FLEXIBLE AND ACTIVE DISTRIBUTION NETWORKS

EDITED BY: Peng Li, Haoran Ji, Yang Mi, Hao Yu, Yue Zhou and Nian Liu
PUBLISHED IN: Frontiers in Energy Research

frontiers Research Topics

frontiers

ISSN 1664-8714
ISBN 978-2-88971-125-3
DOI 10.3389/978-2-88971-125-3

About Frontiers

Frontiers is more than just an open-access publisher of scholarly articles: it is a pioneering approach to the world of academia, radically improving the way scholarly research is managed. The grand vision of Frontiers is a world where all people have an equal opportunity to seek, share and generate knowledge. Frontiers provides immediate and permanent online open access to all its publications, but this alone is not enough to realize our grand goals.

Frontiers Journal Series

The Frontiers Journal Series is a multi-tier and interdisciplinary set of open-access, online journals, promising a paradigm shift from the current review, selection and dissemination processes in academic publishing. All Frontiers journals are driven by researchers for researchers; therefore, they constitute a service to the scholarly community. At the same time, the Frontiers Journal Series operates on a revolutionary invention, the tiered publishing system, initially addressing specific communities of scholars, and gradually climbing up to broader public understanding, thus serving the interests of the lay society, too.

Dedication to Quality

Each Frontiers article is a landmark of the highest quality, thanks to genuinely collaborative interactions between authors and review editors, who include some of the world's best academicians. Research must be certified by peers before entering a stream of knowledge that may eventually reach the public - and shape society; therefore, Frontiers only applies the most rigorous and unbiased reviews.
Frontiers revolutionizes research publishing by freely delivering the most outstanding research, evaluated with no bias from both the academic and social point of view. By applying the most advanced information technologies, Frontiers is catapulting scholarly publishing into a new generation.

What are Frontiers Research Topics?

Frontiers Research Topics are very popular trademarks of the Frontiers Journals Series: they are collections of at least ten articles, all centered on a particular subject. With their unique mix of varied contributions from Original Research to Review Articles, Frontiers Research Topics unify the most influential researchers, the latest key findings and historical advances in a hot research area! Find out more on how to host your own Frontiers Research Topic or contribute to one as an author by contacting the Frontiers Editorial Office: frontiersin.org/about/contact

FLEXIBLE AND ACTIVE DISTRIBUTION NETWORKS

Topic Editors:
Peng Li, Tianjin University, China
Haoran Ji, Tianjin University, China
Yang Mi, Shanghai University of Electric Power, China
Hao Yu, Tianjin University, China
Yue Zhou, Cardiff University, United Kingdom
Nian Liu, North China Electric Power University, China

Citation: Li, P., Ji, H., Mi, Y., Yu, H., Zhou, Y., Liu, N., eds. (2021). Flexible and Active Distribution Networks. Lausanne: Frontiers Media SA.
doi: 10.3389/978-2-88971-125-3

Table of Contents

frontiers in Energy Research

EDITORIAL
published: 04 June 2021
doi: 10.3389/fenrg.2021.687129

Editorial: Flexible and Active Distribution Networks

Peng Li[1], *Yang Mi*[2], *Nian Liu*[3], *Yue Zhou*[4], *Hao Yu*[1] *and Haoran Ji*[1]*

[1]School of Electrical and Information Engineering, Tianjin University, Tianjin, China, [2]School of Electric Power Engineering, Shanghai University of Electric Power, Shanghai, China, [3]School of Electrical and Electronic Engineering, North China Electric Power University, Beijing, China, [4]School of Engineering, Cardiff University, Cardiff, United Kingdom

Keywords: active distribution network, distributed generator, flexible distribution device, operational flexibility, operation and planning

Editorial on the Research Topic

Flexible and Active Distribution Networks

INTRODUCTION

With the increasing penetration of distributed generators (DG), distribution networks are gradually transforming from passive networks to active distribution networks (ADN) (Ji et al., 2019a). However, the intermittent power generation of DGs has significant uncertainties in spatial and temporal distribution. These uncertainties bring challenges and put forward higher requirements for operational flexibility in ADN (Mi et al., 2019). Simultaneously, accurate and fast power flow control by flexible distribution devices, represented by soft open point (SOP) (Bloemink and Green, 2010), solid transformer, distribution unified power flow controller, can significantly improve the operational flexibility of ADNs. The wide application of power electronic devices provides opportunities for the further improvement on the performances of distribution networks (Lee et al., 2019).

This Research Topic is organized to introduce the recent progresses on the modeling, simulation, operation and planning of ADNs with various flexible distribution equipment (power electronic devices). Finally, fifteen papers have been accepted for this Research Topic, which can be sorted into the following three categories including 1) Efficient modeling, simulation and analysis methods; 2) Operation control and energy management under uncertainties; 3) Flexibility and resilience evaluation and enhancement. The three sections below respectively introduce the major researches and contributions of the papers covered in each category.

Efficient Modeling, Simulation and Analysis Methods

Mathematically, the optimal operation of distribution networks generally belongs to large-scale, non-convex and non-linear optimization problems. The integration of power electronic devices in ADNs also increases the complexities in modeling, simulation and analysis (Li et al., 2017). It is necessary to develop efficient methods for optimal operation and control issues in ADNs.

Fu et al. propose an optimal power flow calculation method for the three-phase four-wire low-voltage distribution system. Through improving the node admittance matrix, the complexity of problem solving is effectively reduced.

Li et al., 2017 establish an analysis model to evaluate the wind power consumption capacity. The influence of adjustable parameters on the consumption capacity is quantitatively analyzed.

OPEN ACCESS

Edited and reviewed by:
Rakibuzzaman Shah,
Federation University Australia,
Australia

***Correspondence:**
Haoran Ji
jihaoran@tju.edu.cn

Specialty section:
This article was submitted to Smart Grids, a section of the journal Frontiers in Energy Research

Received: *29 March 2021*
Accepted: *24 May 2021*
Published: *04 June 2021*

Citation:
Li P, Mi Y, Liu N, Zhou Y, Yu H and Ji H (2021) Editorial: Flexible and Active Distribution Networks. Front. Energy Res. 9:687129. doi: 10.3389/fenrg.2021.687129

Li et al., 2017 present a positive sequence voltage fault component polarization impedance criterion. It can adaptively follow the fault resistance variation with less affected by the fault response characteristics of inverter interfaced DGs.

Sun et al. develop a linearized model for modular multilevel converter (MMC) considering diverse failure scenarios. Then, an analytical calculation method is proposed to solve the problem of single-pole grounding short-circuit.

Wang et al. design the DG-load matching degree and the accommodation ratio to analyze DG accommodation in ADN. The simulation model of sequential production is further proposed to calculate the DG-network-load accommodation ratio.

Operation Control and Energy Management Under Uncertainties

The integration of volatile DG and various demand-side resources with uncertainties makes the operation more complex and challenging (Liu et al., 2018). Thus, it is important to investigate the optimal control and energy management methods to deal with the uncertainties (Ma et al., 2019).

Hu et al. develop a two-stage framework for complementary power generation of wind, hydropower and pumped storage systems. The forecast evolution model is established to describe the uncertainties of wind power in different regions.

Luo et al. present a bi-level dispatch model based on virtual power plants (VPPs), which arranges DGs, ESSs and demand response resources as a VPP. VPPs are utilized to alleviate the peak load level of distribution systems.

Song et al. develop a coordinated stochastic scheduling model of integrated electricity and natural gas systems to address the uncertainty of DGs and loads. It helps to accommodate wind power and provide additional flexible ramping capacities.

Qazi et al. utilize cooperative game theory for the optimal operation of isolated microgrid-clusters. To mitigate uncertainties from DGs and loads, the frequency is regulated in real-time and a dynamic droop control process is adopted.

Wang et al. consider load aggregators (LAs) and ADNs as two stakeholders and adopt a distributed method to establish different economic optimization goals.

Flexibility and Resilience Evaluation and Enhancement

Flexibility and resilience enhancement are increasingly important for the operation of ADN (Parvania et al., 2020). Meanwhile, the quantitative evaluation of flexibility and resilience has become a major concern for the system operation (Ji et al., 2019b).

Cai et al. propose a reliability calculation model with ESS integration. The impacts of different prices and incentive policies are analyzed for flexibility and reliability improvement.

Hou et al. present an improved reliability evaluation approach of ADN. The impact increment method and shadow price are adopted to address the high penetration level of renewable energy.

Huo et al. design a multi-station topology to realize the flexible connection of distribution networks. A coordinated control strategy is proposed to ensure the reliable and efficient operation of multi-station system.

Wang et al. develop an operation strategy for SOP-based ESSs with the consideration of battery life. ESSs are regulated to promote DG penetration and reduce the operational cost of ADNs.

Xing et al. propose an optimal dispatch model to facilitate DG integration. Multiple devices are coordinated and the benefits for dispatchable resources are considered in a multi-objective framework.

CONCLUSION

The papers in this Research Topic cover various technical solutions for flexible operation problems of distribution networks, such as the efficient analytical methods with high penetration of DG, flexible operation methods under uncertainties, and system planning with flexible distribution devices. The research will facilitate the enhanced flexibility, efficiency, and reliability of distribution networks under complex environments brought by high DG penetration.

AUTHOR CONTRIBUTIONS

All authors listed have made a substantial, direct, and intellectual contribution to the work and approved it for publication.

ACKNOWLEDGMENTS

Authors would like to acknowledge the National Natural Science Foundation of China (U1866207, 61873159, 52007131, 51907139), and National Key Research and Development of China (2018YFB1503001), which have made this Frontiers Research Topic possible.

REFERENCES

Bloemink, J. M., and Green, T. C. (2010). Increasing Distributed Generation Penetration Using Soft Normally-Open Points, July 25-29, 2010, Minneapolis, MN, IEEE Power and Energy Society General Meeting. Providence, RIPiscataway, NJ: IEEE. doi:10.1109/pes.2010.5589629

Ji, H., Wang, C., Li, P., Ding, F., and Wu, J. (2019a). Robust Operation of Soft Open Points in Active Distribution Networks with High Penetration of Photovoltaic Integration. *IEEE Trans. Sustain. Energ.* 10 (1), 280–289. doi:10.1109/TSTE.2018.2833545

Ji, H., Wang, C., Li, P., Song, G., Yu, H., and Wu, J. (2019b). Quantified Analysis Method for Operational Flexibility of Active Distribution Networks with High Penetration of Distributed Generators. *Appl. Energ.* 239, 706–714. doi:10.1016/j.apenergy.2019.02.008

Lee, T., Zhou, Y., Chao, L., Jianzhong, Wu., and Nick, J. (2019). A General Form of Smart Contract for Decentralized Energy Systems Management. *Nat. Energ.*, 4 (2), 140–149. doi:10.1038/s41560-018-0317-7

Li, P., Ji, H., Wang, C., Zhao, J., Song, G., Ding, F., et al. (2017). Coordinated Control Method of Voltage and Reactive Power for Active Distribution Networks Based on Soft Open point. *IEEE Trans. Sustain. Energ.* 8 (4), 1430–1442. doi:10.1109/TSTE.2017.2686009

Liu, N., Cheng, M., Yu, X., Zhong, J., and Lei, J. (2018). Energy-Sharing Provider for PV Prosumer Clusters: A Hybrid Approach Using Stochastic Programming and Stackelberg Game. *IEEE Trans. Ind. Electron.* 65 (8), 6740–6750. doi:10.1109/TIE.2018.2793181

Ma, L., Liu, N., Zhang, J., and Wang, L. (2019). Real-time Rolling Horizon Energy Management for the Energy-Hub-Coordinated Prosumer Community from a Cooperative Perspective. *IEEE Trans. Power Syst.* 34 (2), 1227–1242. doi:10.1109/TPWRS.2018.2877236

Mi, Y., Chen, X., Ji, H., Ji, L., Fu, Y., Wang, C., et al. (2019). The Coordinated Control Strategy for Isolated DC Microgrid Based on Adaptive Storage Adjustment without Communication. *Appl. Energ.* 252, 113465. doi:10.1016/j.apenergy.2019.113465

Parvania, M., Bindner, H. W., and Qadrdan, M. (2020). Guest Editorial: Maximising Flexibility through Energy Systems Integration. *IET Energ. Syst. Integration* 2 (2), 67–68. doi:10.1049/iet-esi.2020.0054

Conflict of Interest: The authors declare that the research was conducted in the absence of any commercial or financial relationships that could be construed as a potential conflict of interest.

frontiers in Energy Research

ORIGINAL RESEARCH
published: 05 November 2020
doi: 10.3389/fenrg.2020.596774

Two-Stage Stochastic Scheduling of Integrated Electricity and Natural Gas Systems Considering Ramping Costs With Power-to-Gas Storage and Wind Power

Xiaozhe Song[1], Chuqiao Lin[2], Rufeng Zhang[2], Tao Jiang[2] and Houhe Chen[2]*

[1]State Grid Jilin Electric Power Company Limited, Changchun, China, [2]Department of Electrical Engineering, Northeast Electric Power University, Jilin, China

Power-to-gas (P2G) facilities and natural gas fired power units provide flexibility to integrated electricity and natural gas systems (IENGS) for wind power accommodation and ramp deployment. This paper proposes a stochastic coordinated scheduling model for IENGS considering ramping costs with P2G storage and wind power. The operation model of natural gas system with P2G is presented, and the benefits of P2G integration are analyzed. To address the uncertainties of wind power and energy loads, multiple representative scenarios are generated. The flexible ramping requirements and costs are incorporated and analyzed, and flexible ramp can be provided by P2G in this work. The coordinated scheduling model for IENGS is formulated as a two-stage stochastic programming problem, in which day-ahead scheduling for electricity systems is modeled in the first stage model and scheduling of natural gas systems is carried out in the second stage model. Numerical case studies on a modified PJM 5-bus electricity system with a 7-node natural gas system and the IEEE 118-bus system with a 20-node Belgian natural gas system verify that P2G can help accommodate wind power, provide additional flexible ramping capacities, and reduce the gas supply from gas suppliers and gas load shedding.

Keywords: power-to-gas, ramping cost, wind power accommodation, stochastic programming, natural gas system

OPEN ACCESS

Edited by:
Peng Li,
Tianjin University, China

Reviewed by:
Jian Chen,
Shandong University, China
Xiandong Xu,
Cardiff University, United Kingdom

****Correspondence:***
Tao Jiang
tjiang@neepu.edu.cn

Specialty section:
This article was submitted to Smart Grids, a section of the journal Frontiers in Energy Research

Received: *20 August 2020*
Accepted: *02 October 2020*
Published: *05 November 2020*

Citation:
Song X, Lin C, Zhang R, Jiang T and Chen H (2020) Two-Stage Stochastic Scheduling of Integrated Electricity and Natural Gas Systems Considering Ramping Costs With Power-to-Gas Storage and Wind Power. Front. Energy Res. 8:596774. doi: 10.3389/fenrg.2020.596774

INTRODUCTION

In the last decade, the use of natural gas for power generation has increased significantly throughout the world (Zhang et al., 2020). The growth of natural gas-fired generation increases the interaction between electricity systems and natural gas systems (Li et al., 2008; Chaudry et al., 2014), and, together with renewable generation, makes the operation of electricity systems more environmentally friendly (Zhang et al., 2016).

In integrated electricity and natural gas systems (IENGS), the integration of large-scale intermittent and uncertain renewable energy brings major challenges to the operation of the electricity system. Curtailment of renewable energy frequently occurs due to the lack of system flexibility. As the variability increases, fast-ramp thermal units can provide flexible ramp deployment to maintain power balance (Wang et al., 2008). The fast ramping capacities of gas-fired generation units can provide operational flexibility (Baldick, 2014).

In (Zhang et al., 2016) and (Alabdulwahab et al., 2015), stochastic day-ahead scheduling and security-constrained unit commitment models are proposed, respectively, and the flexibility and quick ramping capability of gas-fired generation units demonstrate the possibility of firming the variability of wind power when it is constrained by the natural gas network.

Power-to-gas (P2G) technology can achieve the conversion of electric energy to hydrogen or synthetic natural gas (SNG). Gas-fired generation units and P2G facilities realize bidirectional coupling of IENGS (Clegg and Mancarella, 2016; He et al., 2017). P2G technology is treated as a promising approach to realize high penetration of renewables and low carbon emission in (Li et al., 2017a; Yang et al., 2019). The electricity consumption of P2G can reshape the load profile, reducing wind power curtailment in valley periods and the load difference between peak and valley periods. The SNG produced as a result can then be stored or utilized in the gas network. Some existing publications have studied the operation strategy for P2G. Day-ahead scheduling of P2G storage is studied in (Khani and Farag, 2018), in which P2G storage is optimally scheduled in both electricity and gas markets. In (Clegg and Mancarella, 2015), a methodology to investigate various P2G processes is proposed and their impacts on electricity and gas networks are analyzed. In (Alkano and Scherpen, 2018), the coordination of supply from P2G facilities is studied based on a model predictive control approach. The above works verify that P2G with storage can reduce renewable energy curtailment and that P2G can play a role in the operation of natural gas systems. P2G can also help ramp by regulating the amount of consumed electricity energy. However, the benefit of P2G on flexible ramp deployment has not been considered in the existing works.

Variability and uncertainty of large-scale wind power can be handled by ramping capacities of thermal units, including gas-fired generation units. The fast ramping capability of gas-fired units makes them an important resource for providing flexibility and addressing uncertainties in a power system. Thus, the natural gas network needs to be optimally scheduled to ensure an available fuel supply for the gas-fired units to address any realization of uncertain scenarios. Moreover, the ramping costs should be included. The existing works on coordinated optimal operation of IENGS mainly focus on integrated planning (Zhang et al., 2015; Zhang et al., 2016), day-ahead scheduling (Liu et al., 2010; Alabdulwahab et al., 2015; Bai et al., 2016; He et al., 2017), unit commitment (Wang et al., 2008), and reserve scheduling (Liu et al., 2019). However, the optimal scheduling of natural gas system is barely considered.

To bridge these gaps, a coordinated stochastic scheduling model of IENGS with P2G and wind power is proposed in this paper. The primary goal of this work is to carry out coordinated stochastic optimal scheduling of IENGS utilizing P2G storage to promote wind power integration and reduce ramping costs for electricity systems. The major contributions are summarized as below.

(1) Compared to the work in (Li et al., 2017b), the coordinated scheduling model is formulated as a two-stage stochastic programming problem. Uncertainties of wind power, electricity loads, and natural gas loads are considered. Day-ahead stochastic scheduling of electricity systems is carried out in the first stage to determine the gas loads of gas-fired generation units and produced SNG of P2G for all scenarios, which are utilized in the second stage optimization model. Stochastic scheduling of natural gas systems is modeled in the second stage model to check the feasibility of natural gas transmission for all scenarios and optimally schedule the gas supply and P2G storage. The two stage models are formulated as a linear programming (LP) problem and a mixed-integer linear programming (MILP) problem, respectively.
(2) The benefits of the integration of P2G storage for IEGNS are analyzed in this paper. For electricity systems, a P2G facility can regulate its power consumption to change the electricity load profile to reduce wind power curtailments and ramping costs. For natural gas systems, the produced SNG in P2G storage can participate in the operation of natural gas systems to reduce the gas consumption from natural gas suppliers and help reduce gas load shedding, especially for loads of gas-fired generation units under uncertain scenarios.
(3) Flexible ramping requirements and costs are analyzed and presented. Ramping costs are considered, and flexible ramps can be provided by P2G storage. Natural gas network constraints with P2G storage are considered, and an evaluation of the optimal scheduling of gas suppliers and storage is conducted.

The rest of this paper is organized as follows. In *Natural Gas Networks Model With Power-to-Gas Storage*, a model of a natural gas network with P2G is presented. *Uncertainties of Wind Power Sources and Energy Loads and Flexible Ramp* presents the uncertainties of wind power, energy loads, and flexible ramps. In *Stochastic Coordinated Scheduling Model*, the stochastic day-ahead scheduling model is formulated, and the solution approach is proposed. In *Case Studies*, case studies are conducted to demonstrate the effectiveness of the model. Concluding remarks are presented in *Conclusion*.

NATURAL GAS NETWORKS MODEL WITH POWER-TO-GAS STORAGE

Natural Gas Network

In natural gas systems, the network consists of gas wells (gas suppliers), pipelines, storage, and compressors. The majority of natural gas is produced from gas wells. The gas supply S_j from gas wells is limited by upper and lower boundaries $S_{j,\max}$ and $S_{j,\min}$, as shown in **Eq. 1**:

$$S_{j,\min} \le S_j \le S_{j,\max} \tag{1}$$

The pipeline flow F_{mj} relates to pressures of node m and j in **Eq. 2** and the nodal pressure is constrained in **Eq. 3**:

$$\begin{aligned} F_{mj} &= \mathrm{sgn}\left(\pi_m, \pi_j\right) \cdot C_{mj}\sqrt{\left|\pi_m^2 - \pi_j^2\right|} \\ \mathrm{sgn}\left(\pi_m, \pi_j\right) &= \begin{cases} 1 & \pi_m \ge \pi_j \\ -1 & \pi_m < \pi_j \end{cases} \end{aligned} \tag{2}$$

$$\pi_m^{\min} \le \pi_m \le \pi_m^{\max} \tag{3}$$

where sgn () represents sign function, which shows gas flows from a high pressure node to a low pressure node.

The compressor can be driven by power from the electricity power grid (Li et al., 2017b). The power consumption is:

$$H_{com} = BF_{ij}\left[\left(\frac{\pi_i}{\pi_j}\right)^Z - 1\right] \quad (4)$$

$$P_{com} = H_{com}\left(0.7479 \times 10^{-5}\right) \quad (5)$$

Power-to-Gas Process

P2G facilities are suppliers in natural gas systems and loads in electricity systems. SNG produced by P2G facilities can be stored for use in later scheduling periods. Faster ramping rates of P2G facilities with the technology of a proton exchange membrane (PEM) can better follow power fluctuations (Grond et al., 2013; Clegg and Mancarella, 2015). In this paper, the motivation behind studying P2G and the benefits of considering P2G can be summarized as follows:

(1) From the perspective of wind power accommodation, P2G can reduce wind power curtailment by increasing electricity load. In valley electricity load periods, thermal power units cover a large portion of the power load due to lower output limits and spinning reserve constraints, resulting in a heavy curtailment of wind power. P2G can utilize the surplus wind power to generate SNG.
(2) The power consumption regulating ability of P2G can provide additional flexible ramping capacities to account for power fluctuations and uncertainties. During periods in which thermal units should ramp down dramatically to follow power load and wind power fluctuation and uncertainty, P2G can increase load values and hence reduce ramping requirements.
(3) The SNG generated by P2G can be utilized in a natural gas system to reduce gas consumption from natural gas suppliers and may help to reduce gas load shedding when the P2G storage is integrated at certain nodes. The operation constraints of P2G are stated as **Eqs 6–8**

$$E_{P2G,t,\text{gas}} = \eta_{P2G} D_{P2G,t} \quad (6)$$

$$S_{P2G,t,\text{gas}} = \frac{E_{P2G,t,\text{gas}}}{\text{HHV}_{\text{gas}}} \quad (7)$$

$$0 \le S_{P2G,t,\text{gas}} \le S^{\max}_{P2G,\text{gas}} \quad (8)$$

The energy conversion process of P2G can be described by **Eq. 6**, and volumetric quantity is calculated by **Eq. 7**. The hourly produced SNG should be positive and limited by the upper bounds in **Eq. 8**.

UNCERTAINTIES OF WIND POWER SOURCES AND ENERGY LOADS AND FLEXIBLE RAMP

In this section, uncertainties of wind power, electricity loads, and natural gas loads are represented by a set of scenarios. The flexible ramping requirements and costs are also analyzed.

Wind Power and Energy Loads Uncertainty and Sampling Method

Uncertainties of wind power, electricity loads, and natural gas loads with inevitable forecasting errors are modeled based on probability distribution functions. Normal distribution function has been utilized to obtain hourly wind power and energy load forecasting errors.

To simulate the uncertainties of wind power and electricity and natural gas loads, the Monte Carlo method is utilized to generate proper number of uncertain scenarios. Large numbers of scenarios would increase the computation burden, and scenario reduction techniques should be utilized. The scenario reduction algorithms would determine a scenario subset and assign new probabilities to the preserved scenarios. In this paper, the SCENRED tool in the General Algebraic Modeling System (GAMS) is executed for scenario reduction process, which contains several reduction algorithms. In this paper, fast backward reduction method is employed. The probabilities for all generated scenarios before reduction are assumed to be the same, with a cumulative sum equal to one ($\Sigma Ps = 1$). After reduction, smaller number of scenarios would be obtained with corresponding probabilities.

Flexible Ramping Requirements and Costs

Controllable thermal power units in traditional power systems are adjusted to follow load fluctuations. However, the integration of renewable energy sources (RES) increases variability in power system operation. The net load, which equals to total load minus total available RES generation, is more volatile and requires more ramping capability from thermal units between operating periods in case of power imbalance. Moreover, the forecasting errors of loads and RES should also be balanced by upward and downward flexible ramping of thermal units. Hence, the flexible ramping requirements of thermal units include the following two parts:

- Flexible ramping requirements must follow hourly net load fluctuation. Thermal generation units ramp up/down to follow net load fluctuation between scheduling periods. The more volatile the net load is, the more ramping requirements are expected. The ramping capacity of a thermal generation unit is constrained by its ramping rate and minimum/maximum output limits. In the day-ahead electricity market, the flexible ramping offer is included in a generator's offer and cleared at the bidding prices of up/down ramping together with the energy offer (Wu et al., 2015). The costs for flexible ramping between adjacent scheduling periods are calculated as:

$$\begin{aligned} \text{CRU}^0_{i,t} &= \text{cru}_i \cdot \left(P^0_{i,t} - P^0_{i,t-1}\right) \\ \text{CRD}^0_{i,t} &= \text{crd}_i \cdot \left(P^0_{i,t} - P^0_{i,t+1}\right) \end{aligned} \quad (9)$$

- Flexible ramping requirements must guarantee secure operation under uncertainties of load and RES, as represented in the uncertain scenarios. In each scenario, a ramping cost similar to that of the base case is considered. Moreover, flexible ramping can ensure a transition from the scheduled operation status of the base case to all possible scenarios. The feasible corrective dispatch of thermal units from the base case to all possible scenarios ensures the power balance, but the ramp offer should be optimally determined and allocated. The corrective ramping costs are calculated as:

$$\begin{aligned} \mathrm{CRU}_{i,t}^{s} &= \mathrm{cru}_i \cdot \left(P_{i,t}^{s} - P_{i,t}^{0}\right) + \mathrm{cru}_i \cdot \left(P_{i,t}^{s} - P_{i,t-1}^{s}\right) \\ \mathrm{CRD}_{i,t}^{s} &= \mathrm{crd}_i \cdot \left(P_{i,t}^{0} - P_{i,t}^{s}\right) + \mathrm{crd}_i \cdot \left(P_{i,t}^{s} - P_{i,t+1}^{s}\right) \end{aligned} \tag{10}$$

The bidding prices of flexible ramping are assumed to be the same as up and down ramping costs in the base case.

The total ramping costs are shown as:

$$\begin{aligned} \mathrm{CRU}_{i,t} &= \mathrm{CRU}_{i,t}^{0} + \sum_{s}^{N_s} \mathrm{CRU}_{i,t}^{s} \\ \mathrm{CRD}_{i,t} &= \mathrm{CRD}_{i,t}^{0} + \sum_{s}^{N_s} \mathrm{CRD}_{i,t}^{s} \end{aligned} \tag{11}$$

Remark 1: Natural gas-fired units can provide operational flexibility through their fast-ramp capacities. However, the power output of gas-fired units relates to natural gas consumption, which is constrained by the limits of the natural gas network. So the flexible ramp provided by natural gas-fired units is also constrained, especially in peak natural gas load periods. In these periods, heavy nodal loads lead to violations of the natural gas network, such as the nodal pressure of an end node of long pipeline falling below its lower limit.

STOCHASTIC COORDINATED SCHEDULING MODEL

In this section, the proposed two stage stochastic scheduling model is formulated.

First Stage Model

The objective function of the first stage stochastic scheduling model for electricity system is to minimize the expected operation cost of the electricity system, including electricity bidding costs, wind power curtailment costs, ramping costs and P2G operation costs, as shown in **Eq. 12**.

Objective Function

$$\min \sum_{t}^{T} \left\{ \begin{array}{l} \sum_{i=1}^{N}\left(c_i P_{i,t}^{0}\right) + \sum_{w}^{N_w} c_w P_{\mathrm{wind},t}^{0} \\ +c_{wc}\left(P_{\mathrm{wind},t}^{\mathrm{forecast},0} - P_{\mathrm{wind},t}^{0}\right) \\ +\sum_{i=1}^{N}\left(\mathrm{CRU}_{i,t}^{0}\right) + \sum_{i=1}^{N}\left(\mathrm{CRD}_{i,t}^{0}\right) \\ +c_{P2G} D_{P2G,t}^{0} \end{array} \right\} +$$

$$\sum_{s}^{N_s} Ps \times \left\{ \sum_{t}^{T} \left\{ \begin{array}{l} \sum_{i=1}^{N}\left(c_i P_{i,t}^{s}\right) + \sum_{w}^{N_w} c_w P_{\mathrm{wind},t}^{s} \\ +c_{wc}\left(P_{\mathrm{wind},t}^{\mathrm{forecast},s} - P_{\mathrm{wind},t}^{s}\right) \\ +\sum_{i=1}^{N}\left(\mathrm{CRU}_{i,t}^{s}\right) + \sum_{i=1}^{N}\left(\mathrm{CRD}_{i,t}^{s}\right) \\ +c_{P2G} D_{P2G,t}^{s} \end{array} \right\} \right\}$$

Constraints

$$\sum_{i}^{N} P_{i,t}^{s} + P_{\mathrm{wind},t}^{s} = D_{t}^{e,s} + D_{P2G,t}^{s} \tag{13}$$

$$P_{i\min} \le P_{i,t}^{s} \le P_{i\max} \tag{14}$$

$$0 \le P_{\mathrm{wind},t}^{s} \le P_{\mathrm{wind},t}^{\mathrm{forecast},s} \tag{15}$$

$$P_{i,t,gas} = \eta_{G2P} GL_{m,t,\mathrm{gas}} \tag{16}$$

$$GL_{m,t,\mathrm{gas}} \le GL_{m,\max} \tag{17}$$

$$\left\{ \begin{array}{l} P_{\mathrm{i},t}^{s} - P_{\mathrm{i},t-1}^{s} \le \mathrm{Ramp}_i^{u} \\ P_{\mathrm{i},t}^{s} - P_{\mathrm{i},t-1}^{s} \le \mathrm{Ramp}_i^{d} \end{array} \right. \tag{18}$$

$$\left\{ \begin{array}{l} P_{i,t}^{s} - P_{i,t}^{0} \le \mathrm{Ramp}_i^{u} \\ P_{i,t}^{0} - P_{i,t}^{s} \le \mathrm{Ramp}_i^{d} \end{array} \right. \tag{19}$$

$$\sum_{i=1}^{N}\left(P_{i\max} - P_{i,t}^{s}\right) \ge R_d \tag{20}$$

$$\sum_{i=1}^{N}\left(P_{i,t}^{s} - P_{i\min}\right) \ge R_d \tag{21}$$

$$-\mathrm{Limit}_l \le \sum_{i=1}^{N} \mathrm{GSF}_{l-i} \times \left(P_{i,t}^{s} + P_{\mathrm{wind},t}^{s} - D_{i,t}^{e,s} - D_{P2G,t}^{s}\right) \le \mathrm{Limit}_l \tag{22}$$

P2G constraints: **Eqs 6–8**

For each scenario *s*, the electricity balance constraint is shown in **Eq. 13**, power generation constraints of thermal units and wind power are shown in **Eqs 14 and 15**. Ramping and spinning reserve constraints are presented in **Eqs 18–21**. Constraint **Eq. 19** ensures the transition of operation status from the base case to all scenarios. Transmission constraints based on a DC power flow model are shown in **Eq. 22**.

Second Stage Model

In the second stage, the stochastic scheduling for natural gas systems is carried out based on the scheduling results of the first stage model. The hourly gas loads (including those of gas fired power units) are optimally allocated among different gas suppliers according to various bidding prices. Moreover, P2G storage can participate in the optimal operation of natural gas systems. The storage can charge gas flow from the P2G process and gas network and discharge it as gas supply.

Objective Function

The objective function of the stochastic scheduling model of natural gas systems is to minimize the expected purchasing costs. The objective function is formulated as:

$$\min \sum_{s=1}^{N_s} Ps \times \sum_{t}^{T} \sum_{j}^{N_j} \left(C_{j,\mathrm{gas}} S_{j,t} + C_{ls} Ls_t\right) \tag{23}$$

Constraints

Constraints **Eqs 1–5** in each scenario *s*:

Natural gas balance:

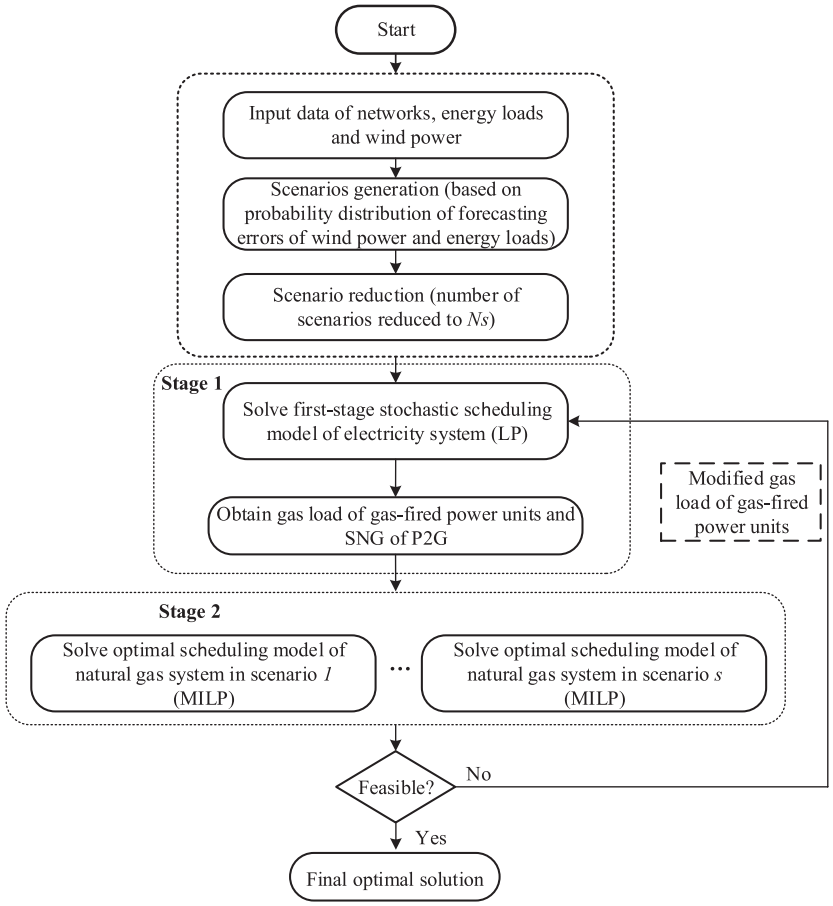

FIGURE 1 | Flowchart of the proposed stochastic scheduling model.

$$\sum_{m}^{Ng} S_m^s = \sum_{m}^{Ng} GL_m^s + GS_t^s \tag{24}$$

Constraints of gas storage integrated with P2G:

$$ST_{P2G,t}^s = ST_{P2G,t-1}^s + S_{P2G,t,\text{gas}}^s - S_{P2G,t}^s \tag{25}$$

$$ST_{\min} + ST_{P2G}^{\text{Res}} \le ST_{P2G,t}^s \le ST_{\max} - ST_{P2G}^{\text{Res}} \tag{26}$$

$$-S_{c,\max}\Delta t \le S_{P2G,t}^s \le S_{d,\max}\Delta t \tag{27}$$

$$\begin{aligned} ST_{P2G,t}^s &= ST_{\text{ini}} \quad t = 1 \\ ST_{P2G,t}^s &\ge ST_{\text{ini}} \quad t = 24 \end{aligned} \tag{28}$$

Eq. 25 gives the calculation of state of charge (SOC) of P2G storage. $S_{P2G,t}^s$ is the exchanged gas flow of P2G storage to the natural gas network. The positive values correspond to discharging flow and the negative values correspond to charging flow. **26 and 27** state the upper and lower limits of the SOC and charging and discharging flow, respectively. $ST_{P2G,t}^{\text{Res}}$ is added to set the lower and upper bounds of the SOC at a value that leaves reserves. **Eq. 28** gives the initial SOC of P2G storage. The SOC of $t = 24$ should meet or exceed the initial SOC if it is to be used in the next scheduling horizon.

To handle the nonlinear constraints of natural gas pipeline flow, the linearization method of our previous work (Li et al., 2017b) is introduced in this paper, and the second stage scheduling model can be formulated as a MILP problem.

Solution Approach

The flow chart of the solution approach for the proposed stochastic scheduling model is shown in **Figure 1**. Major steps of this method are summarized as follows.

Step 1: Input data of networks, wind power and energy loads in IENGS. The initial stochastic scenarios are generated by Monte Carlo. In this paper, the SCENRED tool in the GAMS is applied to perform scenario reduction to reduce computation burden (GAMS/SCENRED Documentation, 2002), and the fast backward reduction method is employed.

Step 2: Solve the first stage stochastic scheduling model of the electricity system considering P2G and ramping costs, which is formulated as a LP problem and solved to obtain gas demand of gas-fired power units and SNG produced by P2G.

Step 3: Solve the second stage stochastic optimal scheduling model of natural gas systems, which is formulated as a MILP problem and the variable of virtual load shedding of natural gas is introduced to ensure that the second stage scheduling problem is feasible.

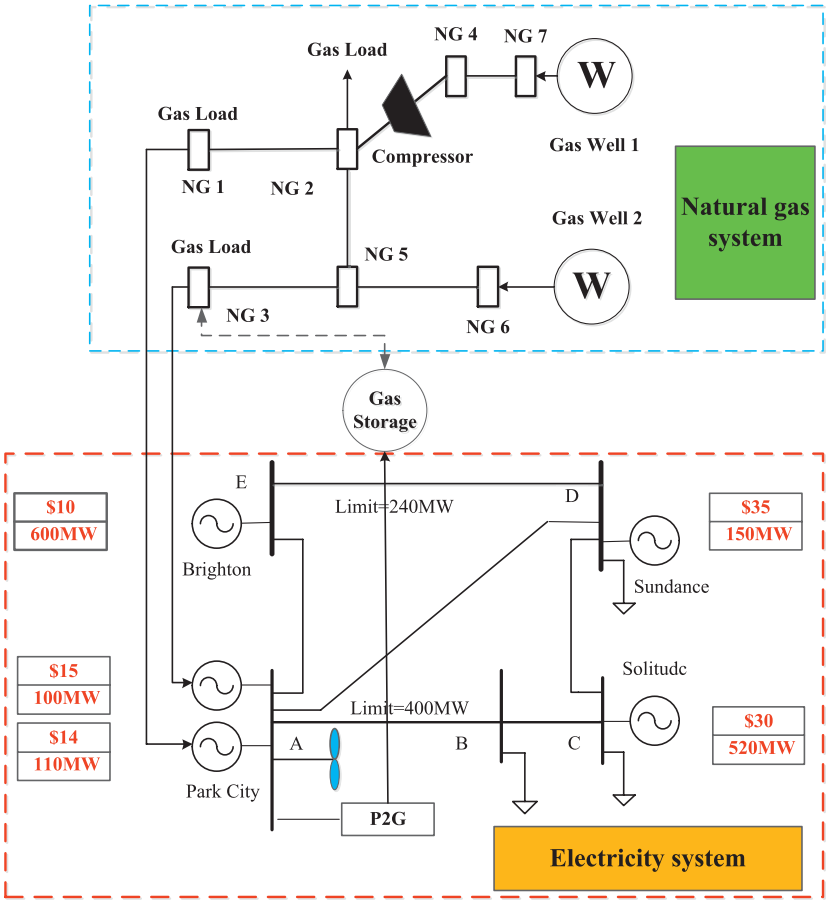

FIGURE 2 | Structure of integrated PJM 5-bus power system and 7-node natural gas system.

Step 4: Given the results, if the load shedding results of gas-fired units are not equal to 0, the gas demand of gas-fired units would be modified based on the load shedding results and added into the first stage model with fixed values.

Step 5: The first stage model would be resolved until the load shedding results of gas-fired units in the second stage model equal to 0, and the results would be output and analyzed.

Remark 2: It's noted that the modified gas demand of gas-fired units would lead to different scheduling results of P2G. To ensure the operation feasibility of P2G storage in a natural gas network, the created reserve margin $ST^{\mathrm{Res}}_{P2G,t}$ is utilized to balance the gas flow mismatches.

The scheduling model is implemented in GAMS, and the LP and MILP optimization models are solved utilizing CPLEX.

CASE STUDIES

In this section, the proposed day-ahead stochastic scheduling model is performed on a PJM 5-bus power system integrated with a 7-node natural gas system and on the IEEE 118-bus power system with the Belgian natural gas system.

PJM 5-Bus System

Figure 2 provides a diagram of the utilized IENGS network including a PJM 5-bus power system integrated with a seven-node natural gas system, in which the generation capacities and bidding prices are also shown. The ramping bids factor is 20%, which means ramping bids are 20% of bidding prices of thermal units. A wind farm with a capacity of 400 MW is installed at Bus A, and the bidding cost is set to $8 per MW. The P2G operation cost coefficient is $2 per MW and the wind power curtailment cost coefficient is $60 per MW. Unit one and two at Bus A are assumed to be gas-fired power units, which are integrated at NG one and three in the natural gas network. The residential and industrial natural gas load is distributed to three load buses. The detailed parameters of the natural gas system can be found in (Liu et al., 2009). The initial state of P2G storage is 2300 kcf. The up and down spinning reserve requirements are 0.1 of hourly forecasting electricity load. The forecasted output of wind power and energy loads (including residential natural gas loads and electricity loads)

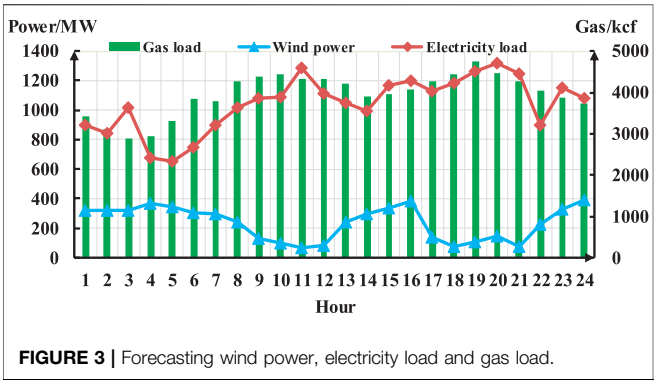

FIGURE 3 | Forecasting wind power, electricity load and gas load.

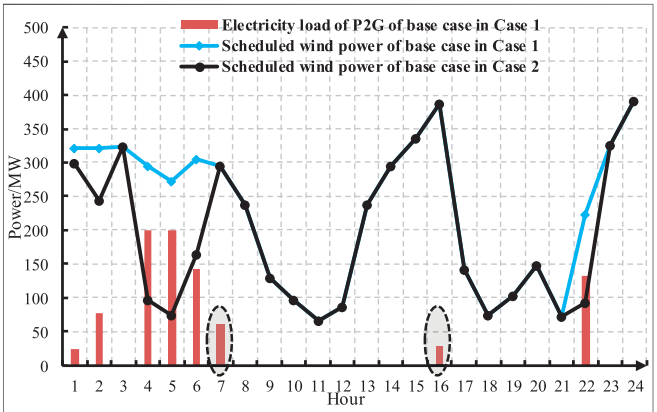

FIGURE 4 | Comparison of scheduled wind power and electricity load of P2G in Case 1 and 2 in base case.

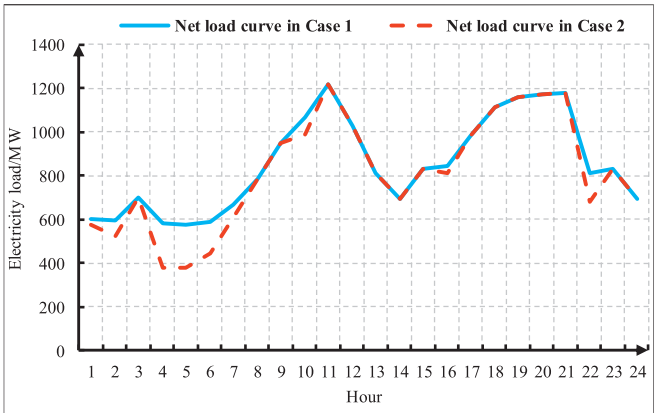

FIGURE 5 | Net load curves in Case 1 and 2.

TABLE 1 | Comparison of scheduling results of electricity systems in Case 1 and 2.

Case	Expected total cost (10^5)	Expected ramping cost (10^4)	Wind power utilization rate in base case
Case 1	8.24	2.54	97.4%
Case 2	9.06	2.65	83.6%

are shown in **Figure 3**. The wind power and energy loads forecasting errors are simulated by 1,000 scenarios generated by Monte Carlo simulation. The number of scenarios is reduced to seven in GAMS.

To verify the impact of P2G on the scheduling results of IENGS, the following two cases are conducted:

Case 1: Stochastic scheduling with P2G and storage.
Case 2: Stochastic scheduling without P2G but with storage. The gas storage is integrated in the natural gas system.

The scheduling results of the two cases are compared to illustrate the impact of P2G on the electricity system and the natural gas system, respectively.

Impact of Power-to-Gas on Electricity System

The impact of P2G on electricity systems primarily assists in wind power accommodation and provides additional flexible ramping capacities to account for power fluctuations and uncertainties by increasing electricity load in certain periods. The results of scheduled wind power and the electricity consumed by P2G in Case 1 and 2 in the base case are compared in **Figure 4**. As depicted in **Figure 4**, more wind power is scheduled in Case 1 in periods 1, 2, 4–6 and 22 compared to Case 2. It can be seen that in those periods, which are off-peak hours, the P2G facility consumes power to increase electricity load and more wind power can be utilized in Case 1, while wind power would be curtailed in Case 2. The results verify that P2G can reduce wind power curtailments and aid wind power accommodation.

It should be noted that in periods 7 and 16 in **Figure 4**, the utilized wind power is the same in Case 1 and 2, but P2G facility consumes a certain amount of electricity. The reason is that the flexible ramping cost is considered in the proposed scheduling model, and in these periods P2G can provide additional flexible ramping capacities to reduce ramping costs. Moreover, electricity load by P2G can flatten the net load profile by reducing the difference between peak and valley net loads, which also reduces the ramping requirements across the scheduling horizon. A comparison of net load profiles in Case 1 and 2 is shown in **Figure 5**. Hourly net load in Case 1 equals to fixed electricity load plus the electricity load of P2G and minus wind power forecasting value, while Case 2 does not include a P2G electricity load. The net load curve in Case 1 fluctuates between a smaller range than the Case 2 curve. The difference between peak and valley loads is reduced from 842.86 to 642.86 MW. The above results show that a P2G facility can provide additional flexible ramping capacities and flatten the net load profile.

TABLE 2 | Comparison of scheduling results of natural gas systems in different cases.

Case	Expected production cost ($\$10^5$)	Expected total supply (10^5 kcf)	Total gas load shedding (kcf)
Case 1	3.719	1.45	12.1
Case 2	3.821	1.49	17.7
Case 3	3.820	1.49	61.4

To further demonstrate the impact of P2G on the scheduling of electricity systems, a comparison of the scheduling results of Case 1 and 2 is shown in **Table 1**. Comparing Case 1 and 2, the expected total cost in Case 1 is reduced to \$8.24 * 10^5 from \$9.06 * 10^5 of Case 2. The expected ramping cost in Case 1 is lower than that of Case 2, which demonstrates that P2G can help reduce the ramping cost. The wind power utilization rate in Case 1 is increased 13.8% compared to Case 2.

The above results illustrate that integration of P2G facility can reduce wind power curtailment and provide additional flexible ramping capacities to reduce ramping costs for electricity systems.

Impact of Power-to-Gas Storage on Natural Gas Systems

A P2G facility generates SNG utilizing electricity energy, and the obtained SNG can be stored in P2G storage. The storage can be scheduled as either load or supply. To verify the impact of P2G storage on natural gas systems, the following case (Case 3) is conducted:

Case 3: Stochastic scheduling without P2G and storage.

The comparison of scheduling results of natural gas systems for Case 1–3 is listed in **Table 2**. It shows that the expected production cost in Case 1 will be decreased by almost \$1,000, and the expected total supply from gas wells will be decreased 400 kcf if P2G is considered. SNG from P2G decreases the supply from gas wells. Note that the expected costs and supplies in Case 2 and 3 are almost the same because no other gas supply (P2G) is integrated, but more gas load shedding occurs in Case 3. Case 1 features the least gas load shedding, while Case 3 features the most because gas storage can regulate the gas load by charging and supply nodal loads by discharging during the scheduling horizon. SNG from P2G in storage can supply nodal gas loads, replacing gas from gas wells. The results in **Table 2** suggest that the integration of P2G can reduce production cost and gas supply of natural gas system, and gas storage can help reduce load shedding, which is more effective with P2G. Natural gas storage can improve security by supplying additional gas reserves to gas-fired power units. It should be noted that the impact of gas storage on gas load shedding and operation cost relates to the location node of the storage, which can be included in the co-planning of an electricity system and natural gas system.

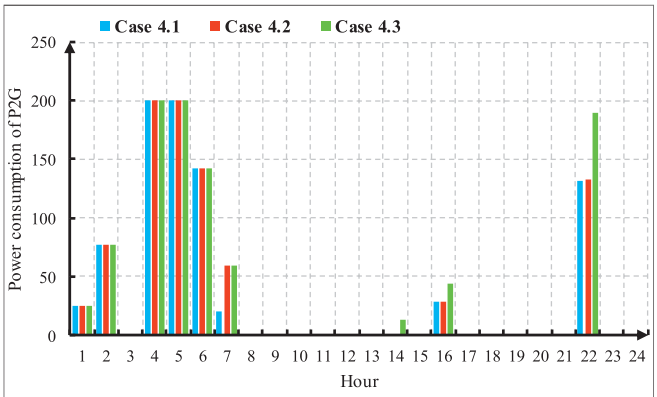

FIGURE 6 | Power consumption of P2G in different cases.

Impact of Ramping Cost Coefficient

In this subsection, we compare the following three cases with various ramping bid factors to illustrate the impact of the ramping cost coefficient on the scheduling of P2G.

Case 4.1: Ramping bid factor is 0;
Case 4.2: Ramping bid factor is 20%;
Case 4.3: Ramping bid factor is 50%;

Hourly power consumption results of P2G in Cases 4.1–4.3 are shown in **Figure 6**. In Case 4.1, the flexible ramping cost is not considered. Total power consumptions of P2G in Cases 4.1–4.3 are 7,148.11, 7644.69, 8,533.056 MW, respectively. The power consumption of P2G increases as we increase the ramping bid factor, especially in hours 14, 16 and 22 as shown in **Figure 6**. When the ramping cost coefficient increases, the P2G facility is operated to provide additional flexible ramping capacities and flatten the net load profile to reduce total costs. The results once again demonstrate the benefits of P2G on an electricity system for providing additional flexible ramping capacities and flattening the net load profile.

IEEE 118-Bus System

The IEEE 118-bus system integrated with the 20-node Belgian natural gas system, shown in **Figure 7**, is applied here to further demonstrate the applicability of the proposed model on large systems. The generator bidding data are similar to those in (Fang et al., 2015). The detailed data of Belgian natural gas system can be found in (Wolf and Smeers, 2000). Wind farms and P2G devices with the same

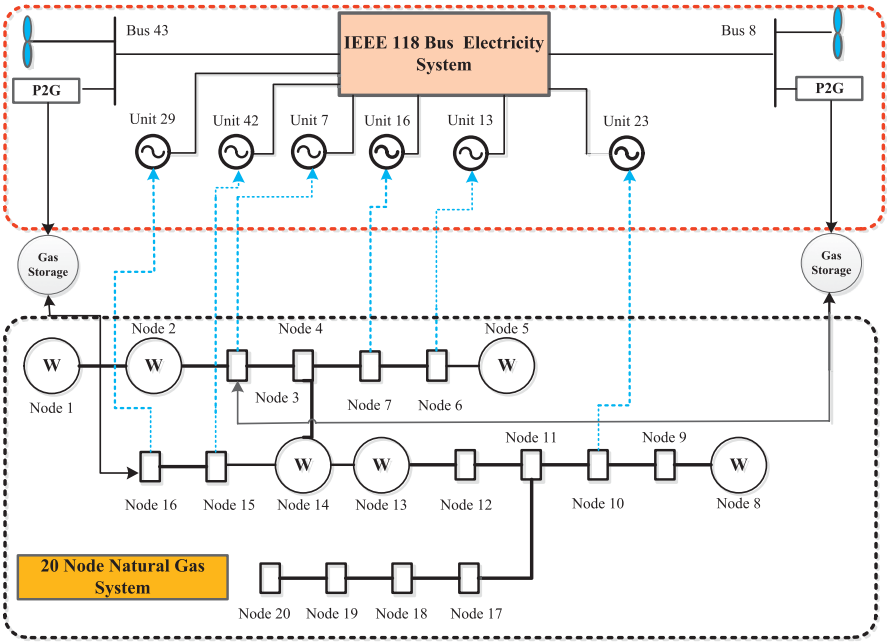

FIGURE 7 | Structure of integrated IEEE 118-bus power system and 20-node natural gas system.

TABLE 3 | Scheduling results of different scenarios.

Scenario	S1	S2	S3	S4	S5
Probability	0.214	0.106	0.258	0.172	0.25
Total cost of electricity system (10^6)	2.025	2.056	2.009	2.118	2.053
Ramping cost (10^4)	5.13	5.18	5.25	6.55	5.56
Corrective ramping cost (10^4)	1.67	1.46	1.80	1.71	1.81
Utilized wind power (MW)	10,718	11,401	10,596	11,068	11,535
Production cost of gas suppliers (10^5)	3.221	3.142	3.136	3.171	3.151

parameters as the PJM 5-Bus system are connected at Buses 8 and 43 and node 16 and three in the natural gas network. Nine generators are assumed to be gas-fired units, and gas loads at nodes 3, 6, 7, 10, 15 and 16 are consumed by power units 7, 13, 16, 23, 42 and 29. Hourly residential gas loads are the 80% of those of the 7-node natural gas system and distributed at load nodes according to the proportion in (Fang et al., 2015). 1,000 initial scenarios are generated, and then reduced to five scenarios.

Table 3 presents the scheduling results for the five uncertain scenarios. The operation cost for the base case of electricity system is $2.036 * 10^4$. The production cost of gas suppliers in Scenario one is the largest. The corrective ramping cost and utilized wind power in S5 are the largest. The reason is that greater corrective ramping capacities are required for greater utilization of wind power. The net load in S4 is the most fluctuant with the largest standard deviation of 998.8 MW, resulting in the largest ramping cost. The results verify the effectiveness of the proposed model on larger systems.

CONCLUSION

In this paper, a novel stochastic day-ahead scheduling model for IENGS considering ramping costs with P2G and wind power is proposed. The uncertainties of wind power and energy loads are represented in multiple scenarios. Natural gas network constraints are considered to ensure the availability of output of gas-fired units. P2G facility with storage is integrated to reduce wind power curtailment, provide ramping capacities, and reduce supply and load shedding in natural gas systems. The coordinated scheduling model is formulated as a two-stage stochastic programming problem, and the solution method is proposed. Numerical case studies on a modified PJM 5-bus electricity system with a 7-node natural gas system and the IEEE 118-bus system with the 20-node Belgian natural gas system demonstrate the rationality and effectiveness of the proposed model. The key findings of the case studies are summarized as follows.

(1) By utilizing abundant wind power, the integration of P2G can reduce wind power curtailment. The increment on wind power utilization rate can reach 13.8% in the test system.
(2) P2G facility provides additional flexible ramping capabilities, smoothing the net load profile and reducing total ramping costs in electricity system.
(3) The integration of P2G can reduce the total production cost, gas supply and load shedding of a natural gas system. It is more effective to reduce load shedding when gas storage works with P2G coordinately.

(4) A larger ramping cost coefficient would result in increased P2G power consumption.

The impact and benefits of P2G integration with storage relate to its capacity and location in an IENGS. Therefore, future research will focus on studying the siting and sizing of P2G facilities with storage.

DATA AVAILABILITY STATEMENT

The original contributions presented in the study are included in the article/Supplementary Material, further inquiries can be directed to the corresponding author/s.

AUTHOR CONTRIBUTIONS

XS: data curation, writing and software. CL: supervision, writing - reviewing and editing. RZ: conceptualization and methodology. TJ: software and formal analysis. HC: project administration.

FUNDING

This paper was supported in part by science and technology project of State Grid Jilin Corporation (SGJL0000DKJS2000287). The authors declare that this study received funding from science and technology project of State Grid Jilin Corporation. The funder had the following involvement with the study data collection.

REFERENCES

Alabdulwahab, A., Abusorrah, A., Zhang, X. P., and Shahidehpour, M. (2015). Coordination of interdependent natural gas and electricity infrastructures for firming the variability of wind energy in stochastic day-ahead scheduling. *IEEE Trans. Sustain. Energy.* 6 (2), 606–615. doi:10.1109/tste.2015.2399855

Alkano, D., and Scherpen, J. M. A. (2018). Distributed supply coordination for power-to-gas facilities embedded in energy grids. *IEEE Trans. Smart Grid.* 9 (2), 1012–1022. doi:10.1109/tsg.2016.2574568

Bai, L., Li, F., Cui, H., Jiang, T., Sun, H., and Zhu, J. (2016). Interval optimization based operating strategy for gas-electricity integrated energy systems considering demand response and wind uncertainty. *Appl. Energy.* 167, 270–279. doi:10.1016/j.apenergy.2015.10.119

Baldick, R. (2014). Flexibility and availability: can the natural gas supply support these needs?. *IEEE Power Energy Mag.* 12 (6), 101–104. doi:10.1109/mpe.2014.2340774

Chaudry, M., Jenkins, N., Qadrdan, M., and Wu, J. (2014). Combined gas and electricity network expansion planning. *Appl. Energy.* 113 (6), 1171–1187. doi:10.1016/j.apenergy.2013.08.071

Clegg, S., and Mancarella, P. (2015). Integrated modeling and assessment of the operational impact of power-to-gas (P2G) on electrical and gas transmission networks. *IEEE Trans. Sustain. Energy.* 6 (4), 1234–1244. doi:10.1109/tste.2015.2424885

Clegg, S., and Mancarella, P. (2016). Storing renewables in the gas network: modelling of power-to-gas seasonal storage flexibility in low-carbon power systems. *IET Gener. Transm. Distrib.* 10 (3), 566–575. doi:10.1049/iet-gtd.2015.0439

Fang, X., Hu, Q., Li, F., and Wang, B. (2015). Coupon-based demand response considering wind power uncertainty: a strategic bidding model for load serving entitie. *IEEE Trans. Power Syst.* 31 (2), 1025–1037. doi:10.1109/tpwrs.2015.2431271

GAMS/SCENRED Documentation (2002). [Online]. Available: http://www.gams.com/docs/document.htm

Grond, L., Schulze, P., and Holstein, J. (2013). Tech. Rep. GL 13.R.23579. Systems analyses power to gas: technology review. Groningen, The Netherlands: DNV KEMA Energy Sustainability.

He, C., Wu, L., Liu, T., and Shahidehpour, M. (2017). Robust co-optimization scheduling of electricity and natural gas systems via ADMM. *IEEE Trans. Sustain. Energy.* 8 (2), 658–670. doi:10.1109/tste.2016.2615104

Khani, H., and Farag, H. E. Z. (2018). Optimal day-ahead scheduling of power-to-gas energy storage and gas load management in wholesale electricity and gas markets. *IEEE Trans. Sustain. Energy.* 9 (2), 940–951. doi:10.1109/tste.2017.2767064

Li, T., Eremia, M., and Shahidehpour, M. (2008). Interdependency of natural gas network and power system security. *IEEE Trans. Power Syst.* 23 (4), 1817–1824. doi:10.1109/tpwrs.2008.2004739

Li, G., Zhang, R., Jiang, T., Chen, H., Bai, L., and Li, X. (2017a). Security-constrained bi-level economic dispatch model for integrated natural gas and electricity systems considering wind power and power-to-gas process. *Appl. Energy.* 194, 696–704. doi:10.1016/j.apenergy.2016.07.077

Li, G., Zhang, R., Jiang, T., Chen, H., Bai, L., Cui, H., et al. (2017b). Optimal dispatch strategy for integrated energy systems with CCHP and wind power. *Appl. Energy.* 192, 408–419. doi:10.1016/j.apenergy.2016.08.139

Liu, C., Shahidehpour, M., Fu, Y., and Li, Z. (2009). Security-constrained unit commitment with natural gas transmission constraints. *IEEE Trans. Power Syst.* 24 (3), 1523–1536. doi:10.1109/tpwrs.2009.2023262

Liu, C., Shahidehpour, M., and Wang, J. (2010). Application of augmented Lagrangian relaxation to coordinated scheduling of interdependent hydrothermal power and natural gas systems. *IET Gener. Transm. Distrib.* 4 (12), 1314–1325. doi:10.1049/iet-gtd.2010.0151

Liu, F., Bie, Z., and Wang, X. (2019). Day-ahead dispatch of integrated electricity and natural gas system considering reserve scheduling and renewable uncertainties. *IEEE Trans. Sustain. Energy.* 10 (2), 646–658. doi:10.1109/tste.2018.2843121

Wang, J., Shahidehpour, M., and Li, Z. (2008). Security-constrained unit commitment with volatile wind power generation. *IEEE Trans. Power Syst.* 23 (3), 1319–1327. doi:10.1109/tpwrs.2008.926719

Wolf, D. D., and Smeers, Y. (2000). The gas transmission problem solved by an extension of the simplex algorithm. *Manag. Sci.* 46 (11), 1454–1465. doi:10.1287/mnsc.46.11.1454.12087

Wu, H., Shahidehpour, M., Alabdulwahab, A., and Abusorrah, A. (2015). Thermal generation flexibility with ramping costs and hourly demand response in stochastic security-constrained scheduling of variable energy sources. *IEEE Trans. Power Syst.* 30 (6), 2955–2964. doi:10.1109/tpwrs.2014.2369473

Yang, J., Zhang, N., Cheng, Y., Kang, C., and Xia, Q. (2019). Modeling the operation mechanism of combined P2G and gas-fired plant with CO_2 recycling. *IEEE Trans. Smart Grid.* 10 (1), 1111–1121. doi:10.1109/tsg.2018.2849619

Zhang, X., Shahidehpour, M., Alabdulwahab, A. S., and Abusorrah, A. (2015). Security-constrained co-optimization planning of electricity and natural gas transportation infrastructures. *IEEE Trans. Power Syst.* 30 (6), 2984–2993. doi:10.1109/tpwrs.2014.2369486

Zhang, X., Che, L., Shahidehpour, M., Alabdulwahab, A., and Abusorrah, A. (2016). Electricity-natural gas operation planning with hourly demand response for deployment of flexible ramp. *IEEE Trans. Sustain. Energy.* 7 (3), 996–1004. doi:10.1109/tste.2015.2511140

Zhang, R., Jiang, T., Li, F., Li, G., Chen, H., and Li, X. (2020). Coordinated bidding strategy of wind farms and power-to-gas facilities using a cooperative game approach. *IEEE Trans. Sustain. Energy.* 11, 2545. doi:10.1109/TSTE.2020.2965521

Conflict of Interest: Author XS was employed by the company State Grid Jilin Electric Power Company Limited, China.

The remaining authors declare that the research was conducted in the absence of any commercial or financial relationships that could be construed as a potential conflict of interest.

GLOSSARY

$\boldsymbol{\pi_m/\pi_j}$ nodal pressure at node m/j

$\pi_m^{\max}/\pi_m^{\min}$ maximum/minimum pressure limit at node m

$\boldsymbol{\eta_{P2G}}$ energy conversion efficiency of P2G

$\boldsymbol{B/Z}$ constant parameter of compressor

$\boldsymbol{c_i/c_w}$ bidding prices of conventional unit/wind power

$\boldsymbol{C_{j,\mathrm{gas}}}$ bidding prices of gas suppliers

$\boldsymbol{C_{mj}}$ pipeline constant

$\mathbf{CRD}_{i,t}^0/\mathbf{CRU}_{i,t}^0$ down/up ramping costs in base case

$\mathbf{CRD}_{i,t}^s/\mathbf{CRU}_{i,t}^s$ corrective down/up ramping costs

$\mathbf{CRU}_{i,t}/\mathbf{CRD}_{i,t}$ total up and down flexible ramping costs

$\mathbf{cru_i/crd_i}$ bidding prices of up/down ramp

$\boldsymbol{c_{wc}/c_{P2G}}$ wind power curtailment/P2G cost coefficient

$D_{P2G,t}^0/D_{P2G,t}^s$ power load of P2G in base case/scenario s

$D_t^{e,s}$ electricity load in period t and scenario s

$D_{P2G,t}/E_{P2G,t,\mathbf{gas}}$ consumed electricity/energy content of P2G

$\boldsymbol{F_{mj}}$ gas flow of pipeline mj

$\boldsymbol{GL_{m,\max}}$ maximum gas load of gas fired units

$\boldsymbol{GL_{m,t,\mathrm{gas}}}$ gas load of gas-fired units

GSF generation shift factor

GS_t^s residential natural gas load

$\mathbf{HHV_{gas}}$ higher heating values of natural gas

$\mathbf{Limit_l}$ limit for power flow of line l

$P_{i,t}^0/P_{i,t}^s$ output of unit i in base case/scenario s

$P_{\mathbf{wind},t}^0/P_{\mathbf{wind},t}^s$ wind power in base case/scenario s

$\boldsymbol{H_{\mathrm{com}}/P_{\mathrm{com}}}$ energy/electricity consumed by compressor

$P_{\mathbf{wind},t}^{\mathbf{forecast},0}/P_{\mathbf{wind},t}^{\mathbf{forecast},s}$ forecast wind power in base case/scenario s

$\boldsymbol{P_{i,t,\mathrm{gas}}}$ power output of gas-fired unit i

$\boldsymbol{P_{i\max}/P_{i\min}}$ maximum/minimum limit of thermal units

Ps Probability

$\mathbf{Ramp}_i^d/\mathbf{Ramp}_i^u$ down/up ramping rate of power unit i

$\boldsymbol{R_d}$ reserve requirement of electricity system

$S_{P2G,t,\mathbf{gas}}^{\max}$ maximum volumetric limit of SNG

$\boldsymbol{S_{c,\max}/S_{d,\max}}$ maximum charging/discharging flow

$\boldsymbol{S_{P2G,t,\mathrm{gas}}}$ volumetric quantity of SNG

$S_{P2G,t}^S/S_{P2G,t,\mathbf{gas}}^S$ exchanged/charging gas flow of P2G storage

$ST_{P2G,t}^S$ The SOC of P2G storage

$\boldsymbol{ST_{\mathrm{ini}}}/ST_{P2G}^{\mathbf{Res}}$ initial/reserve SOC of P2G storage

$\boldsymbol{ST_{\max}/ST_{\min}}$ maximum/minimum SOC of P2G storage

frontiers in Energy Research

ORIGINAL RESEARCH
published: 11 December 2020
doi: 10.3389/fenrg.2020.596817

Bi-Level Load Peak Shifting and Valley Filling Dispatch Model of Distribution Systems With Virtual Power Plants

Fengzhang Luo[1], Xin Yang[1], Wei Wei[1], Tianyu Zhang[2], Liangzhong Yao[3], Lingzhi Zhu[4] and Minhui Qian[4]*

[1]Key Laboratory of Smart Grid of Ministry of Education, Tianjin University, Tianjin, China, [2]Economic and Technology Research Institute, State Grid Tianjin Electric Power Company, Tianjin, China, [3]School of Electrical Engineering and Automation, Wuhan University, Wuhan, China, [4]China Electric Power Research Institute, Beijing, China

Distributed energy resources (DERs) have been widely involved in the optimal dispatch of distribution systems which benefit from the characteristics of reliability, economy, flexibility, and environmental protection. And distribution systems are gradually transforming from passive networks to active distribution networks. However, it is difficult to manage DERs effectively because of their wide distribution, intermittency, and randomness. Virtual power plants (VPPs) can not only coordinate the contradiction between distribution systems and DERs but also consider the profits of DERs, which can realize the optimal dispatch of distribution systems effectively. In this paper, a bi-level dispatch model based on VPPs is proposed for load peak shaving and valley filling in distribution systems. The VPPs consist of distributed generations, energy storage devices, and demand response resources. The objective of the upper-level model is smoothing load curve, and the objective of the lower-level model is maximizing the profits of VPPs. Meanwhile, we consider the quadratic cost function to quantify the deviation between the actual output and the planned output of DGs. The effectiveness of the bi-level dispatch model in load shifting and valley filling is proved by various scenarios. In addition, the flexibility of the model in participating in distribution system dispatch is also verified.

Keywords: distribution systems, distributed generations, energy storage devices, flexible load, demand response, virtual power plants, bi-level dispatch model

OPEN ACCESS

Edited by:
Yue Zhou,
Cardiff University, United Kingdom

Reviewed by:
Jian Chen,
Shandong University, China
Quan Lyu,
Dalian University of Technology, China

****Correspondence:***
Wei Wei
weiw@tju.edu.cn

Specialty section:
This article was submitted to Smart Grids, a section of the journal Frontiers in Energy Research

Received: *20 August 2020*
Accepted: *19 October 2020*
Published: *11 December 2020*

Citation:
Luo F, Yang X, Wei W, Zhang T, Yao L, Zhu L and Qian M (2020) Bi-Level Load Peak Shifting and Valley Filling Dispatch Model of Distribution Systems With Virtual Power Plants. Front. Energy Res. 8:596817. doi: 10.3389/fenrg.2020.596817

INTRODUCTION

With the continuous development of the economy and the growth of electricity demand, the problem of peak load of the power grid has become more and more significant, which has a great impact on distribution systems' operation and resource utilization. Under the dual pressure of environmental pollution and shortage of fossil energy, renewable energy generation technologies have developed rapidly. The technologies of joint dispatching of distributed generations (DGs) and energy storage devices (ESS) for load peak shaving and valley filling are widely concerned (Sigrist et al., 2013; Setlhaolo and Xia, 2015; Aneke and Wang, 2016; and Sahand et al., 2019). Li et al., 2017, proposed a charging/discharging strategy of ESS considering time of use (TOU) price and DGs, and the strategy had good economic benefit and obvious peak load shifting effect. The traditional pumped storage power station was combined with wind power station by Sheng and Sun, 2014, which made the output of wind-storage devices into a stable and schedulable power source to participate in peak load regulation and load curve smoothing. Yang et al., 2018, proposed a variable parameter power control

strategy for ESS considering the effect of peak shaving and valley filling and state of charge interval, which reduced the peak valley difference of the system significantly.

Meanwhile, with the gradual development of power markets, demand response (DR) has been widely studied as an important measure which can optimize the utilization of demand side resources (Setlhaolo et al., 2014; Shafie-Khah et al., 2016; and Chen et al., 2018). Xu et al., 2014, considered the charging demand and load demand establishing a charging control strategy model of electric vehicles' (EVs) charging station based on dynamic TOU, which realized load peak shifting and valley filling effectively. Zhao et al., 2019, considered the uncertainty of flexible load in actual response and proposed a multitime scale model of day ahead, intraday, and real time. The model had a good effect on load peak shaving and valley filling, and it consumed renewable energy resources adequately. Rasheed et al., 2015, considered the user comfort, power consumption cost, and the reduction degree of power consumption peak to optimize the residential load and adopted different optimization algorithms to solve the model.

However, it is difficult to manage DGs effectively because of their small capacity, wide distribution, intermittency, and randomness. In addition, the load of middle-sized and small-sized users is scattered and highly uncertain which makes it hard to participate in the distribution systems' dispatch and power markets' transaction. The contradiction between DGs, DR, and power grid is well solved through virtual power plants (VPPs). VPPs can realize the aggregation, coordination, and optimization of active resources such as DGs, ESS, flexible load, and EVs, which participate in the power markets and power grids operation as special power plants by integrating the above resources (Wei et al., 2013). Therefore, a series of studies on VPPs participating in power systems' dispatch is in full swing (Bai et al., 2015; Ju et al., 2016b; Koraki and Strunz, 2018; and Zahid et al., 2019). Pandzic et al., 2013, aggregated wind power plants, photovoltaic power plants, conventional gas turbine power plants, and pumped hydro storages as a VPP and realized midterm dispatch by maximizing the profits of the VPP. Yi et al., 2020, proposed a bi-level planning model, which effectively improved the security and economy of the system by pricing the reactive power appropriately. In Ref. (Liu et al., 2018), the dispatch model of VPPs was established considering DR and carbon emissions, which studied the impact of environmental protection characteristics on the economy of VPPs. Ju et al., 2016a, established an optimization model which can reduce the fluctuation of wind power output by using variable load and improve VPPs' profits.

Based on the studies mentioned above, a bi-level dispatch model based on VPPs is proposed in this paper for load peak shaving and valley filling, which arranges the DGs, ESS, and DR as a VPP to smooth the load curve and alleviates the peak load problem of distribution systems. The objective of the upper-level model is smoothing load curve, and the objective of the lower-level model is maximizing the profits of VPPs. Meanwhile, we consider the quadratic cost function to quantify the deviation between the actual output and the planned output of DGs, which is used to reduce the waste of renewable energy resources. The model can not only effectively improve the adjustability of all kinds of distributed energy resources (DERs) in load peak shifting and valley filling but also can improve the economic profits of VPPs. Finally, the effectiveness of the bi-level dispatch model in load peak shifting and valley filling is proved by various scenarios. In addition, the flexibility of the model in participating in distribution systems' dispatch is also verified.

The remainder of this paper is organized as follows. The related theoretical models and concepts are introduced in *Preliminary*. The structure and organization process of the model are given in *Bi-Level Dispatch Model of Distribution Systems with Virtual Power Plants*. The flowchart of the bi-level dispatch model, detailed objective functions, and constraints are also presented in *Bi-Level Dispatch Model of Distribution Systems with Virtual Power Plants*. Case studies are provided in *Case Study*. *Conclusion* gives the conclusions of this paper.

PRELIMINARY

The Structure of Virtual Power Plant

VPPs are management systems which integrate different types of DERs such as distributed generators, ESS, flexible load, and EVs through advanced control, measurement, and communication technologies. They are used to participate in the power markets' transactions and distribution systems' dispatch, so as to realize the effective regulation and control of DERs. The structure of VPPs is shown in **Figure 1**.

The Model of Flexible Load

In the case of peak load problem which is constantly prominent, DR as an important measure of load regulation and control has been widely concerned by experts and scholars. Flexible load as a key resource in demand side can alleviate the power supply pressure of power grid greatly by participating in DR, and it can achieve peak shifting and peak avoidance to a certain extent. The strategies of DR are divided into price-based DR (PBDR) and incentive-based DR (IBDR). The PBDR is divided into TOU pricing, critical peak pricing, and spot pricing. TOU is a common electricity price strategy in China, which can effectively reflect the difference of power supply cost in different periods of power grids. The main measures are increasing the price in the peak period and reducing the price in the low period appropriately, which are used to reduce the peak-valley difference. Transferable load is a main expression form of PBDR strategy. And the IBDR includes direct load control, interruptible load, demand side bidding, emergency DR, capacity market project, and auxiliary service project. Before the implementation of IBDR, the DR implementation agency should sign a contract with the participating users, which includes the limits of load curtailment, response duration, and maximum response times. Curtailable load is a main expression form of IBDR strategy. Therefore, we quantify DR as transferable load and curtailable load in this paper.

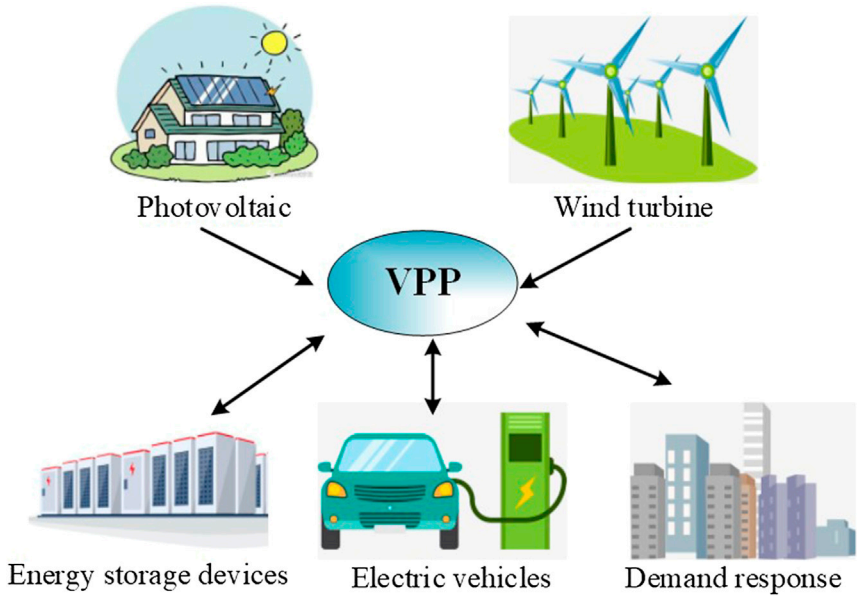

FIGURE 1 | The structure of VPP.

Transferable Load

Transferable load refers to the load whose power supply time can be changed while the total electricity consumption remains unchanged before and after the transferring. It can be flexibly adjusted according to the needs of users or power grids, such as EV power stations, ice storages, ESS, and partial load of industrial and commercial users (Wang et al., 2014). The model of transferable load is shown as follows:

$$\begin{cases} P_{L1}(t) = (1-\lambda)P_{L0}(t), \\ P_{L1}(t+\Delta t) = P_{L0}(t+\Delta t) + \eta P_{L0}(t) \end{cases} \quad (1)$$

where $P_{L0}(t)$ is the original load at time t; $P_{L1}(t)$ is the load after transferring at time t; λ is the proportion of the load transferred out at time t; and η is the proportion of the load transferred in at time t.

Curtailable Load

Curtailable load refers to the load whose total electricity consumption will decrease after responding the DR strategies. The model of curtailable load is shown as follows:

$$P_{L2}(t) = (1-\beta\times\gamma)P_{L0}(t) \quad (2)$$

where $P_{L2}(t)$ is the load after curtailing at time t; β is the proportion of curtailing at time t; and γ is the curtailing degree, which is accepted by users at time t.

The Organization Process of the Dispatch Model

The main structure and organization process of the dispatch model of an active distribution network (ADN) with VPPs is formulated in **Figure 2**, and the detailed implementation procedures of the model are as follows:

(1) VPP agent aggregates the DERs such as photovoltaics (PVs), ESS, and some controllable resources such as curtailable load and transferable load firstly. Then, VPP agent submits the related parameters and aggregation model to the distribution system operator (DSO).
(2) According to the related parameters and aggregation model of VPP agent, the DSO will conduct the optimal dispatch scheme for the active distribution network which can smooth the load curve.
(3) According to the parameters of DERs and DR, VPP agent will conduct the optimal dispatch schemes of each individual resource in the VPPs with the goal of maximizing the profits of VPPs.

BI-LEVEL DISPATCH MODEL OF DISTRIBUTION SYSTEMS WITH VIRTUAL POWER PLANTS

Basic Framework of the Bi-Level Dispatch Model

The distribution system side, VPP side and user side have different requirements in the dispatch process. Therefore, a bi-level dispatch model is proposed in this paper. The objective of distribution system side is smoothing load curves, which is in the upper-level model. The objective of VPP side is maximizing the profits, which is in the lower-level model. In addition, we also consider DR in the lower-level model, which by introducing the flexible load of user side for dispatching. Meanwhile, we consider the quadratic cost function to quantify the deviation between the actual output and the planned output of DGs, which is used to reduce the waste of renewable energy resources. The bi-level

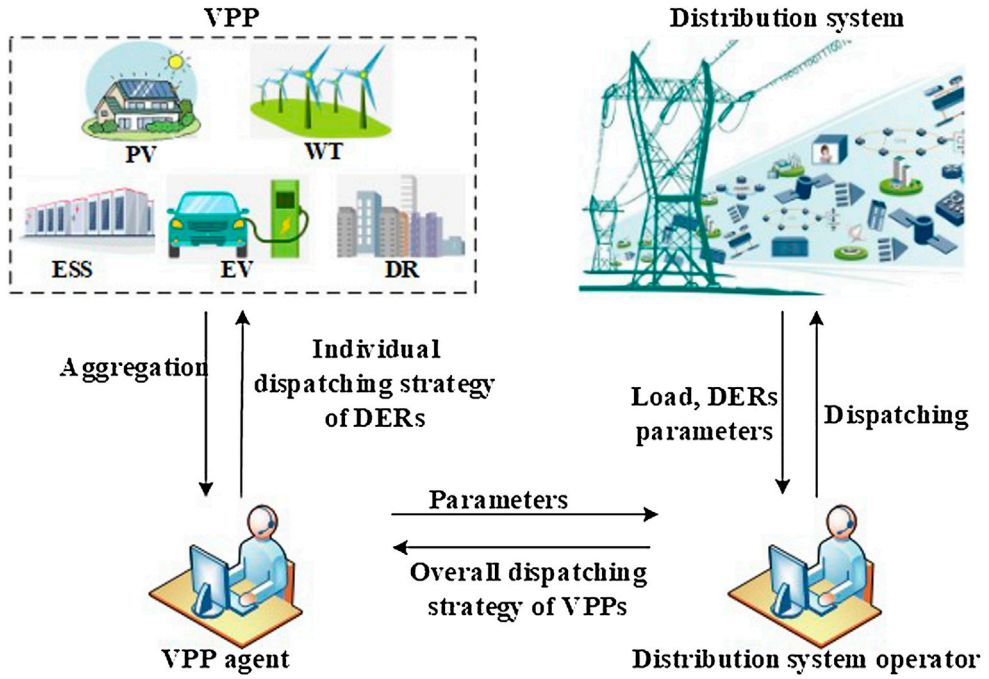

FIGURE 2 | The structure and organization process of the dispatch model.

model satisfies a series of constraints such as power balance restriction, VPP output restriction, DG output restriction, ESS restriction, and flexible load restriction. In order to ensure the effectiveness in load peak shaving and valley filling, the distribution system level objective is the main focus, while the profits of VPPs are secondary. The specific dispatch strategies of individual resources in VPPs are obtained at last. There is a brief introduction to the iteration process. Firstly, the DSO of the upper-level sends the dispatch plan to the VPPs in the lower-level, and the VPPs in the lower-level make the response to the dispatch plan under the condition of satisfying their own operation constraints and then send the dispatch plan to the upper-level model. However, there are many constraints need to be satisfied of the units of VPPs, and VPPs may not be able to fully respond to the dispatch plan of distribution systems' layer. If the VPPs' output of the lower level does not fully respond to the planned output of the upper level, a new output will be generated in the VPPs' layer and if the VPP output deviation between the upper-level and the lower level exceeds σ, the new output will be sent to the upper-level for a new iteration. The distribution system will make adjustments and resend the new dispatch strategies. **Figure 3** shows the flow chart of the bi-level dispatch model.

The Description of the Upper-Level Model

Objective Function

The upper-level model is the distribution system side dispatch model, and the objective is minimizing the peak valley difference of distribution systems and minimizing the VPP output deviation between the upper-level and lower-level. The expression of the upper-level model is as follows:

(1) Minimizing the peak valley difference of distribution systems

$$\min\left(\left(\max P_L(t)\right) - \left(\min P_L(t)\right)\right) \tag{3}$$

$$P_L(t) = P_0(t) - \sum_{i=1}^{N_{VPP}} P_i^{VPP}(t) \tag{4}$$

$$\sum_{i=1}^{N_{VPP}} P_i^{VPP}(t) = \sum_{i=1}^{N_{VPP}} \left(\sum_{j=1}^{N_{DG}} P_{ij}^{DG}(t) + \sum_{j=1}^{N_{ESS}} P_{ij}^{ESS}(t) + \sum_{j=1}^{N_{DR}} P_{ij}^{DR}(t) \right) \tag{5}$$

where $P_L(t)$ is the load at time t after VPPs dispatch; $P_0(t)$ is the original load at time t; $P_i^{VPP}(t)$ is the output of the i^{th} VPP at time t in the upper level; $P_{ij}^{DG}(t)$ is the output of the j^{th} DG in the i^{th} VPP at time t; $P_{ij}^{ESS}(t)$ is the output of the j^{th} ESS in the i^{th} VPP at time t; $P_{ij}^{DR}(t)$ is the output of the j^{th} controllable user in the i^{th} VPP at time t; N_{VPP} is the number of VPPs in the system; N_{DG} is the number of DGs in the i^{th} VPP; N_{ESS} is the number of ESS in the i^{th} VPP; and N_{DR} is the number of controllable users in the i^{th} VPP.

(2) Minimizing the VPP output deviation

$$\min \sum_{t-1}^{24} \sum_{i-1}^{N_{VPP}} \left| P_i^{VPP}(t) - \overline{P_i^{VPP}}(t) \right| \tag{6}$$

where $\overline{P_i^{VPP}}(t)$ is the output of the i^{th} VPP at the time t in the lowe-level.

Constraints

(1) Power balance equation:

$$\sum_{t=1}^{24} P_L(t) + \sum_{t=1}^{24} \sum_{i=1}^{N_{VPP}} P_i^{VPP}(t) = \sum_{t=1}^{24} P_0(t) \tag{7}$$

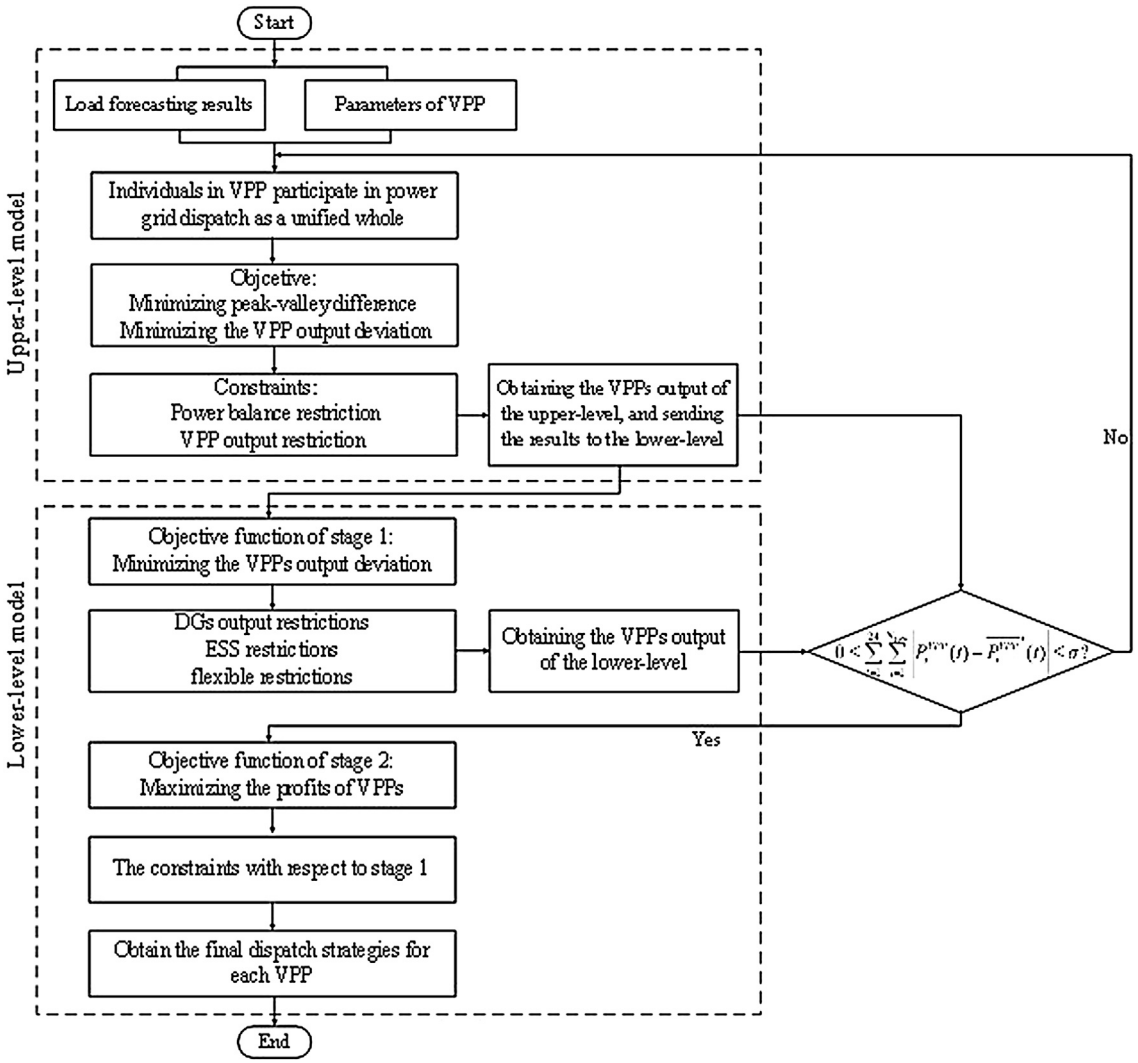

FIGURE 3 | The flow chart of the bi-level dispatch model.

(2) VPPs' output constraints:

$$P_{i,VPP}^{\min} \le P_i^{VPP}(t) \le P_{i,VPP}^{\max} \tag{8}$$

where $P_{i,VPP}^{\min}$ is the minimum output of the ith VPP and $P_{i,VPP}^{\max}$ is the maximum output of the ith VPP.

The Description of the Lower-Level Model

Objective Function

Objective Function of Stage 1

There are many constraints need to be satisfied of the units of VPPs, VPPs may not be able to fully respond to the dispatch plan of distribution systems' layer. Therefore, before the optimization of the lower-level model, we set the objective of minimizing the VPP output deviation between the upper level and lower level to obtain the actual output of the lower level. The objective can be described as follows:

$$\min \sum_{t=1}^{24} \sum_{i=1}^{N_{VPP}} \left| \overline{P_i^{VPP}}(t) - P_i^{VPP}(t) \right| \tag{9}$$

If the VPPs' output of the lower level fully responds to the planned output of the upper level, no new $P_i^{VPP}(t)$ will be generated; if not, a new $\overline{P_i^{VPP}}(t)$ will be generated in the VPP layer. $\overline{P_i^{VPP}}(t)$ will be sent to the upper-level model for a new round of iteration. The $\overline{P_i^{VPP}}(t)$ of the lower-level model is taken as the constraint of the output of the upper-level model.

Objective Function of Stage 2

The lower-level model is the VPP side dispatch model, and the objective is to maximize the profits of VPPs. In this paper, the

profits of VPPs include the generation income of DGs, the compensation income of DR, and the peak-shaving income of ESS. It is worth noting that the peak-shaving income of ESS includes not only the electricity cost/income due to ESS charging/discharging but also the compensation for peak-shaving ancillary service and even some environmental profits in the process of peak shaving. However, due to the lack of appropriate ancillary service prices and the difficulty in collecting pollutant density of thermal power units, we only consider the charging and discharging income of ESS in this paper. The detailed description of the lower-level model is as follows:

$$\max \sum_{i=1}^{N_{VPP}} \left(\sum_{j=1}^{N_{DR}} \sum_{t=1}^{24} C_{ij}^{DR}(t) + \sum_{j=1}^{N_{ESS}} \sum_{t=1}^{24} C_{ij}^{ESS}(t) + \sum_{j=1}^{N_{DG}} \sum_{t=1}^{24} \left(C_{ij,sell}^{DG}(t) - C_{ij,pub}^{DG}(t) \right) \right) \tag{10}$$

$$C_{ij}^{DR}(t) = \rho_{ij}^{ZY}(t) \cdot \mu_{ij}^{ZY}(t) \cdot \Delta P_{ij}^{ZY}(t) + \rho_{ij}^{XJ}(t) \cdot \mu_{ij}^{XJ}(t) \cdot \Delta P_{ij}^{XJ}(t) \tag{11}$$

$$C_{ij}^{ESS}(t) = \rho(t) \cdot \mu_{ij}^{d}(t) \cdot P_{ij}^{d}(t) - \rho(t) \cdot \mu_{ij}^{c}(t) \cdot P_{ij}^{c}(t) \tag{12}$$

$$C_{ij,sell}^{DG}(t) = \rho(t) \cdot \mu_{ij}^{DG}(t) \cdot P_{ij}^{DG}(t) \tag{13}$$

$$C_{ij,pub}^{DG}(t) = a_h \cdot \left(P_{ij}^{pre}(t) - \mu_{ij}^{DG}(t) \cdot P_{ij}^{DG}(t) \right)^2 + b_h \cdot \left(P_{ij}^{pre}(t) - \mu_{ij}^{DG}(t) \cdot P_{ij}^{DG}(t) \right) \tag{14}$$

where $C_{ij}^{DR}(t)$ is the compensation income of the jth user in the ith VPP at time t; $C_{ij}^{ESS}(t)$ is the peak shaving income of the jth ESS in the ith VPP at time t; $C_{ij,sell}^{DG}(t)$ is the electricity sales revenue of the jth DG in the ith VPP at time t; $C_{ij,pub}^{DG}(t)$ is a quadratic cost function, which represents the penalty cost of the jth DG in the ith VPP at time t; $\Delta P_{ij}^{ZY}(t)$ is the transferable load response capacity of the jth user in the ith VPP at time t; $\Delta P_{ij}^{XJ}(t)$ is the curtailable load response capacity of the jth user in the ith VPP at time t; $P_{ij}^{c}(t)$ is the charging power of the jth ESS in the ith VPP at time t; $P_{ij}^{d}(t)$ is the discharging power of the jth ESS in the ith VPP at time t; $\mu_{ij}^{XJ}(t)$ is the curtailment state of the jth users in the ith VPP at time t; $\mu_{ij}^{ZY}(t)$ is the transfer state of the jth users in the ith VPP at time t; $\mu_{ij}^{c}(t)$ is the charging state of the jth ESS in the ith VPP at time t; $\mu_{ij}^{d}(t)$ is the discharging state of the jth ESS in the ith VPP at time t; $\mu_{ij}^{DG}(t)$ is the operation state of the jth DG in the ith VPP at time t; $\rho_{ij}^{DR}(t)$ is the unit capacity compensation price of the jth DR in the ith VPP at time t; $\rho(t)$ is the electricity price at time t; a_h and b_h are the coefficients of quadratic cost function (Wang et al., 2019); and $P_{ij}^{pre}(t)$ is the forecasting output of the jth DG in the ith VPP at time t.

Constraints

The Constraints of Stage 1

(1) The supply and demand balance of VPPs:

$$\sum_{i=1}^{N_{VPP}} \left(\sum_{j=1}^{N_{DG}} \mu_{ij}^{DG}(t) \cdot P_{ij}^{DG}(t) + \sum_{j=1}^{N_{ESS}} \mu_{ij}^{d}(t) \cdot P_{ij}^{d}(t) + \sum_{j=1}^{N_{DR}} \mu_{ij}^{ZY}(t) \cdot \Delta P_{ij}^{ZY}(t) \right) = \sum_{i=1}^{N_{VPP}} \overline{P_i^{VPP}}(t) - \sum_{i=1}^{N_{VPP}} \sum_{j=1}^{N_{DR}} \mu_{ij}^{XJ}(t) \cdot \Delta P_{ij}^{XJ}(t) + \sum_{i=1}^{N_{VPP}} \sum_{j=1}^{N_{ESS}} \mu_{ij}^{c}(t) \cdot P_{ij}^{c}(t) \tag{15}$$

(2) DGs' constraints:

$$0 \le P_{ij}^{DG}(t) \le \mu_{ij}^{DG}(t) \cdot P_{ij,DG}^{\max}(t) \tag{16}$$

where $P_{ij,DG}^{\max}(t)$ is the maximum output of the jth DG in the ith VPP at time t.

(3) ESS constraints:

Equations 17–22 are the constraints of ESS. **Equation 17** is the relationship between stored energy and charging/discharging power of ESS at time t, **Equation 18** is the capacity constraint of ESS, **Equations 19** and **20** are charging power and discharging power constraint, respectively, **Equation 21** is working state constraint of ESS, and the working state can be divided into idle, charging, and discharging, and it can only be in one state in a moment; **Equation 22** is the periodic constraint of ESS:

$$S_{ij}^{ESS}(t) = S_{ij}^{ESS}(t-1) + \eta_c P_{ij}^{c}(t) + \frac{P_{ij}^{d}(t)}{\eta_d} \tag{17}$$

$$S_{ij,ESS}^{STO} \cdot C_{ij,ESS}^{\min} \le S_{ij}^{ESS}(t) \le S_{ij,ESS}^{STO} \cdot C_{ij,ESS}^{\max} \tag{18}$$

$$0 \le P_{ij}^{c}(t) \le P_{ij,ESS}^{\max} \cdot \mu_{ij}^{c}(t) \tag{19}$$

$$0 \le P_{ij}^{d}(t) \le P_{ij,ESS}^{\max} \cdot \mu_{ij}^{d}(t) \tag{20}$$

$$0 \le \mu_{ij}^{c}(t) + \mu_{ij}^{d}(t) \le 1 \tag{21}$$

$$S_{ij}^{ESS}(1) = S_{ij}^{ESS}(T) = 0.2 S_{ij,ESS}^{STO} \tag{22}$$

where $S_{ij}^{ESS}(t)$ is the energy of the jth ESS in the ith VPP at time t; η_c is the charging efficiency of ESS; η_d is the discharging efficiency of ESS; $P_{ij,ESS}^{\max}$ is the maximum charging/discharging power of the jth ESS in the ith VPP; $S_{ij,ESS}^{STO}$ is the rated capacity of the jth ESS in the ith VPP; $C_{ij,ESS}^{\max}$ and $C_{ij,ESS}^{\min}$ are the maximum/minimum state of charge of the jth ESS in the ith VPP; and the value are 0.8 and 0.2, respectively, in this paper.

(4) Flexible Load Constraints:

Equations 23–26 are the curtailable load constraints, and **Equations 27** to **29** are the transferable load constraints. **Equation 23** is the user comfort and acceptance constraint, which

limits the upper and lower limit of curtailable load capacity at time *t*. **Equation 24** is the curtailable number constraint. **Equation 25** is the upper and lower limit constraint of the response capacity of curtailable load in one user. **Equation 26** is the constraint of the total response capacity of curtailable load in one VPP. **Equation 27** is the user comfort and acceptance constraint, which limits the upper and lower limit of transferable load capacity at time *t*. **Equation 28** is the upper and lower limit constraint of the response capacity of transferable load in one user. **Equation 29** is the constraint of the total response capacity of transferable load in one VPP:

$$\mu_{ij}^{XJ}(t)\cdot\Delta P_{ij,XJ}^{\min}(t)\le\Delta P_{ij}^{XJ}(t)\le\mu_{ij}^{XJ}(t)\cdot\Delta P_{ij,XJ}^{\max}(t) \tag{23}$$

$$\sum_{t=1}^{24}\mu_{ij}^{XJ}(t)\le N_{ij}^{\max} \tag{24}$$

$$\Delta P_{ij,XJ}^{\min}\le\sum_{t=1}^{24}\Delta P_{ij}^{XJ}(t)\le\Delta P_{ij,XJ}^{\max} \tag{25}$$

$$\sum_{j=1}^{N_{DR}}\sum_{t=1}^{24}\Delta P_{ij}^{XJ}(t)=\Delta P_{ij,XJ}^{total} \tag{26}$$

$$\mu_{ij}^{ZY}(t)\cdot\Delta P_{ij,ZY}^{\min}(t)\le\Delta P_{ij}^{ZY}(t)\le\mu_{ij}^{ZY}(t)\cdot\Delta P_{ij,ZY}^{\max}(t) \tag{27}$$

$$\Delta P_{ij,ZY}^{\min}\le\sum_{t=1}^{24}\Delta P_{ij}^{ZY}(t)\le\Delta P_{ij,ZY}^{\max} \tag{28}$$

$$\sum_{j=1}^{N_{DR}}\sum_{t=1}^{24}\Delta P_{ij}^{ZY}(t)=\Delta P_{ij,ZY}^{total} \tag{29}$$

where $\Delta P_{ij,XJ}^{\min}(t)$ is the lower limit of the curtailable load of the *j*th user in the *i*th VPP at time *t*; $\Delta P_{ij,XJ}^{\max}(t)$ is the upper limit of the curtailable load of the *j*th user in the *i*th VPP at time *t*; $\Delta P_{ij,XJ}^{\min}$ is the lower limit of the curtailable load of the *j*th user in the *i*th VPP in one dispatch cycle; $\Delta P_{ij,XJ}^{\max}$ is the upper limit of the total curtailable load of the *j*th user in the *i*th VPP in one dispatch cycle; $N_{ij}^{\max}$ is the upper limit of curtailable number of the *j*th user in the *i*th VPP in one dispatch cycle and the value is 16 in this paper; $\Delta P_{ij,XJ}^{total}$ is the curtailable load capacity of all users in the *i*th VPP in one dispatch cycle; $\Delta P_{ij,ZY}^{\min}(t)$ is the lower limit of the transferable load of the *j*th user in the *i*th VPP at time *t*; $\Delta P_{ij,ZY}^{\max}(t)$ is the upper limit of the transferable load of the *j*th user in the *i*th VPP at time *t*; $\Delta P_{ij,ZY}^{\min}$ is the lower limit of the transferable load of the *j*th user in the *i*th VPP in one dispatch cycle; $\Delta P_{ij,ZY}^{\max}$ is the upper limit of the transferable load of the *j*th user in the *i*th VPP in one dispatch cycle; and $\Delta P_{ij,ZY}^{total}$ is the transferable load capacity of all users in the *i*th VPP in one dispatch cycle. One dispatch cycle is 24 h in this paper.

The Constraints of Stage 2

1) VPPs' output constraints:

$$\begin{aligned}&\sum_{i=1}^{N_{VPP}}\left(\sum_{j=1}^{N_{DG}}\mu_{ij}^{DG}(t)\cdot P_{ij}^{DG}(t)+\sum_{j=1}^{N_{ESS}}\mu_{ij}^{d}(t)\cdot P_{ij}^{d}(t)\right.\\&\quad\left.+\sum_{j=1}^{N_{DR}}\mu_{ij}^{ZY}(t)\cdot\Delta P_{ij}^{ZY}(t)\right)\\&=\sum_{i=1}^{N_{VPP}}\overline{P_i^{VPP\prime}}(t)-\sum_{i=1}^{N_{VPP}}\sum_{j=1}^{N_{DR}}\mu_{ij}^{XJ}(t)\cdot\Delta P_{ij}^{XJ}(t)+\sum_{i=1}^{N_{VPP}}\sum_{j=1}^{N_{ESS}}\mu_{ij}^{c}(t)\cdot P_{ij}^{c}(t)\end{aligned} \tag{30}$$

where $\overline{P_i^{VPP\prime}}(t)$ is the output of VPPs which obtained from objective function of stage 1.

Other constraints of stage 2 are the same as that of stage 1.

Model Processing and Implement Method

The upper-level model of the bi-level dispatch model proposed in this paper is a typical mixed integer linear programming model. The lower-level model contains nonlinear objective functions, which is a mixed integer nonlinear programming model. The objective function in the lower-level model is transformed into linear description by KKT condition (Zhang et al., 2018, and Wei et al., 2015). Then, we can solve the model by calling optimization software CPLEX through YALMIP in MATLAB. The convergent gap value of CPLEX solver is set to 0.01%.

CASE STUDY

Case Introduction

We consider two VPPs participating in the distribution system dispatch. One VPP consists two photovoltaic systems and one ESS. The installed capacity of PV is 100 kW, the capacity of the ESS is 1,800 kWh, and the rated power is 300 kW. The other VPP consists one photovoltaic system and one ESS. The installed capacity of PV is 200 kW, the capacity of the ESS is 900 kWh and the rated power is 150 kW. The load data are from a typical day of a city in southern China. DR resources contain transferable load and curtailable load in this paper. The transferable load accounts for 3% of the total load and the curtailable load accounts for 1% of the total load in the first VPP system. In the second VPP system, the transferable load accounts for 2% of the total load and the curtailable load accounts for 1% of the total load. We adopt TOU in this paper. The division of peak-valley time period and the electricity price of each period are shown in **Table 1**. The rated output of PV is shown in **Table 2**. In this paper, the system electricity price at the curtailable time is used to compensate for the curtailable load (Luo and Song, 2015), and 80% of the system electricity price at the transferable time is used to compensate the transferable load (Liu et al.,) $a_h = 0.1$ and $b_h = 0$ (Wang et al., 2019).

Result Analysis

Scenario Setting

This paper simulates four different scenarios to analyze the optimization effect on the load curve by VPPs when aggregating different types of DERs. Scenario 1 is the benchmark scenario, which considers the optimization of load curve only with DGs; scenario 2 does not consider the DR, but only considers the DGs and ESS to optimize the load curve; scenario 3 does not consider ESS, but only considers DGs and DR to optimize the load curve; scenario 4 is a comprehensive

TABLE 1 | The division of TOU.

	Time	Price (RMB/kW·h)
Peak periods	8:00–11:00; 17:00–20:00	1.082
Normal periods	12:00–16:00; 21:00–23:00	0.649
Valley periods	0:00–7:00	0.316

TABLE 2 | The output of PV (p.u.).

Time	PV	Time	PV
0:00	0.000	12:00	1.000
1:00	0.000	13:00	0.969
2:00	0.000	14:00	0.725
3:00	0.000	15:00	0.734
4:00	0.000	16:00	0.524
5:00	0.000	17:00	0.232
6:00	0.105	18:00	0.051
7:00	0.382	19:00	0.000
8:00	0.643	20:00	0.000
9:00	0.838	21:00	0.000
10:00	0.955	22:00	0.000
11:00	0.954	23:00	0.000

TABLE 3 | Different scenarios of VPPs.

Scenarios	DG	ESS	DR
Scenario 1	√	×	×
Scenario 2	√	√	×
Scenario 3	√	×	√
Scenario 4	√	√	√

"√" represents that the resource is considered and "×" represents that the resource is not considered.

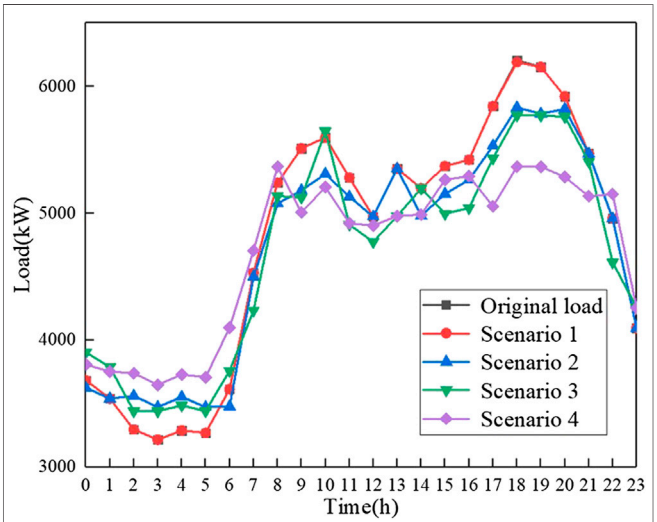

FIGURE 4 | Optimized load curve in different scenarios.

scenario, considering DGs, ESS, and DR to optimize the load curve. **Table 3** shows the scenarios in detail.

Optimization Effect and Analysis

Figure 4 shows the optimized load curve in different scenarios. In scenario 1, the peak period of DGs does not completely match with the peak period of load demand, so DGs power output cannot be fully absorbed, which causes the problem of resource waste. The effect of the optimization is not obvious. Scenario 2 considers the combination of DGs and ESS for dispatching. ESS smooths the load curve by discharging at peak

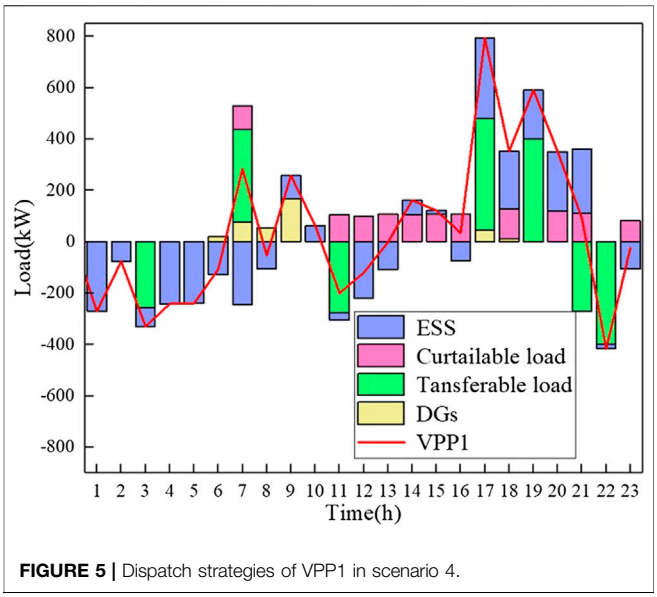

FIGURE 5 | Dispatch strategies of VPP1 in scenario 4.

periods and charging at valley periods. Meanwhile, the introduction of ESS can realize the local absorption of DGs, which can greatly improve the renewable energy resource utilization rate. Scenario 3 considers DR for optimizing load curve, and the introduction of DR can effectively reduce the load peak valley difference. In addition, due to the lack of ESS coordination, the waste of DGs is serious. Scenario 4 considers all the resources comprehensively. It can be seen from **Figure 4** that the smoothness performance of load curve and the peak valley difference are optimal in scenario 4. Aggregating DGs, ESS, and DR as VPPs for distribution systems' dispatch can relieve the pressure of power grid more.

Virtual Power Plant Dispatch Strategies and Analysis

Figures 5 and **6** show the dispatch strategies of the two VPPs in scenario 4, respectively. **Figure 7** shows the total dispatch strategies of VPPs in scenario 4. We can see that the ESS charging in the valley period of TOU price and discharging in the peak period of TOU price. Meanwhile, the transferable load is transferred from the peak period to the valley period, and the curtailable load is curtailed in the peak period. DGs output is close to the rated output, which greatly improves the utilization of resources and the profits of VPPs.

Table 4 shows the optimization performance of VPPs with some typical indexes of load curve in scenario 4. It can be clearly seen from **Table 4** that aggregating DGs, ESS, and DR as VPPs to optimize the distribution systems load can improve the relevant indexes greatly, which can realize the load peak shaving and valley filling of the distribution systems effectively. Moreover, it can alleviate the pressure of the distribution systems greatly and provide scientific guidance for distribution systems planning, construction, and management.

CONCLUSION

The problem of large peak valley difference and the peak load problem have a negative impact on the distribution systems'

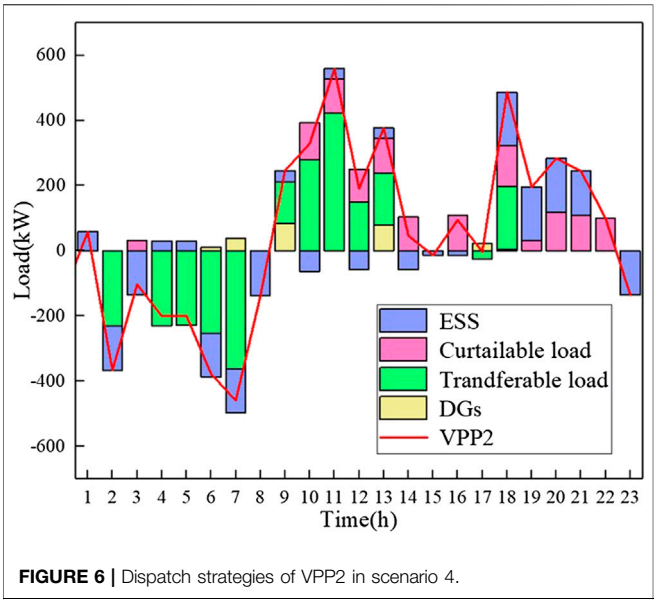

FIGURE 6 | Dispatch strategies of VPP2 in scenario 4.

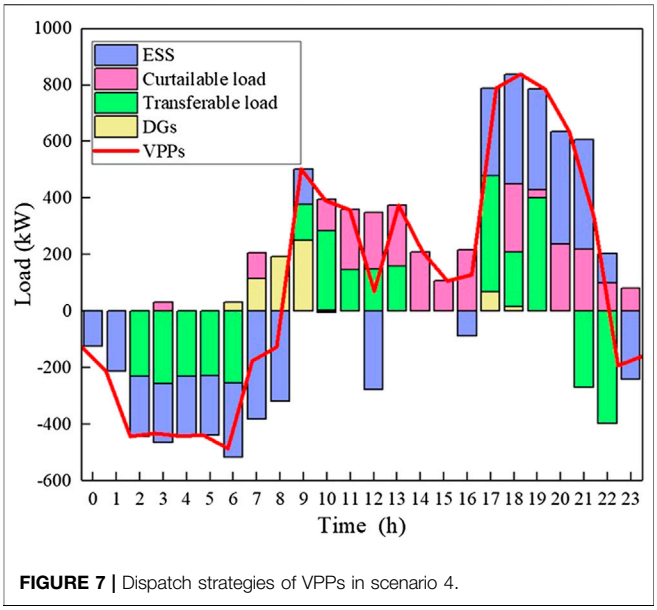

FIGURE 7 | Dispatch strategies of VPPs in scenario 4.

TABLE 4 | The optimization performance measured by typical indexes.

Indexes	Original load curve	Scenario 4 load curve	Optimization performance
Maximum load (kW)	6,207.02	5,368.45	↓13.51%
Minimum load (kW)	3,215.37	3,646.88	↑13.42%
Average load (kW)	4,793.39	4,697.52	↓2.00%
Peak valley difference (kW)	2,991.65	1,721.58	↓42.45%
Peak valley ratio (%)	48.20%	32.07%	↓33.47%
Load rate (%)	77.23%	87.50%	↑13.31%
Load dispersion	992.41	619.54	↓37.57%
VPP profits (RMB)	—	8,835.54	—

operation and resource utilization rate. A bi-level dispatch model of distribution systems with VPPs is proposed in this paper to solve the problems mentioned above. The objective of the upper-level model is smoothing load curve, and the objective of the lower-level model is maximizing the profits of VPPs. The effectiveness of the bi-level dispatch model in load peak shifting and valley filling is proved by various scenarios. In addition, the flexibility of the model in participating in distribution systems dispatch is verified as well. Through the analysis of the case studies, the following conclusions can be drawn:

(1) Active resources play an important role in solving the large peak valley difference and the peak load problem of distribution systems. In this paper, we aggregate various kinds of active resources as VPPs to participate in distribution systems' dispatch, which solve the problem of high uncertainty and difficulty in management of the active resources. The model reflects the high flexibility of the VPPs in the process of distribution systems' dispatch.
(2) The flexible load and ESS have a very significant performance in the smoothing load curve. In addition, the ESS can rely on their own charging and discharging characteristics to cooperate with the DGs in VPPs, which increases the utilization rate of resources.
(3) The bi-level dispatch model in this paper can not only maximize the local consumption of DGs and improve the economy of VPPs but also smooth the load curve and reduce the peak valley difference. Moreover, it can provide more scientific and accurate guidance for the future distribution systems' planning.

DATA AVAILABILITY STATEMENT

The original contributions presented in the study are included in the article/**Supplementary Material**; further inquiries can be directed to the corresponding author.

AUTHOR CONTRIBUTIONS

FL contributed toward supervision, conceptualization, and writing—review and editing. XY contributed toward

methodology, software, data curation, and writing—original draft. WW, TZ, LY, LZ, and MQ contributed toward writing—review and editing.

FUNDING

This work was supported in part by the National Key Research and Development Program of China under Grant 2016YFB0900100, National Natural Science Foundation of China under Grant 51977140, Grant U1866207, and Grant 51207101, and Natural Science Foundation of Tianjin under Grant 19JCYBJC21300.

ACKNOWLEDGMENTS

Thanks for the data support provided by the project team members of National Key Research and Development Program of China, the National Natural Science Foundation of China, and the Natural Science Foundation of Tianjin.

SUPPLEMENTARY MATERIAL

The Supplementary Material for this article can be found online at: https://www.frontiersin.org/articles/10.3389/fenrg.2020.596817/full#supplementary-material

REFERENCES

Aneke, M., and Wang, M. (2016). Energy storage technologies and real-life applications-A state of the art review. *Appl. Energy* 179, 350–377. doi:10.1016/j.apenergy.2016.06.097

Bai, H., Miao, S., Ran, X., and Ye, C. (2015). Optimal dispatch strategy of a virtual power plant containing battery switch stations in a unified electricity market. *Energies* 8, 2268–2289. doi:10.3390/en8032268

Chen, X., Wang, J., Xie, J., Xu, S., and Gan, L. (2018). Demand response potential evaluation for residential air conditioning loads. *IET Gener. Transm. Distrib.* 12, 4260–4268. doi:10.1049/iet-gtd.2018.5299

Ju, L., Li, H., Zhao, J., Chen, K., Tan, Q., and Tan, Z. (2016a). Multi-objective stochastic scheduling optimization model for connecting a virtual power plant to wind -photovoltaic-electric vehicles considering uncertainties and demand response. *Energy Convers. Manag.* 128, 160–177. doi:10.1016/j.enconman.2016.09.072

Ju, L., Tan, Z., Yuan, J., Tan, Q., Li, H., and Dong, F. (2016b). A bi-level stochastic scheduling optimization model for a virtual power plant connected to a wind-photovoltaic-energy storage system considering the uncertainty and demand response. *Appl. Energy* 171, 184–199. doi:10.1016/j.apenergy.2016.03.020

Koraki, D., and Strunz, K. (2018). Wind and solar power integration in electricity markets and distribution networks through service-centric virtual power plants. *IEEE Trans. Power Syst.* 33, 473–485. doi:10.1109/PESGM.2018.8586267

Li, X., Geng, G., Ji, Y., and Lu, L. (2017). Operation strategy of battery energy storage system in distribution network with distributed generation. *Electric Power Automation Equipment* 37, 59–65 [in Chinese, with English summary]. doi:10.16081/j.issn.1006-6047.2017.11.010

Liu, X., Wu, H., Wang, J., and Lu, J. (2020) Economic dispatch of a virtual power plant considering demand response in electricity market environment. *Electr. Power*, 53, 172–180 [in Chinese, with English summary]. doi:10.11930/j.issn.1004-9649.202001092

Liu, Z., Zheng, W., Qi, F., Wang, L., Zou, B., Wen, F., et al. (2018). Optimal dispatch of a virtual power plant considering demand response and carbon trading. *Energies*, 11, 1488–1506. doi:10.3390/en11061488

Luo, Q., and Song, Y. (2015). Marketing strategy in competitive retail market considering interruptible load. *Autom. Electr. Power Syst.* 39, 134–139 [in Chinese, with English summary]. doi:10.7500/AEPS20140910001

Pandzic, H., Kuzle, I., and Capuder, T. (2013). Virtual power plant mid-term dispatch optimization. *Appl. Energy* 10, 134–141. doi:10.1016/j.apenergy.2012.05.039

Rasheed, M., Javaid, N., Ahmad, A., Khan, Z. A., Qasim, U., and Alrajeh, N. (2015). An efficient power scheduling scheme for residential load management in smart homes. *Appl. Sci.* 5, 1134–1163. doi:10.3390/app5041134

Sahand, G., Amin, R., Mojtaba, J., Ali, A., Li, L., and Zhang, J. (2019). Risk-constrained demand response and wind energy systems integration to handle stochastic nature and wind power outage. *IET Energy Sys. Int.* 1, 114–120. doi:10.1049/iet-esi.2018.0022

Setlhaolo, D., and Xia, X. (2015). Optimal scheduling of household appliances with a battery storage system and coordination. *Energy Build.* 94, 61–70. doi:10.1016/j.enbuild.2015.02.051

Setlhaolo, D., Xia, X., and Zhang, J. (2014). Optimal scheduling of household appliances for demand response. *Elec. Power Syst. Res.* 116, 24–28. doi:10.1016/j.epsr.2014.04.012

Shafie-Khah, M., Kheradmand, M., Javadi, S., Azenhad, M., de Aguiarc, J. L. B., Castro-Gomes, J., et al. (2016). Optimal behavior of responsive residential demand considering hybrid phase change materials. *Appl. Energy*, 163, 81–92. doi:10.1016/j.apenergy.2015.11.013

Sheng, S., and Sun, X. (2014). An economic dispatching strategy of peak load shifting by wind farm and pumped storage plant. *Power Syst. Technol.* 38, 2484–2489 [in Chinese, with English summary]. doi:10.13335/j.1000-3673.pst.2014.09.027

Sigrist, L., Lobato, E., and Rouco, L. (2013). Energy storage systems providing primary reserve and peak shaving in small isolated power system: an economic assessment. *Int. J. Electr. Power Energy Syst.* 53, 675–683. doi:10.1016/j.ijepes.2013.05.046

Wang, K., Yao, J., Yao, L., Yang, S., and Yong, T. (2014). Survey of Research on flexible loads scheduling technologies. *Autom. Electr. Power Syst.* 38, 127–135 [in Chinese, with English summary]. doi:10.7500/AEPS20140422005

Wang, Z., Liu, M., and Xie, M. (2019). Decentralized saddle-point dynamics solution for optimal power flow of distribution networks with high photovoltaic penetration. *Proc. CSEE* 39, 459–468+643 [in Chinese, with English summary]. doi:10.13334/j.0258-8013.pcsee.171395

Wei, W., Chen, Y., Liu, F., Mei, S. W., Tian, F., and Zhang, X. (2015). Stackelberg game based retailer pricing scheme and EV charging management in smart residential area. *Power Syst. Technol.* 39, 134–139 [in Chinese, with English summary]. doi:10.13335/j.1000-3673.pst.2015.04.010

Wei, Z., Yu, S., Sun, G., Sun, Yi., Yuan, Y., and Wang, D. (2013). Concept and development of virtual power plant. *Autom. Electr. Power Syst.* 37, 1–9 [in Chinese, with English summary]. doi:10.3390/app5041134

Xu, Z., Hu, Z., Song, Y., Zhang, H., and Chen, X. (2014). Coordinated charging strategy for PEV charging stations based on dynamic time-of-use tariffs. *Proc. CSEE* 34, 3638–3646. doi:10.13334/j.0258-8013.pcsee.2014.22.008

Yang, X., Dong, D., Li, X., Ma, X., Di, N., and Jia, X. (2018). Active power coordinated control strategy of peak load shifting for energy storage system in business park. *Power Syst. Technol.* 42, 2551–2561. doi:10.13335/j.1000-3673.pst.2017.2098

Yi, Z., Xu, Y., Zhou, J., Wu, W., and Sun, H. (2020). Bi-level programming for optimal operation of an active distribution network with multiple virtual power plants. *IEEE Trans. Sustain. Energy* 11, 2855–2869. doi:10.1109/TSTE.2020.2980317

Zahid, U., Geev, M., Felician, C., and Yim, F. (2019). Comprehensive review of VPPs planning, operation and scheduling considering the uncertainties related to renewable energy sources. *IET Energy Sys. Int.* 1, 147–157. doi:10.1049/iet-esi.2018.0041

Zhang, G., Wang, X., and Jiang, C. (2018). Stackelberg game based coordinated dispatch of virtual power plant considering electric vehicle management.

Autom. Electr. Power Syst. 42, 48–55 [in Chinese, with English summary]. doi:10.7500/AEPS20170607005

Zhao, D., Song, Y., Yin, J., and Xu, C. (2019). Coordinated scheduling model with multiple time scales considering response uncertainty of flexible load. *Autom. Electr. Power Syst.* 43, 21–32 [in Chinese, with English summary]. doi:10.7500/AEPS20190428008

Conflict of Interest: Author TZ was employed by State Grid Tianjin Electric Power Company. Author LZ and MQ were employed by China Electric Power Research Institute.

The remaining authors declare that the research was conducted in the absence of any commercial or financial relationships that could be construed as a potential conflict of interest.

frontiers in Energy Research

METHODS
published: 22 December 2020
doi: 10.3389/fenrg.2020.614292

A Specialized System-on-Chip Based Distance Protection for Distribution Grids with Inverter Interfaced Distributed Generation

*Peng Li[1], Wei Xi[1], Xianggen Yin[2], Xiangjun Zeng[3], Licheng Li[4], Qixun Yang[5] and Wei Chen[2]**

[1]Artificial Intelligence and Chip Application Research Department, Digital Grid Research Institute, CSG, Guangzhou, China, [2]State Key Laboratory of Advanced Electromagnetic Engineering and Technology, Huazhong University of Science and Technology, Wuhan, China, [3]School of Electrical and Information Engineering, Changsha University of Science and Technology, Changsha, China, [4]CSG, Guangzhou, China, [5]Sifang Automation Co., Ltd., Beijing, China

Legacy protection schemes face new challenges as Inverter Interfaced Distribution Generation (IIDG) significantly changes the transient fault response of the distribution grid. The performance of the protection near the IIDG side is adversely affected by Low Voltage Ride Through (LVRT) and the negative sequence current suppression control characteristics of the IIDG. The operational characteristics of the protection are very different from those of the legacy protection schemes used in the distribution grid. Traditional overcurrent protection schemes cannot meet the requirements of selectivity and sensitivity. This paper analyses the influence of the IIDG on the protection schemes used in the distribution grid. Based on the positive sequence voltage polarization impedance criterion this study proposes a polarizing impedance criterion based on the fault component of positive sequence voltage, which can adaptively follow the fault resistance variation to satisfy the requirements of grid operation. The simulation results show that: (a) the proposed criterion is immune to the adverse effects of the transient characteristics of the IIDG; and, (b) it can adaptively follow the change of fault resistance making it suitable for application in short distribution lines. Using specialized System-on-Chip technology, a new distance protection device has been developed and tested on an industrial site. Simulation results and field tests showed that the new distance protection meets the requirements of the distribution grid with IIDGs.

Keywords: distribution grid, inverter interfaced distributed generation, low voltage ride through, positive sequence voltage polarization, system-on-chip based protection

OPEN ACCESS

Edited by:
Yang Mi,
Shanghai University of Electric Power, China

Reviewed by:
Tai Nengling,
Shanghai Jiao Tong University, China
Tao Lin,
Wuhan University, China
Xiaohua Li,
South China University of Technology, China

****Correspondence:***
Wei Chen
weichen@hust.edu.cn

Specialty section:
This article was submitted to Smart Grids, a section of the journal Frontiers in Energy Research

Received: *05 October 2020*
Accepted: *24 November 2020*
Published: *22 December 2020*

Citation:
Li P, Xi W, Yin X, Zeng X, Li L, Yang Q and Chen W (2020) A Specialized System-on-Chip Based Distance Protection for Distribution Grids with Inverter Interfaced Distributed Generation. Front. Energy Res. 8:614292. doi: 10.3389/fenrg.2020.614292

INTRODUCTION

With the rapid developments in new generation technologies in recent years, various forms of new energy sources have been connected to the grid in the form of the IIDG. The dynamic response characteristics of the IIDG are determined by the nonlinear control strategy of the inverter. The complicated response characteristics of the IIDG, which largely change the characteristics and distribution of the fault current, lead to increased difficulties in fault analysis in the distribution grid. Conventional overcurrent protection schemes can no longer meet the operational requirements of the distribution grid with the IIDG.

The power system requires the IIDG to adopt an LVRT control strategy, suppressing negative sequence current control strategy and fault current limiting measures, which makes the fault current characteristics of the IIDG different from that of the inertial power system. The conventional protection principles and relay coordination cannot meet the requirements of power system protection. In serious situations, this can lead to the failure or maloperation of the protection scheme.

Aiming at solving these issues, many researchers have made attempts to address the problems caused by the IIDG. In one study (Huang et al., 2014), the fault characteristics of the IIDG were analyzed when an asymmetrical or asymmetric fault occurs. The authors (Huang et al., 2014) concluded that the IIDG only feeds positive sequence current, but no negative sequence. Another study (Li et al., 2019), analyzed the output current of the inverter, which depends on the pre-fault operation state of the inverter and the positive sequence voltage drop on the post-fault. Other studies (Telukunta et al., 2017; Mahamedi and Fletcher, 2019) have pointed out that the integration of IIDG in the power grid will change the fault level and network topology. These fault levels are intermittent, and existing protection schemes may fail to operate due to pre-set conditions. This was addressed in a study (Fang et al., 2019) in which the analytical expression for the fault current of IIDG was derived based on predecessors, and it discusses the basic pattern of change of the short-circuit current characteristics.

One study proposed (Han et al., 2016) a multi-terminal transmission line differential protection scheme based on master-slave topology is proposed, according to the characteristics of the multi-point access of the IIDG, but this is only applicable to the distribution grid. In another experiment (Li et al., 2017), the power system connected with the IIDG was divided into strong and weak operation modes and studied respectively. It proved that phase current differential protection may have the risk of failed operation under weak system status. When the system is strong, it can still operate correctly, even though protection sensitivity is reduced. In (Han et al., 2018), a negative sequence current differential protection scheme and a multi-terminal current differential protection scheme are proposed according to the characteristics of suppressing the negative sequence current of new energy sources, which are mainly applicable to the IIDG with multi-T-connected. In (Chen et al., 2020), the differential impedance protection principle is proposed based on the variation relationship of the differential impedance and constrained impedance between normal operation, external faults, and internal faults. However, due to the use of voltage, it is necessary to consider the adverse effects of potential transformer disconnection, short-circuit faults, and other factors. Based on the short-circuit current output characteristics of IIDG, another study (Li et al., 2017) examined the relationship between the phase angle of the output current lagging voltage and the voltage drop at the grid connection point. According to the correlation, a protection criterion based on phase comparison was proposed. With the development of computer and communication technology, some studies (Zhang et al., 2019; Singh and Agrawal, 2019) have proposed a wide area protection scheme for distribution grid by using wide-area information and intelligent agent technology, which can better adapt to the operational conditions of the distribution grid, with various operation modes and complex fault characteristics. However, the application scenarios are limited due to heavy reliance on wide-area communication.

One study examined the impact mechanism of the IIDG on directional relay based on various fault components (Yang et al., 2016), concluding that the positive sequence and negative sequence directional elements are not available, while the zero-sequence directional relay is available. However, the zero-sequence directional relay can only reflect an asymmetric grounding fault. When gap grounding mode is adopted for the neutral point of the step-up transformer, there is no zero-sequence current on the IIDG side, making the application of zero-sequence directional relay difficult. In (Jia et al., 2017), a direction discrimination method based on phase comparison of positive sequence fault current and memory voltage is proposed. However, the memory voltage can only be used for a short time, and the proposed method is mainly for the distribution grid. To overcome the problems of insufficient sensitivity and reduced reliability of the traditional overcurrent protection, a protection scheme using the positive sequence components of the fault current is proposed in (Yang et al., 2018). However, the accuracy of the fault component measurement needs further research when grid-connected IIDG is present. Based on the impact analysis of the inverter grid connection on directional protection, the wavelet analysis is proposed in (Jia et al., 2019; Yang et al., 2020), to extract fault components lower than 3 kHz for the direction criterion. Since the inverter output also contains certain high-frequency components, its impact on the criterion needs to be further studied. According to the requirements of selectivity and the rapidity of wind power integration, two schemes of inverse time protection and directional protection are proposed in (Song et al., 2016; Tang et al., 2016) by using the least square method.

Due to the many challenges faced by the application of overcurrent protection, some researchers try to apply distance protection to the distribution grid with grid-connected IIDG. The main problem of distance protection in the neutral non-effective grounded distribution grid is that the lines are relatively short, and the measured impedance is too small to guarantee the measurement accuracy. The line impedance is smaller than the system impedance, and the phase to phase impedance relay is significantly affected by the fault resistance. The use of a positive sequence fault component to form pilot protection is proposed in another study (Zhou et al., 2019). This scheme is less affected by the fault characteristics of the IIDG connection, but it relies on the communication channel to exchange the direction information at both ends. The transient characteristics of the positive sequence voltage polarized impedance relay used for the grid-connected wind power plants are analyzed in a study (Li et al., 2012). The authors (Li et al., 2012) proposed the possible overreach risk of the zone I protection, while the zone II and zone III protection have the problem of delay in operation time. Aiming to address the problem of distance protection, which is easily affected by fault resistance, another study (Li et al., 2003)

proposed an adaptive protection scheme based on bus voltage sudden variable. This method could solve the problem of distance protection, overcoming fault resistance to a certain extent. However, this paper mainly focuses on the single-phase grounding fault of high-voltage and ultra-high-voltage transmission lines, and ways of applying them in the distribution grid with the IIDG needs further research.

Although some research has been carried out on the short-circuit current characteristics of new energy sources and their adverse impact on protection schemes, there are still many issues that remain unexplored. This article analyzes the impact of the IIDG on the operation of protection schemes in the distribution grid. The LVRT and the negative sequence current suppression control strategy modify the fault transient characteristics of the grid. This modification makes the application of traditional overcurrent protection all the more difficult. The requirements of selectivity and the sensitivity of the protection system in the distribution grid can no longer be met by legacy protection schemes in the presence of the IIDG. This paper proposes a positive sequence voltage fault component polarization impedance criterion, which can adaptively follow the fault resistance variation. Simulation verification shows that the criterion are less affected by the fault response characteristics of the IIDG. The distribution grid protection device based on the specialized SoC chip for power system has been developed on this basis and a trial-run has been successfully carried out on the industrial site.

ANALYSIS OF FAULT TRANSIENT CHARACTERISTICS OF DISTRIBUTION GRID WITH THE IIDG

The new energy source is directly connected to the grid through the inverter, and the photovoltaic array or wind turbine is isolated from the inverter through the DC bus. During the normal operation, active power is generated. When the power grid fails, the active power and reactive power control are carried out according to the LVRT strategy. When asymmetric faults such as phase-to-phase faults occur in the power grid, the output of the IIDG can suppress the negative sequence current.

Low Voltage Ride Through (LVRT) Control Strategy

The output power of the inverter is generally controlled by the decoupling control method of d and q vectors. The positive sequence voltage of the power grid is generally directed to the d-axis. The active and reactive power fed by the inverter to the power grid can be expressed as (1) in d and q coordinate:

$$\begin{cases} P = u_{gd}i_d + u_{gq}i_q = U_g i_d \\ Q = u_{gq}i_d - u_{gd}i_q = -U_g i_q \end{cases} \tag{1}$$

where u_{gd} and u_{gq} are the d and q axis components of the IIDG terminal voltage, i_d and i_q are the d and q axis components of output current from the inverter to the power grid, U_g is the terminal voltage of the IIDG. From **Eq. 1**, the active power output P by the inverter is proportional to the vector modulus of the grid voltage U_g and the d-axis component of the current. The output reactive power is inversely proportional to the vector modulus of the grid voltage U_g and the q-axis component of the current. The output active and reactive power can be controlled by adjusting the current of the d-axis and q-axis.

The LVRT control strategy requires that when a short circuit fault occurs in the power grid, the IIDG should not only remain grid-connected but also provide reactive power support as far as possible according to the depth of voltage drop. In addition, according to the current carrying capacity of the inverter, the current margin is used to generate active power as much as possible to reduce the influence of active power imbalance. It is generally believed that the over-current capacity of IIDG does not exceed two times the rated current. The requirements of different regions are slightly different. For example, in the grid code of the State Grid Corporation of China, the over-current capacity is required to be 1.2 times the rated current, and the limiting link is added at the output end of the power outer loop to limit the active and reactive current instructions. During LVTR, the output active and reactive current of distributed generation (I_{gdf}, I_{gqf}) (per unit) can be expressed as:

$$I_{gqf} = \begin{cases} 0, & \alpha > 0.9 \\ 2(1-\alpha), & 0.4 \le \alpha \le 0.9 \\ 1.2, & \alpha \le 0.4 \end{cases} \tag{2}$$

$$I_{gdf} = \min\left\{ I_{gdf0}, \quad \sqrt{1.2^2 - I_{gqf}^2} \right\} \tag{3}$$

where I_{gdf0} is the active current in the inner loop under normal operation; α is the positive sequence voltage amplitude at the terminal of the IIDG with lagging voltage drop.

Based on the above LVRT operation characteristics, the IIDG can be equivalent to a voltage controlled current source model. The expression is:

$$\dot{I}_{gf} = \sqrt{I_{gdf}^2 + I_{gqf}^2} \angle \arctan\left(I_{gqf} / I_{gdf} \right) \tag{4}$$

Fault Characteristics Under Asymmetric Fault Conditions

In the event of an asymmetric fault in the power grid, the terminal voltage of the IIDG will contain a positive sequence component and a negative sequence component. After Park's transformation, the negative sequence component will be changed into a frequency multiplication component in d-q coordinate, which makes the active and reactive power of IIDG output unable to accurately track the reference power, and becomes the superposition of DC and frequency multiplication AC. Moreover, the fluctuation degree of frequency multiplication AC increases with the increase of i_{dref}, that is, the more serious the voltage drop of the grid, the more obvious the fluctuation of frequency multiplication power component. To avoid the fluctuation of output power and track the reference power accurately, the phase-locked loop principle is often used to

calculate the amplitude of positive sequence voltage and fix the phase of positive sequence voltage in the case of asymmetric faults. By adopting the symmetrical positive sequence control method, IIDG only outputs positive sequence fault current after asymmetric fault, and the amplitude and phase of current are only related to the pre-fault operating state and the post-fault positive sequence voltage. This is quite different from the fault current characteristics of the traditional synchronous generator under asymmetric fault.

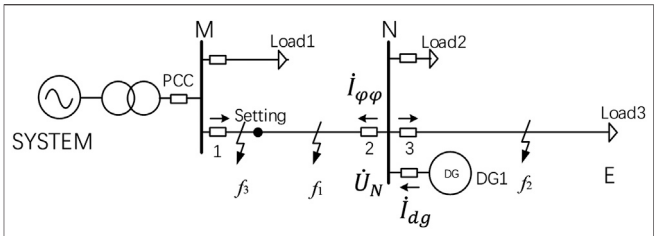

FIGURE 1 | Diagram of the distribution grid, connected with the IIDG.

Fault Characteristics Under Symmetric Fault Conditions

When a symmetrical fault occurs, like the analysis of asymmetric fault characteristics, the amplitude of fault current is related to the pre-fault state and the voltage drop is related to the post-fault. The maximum value is the current limiting value of the inverter, such as 1.2 times the rated current. The phase relationship between the terminal voltage and output current depends on the ratio of fault current d, q axis component i_d and i_q. If no load before failure, $i_d = 0$, the phase of short-circuit current will reach 90°. When the system operates at full load before failure, if the post-fault voltage drop is less, then i_d is larger, i_q is small, the phase of short-circuit current will be close to 0°. Therefore, in the case of a symmetrical fault, the variation range of the phase difference between the output current of the inverter and the terminal voltage is much larger than that of the synchronous generator, and the amplitude characteristics are also very different.

To summarize, the traditional protection system cannot adequately meet the requirements of distribution grid with the large presence of the IIDG, whether for symmetrical fault or asymmetric fault.

PRINCIPLES OF ADAPTIVE PROTECTION

Since the traditional overcurrent protection schemes are significantly affected by the operation mode of the system, it can no longer meet the requirements of the protection system and therefore needs to be complemented by a protection scheme adapted specifically for the distribution grid with the IIDG. To maintain adequate sensitivity without losing the selectivity of the protection scheme in the distribution grid with the IIDG, a new protection principle should be adapted that is least affected by the system impedance at the back side of the protection. Two main protection categories are less affected by the operation mode of the system: (1) pilot differential protection, which uses the current and voltage of each side; and, (2) impedance protection reflecting the impedance of the protected line.

Considering that the pilot differential protection relies on double-ended communication, this will add the burden of equipping the distribution grid with the communication infrastructure. In this paper, distance protection is used as the main protection scheme for the distribution grid with the IIDG. The main challenge of the distance protection scheme in this scenario is that the distances are relatively short in the distribution grid. With short lines, the operation characteristics of phase to phase distance protection are greatly affected by the fault resistance. If the neutral point is not directly grounded, it is not necessary to consider the influence of a single-phase grounding fault. Research on the influence of the fault resistance of phase to phase distance protection has not received much attention.

The key to improving the ability of distance protection to overcome the effect of fault resistance lies in the selection of appropriate polarization and the constitution of the phase comparison criterion. Based on the conventional positive sequence voltage polarization impedance relay, this paper proposes an adaptive protection criterion C1 with positive sequence voltage fault components as polarization quantity, as shown in **Eq. 5**:

$$C1: -90° \le \arg\frac{\dot{U}_{\varphi\varphi op}}{\dot{U}_{\varphi\varphi 1} - \dot{U}_{\varphi\varphi 1[0]}} \le 90° \tag{5}$$

In **Eq. 5**, $\dot{U}_{\varphi\varphi 1}$ is the busbar positive sequence component of post-fault voltage, and $\dot{U}_{\varphi\varphi 1[0]}$ is the corresponding busbar positive sequence component of pre-fault voltage. The compensation voltage $\dot{U}_{\varphi\varphi op}$ is as follows:

$$\dot{U}_{\varphi\varphi op} = \dot{U}_{\varphi\varphi} - \dot{I}_{\varphi\varphi} Z_{set} \tag{6}$$

where $\dot{U}_{\varphi\varphi}$、$\dot{I}_{\varphi\varphi}$ are the line voltage and line current measured by the protection device, Z_{set} is the setting impedance, $\varphi\varphi$ = AB , BC , CA.

In the distribution grid with a typical inverter connected, as shown in **Figure 1**, the research object is protection 2, close to bus N. When a two-phase short circuit occurs at f_1 point, $\dot{U}_{\varphi\varphi 1}$ and $\dot{U}_{\varphi\varphi 1[0]}$ at protection 2 can be expressed by **Eq. 7**, **8** respectively.

$$\begin{aligned}\dot{U}_{\varphi\varphi 1} &= \dot{E}_{\varphi\varphi N} - \dot{I}_{\varphi\varphi 1} Z_{N1} \\ &= \left(1 - C_{1N}\frac{Z_{N1}}{Z_{\Sigma 1} + Z_{\Sigma 2} + R_f}\right)\dot{E}_{\varphi\varphi N} \\ &= \left(1 - C_{1N}\frac{Z_{N1}}{Z_{\Sigma 1} + Z_{\Sigma 2} + R_f}\right)\left[\dot{I}_{\varphi\varphi}\left(Z_{N1} + Z_{Nm}\right)\right]\end{aligned} \tag{7}$$

$$\dot{U}_{\varphi\varphi 1[0]} \approx \dot{E}_{\varphi\varphi N} = \dot{I}_{\varphi\varphi}\left(Z_{N1} + Z_{Nm}\right) \tag{8}$$

In **Eq. 7**, **8**, $\dot{E}_{\varphi\varphi N}$ is the equivalent phase-to-phase potential of the N-side system in the composite sequence network, Z_{N1} is the positive sequence impedance of the N-side system, $\dot{I}_{\varphi\varphi 1}$ is the positive sequence component of the line current corresponding to the fault phase after the fault, $Z_{\Sigma 1}$ and $Z_{\Sigma 2}$ are the positive and negative sequence impedance of the equivalent system, R_f is the fault resistance of the short-circuit point, C_{1N} is the shunt

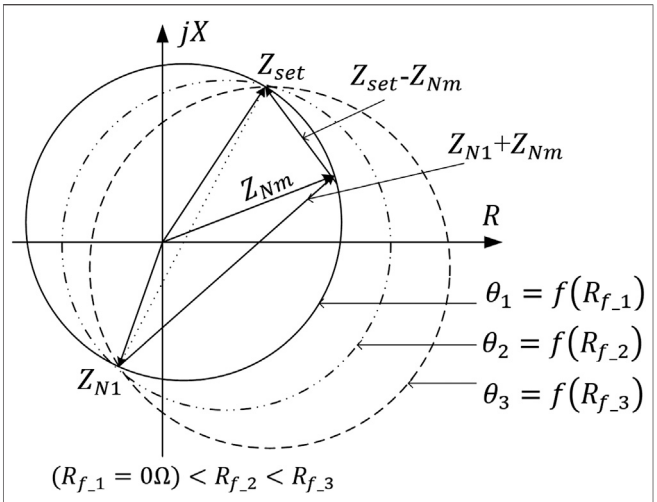

FIGURE 2 | Adaptive characteristics with the fault resistance of positive sequence voltage fault component polarized impedance relay when forward fault occurs.

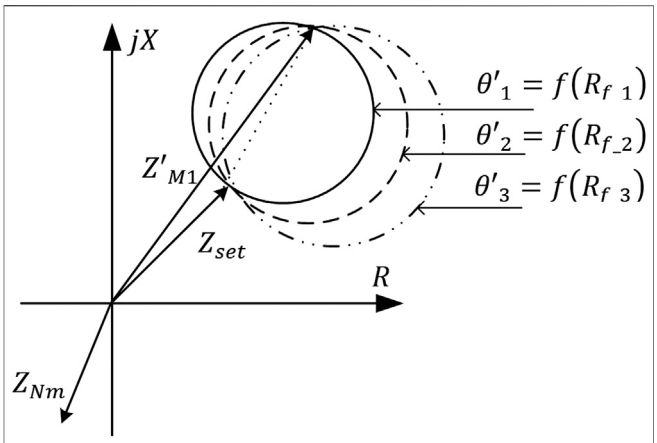

FIGURE 3 | Adaptive characteristics with the fault resistance of fault component positive sequence voltage polarized impedance relay when backward fault occurs.

coefficient of the positive sequence current N-side, and Z_{Nm} is the measured impedance of the N-side.

In **Eq. 7**, let:

$$K_c = \left(1 - C_{1N}\frac{Z_{N1}}{Z_{\Sigma 1} + Z_{\Sigma 2} + R_f}\right) \tag{9}$$

Therefore, (7) can be simplified as follows:

$$\dot{U}_{\varphi\varphi 1} = K_c\left[\dot{I}_{\varphi\varphi}\left(Z_{N1} + Z_{Nm}\right)\right] \tag{10}$$

By introducing (6), (8), and (10) into (5), we can get the following result:

$$-90° \le \arg\frac{\dot{U}_{\varphi\varphi} - \dot{I}_{\varphi\varphi}Z_{set}}{(K_c - 1)\dot{I}_{\varphi\varphi}\left(Z_{N1} + Z_{Nm}\right)} \le 90° \tag{11}$$

where $\dot{U}_{\varphi\varphi} = \dot{I}_{\varphi\varphi}Z_{Nm}$. By further simplification of **Eq. 11**, we achieve the following result:

$$-90° \le \arg\frac{Z_{Nm} - Z_{set}}{(K_c - 1)\left(Z_{Nm} + Z_{N1}\right)} \le 90° \tag{12}$$

By introducing (9) into $1/(K_c - 1)$ in **Eq. 12**, **13** is obtained as follows:

$$\frac{1}{(K_c - 1)} = -\frac{1}{C_{1N}}\frac{Z_{\Sigma 1} + Z_{\Sigma 2} + R_f}{Z_{N1}} \tag{13}$$

It is observed from **Eq. 13** that after neglecting the influence of the phase angle difference of $Z_{\Sigma 1}$, $Z_{\Sigma 2}$ and Z_{N1}, the influence of $1/(K_c - 1)$ on the phase comparison result of **Eq. 12** mainly comes from R_f. The characteristic of part $\arg\frac{Z_{Nm} - Z_{set}}{Z_{Nm} + Z_{N1}}$ in **Eq. 12** is completely consistent with that of the distance relay with positive sequence voltage polarization. As shown in **Figure 2**, the operation characteristics of the positive sequence voltage polarization impedance criterion are deflected by $\theta = f(R_f) = \arg\left(-\frac{1}{C_{1N}}\frac{Z_{\Sigma 1} + Z_{\Sigma 2} + R_f}{Z_{N1}}\right)$ with the change of R_f

Therefore, the operation characteristics of **Eq. 12** can be expressed as follows:

$$-90° - \theta \le \arg\frac{Z_{Nm} - Z_{set}}{Z_{Nm} + Z_{N1}} \le 90° - \theta \tag{14}$$

The dynamic adjustment of the operation characteristics can adaptively change the protection zone, and the ability of the protection criterion to overcome the influence of the fault resistance is significantly improved.

As can be seen from **Figure. 2**, when the forward fault occurs the operation characteristic contains the installation position, that is, the origin of coordinates. The positive sequence fault component, as a polarization quantity, can avoid the influence of the dead zone caused by the low positive sequence voltage of metallic fault at the near end of protection installation. Compared with the traditional positive sequence voltage polarization impedance relay, this characteristic is also suitable for a three-phase short circuit in the near zone and has a wide range of adaptability.

In the case of the phase-to-phase short circuit at point f_2 in the opposite direction of protection 2 in **Figure 1**, the current direction measured by protection 2 is opposite to the specified positive direction, i.e. $\dot{U}_{\varphi\varphi} = -\dot{I}_{\varphi\varphi}Z_{Nm}$.

Here

$$\begin{aligned}\dot{U}_{\varphi\varphi 1} &= \dot{E}_{\varphi\varphi M} + \dot{I}_{\varphi\varphi 1}Z'_{M1} \\ &= \left(1 - C_{1M}\frac{Z'_{M1}}{Z_{\Sigma 1} + Z_{\Sigma 2} + R_f}\right)\dot{E}_{\varphi\varphi M} \\ &= K'_c\left[-\dot{I}_{\varphi\varphi}\left(Z'_{M1} + Z_{Nm}\right)\right]\end{aligned} \tag{15}$$

In(15)

$$K'_c = \left(1 - C_{1M}\frac{Z'_{M1}}{Z_{\Sigma 1} + Z_{\Sigma 2} + R_f}\right) \tag{16}$$

$\dot{E}_{\varphi\varphi M}$ is the equivalent phase-to-phase potential of the M-side system in the composite sequence network, Z'_{M1} is the sum of

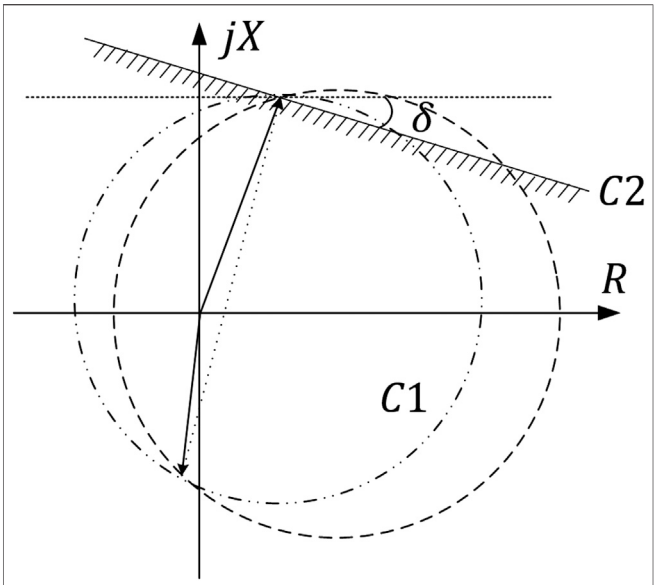

FIGURE 4 | Composite adaptive characteristics of the positive sequence voltage fault component polarized impedance relay when forward fault occurs.

positive sequence impedance of the M-side system and protected line. C_{1M} is the M-side shunt coefficient of the positive sequence current.

The pre-fault positive sequence voltage $\dot{U}_{\varphi\varphi 1[0]}$ is as follows:

$$\dot{U}_{\varphi\varphi 1[0]} \approx \dot{E}_{\varphi\varphi M} = -\dot{I}_{\varphi\varphi}\left(Z'_{M1} + Z_{Nm}\right) \tag{17}$$

By introducing (15) and (17) into **Eq. 5**, we can get the following result:

$$-90° \le \arg \frac{\dot{U}_{\varphi\varphi} - \dot{I}_{\varphi\varphi} Z_{set}}{-\left(K'_c - 1\right)\dot{I}_{\varphi\varphi}\left(Z'_{M1} + Z_{Nm}\right)} \le 90° \tag{18}$$

Eq. 18 is further simplified:

$$-90° \le \arg \frac{Z_{Nm} + Z_{set}}{-\left(K'_c - 1\right)\left(Z'_{M1} + Z_{Nm}\right)} \le 90° \tag{19}$$

By introducing **Eq. 16** into $1/-(K'_c - 1)$ in **Eq. 19**, we can obtain that:

$$\frac{1}{\left(K'_c - 1\right)} = -\frac{1}{C_{1M}} \frac{Z_{\Sigma 1} + Z_{\Sigma 2} + R_f}{Z'_{M1}} \tag{20}$$

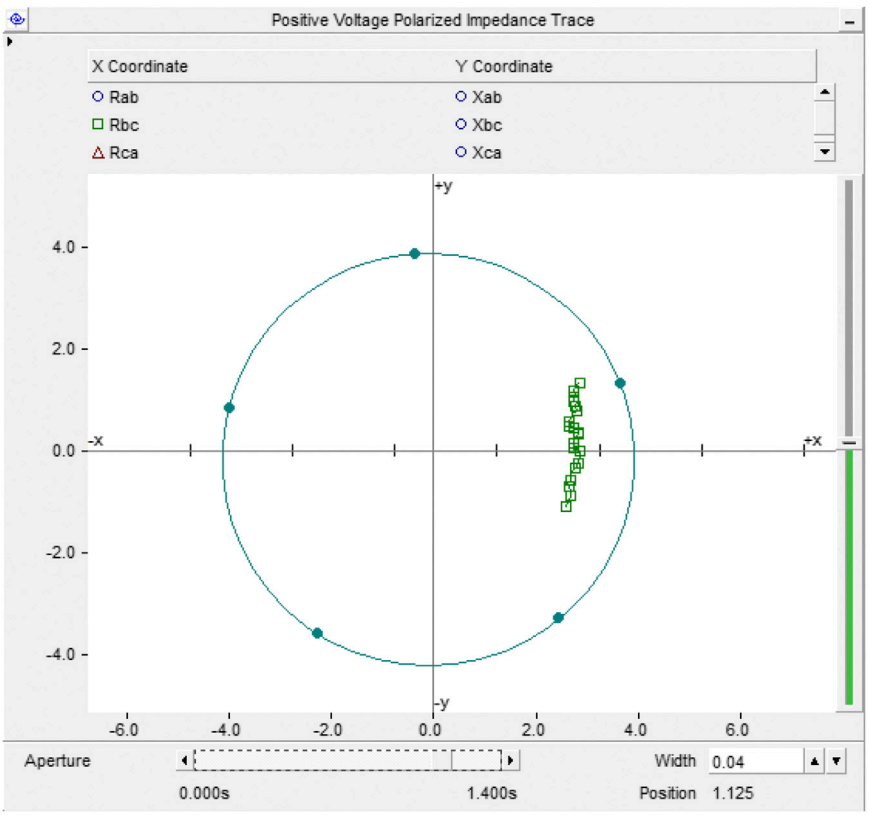

FIGURE 5 | When the protection is at the receiving end, the PCC is connected to the grid. The measured impedance trajectory and operation characteristics of the positive sequence voltage fault component polarized impedance relay at a BC phase fault with a fault resistance (2Ω) at 2.5 km forward.

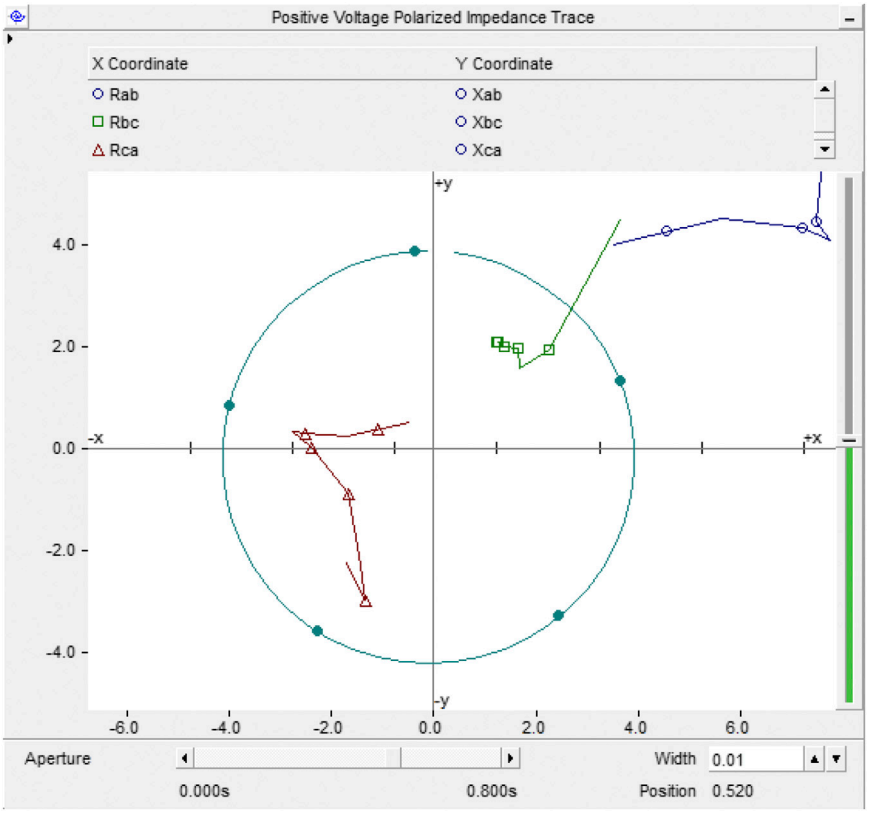

FIGURE 6 | When the protection is at the sending end, the PCC is disconnected from the grid. The measured impedance trajectory and operation characteristics of the positive sequence voltage fault component polarized impedance relay at a BC phase fault with a fault resistance (2Ω) at 2.5 km forward.

With the increase of the transition resistance, the operation characteristics will be deflected in the angle of $\theta' = f(R_f) = \arg\left(-\frac{1}{C_{1M}}\frac{\dot{Z}_{\Sigma 1}+\dot{Z}_{\Sigma 2}+R_f}{\dot{Z}'_{M1}}\right)$. Therefore, the operation characteristics of **Eq. 19** can be expressed as follows:

$$-90° - \theta' \le \arg\frac{Z_{Nm} + Z_{set}}{-\left(Z_{Nm} + Z'_{M1}\right)} \le 90° - \theta' \tag{21}$$

Figure. 3 shows the operation characteristics of positive sequence fault component polarization impedance relay under the reverse direction fault. The influence of the fault resistance makes the protection zone deviate. However, when the fault occurs in the opposite direction, the measured impedance falls in quadrants III and IV which is far away from the operating area of the throw-up circle, so the characteristic still has explicit directionality.

As this is affected by the fault resistance in a short transmission line, relay over-reaching problems may exist. In coordination with the operation characteristics shown in **Eq. 5**, a reactance line C2 with downward deflection angle is added at the end of the protection range, as shown in **Eq. 22**:

$$C2: 180° + \varphi \le \arg(Z_{Nm} - Z_{set}) \le 360° + \varphi \tag{22}$$

The "AND" logic is composed of two characteristics of **Eq. 5**, **22**, that is, $C1 \cap C2$ combination constitutes the operation characteristics of protection, as shown in **Figure. 4**.

CASE STUDY

The proposed protection principle is verified and analyzed by using a typical distribution grid simulation test system with the IIDG connected as shown in **Figure. 1**. The system voltage level is 10kV, the transformer capacity is 10MVA, and the neutral point is grounded by Petersen Coil. The length of the overhead line MN in the distribution grid is 5km, the parameter is $x_1 = 0.343\Omega$/km, $r_1 = 0.276\Omega$/km. The maximum output current of grid connected photovoltaic inverter is limited to 1.2 times of the rated current, and the rated capacity is 1MVA. Considering the similar fault transient characteristics of the grid-connected photovoltaic power converters and direct-driven wind power converters, only the influence of grid-connected photovoltaic power converters is used in the simulation described in this paper, which assessed whether the proposed scheme could be applied. Under the normal operating conditions of the system, PQ control is adopted, and active power is delivered according to the maximum power factor of 0.9. When the fault occurs, the distributed generation adopts LVRT control strategy. The setting range of protection Zone I is set

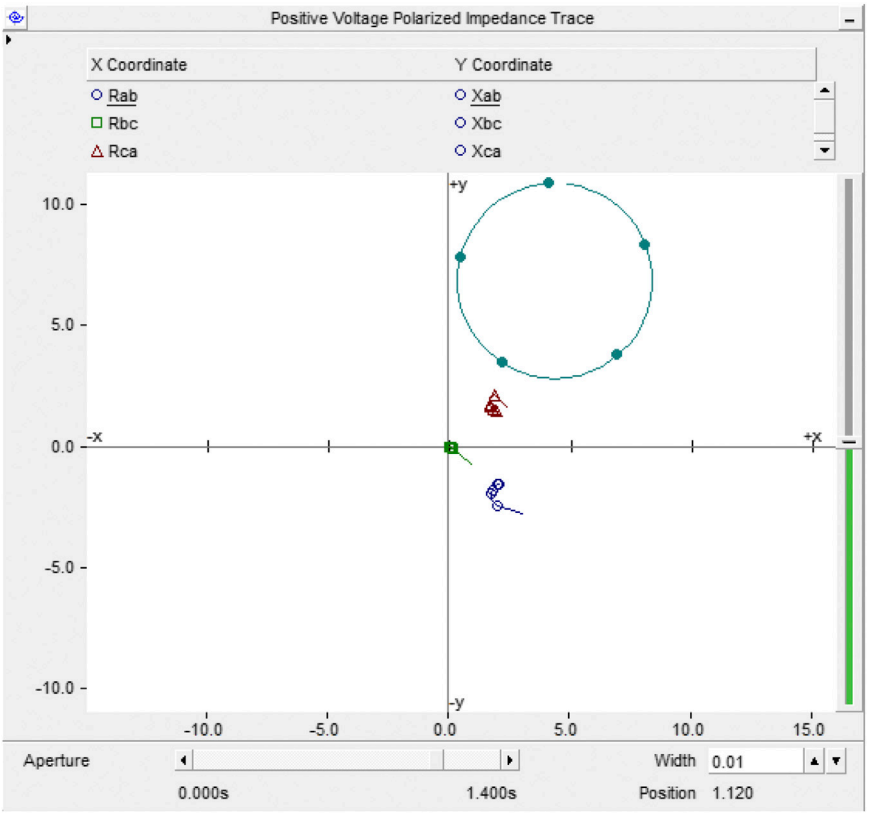

FIGURE 7 | When the protection is at the receiving end, the PCC is connected to the grid. The measured impedance trajectory and operation characteristics of the positive sequence voltage fault component polarized impedance relay at a BC phase metallic fault 0.1 km backward.

according to 80% of line impedance. Based on PSCAD/EMTDC simulation platform, the simulation model is established to simulate the phase-to-phase fault and three-phase fault at different positions of f_1, f_2 and f_3 of the IIDG under different output conditions. The principle of adaptive positive sequence voltage fault component polarization impedance relay, as proposed in *Analysis of Fault Transient Characteristics of Distribution Grid with the IIDG*, was calculated and verified by using the simulation output, and its rules for change were analyzed.

In the simulation system shown in **Figure 1**, the point of common coupling (PCC) is closed, the IIDG is connected to the grid, and protection 2 is at the receiving end. When the protected line is 2.5 km away from the protection installation, a short circuit between the BC phase with a 2Ω fault resistance occurs. The trajectory of the protection measurement impedance 20ms after the fault occurs is shown in **Figure 5**. The operation characteristic of C1 shown in **Eq. 5** fluctuates about $\alpha_{BC} = \arg\frac{\dot{U}_{BCop}}{\dot{U}_{BC1}-\dot{U}_{BC1[0]}} = 69°$ during the steady-state fault process. The operation conditions of **Eq. 5** are satisfied.

Figure 6 shows the track of measured impedance when the protection is at the sending end after the PCC is disconnected and the same fault occurs. At the same time, $\alpha_{BC} = -2°$ and the operation criterion C1 also meets the requirements.

TABLE 1 | Simulation Result of phase BC fault occurring under the protection operation in receiving end.

Fault Resistance	Fault Location					
	Internal			Backward		Forward out range
	0.1 km	2.5 km	3.8 km	0.1 km	2 km	7 km
0.5Ω	35°	11.7°	75°	−178°	−193°	131°
2.0Ω	73°	69°	82°	−182°	−202°	155°
4.0Ω	*109°*	*129°*	*115°*	−210°	−210°	193°

TABLE 2 | Simulation Result of Phase-to-Phase fault occurring under the protection operation in sending end.

Fault Resistance	Fault Location					
	Internal			Backward		Forward out range
	0.1 km	2.5 km	3.8 km	0.1 km	2 km	7 km
0.5Ω	−74°	−54°	−30°	−177°	−196°	143°
2.0Ω	−7°	−2°	5°	183°	179°	191°
4.0Ω	40°	51°	50°	157°	167°	207°

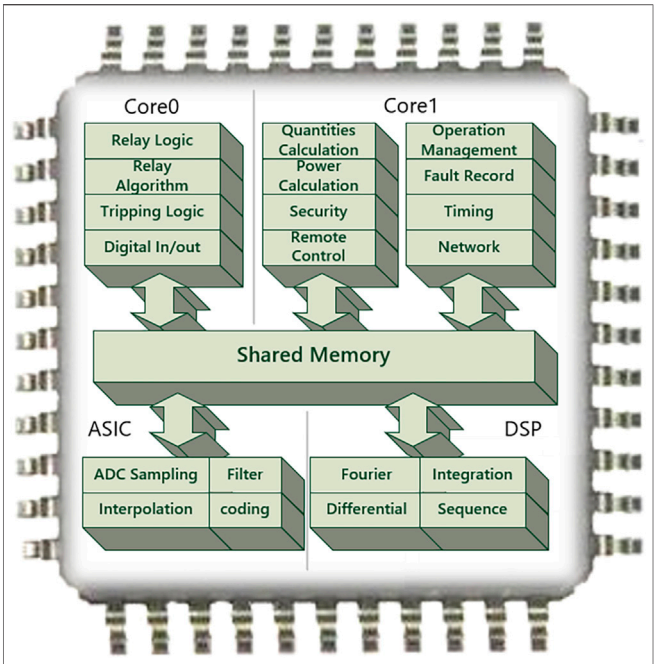

FIGURE 8 | Schematic diagram of specialized multi-core heterogeneous SoC chip for power system.

Figure 7 shows the operation trajectory of impedance measurement when the protection is at the receiving end and the close-in fault occurs in the opposite direction. When $\alpha = -182°$ in the criterion C1, the condition of the criterion is not satisfied. It can be seen from **Figure 7** that the protection cannot operate correctly according to the principle of measurement impedance.

For the other faults, according to the opening and closing of the PCC switch, various fault types of protection 2 under the sending end and receiving end are simulated respectively. The simulation results of the two-phase short circuit are shown in **Table 1** and **Table 2**. The simulation results of the three-phase short-circuit fault are the same as that of the phase-to-phase short-circuit fault. For the sake of brevity, not all are listed here.

For common faults, **Table 1** and **Table 2** show that the protection can normally clear various types of faults. However, when the protection system operates at the receiving end, the system impedance is far less than the distribution composite equivalent impedance including the IIDG. Due to the strong effect of the opposite side system and the short distribution line, when the phase to phase short circuit with the transition resistance of 4.0 Ω occurs, the operating condition of the protection criterion cannot be satisfied. In this case, the selectivity of operation can only be ensured by the backup protection or the protection principle based on both-end information.

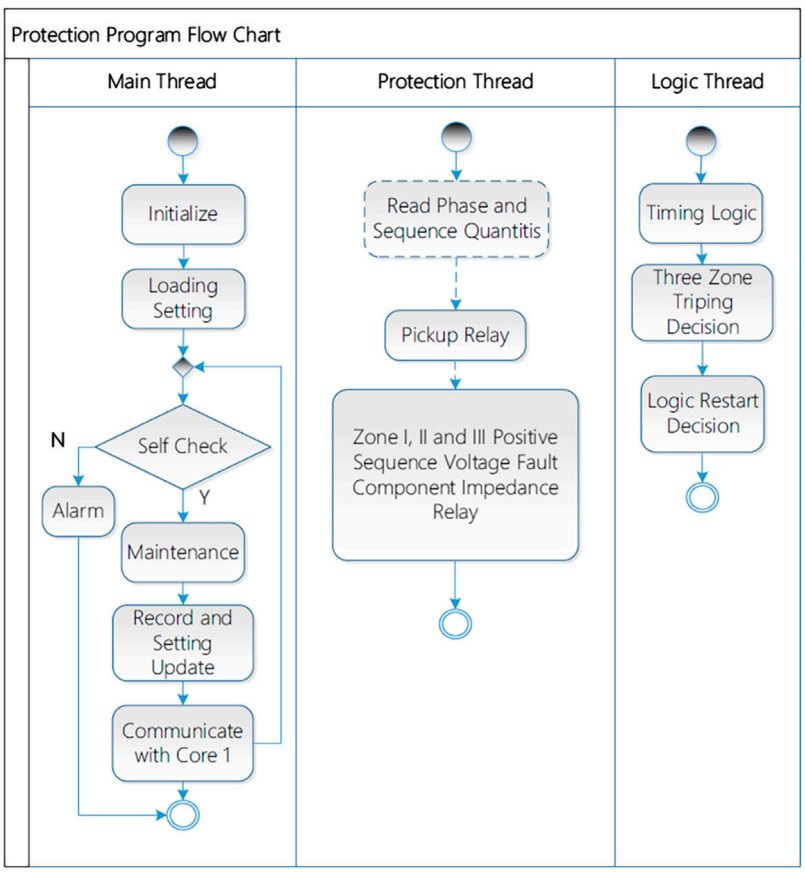

FIGURE 9 | Flow chart of distance protection program running on core0 of SoC chip for power system.

FIGURE 10 | The photos of distance protection device based on SoC chip special for power system and industrial field testing.

IMPLEMENTATION OF DISTRIBUTION GRID PROTECTION BASED ON SPECIALIZED SOC FOR POWER SYSTEM

To make the proposed protection principle applicable, a 35 kV/10kV distance protection based on the specialized multi-core heterogeneous SoC (FUXI-M) for the power system was developed. The chip fully considers the requirements of high-efficiency parallel processing units of a power-specific algorithm, power consumption, and application economy. It combines the Discrete Fourier algorithm, sequence quantities calculation, filtering, interpolation, and the other calculation tasks originally implemented by general-purpose CPUs, as well as communication encoding and decoding. General tasks such as security encryption are integrated into an independent core on-chip for realizing power-specific algorithms, forming a power-specific multi-core heterogeneous SoC chip as shown in **Figure 8**. The functional calculation of distribution grid protection is realized by using the parallel calculation of independent hardware units in the chip, which greatly improves the execution efficiency of the algorithm.

According to the positive sequence voltage fault component polarization impedance criterion proposed in this paper, it constitutes three-zone distance protection adapted to the operational requirements of the distribution grid. Since the primary computing architecture has been integrated into parallel processing in independent ASIC core and signal processing co-processors (DSP), the distance protection program and logic calculation operating at Core 0 is simple and efficient. As shown in **Figure 9**, the program flow is divided into three main threads for execution. The protection and logic threads only need to maintain simple sequential execution. The thread processing and program logic structure are greatly simplified, and the execution time is also significantly reduced.

The developed protection device is shown in **Figure 10**. It was put into trial operation at a 110kV Ruiyan substation in Foshan, China in early 2019. During several external fault tests, no maloperation of external fault was observed.

CONCLUSION

This article has analyzed the impact of the IIDG on the protection system of the distribution grid. For the protection system installed on the near-IIDG side, due to the LVRT control characteristics of the IIDG, the current fed to the fault point was closely related to the busbar voltage of the IIDG, and the maximum short-circuit current was also limited to a low level. The negative sequence current suppression control strategy also changes the transient characteristics measured by the protection scheme. This makes the application of traditional overcurrent protection difficult and the requirements of selectivity and sensitivity can no longer be met by the legacy protection schemes in the distribution grid.

Based on the positive sequence voltage polarization impedance criterion, this paper proposes an impedance criterion based on positive sequence voltage fault component polarization, which can adaptively follow the fault resistance variation. Verification of

these findings with a simulation showed that the criterion was less affected by the fault response characteristics of the IIDG under fault conditions. A distribution grid protection device, based on the specialized SoC for a power system, was developed and a trial-run on the industrial site has been carried out. The operating performance of the new protection device meets the requirements of the distribution grid with the IIDG. The proposed protection scheme and the implementation has broad application opportunities in the distribution grid with the IIDG.

DATA AVAILABILITY STATEMENT

The raw data supporting the conclusions of this article will be made available by the authors, without undue reservation.

ETHICS STATEMENT

Written informed consent was obtained from the individual for the publication of any potentially identifiable images or data included in this article.

AUTHOR CONTRIBUTIONS

PL conceived of the proposed idea and supervised the work. WX performed the device development. XY planned and carried out the simulations. XZ carried out the experiments. LL verified the analytical methods. QY contributed to the interpretation of the results. WC developed the theory and took the lead in writing the manuscript. All authors provided critical feedback and helped shape the research, analysis and manuscript.

FUNDING

This work was supported by the National Key R&D Program of China under Grant 2018YFB0904900, 2018YFB0904902.

SUPPLEMENTARY MATERIAL

The Supplementary Material for this article can be found online at: https://www.frontiersin.org/articles/10.3389/fenrg.2020.614292/full#supplementary-material.

REFERENCES

Chen, G., Liu, Y., and Yang, Q. (2020). Impedance differential protection for active distribution network. *IEEE Transactions on Power Delivery* 35, 25–36. doi:10.1109/TPWRD.2019.2919142

Fang, Y., Jia, K., Yang, Z., Li, Y., and Bi, T. (2019). Impact of inverter-interfaced renewable energy generators on distance protection and an improved scheme. *IEEE Transactions on Industrial Electronics* 66, 7078–7088. doi:10.1109/TIE.2018.2873521

Han, B., Li, H., Wang, G., Zeng, D., and Liang, Y. (2018). A Virtual multi-terminal current differential protection scheme for distribution networks with inverter-interfaced distributed generators. *IEEE Transactions on Smart Grid* 9, 5418–7088. doi:10.1109/TSG.2017.2749450

Han, B., Wang, G., Li, H., and Zeng, D. (2016). "An improved pilot protection for distribution network with inverter-interfaced distributed generations," in 2016 IEEE PES asia-pacific power and energy engineering conference (APPEEC), Xi'an, October 25–28, 2016. doi:10.1109/APPEEC.2016.7779949

Huang, W., Nengling, T., Zheng, X., Fan, C., Yang, X., and Kirby, B. J. (2014). An impedance protection scheme for Feeders of active distribution networks. *IEEE Transactions on Power Delivery* 29, 1591–1602. doi:10.1109/TPWRD.2014.2322866

Jia, K., Gu, C., Xuan, Z., Li, L., and Lin, Y. (2017). Fault Characteristics analysis and line protection design within a large-scale photovoltaic power plant. *IEEE Transactions on Smart Grid*.9, 4099–4108. doi:10.1109/TSG.2017.2648879

Jia, K., Yang, Z., Fang, Y., Tianshu, B., and Sumner, M. (2019). Influence of inverter-interfaced renewable energy generators on directional relay and an improved scheme. *IEEE Transactions on Power Electronics* 34, 11843–11855. doi:10.1109/TPEL.2019.2904715

Li, Q., Yong-jun, Z., Wei-peng, Y., and Feng, L. (2012). "A study on influence of wind power on positive sequence voltage polarized impedance relay," in 2012 Power Engineering and Automation Conference, Wuhan, September 18–20, 2012. doi:10.1109/PEAM.2012.6612485

Li, Y., Jia, K., Bi, T., Yan, R., Li, W., and Liu, B. (2017). "Analysis of line current differential protection considering inverter-interfaced renewable energy power plants," in 2017 IEEE PES Innovative Smart Grid Technologies Conference Europe (ISGT-Europe), Torino, September 26–28, 2017. doi:10.1109/ISGTEurope.2017.8260157

Li, W., He, J., Zhang, D., and Zhang, Q. (2017). Directional pilot protection based on fault current for distribution network with Distributed Generation (DG). *The Journal of Engineering* 2017, 1327–1331. doi:10.1049/joe.2017.0546

Li, P., Kong, X., Han, J., Zhang, Z., and Yin, X. (2019). "Research on low voltage ride through strategy and fault calculation equivalent model of power electronic transformer," in 2019 4th international conference on intelligent green building and Smart grid (IGBSG), Hubei, Yichang, China. September 6–9, 2010. doi:10.1109/IGBSG.2019.8886267

Li, B., De-shu, C., Xiang-gen, Y., Yi, Z., and Yu-feng, H. (2003). Study on the new adaptive MHO relay. *Proceedings of the CSEE* 23, 80–83.

Mahamedi, B., and Fletcher, J. E. (2019). Trends in the protection of inverter-based microgrids. *IET Generation, Transmission and Distribution* 13, 4511–4522. doi:10.1049/iet-gtd.2019.0808

Singh, M., and Agrawal, A. (2019). Voltage–current–time inverse-based protection coordination of photovoltaic power systems. *IET Generation, Transmission and Distribution* 13, 794–804. doi:10.1049/iet-gtd.2018.6143

Song, G., Wang, X., Chang, Z., Tang, J., and Liu, P. (2016). "A novel protection method of collecting power lines in PMSG wind farm," in 2016 IEEE PES asia-pacific power and energy engineering conference (APPEEC), Xi'an, October 25–28, 2016. doi:10.1109/APPEEC.2016.7779854

Tang, J., Song, G., Wang, X., and Chang, W. (2016). "A novel directional relay applicable to power system with wind farms," in 2016 IEEE PES asia-pacific power and energy engineering conference (APPEEC), Xi'an, October 25–28, 2016. doi:10.1109/APPEEC.2016.7779860

Telukunta, V., Pradhan, J., Agarwal, A., Singh, M., and Srivani, S. G. (2017). Protection challenges under bulk penetration of renewable energy resources in power systems: a review. *CSEE Journal of Power and Energy Systems* 3, 365–379. doi:10.17775/CSEEJPES.2017.00030

Yang, J., Zhou, C., and Zou, G. (2018). "A protection scheme based on positive sequence fault component for active distribution networks," in 2018 2nd IEEE Conference on Energy Internet and Energy System Integration (EI2), Beijing, October 20–22, 2018. doi:10.1109/EI2.2018.8582469

Yang, Z., Jia, K., Fang, Y., Zhu, Z., Yang, B., and Bi, T. (2020). High-frequency Fault Component-based distance protection for large renewable power plants. *IEEE Transactions on Power Electronics* 35, 10352–10362. doi:10.1109/TPEL.2020.2978266

Yang, H., Zhang, Z., Yin, X., Xiao, F., Qi, X., and Ye, Y. (2016). "Study of the collector-line-current-protection setting in centralized accessed double-fed wind farms," in 2016 IEEE Power and Energy Society General Meeting (PESGM), Boston, MA, October 20–22, 2018. doi:10.1109/PESGM.2016.7741664

Zhang, F., Mu, L., and Guo, W. (2019). An integrated wide-area protection scheme for active distribution networks based on fault components principle. *IEEE Transactions on Smart Grid* 10, 392–402. doi:10.1109/TSG.2017.2741060

Zhou, C., Zou, G., Yang, J., and Lu, X. (2019). "Principle of pilot protection based on positive sequence fault component in distribution networks with inverter-interfaced distributed generators," in 2019 IEEE PES GTD grand international conference and exposition asia (GTD asia), Bangkok, Thailand, March 19–23, 2019. doi:10.1109/GTDAsia.2019.8716011

Conflict of Interest: PL, WX, and LL was employed by the CSG, Guangzhou, China. QY was employed by the Sifang Automation Co., Ltd., Beijing, China.

The remaining authors declare that the research was conducted in the absence of any commercial or financial relationships that could be construed as a potential conflict of interest.

frontiers in Energy Research

ORIGINAL RESEARCH
published: 08 January 2021
doi: 10.3389/fenrg.2020.615870

Three-Phase Four-Wire OPF-Based Collaborative Control of PV Inverter and ESS for Low-Voltage Distribution Networks With High Proportion PVs

*Jinwei Fu[1], Tianrui Li[2], Shilei Guan[1], Yan Wu[1], Kexin Tang[1], Yan Ding[1] and Zhi Song[2]**

[1]Beijing Key Laboratory of Distribution Transformer Energy-Saving Technology, China Electric Power Research Institute, Beijing, China, [2]College of Information and Electrical Engineering, China Agricultural University, Beijing, China

The use of photovoltaic reactive power and energy storage active power can solve the problems of voltage violation, network loss, and three-phase unbalance caused by photovoltaic connection to low-voltage distribution networks. However, the three-phase four-wire structure of the low-voltage distribution network brings difficulties to power flow calculation. In order to achieve photovoltaic utilization through optimal power flow, a photovoltaic-energy storage collaborative control method for low-voltage distribution networks based on the optimal power flow of a three-phase four-wire system is proposed. Considering the amplitude and phase angle of voltage and current, a three-phase four-wire node admittance matrix was used to establish the network topology of the low-voltage distribution network. Also, to minimize the network loss, the three-phase unbalance and voltage deviation. a multi-objective optimization model based on three-phase four-wire network topology was established considering the voltage constraints, reverse power flow constraints and neutral line current constraints. Through improving the node admittance matrix and model convexity, the complexity of solving the problem is reduced. The CPLEX algorithm package was used to solve the problem. Based on a 21-bus three-phase four-wire low-voltage distribution network, a 24-h multi-period simulation was undertaken to verify the feasibility and effectiveness of the proposed scheme.

Keywords: low voltage distribution network, optimal power flow, voltage violation, three-phase unbalance, network losses, energy storage system

OPEN ACCESS

Edited by:
Haoran Ji,
Tianjin University, China

Reviewed by:
Lv Chaoxian,
China University of Mining and Technology, China
Xiaoxue Wang,
Hebei University of Technology, China

****Correspondence:***
Zhi Song
sy20193081440@cau.edu.cn

Specialty section:
This article was submitted to Smart Grids, a section of the journal Frontiers in Energy Research

Received: *10 October 2020*
Accepted: *19 November 2020*
Published: *08 January 2021*

Citation:
Fu J, Li T, Guan S, Wu Y, Tang K, Ding Y and Song Z (2021) Three-Phase Four-Wire OPF-Based Collaborative Control of PV Inverter and ESS for Low-Voltage Distribution Networks With High Proportion PVs. Front. Energy Res. 8:615870. doi: 10.3389/fenrg.2020.615870

INTRODUCTION

In recent years, with the rapid development of economy, environmental pollution and the energy crisis are being increasingly prominent. In order to achieve the sustainable energy development, photovoltaic and other renewable energy power generation has been vigorously promoted (Zehar and Sayah, 2008). However, large-scale household photovoltaic integration will affect the node voltage and network losses of the three-phase four-wire structure of the low-voltage distribution network. The mismatch between household photovoltaic generation and household loads causes the violation of the upper voltage limit during the day and the lower limit in the evening (Aziz and Ketjoy, 2017). In addition, the three-phase four-wire structure of the low-voltage distribution network will lead to three-phase unbalances if there are three-phase loads and asymmetric line

parameters (Pansakul and Hongesombut, 2014). Therefore, it is significant to research on the photovoltaic utilization for a three-phase four-wire system of the low-voltage distribution network.

At present, a large amount of literature has been carried out on photovoltaic utilization in the distribution network. Voltage control can be performed by adjusting the on-load tap-changer tap position (Liu et al., 2012). However, as a result of the limitation in the tap position, the amount of voltage regulation is non-continuous. Also, frequently regulation of taps will cause the reduction in transformers service life. Another method is to reduce the photovoltaic active power (Tonkoski, 2009; Reinaldo et al., 2011) to suppress the occurrence of over-voltage, however, this will reduce the income of photovoltaic owners. In addition, this method only performs voltage control and will not improve the photovoltaic utilization of the distribution network. The photovoltaic inverter's reactive power regulation capability (Qian et al., 2018) can be used to achieve photovoltaic utilization. Compared with the previous two methods, this method has a smoother controllable volume, and will not require additional investment or loss of generation revenues. However, there may be shortcomings of insufficient reactive power resulting in unsatisfactory voltage control. At present, energy storage equipment is also widely used in the voltage control after the low-voltage distribution network is connected to photovoltaic. In particular, a large number of literatures have studied the coordinated control method of energy storage and reactive power inverter (Zhang et al., 2020). This strategy can effectively suppress the voltage over limit, make full use of equipment capacity through the coordination of equipment, greatly reduce the cost of voltage regulation and network loss. Although there is one more neutral line in the three phase four wire system than the three phase four wire system, the control strategy adopted by the three phase three wire system is still applicable to the three phase four wire system. Therefore, if the investment cost is considered, for the three-phase three-wire low-voltage distribution network and the three-phase four-wire low-voltage distribution network with the same load and control equipment, there is only a neutral line gap in their investment costs.

The OPF problem of the distribution network needs to consider the feasibility of the model and the solution. In terms of the model, the OPF problem is to find the optimal state of a controllable variable of the power grid, so that the objective functions such as network loss and operating cost of the distribution network will reach the optimization. Literature (Gill et al., 2014) is based on the premise of ensuring the safe operation of the power grid, and aims at maximizing the photovoltaic power generation and its benefits to establish a dynamic optimal power flow model of an active power distribution network. Literature (Alsenani and Paudyal, 2018) aims to minimize the network loss by proposing an OPF model to solve the three-phase unbalance in the distribution network. However, the above literature ignores that the low-voltage distribution network is actually a three-phase four-wire system. The neutral wire makes the three-phase three-wire system and the three-phase four-wire system essentially different in calculation methods and other aspects (Bozchalui and Sharma, 2014). The neutral line voltage and current, and the phase line voltage and current should meet the Kirchhoff's law, which cannot be directly obtained through methods similar with the symmetrical components in a three-phase three-wire system. The three-phase three-wire model cannot accurately reflect the three-phase unbalance. However, there are relatively few researches on the OPF model of three-phase four-wire system.

For the OPF solution, scholars have established the OPF model as a linear or non-linear programming model and directly solved it based on artificial intelligence algorithms such as genetic algorithm (Martins and Carmenlt, 2011), particle swarm algorithm (Niknam et al., 2012), etc. However, the solution speed is slow and can easily fall into local optimization instead of the global. Other scholars used the convex model of convexity relaxation, which first eliminated the phase angle of voltage and current, and then used a second-order cone relaxation to convexify the original model (Bose et al., 2016; Tian et al., 2016; Ju et al., 2017; Zafar et al., 2020). However, since OPF solutions such as second-order cones need to eliminate the phase angle between voltage and current, this method cannot calculate the voltage and current on the neutral line. Therefore, it cannot be applied to three-phase four-wire system. The research at present is only to solve some specific problems, such as the minimization of network loss, three-phase unbalance, etc. Few Hardly any attention has been paid to the actual three-phase four-wire system model of low-voltage distribution networks. No effective solution method has been proposed for the three-phase four-wire OPF model. It is hence necessary to propose a calculation method for OPF of a three-phase four-wire distribution network.

The main contributions of this paper are summarized as follows.

(1) Due to the lack of research on three-phase four-wire SYSTEM OPF model in existing literature studies, this paper establishes an OPF model based on the optimal coordinated control of photovoltaic power generation and energy storage for three-phase four-wire low-voltage distribution network, aiming at network loss, three-phase imbalance and voltage deviation, and taking neutral line voltage, photovoltaic and energy storage as constraints.
(2) As it is discussed that the OPF solution method in present research is not applicable to the model in this paper, a convex process solution of optimal power flow model based on photovoltaic utilization in the low-voltage distribution network is proposed. Based on the established three-phase four-wire low-voltage distribution network optimal power flow model, all the concave functions in the model are converted into convex functions, Thereafter, the three-phase four-wire OPF model can be efficiently solved.

The remaining paper is structured as follows. **Section 2** provides the mathematical formulations of the three-phase four-wire low-voltage distribution network topology and low-voltage components containing photovoltaic and energy storage.

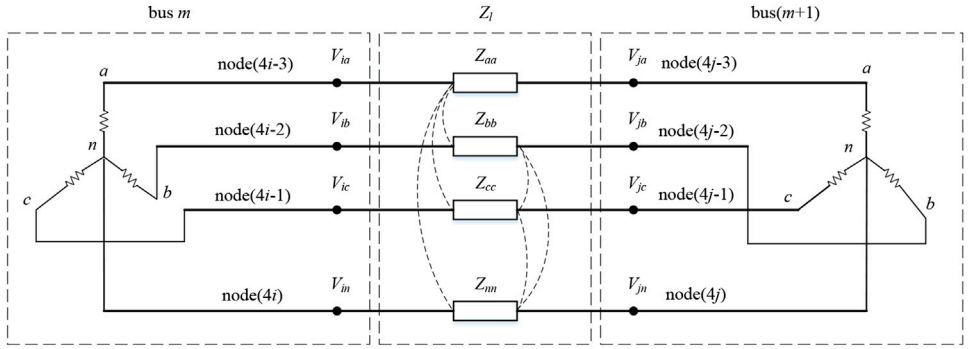

FIGURE 1 | Model of the three-phase four-wire low voltage distribution network.

Section 3 establishes the coordinated control model of photovoltaic and energy storage in a three-phase four-wire system low-voltage distribution network. **Section 4** proposes a solution method based on the three-phase four-wire optimal power flow. **Section 5** obtains the effectiveness of the proposed optimization method through simulation. **Section 6** concludes the study.

THREE-PHASE FOUR-WIRE LOW VOLTAGE DISTRIBUTION NETWORK EQUATION WITH PHOTOVOLTAIC AND ENERGY STORAGE HEADINGS

Network Equations Containing Photovoltaic and Energy Storage in a Three-phase Four-Wire Low Voltage Distribution Network

Network Topology of a Three-phase Four-Wire Low Voltage Distribution Network

The low-voltage distribution network (LVDN) in China adopts a three-phase four-wire structure. The distribution network model between two busbars (m-1) and m is shown in **Figure 1**. This model has only one reference node, which is the neutral node at the beginning of the line. All other nodes take this as the reference point. The model contains two busbars (m-1) and m. Each busbar consists of four nodes, which are (4i-3), (4i-2), (4i-1), (4i), and (4j-3), (4j-2), (4j-1), and (4j) representing the three phases of a, b, and c on busbars (m-1) and m respectively, and the neutral line n. Each phase line has its own impedance, and the coupling relationship between each phase line is expressed by mutual impedance. Phase a, b, and c lines are connected to the neutral line through a load to form a closed loop.

Branch Model

According to the topology of the LVDN, the three-phase four-wire system between any two busbars (m-1) and m can be represented by a 4 × 4 series impedance matrix.

$$Z_{l,m} = \begin{bmatrix} Z_{aa} & Z_{ab} & Z_{ac} & Z_{an} \\ Z_{ba} & Z_{bb} & Z_{bc} & Z_{bn} \\ Z_{ca} & Z_{cb} & Z_{cc} & Z_{cn} \\ Z_{na} & Z_{nb} & Z_{nc} & Z_{nn} \end{bmatrix} \tag{1}$$

where Z_{gg} is the diagonal element of the series impedance matrix, which is the self-impedance of the three phases of a, b, and c and the neutral line n; Z_{gh} is the off-diagonal element of series impedance matrix $(g \neq h)$ which is the mutual impedance between three-phase a, b, c and neutral line n.

In order to obtain the overall model of the LVDN, the calculation formulas are all in matrix. Therefore, the admittance matrix Y of a LVDN node with m buses can be expressed as:

$$Y_l = \begin{bmatrix} Z_{l,1}^{-1} + \sum\limits_{k \in c(1)} Z_{l,k}^{-1} & \cdots & -\left(Z_{l,m}^{-1} + \sum\limits_{k \in c(m)} Z_{l,k}^{-1}\right) \\ \vdots & \ddots & \vdots \\ -\left(Z_{l,m}^{-1} + \sum\limits_{k \in c(m)} Z_{l,k}^{-1}\right) & \cdots & Z_{l,m}^{-1} + \sum\limits_{k \in c(m)} Z_{l,k}^{-1} \end{bmatrix} \tag{2}$$

where c (m) represents the set of busbars connected with the busbar m; $Z_{l,m}^{-1}$ is the inverse matrix of the series impedance matrix connected between the busbars (m-1) and m; $\sum\limits_{k \in c(m)} Z_{l,k}^{-1}$ is the sum of the inverse matrices of all the series impedance matrix connected to busbar m.

Substituting **Eq 1** into **Eq 2**, the overall node admittance matrix of the LVDN can be obtained.

$$Y = \begin{bmatrix} Y_{l11} & Y_{l12} & \cdots & Y_{l12} & \cdots & Y_{l1N} \\ Y_{l21} & Y_{l22} & \cdots & Y_{l2i} & \cdots & Y_{l2N} \\ \vdots & \vdots & \ddots & \vdots & \ddots & \vdots \\ Y_{li1} & Y_{li2} & \cdots & Y_{lii} & \cdots & Y_{liN} \\ \vdots & \vdots & \ddots & \vdots & \ddots & \vdots \\ Y_{lN1} & Y_{lN2} & \cdots & Y_{lNN} & \cdots & Y_{lNN} \end{bmatrix} \tag{3}$$

where N represents the number of nodes in the LVDN.

Load Connections in an Low-Voltage Distribution Network

Photovoltaic energy storage into low-voltage distribution network technology is very common, effective use of clean

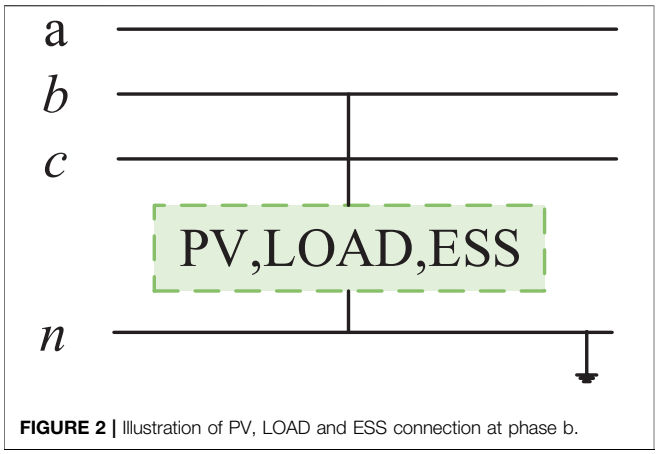

FIGURE 2 | Illustration of PV, LOAD and ESS connection at phase b.

energy and distribution network voltage control has a very obvious effect.

As shown in **Figure 2**, taking phase b as an example. The photovoltaic, load and energy storage are connected to a single-phase in the distribution network. Phase b and the neutral line n are connected to form a closed loop.

Photovoltaic, load and energy storage all use a constant power model to obtain the injection current at node i.

$$I_i(t) = \frac{\left(P_{PV,i}(t) + P_{ESS,i}(t) - P_{LOAD,i}(t)\right) - j\left(Q_{PV,i}(t) - Q_{LOAD,i}(t)\right)}{U^*_{\varphi,i}} \tag{4}$$

where $P_{PV,i}(t)$, $Q_{PV,i}(t)$ represent the photovoltaic active power and reactive power of node i at time t; $P_{LOAD,i}(t)$, $Q_{LOAD,i}(t)$ represent the active and reactive power of load at node i at time t; $P_{ESS,i}(t)$ represents the active power of energy storage at node i at time t. If no energy storage is connected, the value is 0.

Storage Model

Regulating the energy storage charge and discharge power is an effective way to control the voltage. When the photovoltaic power generation is large during the day and cannot be completely absorbed by the power grid, excessive energy can be absorbed through energy storage. Energy storage releases active power to compensate for the power shortage of the grid in the evening when photovoltaic is not generating and the power demand is high. The State of Charge (SOC) of energy storage is an important indicator for measuring the capacity of charge and discharge of energy storage. It represents the ratio of the remaining charge and discharge capacity of the energy storage system to its fully storage capacity. It is expressed as a percentage. The value range is [0,1]. The SOC at the next time step is closely related to the SOC at the present time step. The energy storage SOC can be expressed as:

$$SOC_{ESS,i}(t+\Delta t) = SOC_{ESS,i}(t) - \frac{P_{charge,i}(t)\eta_{charge}\Delta t}{E_N} + \frac{P_{discharge,i}(t)\Delta t}{\eta_{discharge}E_N} \tag{5}$$

where $SOC_{ESS,i}(t)$ represents the energy storage SOC of node i at time t; $SOC_{ESS,i}(t+\Delta t)$ represents the energy storage SOC of node i at the next time step; Δt is the time interval; E_N is the energy storage capacity; η_{charge}, $\eta_{discharge}$ are the charging efficiency and discharge efficiency of the energy storage; At time t, $P_{charge,i}(t)$, $P_{discharge,i}(t)$ represents the storage charging power and discharging power of node i.

Photovoltaic Inverter Model

The model makes full use of the reactive power of photovoltaic inverters for voltage regulation. The photovoltaic absorbs reactive power to reduce the overvoltage and generates reactive power to raise the undervoltage. The relationship between the adjustable reactive power capacity and inverter is

$$Q^{max}_{PV,\varphi} = \pm\sqrt{S^2_{PV,\varphi} - P^2_{PV,\varphi}}, \varphi \in abc \tag{6}$$

where $Q^{max}_{PV,\varphi}$ is the maximum output of reactive power of the inverter that is installed in the phase φ (node i). $S_{pv,\varphi}$ is the rated capacity of the PV inverter installed in phase φ, which is 1.1 times of the rated active power. $P_{pv,\varphi}$ is the Photovoltaic active power installed in the phase φ.

Matrix of Three-phase Four-Wire Power Flow Algorithm for Low-Voltage Distribution Network

According to the circuit theory, the node voltage and current should satisfy the node voltage equation. In the three-phase four-wire system, the node voltage equation of the LVDN can be obtained through the node admittance matrix.

$$[Y]\cdot[V(t)] = [I_{in}(t)] \tag{7}$$

where $[V(t)]$ represents a matrix containing the voltage of each node at time t, its dimension is N × 1; $[I_{in}(t)]$ is a matrix composed of the current injected by each node at time t, and its dimension is N × 1. Each element $I_i(t)$ of the matrix $[I_{in}(t)]$ can be obtained by **Eq 4**.

In order to obtain the voltage of each node, **Eq 7** can be modified

$$[V(t)] = [Y]^{-1}[I_{in}(t)] \tag{8}$$

By solving **Eq 8**, the voltage of each node can be obtained.

$$\begin{bmatrix} V_1(t) \\ V_2(t) \\ \vdots \\ V_i(t) \\ \vdots \\ V_N(t) \end{bmatrix} = \begin{bmatrix} Y_{l11} & Y_{l12} & \cdots & Y_{l1i} & \cdots & Y_{l1N} \\ Y_{l21} & Y_{l22} & \cdots & Y_{l2i} & \cdots & Y_{l2N} \\ \vdots & \vdots & \ddots & \vdots & \ddots & \vdots \\ Y_{li1} & Y_{li2} & \cdots & Y_{lii} & \cdots & Y_{liN} \\ \vdots & \vdots & \ddots & \vdots & \ddots & \vdots \\ Y_{lN1} & Y_{lN2} & \cdots & Y_{lNi} & \cdots & Y_{lNN} \end{bmatrix}^{-1} \begin{bmatrix} I_1(t) \\ I_2(t) \\ \vdots \\ I_i(t) \\ \vdots \\ I_N(t) \end{bmatrix} \tag{9}$$

However, the node admittance matrix $[Y]$ is singular matrix, which can not be inverse. Therefore, it is necessary to improve the node admittance matrix $[Y]$.

$$Y^{'} = \begin{bmatrix} E & 0 & \cdots & 0 & \cdots & 0 \\ Y_{l51} & Y_{l52} & \cdots & Y_{l5i} & \cdots & Y_{l5N} \\ \vdots & \vdots & \ddots & \vdots & \ddots & \vdots \\ Y_{li1} & Y_{li2} & \cdots & Y_{lii} & \cdots & Y_{liN} \\ \vdots & \vdots & \ddots & \vdots & \ddots & \vdots \\ Y_{lN1} & Y_{lN2} & \cdots & Y_{lNi} & \cdots & Y_{lNN} \end{bmatrix} \tag{10}$$

where E is identity matrix with a dimension of 4 × 4.

The Coordinated Control Model of Photovoltaic and Energy Storage in Three-phase Four-Wire Low-Voltage Distribution Network

The coordinated control method of photovoltaic and energy storage for the three-phase four-wire low-voltage distribution network proposed in this paper refers to the control idea proposed in (Zhang et al., 2020), which is a two-stage distributed control strategy for inverter and energy storage. It adjusts the reactive power of the inverter first and then adjusts the active power of the energy storage during voltage control.

Objective Function

The optimization control of the LVDN involves multiple optimization objectives. In this paper, minimize the network loss, the three-phase unbalance and the voltage deviation are the objectives. The three-phase four-wire system OPF model is established. The optimization variables are photovoltaic reactive power and energy storage active power. The multi-objectives problem is converted to a single-objective problem by weighting. The overall objective function can be expressed as

$$\min F = \omega_1 F \Big/ F_{1ref}{}_1 + \omega_2 F_2 \Big/ F_{2ref} + \omega_3 F_3 \Big/ F_{3ref} \tag{11}$$

where F is the objective function value; F_1, F_2, F_3 are the objective function value of network loss, three-phase unbalance and voltage deviation; F_{1ref}, F_{2ref}, and F_{3ref} are the reference values of each objective function, which is used as a reference to standardize each objective function to per unit. In this paper, the network loss, three-phase unbalance and voltage deviation without control are used as the reference values. ω_1, ω_2 and ω_3 are the weight values of each objective function, and should meet $\omega_1 + \omega_2 + \omega_3 = 1$, and $\omega_1 \geq 0$, $\omega_2 \geq 0$, $\omega_3 \geq 0$.

(1) Network losses

Network loss is an important indicator for measuring the economy of the LVDN. The objective function for calculating the network losses of the LVDN is:

$$F_1 = \sum_{t=1}^{T} P_{loss}(t) \cdot \Delta t = \sum_{t=1}^{T} \left[[I_{line}(t)]^* \otimes [I_{line}(t)] \right]^T \cdot [R] \cdot \Delta t \tag{12}$$

where $[I_{line}(t)] = [I^{abc}_{line,1}(t) I^{n}_{line,1}(t) \cdots I^{abc}_{line,(m-1)}(t) I^{abc}_{line,(m-1)}(t)]^T$; $[R] = [R^{abc}_1 R^n_1 \cdots R^{abc}_{(m-1)} R^n_{(m-1)}]^T$; $[I_{line}(t)]$ represents a complex matrix containing the amplitude and phase angle of the branch current at time t, with a dimension of l×1, where l represents the number of branches in the distribution network; $[I^{abc}_{line,m}(t)]$ represents the three phases currents of a, b and c on the m-segment line at time t, with a dimension of 3 × 1; $[I^{n}_{line,m}(t)]$ represents the current of the neutral line n on the m-segment line at time t, with a dimension of l × 1; R is the branch resistance with a dimension of l × 1; R^{abc}_m includes the resistance value of three phases of a, b and c on the m-segment line, with a dimension of 3 × 1; R^n_m represents the resistance value of neutral line n on the m-segment line, with dimension of l × 1. A new operation symbol ⊗ is defined, which represents the multiplication of the corresponding elements of two matrices.

(2) Three-phase unbalance factor

Voltage Unbalance Factor (VUF) is also an important indicator in LVDN. The definition can be the ratio of the negative sequence fundamental component to the positive sequence fundamental component.

$$U_{\mathrm{VUF},m}(t) = \left| \frac{V_{-,m}(t)}{V_{+,m}(t)} \right| = \left| \frac{V_{\mathrm{a},m}(t) + \alpha V_{\mathrm{b},m}(t) + \alpha^2 V_{\mathrm{c},sm}(t)}{V_{\mathrm{a},m}(t) + \alpha^2 V_{\mathrm{b},m}(t) + \alpha V_{\mathrm{c},m}(t)} \right| \tag{13}$$

where $V_{\mathrm{a},m}(t)$, $V_{\mathrm{b},m}(t)$, $V_{\mathrm{c},m}(t)$ represent the voltage of each phase at bus m; $V_{-,m}(t)$ represents the negative sequence voltage; $V_{+,m}(t)$ represents the positive sequence voltage; $\alpha = 1\angle 120^\circ$.

Take the minimization of the three-phase unbalance of each bus in the distribution network as the objective function:

$$F_2 = \sum_{t=1}^{T} \sum_{i=1}^{l} U_{\mathrm{VUF},m}(t) \tag{14}$$

where l represents the number of branches in LVDN.

(3) Voltage deviation

The difference between the actual voltage of each point and the nominal voltage of the system is called the voltage deviation. The objective function for calculating the voltage deviation of the LVDN is:

$$\Delta U_\varphi = \left(\frac{U_{\varphi,m}(t) - U_N}{U_N} \right)^2 \tag{15}$$

$$F_{3=} \sum_{t=1}^{T} \sum_{m} \sum_{\varphi \in abc} \Delta U_\varphi \tag{16}$$

where ΔU_φ represents the voltage deviation of a certain phase at a certain node at a certain time; U_N represents the standard voltage of the system.

The selection of the target weight mainly considers the importance of different indicators in the optimization model. As the network losses is closely related to the operating cost of the distribution network, the smaller the value, the better the results. The three-phase unbalance is according to the requirements of GB/T 12,325–2008 "Power Quality Three-Phase Voltage Unbalance". The allowable value of the voltage unbalance at the public connection point of the power system during normal operation of the power grid is 2%, and it must not exceed 4% in a short time. That is, the VUF that is less than 2% can meet the requirements. Therefore, economics (network losses) is the primary concern of the optimization model in this paper, and its weight should be greater than the three-phase unbalance weight. This paper first takes the weights of the two objective functions as 0.85 and 0.15. The effect of different weights on the control effect will be analyzed in more detail in the case study section.

Constraints

(1) Branch current constraints

$$\left|I_{ij}(t)\right| \le I_{ij,max} \tag{17}$$

where $I_{ij}(t)$ represents the current of branch ij that connects node i and node j; $I_{ij,max}$ represents the maximum allowable value of the branch current. This paper uses 100A.

(2) Voltage constraints

For the voltage amplitude of each node on a, b, and c phase, according to national standards, there should be a maximum and minimum limit to ensure the safe operation of the power grid.

$$V_{i,min} \le |V_i(t)| \le V_{i,max} \tag{18}$$

where $|V_i(t)|$ represents the voltage amplitude of node i at time t; $V_{i,min}$ represents the minimum allowable voltage at node i, $V_{i,max}$ represents the maximum allowable voltage. According to GB/T 12,325–2008 "Power Quality Voltage Allowable Range", the 220V single-phase supply voltage deviation is −10%–7% of the nominal voltage.

(3) Neutral line voltage constraints

$$\left|V_{i,neutral}(t)\right| \le V_{neutral,max}, i \in n \tag{19}$$

where $\left|v_{i,neutral}(t)\right|$ represents the voltage amplitude of node i on the neutral line at time t; $V_{neutral,max}$ represents the maximum allowable value of the neutral line voltage. According to DL/T 620–1997 "Overvoltage Protection and Insulation Coordination for AC Electrical Installations", the neutral point voltage displacement rate should be less than 15% of the phase voltage.

(4) Photovoltaic inverter capacity constraints

The reactive power of photovoltaic inverters is not unlimited, and the active power and capacity of photovoltaic inverters must meet certain constraints.

$$P_\varphi^2 + Q_\varphi^2 \le S_\varphi^2, \varphi \in abc \tag{20}$$

where P_φ indicates the active power of the photovoltaic inverter connected to the phase $^\varphi$; Q_φ indicates the reactive power of the photovoltaic inverter connected to the phase $^\varphi$; $S_\varphi$indicates the capacity of the photovoltaic inverter connected to the phase $^\varphi$.

(5) Energy storage constraints

The limits of SOC at time t:

$$SOC_{ESS,min} \le SOC_{ESS,i}(t) \le SOC_{ESS,max} \tag{21}$$

where $SOC_{ESS,min}$, $SOC_{ESS,max}$ represent the minimum and maximum allowable SOC of energy storage. This paper takes 20 and 80%.

Take a day as a charge and discharge cycle of the energy storage device, the initial state of each cycle should be the same.

$$SOC_{ESS,i}(t_0) = SOC_{ESS,i}(t_n) \tag{22}$$

where $SOC_{ESS,i}(t_0)$ represents the initial SOC of a day, $SOC_{ESS,i}(t_n)$ represents the SOC at the end of a day.

In addition, energy storage should meet the charging and discharging power constraints.

$$\begin{cases} P_{charge,i,min} D_{charge,i}(t) \le P_{charge,i}(t) \le P_{charge,i,max} D_{charge,i}(t) \\ P_{discharge,i,min} D_{discharge,i}(t) \le P_{discharge,i}(t) \le P_{discharge,i,max} D_{discharge,i}(t) \\ D_{charge,i}(t) + D_{discharge,i}(t) \le 1 \end{cases} \tag{23}$$

where $P_{charge,i,min}$, $P_{charge,i,max}$ represent the minimum and maximum values of energy storage charging power; $P_{discharge,i,min}$, $P_{discharge,i,max}$ represent the minimum and maximum values of energy storage discharge power; $D_{charge,i}(t)$, $D_{discharge,i}(t)$ are binary variables.

(6) Tie line power constraints

After a high proportion of photovoltaics are integrated, there will be a phenomenon of power flow from the LVDN to the upper-level power grid. In order to ensure the normal operation of each device, the tie line between the low voltage station area and the upper-level power grid should meet the power limit.

$$P_{con,min} \le P_{con}(t) \le P_{con,max} \tag{24}$$

where $P_{con,min}$, $P_{con,max}$ represent the upper and lower limit of the tie line. The value should not be greater than the rating of the distribution transformer. $P_{con}(t)$ represents the actual power of the tie line at time t.

Solution Method Based on Optimal Power Flow Model in a Three-phase Four-Wire System

This paper uses the complex form to represent both the magnitude and phase angle of the variables, and the optimization model contains non-convex nonlinear constraints. Therefore, the OPF problem is a non-convex programming problem. It is difficult to obtain a global optimal solution. In order to solve the problem, all variables are split into real part and imaginary part. For **Eq 8**, it can be simplified by the following formula.

$$[V] = \left[V_{re} + jV_{re}\right] = [\mathrm{Re}(Y) + \mathrm{Im}(Y)]^{-1} \cdot \left[I_{in,re} + jI_{in,im}\right] \tag{25}$$

Therefore, the real and imaginary part of each node voltage can be represented:

$$[V_{re}] = [\mathrm{Re}(Y)]^{-1} \cdot \left[I_{in,re}\right] - [\mathrm{Im}(Y)]^{-1} \cdot \left[I_{in,im}\right] \tag{26}$$

$$[V_{im}] = [\mathrm{Im}(Y)]^{-1} \cdot \left[I_{in,re}\right] + [\mathrm{Re}(Y)]^{-1} \cdot \left[I_{in,im}\right] \tag{27}$$

(1) Upper voltage constraint

The voltage is split into real and imaginary parts. The essence of the upper voltage constraint is that the modulus length of the complex number is less than the specified value.

$$V_{i,re}^2(t) + V_{i,im}^2(t) \le V_{i,max}^2 \tag{28}$$

where $V_{i,re}(t)$ represents the real part of node i voltage at time t; $V_{i,re}(t)$ represents the imaginary part of node i voltage at time t; $V_{i,max}$ represents the maximum allowable value of node i voltage.

(2) Lower voltage constraint

The voltage lower voltage constraint is a concave function, which is difficult to solve and hard to maintain the optimality of the solution. Therefore, this constraint can be linearized to ensure the optimization of the convex function.

$$-D_{1a}\left[V_{i,re}(t)\right] - D_{2a}\left[V_{i,im}(t)\right] \le -V_{i,min}, i \in a \tag{29}$$

$$-D_{1b}\left[V_{i,re}(t)\right] - D_{2b}\left[V_{i,im}(t)\right] \le -V_{i,min}, i \in b \tag{30}$$

$$-D_{1c}\left[V_{i,re}(t)\right] - D_{2c}\left[V_{i,im}(t)\right] \le -V_{i,min}, i \in c \tag{31}$$

where $D_{1a,}$ D_{2b}, D_{1a}, D_{2b}, D_{1a}, D_{2b} represents the coefficients of the a, b, and c phase lower voltage constraint, the results of the solution method are 1.001, 0, −0.5005, −0.8668, −0.5005, and 0.8668, respectively. $V_{i,min}$ is the minimum allowable voltage.

(3) Three-phase unbalance

Although the negative and positive components of the current are both convex functions, the ratio of the two is a concave function. Therefore, the three-phase unbalance constraint must be convex. In the actual distribution network, the positive sequence current value of the branch current is much larger than the negative sequence current value. The module length could be approximately equal to the average current of the branch. Hence, the three-phase unbalance formula can be approximated as:

$$U_{\mathrm{VUF},m}(t) = \left|\frac{V_{-,m}(t)}{V_{+,m}(t)}\right| \cong \left|\frac{V_{\varphi}(t)}{V_{\mathrm{a},m}(t) + \alpha^2 V_{\mathrm{b},m}(t) + \alpha V_{\mathrm{c},m}(t)}\right| \tag{32}$$

where $V_{\varphi}(t)$ indicates the rated voltage of phase φ.

Therefore, the constraint of unbalance can be represented by:

$$VUF_{bus}^2(t) \le VUF_{bus,max}^2 \tag{33}$$

(4) Neutral line voltage constraint

The neutral line voltage is split into real and imaginary part.

$$V_{i,re}^2(t) + V_{i,im}^2(t) \le V_{neutral,max}^2, i \in N \tag{34}$$

where $V_{neutral,max}$ represents the maximum allowable value of the neutral line voltage.

(5) Branch current constraints

The value of the branch current is limited by:

$$\left|I_{ij}(t)\right| \le I_{ij,max} \tag{35}$$

where $I_{ij}(t)$ represents the current of the branch ij connecting the node i and the node j at time t; $I_{ij,max}$ represents the maximum allowable value of the branch current.

Use the plural form when solving I_{ij}.

$$I_{ij} = Y_{ij}V_{ij} = Y_{ij}\left(V_i - V_j\right) \tag{36}$$

The left side of **Eq. 35** can be:

$$\left|I_{ij}\right| = \left|Y_{ij}\right|\left|V_{ij}\right| = \sqrt{\left(G_{ij}^2 + B_{ij}^2\right)} \cdot \sqrt{\left(V_{i,re} - V_{j,re}\right)^2 + \left(V_{i,im} - V_{j,im}\right)^2} \tag{37}$$

Remove the radical and further convex the calculation formula:

$$\begin{aligned}\left|I_{ij}\right|^2 &= \left|Y_{ij}\right|^2 \cdot \left|V_{ij}\right|^2 \\ &= \left(G_{ij}^2 + B_{ij}^2\right) \cdot \left[\left(V_{i,re} - V_{j,re}\right)^2 + \left(V_{i,im} - V_{j,im}\right)^2\right]\end{aligned} \tag{38}$$

Hence, the branch current constraint can be:

$$\left|I_{ij}(t)\right|^2 \le I_{ij,max}^2 \tag{39}$$

Through the convex processing of the model, the original non-convex nonlinear problem is transformed into an easy-to-solve convex programming problem. The original problem has global optimality. It is solved by the branch and bound method and the cut plane method included in the mature CPLEX algorithm package. This paper uses the YALMIP platform to develop the OPF-based photovoltaic-storage coordinated control program under the MATLAB operating environment, which calls the professional CPLEX algorithm package, and directly calculates the global optimal solution of the original optimal control problem.

Simulation Settings

A 21-bus three-phase four-wire low voltage distribution network was used for simulation studies, see **Figure 3**. The length of all lines is \50 m. The rated voltage is 380 V. The line self-impedance is $Z_{ii} = 0.650 + j0.412\,\Omega$/km, mutual impedance is $Z_{ij} = (0.01 \times Z_{ii})\,\Omega$/km. Each bus can be connected with single-phase or three-phase photovoltaic, and the three-phase can be regulated independently. The rated power of single-phase photovoltaic power generation is 5 kW, and the capacity of inverter is 1.1 times the rated active power capacity. Energy storage is connected at bus four and bus 13 via three phase connection and can be regulated independently. The rated energy capacity of energy storage is 20 kWh. The charging and discharging efficiency is 0.94. The upper limit of the energy storage power of each phase is 4 kW. The weight factors are $\omega_1 = 0.7$, $\omega_2 = 0.2$ and $\omega_2 = 0.1$.

The power curve of PV is shown in **Figure 4A**. The value is the per unit value with the peak value to be the base. As the actual power transmission distance of the low-voltage distribution network is short, the conditions such as temperature and light will not be much different. The typical daily photovoltaic power curves connected to each node are hence similar. A typical daily load curve is shown in **Figure 4B** which is also per unit value. The per unit value of the typical load curves at each bus are similar. For details of the PV and load base data of each node.

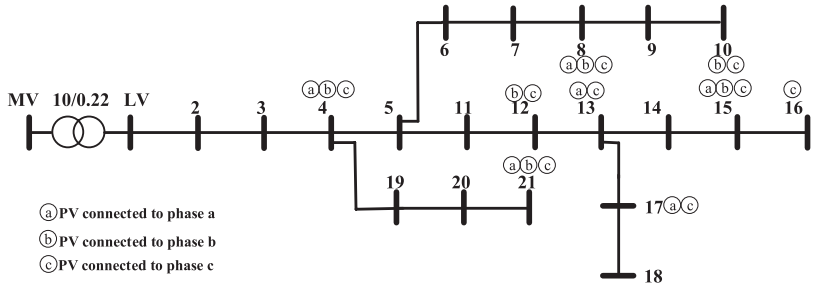

FIGURE 3 | Low voltage distribution network with 21 buses.

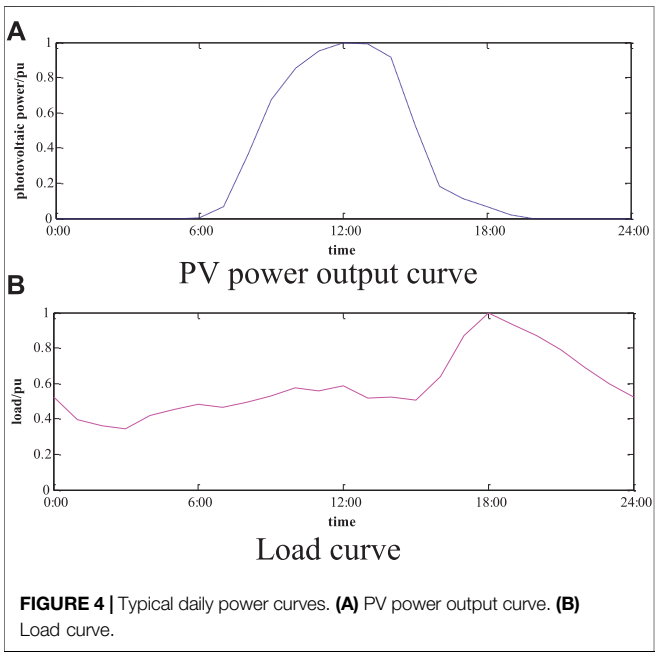

FIGURE 4 | Typical daily power curves. **(A)** PV power output curve. **(B)** Load curve.

Enhancement in Voltage Violation, Network Loss and Three-phase Unbalance

The effectiveness of the control method in this paper is verified by comparing the calculation results of various indicators of the distribution network with "without control" and "under control".

(1) Voltage comparison

As the load at phase b is higher than other two phases and the PV integration at phase b is the highest, phase b is taken as an example to compare the voltage with and without the control. See **Figure 5** for the simulation results. The blue bar indicates the voltage before the control. When the photovoltaic power generation is high during the day, the loads are at the low consumption period and the voltage exceeds the upper limit. This will lead to reverse power flow and three-phase unbalance. In the evening, there is no power output from photovoltaics, and loads are at the peak consumption period. The voltage is lower than the lower limit. The timing mismatch between photovoltaics and loads results in a higher voltage during the day and a lower voltage in the evening. The red bar indicates the proposed control scheme, and it can be seen that the voltage violation can be effectively suppressed. When the daytime voltage exceeds the upper limit, the photovoltaic inverter absorbs reactive power and suppresses the voltage violation. When the inverter reactive power is insufficient, the energy storage is charged, and the voltage is maintained through the coordinated control of the photovoltaic inverter and energy storage. The voltage is controlled within 1.07 pu. This can not only make up for the shortcomings of exceeding the inverter's reactive power margin when the voltage exceeds the limit, but also for the shortage that the SOC reaches the limit and cannot further charge or discharge. The cooperative control of the two enables the voltage control to be optimal. In the evening, when the power supply is insufficient, the energy stored in the energy storage during the day is fully utilized to maintain the power grid voltage above 0.9 pu.

(2) Three phase unbalance comparison

Without the control, as the load is unbalance connected and PV is connected via single phase, this lead to severe three phase unbalance. The unbalance can reach 10.8%. With the control proposed in this paper, all unbalance is limited within 2%. The max value is 0.59% at 12:00. This is because the photovoltaic power generation is sufficient and the load is low, the large-scale single-phase photovoltaic connection leads to the maximum three-phase unbalance. However, the unbalance is still less than the required 2%. Therefore, the proposed control method effectively reduced the three phase unbalance.

(3) Network loss comparison

The total distribution network loss without control is 83.21 kWh. When the upper limit of the voltage during the day or when the lower limit of the voltage during the night, the network loss is the largest in the day. This is because the reverse power flow that occurs when the photovoltaic power is large during the day generates extra network losses in the grid, and the heavy load will increase the network loss in the evening. In addition, the three-phase unbalance caused by the asymmetric connection of photovoltaics and loads causes the neutral line to generate current which further increases the network loss. Under

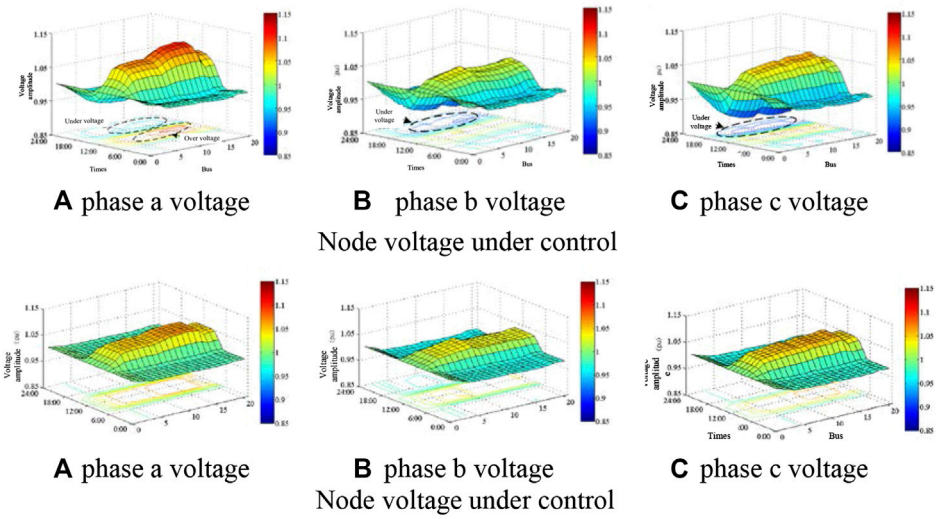

FIGURE 5 | Control method under node voltage. Node voltage under control. **(A)** phase a voltage **(B)** phase b voltage **(C)** phase c voltage. Node voltage under control. **(A)** phase a voltage **(B)** phase b voltage **(C)** phase c voltage.

the control scheme, the total network loss is 65.87 kWh, and the network loss is large when the photovoltaic power is large during the day. At the same time, the three-phase unbalance is improved, which reduces the neutral current to zero and further reduces network loss. Therefore, the method proposed in this paper effectively reduces the network loss.

(4) PV and energy storage SOC changes with the proposed control

The PV reactive power at bus 16 is given in **Figure 7**. As the bus is located at the end of the line, the voltage violation is most likely to occur. Through the proposed scheme, the photovoltaic reactive power is controlled to improve the voltage over-limit and three-phase unbalance. It can be seen that when the upper limit of the voltage during the day is obvious. The photovoltaic absorbs reactive power and mitigate the voltage violation of the upper limit.

Figure 8 shows the energy storage charging and discharging power at bus 13. As the bus is located at the end of the line, it is also the point where the voltage violation is most likely to occur. In the daytime, excess energy is used to charge energy storage. In the evening, when demand for electricity is high, energy storage is discharged to supply the demand.

Figure 9 shows the changes of the energy storage SOC at bus 13. Around 10:00, photovoltaic power generation continues to increase with the increase in light intensity. At this time, the load is the minimum value throughout the day. The energy storage starts to enter into the charging state, and SOC continues to increase from 20%. At around 15:00, the energy storage reaches the maximum energy limit at 80%. At the time of sunset, following the decrease in light intensity, the power from PV inverter continuously decreases while loads start to increase to peak demand period. Energy storage starts to discharge to supply the load. SOC starts to drop until reaching the low energy limit at 20%. This will not affect the action of energy storage in the next cycle.

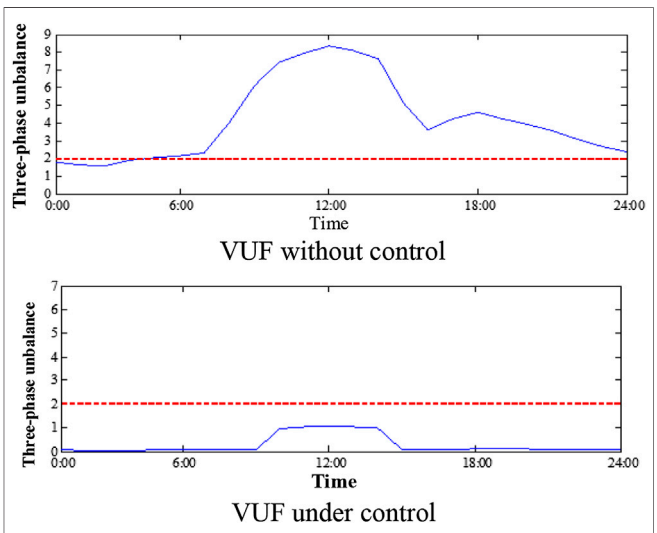

FIGURE 6 | Comparison of three–phase imbalances. VUF without control. VUF under control.

Results Comparison of Different Control Method

The target weight indicates the importance of each index in the objective function. Hence, the control performance is related to the value of the weight. Among the three objective functions in the model, the network losses and three-phase unbalance factor are the most important. In this section, the weight of the voltage deviation is always maintained at 0. The control performance with different weights of network losses and three-phase

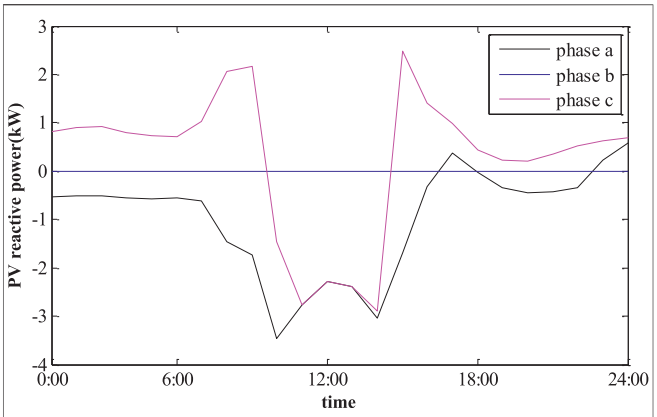

FIGURE 7 | PV reactive power under control.

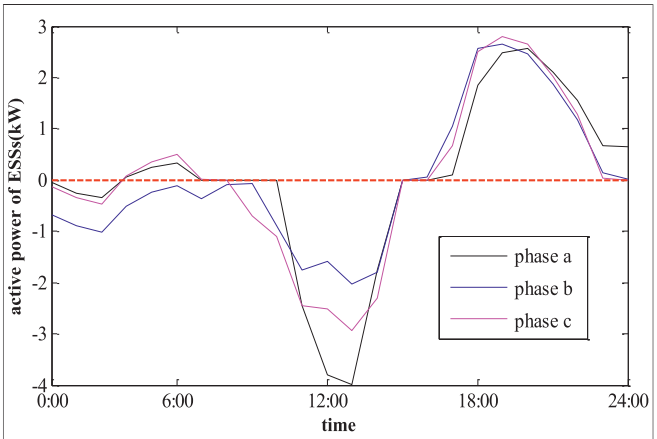

FIGURE 8 | Active power of ESSs under control.

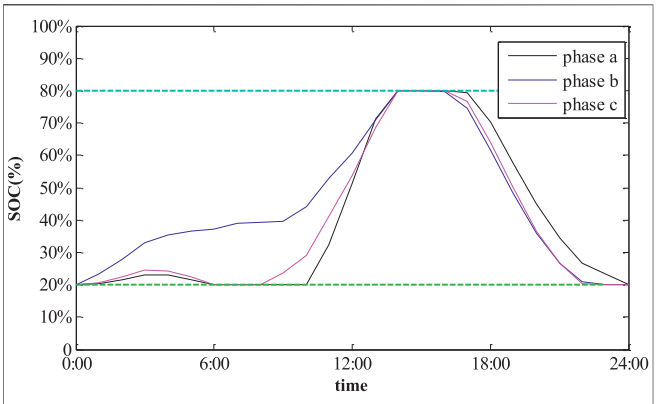

FIGURE 9 | SOC of ESSs under control.

unbalance factor is analyzed. **Figure 9** lists the control results of different weighting schemes.

It can be seen from the results that the variation of the voltage deviation in the objective function has a very small influence on the results, almost no change, so the weight of the voltage deviation can be ignored here, and the influence of the network loss and the weight of the three-phase imbalance on the results can be analyzed. The following conclusions are drawn.

TABLE 1 | Result under different strategies.

Control scheme	ω_1	ω_2	ω_3	The network losses/ (kW.h)	Three-phase unbalance/ %	Voltage deviation
1	0	1	0	78.31	0.52	51.25
2	0.05	0.9	0.05	62.93	0.52	51.32
3	0.15	0.7	0.15	62.49	0.52	52.28
4	0.25	0.5	0.25	62.14	0.56	52.30
5	0.35	0.3	0.35	61.13	0.54	52.32
6	0.45	0.1	0.45	57.59	1.07	52.35
7	0.5	0	0.5	45.77	9.48	52.36
8	1	0	0	34.64	9.32	51.25
9	0	0	1	63.92	9.27	54.86

(1) Only the three-phase unbalance index is considered. At this time, the distribution network three-phase unbalance control effect is the optimal, reaching a minimum value of 0.52%. However, the network loss is extremely deteriorated, reaching a maximum value of 78.31 kWh.
(2) When the network loss weight is 0.05 and the three-phase unbalance weight is 0.9, the weight is only adjusted slightly. The network loss index changes dramatically. Although the network loss is much smaller, the three-phase unbalance is still 0.52%.
(3) The network loss weight is further increased, and the three-phase unbalance weight is further smaller. The network loss is slightly decreased but not obvious, and the three-phase unbalance is 0.52%. When the three-phase unbalance weight reduce to 0.1, only minor changes can be seen, however still within the national standard (2%).
(4) Consider only the network loss index. Although the network loss can reach a minimum value of 45.77 kWh, the control effect on the three-phase unbalance of the network is not obvious. At this time, the three-phase unbalance is 9.48%, which is far beyond the specified 2%.

In summary, on the premise that the network loss and the three-phase unbalance are within the national standard range, the reasonable weight value is determined based on the principle that the three-phase unbalance and the network loss are not significantly increased. This can ensure the security of the power grid operation and also reduce the operating cost of the power grid. Hence, the three-phase unbalance index takes less weight.

Three-phase Three-Wire and Three-phase Four-Wire System Model Simulation Comparison

In order to verify the superiority of the control method proposed in this paper, a three-phase three-wire system using a second-order cone relaxation solution and a three-phase four-wire system based on OPF proposed in this paper are compared and analyzed. As the second-order cone optimization model cannot calculate the three-

TABLE 2 | Result under different line structure.

Control scheme	Network loss					Voltage deviation
	Phase a (kWh)	Phase b (kWh)	Phase c (kWh)	Phase n (kWh)	Total loss (kWh)	
Three-phase three-wire system	15.84	22.79	33.65	–	69.28	58.28
Three-phase four-wire system	18.79	20.97	22.04	4.07	65.87	51.76

phase unbalance, the results of this method are compared with the results of the second-order cone model based on the three-phase three-wire system.

As can be seen from **Table 2**, compared with the three-phase three-wire system and the three-phase four-wire system, the total network loss differs by 3.41 kWh and the three-phase four-wire neutral line loss is 4.07 kWh. Under the same simulation condition, the difference between the total network losses of the two types of distribution network is approximately equal to the neutral line loss. In addition, the losses of each phase of the two models are quite different. For example, loss of a-phase of the three-phase three-wire system is 15.84 kWh, while the loss of a-phase of the three-phase four-wire system is 18.79 kWh. At this time, the network loss and voltage deviation of three-phase three-wire system has high errors. Therefore, in a three-phase balanced low-voltage distribution network, the neutral line has no current. The two types of distribution networks can be approximately equivalent. For a three-phase unbalanced low-voltage distribution network, the calculation of a three-phase three-wire system will produce errors.

CONCLUSION

In this paper, the problems of large-scale domestic photovoltaic connecting to the three-phase four-wire low-voltage distribution network including voltage violation and three-phase unbalance were studied. A low-voltage photovoltaic-energy storage based on the three-phase four-wire network OPF cooperative control method is proposed.

(1) For a low-voltage distribution network with a high proportion of photovoltaics, the proposed photovoltaic-energy storage collaborative control method can comprehensively improve the technical indicators of the power grid. The node voltage can be controlled within the range of 0.9–1.07 pu, and also effectively reduce the three-phase unbalance and the network loss.
(2) The proposed three-phase four-wire optimal power flow algorithm overcomes the shortcomings that the existing method that cannot accurately calculate the neutral line voltage and current. This ensures the correctness of the network optimization calculation results in the case of three-phase unbalance. It has good adaptability to low-voltage distribution network.
(3) In the objective function, the network loss, the three-phase unbalance and the voltage deviation weight have different effects on the control results. The network loss weight is more sensitive to the objective function than the three-phase unbalance and the voltage deviation. The control effect is better when the network loss weight is set in the range of 0.7–0.9.

DATA AVAILABILITY STATEMENT

The original contributions presented in the study are included in the article/Supplementary Material, further inquiries can be directed to the corresponding author.

AUTHOR CONTRIBUTIONS

The paper was a collaborative effort between the authors. JF designed the coordinated control model, TL contributed to the Introduction, SG and YW contributed to the multi-state models of REG active power considering forecast errors, KT and YD contributed to case study.

FUNDING

This research was funded by Beijing Key Laboratory of Distribution Transformer Energy-Saving Technology (China Electric Power Research Institute), grant number 51201901230.

REFERENCES

Alsenani, T. R., and Paudyal, S. (2018). "Distributed approach for solving optimal power flow problems in three-phase unbalanced distribution networks," in 2018 Australasian universities power engineering conference (AUPEC), Auckland, NZ, November 29–30, 2018 (IEEE), 1–6.

Aziz, T., and Ketjoy, N. (2017). PV penetration limits in low voltage networks and voltage variations. *IEEE Access* 5 (99), 1. doi:10.1109/ACCESS.2017.2747086

Bose, A., Tian, Z., Wu, W., and Zhang, B. (2016). Mixed-integer second-order cone programing model for VAR optimisation and network reconfiguration in active distribution networks. *IET Gener. Transm. Distrib.* 10 (8), 1938–1946. doi:10.1049/iet-gtd.2015.1228

Bozchalui, M., and Sharma, R. (2014). *Optimal operation of energy storage in distribution systems with renewable energy resources*. 2014 Clemson university power systems conference, Clemson, SC, March 11–14, 2014 (IEEE).

Gill, S., Kockar, I., and Ault, G. (2014). Dynamic optimal power flow for active distribution networks. *IEEE Trans. Power Syst.* 29 (1), 121–131. doi:10.1109/TPWRS.2013.2279263

Ju, Y., Wu, W., Lin, Y., Ye, L., and Ge, F. (2017). *Three-phase optimal load flow model and algorithm for active distribution networks*. 2017 IEEE Power and energy society general meeting, Chicagol, IL, July 16–20, 2017 (IEEE), 1–5.

Liu, X., Aichhorn, A., Liu, J., and Li, H. (2012). Coordinated control of distributed energy storage system with tap changer transformers for voltage rise mitigation under high photovoltaic penetration. *IEEE Trans. Smart Grid* 3 (2), 897–906. doi:10.1109/TSG.2011.2177501

Martins, V. F., and Carmenlt, L. T. B. (2011). Active distribution network integrated planning incorporating distributed generation and load response uncertainties. *IEEE Trans. Power Syst.* 26 (4), 2164–2172. doi:10.1109/TPWRS.2011.2122347

Niknam, T., Narimani, M. R., Aghaei, J., and Azizipanah-Abarghooee, R. (2012). Improved particle swarm optimisation for multi-objective optimal power flow considering the cost, loss, emission and voltage stability index. *IET Gener. Transm. Distrib.* 6 (6), 515–527. doi:10.1049/iet-gtd.2011.0851

O'Neill, R. P., Castillo, A., and Cain, M. (2012). *The IV formulation and linear approximations of the AC optimal power flow problem*. Washington, DC: Federal Energy Regulation Commission Staff Tech. Paper.

Pansakul, C., and Hongesombut, K. (2014). *Analysis of voltage unbalance due to rooftop PV in low voltage residential distribution system*. 2014 International electrical engineering congress (iEECON), Chonburi, Thailand, March 19–21, 2014 (IEEE).

Qian, M., Qin, H., Zhao, D., Chen, N., Jiang, J., Wang, B., et al. (2018). *A multi-level reactive power control strategy for PV power plant based on sensitivity analysis*. 2018 China international conference on electricity distribution (CICED), Tianjin, China, September 17–19, 2018 (IEEE), 1838–1842.

Reinaldo, T., Lopes, L., and Tarekhm, H. M. E.-F. (2011). Coordinated active power curtailment of grid connected PV inverters for overvoltage prevention. *IEEE Trans. Sustain. Energy* 2 (2), 139–147. doi:10.1109/TSTE.2010.2098483

Tian, Z., Wu, W., Zhang, B., and Bose, A. (2016). Mixed-integer second-order cone programing model for VAR optimisation and network reconfiguration in active distribution networks. *IET Gener. Transm. Distrib.* 10 (8), 1938–1946. doi:10.1049/iet-gtd.2015.1228

Tonkoski, L. (2009). *Voltage regulation in radial distribution feeders with high penetration of photovoltaic*. 2009 IEEE energy 2030 conference, Atlanta, GA, September 1–7, 2009 (IEEE).

Zafar, R., Ravishankar, J., Fletcher, J. E., and Pota, H. R. (2020). Optimal dispatch of battery energy storage system using convex relaxations in unbalanced distribution grids. *IEEE Trans. Indust. Inform.* 16 (1), 97–108. doi:10.1109/TII.2019.2912925

Zehar, K., and Sayah, S. (2008). Optimal power flow with environmental constraint using a fast successive linear programming algorithm: application to the algerian power system. *Energy Convers. Manag.* 49 (11), 3362–3366. doi:10.1016/j.enconman.2007.10.033

Zhang, B., Tang, W., Cai, Y., Wang, Z., Li, T., and Zhang, H. (2020). Distributed control strategy of residential photovoltaic inverter and energy storage based on consensus algorithm. *Auto. Elect. Power Syst.* 44 (02), 86–96. doi:10.7500/AEPS20190305005

Conflict of Interest: The authors declare that the research was conducted in the absence of any commercial or financial relationships that could be construed as a potential conflict of interest.

TABLE A1 | Three-phase four-wire 21-bus test system.

Branch number	Front node	End node	Base load value/Ω					
			Pa	Qa	Pb	Qb	Pc	
1	0	1	2.004	0.8017	0.945	0.3780	1.640	0
2	1	2	1.787	0.7148	2.352	0.9408	1.440	0
3	2	3	1.546	0.6182	1.302	0.5208	1.700	0
4	3	4	1.352	0.5409	1.764	0.7056	2.340	0
5	4	5	0	0	0	0	4.680	1
6	5	6	3.284	1.314	4.032	1.613	2.900	1
7	6	7	0	0	2.541	1.016	2.960	1
8	7	8	0	0	2.583	1.033	3.120	1
9	8	9	2.995	1.198	1.428	0.5712	1.700	0
10	9	10	2.125	0.8501	2.100	0.8400	2.480	0
11	10	11	0	0	2.373	0.9492	3.000	1
12	11	12	2.077	0.8308	1.407	0.5628	1.960	0
13	12	13	1.860	0.7438	0.777	0.3108	1.960	1
14	13	14	0	0	2.100	0.8400	1.960	0
15	14	15	3.429	1.372	2.226	0.8904	0	
16	15	16	1.280	0.5120	2.079	0.8316	1.560	0
17	16	17	0	0	1.155	0.4620	0.9200	0
18	17	18	0	0	3.675	1.470	3.100	1
19	18	19	1.860	0.7438	3.024	1.210	3.980	1
20	19	20	3.212	1.285	2.079	0.8316	2.880	1

frontiers in Energy Research

ORIGINAL RESEARCH
published: 10 February 2021
doi: 10.3389/fenrg.2020.633401

Optimal Operation of Soft Open Points-Based Energy Storage in Active Distribution Networks by Considering the Battery Lifetime

*Jian Wang, Niancheng Zhou, Anqi Tao and Qianggang Wang**

State Key Laboratory of Power Transmission Equipment and System Security and New Technology, Chongqing University, Chongqing, China

Soft open point-based energy storage (SOP-based ES) can transfer power in time and space and also regulate reactive power. These characteristics help promote the integration of distributed generations (DGs) and reduce the operating cost of active distribution networks (ADNs). Therefore, this work proposed an optimal operation model for SOP-based ES in ADNs by considering the battery lifetime. First, the active and reactive power equations of SOP-based ES and battery degradation cost were modeled. Then, the optimal operation model that includes the operation cost of ADNs, loss cost, and battery degradation cost was established. The mixed integer nonlinear programming model was transformed to a mixed integer linear programming model derived through linearization treatment. Finally, the feasibility and effectiveness of the proposed optimization model are verified by the IEEE33 node system.

Keywords: active distribution networks, soft open point, energy storage, battery lifetime, optimal operation

OPEN ACCESS

Edited by:
Hao Yu,
Tianjin University, China

Reviewed by:
Qunhai Huo,
Chinese Academy of Sciences, China
Lu Zhang,
China Agricultural University, China

****Correspondence:***
Qianggang Wang
yitagou@cqu.edu.cn

Specialty section:
This article was submitted to Smart Grids, a section of the journal Frontiers in Energy Research

Received: *25 November 2020*
Accepted: *29 December 2020*
Published: *10 February 2021*

Citation:
Wang J, Zhou N, Tao A and Wang Q (2021) Optimal Operation of Soft Open Points-Based Energy Storage in Active Distribution Networks by Considering the Battery Lifetime. Front. Energy Res. 8:633401. doi: 10.3389/fenrg.2020.633401

INTRODUCTION

Renewable energy power generation is a key measure to solve the contradiction between load growth, environmental protection, and energy shortage (Habibollahzade et al., 2018; Zhao and Chen, 2018). Renewable energy power generation is usually connected to the distribution network in the form of distributed generation (DG) (Badran et al., 2018; Naderi et al., 2018). The increasing integration of DG has a profound impact on the distribution network. In a traditional distribution network, power flows in a one-way radial from the slack bus to the load side; meanwhile, a DG may make power flow in multiple directions from multiple points inside the distribution network, an occurrence which will raise the voltage (Su et al., 2014). Flexible and controllable equipment are present in active distribution networks (ADNs) and can improve the operation efficiency and management level of ADNs.

A soft open point (SOP) is a new type of power electronic equipment which consists of two back-to-back voltage source converters (VSCs) and can replace the traditional tie switch (Bloemink and Green, 2010). An SOP's flexible control characteristics and rapid response capability effectively deal with renewable energy fluctuation. An SOP can transfer power flow and regulate reactive power, thereby promoting the access level of DGs. Energy storage (ES) transfers the electric energy through the storage and release of the said energy, a feature which can effectively reduce the operating cost of the ADNs under the time-of-use (TOU) electricity price environment (Imani et al., 2019). The battery module of the ES can be connected to the DC bus of the SOP through a DC–DC converter to form an SOP-based ES. By controlling two VSCs and one DC–DC converter, the SOP-based ES has

multiple functions such as energy storage, power flow transfer, and reactive power regulation (Yao et al., 2018). Therefore, investigating the optimal operation of SOP-based ES for reducing the operation cost and improving the operation efficiency of ADNs is of great significance.

Numerous research achievements exist on the operation strategy of an SOP in the ADNs. Ref. (Cao et al., 2016) reduced the loss of the distribution network by controlling an SOP. In fact, the control ability of the SOP is reflected not only in the loss reduction, but also in its voltage regulation ability. Most studies consider both loss and voltage quality and adopt a multi-objective optimization model to solve the problem. Ref. (Long et al., 2016; Ji et al., 2017; Li et al., 2017; Qi et al., 2017; Ji et al., 2018; Li et al., 2019; Shafik et al., 2019) proposed a variety of multi-objective optimization operation models of the active distribution network and used an SOP to reduce the distribution network loss and improve system voltage deviation. Some studies also considered load balancing. In (Sun et al., 2021), a long-term and short-term two-stage distribution network optimization model is established by considering the uncertainty of the renewable energy output. In the long-term model, the minimum loss and voltage unbalance are taken as the optimization objectives, and the operation point of the SOP is obtained. Then, according to the actual output of renewable energy sources, the short-term model responds to the actual output of renewable energy through droop control. Ref. (Shafik et al., 2019) improves the renewable energy utilization efficiency by controlling the tie switch and SOPs. Ref. (Lou et al., 2020; Wang et al., 2020) further reduces the voltage unbalance in the unbalanced distribution network by controlling the three-phase power of SOPs. In (Chen et al., 2020; Ding et al., 2020), the SOP was used to enhance the service restoration ability of a distribution network. As for the reliability of the distribution network, (Escalera et al., 2020; Yan et al., 2020) shows that the substitution of an SOP for a tie switch can improve distribution network reliability, especially for ADNs with DGs. However, research on SOP-based ES operation strategy is scant, and only Ref (Yao et al., 2018) utilized an SOP-based ES to reduce the loss of ADNs. This approach does not maximize the ability of ESs to transfer power in time to reduce the operating cost of the ADNs. In addition, the frequent charge and discharge of ES directly affects the lifetime of the battery module (Tran and Khambadkone, 2013). Therefore, the influence of SOP-based ES on the operating cost of the ADNs and the consideration of the battery lifetime are necessary.

To fill the aforementioned gaps, an optimal operation model for an SOP-based ES in the ADNs with regard for battery lifetime is proposed in this article. The main contributions of this work can be summarized as follows:

(1) The active and reactive power equations of an SOP-based ES are established, and the cost of battery degradation is deduced.
(2) An optimal operation model is established and considers the power exchange cost, loss cost, and battery degradation cost of the distribution network. Moreover, the original mixed integer nonlinear programming (MINLP) problem is transformed into a mixed integer linear programming (MILP) problem by linearization, thereby improving the solving efficiency and convergence.
(3) The effectiveness of the proposed optimization model is verified by the IEEE 33-node test system (Baran and Wu, 1989).

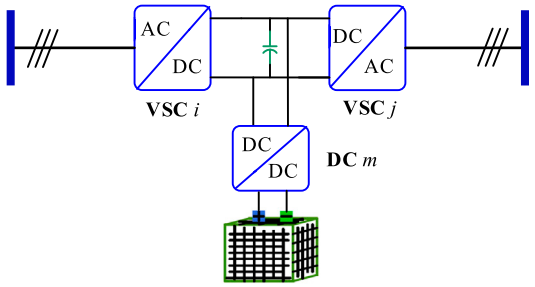

FIGURE 1 | The structure of SOP-based ES.

The remainder of this paper is organized as follows. The SOP-based ES is modeled in Section *Modeling of SOP-Based ES*. The optimal operation model of the SOP-based ES in the ADNs is established in Section *Problem Formulation*. Case studies are presented in Section Case Studies. Conclusions are drawn in Section *Conclusion*.

MODELING OF SOP-BASED ES

Active and Reactive Power Equations of the SOP-Based ES

The structure of an SOP-based ES is shown in **Figure 1**. The SOP-based ES has two VSCs and a DC–DC converter. The DC sides of the two VSCs are connected with the DC–DC converter, the AC sides are connected to the feeders, and the other side of the DC–DC converter is linked to the battery. The SOP-based ES can transfer the active power between feeders and store energy, and the AC side of VSCs can also regulate the reactive power. The power of the SOP-based ES meets the following constraints (Yao et al., 2018):

$$P^{t}_{i,\mathrm{VSC}} + P^{t}_{j,\mathrm{VSC}} + P^{t}_{m,\mathrm{ES}} + P^{\mathrm{L},t}_{i,\mathrm{VSC}} + P^{\mathrm{L},t}_{j,\mathrm{VSC}} + P^{\mathrm{L},t}_{m,\mathrm{DC}} = 0, \tag{1}$$

$$\begin{cases} P^{\mathrm{L},t}_{i,\mathrm{VSC}} = A_{i,\mathrm{VSC}}\sqrt{\left(P^{t}_{i,\mathrm{VSC}}\right)^2 + \left(Q^{t}_{i,\mathrm{VSC}}\right)^2}, \\ P^{\mathrm{L},t}_{j,\mathrm{VSC}} = A_{j,\mathrm{VSC}}\sqrt{\left(P^{t}_{j,\mathrm{VSC}}\right)^2 + \left(Q^{t}_{j,\mathrm{VSC}}\right)^2}, \\ P^{\mathrm{L},t}_{m,\mathrm{DC}} = A_{ij,\mathrm{DC}}\left|P^{t}_{m,\mathrm{ES}}\right|, \end{cases} \tag{2}$$

$$\begin{cases} \sqrt{\left(P^{t}_{i,\mathrm{VSC}}\right)^2 + \left(Q^{t}_{i,\mathrm{VSC}}\right)^2} \le S_{i,\mathrm{VSC}}, \\ \sqrt{\left(P^{t}_{j,\mathrm{VSC}}\right)^2 + \left(Q^{t}_{j,\mathrm{VSC}}\right)^2} \le S_{j,\mathrm{VSC}}, \\ -S_{m,\mathrm{DC}} \le P^{t}_{m,\mathrm{ES}} \le S_{m,\mathrm{DC}}, \end{cases} \tag{3}$$

$$\begin{cases} Q^{\min}_{i,\mathrm{VSC}} \le Q^{t}_{i,\mathrm{VSC}} \le Q^{\max}_{i,\mathrm{VSC}}, \\ Q^{\min}_{j,\mathrm{VSC}} \le Q^{t}_{j,\mathrm{VSC}} \le Q^{\max}_{j,\mathrm{VSC}}, \end{cases} \tag{4}$$

where $P^t_{i,\mathrm{VSC}}$ and $P^t_{i,\mathrm{VSC}}$ are the active power injections of VSC i and j at time t. $P^t_{m,\mathrm{ES}}$ is the active power consumption of the ES. $P^{L,t}_{i,\mathrm{VSC}}$ and $P^{L,t}_{j,\mathrm{VSC}}$ are the power losses of VSC i and j, respectively. $P^{L,t}_{m,\mathrm{DC}}$ is the power loss of the DC–DC converter ij. $A_{i,\mathrm{VSC}}$, $A_{j,\mathrm{VSC}}$ and $A_{ij,\mathrm{DC}}$ are the power loss coefficients. $Q^t_{i,\mathrm{VSC}}$ and $P^t_{j,VSC}$ are the reactive power injections of VSC i and j. $S_{i,\mathrm{VSC}}$, $S_{j,\mathrm{VSC}}$, and $S_{ij,\mathrm{DC}}$ are the capacities of the VSC and DC–DC converter. $Q^{min}_{i,\mathrm{VSC}}$ and $Q^{max}_{i,\mathrm{VSC}}$ are the minimum and maximum reactive power injections of VSC i. $Q^{min}_{j,\mathrm{VSC}}$ and $Q^{max}_{J,\mathrm{VSC}}$ are the minimum and maximum reactive power injections of VSC j.

Eq. 1 is the active power balance of the SOP-based ES. **Eq. 2** is the power loss equation. **Eqs. 3**, **4** are the capacity and reactive power constraints, respectively.

ES must also meet the following constraints:

$$\begin{cases} P^t_{m,\mathrm{ES}} = P^t_{m,\mathrm{ch,ES}} - P^t_{m,\mathrm{dis,ES}}, \\ 0 \le P^t_{m,\mathrm{ch,ES}} \le \lambda^t_m M, 0 \le P^t_{m,\mathrm{dis,ES}} \le (1-\lambda^t_m)M, \end{cases} \tag{5}$$

$$SoC^t_m = SoC^0_m + \sum_{t_0=1}^{t}\left(\eta_{m,\mathrm{ES}} P^{t_0}_{m,\mathrm{ch,ES}} - \frac{P^{t_0}_{m,\mathrm{dis,ES}}}{\eta_{m,\mathrm{ES}}}\right)\frac{\Delta t}{Cap_m}, \tag{6}$$

$$SoC^{\min}_m \le SoC^t_m \le SoC^{\max}_m, \tag{7}$$

$$SoC^T_m = SoC^0_m, \tag{8}$$

where $P^t_{\mathrm{m,ch,ES}}$ and $P^t_{\mathrm{m,dis,ES}}$ are the charging and discharging powers of ES m. λ^t_m is a binary variable if ES m is in the charging state, λ^t_m =1, otherwise, λ^t_m =0. $\mathrm{SoC}^{\,t}_{\mathrm{m}}$ is the state of charge of ES m, and $\mathrm{SoC}^{\,0}_{\mathrm{m}}$ is the initial SOC. Δt is the time interval and equals one hour in this work. Cap_m is the energy capacity of ES m. $\eta_{m,\mathrm{ES}}$ is the ES efficiency. M is a sufficiently large number. $\mathrm{SoC}^{\min}_m$ and $\mathrm{SoC}^{\min}_m$ are the SOC limits of ES m. T is the total time intervals of an operation cycle.

Eq. 5 is used to obtain the charging and discharging powers. **Eq. 6** is the relationship between SOC and the charging and discharging powers. **Eq. 8** is the lower and upper limits of SOC. **Eq. 9** indicates the SOC of ES in the last time interval and equals the initial SOC.

Lifetime Model of the Battery

The depth of cycle discharge is the key factor affecting the battery lifetime (Tran and Khambadkone, 2013). The charge and discharge cycles of a battery constitute the process from discharging to charging. That is,

$$\begin{cases} cyc^t_m \ge \lambda^t_m - \lambda^{t-1}_m, \\ cyc^t_m \le \lambda^t_m, \\ cyc^t_m \le 1 - \lambda^{t-1}_m, \end{cases} \tag{9}$$

where *cyc^t_m is a binary variable and indicates the battery changes from a discharging to a charging state when cyc^t_m = 1.*

The cycle discharge depth $dt^{-1}_{m,cyc}$ of the battery refers to the discharge depth dt^{-1}_m at the moment before charging and can be expressed as

$$\begin{cases} -cyc^t_m M \le d^{t-1}_{m,cyc} \le cyc^t_m M, \\ d^{t-1}_m - (1-cyc^t_m)M \le d^{t-1}_{m,cyc} \le d^{t-1}_m + (1-cyc^t_m)M, \end{cases} \tag{10}$$

$$d^t_m = 1 - SoC^t_m. \tag{11}$$

The cycle life $N^t_{m,d}$ *of the battery can be expressed as the cycle discharge depth. That is,*

$$N^t_{m,d} = N_0\left(d^t_{m,cyc}\right)^{-k_p}, \tag{12}$$

where N_0 is the cycle number of the charge and discharge of a battery at 100% discharge depth. k_p is a constant that usually between 1.1 and 2.1 (Tran and Khambadkone, 2013; Duggal and Venkatesh, 2014).

The equivalent life degradation $N_{m,de}$ of the daily charge and discharge cycle can be expressed as (Duggal and Venkatesh, 2014)

$$N_{m,de} = \sum_{t=1}^{T}\frac{N_0}{N^t_{m,d}} = \sum_{t=1}^{T}\left(d^t_{m,cyc}\right)^{k_p}. \tag{13}$$

The battery cycle life in years $T_{m,\mathrm{life}}$ and the daily degradation cost $C_{m,\mathrm{ES}}$ can be formulated as:

$$T_{m,\mathrm{life}} = \frac{N_0}{(365 \cdot N_{m,de})}, \tag{14}$$

$$C_{m,\mathrm{ES}} = C_{m,\mathrm{inv,ES}}\frac{1}{365}\cdot\frac{r(1+r)^{T_{m,\mathrm{life}}}}{(1+r)^{T_{m,\mathrm{life}}}-1}, \tag{15}$$

where $C_{m,\mathrm{inv,ES}}$ is the investment cost of ES and r is discount rate.

PROBLEM FORMULATION

Optimization Model

The objective function is to minimize the total daily operation cost C, including the power exchange cost, network loss cost, and battery degradation cost.

$$\min C = \left(\sum_{t\in T}\left(c^t_{\mathrm{b}}P^t_{\mathrm{b,grid}} - c^t_{\mathrm{s}}P^t_{\mathrm{s,grid}}\right) + c_{\mathrm{L}}\sum_{t\in T}P^{L,t}\right)\Delta t + \sum_{m\in\Omega_{ES}}C_{m,ES}, \tag{16}$$

$$P^{L,t} = \left(\sum_{ij\in\Omega_l}P^{L,t}_{ij} + \sum_{i,j,m\in\Omega_{\mathrm{SOP-ES}}}\left(P^{L,t}_{i,\mathrm{VSC}} + P^{L,t}_{j,\mathrm{VSC}} + P^{L,t}_{m,\mathrm{DC}}\right)\right), \tag{17}$$

where c^t_{b}, *ct s*, and c_{L} are the electricity purchase price, electricity selling price, and loss cost, respectively. $P^t_{b,grid}$ *and* $\mathrm{P}^{\mathrm{t}}_{b,grid}$ are the active power purchase and selling. $P^{L,t}$ is the total power loss and includes the line loss $P^{L,t}_{ij}$ and the VSC and DC–DC converter loss. Ω_l and $\Omega_{\mathrm{SOP\text{-}ES}}$ are the sets of the branch and SOP-based ES, respectively.

The constraints of the optimization model include the power flow, PV generation, and network operation constraints.

Linearized DistFlow Equations

The power flow equations of an ADN can be expressed as

$$\sum_{i\in u(j)}\left(P^t_{ij} - P^{L,t}_{ij}\right) + P^t_j = \sum_{k\in v(j)}P^t_{jk}, \tag{18}$$

$$\sum_{i\in u(j)}\left(Q^t_{ij} - Q^{L,t}_{ij}\right) + Q^t_j = \sum_{k\in v(j)}Q^t_{jk}, \tag{19}$$

$$P^t_j = P^t_{j,\mathrm{VSC}} + P^t_{j,\mathrm{PV}} - P^t_{j,Load}, \tag{20}$$

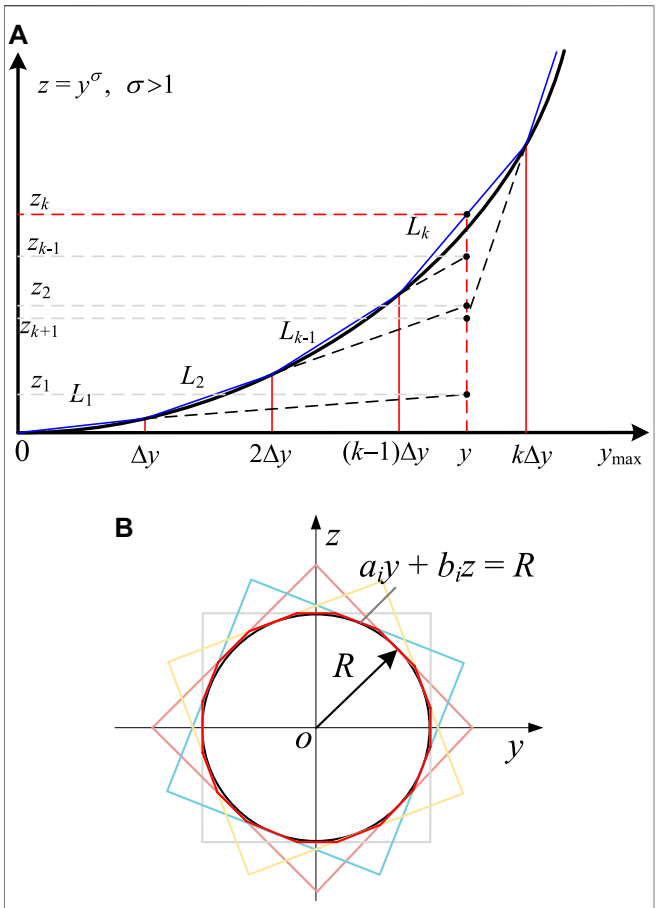

FIGURE 2 | Piecewise linearization for the power function term and circle term; **(A)** power function term; and **(B)** circle term.

$$Q_j^t = Q_{j,\mathrm{VSC}}^t + Q_{j,\mathrm{PV}}^t - Q_{j,Load}^t, \tag{21}$$

$$V_j^t = \frac{V_i^t - \left(r_{ij}P_{ij}^t + x_{ij}Q_{ij}^t\right)}{V_N}, \tag{22}$$

where P_{ij}^t and Q_{ij}^t are the active and reactive powers of the branch from nodes i to j. P_j^t and Q_j^t are the active and reactive power injections at node j, respectively. $P_{j,\mathrm{PV}}^t$ and $Q_{j,\mathrm{PV}}^t$ are the active and reactive power injections of the PV generations, respectively. $P_{j,Load}^t$ and $Q_{j,Load}^t$ are the active and reactive powers of the load, respectively. V_i^t and V_N are the node voltage and its rated value, respectively. r_{ij} and x_{ij} are the resistance and reactance of branch ij, respectively. Constraints **Eqs. 18–21** are the linearized DistFlow equations with power loss (Zhang et al., 2019). The power loss equation can be expressed as follows:

$$P_{ij}^{L,t} = \frac{r_{ij}\left[\left(P_{ij}^t\right)^2 + \left(Q_{ij}^t\right)^2\right]}{\left(V_N\right)^2}, \tag{23}$$

$$Q_{ij}^{L,t} = \frac{x_{ij}\left[\left(P_{ij}^t\right)^2 + \left(Q_{ij}^t\right)^2\right]}{\left(V_N\right)^2}. \tag{24}$$

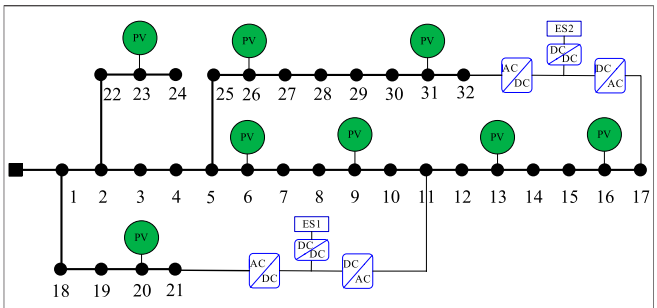

FIGURE 3 | IEEE 33-node system with SOP-based ES and PV generations.

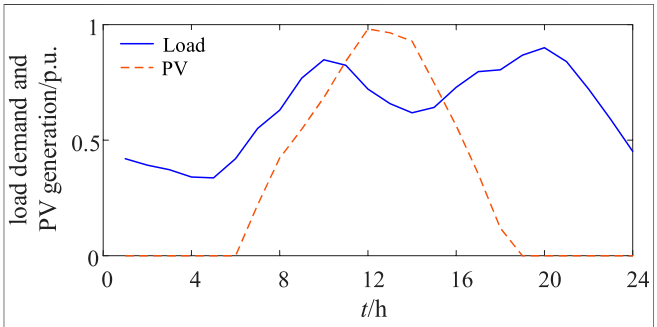

FIGURE 4 | Load demand and PV generation.

PV Generations Constraints

$$P_{i,\mathrm{PV}}^t = P_{i,\mathrm{PV}}^{t,\mathrm{rated}}, \tag{25}$$

$$Q_{i,\mathrm{PV}}^t = P_{i,\mathrm{PV}}^t \tan\varphi_{\mathrm{PV}}, \tag{26}$$

where $\tan\varphi_{\mathrm{PV}}$ is the power factor of a PV converter.

Network Operation Constraints

$$V^{\min} \le V_i^t \le V^{\max}, \tag{27}$$

$$\sqrt{\left(P_{ij}^t\right)^2 + \left(Q_{ij}^t\right)^2} \le S_{ij}^{\max}, \tag{28}$$

where $V^{\min}$ and $V^{\max}$ are the minimum and maximum node voltages, respectively. $S_{ij}^{\max}$ is the branch capacity. Constraints **Eqs. 22**, **23** are the node and branch capacity constraints, respectively.

Model Linearization

Constraints **Eqs. 2**, **3**, **13–15**, **23**, **24**, **28** are nonconvex and nonlinear, and will affect the solution efficiency and convergence. Linearization can help solve this problem.

Constraints **Eqs. 14**, **15** can be approximately treated as the following linear function (He et al., 2017)

$$C_{m,\mathrm{ES}} = L_{m,de}N_{m,de} + K_{m,de}, \tag{29}$$

where $L_{\mathrm{m,de}}$ and $K_{\mathrm{m,de}}$ are linear parameters that can be obtained by linear fitting.

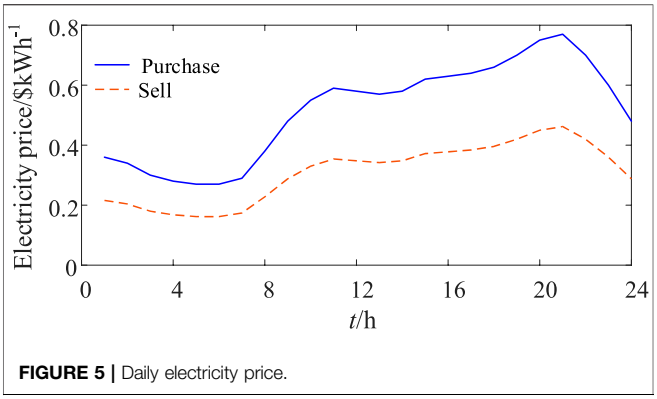

FIGURE 5 | Daily electricity price.

The power function terms $z = y^{\sigma}$ ($\sigma > 1$) in Constraints **Eqs. 13**, **23**, **24** are linearized as **Eq. 30** (Wang et al., 2020),

$$\begin{cases} z_k = L_k y + K_k, (k-1)\Delta y \le y \le k\Delta y, \\ L_k = \left[k^{\sigma} - (k-1)^{\sigma}\right]\Delta y^{\sigma-1}, \\ K_k = \left(k^{\sigma} - k^{\sigma+1} + k(k-1)^{\sigma}\right)\Delta y^{\sigma}, \\ z \ge z_k, y \ge y_0, y \ge -y_0, \end{cases} \tag{30}$$

where $y_0 \in \{(d^t_{m,cyc})^{k_p}, P^t_{ij}, Q^t_{ij}\}$, y is a positive value that is greater than the absolute value of y_0. L_k is the slope at the linear function of segment k. y will converge to the absolute value of y_0 because the objective function minimizes line power loss. **Figure 2A** shows that $z_k \ge \max\{z_1, z_2, \ldots, z_{k-1}, z_{k+1}, \ldots\}$ when $(k-1)\ \Delta y \le y \le k\ \Delta y$. Therefore, $z \ge z_k$ provides a lower bound for z, and the objective function helps z converge to z_k. This proposed linearization method excludes the integer variables and improves the solving efficiency.

The circle terms in Constraints **Eqs. 2**, **3**, **28** can be linearized with the replacement of a regular polygon, as shown in **Figure 2B**. Constraint **Eq. 2** is an equation constraint and should be relaxed to an inequality constraint (Yao et al., 2018). These convex second-order conic models $y^2 + z^2 \le R^2$ can be linearized as follows:

$$a_i y + b_i z \le R, \tag{31}$$

where a_i and b_i are the linear equation coefficients.

The absolute value constraint in Constraint **Eq. 2** can be linearized as follows:

$$\begin{cases} P^{L,t}_{m,DC} \ge A_{ij,DC} P^t_{m,ES}, \\ P^{L,t}_{m,DC} \ge -A_{ij,DC} P^t_{m,ES}. \end{cases} \tag{32}$$

CASE STUDIES

The IEEE 33-node test system is used to verify the feasibility and efficiency of the proposed model. The simulation program is tested on the MATLAB R2016b-YALMIP platform (Lofberg, 2004), and the optimization models are solved by CPLEX (IBM ILOG CPLEX Optimization Studio, 2020). YALMIP is an open source software that provides interfaces for MATLAB and solvers. CPLEX is a mathematical programming solver developed by IBM and can effectively solve MILP problems. The hardware device is a computer with Intel Core i7-8700 @ 3.2 GHz and 16 GB RAM.

Parameter Settings

The IEEE 33-node system has two SOP-based ESs and eight PV generations (**Figure 3**). The system parameters can be found in (Baran and Wu, 1989). Each SOP-based ES include two VSCs, a DC–DC converter and an ES. The capacity of each VSC is 300 kVA, and the DC–DC capacity is 300 kW. The energy capacities of ES one and two are both 2000 kWh. The power loss coefficient of the VSC and DC–DC converter is 0.02. The capacity PV converter is 500 kVA. The voltage limits are (0.95, 1.05) p.u.. The load demand and PV generation and electricity price are shown in **Figures 4**, **5**, respectively. The network loss cost is $0.5/kWh. The investment cost of the ES one and two are both $200/kWh, the cycle number of ES one and two N_0 = 1,591, and the constant k_p = 2.09. The initial SOC values of ES one and two are both 0.5, and the minimum and maximum SOC values of ES one and two are 0.2 and 0.9, respectively.

Optimization Results Analysis

Four cases are used to evaluate the effect of the SOP-based ES and battery degradation.

Case 1: Without SOP-based ES.
Case 2: Two SOPs exist in the system, and no ES connects to the SOP DC side.
Case 3: Two SOP-based ESs exist in the system (**Figure 4**), and the battery degradation is not considered.
Case 4: Two SOP-based ESs exist in the system (**Figure 4**), and the battery degradation is considered.

TABLE 1 | Optimization results.

Case	Electricity purchase cost/$	Electricity selling benefits/$	Loss cost/$	Degradation of battery			Total cost//$
				Degradation cost/$	Cycle life of ES 1/year	Cycle life of ES 2/year	
1	18,440	1,576	747	\	\	\	17,611
2	18,350	1,627	607	\	\	\	17,330
3	16,952	1,048	709	419	8.3	7.5	17,031
4	17,209	1,292	733	283	15.1	10.7	16,934

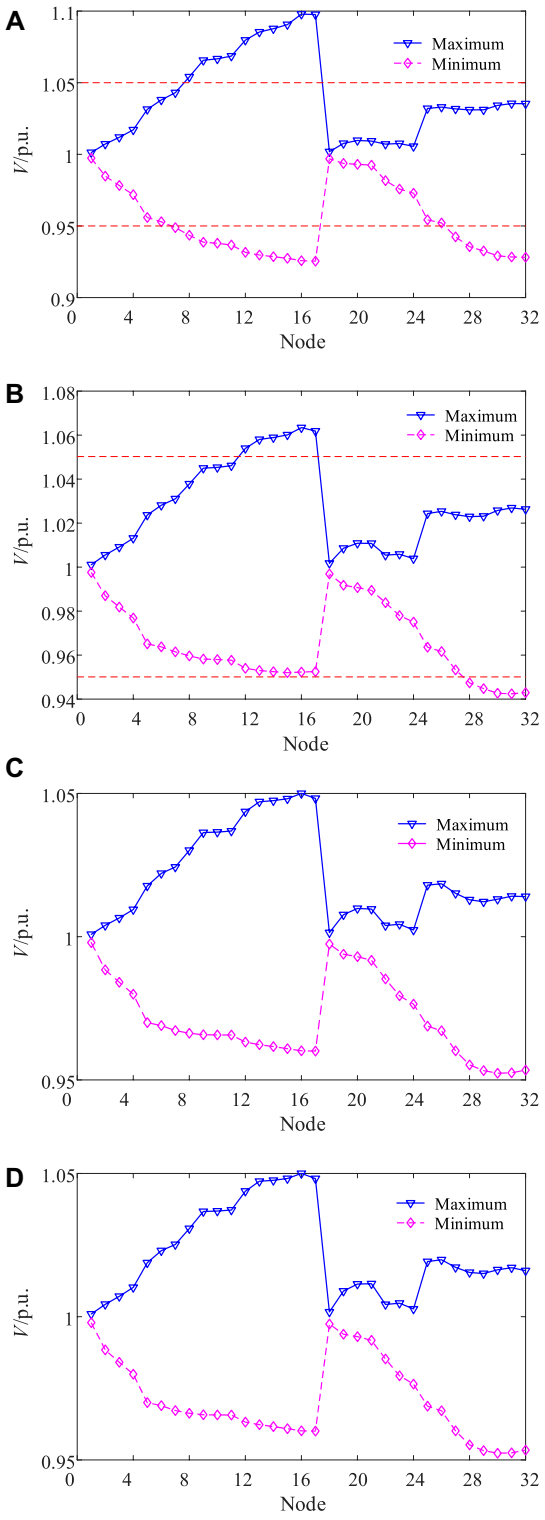

FIGURE 6 | Voltage profile of ADN in Cases 1–4; **(A)** Case 1, **(B)** Case 2, **(C)** Case 3 and **(D)** Case 4.

The optimization results are shown in **Table 1**. As no ES exists in Cases 1 and 2, the difference in the TOU electricity price cannot be fully utilized to reduce the operating cost of the ADN. The SOP in Case 2 reduces power losses, thereby resulting in lower power purchase costs and loss costs and increase in revenue from electricity sales. Therefore, the total cost in Case 2 is slightly lower than that in Case 1 and the total cost is highest for Case 1. In Cases 3 and 4, the operating cost of the ADN is reduced by controlling the storage and release of energy. Although SOP-based ES loss is included in Cases 3 and 4, the total loss cost is lower than that in Cases 1 and 2. Given that SOP-based ES can balance the feeder load and compensate for reactive power, this feature helps reduce the line loss. In addition, the ES degradation cost is considered in Case 3, so the degradation cost in Case 3 is lower than that in Case 2. The cycle life of ES one and of ES two in Case 3 can reach 15.1 and 10.7 years, respectively. By contrast, the cycle life of ES one and of ES two in Case 2 are only 8.3 and 7.5 years, respectively.

Figure 6 depicts the maximum and minimum voltage profiles of ADN in Cases 1–4. In Case 1, the maximum voltage of Nodes 8–17 violates the voltage upper limit, while the minimum voltage is less than the voltage lower limit. Given the peak output of PV generation, the power flow reverses, thereby causing the voltage at the end node to rise. When the PV output is low, the load causes the voltage to decrease. The SOP in Case 2 improves the voltage profile by transferring power flow and adjusting reactive power, but some nodes (Nodes 12–17 and 28–32) still violate the voltage constraint. However, the SOP-based ESs in Cases 2 and 3 not only have the functions of transferring active power and regulating reactive power, but also have the ability to store and release active power, so the voltage profile is significantly improved.

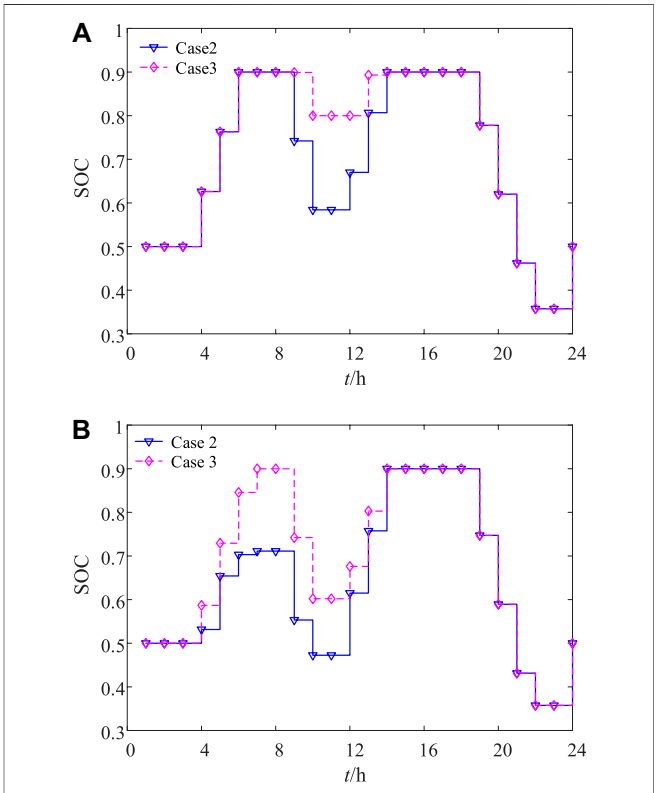

FIGURE 7 | The SOC of ES in Cases 2 and 3, **(A)** ES 1, and **(B)** ES 2.

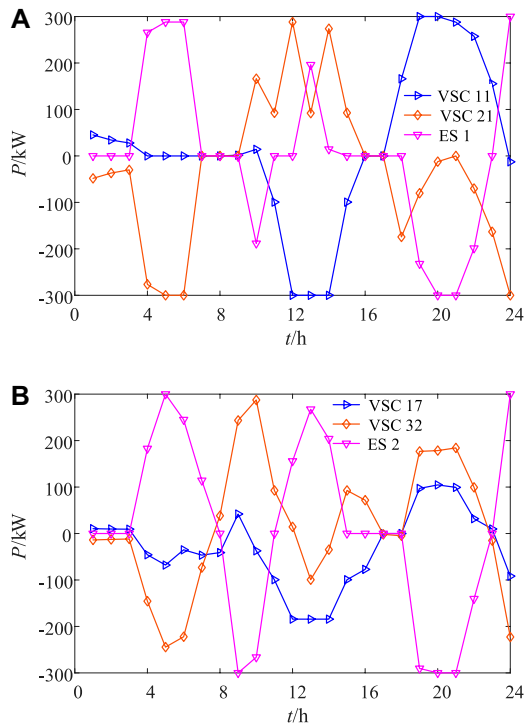

FIGURE 8 | Active power of SOP-based ESs in Case 4; **(A)** SOP -based ES 1, **(B)** SOC-based ES 2

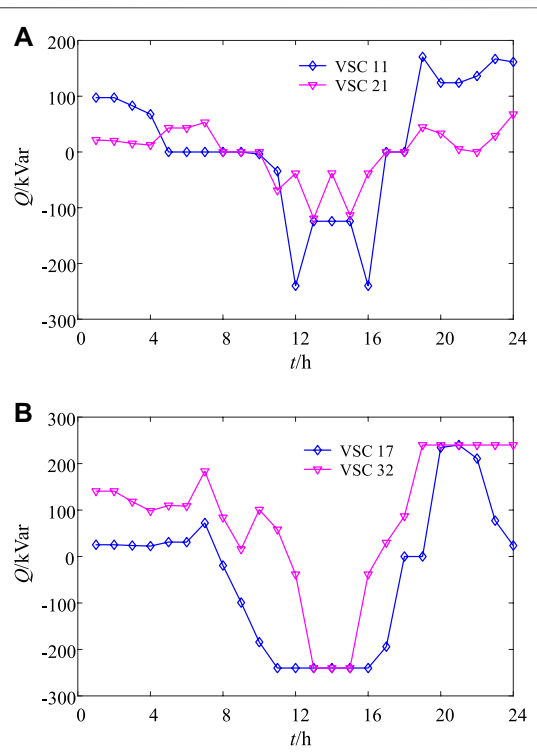

FIGURE 9 | Reactive power of SOP-based ESs in Case 4 **(A)** SOP -based ES one and **(B)** SOC-based ES 2

TABLE 2 | Convergence and solving efficiency of different models.

Model	Objective function value/$	Computing time/s
MINLP	\	>3,600
MILP	16,934	19.2

The SOC of ESs one and two in Cases 3 and 4 are shown in **Figure 7**. The ESs are in the charging state from t = 4 to 6 h because of the low price of electricity. In t = 9 and 10 h, the ESs discharge because electricity prices and load demand increase. From t = 12 to 14 h, the SOC increases again because the PV output increases but the load decreases. From t = 19 h, the ES discharged due to the increased load. Moreover, the SOC in Case 3 is higher than that in Case 2, a situation which can avoid excessive discharge and extend the battery life.

Figure 8 depicts the active power of the SOP-based ESs in Case 3. The active power of VSC 21 and ES one are positive and negative, respectively, from t = 4 to 6 h. Thus, the SOP-based ES one transfers the active power from Node 21 to ES 1. As the PV output is 0 and Node 21 is close to the slack bus, Node 11 is far from the slack bus with a lower voltage. Similarly, SOP-based ES two mainly transfers the active power from Node 32 to ES two at this period. From t = 9 h, the ES starts to discharge. As the PV output is higher, the voltage at the end nodes of the branch increases, so VSCs 21 and 32 inject active power, while VSCs 11 and 17 absorb active power. From t = 12 h, the ESs start to charge again when the PV output is highest. Given that VSC 21 is close to the balance node, the active power of VSC 21 is injected into Node 21, while other VSCs absorb active power. From t = 18 h, the PV output is 0, and the voltage at the end node is relatively low. Thus, VSC 21 absorbs active power, whereas other VSCs inject active power.

Figure 9 shows the reactive power of SOP-based ESs in Case 4. When the PV output is low or absent (t = 1–6 h and 19–24 h), all the output reactive power of VSCs improves the system voltage and reduces the power loss. When the PV output is high (t = 11–16 h), power flow reverse leads to voltage increase and the VSC absorption reactive power reduces system voltage.

Computing Performance

To verify the validity and convergence of the proposed linearized model, **Table 2** provides the comparison of optimization results and the computing time between the proposed MILP model and the original MINLP model solved by Knitro (Artelys Knitro, 2020). The solving efficiency of the MILP model is noticeably improved by linearization. The original MINLP problem is a nonconvex one for which obtaining the optimal solution is difficult. The nonconvex problem is transformed into a convex optimization problem by linearization, and its convergence is further improved.

CONCLUSION

In this study, the optimization operation model of SOP-based ESs in ADNs is presented, and the battery degradation cost is considered. The effectiveness and performance of the proposed model is validated by case studies. The ability of SOP-based ESs to

transfer power in time and space not only promotes the integration of DG, but also reduces the operating cost of the ADNs. By considering the battery degradation cost in the optimization model, excessive discharge can be avoided and battery life can be prolonged. The MILP proposed in this paper further improves the solving efficiency and convergence of the optimization model and helps identify the optimal solution. The research in this work is helpful for improving the operation management of ADNs and promoting the further development of renewable energy.

DATA AVAILABILITY STATEMENT

The original contributions presented in the study are included in the article/Supplementary Material, further inquiries can be directed to the corresponding author.

AUTHOR CONTRIBUTIONS

JW: Software, Validation, Writing- Original draft preparation NZ: Supervision, Writing-Reviewing and Editing AT: Data curation QW: Investigation, Conceptualization, Methodology.

FUNDING

This work was supported by the National Natural Science Foundation of China (Grant No. 52077017), Chongqing Technology Innovation and Application Development Special Key Project (cstc2019jscx-mbdxX0017) and the Fundamental Research Funds for the Central Universities (Grant No. 2019CDXYDQ0010).

REFERENCES

Artelys Knitro (2020). Available at: https://www.artelys.com/solvers/knitro/.

Badran, O., Mokhlis, H., Mekhilef, S., Dahalan, W., and Jallad, J. (2018). Minimum switching losses for solving distribution NR problem with distributed generation. *IET Gener., Transm. Distrib.* 12 (8), 1790–1801. doi:10.1049/iet-gtd.2017.0595

Baran, M. E., and Wu, F. F. (1989). Optimal capacitor placement on radial distribution systems. *IEEE Trans. Power Deliv.* 4 (1), 725–734. doi:10.1109/61.19265

Bloemink, J. M., and Green, T. C. (2010). "Increasing distributed generation penetration using soft normally-open points," in 2010 IEEE Power and Energy Society General Meeting, Providence, RI, July 25–29, 2010 (Piscataway, NJ: IEEE). doi:10.1109/pes.2010.5589629

Cao, W., Wu, J., Jenkins, N., Wang, C., and Green, T. (2016). Operating principle of soft open points for electrical distribution network operation. *Appl. Energy* 164 (15), 245–257. doi:10.1016/j.apenergy.2015.12.005

Chen, W., Lou, X., Ding, X., and Guo, C. (2020). Unified data-driven stochastic and robust service restoration method using non-parametric estimation in distribution networks with soft open points. *IET Gener., Transm. Distrib.* 14 (17), 3433–3443. doi:10.1049/iet-gtd.2019.1895

Ding, T., Wang, Z., Jia, W., Chen, B., and Shahidehpour, M. (2020). Multiperiod distribution system restoration with routing repair crews, mobile electric vehicles, and soft-open-point networked microgrids. *IEEE Trans. Smart Grid* 11 (6), 4795–4808. doi:10.1109/tsg.2020.3001952

Duggal, I., and Venkatesh, B. (2014). Short-term scheduling of thermal generators and battery storage with depth of discharge-based cost model. *IEEE Trans. Power Sys.* 30 (4), 2110–2118. doi:10.1109/TPWRS.2014.2352333

Escalera, A., Prodanović, M., Castronuovo, E. D., and Roldan-Perez, J. (2020). Contribution of active management technologies to the reliability of power distribution networks. *Appl. Energy* 267, 114919. doi:10.1016/j.apenergy.2020.114919

Habibollahzade, A., Houshfar, E., Ashjaee, M., Behzadi, A., Gholamian, E., and Mehdizadeh, H. (2018). Enhanced power generation through integrated renewable energy plants: solar chimney and waste-to-energy. *Energy Convers. Manag.* 166, 48–63. doi:10.1016/j.enconman.2018.04.010

He, G., Chen, Q., Kang, C., Pinson, P., and Xia, Q. (2017). Optimal bidding strategy of battery storage in power markets considering performance-based regulation and battery cycle life. *IEEE Trans. Smart Grid* 7 (5), 2359–2367. doi:10.1109/TSG.2015.2424314

IBM ILOG CPLEX Optimization Studio (2020). Available at: https://www.ibm.com/products/ilog-cplex-optimization-studio.

Imani, M. H., Niknejad, P., and Barzegaran, M. R. (2019). Implementing Time-of-Use Demand Response Program in microgrid considering energy storage unit participation and different capacities of installed wind power. *Elec. Power Syst. Res.* 175, 105916. doi:10.1016/j.epsr.2019.105916

Ji, H., Wang, C., Li, P., Ding, F., and Wu, J. (2018). Robust operation of soft open points in active distribution networks with high penetration of photovoltaic integration. *IEEE Trans. Sustain. Energy* 10 (1), 280–289. doi:10.1109/TSTE.2018.2833545

Ji, H., Wang, C., Li, P., Zhao, J., Song, G., Ding, F., et al. (2017). An enhanced SOCP-based method for feeder load balancing using the multi-terminal soft open point in active distribution networks. *Appl. Energy* 208, 986–995. doi:10.1016/j.apenergy.2017.09.051

Li, P., Ji, H., Wang, C., Zhao, J., Song, G., Ding, F., et al. (2017). Coordinated control method of voltage and reactive power for active distribution networks based on soft open point. *IEEE Trans. Sustain. Energy* 8 (4), 1430–1442. doi:10.1109/tste.2017.2686009

Li, P., Ji, H., Yu, H., Zhao, J., Wang, C., Song, G., et al. (2019). Combined decentralized and local voltage control strategy of soft open points in active distribution networks. *Appl. Energy* 241, 613–624. doi:10.1016/j.apenergy.2019.03.031

Lofberg, J. (2004). "YALMIP: a toolbox for modeling and optimization in MATLAB," in 2004 IEEE international conference on robotics and automation (IEEE Cat. No. 04CH37508), New Orleans, LA, September 2–4, 2004 (Piscataway, NJ: IEEE), 284–289.

Long, C., Wu, J., Thomas, L., and Jenkins, N. (2016). Optimal operation of soft open points in medium voltage electrical distribution networks with distributed generation. *Appl. Energy* 184, 427–437. doi:10.1016/j.apenergy.2016.10.031

Lou, C., Yang, J., Li, T., and Vega-Fuentes, E. (2020). New phase-changing soft open point and impacts on optimising unbalanced power distribution networks. *IET Gener., Transm. Distrib.* 14 (23), 5685–5696. doi:10.1049/iet-gtd.2019.1660

Naderi, Y., Hosseini, S. H., Ghassem Zadeh, S., Mohammadi-Ivatloo, ., and Guerrero, J. M. (2018). An overview of power quality enhancement techniques applied to distributed generation in electrical distribution networks. *Renew. Sustain. Energy Rev.* 93, 201–214. doi:10.1016/j.rser.2018.05.013

Qi, Q., Wu, J., and Long, C. (2017). Multi-objective operation optimization of an electrical distribution network with soft open point. *Appl. Energy* 208, 734–744. doi:10.1016/j.apenergy.2017.09.075

Shafik, M. B., Chen, H., Rashed, G. I., El-Sehiemy, R. A., Elkadeem, M. R., and Wang, S. (2019). Adequate topology for efficient energy resources utilization of active distribution networks equipped with soft open points. *IEEE Access* 7, 99003–99016. doi:10.1109/access.2019.2930631

Su, X., Masoum, M. A. S., and Wolfs, P. J. (2014). Optimal pv inverter reactive power control and real power curtailment to improve performance of unbalanced four-wire lv distribution networks. *IEEE Trans. Sustain. Energy* 5 (3), 967–977. doi:10.1109/tste.2014.2313862

Sun, F., Ma, J., Yu, M., and Wei, W. (2021). Optimized two-time scale robust dispatching method for the multi-terminal soft open point in unbalanced active distribution networks. *IEEE Trans. Sustain. Energy* 12 (1), 587–598. doi:10.1109/tste.2020.3013386

Tran, D., and Khambadkone, A. M. (2013). Energy management for lifetime extension of energy storage system in micro-grid applications. *IEEE Trans. Smart Grid* 4 (3), 1289–1296. doi:10.1109/tsg.2013.2272835

Wang, J., Zhou, N., Ran, Y., and Wang, Q. (2020). Reducing the active power curtailment of distributed generation based on soft open points in unbalanced distribution networks. *IET Renew. Power Gener.* 14, 3252. doi:10.1049/iet-rpg.2020.0301

Yan, F., Chen, X., Tang, W., Yan, R., and Wu, H. (2020). Reliability and power supply capability evaluation of active distribution networks with four-terminal soft open points. *IET Smart Grid* 3 (5), 657–666. doi:10.1049/iet-stg.2019.0353

Yao, C., Zhou, C., Yu, J., Xu, K., Li, P., and Song, G. (2018). A sequential optimization method for soft open point integrated with energy storage in active distribution networks. *Energy Procedia* 145, 528–533. doi:10.1016/j.egypro.2018.04.077

Zhang, C., Xu, Y., and Dong, Z. Y. (2019). Robustly coordinated operation of a multi-energy micro-grid in grid-connected and islanded modes under uncertainties. *IEEE Trans. Sustain. Energy* 11 (2), 640–651. doi:10.1109/TSTE.2019.2900082

Zhao, Z.-Y., and Chen, Y.-L. (2018). Critical factors affecting the development of renewable energy power generation: evidence from China. *J. Clean. Prod.* 184, 466–480. doi:10.1016/j.jclepro.2018.02.254

Conflict of Interest: The authors declare that the research was conducted in the absence of any commercial or financial relationships that could be construed as a potential conflict of interest.

frontiers in Energy Research

ORIGINAL RESEARCH
published: 03 March 2021
doi: 10.3389/fenrg.2021.635071

Reliability Assessment of Power Systems with High Renewable Energy Penetration Using Shadow Price and Impact Increment Methods

Kai Hou[1,2], *Puting Tang*[1,2], *Zeyu Liu*[1,2]*, *Hongjie Jia*[1,2] *and Lewei Zhu*[1,2,3]

[1]Key Laboratory of Smart Grid of Ministry of Education, Tianjin University, Tianjin, China, [2]Key Laboratory of Smart Energy and Information Technology of Tianjin Municipality, Tianjin University, Tianjin, China, [3]Tianjin Key Laboratory for Control Theory and Applications in Complicated Industry Systems, Maritime College, Tianjin University of Technology, Tianjin, China

With the ever-increasing penetration of renewable resources, more complexities and uncertainties are introduced in power system reliability assessment. This entails an enormous number of contingency states to represent the characteristics of renewable energy. As a result, the unbearable computation burden is the main challenge toward the efficiency of the state enumeration (SE) method. To address that, this paper proposes an improved reliability evaluation approach that can not only increase the accuracy but also accelerate the analysis. In detail, the impact increment method is first employed to decrease the proportion of higher-order contingency states, leading to accuracy improvement. Then, the shadow price is used to solve the optimal power flow (OPF) problem in a faster manner. This shadow price (SP) method allows us to obtain the optimal load curtailment directly from linear functions rather than the time-consuming OPF algorithms. In addition, one hundred percent criterion is used to match shadow-price-based linear functions with system states. Case studies are performed on the RTS-79 system and IEEE 118-bus system, in which test scenarios include loads, photovoltaics (PV), and wind turbines (WT). Results indicate that the proposed method can significantly ease the computation burden and outperform traditional reliability assessment methods in terms of both computing time and accuracy.

Keywords: shadow price, impact increment, reliability assessment, optimal load curtailment, renewable energy, optimal power flow

OPEN ACCESS

Edited by:
Nian Liu,
North China Electric Power University, China

Reviewed by:
Kenneth Okedu,
Caledonian College of Engineering, Oman
Minh Quan Duong,
The University of Danang, Vietnam

***Correspondence:**
Zeyu Liu
tjulzy@tju.edu.cn

Specialty section:
This article was submitted to Smart Grids, a section of the journal Frontiers in Energy Research

Received: *29 November 2020*
Accepted: *15 January 2021*
Published: *03 March 2021*

Citation:
Hou K, Tang P, Liu Z, Jia H and Zhu L (2021) Reliability Assessment of Power Systems with High Renewable Energy Penetration Using Shadow Price and Impact Increment Methods. Front. Energy Res. 9:635071. doi: 10.3389/fenrg.2021.635071

INTRODUCTION

With the increasingly great attention to the low-carbon emission and sustainability, the conventional generations using fossil fuels are withdrawing and renewable resources are rapidly developing. Whereas, the expanding share of renewable energy brings more uncertainties in reliability assessment. Unlike conventional energy, the outputs of PV and WT are determined by solar radiation, wind velocity, etc. The fluctuation and unpredictable characteristics of these nature factors make the outputs of renewable generation stochastic and intermittent. Therefore, this raises the concern of generation adequacy in the power system with high renewable energy penetration.

Indeed, there is a growing interest in evaluating the impact of high penetration of wind power and photovoltaics on power system reliability (Alotaibi and Salama, 2016). The authors in (Ding et al., 2011) develops the output models of wind turbines in a wind farm considering wind speed

correlation. A new wind power probabilistic interval prediction model is proposed to describe the uncertain scenario of wind power (Yang et al., 2020). Moreover, an efficient framework that enables a fast cascading path searching under high penetration of wind power (Liu et al., 2020a) is proposed. The universal generating functions are used to evaluate the time-varying reliabilities of power systems with high wind power penetration (Ding et al., 2014). The Copula theory can capture the correlation between wind turbines in different locations (Tomasson and Soder, 2018). It inevitably entails a large number of scenarios and variables to represent the fluctuating outputs of renewable resources. Moreover, the detailed hourly load models and massive contingency states also need to be considered in the reliability assessment. Thus, with the expansion of power systems and the increasing penetration of renewable energy, the number of system states exponentially grows, which results in an unacceptable computation burden.

In general, two major methods, Monte Carlo simulation (MCS) method and analytical method, are utilized to assess the reliability of power systems (Billinton and Li, 1994). Both have their applications and limitations. The MCS method randomly samples the system states to be analyzed, and variance reduction technique (Sankarakrishnan and Billinton, 1995), state-space pruning approach (Singh and Mitra, 1997), cross-entropy method (Gonzalez-Fernandez and da Silva, 2011), etc., have been successfully employed to promote its efficiency. However, the MCS usually requires a longer sampling time to encounter a failure state with a low probability of occurrence, when applied to evaluate highly reliable power systems (Li, 2014). On the other hand, the analytical method is very useful and more efficient for power system planning (Ding et al., 2011). The State Enumeration technique, a typical analytical method, enumerates system states until the stopping criteria are met. However, exponentially growing system states would result in such a heavy computation burden that the SE method cannot bear.

Various methods are proposed to ease the computation burden of the SE method for power system reliability evaluation considering PV and WT. Combining high-dimensional Copula theory with the discrete convolution method, an efficient approach (Wang et al., 2018) is proposed to handle high-dimensional dependencies. Generally, most literatures are investigated to reduce the number of system states. The maximum order of contingency states is commonly used as the stopping criterion to neglect the high-order states. Since the probability of a high-order contingency may be larger than that of a low-order contingency, this criterion may make the reliability results lower than the actual value. To deal with that, techniques such as fast sorting (Liu et al., 2008) are used to arrange contingencies based on the probability of occurrence. However, a low probability state may have larger impact on system reliability indices than a high probability state due to different outage capacities. To address this issue, an impact-increment-based state enumeration (IISE) approach (Hou et al., 2016; Hou et al., 2018) is used to transfer partial impacts of higher-order states to the corresponding lower-order ones. In this way, the proportion of high-order contingencies is decreased implicitly, and the neglecting of higher-order states will no longer bring unacceptable errors, albeit using the maximum order criterion. As a result, we can achieve a remarkable accuracy improvement for the SE method. Furthermore, an incremental reliability assessment approach (IRAA) (Lei et al., 2018) is proposed to apply IISE to transmission expansion planning. In this way, more reliable references could be provided for system planners to select the best optimal planning scheme.

Compared with the number of system states, studies of the state analysis acceleration are relatively rare. The state analysis requires repeated computations for OPF problems corresponding to numerous system states, therefore the state analysis is the most time-consuming process for the reliability assessment. An improved stochastic fractal search algorithm (ISFSA) (Nguyen et al., 2020) is proposed to improve the OPF solving process, in terms of optimal solution quality, execution speed as well as success rate. Time in an OPF optimization can be saved, and the enhancement is considerable in the whole process. Followed by that, Direct Current (DC) OPF (Geng et al., 2018), parallel computation (Gubbala and Singh, 1995), post optimal analysis (Safdarian et al., 2013), etc., are utilized to speed up the state analysis, but they cannot decrease the number of OPF optimizations. The multi-parametric linear programming approach (Yong et al., 2019) is used to decrease the OPF calculations for the MCS method. The Lagrange multiplier based state enumeration (LMSE) approach (Liu et al., 2020b) is proposed to accelerate the analysis without loss of accuracy. A shadow-price-based linear function is present in this paper to solve the OPF problem by matrix multiplications. In this manner, the optimal load curtailment can be obtained directly, rather than the time-consuming OPF computations. Therefore, we can significantly accelerate the evaluations of most system states to ease the computation burden for the SE method.

In this paper, we propose an improved state enumeration method based on the shadow price and impact-increment (SPIISE) method. The accuracy and speed of reliability assessment can be enhanced by the IISE method and shadow price (SP) method, respectively. Furthermore, by integrating the SP into the IISE, we can evaluate the reliability of power systems with high renewable energy penetration more efficiently. In summary, the main contributions are as follows:

(1) Shadow-price-based linear functions are constructed to establish the relationship between the system state and optimal load curtailment. By avoiding a myriad of OPF optimizations, we can achieve significantly reduce the computing time of reliability assessment.
(2) One hundred percent criterion is proposed to match the states with the shadow price, which can ensure the accuracy of the shadow-price-based linear functions.
(3) An impact-increment-based state enumeration method is used to evaluate the impact of renewable energy on reliability. This allows us to ease the heavy computation burden and improve the accuracy of the traditional SE method.

The remainder of this paper is organized as follows. Section *The Methodology of Reliability Assessment* introduced the framework of the proposed reliability assessment methodology.

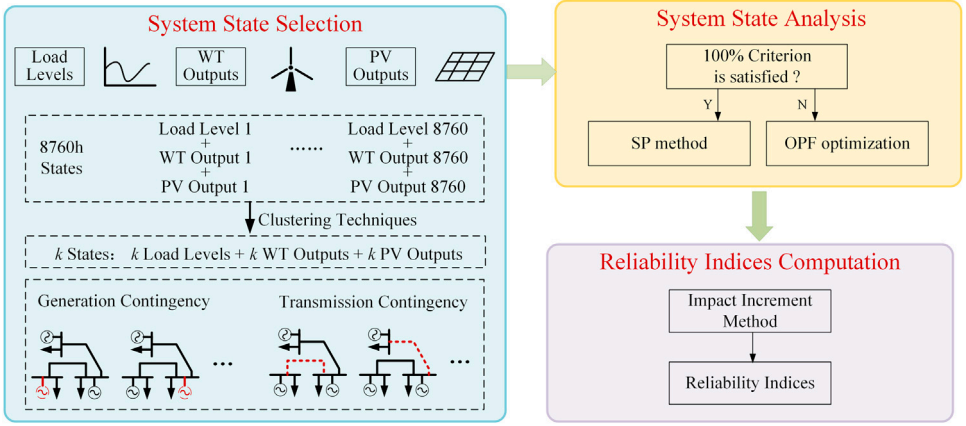

FIGURE 1 | The framework of the proposed method.

In Section *Reliability Assessment Method Based on Shadow Price and Impact Increment Methods*, the IISE method and the shadow price method are illustrated in detail. Case studies are performed in Section *Case Studies* and conclusions are drawn in Section *Conclusion*.

THE METHODOLOGY OF RELIABILITY ASSESSMENT

The framework of reliability evaluation of power systems with high renewable energy penetration is shown in **Figure 1**, which consists of three main processes: 1) system state selection 2) system state analysis 3) reliability indices computation.

System state selection is used to enumerate all possible contingencies by the SE method. The contingencies include generation and transmission. In the SE method, the reliability assessment indices can be obtained by calculating the possibility and impact of each system state. The mathematical expression is as follows:

$$R = \sum_{s \in \Omega} I(s)P(s) \tag{1}$$

$$P(s) = \prod_{i \in s} u_i \prod_{j \notin s} a_j \tag{2}$$

where $I(s)$ is the impact of the system state s, which can be calculated by system state analysis.

System state analysis uses the OPF model to calculate the influence of state contingency states. When some contingencies occur in power systems, resulting in line overload or system disconnection, the generator output must be readjusted, and if necessary, load shedding should be carried out to ensure the normal operation of the system. The optimal load curtailment is determined by the DC-OPF model, which is composed of three aspects: decision variables, objective function, and constraints.

The decision variable $\boldsymbol{x} = [\boldsymbol{\theta}, \boldsymbol{P_C}, \boldsymbol{P_G}]^{\mathrm{T}}$ includes the generation output $\boldsymbol{P_G} = [P_{G,1}, P_{G,2}, \ldots, P_{G,g}]^{\mathrm{T}}$, the voltage phase $\boldsymbol{\theta} = [\theta_1, \theta_2, \ldots, \theta_n]^{\mathrm{T}}$, and the load curtailment $\boldsymbol{P_C} = [P_{C,1}, P_{C,2}, \ldots, P_{C,n}]^{\mathrm{T}}$. The objective function is the minimum total load curtailment P_{LC}. The constraints include the power flow limits, the upper and lower limits of generation output, the branch flow limits, and the upper and lower limits of load curtailment. Then, the optimal load curtailment (OLC) model is

$$\begin{aligned}
&\min \quad f(\boldsymbol{x}) = P_{LC} = \sum_{i=1}^{n} P_{C,i} \\
&s.t. \quad P_{G,i} - P_{L,i} + P_{C,i} = \sum_{j \in i} \frac{\theta_i - \theta_j}{x_{ij}} \qquad i = 1, 2, \ldots, n \\
&\qquad 0 \le P_{G,i} \le P_{\mathrm{Gmax},i} \qquad i = 1, 2, \ldots, g \\
&\qquad 0 \le P_{C,i} \le P_{L,i} \qquad i = 1, 2, \ldots, n \\
&\qquad -P_{\mathrm{Bmax},ij} \le \frac{\theta_i - \theta_j}{x_{ij}} \le P_{\mathrm{Bmax},ij} \qquad j \in i \\
&\qquad \theta_i \ge 0 \qquad i = 1, 2, \ldots n
\end{aligned} \tag{3}$$

Reliability indices computation is to calculate the reliability assessment indices. After calculating all the enumerated contingencies states based on the optimal power flow model, the reliability assessment indices can be obtained. The common reliability indices include expected energy not supplied (EENS), probability of load curtailments (PLC), average energy not supplied (AENS), and expected demand not supplied (EDNS). This paper uses EENS as the reliability assessment index. According to (**Eq. 1**), it can be calculated by:

$$\mathrm{EENS} = T \sum_{s \in \Omega} I(s)P(s) \tag{4}$$

where T is the time period of reliability assessment. $I(s)$ is the load curtailment of state s.

RELIABILITY ASSESSMENT METHOD BASED ON SHADOW PRICE AND IMPACT INCREMENT METHODS

In this paper, the impact increment method and shadow price method are used to improve the system state selection and system state analysis, respectively. The impact increment method can transfer partial impacts of higher-order states to the corresponding lower-order ones, which can reduce the number of system states implicitly. SP method can establish the linear function between the system state and optimal load curtailment, which can avoid a myriad of OPF optimizations.

The Impact-Increment-Based State Enumeration Method

The traditional SE method needs to enumerate a large number of contingency states. In this way, some high-order states are ignored to improve the calculation speed at the cost of accuracy. In order to solve this problem, the IISE reliability assessment approach is used in this paper.

According to the reliability indices calculation **Eq. 1**, the reliability indices calculation equation based on impact increment can be deduced. Taking a three-components system as an example, we have,

$$\begin{aligned} R = {} & a_1a_2a_3I_\phi + u_1a_2a_3I_1 + a_1u_2a_3I_2 + a_1a_2u_3I_3 \\ & + u_1u_2a_3I_{12} + u_1a_2u_3I_{13} + a_1u_2u_3I_{23} + u_1u_2u_3I_{123} \end{aligned} \tag{5}$$

Equation 5 is a polynomial with eight terms, including one normal state and seven contingency states. Then, this equation can be simplified by replacing the availability with unavailability,

$$\begin{aligned} R = {} & I_\phi + u_1\left(I_1 - I_\phi\right) + u_2\left(I_2 - I_\phi\right) + u_3\left(I_3 - I_\phi\right) \\ & + u_1u_2\left(I_{12} - I_1 - I_2 + I_\phi\right) + u_1u_3\left(I_{13} - I_1 - I_3 + I_\phi\right) \\ & + u_2u_3\left(I_{23} - I_2 - I_3 + I_\phi\right) \\ & + u_1u_2u_3\left(I_{123} - I_{12} - I_{13} - I_{23} + I_1 + I_2 + I_3 - I_\phi\right) \end{aligned} \tag{6}$$

It can be seen from the above equation that the impact has been changed into the form of impact increment. Thus, the impact increment of system state s is defined as follows,

$$\Delta I_s = \sum_{k=0}^{n_s} (-1)^{n_s-k} \sum_{u \in \Omega_s^k} I_u \tag{7}$$

$$\Omega_s^k = \{u | u \subset s, Card(u) = k\} \tag{8}$$

where $Card(u)$ is the order of contingency states u. Therefore, **Eq. 6** can be simplified to,

$$\begin{aligned} R = {} & \Delta I_\phi + u_1\Delta I_1 + u_2\Delta I_2 + u_3\Delta I_3 + u_1u_2\Delta I_{12} \\ & + u_1u_3\Delta I_{13} + u_2u_3\Delta I_{23} + u_1u_2u_3\Delta I_{123} \end{aligned} \tag{9}$$

Compared with **Eqs 5**, **9**, it can be seen that the number of terms to be calculated is the same in the two equations, but the content of each term is different. The system state probability of the first equation is replaced by the impact-increment probability, which is eliminating the availability of available components. Also, the system state impact in **Eq. 5** is replaced by the impact-increment. In this way, the proportion of the impact of low-order contingencies in the total impact is increased. As a result, the calculation efficiency can be improved when the high-order contingencies are ignored in some scenarios. Furthermore, **Eq. 9** of the three-component system can be extended to the N-component system,

$$\begin{aligned} \Delta P_s &= \prod_{i \in s} u_i \\ \Delta I_s &= \sum_{k=0}^{n_s} (-1)^{n_s-k} \sum_{u \in \Omega_s^k} I_u \\ R &= \sum_{k=0}^{N} \sum_{s \in \Omega_s^k} \Delta P_s \Delta I_s \end{aligned} \tag{10}$$

A Shadow-Price-Based Optimal Load Curtailment Calculation Method

The OLC model solving process is the most time-consuming in the reliability assessment. In this paper, the OLC model **Eq. 3** is a linear programming problem, which can be expressed as follows:

$$\begin{aligned} \min \quad & \boldsymbol{z} = \boldsymbol{cx} \\ s.t. \quad & \boldsymbol{Ax} = \boldsymbol{b} \\ & \boldsymbol{x} \geq \boldsymbol{0} \end{aligned} \tag{11}$$

where $\mathbf{c} = (c_1, c_2, \ldots, c_n), \mathbf{x} = (x_1, x_2, \ldots, x_n)^{\mathrm{T}}$,

$$\boldsymbol{A} = \begin{bmatrix} a_{11} & a_{12} & \cdots & a_{1n} \\ a_{21} & a_{22} & \cdots & a_{2n} \\ \vdots & \vdots & & \vdots \\ a_{m1} & a_{m2} & \cdots & a_{mn} \end{bmatrix}, \boldsymbol{b} = \begin{bmatrix} b_1 \\ b_2 \\ \vdots \\ b_m \end{bmatrix}, \boldsymbol{0} = \begin{bmatrix} 0 \\ 0 \\ \vdots \\ 0 \end{bmatrix}$$

The simplex method is generally used to solve linear programming problems (Vanderbei, 1998). Then we get,

$$\begin{aligned} \boldsymbol{x_B} &= \boldsymbol{B}^{-1}\boldsymbol{b}, \\ z &= \boldsymbol{c_B}\boldsymbol{B}^{-1}\boldsymbol{b}, \\ \boldsymbol{\sigma} &= \boldsymbol{c} - \boldsymbol{c_B}\boldsymbol{B}^{-1}\boldsymbol{A} \end{aligned} \tag{12}$$

where $\boldsymbol{B}$ is the optimal basis. $\boldsymbol{x_B}$ and $\boldsymbol{c_B}$ are the solution and cost coefficient vector corresponding to $\boldsymbol{B}$, respectively. As long as the criterion $\boldsymbol{x_B} \geq 0$ and $\boldsymbol{\sigma} \geq 0$ are satisfied, $\boldsymbol{x}$ is the optimal solution and z is the optimal objective function.

This paper considers various load levels and renewable generation outputs. The load level $P_{L,i}$ changes with time and there are 8,760 load levels in a year. All generator buses are divided into three categories: conventional generators, PVs, and WTs. The maximum power output P_{Gmax} of conventional generators is constant, while that of renewable generations changes with time. When dealing with a specific contingency, each load level and generator output should be calculated by the optimal load curtailment model to obtain reliability indices. However, the OPF calculation requires too much time because the number of contingency states is very large.

To address that, a shadow-price-based optimal load curtailment calculation method (SP) is proposed to accelerate the solving process of the optimal load curtailment model. It can be observed that the only different part of the OPF model is

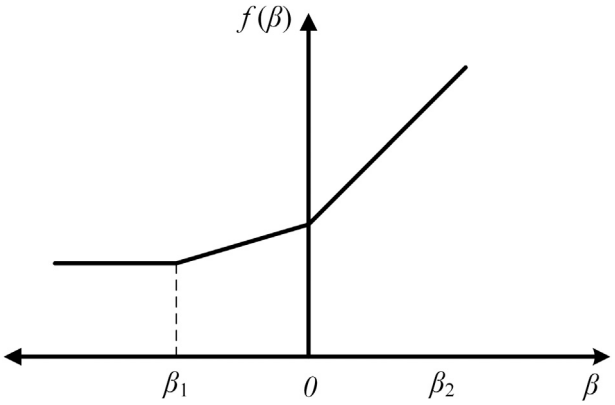

FIGURE 2 | $\beta = 0$ is a breakpoint.

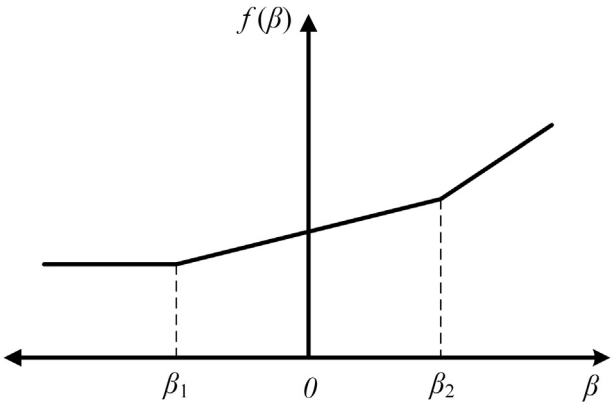

FIGURE 3 | $\beta = 0$ is in the interior of the linearity interval.

matrix $\boldsymbol{b}$ between different load levels and generator outputs. And the shadow price can be used to represent the influence of these changes on the optimal load curtailment. Based on **Eq. 12**, the reduced cost $\boldsymbol{\sigma}$ is always positive when matrix $\boldsymbol{b}$ changes. Therefore, once $\boldsymbol{x_B} \geq 0$ is satisfied, the change of optimal load curtailment can be calculated by the shadow price, as shown in **Eq. 12**.

Furthermore, through the criterion $\boldsymbol{x_B} \geq 0$, the variation range of $\boldsymbol{b}$ can be obtained, which can be expressed as $[\beta_1, \beta_2]$. Therefore, the new linear programming problem can be directly solved by using the last calculation result if the changed $\boldsymbol{b}$' is still in this range. In this case, the optimal base matrix $\boldsymbol{B}$ is unchanged, and the optimal load curtailment of the new state can be obtained by **Eq. 12**. Hence, $f_{bi}(\beta)$ is the optimal objective value as a function of varying b_i with the other bounds fixed. It should be noted that $f_{bi}(\beta)$ is a piecewise linear and convex function, as shown in **Figures 2**, **3**.

Obviously, if $f_{bi}(\beta)$ does not change, then we can easily obtain the optimal objective function of different b_i. The gradient $f'_{bi}(\beta)$ is called the shadow price related to b_i, thus

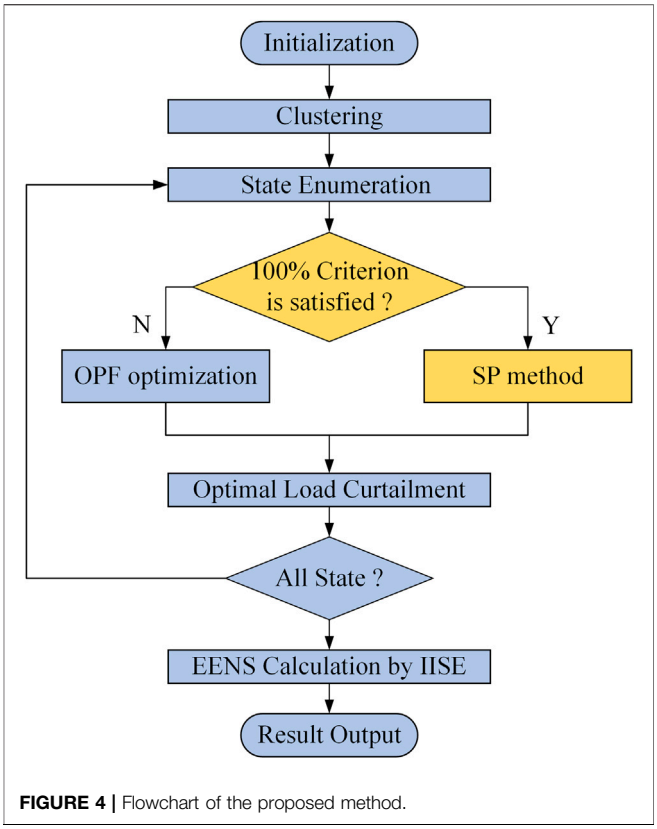

FIGURE 4 | Flowchart of the proposed method.

the shadow-price-based linear functions can represent the change of objective function for small changes of β around zero. Moreover, we are interested in the linearity interval $\beta \in [\beta_1, \beta_2]$ for which $f'_{b_i}(\beta) = f'_{b_i}(0)$.

However, the change in $\boldsymbol{b}$ is usually composed of multiple components. Therefore, one hundred percentage criterion is considered: for all the constant data in the changing constraint conditions, when the sum of all allowable increase percentages and allowable decrease percentages does not exceed one hundred percent, the shadow price of this problem is unchanged, as follows:

$$\sum_{\Delta\beta>0} \frac{\Delta\beta}{\beta_1} + \sum_{\Delta\beta<0} \frac{\Delta\beta}{\beta_2} \leq 100\% \tag{13}$$

Consequently, for the linear programming problem with changes in $\boldsymbol{b}$, when one hundred percentage criterion is satisfied, the optimal load curtailment can be obtained directly by $z = \boldsymbol{c_B B^{-1} b} = \boldsymbol{wb}$, in which $\boldsymbol{w}$ is the shadow price. This simple calculation can eliminate the cumbersome iterative OPF optimizations because the new solution can be calculated by the previous solutions.

Process of the Proposed Approach

The overall process of the proposed SPIISE method is shown in **Figure 4** and elaborated as follows:

Step 1: Initialization. Input power system data, load level data, PV and WT output data. Set the maximum contingency order.

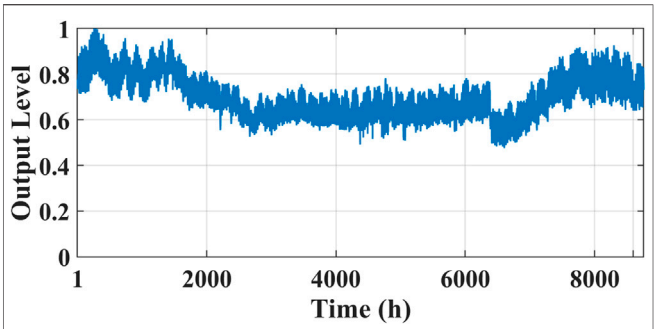

FIGURE 5 | Annual load curve.

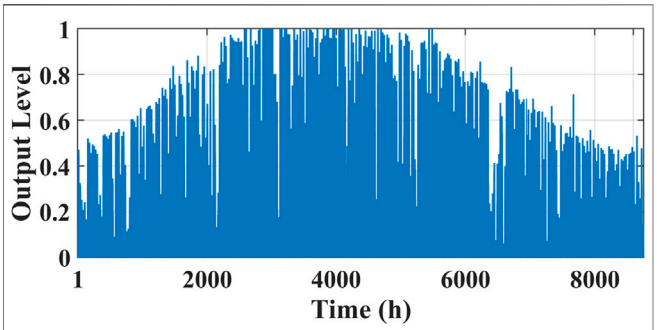

FIGURE 6 | PV annual curve.

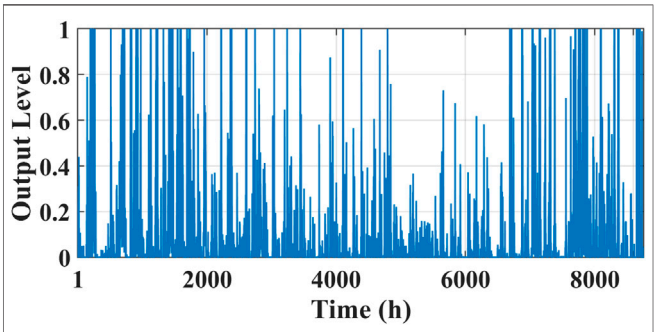

FIGURE 7 | WT annual curve.

Step 2: Clustering. Reduce the load levels and renewable generation outputs by the *k*-means clustering technique.

Step 3: System state enumeration. Enumerate all contingency states, and select a system state to analyze.

Step 4: The judgment of one hundred percentage criterion. Determine whether **Eq. 13** is satisfied, then use the SP method or OPF optimization algorithm to solve the optimal load curtailment model, and obtain the optimal load curtailment of the system state.

Step 5: EENS computation. Calculate the reliability assessment index (EENS) by the impact-increment-based state enumeration approach, as shown in **Eqs 4**, **10**.

Step 6: Output Results.

CASE STUDIES

The RTS-79 system (Subcommittee, 1979) and IEEE 118-bus system (IEEE 118-Bus System, 1962) are used to demonstrate the effectiveness of the proposed SPIISE method. The performance of IISE and SP methods are verified. Finally, the impacts of renewable energy penetration on the power system reliability are analyzed in detail. The performance of studies is parallel tested on a PC equipped with dual Intel Xeon Platinum 8180 CPU (ES) 28 × 1.8 GHz and 128 GB RAM.

Annual load curves (**Figure 5**) is the actual annual load data in Alberta (Alberta Electric System Operator, 2017). Annual output curves of PV and WT (**Figures 6**, **7**) are from NREL National Wind Technology Center (Renewable Resource Data Sets, 2019). The fault component, analyzed in this paper, includes branches and generations. The unavailability of components in the RTS-79 system and branches in the IEEE-118 bus system are calculated by (Subcommittee, 1979). The unavailability of generations in the IEEE-118 bus system is 1.5%. The MCS result with 1×10^8 samples is regarded as the actual result of reliability assessment, which can be used as a benchmark to evaluate the accuracy of other methods.

RTS-79 System

RTS-79 system is a composite power system with 24 buses, 33 generator units, and 38 branches. The total generation capacity is 34.05 MW and the peak load is 28.5 MW. In this case, 5% capacity of conventional generation is replaced by PV and WT. The ratio of PV to WT is 1:1. The cluster number is 100. The maximum contingency order is 5 and transmission contingencies above third-order are ignored. The SPLMSE is applied in the RTS-79 system to test its performance. SPSE denotes the method that combines the SP method and SE method. IISE, SPSE, SE, and MCS approaches are also utilized as comparisons.

Accuracy and Efficiency

As shown in **Table 1**, reliability indices EENS yielded by two approaches (SPSE and SE) are equal, however, the computation speed is increased by over 5 times. This is because the number of OPF optimizations per contingency is reduced from 100 to 14.10, so over 80% of OPF optimizations are substituted by shadow-price-based linear functions. Compared with the traditional approach (SE), the IISE method can achieve more accurate reliability results. It can be seen in **Figure 8** that the position of SPIISE is located at the bottom left of all others. Thus, combined with the SP method and IISE method, SPIISE performs high efficiency in terms of both computation time and accuracy. Furthermore, efficiencies of MCS and SPIISE are approximately equal. Consequently, the superiority of the LMIISE is confirmed, and using the analytical method (SE) to evaluate power systems with 5% penetration of renewable energy becomes feasible and effective.

TABLE 1 | Reliability assessment results of SPIISE, SPSE, IISE, SE and MCS (RTS-79).

Method	EENS (MWh/y)		OPF optimizations number	CPU Time(s)	Speed multiple
	Value	Relative error (%)			
Actual result*	4,525.68	0	—	—	—
SPIISE	4,452.67	1.61	14.10	265	5.84
SPSE	3,823.80	15.51	14.10	265	5.84
IISE	4,452.67	1.61	100	1,548	1
SE	3,823.80	15.51	100	1,548	1

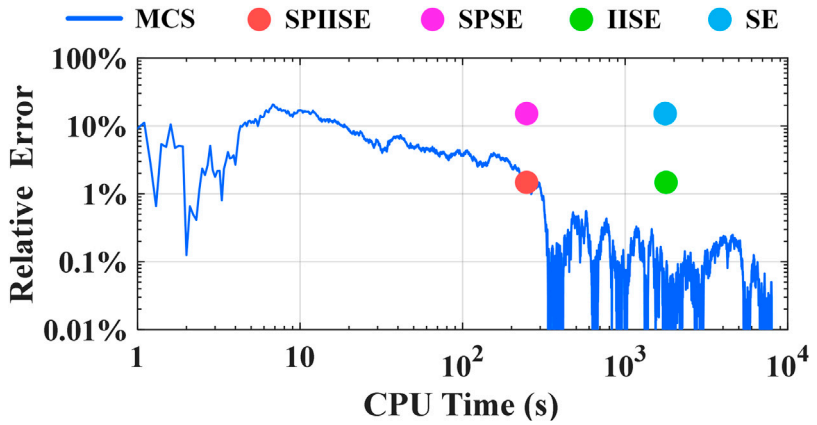

FIGURE 8 | Comparisons of computation efficiencies of five methods (RTS-79).

TABLE 2 | The Impact of Cluster Number on Reliability assessment results (RTS-79).

Cluster number	EENS (MWh/y)		OPF optimizations number	CPU Time(s)	Speed multiple
	Value	Relative error (%)			
10	4,179.80	7.64	6.63	120	1.36 (163 s)
50	4,438.22	1.93	11.60	212	3.77 (799 s)
100	4,452.67	1.61	14.10	265	5.84 (1,548 s)
200	4,453.66	1.59	16.97	331	9.34 (3,092 s)
300	4,482.69	0.95	18.36	372	12.79 (4,758 s)
500	4,436.08	1.98	19.12	410	18.93 (7,763 s)
1,000	4,413.79	2.47	20.36	507	31.46 (15950 s)
8,760	4,426.75	2.19	21.34	1,550	85.44 (132434 s)

The clustering technique is used in the proposed methodology to ease the computation burden of the SE method. As shown in **Figure 2**, the massive scenarios of loads, PVs, and WTs are reduced to representative system states. As shown in **Table 2**, the relative errors can reach 2% when the cluster number is over 100. Therefore, the clustering technique could achieve a good trade-off between speed and accuracy, so 100 is used as the cluster number in this paper. Also, the acceleration performance of the proposed SPIISE method is getting better for the larger cluster number.

Impact of Renewable Energy Penetration

In this paper, renewable generation penetration ζ is defined as follow:

TABLE 3 | The impact of renewable energy penetration on EENS in cases 1 and 2 (RTS-79).

ζ (%)	EENS (MWh/y)	
	Case I	Case II
0	2,085	2,085
5	4,453	1,842
10	9,814	1,618
15	22,592	1,475
20	50,445	1,371
25	104,322	1,283

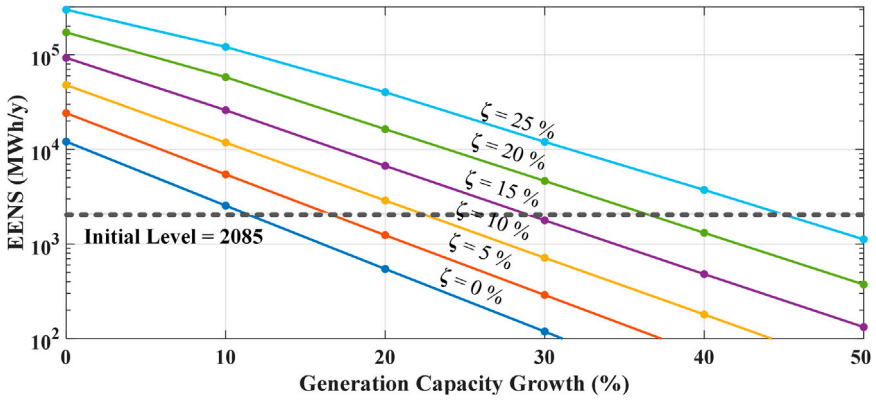

FIGURE 9 | Reliability results of generation capacity growth at different renewable energy penetrations in Case 3.

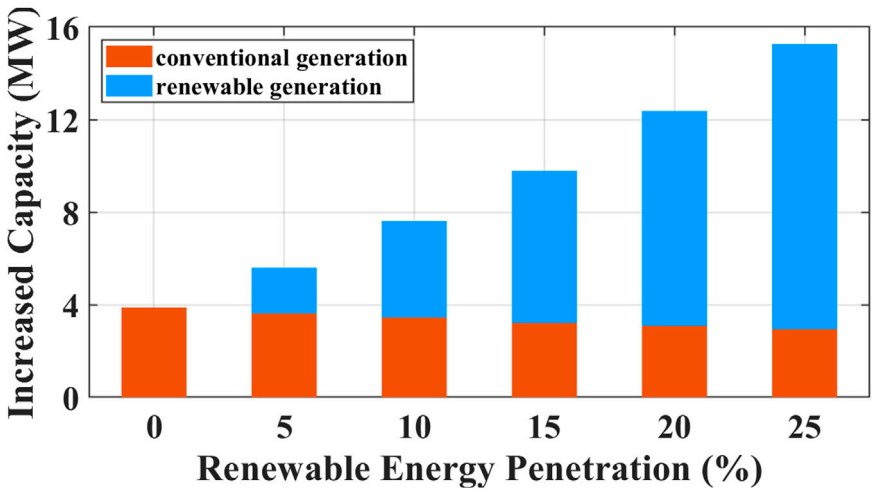

FIGURE 10 | Increased generation capacity at different renewable energy penetrations in Case 3.

$$\zeta = \frac{P_{re}}{P_g + P_{re}} \tag{14}$$

where P_g represents the total capacity of convention generators; P_{re} represents the capacity of renewable generators. In this subsection, we compare the following three cases with growing renewable energy penetration to illustrate the impact of renewable energy penetration.

Case 1: The convention generation is being replaced by the renewable generation with growing penetration, that is the total generation capacity $P_g + P_{re}$ remains unchanged.

Case 2: The renewable generation is being newly added in power systems with growing penetration, that is the convention generation capacity P_g remains unchanged.

Case 3: the load increased by 10%, and total generation capacity $P_g + P_{re}$ is increasing at different renewable energy penetrations.

Table 3 presents the reliability assessment results of the RTS-79 system at different renewable energy penetrations in Cases I and II. It can be found that the higher penetration of renewable energy can improve the reliability in Case I while deteriorate the reliability in Case II. This is because that intermittent renewable energy cannot satisfy the generation adequacy at all the time, unlike the convention generators. Moreover, the reliability results of Case 3 are shown in **Figure 9**. Load growth decreases the reliability of power systems. The initial reliability level is 2085 MWh/y, which is the EENS of the RTS-79 system without renewable energy and increased load. To reach the initial reliability level, both convention generation and renewable generation are needed to be expanded, as shown in **Figure 10**. Thus, in this case, the convention generation is a necessary support for the reliability of power systems with high renewable energy penetration.

IEEE 118-Bus System

IEEE 118-bus system consists of 118 buses, 54 generation units, and 186 branches. The total generation capacity is 99,662 MW and the peak load is 42,420 MW. Similar to the RTS-79 system, renewable generation penetration ζ = 5%, the cluster number is 100, and the

TABLE 4 | Reliability assessment results of SPIISE, SPSE, IISE, SE and MCS (IEEE 118-bus).

Method	EENS (MWh/y)		OPF optimizations number	CPU Time(s)	Speed multiple
	Value	Relative error (%)			
Actual result*	280.71	0	—	—	—
SPIISE	275.06	2.01	22.58	262	2.91
SPSE	195.67	30.29	22.58	262	2.91
IISE	275.06	2.01	—	763	1
SE	195.67	30.29	—	763	1

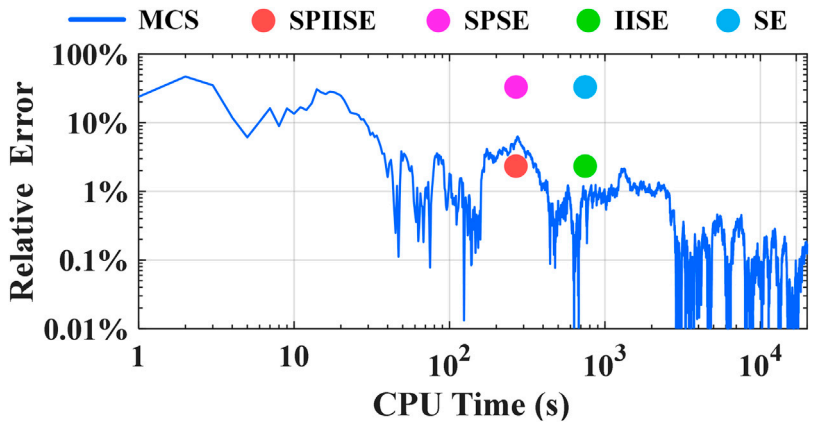

FIGURE 11 | Comparisons of computation efficiencies of five methods (IEEE 118-bus).

maximum contingency order is 2. SPIISE, SPSE, IISE, SE, MCS are applied in the IEEE 118-bus system.

As shown in **Table 4**, SPIISE still outperforms the other methods in the IEEE 118-bus system. Based on the IISE method, the relative errors are reduced to 2.01% from 30.29%. About 80% of system states are calculated by the SP method, rather than the time-consuming OPF optimizations. Therefore, the position of LMIISE is located at the bottom left of others, as shown in **Figure 11**. Also, the efficiency of the proposed approach can reach or even exceed that of the MCS. In addition, since the IEEE-118 bus system is more complicated than the RTS-79 system, more OPF optimizations are needed in this case.

CONCLUSION

This paper proposes a shadow-price-and-impact-increment-based reliability evaluation approach to improve the efficiency of reliability assessment for power systems with high renewable energy penetration. Based on the impact increment method, more precise indices could be obtained with only low-order contingency. On the other hand, the shadow-price-based linear functions are constructed to calculate the optimal load curtailment in a faster manner. Moreover, one hundred percent criterion is applied to determine the shadow price of states. The results indicate that about over 80% OPF optimizations can be obtained directly by matrix multiplications, rather than the time-consuming optimization algorithms. Consequently, the proposed methodology can significantly improve computational efficiency. Moreover, a detailed analysis shows that convention generation may be an effective and necessary way to ensure the reliability of power systems with high renewable energy penetration. In addition, the one hundred percent criterion may be conservative for state matching, therefore, future research will focus on further decreasing the number of OPF calculations.

DATA AVAILABILITY STATEMENT

The original contributions presented in the study are included in the article/Supplementary Material, further inquiries can be directed to the corresponding author.

AUTHOR CONTRIBUTIONS

KH: supervision, literature review, and writing-reviewing. PT: mathematical analysis, writing, and software. ZL: simulation, framework formation, and writing. HJ: supervision and project administration. LZ: methodology, writing-reviewing and editing.

FUNDING

This work was supported by the National Natural Science Foundation of China (52061635103, 51707129).

REFERENCES

Alberta Electric System Operator (2017). Hourly load by area and region 2011 to 2017. Available at: https://www.aeso.ca/

Alotaibi, M. A., and Salama, M. M. A. (2016). An efficient probabilistic-chronological matching modeling for DG planning and reliability assessment in power distribution systems. *Renew. Energ.* 99, 158–169. doi:10.1016/j.renene.2016.06.058

Billinton, R., and Li, W. (1994). *Reliability assessment of electrical power systems using Monte Carlo methods*. New York: Springer

Ding, Y., Singh, C., Geol, L., Ostergaard, J., and Wang, P. (2014). Short-term and medium-term reliability evaluation for power systems with high penetration of wind power. *IEEE Trans. Sustain. Energ.* 5 (3), 896–906. doi:10.1109/TSTE.2014.2313017

Ding, Y., Wang, P., Goel, L., Loh, P., and Wu, Q. (2011). Long-term reserve expansion of power systems with high wind power penetration using universal generating function methods. *IEEE Trans. Power Syst.* 26 (2), 766–774. doi:10.1109/TPWRS.2010.2054841

Geng, L., Zhao, Y., and Chen, G. (2018). Simplified sequential simulation of bulk power system reliability via chronological probability model of load supplying capability. *IEEE Trans. Power Syst.* 33 (3), 2349–2358. doi:10.1109/TPWRS.2017.2757033

Gonzalez-Fernandez, R. A., and da Silva, A. M. L. (2011). Reliability assessment of time-dependent systems via sequential cross-entropy monte carlo simulation. *IEEE Trans. Power Syst.* 26 (4), 2381–2389. doi:10.1109/TPWRS.2011.2112785

Gubbala, N. V., and Singh, C. (1995). Models and considerations for parallel implementation of monte carlo simulation methods for power system reliability evaluation. *IEEE Trans. Power Syst.* 10 (2), 779–787. doi:10.1109/59.387917

Hou, K., Jia, H., Li, X., Xu, X., Mu, Y., Jiang, T., et al. (2018). Impact-increment based decoupled reliability assessment approach for composite generation and transmission systems. *IET Gener. Transmiss. Distrib.* 12 (3), 586–595. doi:10.1049/iet-gtd.2017.0745

Hou, K., Jia, H., and Xu, X. (2016). An impact increment-based state enumeration reliability assessment approach and its application in transmission systems. *IEEE Trans. Power App. Syst. Pas* 98 (6), 2047–2054. doi:10.1109/TPAS.1979.319398K

IEEE 118-Bus System, Illinois center for a smarter electric grid (1962). Available at: http://publish.illinois.edu/smartergrid/ieee-118-bus-system/

Lei, Y., Zhang, P., Hou, K., Jia, H., Mu, Y., and Sun, B. (2018). An incremental reliability assessment approach for transmission expansion planning. *IEEE Trans. Power Syst.* 33 (3), 2597–2609. doi:10.1109/TPWRS.2017.2756261

Li, W. (2014). *Risk assessment of power systems: models methods and applications*. Hoboken: Wiley

Liu, H., Sun, Y., Wang, P., Cheng, L., and Goel, L. (2008). A novel state selection technique for power system reliability evaluation. *Electr. Power Syst. Res.* 78 (6), 1019–1027. doi:10.1016/j.epsr.2007.08.002

Liu, Y., Wang, Y., Yong, P., Zhang, N., Kang, C., and Lu, D. (2020a). Fast power system cascading failure path searching with high wind power penetration. *IEEE Trans. Sustain. Energ.* 11 (4), 2274–2283. doi:10.1109/TSTE.2019.2953867

Liu, Z., Hou, K., Jia, H., Zhao, J., Wang, D., Mu, Y., et al. (2020b). A Lagrange multiplier based state enumeration reliability assessment for power systems with multiple types of loads and renewable generations. *IEEE Trans. Power Syst.* doi:10.1109/TPWRS.2020.3045021

Nguyen, T. T., Nguyen, T. T., Duong, M. Q., and Doan, A. T. (2020). Optimal operation of transmission power networks by using improved stochastic fractal search algorithm. *Neural Comput. Appl.* 32 (13), 9129–9164. doi:10.1007/s00521-019-04425-0

Renewable Resource Data Sets, National renewable energy laboratory (2019). Available at: https://www.nrel.gov/grid/data-tools.html

Safdarian, A., Firuzabad, M. F., and Aminifar, F. (2013). Composite power system adequacy assessment based on postoptimal analysis. *Turk. J. Elec. Eng. Comput. Sci.* 21 (1), 90–106. doi:10.3906/elk-1104-36

Sankarakrishnan, A., and Billinton, R. (1995). Sequential Monte Carlo simulation for composite power system reliability analysis with time varying loads. *IEEE Trans. Power Syst.* 10 (3), 1540–1545. doi:10.1109/59.466491

Singh, C., and Mitra, J. (1997). Composite system reliability evaluation using state space pruning. *IEEE Trans. Power Syst.* 12 (1), 471–479. doi:10.1109/59.575787

Subcommittee, P. M. (1979). IEEE reliability test system. *IEEE Trans. Power App. Syst. Pas* 98 (6), 2047–2054. doi:10.1109/TPAS.1979.319398K

Tomasson, E., and Soder, L. (2018). Generation adequacy analysis of multi-area power systems with a high share of wind power. *IEEE Trans. Power Syst.* 33 (4), 3854–3862. doi:10.1109/TPWRS.2017.2769840

Vanderbei, R. J. (1998). *Vanderbei, linear programming foundations and extensions*. Boston: Kluwer

Wang, Y., Zhang, N., Kang, C., Miao, M., Shi, R., and Xia, Q. (2018). An efficient approach to power system uncertainty analysis with high-dimensional dependencies. *IEEE Trans. Power Syst.* 33 (3), 2984–2994. doi:10.1109/TPWRS.2017.2755698

Yang, X., Yang, Y., Liu, Y., and Deng, Z. (2020). A reliability assessment approach for electric power systems considering wind power uncertainty. *IEEE Access* 8, 12467–12478. doi:10.1109/ACCESS.2020.2966275

Yong, P., Zhang, N., Kang, C., Xia, Q., and Lu, D. (2019). MPLP-based fast power system reliability evaluation using transmission line status dictionary. *IEEE Trans. Power Syst.* 34 (2), 1630–1640. doi:10.1109/TPWRS.2018.2878324

Conflict of Interest: The authors declare that the research was conducted in the absence of any commercial or financial relationships that could be construed as a potential conflict of interest.

NOMENCLATURE

Abbreviations

EENS Expected energy not supplied

IISE Impact-increment-based SE method

MCS Monte Carlo simulation method

OLC Optimal load curtailment

OPF Optimal power flow

SE State Enumeration method

SPIISE shadow-price-based IISE method

SPSE shadow-price-based SE method

Variables

a_j the availability rate of component j

g the numbers of generators

$I(s)$ the impact of the system state s

n the numbers of buses

n_s the number of contingency components of the system state s

$P(s)$ the probability of occurrence of system state s

$P_{Bmax,ij}$ the maximum power flow of branch ij

$P_{C,i}$ the load curtailment of node i

$P_{G,i}$ the generation output of generator i

$P_{Gmax,i}$ the maximum output of the generator i

$P_{L,i}$ the load of node i

P_{LC} the total system load curtailment

R the reliability assessment index

s the system state

u_i the unavailability rate of component i

x_{ij} the reactance of branch ij

θ_i the voltage phase of node i

Sets

Ω the set of enumerated system states

Ω_s^k the k-order contingency subset of s

frontiers in Energy Research

METHODS
published: 04 March 2021
doi: 10.3389/fenrg.2021.634232

Calculation of Short-Circuit Current in DC Distribution System Based on MMC Linearization

Peixiao Sun, Zaibin Jiao and Hanwen Gu*

Department of Electrical Engineering, Xi'an Jiaotong University, Xi'an, China

The calculation of the short-circuit current is an important basis for fault detection and equipment selection in the DC distribution system. This paper proposes a linearized model for modular multilevel converter (MMC) considering different grounding methods and different failure scenarios. This model can be used in different fault conditions before MMC's block. Under different fault forms, the model has different manifestations. This paper analyzes and models the DC distribution network with two types of faults: inter-pole short circuit and single-pole grounding short circuit. Among them, the modeling and analysis of single-pole grounding short-circuit uses the method of common- and differential-mode (CDM) transformation. To solve such a model, an analytical calculation method is proposed. As a mean of evaluating the effectiveness and accuracy of the proposed model, the analytical calculation solution is compared to the solution produced by PSCAD/EMTDC. A comparison of the results reveals the efficacy of the proposed model.

Keywords: DC distribution system, short-circuit current calculation, MMC, linearization, common- and differential-mode

OPEN ACCESS

Edited by:
Peng Li,
Tianjin University, China

Reviewed by:
Zhengqing Han,
Southwest Jiaotong University, China
Botong Li,
Tianjin University, China

****Correspondence:***
Zaibin Jiao
jiaozaibin@xjtu.edu.cn

Specialty section:
This article was submitted to Smart Grids, a section of the journal Frontiers in Energy Research

Received: *27 November 2020*
Accepted: *18 January 2021*
Published: *04 March 2021*

Citation:
Sun P, Jiao Z and Gu H (2021) Calculation of Short-Circuit Current in DC Distribution System Based on MMC Linearization. Front. Energy Res. 9:634232. doi: 10.3389/fenrg.2021.634232

INTRODUCTION

With the continuous development of society, people's production methods are becoming more and more abundant, and the demand for the use of electric energy is also increasing. At present, the AC distribution network in some large cities is facing the problem of lack of power supply corridors and insufficient power supply capacity. At the same time, the traditional AC distribution network has problems such as three-phase imbalance and insufficient node reactive power support, which are becoming more and more prominent under the trend of substantial increase in electricity demand. In addition, the rise of many high-tech industries has put forward higher requirements for power supply reliability and power quality. However, high-quality power supply is difficult to achieve due to problems such as harmonics and shock loads caused by converter equipment in the network. This series of problems has promoted the technological innovation of the distribution network (Feng, 2019).

As countries attach importance to renewable energy and the development of power electronics technology, DC power distribution technology has gradually entered people's field of vision. At the same time, the DC distribution network has become a feasible way to solve a series of problems in the traditional AC distribution network with its advantages of large transmission capacity, low line cost, low network loss, high power supply reliability and high power quality (Baran and Mahajan, 2003; Sannino et al., 2003; Starke et al., 2008). What's more, the DC distribution network with converters and a series of power electronic equipment is highly controllable and would be an important part of

flexible and active distribution networks. In the DC distribution network, the converter is one of the key equipment. As a new generation of converters, voltage source converter has the advantages of the ability to manage power flow direction, immunity against commutation failure and easy extension to multi-terminal DC grid (Lyu et al., 2016; Hao et al., 2019). Therefore, the voltage source converter provides the possibility for the DC distribution network. At present, as a kind of voltage source converters, MMC not only has high output waveform quality, but also has low switching frequency and low loss (Xu, 2013). It is currently the key research object of DC technology.

The calculation of the short-circuit current is an important basis for fault detection and equipment selection in the DC distribution system (Li et al., 2018). At present, many researchers have studied the calculation of DC short-circuit current in the DC distribution network formed by MMCs. Franquelo et al. (2008) conducted a qualitative analysis of various types of faults in the multi-terminal DC grid composed of MMCs. Some researchers applied simulation methods to analyze the short circuit on the DC side of the MMC (Bucher and Franck, 2013; Zhang and Xu, 2016; Han et al., 2018; Tünnerhoff et al., 2018). Although such simulation is accurate, the modeling is complicated and time-consuming, so it is not suitable for system planning and design. In order to avoid these shortcomings of simulation, we can use a simplified model for analytical calculations. Zhou et al. (2017) conducted a theoretical analysis of the DC distribution network formed by MMC when the DC side was not grounded, and investigated the equivalent discharge circuit before the MMC is blocked after a short-circuit fault occurred at the outlet of the MMC and a single-pole grounding fault. Based on the circuit model of the equivalent discharge loop, the analytical expression of the fault discharge current is derived. Xu (2013) analyzed the equivalent circuit of the MMC before the MMC is blocked when the output of the MMC is short-circuited. In his research, the steady-state situation after MMC's block was solved and the analytical expression of the whole fault process is revealed. In addition, Xu (2013) also introduced a circuit model that applies the superposition theorem to calculate when facing a complex topology of a multi-terminal DC grid, and simulated the calculation model. In (Wang et al., 2011), the discharge circuit of the sub-module after the inter-electrode short circuit at the outlet of the MMC was divided into two stages before and after the MMC is locked, and the analytical expression of the sub-module overcurrent was presented. Gao et al. (2020) applied a converter model composed of an RLC series circuit and a parallel current source, and performed an effective approximate calculation of the short circuit between poles. Shi and Ma (2020) analyzed the fault circuit under a single-pole grounding short circuit, and calculated the short-circuit current for a two-terminal DC system.

From the previous discussion, in the DC distribution network that widely adopts symmetrical unipolar structure wiring, people have more abundant researches on short-circuit faults between poles at the outlet of MMC, but less on single-pole grounding faults. In addition, when a failure occurs at the line, it is difficult to derive the analytical expression of the fault current in the face of a complex multi-terminal DC system, and the calculation method lacks more detailed research.

To bridge these gaps, this paper presents the linearized model before MMC's block in two types of faults. In addition, for the complex multi-terminal DC distribution network model, an effective solution method is proposed.

The rest of this paper is organized as follows. In *Analysis and Modeling of DC Distribution System*, a model of DC distribution system is presented. In *Model Solution Method*, a method to solve the presented model is proposed. In *Case Studies*, case studies are conducted to evaluate the effectiveness and accuracy of the proposed model. Concluding remarks are presented in *Conclusion*.

ANALYSIS AND MODELING OF DC DISTRIBUTION SYSTEM

The topology of MMC is shown in **Figure 1**. Because the fault characteristics of various sub-modules are basically the same before the MMC is locked, the half-bridge sub-module is taken as a representative here. MMC is a converter that relies on constant switching between sub-modules to approximate a sine wave with a step wave, so MMC is a time-varying circuit. However, if we make the analysis time short enough and believe that the MMC input and bypass sub-modules remain unchanged, we can regard MMC as a linear and time-invariant circuit and use the superposition theorem for analysis. The following research work is based on this assumption.

Analysis and Modeling Under Inter-pole Short-Circuit Faults

When an inter-pole short-circuit fault occurs in a DC distribution network, the superposition theorem can be used at the fault point *f* to divide the inter-pole voltage at the fault point into a normal component and a fault component, as shown in **Figure 2**. Then the response generated by all other excitation sources except the fault component voltage at the fault point is the response of the normal operating state of the circuit. Under the normal operating state, the short-circuit current at the fault point is zero, and the current carried by each line is the current under normal operation. The current under normal operating conditions can be obtained by load flow calculation or direct measurement, and will not be calculated in this article. This paper will calculate the fault component current, which is the zero state response current of the circuit under the excitation of the fault component power supply. If there is no transition resistance, the fault component power supply can be regarded as a voltage source. If there is a transition resistance at the fault point, the fault component current can be expressed by the response under the excitation of the fault component current source. This current source can be obtained by transforming the fault component voltage source and transition resistance through Norton's equivalent law.

When considering the zero-state response of the fault component voltage source in the circuit, MMC can be transformed into an equivalent circuit model as shown in **Figure 3**. *R*, *L*, and *C* in the model are all calculated by **Eq. 1**

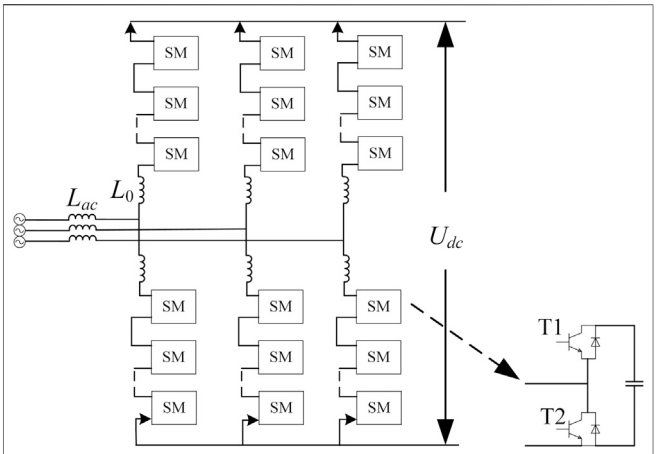

FIGURE 1 | The topology of MMC.

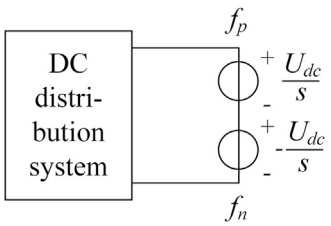

FIGURE 2 | Schematic diagram of the superposition theorem.

(Xu, 2013). If the MMC is grounded through the midpoint of the capacitor, the corresponding capacitance value can be added to C.

$$\begin{cases} R = \frac{2}{3}R_0 + 2R_{dc} \\ L = \frac{2}{3}L_0 + 2L_{dc} \\ C = \frac{6C_0}{N} \end{cases} \#(1)$$

Where R_0 and L_0 are the resistance and inductance of the bridge arm reactor, respectively, R_{dc} and L_{dc} are the resistance and inductance of the smoothing reactor at the converter outlet, respectively, N is the number of sub-modules in each bridge arm, and C_0 is the sub-module capacitance.

The DC line can be described as a π-type equivalent circuit model. In order to make the subsequent calculation easier, the parameters of the model are converted to the positive pole or inter-pole, as shown in **Figure 4**. When calculating with the positive pole current and the voltage between poles, the model before and after the conversion is equivalent.

In **Figure 4**, R_l, L_l and C_l are the equivalent resistance, equivalent inductance, and equivalent capacitance of the positive/negative line, respectively. R, L and C in **Figure 4** are their values after converted to the positive pole or inter-pole. The circuit parameters before and after conversion have the following relationship:

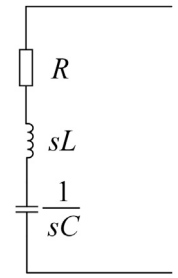

FIGURE 3 | Zero-state response equivalent circuit model of MMC in frequency domain.

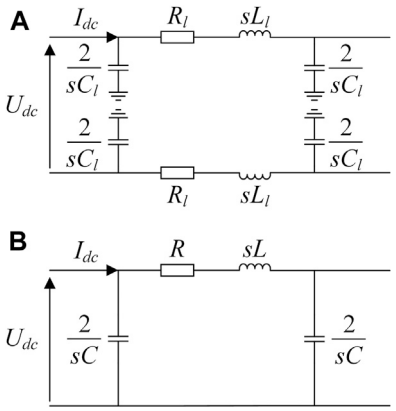

FIGURE 4 | Equivalent circuit model before and after conversion of DC line **(A)** Before conversion. **(B)** After conversion.

$$\begin{cases} R = 2R_l \\ L = 2L_l \\ C = \frac{1}{2}C_l \end{cases} \#(2)$$

Analysis and Modeling Under Single-Pole Grounding Faults

When a single-pole grounding fault occurs, the transient characteristics of the DC distribution network are greatly affected by the grounding method of the AC and DC sides. There will be different fault loops and fault mechanisms under different grounding methods on the AC and DC sides of the DC distribution network. Therefore, before modeling, it is necessary to classify the different grounding methods of the AC and DC sides of the MMC. If there is a zero-sequence path on the AC side of the MMC, the AC side is considered to be grounded. Otherwise, it is considered that the AC side is not grounded. As shown in **Figure 5**, MMC's DC side grounding methods are divided into three types: ungrounded, grounded through the midpoint of the clamp resistance, and grounded through the midpoint of the capacitor (Luo, 2019).

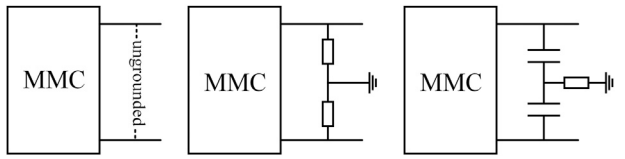

FIGURE 5 | MMC's DC side grounding method.

When modeling the MMC, in order to make the model symmetric about the positive and negative poles, and to facilitate subsequent analysis and calculation, the influence of the bridge arm reactor was ignored. Considering that the inductance of the bridge arm reactor is not too large, it is generally an order of magnitude smaller than the inductance of the smoothing reactor at the converter outlet, so the error caused by the simplified model will not be large, and the conservativeness of the model can also be taken into account.

Under different grounding modes, the zero-state response equivalent circuit of MMC is shown in **Figure 6**. The dashed line indicates that the connection exists only when the AC and DC sides of the MMC are grounded in a corresponding way. L_{ac} represents 1/3 of the zero-sequence inductance on the AC side when the AC side is grounded (Luo, 2019). R_g represents the clamp resistance. C_g represents grounding capacitance. R_{cg} represents the ground resistance at the midpoint of the capacitor.

The DC line can be described as the unconverted equivalent circuit model in **Figure 4**.

The single-pole grounding short circuit will make the circuit asymmetrical. Therefore, we can analyse it with CDM conversion. From the perspective of CDM, it will be divided into two symmetrical circuits that are easy to analyze. The CDM conversion has the following mathematical form (Kimbark, 1970):

$$\begin{bmatrix} I_\Sigma \\ I_\Delta \end{bmatrix} = \frac{1}{2}\begin{bmatrix} 1 & 1 \\ 1 & -1 \end{bmatrix}\begin{bmatrix} I_p \\ I_n \end{bmatrix} \#(3)$$

Where Σ and Δ respectively represent common-mode and differential-mode components. In addition, p and n respectively represent positive and negative parameters. This formula is applicable to both current and voltage.

After CDM conversion of current and voltage, the converter model will become the following form:

(1) Case 1: The AC side is not grounded, and the DC side is grounded through the midpoint of the capacitor.

In this case, the common-mode and differential-mode models of the converter are shown in **Figure 7**.

(2) Case 2: The AC side is not grounded, and the DC side is grounded through the midpoint of the clamp resistor.

In this case, the common-mode and differential-mode models of the converter are shown in **Figure 8**. When the DC side is not grounded, it is equivalent to an open circuit at R_g, so it will not be listed separately later.

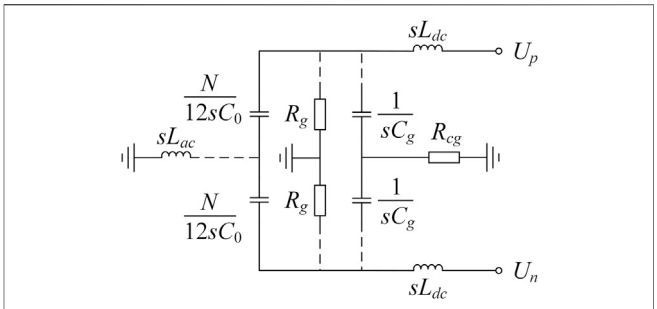

FIGURE 6 | The zero-state response equivalent circuit model of MMC under single-pole grounding faults.

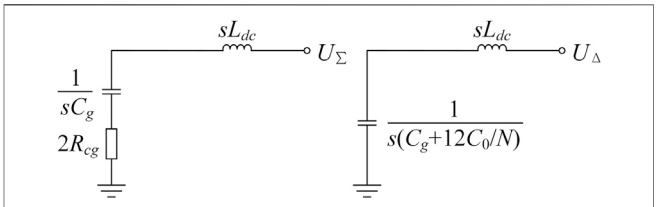

FIGURE 7 | The common-mode **(left)** and differential-mode **(right)** models of the converter in case 1.

(3) Case 3: The AC side is grounded, and the DC side is grounded through the midpoint of the capacitor.

In this case, the common-mode and differential-mode models of the converter are shown in **Figure 9**.

(4) Case 4: The AC side is grounded, and the DC side is grounded through the midpoint of the clamp resistor.

In this case, the common-mode and differential-mode models of the converter are shown in **Figure 10**. When the DC side is not grounded, it is equivalent to an open circuit at R_g, so it will not be listed separately later.

After CDM conversion of current and voltage, the DC line model is shown in **Figure 11**. Its common-mode model is the same as Its differential-mode model.

From the perspective of CDM, the fault boundary conditions of the circuit also need to be converted. Without loss of generality, if we set a negative pole grounding short-circuit fault at the fault point f, the boundary conditions can be expressed as **Eq. 4**.

$$\begin{cases} I_{f,p} = 0 \\ U_{f,n} = R_f I_{f,n} \end{cases} \#(4)$$

Where $U_{f,n}$ is the negative voltage at the fault point, $I_{f,p}$ and $I_{f,n}$ are the positive and negative currents flowing from the fault point to the ground, respectively, and R_f is the transition resistance between the fault point and the ground.

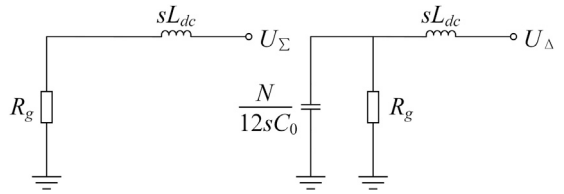

FIGURE 8 | The common-mode **(left)** and differential-mode **(right)** models of the converter in case 2.

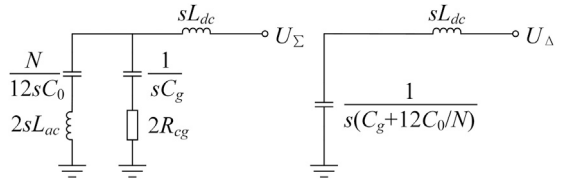

FIGURE 9 | The common-mode **(left)** and differential-mode **(right)** models of the converter in case 3.

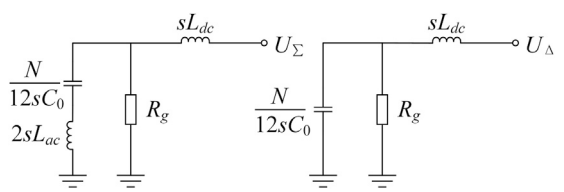

FIGURE 10 | The common-mode **(left)** and differential-mode **(right)** models of the converter in case 4.

Through CDM transformation of **Eq. 4**, the boundary conditions are transformed into **Eq. 5**.

$$\begin{cases} I_{f,\Sigma} + I_{f,\Delta} = 0 \\ U_{f,\Sigma} - U_{f,\Delta} = R_f\left(I_{f,\Sigma} - I_{f,\Delta}\right) \end{cases} \#(5)$$

Where $U_{f,\sum}$ and $U_{f,\Delta}$ are the common-mode and differential-mode voltage at the fault point, respectively, $I_{f,\sum}$ and $I_{f,\Delta}$ are the common-mode and differential-mode current flowing from the fault point, respectively.

Similar to the asymmetric fault analysis of the AC grid, the DC distribution network also has the following relationships at the fault point:

$$\begin{cases} U_{f,\Delta(0)} - U_{f,\Delta} = Z_\Delta I_{f,\Delta} \\ -U_{f,\Sigma} = Z_\Sigma I_{f,\Sigma} \end{cases} \#(6)$$

Where

$$U_{f,\Delta(0)} = \frac{U_{dc}}{2s} \#(7)$$

In **Eq. 6**, $U_{f,\Delta(0)}$ is the normal component of the differential-mode voltage at the fault point, Z_Δ and $Z_\sum$ are the equivalent differential-mode and common-mode impedance of DC distribution network measured from the fault point, respectively. In **Eq. 7**, U_{dc} is the inter-pole voltage at the fault point during normal operation.

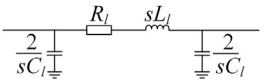

FIGURE 11 | The CDM model of the DC line.

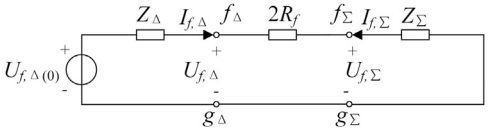

FIGURE 12 | The equivalent CDM network under single-pole grounding fault.

According to **Eq. 5** and **Eq. 6**, an equivalent CDM network as shown in **Figure 12** can be formed.

MODEL SOLUTION METHOD

Solution of Fault Component Current Under Inter-pole Short-Circuit Faults

Since it is difficult to derive analytical formulas for high-order circuits when the DC distribution network has a complex topology, this section introduces an analytical calculation method suitable for computers. The symbolic math toolbox of MATLAB can help us use this method.

Before the calculation, the circuit structure should be classified, and the buses should be classified first:

(1) Voltage bus: The fault component voltage of the bus is known, while the fault component injection current at the bus is unknown. This kind of bus is generally at the fault point.
(2) Current bus: The fault component injection current at the bus is known, while the fault component voltage of the bus is unknown. This kind of bus is generally a non-fault bus or at a fault point with a known fault component current.

After that, the connection structure in the circuit also needs to be classified:

(1) Grounding structure

The grounding structure is shown in **Figure 13**. The ground in the figure is not the ground in the conventional sense, but the reference point of the bus voltage. In this calculation for the inter-pole short-circuit fault, the inter-pole voltage and the positive current are used for calculation, so the ground in **Figure 13** is equivalent to the converted negative circuit in **Figure 4**.

The inter-pole voltage U_n and the positive current I_{nn} in the grounding structure have the following relationship:

$$I_{nn} = Y_{nn}U_n \#(8)$$

Where Y_{nn} is the admittance of grounding structure.

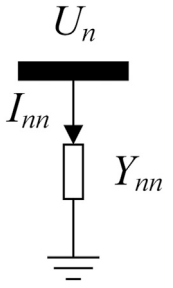

FIGURE 13 | The grounding structure.

(2) Bus connection structure

The bus connection structure is shown in **Figure 14**.

U_n and U_m are the inter-pole voltage at the bus n and m, respectively. The positive current flowing in the bus connection structure I_{nn} and they have the following relationship:

$$I_{nm} = Y_{nm}(U_n - U_m) \# (9)$$

After classifying the structure of the DC distribution network, the fault component current can be solved under the inter-pole short-circuit fault. The following matrix has been defined and used as input of the calculation formula.

Assuming that there are N_b original buses in the circuit, the circuit will have N_b+1 buses after adding a faulty bus (if the fault occurs at an original bus, the number of buses will not change).

(1) Connection matrix F ($(N_b+1)\times(N_b+1)$): It describes the connection of the DC distribution network:
   i) $F_{nm} = 1$, if a line connects buses n and m.
   ii) $F_{nm} = 0$, if no line connects buses n and m.
(2) Admittance matrix Y ($(N_b+1)\times(N_b+1)$): The diagonal element Y_{nn} in the matrix is the ground admittance at bus n, and the non-diagonal element Y_{nm} is the admittance of the DC line connecting buses n and m.

With input matrices F and Y, according to KVL and KCL, we can list the following linear equations at n_i current buses.

$$I_{G_n} = Y_{nn}U_n + \sum_{\substack{m=1 \\ m\neq n}}^{N_b+1} F_{nm}Y_{nm}(U_n - U_m), n \in \mathbb{R}^{n_i} \# (10)$$

Where I_{G_n} is the known injection current at bus n.

In the equation set shown in **Eq. 10**, there are n_i current bus voltages as variables, and this number is the same as the number of equations. Therefore, the expression of the unknown voltage in the frequency domain can be solved by a computer.

After obtained the voltage of each bus, **Eq. 11** can be used to determine the fault component current flowing out of the MMC's outlet at bus n.

$$I_{c-n} = -\frac{U_n}{R_{c-n} + sL_{c-n} + \frac{1}{sC_{c-n}}} \# (11)$$

Where $R_{c\text{-}n}$, $L_{c\text{-}n}$ and $C_{c\text{-}n}$ are the resistance, inductance and capacitance in the MMC equivalent circuit at bus n, respectively.

The fault component current flowing from bus n to bus m can be determined by **Eq. 12**.

$$I_{l-nm} = \frac{1}{2}sC_{l-nm}U_n + \frac{U_n - U_m}{R_{l-nm} + sL_{l-nm}} \# (12)$$

Where $R_{l\text{-}nm}$, $L_{l\text{-}nm}$ and $C_{l\text{-}nm}$ are the resistance, inductance and capacitance in the DC line equivalent circuit between bus n and bus m, respectively.

Then, **Eq. 13** can be used to determine the inter-pole short-circuit current flowing from the positive pole at the fault point f.

$$I_f = I_{c-f} - \sum_{\substack{m=1 \\ m\neq f}}^{N_b+1} F_{nm}I_{l-nm} \# (13)$$

After calculated the fault component currents everywhere, we can use a computer to perform the inverse Laplace transform to obtain the corresponding time-domain expression.

Solution of Fault Component Current Under Single-Pole Grounding Short-Circuit Faults

To solve the fault component current in this case, the CDM currents at the fault point should be calculated first. According to the circuit shown in **Figure 12**, the common-mode current $I_{f,\Sigma}$ and the differential-mode current $I_{f,\Delta}$ flowing from the fault point can be solved by **Eqs. 14**,**15**.

$$I_{f,\Sigma} = -\frac{U_{f,\Delta(0)}}{Z_\Delta + 2R_f + Z_\Sigma} \# (14)$$

$$I_{f,\Delta} = \frac{U_{f,\Delta(0)}}{Z_\Delta + 2R_f + Z_\Sigma} \# (15)$$

Where

$$Z_\Sigma = \frac{Y^*_{ff,\Sigma}}{\det(Y_\Sigma)} \# (16)$$

$$Z_\Delta = \frac{Y^*_{ff,\Delta}}{\det(Y_\Delta)} \# (17)$$

In **Eqs. 16**,**17**, Y_Σ and Y_Δ are the common- and differential-mode admittance matrixes, respectively. $Y^*_{ff,\Sigma}$ and $Y^*_{ff,\Delta}$ are the elements in the f row and f column in the adjoint matrixes of the common- and differential-mode admittance matrixes, respectively. It should be noted that in order to calculate impedance, the Y_Σ and Y_Δ here should be formed according to the following rules: The diagonal element $Y_{nn,\Sigma}$ in the common-mode admittance matrix is the self-admittance of

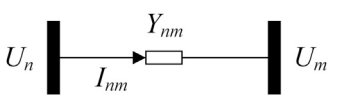

FIGURE 14 | The bus connection structure.

the bus n in the common-mode network, and its value is equal to the sum of the admittances of the branches connected to the bus. $Y_{nm,\Sigma}$ ($n \neq m$) is the mutual admittance of the buses n and m in the common-mode network, and its value is equal to the opposite of the admittance of the branch connected between the two buses. The elements in the differential-mode admittance matrix comply with the same rules.

After obtaining $I_{f,\Sigma}$ and $I_{f,\Delta}$, the solution methods mentioned in the calculation of inter-pole short-circuit can be applied to solve the common- and differential-mode networks respectively. Here, the CDM voltages and currents excited by the fault component current source should be used as unknown variables. After that, the positive and negative currents of the fault components can be obtained through the inverse CDM transformation shown in **Eq. 18**.

$$\begin{bmatrix} I_p \\ I_n \end{bmatrix} = T^{-1} \begin{bmatrix} I_\Sigma \\ I_\Delta \end{bmatrix} = \begin{bmatrix} 1 & 1 \\ 1 & -1 \end{bmatrix} \begin{bmatrix} I_\Sigma \\ I_\Delta \end{bmatrix} \# (18)$$

Finally, the time-domain expression of the fault component current can be obtained through the inverse Laplace transform.

CASE STUDIES

This section presents the case studies that were used for evaluating the effectiveness and accuracy of the proposed linearized model. We will compare the calculated value and the simulated value in the four-terminal ring grid DC distribution system shown in **Figure 15**. This simulation value is provided by PSCAD/EMTDC. **Table 1** provides the corresponding system parameters. The system adopts master-slave control strategy. MMC1 is the master station, and the rest are slave stations. The active powers in the table are the injected powers on the AC side. The injected reactive power of each MMC is zero.

Verification Under Inter-pole Short-Circuit Faults

In the verification under inter-pole short-circuit faults, all the MMCs in **Figure 15** are not grounded, and the transition resistance is zero. After the circuit is stable, set an inter-pole short circuit at the midpoint of the DC line between MMC1 and MMC2 (let t = 0s at this time). The short-circuit currents obtained are shown in **Figure 16**.

From the comparison in **Figure 16**, it can be seen that compared to the simulated value, the calculated value has a small error (no more than 2.64%), and this error would gradually increase over time. I think the reason for this error is that the MMC will no longer maintain the original operating state after the fault, the steady-state component of the fault current would change, and this change would gradually increase over time. Therefore, the calculation method using the superposition theorem in the previous article is only applicable in a very short time after the failure. However, considering that the MMC will be blocked within a very short time after a DC failure, the calculation result is still quite reliable within this time.

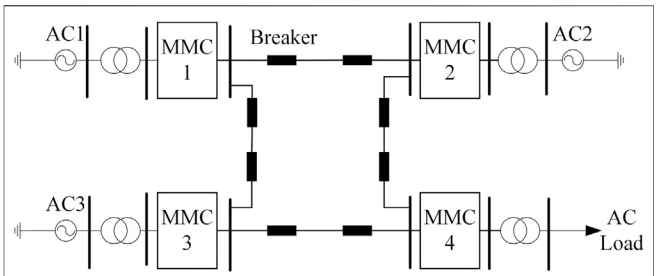

FIGURE 15 | The four-terminal ring grid DC distribution system.

Verification Under Single-Pole Grounding Short-Circuit Faults

In the verification under single-pole grounding short-circuit faults, to verify the MMC models of different grounding methods, the MMCs in **Figure 15** are set with different grounding methods. For MMC1, the AC side is grounded (L_{ac} = 10mH), and the DC side is grounded through the midpoint of the capacitor (C_g = 8mF, R_{cg} = 0.5Ω). For MMC2, the AC side is not grounded, and the DC side is grounded through the midpoint of the clamp resistor (R_g = 4MΩ). For MMC3, the AC side is not grounded, and the DC side is grounded through the midpoint of the capacitor (C_g = 8mF, R_{cg} = 0.5Ω). For MMC4, the AC side is grounded (L_{ac} = 10mH), and the DC side is grounded through the midpoint of the clamp resistor (R_g = 4MΩ). After the circuit is stable, set a negative ground short circuit (R_f = 0) at the midpoint of the DC line between MMC1 and MMC2 (let t = 0s at this time). The short-circuit currents obtained are shown in **Figure 17**.

From the comparison in **Figure 17**, it can be seen that compared to the simulated value, the calculated value has a small error (no more than 4.53%), and this error would gradually increase over time. Not only that, the error in this calculation is larger than that in the calculation of inter-pole short-circuit fault. I think the error in this calculation is not only related to the change in the operating state of the MMC, but also related to the neglect of the bridge arm reactor. This calculation result is not only reliable in a very short time, but also conservative.

CONCLUSION

This paper summarizes the MMC model in the calculation of inter-pole short circuit, and proposes a new linearized model based on CDM transformation for single-pole grounding short-circuit calculation. Through verification with simulation results, this new model is proven to be reliable and

TABLE 1 | The system parameters of four-terminal ring grid DC distribution system.

Item	Parameter	Item	Parameter
AC voltage (kV)	110	AC frequency (Hz)	50
Transformer ratio	110 kV/10 kV	converter level number	5
DC voltage (kV)	±10	Bridge arm resistance (Ω)	0.5
Bridge arm inductance (mH)	6	Sub-module capacitance (mF)	4
Carrier frequency (Hz)	1000	Smoothing reactor (mH)	10
MMC1 Active power (MW)	12.9	MMC2 Active power (MW)	5
MMC3 Active power (MW)	−3	MMC4 Active power (MW)	−12
DC line resistance (Ω)	1.5	DC line inductance (mH)	2.8

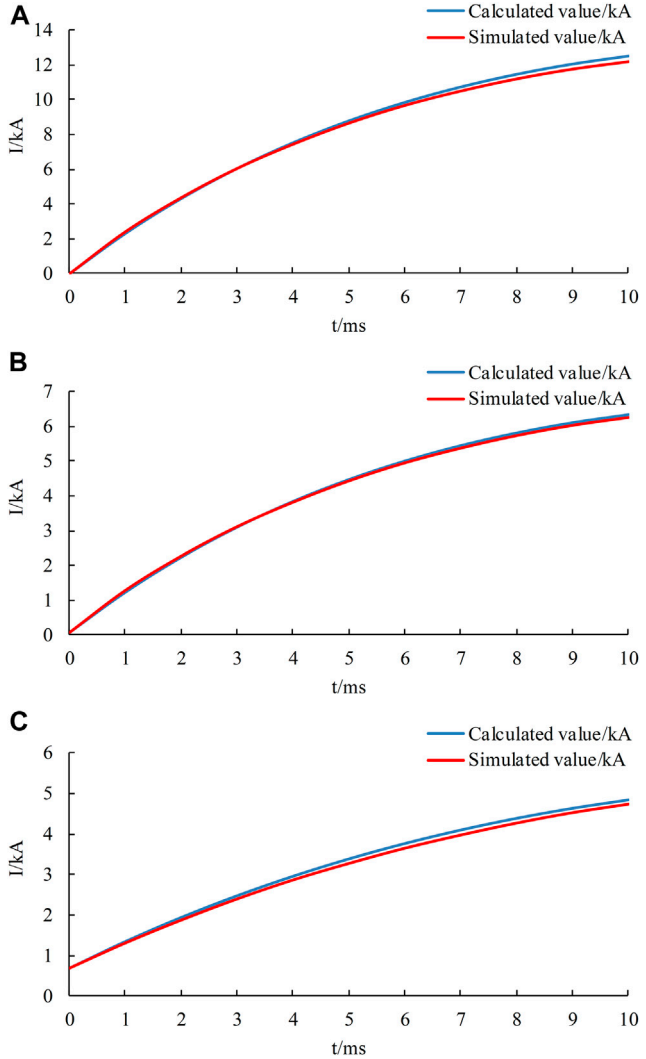

FIGURE 16 | Comparison of the calculated value and the simulated value of the fault current during a inter-pole short circuit **(A)** Short circuit current at fault point. **(B)** Positive current flowing from MMC1 to MMC2 on the fault line. **(C)** Positive current at the outlet of MMC1.

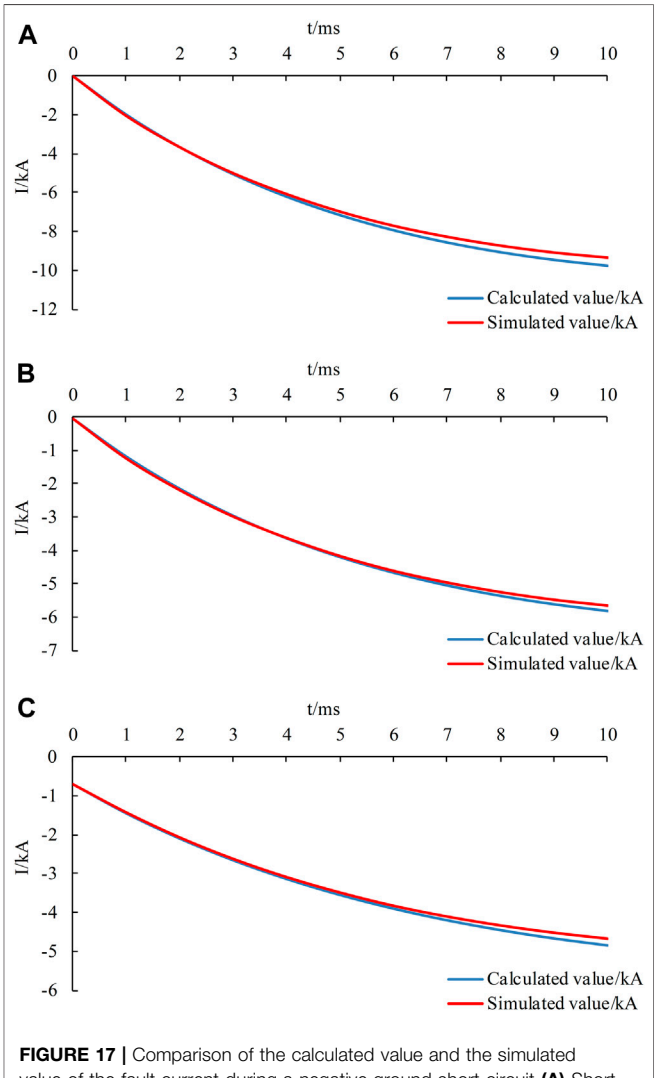

FIGURE 17 | Comparison of the calculated value and the simulated value of the fault current during a negative ground short circuit **(A)** Short circuit current at fault point. **(B)** Negative current flowing from MMC1 to MMC2 on the fault line. **(C)** Negative current at the outlet of MMC1.

conservative. In addition, this paper proposes a frequency domain calculation method suitable for the calculation of complex multi-terminal DC distribution networks. This method can flexibly transform the network topology and has a much faster calculation speed than simulation. The models and method in this paper can be used as a reference for grid planning and equipment selection.

DATA AVAILABILITY STATEMENT

The raw data supporting the conclusions of this article will be made available by the authors, without undue reservation.

AUTHOR CONTRIBUTIONS

PS: analysis, modeling, method, verification and writing. ZJ: advising, supervision, writing-reviewing and editing. HG: simulation model, conceptualization and methodology.

REFERENCES

Baran, M. E., and Mahajan, N. R. (2003). DC distribution for industrial systems opportunities and challenges. *IEEE Transactions on Industry Applications* 39 (6), 1596–1601. doi:10.1109/TIA.2003.818969

Bucher, M. K., and Franck, C. M. (2013). Contribution of fault current sources in multiterminal HVDC cable networks. *IEEE Transactions on Power Delivery* 28 (3), 1796–1803. doi:10.1109/TPWRD.2013.2260359

Feng, T. (2019). Research on transient analysis grounding mode and fault flexible medium voltage DC distribution network. Master's Thesis, China: Xi'an University of Technology.

Franquelo, L. G., Rodriguez, J., Leon, J. I., Kouro, S., Portillo, R., and Prats, M. A. M. (2008). The age of multilevel converters arrives. *IEEE Industrial Electronics Magazine* 2 (2), 28–39. doi:10.1109/MIE.2008.923519

Gao, S., Ye, H., and Liu, Y. (2020). Accurate and efficient estimation of short-circuit current for MTDC grids considering MMC control. *IEEE Transactions on Power Delivery* 35 (3), 1541–1552. doi:10.1109/TPWRD.2019.2946603

Han, X., Sima, W., Yang, M., Li, L., Yuan, T., and Si, Y. (2018). Transient characteristics under ground and short-circuit faults in a ±500kV MMC-based HVDC system with hybrid DC circuit breakers. *IEEE Transactions on Power Delivery* 33 (3), 1378–1387. doi:10.1109/TPWRD.2018.2795800

Hao, Q., Li, Z., Gao, F., and Zhang, J. (2019). Reduced-order small-signal models of modular multilevel converter and MMC-based HVdc grid. *IEEE Transactions on Industrial Electronics* 66 (3), 2257–2268. doi:10.1109/TIE.2018.2869358

Kimbark, E. W. (1970). Transient overvoltages caused by monopolar ground fault on bipolar DC line: theory and simulation. *Power Apparatus Systems IEEE Transactions on PAS* 89 (4), 584–592. doi:10.1109/TPAS.1970.292605

Li, C., Gole, A. M., and Zhao, C. (2018). A fast DC fault detection method using DC reactor voltages in HVdc grids. *IEEE Transactions on Power Delivery* 33 (5), 2254–2264. doi:10.1109/TPWRD.2018.2825779

Luo, F. (2019). Research on grounding method and protection strategy of DC distribution network for power supply in remote areas. Master's Degree, China: Xi'an Jiaotong University.

Lyu, J., Cai, X., and Molinas, M. (2016). Frequency domain stability analysis of MMC-based HVdc for wind farm integration. *IEEE J. Emerging and Selected Topics in Power Electronics* 4 (1), 141–151. doi:10.1109/JESTPE.2015.2498182

Sannino, A., Postiglione, G., and Bollen, M. H. J. (2003). Feasibility of a DC network for commercial facilities. *IEEE Transactions on Industry Applications*. 39 (5), 1499–1507. doi:10.1109/TIA.2003.816517

Shi, X., and Ma, J. (2020). "Analysis of DC-side single Pole grounding fault in MMC-HVDC system considering the influence of control strategy," in 2020 12th IEEE PES Asia-Pacific Power and Energy Engineering Conference, Nanjind, China, September 20–23, 2020. doi:10.1109/APPEEC48164.2020.9220729

Starke, M. R., Tolbert, L. M., and Ozpineci, B. (2008). "AC vs. DC distribution: a loss comparison," in Transmission and Distribution Conference and Exposition, 2008, Chicago, IL, April 21–24, 2008. doi:10.1109/TDC.2008.4517256

Tünnerhoff, P., Ruffing, P., and Schnettler, A. (2018). Comprehensive fault type discrimination concept for bipolar full-bridge-based MMC HVDC systems with dedicated metallic return. *IEEE Transactions on Power Delivery* 33 (1), 330–339. doi:10.1109/TPWRD.2017.2716113

Wang, S., Zhou, X., Tang, G., He, Z., Teng, L., and Bao, H. (2011). Analysis of submodule overcurrent caused by DC pole-to-pole fault in modular multilevel converter HVDC system. *Proceedings of the CSEE* 31 (01), 1–7. doi:10.13334/j.0258-8013.pcsee.2011.01.001

Xu, Z. (2013). *Flexible DC transmission system*. Beijing, China: China Machine Press.

Zhang, Z., and Xu, Z. (2016). Short-circuit current calculation and performance requirement of HVDC breakers for MMC-MTDC systems. *IEEJ Transactions on Electrical and Electronic Engineering* 11 (2), 168–177. doi:10.1002/tee.22203

Zhou, J., Zhao, C., Li, C., Xu, J., and An, T. (2017). Boundary protection scheme for multi-terminal flexible DC grid based on voltage of DC reactor. *Automation of Electric Systems* 41 (19), 89–94. doi:10.7500/AEPS20170331005

Conflict of Interest: The authors declare that the research was conducted in the absence of any commercial or financial relationships that could be construed as a potential conflict of interest.

frontiers in Energy Research

METHODS
published: 05 March 2021
doi: 10.3389/fenrg.2021.629131

Optimal Operation of Isolated Micro-Grids-cluster Via Coalitional Energy Scheduling and Reserve Sharing

Hasan Saeed Qazi[1], Tianyang Zhao[2], Nian Liu[1]*, Tong Wang[1] and Zia Ullah[3]*

[1]State Key Laboratory for Alternate Electrical Power System with Renewable Energy Sources, Department of Electrical and Electronics Engineering, North China Electric Power University, Beijing, China, [2]Energy Research Institute, Nanyang Technological University, Singapore, [3]School of Electrical and Electronics Engineering, Huazhong University of Science and Technology, Wuhan, China

Microgrids (MG) cluster are isolated from the utility grid but they have the potential to achieve better techno-economic performance by using joint energy and reserve sharing among MGs. This paper proposes a techno-economic framework for the optimal operation of isolated MGs-cluster by scheduling cooperative energy sharing and real-time reserve sharing for ancillary services based on the cooperative game theory. In the day-ahead scheduling, a coalitional sharing scheme is formulated as an adjustable robust optimization (ARO) problem to optimally schedule the energy and reserves of distributed generators (DGs) and energy storage systems (ESSs), thereby responding to the uncertainties of photovoltaic systems, wind turbines, and loads. These uncertainties are the main reason for power system imbalance which is mitigated by regulating the frequency in real-time and a dynamic droop control process is used to realize the reserves in a distributed manner. This control process is embedded into the ARO problem, which is formulated as an affine ARO problem and then transformed into a deterministic optimization problem that is solved by off-shore solvers Apart from the reduction in the operation cost, the frequency restoration can be improved jointly, resulting in the coupled techno-economic contribution of the MGs in the coalition. The contribution of each MG is quantified using shapely value, a cooperative game approach. Simulations are conducted for a case study with 4 MGs and the results demonstrate the merits of the proposed cooperative scheduling scheme.

Keywords: coalitional scheduling, jointed energy, reserve energy, microgrid, frequency restoration, techno-economic

OPEN ACCESS

Edited by:
G. M. Shafiullah,
Murdoch University, Australia

Reviewed by:
Jin Yang,
University of Glasgow, United Kingdom
Kenneth Okedu,
Caledonian College of Engineering, Oman
Zhongwen Li,
Zhengzhou University, China

****Correspondence:***
Nian Liu
nianliu@ncepu.edu.com
Hasan Saeed Qazi
hasanqazi1@hotmail.com

Specialty section:
This article was submitted to Smart Grids, a section of the journal Frontiers in Energy Research

Received: *13 November 2020*
Accepted: *18 January 2021*
Published: *05 March 2021*

Citation:
Qazi HS, Zhao T, Liu N, Wang T and Ullah Z (2021) Optimal Operation of Isolated Micro-Grids-cluster Via Coalitional Energy Scheduling and Reserve Sharing. Front. Energy Res. 9:629131. doi: 10.3389/fenrg.2021.629131

1 INTRODUCTION

Due to the interconnection of distributed energy resources (DERs), e.g., wind turbines (WTs), photovoltaic (PV) modules, distributed generators (DGs) (Ma et al., 2016; Hamidi et al., 2017; Lara et al., 2018) and energy storage systems (ESSs), microgrids (MGs) have been playing a crucial role in the development of smart grid technology. MGs are capable of operating in both isolated and grid-connected modes (Faisal et al., 2018; Lv et al., 2016). Other than ensuring the power balancing status among local DERs and loads, MGs can also exchange power flexibly with external systems (Vahedipour-Dahraie et al., 2020), e.g., the utility grid and other MGs. By developing a more

efficient and resilient MGs-cluster, these exchanges cover not only conventional energy sources but also emerging ancillary services, especially for isolated MGs-cluster with high penetration of schedulable DERs (Pourghasem et al., 2019).

The optimal operation of isolated MGs was generally investigated considering the uncertainty of schedulable DERs using stochastic optimization (Hu et al., 2016; Shi et al., 2019) and robust optimization (Ghahramani et al., 2019; Liu et al., 2019). In a grid-connected mode, the MGs-cluster is created by connecting them and the distribution network (Luo et al., 2020). Due to cluster formation and grid-connection, each MG utilizes the local grid resources (Lv and Ai, 2016; Ghadi et al., 2019; Mostafa et al., 2020), as well as those of other MGs (Lv and Ai, 2016; Gao et al., 2017; Ali et al., 2019; Toutounchi et al., 2019).

Regarding the coalitional operation of an MGs-cluster, an energy management problem was extended to a multi-MG in (Liu et al., 2018; Purage et al., 2019) to minimize the cost. The amount of production cannot be controlled in uncontrollable energy sources; therefore, in (Purage et al., 2019), a controllable distributed energy re-source (CDER) was presented such as DGs and ESS where the production amount can be controlled by the energy management system. Energy management approaches for the utilization of energy resources in MGs-cluster and the grid were presented in (Zhang and Xu, 2018). This approach successfully decreases the volume of energy acquired from the grid which significantly increases the MG profit. In (Aktas et al., 2017), a stochastic bi-level model that provided an effective solution for the coordinated operation of the MGs-cluster was proposed. In (Simões et al., 2016), a strategy was recommended for the exchange of information between MGs-cluster to enhance the coordination among the MGs to increase the profit and reduce the operational cost of each member of the cluster. In (Xie et al., 2017), an economic-probabilistic model was presented for the balanced exchange of energy between the MGs-cluster by controlling the energy resources and loads of the MGs.

The stability of the power system is achieved when the generation and load are in equilibrium. However, due to the possibility of errors in the day-ahead forecasted outputs of PV, WT, and load demand, the real-time outputs exhibit fluctuations in the frequency. The scheduling of the controllable DER (CDER) output must be readjusted according to the output of the PV, WT, and load demand to achieve frequency stability (Lin et al., 2018). The isolated MGs-cluster requires a robust frequency regulation that depends on the three-level hierarchical energy management system, i.e., primary, secondary, and tertiary control level (Pinzón et al., 2018). The primary control level is focused on the automatic voltage and frequency control of the inverter-interfaced DERs (IIDERs) (Castilla et al., 2019). For secondary control, researchers have implemented the droop-based control method to model the frequency security in energy management (EM) problem. It should be noted that the dependence of IIDERs on MG frequency is insubstantial, however, to keep the power sharing strategy more secure from over-heating risks, the more advanced P-f droop control method is used (Arani and Mohamed, 2017). The highest control level is the tertiary control when primary and secondary levels are insufficient for frequency excursions; this is executed by the MGs-cluster control center (MGCCC) (Basso et al., 2012). For reserve sharing, a linear quadratic regulator-based technique is used to control the CDERs instead of the traditional proportional-integral derivative-based controller (Ketabi et al., 2017). The fluctuations of the renewable energy sources (RES) significantly influence reserve sharing in the MG and the existing droop control method should be modified to handle RES uncertainty (Liu et al., 2018).

In (Rokrok et al., 2018), a contributing factor was introduced for reserve sharing among MGs and the grid to ensure that the system is in equilibrium with the load demand and that the economic impact due to reserve sharing is distributed among the MGs. Further-more, ancillary services regarding frequency support and voltage regulation could be potentially introduced by MGs (Anvari-Moghaddam et al., 2017).

The existing literature indicates that: 1) previous studies on MGs-cluster have mostly considered energy collaboration, reserve cooperation, and economic benefits; besides, the MGs-cluster are connected to the distribution network. However, power system constraints were not considered and their effect on power quality was neglected; the quality is affected due to the transient nature of PVs and WTs because imbalances in the power supply and demand occur. 2) To maintain the power system in equilibrium, market-based regulation services are provided by different MGs in a cluster; however, the coordination of these services and the provision of economic benefits for the MGs have not been considered.

To address these problems, we propose a scheduling model for energy sharing and reserve sharing for ancillary services to achieve the optimal operation of isolated MGs-cluster. The main contributions of this paper are twofold.

(1) A techno-economic framework is proposed for the optimal operation of isolated MGs-cluster by scheduling cooperative energy sharing and real-time reserve sharing for ancillary services based on the cooperative game theory.
(2) An economic subsidy sharing between MGs-cluster members is achieved by determining the Shapley values of the coordinated distribution of economic benefits. In the coalitional operation of the MGs-clusters, the Shapley values are used to allocate economic benefits to individual MGs

2 COALITIONAL SCHEDULING OF ISOLATED MICROGRIDS-CLUSTER

2.1 Isolated Microgrids-Cluster System

The typical structure of MGs-cluster is shown in **Figure 1**, it includes multiple interconnected MGs. Each MG consists of DGs, WTs, PVs, ESSs, and loads, which are managed by the corresponding MG control center (MGCC). The MGCC is responsible for information acquisition from the respective MG and information exchange with the external systems. All MGs are integrated into a ring configuration with NB buses and NL lines; this represents the MGs-cluster that is supported by the

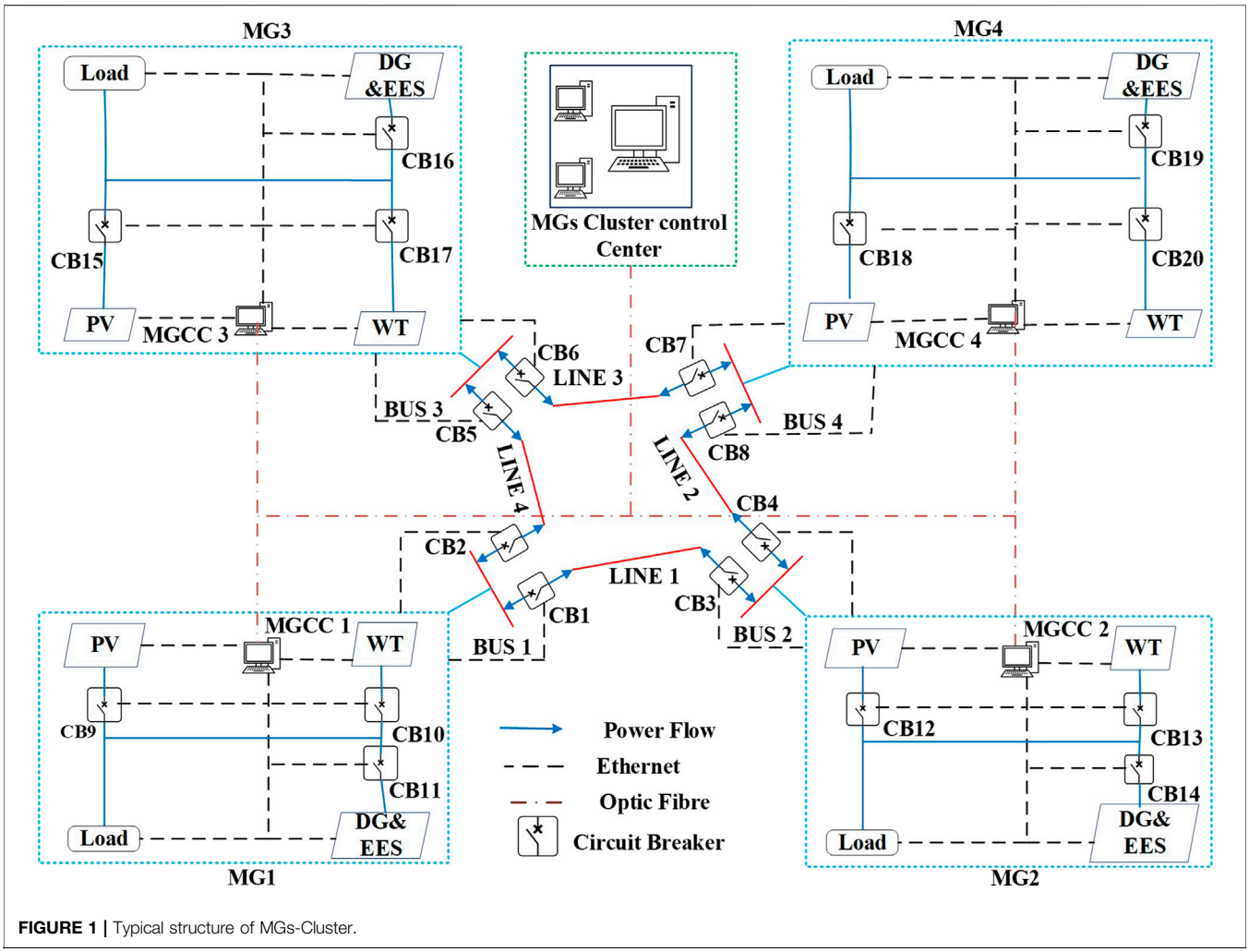

FIGURE 1 | Typical structure of MGs-Cluster.

MGCCC. The MGCCC is responsible for the secure and efficient operation of the MGs-cluster by providing energy and ancillary services, e.g., regulation of reserves and sharing among MGs across multiple scheduling and control processes.

2.2 Operating Process of Microgrids-Cluster

Generally, the operating process of the MGs-cluster includes day-ahead scheduling and reserve sharing for real-time frequency regulation (see **Figure 2**). In the day-ahead scheduling, the forecasted power output of PVs, WTs, and loads (Li et al., 2018; Ullah et al., 2019), as well as the technical information of DGs and ESS, are sent to the MGCCC by each MGCC. After receiving the information, the MGCCC implements the joint energy and reserve optimization to optimally schedule the energy and reserve of the DGs and ESSs in each MGCC; besides, the energy exchange and reserve sharing among MGs for each day is determined. The scheduling plan is sent to each MGCC after the joint energy and reserve optimization. In each operating period, the outputs of the DGs and ESSs are adjusted by the corresponding MGCC according to the day-ahead scheduling plan and in response to the actual power outputs of PVs, WTs, and loads. In this way, the day-ahead scheduling is done by MGCC that includes the power output of DGs and ESSs. The real-time adjustment of the DGs and ESSs is implemented in a distributed manner using a droop control method (Xiao et al., 2017). However, the transient nature of the WT, PV, and load demand is not entirely predictable; therefore, the forecasted information rarely matches the real-time data. To maintain the stability of the MG, real-time scheduling is a challenging task; therefore, the MGCC and the MGCCC coordinate energy and reserve sharing (Xiao et al., 2017). When the load demand is lower than the power generation, the MG can provide excess energy and reserve energy to other MGs and the MGCCC provides economic compensation to that MG. On the other hand, when an MG has a shortage of energy, the MGCCC arranges for other MGs to pro-vide energy to the respective MG. In this way, energy and reserves can be shared and exchanged within the MGs-cluster in real-time for frequency regulation.

Consequently, this paper proposes to address the technical aspect of the framework by doing frequency regulation and economic aspect by addressing the energy and reserve

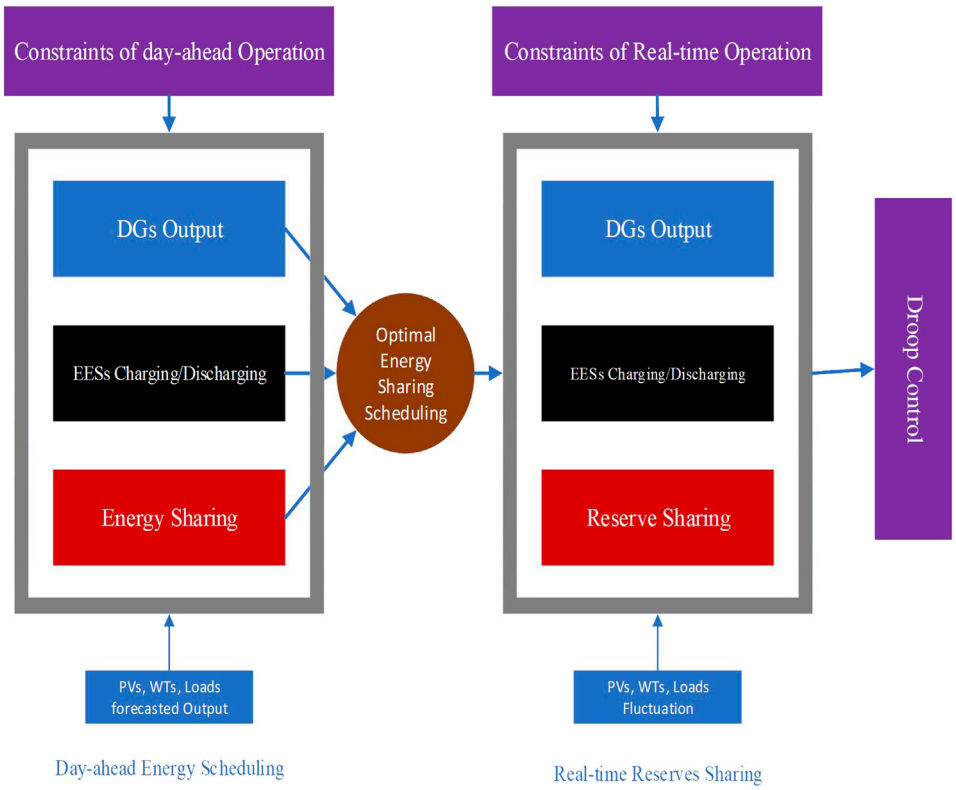

FIGURE 2 | Energy sharing and reserve sharing of isolated MGs-Cluster.

sharing within the MGs-cluster. Therefore, we propose a techno-economic framework for optimal operation of isolated MGs-cluster. Formulations for energy and reserve scheduling for single MG are given in the next section. The coalition scheduling and reserve sharing formulation is discussed in **Section 4**. Details of the economic model are presented in **Section 5**.

3 ENERGY AND RESERVE SCHEDULING FOR SINGLE MICROGRIDS

3.1 Objective Function

The energy and reserve scheduling problem is formulated as an affine adjustable robust optimization problem, where the uncertainties of PVs, WTs, and loads are depicted as a robust set and mitigated by the DGs and ESSs in the real-time frequency regulation. The objective of the MG scheduling is to minimize the total operating cost (OC) of the DGs and ESSs, which is shown in **Equation 1**:

$$C^n = \sum_{t=1}^{T} \left\{ \sum_{g=1}^{N_G^n} \left(C_{G,g}^{n,t,E} + C_{G,g}^{n,t,R} \right) + \sum_{k=1}^{N_B^n} \left(C_{B,k}^{n,t,E} + C_{B,k}^{n,t,R} \right) \right\} \quad (1)$$

where $C_{G,g}^{n,t,E}$ and $C_{G,g}^{n,t,R}$ are the DG OC in the case of energy and reserve sharing for the gth DG in the nth MG during the tth time interval. $n = 1, 2, ..., N_{MG}$, and $N_{MG}$are the number of MGs; g = 1, 2,...,N_G^n, and N_G^n are the number of DGs in the nth MG. $C_{B,k}^{n,t,E}$ and $C_{B,k}^{n,t,R}$ are the ESS OC in case of energy and reserve sharing for the tth ΔESS in the nth MG during the tth time interval respectively. k = 1, 2, ..., N_B^n, and are the number of ESSs in the nth MG. The details on each item is explained in Section 4.3.

3.2 Constraints of Day-Ahead Operation

In the day-ahead operation, the constraints concerning the DGs and ESSs are as follows:

$$p_{G,g}^{n,min} \le p_{G,g,f}^{n,t} \le p_{G,g}^{n,max} \quad (2)$$

$$Ramp_{G,g}^{n,dn} \le \left(p_{G,g,f}^{n,t} - p_{G,g,f}^{n,t-1} \right) \le Ramp_{G,g}^{n,up} \quad (3)$$

$$0 \le p_{B,k,f}^{d,n,t} \le \left(p_{B,k}^{d,n} \right)^{max} \quad (4)$$

$$0 \le p_{B,k,f}^{c,n,t} \le \left(p_{B,k}^{c,n} \right)^{max} \quad (5)$$

$$E_{B,k,f}^{n,t} = E_{B,k,f}^{n,t-1} + \left(p_{B,k,f}^{c,n,t} \eta_k^{c,n} - \frac{p_{B,k,f}^{d,n,t}}{\eta_k^{d,n}} \right) \quad (6)$$

$$E_{B,k}^{n,min} \le E_{B,k}^{n,0} \le E_{B,k}^{n,max} \quad (7)$$

To minimize the OC, the DGs must operate under the constraints defined in **Equations 2**, **3**. The maximum and minimum outputs

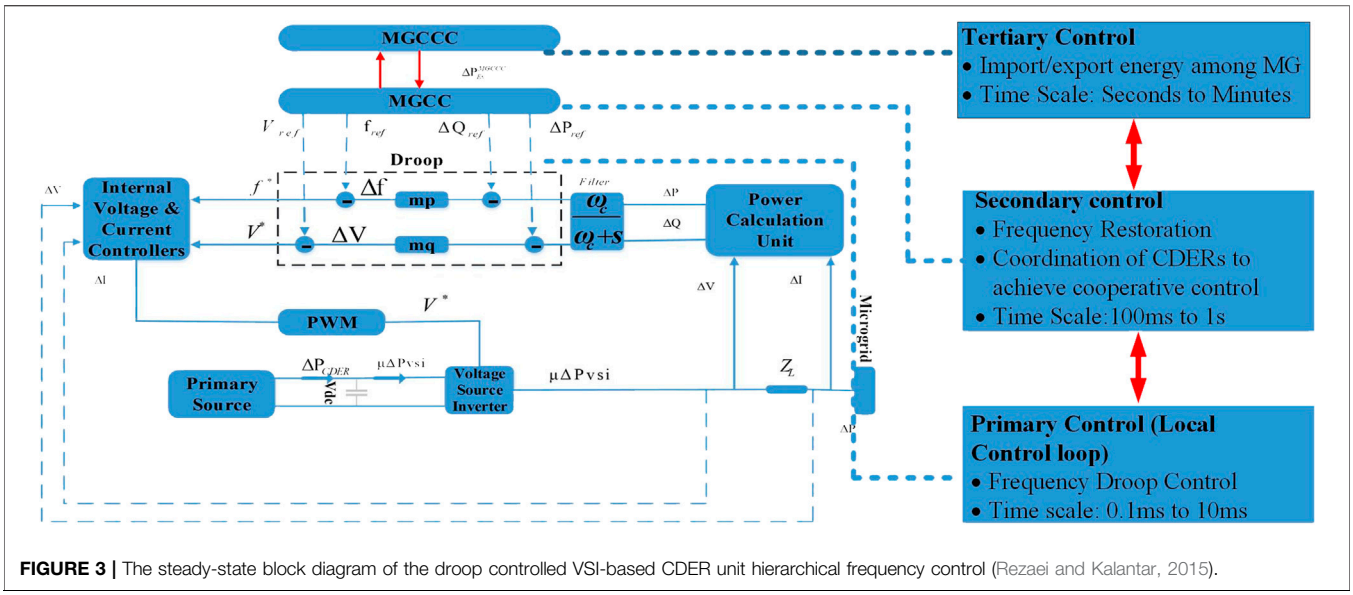

FIGURE 3 | The steady-state block diagram of the droop controlled VSI-based CDER unit hierarchical frequency control (Rezaei and Kalantar, 2015).

of the *g*th DG in the *n*th MG are $p_{G,g}^{n,max}$ and $p_{G,g}^{n,min}$ respectively whereas the ramp-down and ramp-up rate limits are $Ramp_{G,g}^{n,dn}$ and $Ramp_{G,g}^{n,up}$, respectively. In constraints (4)–(5), the maximum charging and discharging power of the *k*th ESS are $(p_{B,k}^{c,n})^{max}$ and $(p_{B,k}^{d,n})^{max}$, respectively. The energy level at the end of the *t*th time interval is $E_{B,k}^{n,t}$. $\eta_k^{c,n}$ and $\eta_k^{d,n}$ are the charging and discharging efficiencies, and $E_{B,k}^{n,max}$ and $E_{B,k}^{n,min}$ are the maximum and minimum capacities of the *k*th ESS, where $p_{G,g,f}^{n,t}$ and $p_{B,k,f}^{n,t}$ are the base-point power output of the *g*th DG and *k*th ESS in the *nth* MG in the *t*th time.

3.3 Constraints for Real Time Operation.

To minimize the OC in real-time, the following constraints must be satisfied. The constraints concerning DGs and ESSs are as follows:

$$p_{G,g}^{n,min} \le p_{G,g,f}^{n,t} + \Delta p_{G,g,q}^{n,t} \le p_{G,g}^{n,max} \tag{9}$$

$$Ramp_{G,g}^{n,dn} \le \left(p_{G,g,f}^{n,t} + \Delta p_{G,g,q}^{n,t}\right) - \left(p_{G,g,f}^{n,t-1} + \Delta p_{G,g,q}^{n,t-1}\right) \le Ramp_{G,g}^{n,up} \tag{10}$$

$$R_{G,g,q}^{n,t} \ge \Delta p_{G,g,q}^{n,t} \tag{11}$$

$$R_{G,g,q}^{n,t} \le -\Delta p_{G,g,q}^{n,t} \tag{12}$$

$$0 \le p_{B,k,f}^{d,n,t} + \Delta p_{B,k,q}^{d,n,t} \le \left(p_{B,k}^{d,n}\right)^{max} \tag{13}$$

$$0 \le p_{B,k,f}^{c,n,t} + \Delta p_{B,k,q}^{c,n,t} \le \left(p_{B,k}^{c,n}\right)^{max} \tag{14}$$

$$R_{B,k,q}^{n,t} \ge \Delta p_{B,k,q}^{n,t} \tag{15}$$

$$R_{B,k,q}^{n,t} \le -\Delta p_{B,k,q}^{n,t} \tag{16}$$

$$E_{B,k}^{n,t} = E_{B,k}^{n,t-1} + \left(p_{B,k,f}^{c,n,t} + \Delta p_{B,k,q}^{c,n,t}\right)\eta_k^{c,n} - \frac{p_{B,k,f}^{d,n,t} + \Delta p_{B,k,q}^{d,n,t}}{\eta_k^{d,n}} \tag{17}$$

$$E_{B,k}^{n,min} \le E_{B,k}^{n,0} \le E_{B,k}^{n,max} \tag{18}$$

The constraint **Equation 9** represents the power capacity limit of DGs, where $\Delta p_{G,g,q}^{n,t}$ is the change in the *q*th control level in the *g*th DG output in the *n*th *MG* in the *t*th time. The index $q \epsilon Q$ denotes that the hierarchical control level is equal to the *pri* (primary) and sec (secondary) control level. The constraints **Equations 11**, **12**, **15**, **16** are the limits of the primary and secondary upward/downward reserve of the DGs and ESSs respectively. $\Delta p_{B,k,q}^{d,n,t}$ is the change in the *q*th control level in the *k*th ESS output in the *n*th MG in the *t*th time. $R_{G,g,q}^{n,t}$ and $R_{B,k,q}^{n,t}$ are define in 4.3.

3.4 Real-Time Frequency Regulation

Normally, the primary control, secondary control, and tertiary control are the hierarchical control approach involve in the frequency regulation of MGs-Cluster. As shown in **Figure 1**, the primary control level, the VSI-based CDER units alleviate the frequency excursions by adjusting their active power outputs in proportion to the frequency excursions (Rezaei and Kalantar, 2015). The primary control has fast response speed and the time scale is between 0.1 ms and 1ms (Wu et al., 2020). However due to inherent errors of the droop controllers, the MG frequency may be stabilizes at a value which may be distinctive to the reference frequency. In such case, the secondary control level, the MGCC can restore the frequency to its reference value by readjusting the active power set-points (Guo et al., 2014). Worth mentioning that, the restoration function should be carried out subject to the MG economic and environmental targets (Li et al., 2019).The response speed of the secondary control is slower than the primary control and the time scale is between 100 ms and 1s (Feng et al., 2017). The tertiary control level is responsible for should coordinate each MG through MGCCC to share active power among them and also regulate the system (de Azevedo et al., 2017; Feng et al., 2017). The tertiary is generally at the slowest level of control and the time scale is in the range of several seconds to minutes (Mohamed et al., 2017).The detailed steady-state model of the droop control function that is shown in **Figure 3** is described in (Rezaei and Kalantar, 2015). Furthermore, the control functions corresponding to internal voltage and current controllers have been neglected in the steady state. Worth to be noted, it is assumed that MG is in the steady-state and all the transients and oscillating modes have been died

down. The frequency depends on the behavior of the droop-controlled inverter-interfaced DGs and ESSs, as defined in **Equations 19**, **20** (Rezaei and Kalantar, 2015) where, m_{pg} and $m_{p,k}$ are frequency droop control gain of VSI base DG and ESS and $\omega_c = 8\ kHz$ The **Equation 21** ensures that the frequency remains within secure limits; $\Delta f^{n,t}_{q,max}$ is the frequency excursion limit.

$$\Delta f^{n,t}_{q} = m_{pg}.\left(\Delta P^{n,t}_{G,g,f} - \Delta p^{n,t}_{G,g,q}\right) \tag{19}$$

$$\Delta f^{n,t}_{q} = m_{p,k}.\left(\Delta P^{n,t}_{B,k,f} - \Delta p^{n,t}_{B,k,q}\right) \tag{20}$$

$$\left|\Delta f^{n,t}_{q}\right| \le \Delta f^{n,t}_{q,max} \tag{21}$$

The frequency depends on the behavior of the droop-controlled inverter-interfaced DGs and ESSs at the primary and secondary control levels. It is noteworthy that, at the primary level, the control functions are processed instantaneously in a few seconds, hence the MGCC does not have enough time to change the base set points of the CDERs. Therefore, $\Delta P^{n,t}_{G,g,f}, \Delta p^{n,t}_{B,k,f} = 0$ for all $q = pri$. (Rezaei and Kalantar, 2015). In contrast, at the secondary control level, the MGCC has more freedom to restore its frequency within its available reserve capacity (Ding et al., 2016). Moreover, if the required energy is not sufficient to restore the frequency, the MGCC has to move to the tertiary control level and purchase energy from another member of the MGs-cluster.

4 COALITIONAL SCHEDULING AND RESERVE SHARING

4.1 Energy Sharing Among Microgrids

The MGCC tries to schedule its DGs and ESSs to match demand and supply within the MG. The MGCCC supervises the MGCC to schedule the DGs and ESSs for energy sharing when other MGs power generation reaches the capacity constraints. Extending the problem **Equations 1–21**, the day-ahead energy sharing within MGs-cluster is to minimize the energy exchange cost. **Equation 22** shows the amount of energy that an MG can exchange (import/export) with the MGCCC. If the value of $p^{n,t}_{Ex,f}$ is positive, it means MGCC will sell energy to MGCCC. On the other hand, if its value is negative MGCC will buy energy from MGCCC. **Equation 23** represents the hourly power balances. The power flow constraint between 2 MGs is expressed in **Equation 24** (Rezaei et al., 2018). The overall energy exchange must be zero for isolated MGs-cluster as shown in **Equation 25**.

$$p^{n,t}_{Ex,f} = \left(p^{n,t}_{W,w,f} + p^{n,t}_{PV,s,f} + p^{n,t}_{G,g,f} + p^{n,t}_{B,k,f}\right) - p^{n,t}_{L,f} \tag{22}$$

$$\sum_{g=1}^{N^n_G} p^{n,t}_{G,g,f} + \sum_{k=1}^{N^n_B} p^{n,t}_{B,k,f} + \sum_{w=1}^{N^n_W} p^{n,t}_{W,w,f} + \sum_{s=1}^{N^n_{PV}} p^{n,t}_{PV,s,f} + p^{n,t}_{Ex,f} - p^{n,t}_{L,f} = 0 \tag{23}$$

$$L^{\star}\left(\left(\sum_{g=1}^{N^n_G} p^{n,t}_{G,g,f} + \sum_{k=1}^{N^n_B} p^{n,t}_{B,k,f}\right) + \left(\sum_{w=1}^{N^n_W} p^{n,t}_{W,w,f} + \sum_{w=1}^{N^n_W} p^{n,t}_{W,w,f} + \sum_{s=1}^{N^n_{PV}} p^{n,t}_{PV,s,f}\right) - \left(p^{n,t}_{L,f}\right) \le p^{max}_{L} \tag{24}$$

$$\sum_{n=1}^{N} p^{n,t}_{Ex,f} = 0 \tag{25}$$

Where, $p^{n,t}_{Ex,f}$ is the scheduled energy sharing among the MGs, where, L represents an $N_L{}^{\star}(N_B\text{-}1)$ matrix of the power transfer distribution factor and explain in detail in (Rezaei et al., 2018).

4.2 Reserve Sharing Among Microgrids

In real-time operation, the MGCC utilizes its reserve to address its mismatch first and then participates in reserve sharing to keep the power system in equilibrium; this is defined in **Equation 26**. The power balance in real-time after reserve sharing is shown in **Equation 27** and the power flow constraint between 2 MGs is defined in **Equation 28**. The sum of the exchanged energy in the isolated MGs-cluster must be equal to zero as shown in **Equation 29**.

$$\Delta p^{n,t}_{Ex} = \left(\Delta p^{n,t}_{W,w} + \Delta p^{n,t}_{s,PV} + \Delta p^{n,t}_{G,g} + \Delta p^{n,t}_{B,k}\right) - \Delta p^{n,t}_{L} \tag{26}$$

$$\sum_{w=1}^{N^n_W}\left(p^{n,t}_{W,w,f} + \Delta p^{n,t}_{W,w}\right) + \sum_{s=1}^{N^n_{PV}}\left(p^{n,t}_{PV,s,f} + \Delta p^{n,t}_{PV,s}\right) + \left(p^{n,t}_{Ex,f} + \Delta p^{n,t}_{Ex}\right) - \left(p^{n,t}_{L,f} + \Delta p^{n,t}_{L}\right) = 0 \tag{27}$$

$$L^{\star}\left(\left(p^{n,t}_{G,g,f} + \Delta p^{n,t}_{G,g,q}\right) + \left(p^{n,t}_{B,k,f} + \Delta p^{n,t}_{E,k,q}\right)\right) + \left(p^{n,t}_{W,w,f} + \Delta p^{n,t}_{W,w}\right) + \left(p^{n,t}_{PV,s,f} + \Delta p^{n,t}_{PV,s}\right) - \left(p^{n,t}_{L,f} + \Delta p^{n,t}_{L}\right) \le \left(p^{max}_{L} + \Delta p^{max}_{L}\right) \tag{28}$$

$$\sum_{n=1}^{N}\left(p^{n,t}_{Ex,f} + \Delta p^{n,t}_{Ex}\right) = 0 \tag{29}$$

where $\Delta p^{n,t}_{Ex}$ is the reserve sharing among the MGs and $\Delta p^{n,t}_{G,g}$ and $\Delta p^{n,t}_{B,k}$ are the power levels of the DG and ESS that participate in the primary and secondary frequency control.

4.3 Microgrid Component Modeling

The MG energy management system usually solves the day-ahead dispatch problem, which is subject to the power balance constraint of the MG and the operational constraints of the MG components. To enable the formulation of this dispatch problem, the cost functions, and the operational constraints of all the MG components are developed in the following paragraphs. The MG generally consists of DGs, ESSs, WTs, PVs, etc. The objective of optimizing the schedule of an MG is to reduce the overall OC, which contains the operational expenses of the DGs and ESSs, as well as the exchange energy cost between the MGs. The basic cost function corresponding to the energy and reserve cost of DGs and ESSs are given as follows:

$$C^{n,t}_{G,g}\left(p^{n,t}_{G,g}\right) = a^{n}_{G,g}\left(p^{n,t}_{G,g}\right) + b^{n}_{G,g} \tag{30}$$

$$C^{n,t,R}_{G,g} = \sum_{q\epsilon Q} c^{n,R}_{G,g,q}.\ R^{n,t}_{G,g,q} \tag{31}$$

$$C^{n,t,E}_{B,k} = a^{n}_{B,k}\left|p^{n,t}_{B,k}\right| \tag{32}$$

$$C^{n,t,R}_{B,k} = \sum_{q\epsilon Q}\left(c^{n,R}_{B,k,q}.R^{n,t}_{B,k,q}\right) \tag{33}$$

The basic OC of DGs in case of the energy $C^{n,t,E}_{G,g}$ and reserve $C^{n,t,R}_{G,g}$ cost is defined in **Equations 30**, **31**, where $p^{n,t}_{G,g}$ and $R^{n,t}_{G,g,q}$ are the active power output and reserve of the *g*th DG. The $a^{n}_{G,g}$ and $b^{n}_{G,g}$ are the OC coefficients and $c^{n,R}_{G,g,q}$ is the reserve cost of the *g*th DG at control level *q*. The OC of the ESS in case of the energy $C^{n,t,E}_{B,k}$ and reserve $C^{n,t,R}_{B,k}$ cost is expressed in **Equations 32**, **33**, where $p^{n,t}_{B,k}$ and $R^{n,t}_{G,g,q}$ are the charging and discharging power and reserve of the *k*th ESS. $c^{n}_{B,k}$ is the OC coefficient and $c^{n,R}_{B,k,q}$ is the reserve cost of the *k*th ESS at control level *q*.

In the day-ahead scheduling, the MGCC schedules its DGs and ESSs within its capacity constraints to match demand and supply in the MG power system as shown in **Equation 34**; if the MGCC is not able to match the load and power generation, the MGCCC is responsible for energy sharing from other MGs, as follows:

$$\sum_{g=1}^{N^n_G} \boldsymbol{p}^{n,t}_{G,g,f} + \sum_{B=1}^{N^n_E} \boldsymbol{p}^{n,t}_{B,k,f} + \sum_{w=1}^{N^n_W} \boldsymbol{p}^{n,t}_{W,w,f} + \sum_{s=1}^{N^n_{PV}} \boldsymbol{p}^{n,t}_{s,PV,f} - \boldsymbol{p}^{n,t}_{L,f} \geq 0 \tag{34}$$

The uncertain nature of PVs and WTs makes it a challenging task to obtain real power output values. Therefore, errors exist in the forecasted value; hence, the real power outputs of PVs and WTs are presented as a sum of the forecast values and errors:

$$\boldsymbol{p}^{n,t}_{W,w} \in \left[\boldsymbol{p}^{n,t}_{W,w,f} - \boldsymbol{\Delta p}^{n,t}_{W,w}, \boldsymbol{p}^{n,t}_{W,w,f} + \boldsymbol{\Delta p}^{n,t}_{W,w}\right] \tag{35}$$

$$\boldsymbol{p}^{n,t}_{PV,s} \in \left[\boldsymbol{p}^{n,t}_{PV,s,f} - \boldsymbol{\Delta p}^{n,t}_{PV,s}, \boldsymbol{p}^{n,t}_{PV,s,f} + \boldsymbol{\Delta p}^{n,t}_{PV,s}\right] \tag{36}$$

Where, $p^{n,t}_{W,w}$, $p^{n,t}_{W,w,f}$, and $\Delta p^{n,t}_{W,w}$ are the actual power, forecast power, and forecast errors of the *w*th WT in *n*th MG in *t*th time. $p^{n,t}_{PV,s}$, $p^{n,t}_{PV,s,f}$; $\Delta p^{n,t}_{PV,s}$ are the actual Power, forecast Power, and forecast errors of the *s*th PV in *n*th MG in *t*th time.

Likewise, the load demand $p^{n,t}_{L}$ is expressed as follows:

$$\boldsymbol{p}^{n,t}_{L} \in \left[\boldsymbol{p}^{n,t}_{L,f} - \boldsymbol{\Delta p}^{n,t}_{L}, \boldsymbol{p}^{n,t}_{L,f} + \boldsymbol{\Delta p}^{n,t}_{L}\right] \tag{37}$$

Where, $p^{n,t}_{L}$, $p^{n,t}_{L,f}$ and $\Delta p^{n,t}_{L}$ are the actual load, the forecasted load, and forecast error respectively during the *t*th time interval, which is displayed in **Equation 37**.

The discrepancy in the power values $\phi^{n,t}$ of the *nth* MG due to the forecast error is defined as follows:

$$\phi^{n,t} = \boldsymbol{p}^{n,t}_{L} - \sum_{g=1}^{N^n_G} \boldsymbol{p}^{n,t}_{G,g,f} \quad - \sum_{k=1}^{N^n_B} \boldsymbol{p}^{n,t}_{B,k,f} - \sum_{w=1}^{N^n_W} \boldsymbol{p}^{n,t}_{W,w} - \sum_{s=1}^{N^n_{PV}} \boldsymbol{p}^{n,t}_{PV,s} \tag{38}$$

And

$$\boldsymbol{p}^{n,t}_{L,max} = \boldsymbol{p}^{n,t}_{L,f} + \boldsymbol{\Delta p}^{n,t}_{L} \tag{39}$$

$$\boldsymbol{p}^{n,t}_{W,w,max} = \boldsymbol{p}^{n,t}_{W,w,f} + \boldsymbol{\Delta p}^{n,t}_{W,w} \tag{40}$$

$$\boldsymbol{p}^{n,t}_{PV,s,max} = \boldsymbol{p}^{n,t}_{PV,s,f} + \boldsymbol{\Delta p}^{n,t}_{PV,s} \tag{41}$$

$$\boldsymbol{p}^{n,t}_{L,min} = \boldsymbol{p}^{n,t}_{L,f} - \boldsymbol{\Delta p}^{n,t}_{L} \tag{42}$$

$$\boldsymbol{p}^{n,t}_{W,w,min} = \boldsymbol{p}^{n,t}_{W,w,f} - \boldsymbol{\Delta p}^{n,t}_{W,w} \tag{43}$$

$$\boldsymbol{p}^{n,t}_{PV,s,min} = \boldsymbol{p}^{n,t}_{PV,s,f} - \boldsymbol{\Delta p}^{n,t}_{PV,s} \tag{44}$$

where $p^{n,t}_{L,max}$, $p^{n,t}_{W,w,max}$, and $p^{n,t}_{PV,s,max}$ are the maximum values of $p^{n,t}_{L}$, $p^{n,t}_{W,w}$, and $p^{n,t}_{PV,s}$, respectively. $p^{n,t}_{L,min}$,$p^{n,t}_{W,w,min}$, and $p^{n,t}_{PV,s,min}$ are the corresponding minimum values. It is evident in **Equations 39–44** that $\phi^{n,t}$ is an interval number and the maximum and minimum values are obtained as follows:

$$\phi^{n,t}_{max} = \sum_{w=1}^{N^n_W} \boldsymbol{\Delta p}^{n,t}_{W,w} + \sum_{s=1}^{N^n_{PV}} \boldsymbol{\Delta p}^{n,t}_{PV,s} + \boldsymbol{\Delta p}^{n,t}_{L} \tag{45}$$

$$\phi^{n,t}_{min} = -\sum_{w=1}^{N^n_W} \boldsymbol{\Delta p}^{n,t}_{W,w} - \sum_{s=1}^{N^n_{PV}} \boldsymbol{\Delta p}^{n,t}_{PV,s} - \boldsymbol{\Delta p}^{n,t}_{L} \tag{46}$$

The differences between the forecasted and real-time values due to the uncertain nature of PVs, WTs, and load demand might result in instability in the power system; therefore, the MGCC tries to utilize the reserve resources to maintain a stable power system. A new approach for real-time OPF was introduced in (Reddy and Bijwe, 2016) by using the 'best-fit' participation factors (PFs) of each power source. The term $\phi^{n,t}$ represents the power imbalance to the base point solution; the PF that provides the power source for each reserve is shown in **Equations 47**, **48**. The actual outputs of the DGs and ESSs can be determined with **Equations 49**, **50**. The MGCC will try to balance the uncertainty with its available resources as shown in **Equation 51** and if the MG reserve resource hits the capacity constraints, the MGCCC is responsible for reserve sharing from other MGs.

$$\boldsymbol{PF}^{n}_{G,g} = \frac{\boldsymbol{p}^{n,t,}_{G,g}}{\sum_{g=1}^{N^n_G} \boldsymbol{p}^{n,t}_{G,g} + \sum_{k=1}^{N^n_B} \boldsymbol{p}^{n,t}_{B,k}} \tag{47}$$

$$\boldsymbol{PF}^{n}_{B,k} = \frac{\boldsymbol{p}^{n,t,}_{E,k}}{\sum_{g=1}^{N^n_G} \boldsymbol{p}^{n,t}_{G,g} + \sum_{k=1}^{N^n_B} \boldsymbol{p}^{n,t}_{B,k}} \tag{48}$$

$$\boldsymbol{p}^{n,t}_{G,g} = \boldsymbol{p}^{n,t}_{G,g,f} + \boldsymbol{PF}^{n}_{G,g}\phi^{n,t} \tag{49}$$

$$\boldsymbol{p}^{n,t}_{E,k} = \boldsymbol{p}^{n,t}_{E,k,f} + \boldsymbol{PF}^{n}_{B,k}\phi^{n,t} \tag{50}$$

$$\sum_{g=1}^{N^n_G}\left(\boldsymbol{p}^{n,t}_{G,g,f} + \boldsymbol{\Delta p}^{n,t}_{G,g}\right) + \sum_{k=1}^{N^n_B}\left(\boldsymbol{p}^{n,t}_{B,k,f} + \boldsymbol{\Delta p}^{n,t}_{B,k}\right) + \sum_{w=1}^{N^n_W}\left(\boldsymbol{p}^{n,t}_{W,w,f} + \boldsymbol{\Delta p}^{n,t}_{W,w}\right)$$

$$+ \sum_{s=1}^{N^n_{PV}}\left(\boldsymbol{p}^{n,t}_{s,PV,f}\right) + \sum_{s=1}^{N^n_{PV}}\left(\boldsymbol{p}^{n,t}_{s,PV,f} + \boldsymbol{\Delta p}^{n,t}_{s,PV}\right) - \left(\boldsymbol{p}^{n,t}_{L,f} + \boldsymbol{\Delta p}^{n,t}_{L}\right) \geq 0 \tag{51}$$

5 ECONOMIC MODEL

5.1 Cooperative Game-Based Energy and Reserve Sharing

The coalitional game for the energy and reserve sharing model is denoted as {*N*, *υ*, *φ*}. The MGs-cluster is denoted by $\varkappa$ where the number of MGs is *N*. Therefore, 2^N possible alliances can cooperate for *N* MG. Furthermore, a 4-MG game comprises 16 possible alliances, including an empty alliance {∅} and the grand alliance {*N*}. υ denotes the characteristic function for a random alliance $S \subset 2^N$ and φ is the vector of payment to be allocated to individual MGs (Li et al., 2018).

The MGs-cluster coalitional operation that is used to quantify the economic benefit is based on the coalitional characteristic function. To achieve equal distribution of benefits/turn over to

each member of the cluster, an allocation framework is adopted. In the cooperative environment, the power exchange should consider energy sharing and the MG can provide reserve sharing for ancillary services to other members of the cluster. The MGCCC is responsible for the determination of the optimal energy and reserve sharing. The benefit function π_S is formulated as follows:

$$\boldsymbol{\pi_s} = -\boldsymbol{C_S} = -\sum_{n=1}^{S} \boldsymbol{C^n} = -\sum_{n=1}^{S}\sum_{t=1}^{T}\left\{\sum_{g=1}^{N_G^n}\left(\boldsymbol{C_{G,g}^{n,E}} + \boldsymbol{C_{G,g}^{n,R}}\right) + \sum_{k=1}^{N_B^n}\left(\boldsymbol{C_{B,k}^{n,E}} + \boldsymbol{C_{B,k}^{n,R}}\right)\right\} \quad (52)$$

where the total OC of the MGs-cluster is denoted by $C_{\mathcal{S}}$ and S is the number of MGs in this coalition. ϕ^t represents the total power mismatch in terms of:

$$\phi^t = \sum_{n=1}^{S}\phi^{n,t} = \sum_{n=1}^{S}\left\{\boldsymbol{p_L^{n,t}} - \sum_{g=1}^{N_G^n}\boldsymbol{p_{G,g,f}^{n,t,}} - \sum_{k=1}^{N_B^n}\boldsymbol{p_{B,k,f}^{n,t}} - \sum_{w=1}^{N_W^n}\boldsymbol{p_{W,w}^{n,t}} - \sum_{s=1}^{N_{PV}^n}\boldsymbol{p_{PV,s}^{n,t}}\right\} \quad (53)$$

Equations 45, **46** indicate that the overall power mismatches with the maximum and minimum values are defined as:

$$\phi_{max}^t = \sum_{n=1}^{S}\left\{\sum_{w=1}^{N_W^n}\boldsymbol{\Delta p_{W,w}^{n,t}} + \sum_{s=1}^{N_{PV}^n}\boldsymbol{\Delta p_{PV,s}^{n,t}} + \boldsymbol{\Delta p_L^{n,t}}\right\} \quad (54)$$

$$\phi_{min}^t = -\sum_{n=1}^{S}\left\{\sum_{w=1}^{N_W^n}\boldsymbol{\Delta p_{W,w}^{n,t}} + \sum_{s=1}^{N_{PV}^n}\boldsymbol{\Delta p_{PV,s}^{n,t}} + \boldsymbol{\Delta p_L^{n,t}}\right\} \quad (55)$$

Therefore, the proposed model of energy sharing scheduling and real-time reserve sharing for the isolated MGs-cluster is defined as follows:

$$\textbf{max}\ \ \boldsymbol{\pi_S}(\boldsymbol{x.u})\ \textbf{or min}\ \ \boldsymbol{C_S}(\boldsymbol{x.u}) \quad (56)$$

$$\textbf{s.t}\ \ \boldsymbol{G}(\boldsymbol{x.u}) = 0 \quad (57)$$

$$\boldsymbol{H}(\boldsymbol{x.u}) \le 0 \quad (58)$$

where x is the vector of the decision variables, including $p_{G,g}^{n,t}$ and $p_{B,k}^{n,t}$, where $(n = 1, 2, \ldots\ldots\ldots, N)$. The uncertain variables of the MGs-cluster are denoted by u and consist of $p_{W,w}^{n,t}$, $p_{PV,s}^{n,t}$, and $p_L^{n,t}$. $G(x.u)$ are the equality constraints, which include **Equations 6**, **17**, **19**, **20**, **22**, **23**, **25–27**, **29**, **51** whereas $H(x.u)$are the inequality constraints, comprised of **Equations 2–5**, **7**, **9–21**, **24**, **28**, **34–38**, **46–50**, **53–54**. Note that "max$\pi_S(x.u)$" is equivalent to "min$C_S(x.u)$" based on **Equation 1**.

To solve the optimization problem that is shown in **Equations 46–48**, the uncertain variables have to be determined. One of the best approaches to solve this problem is the affine ARO (Kumar et al., 2017). The off-shore solvers used is CPLEX.

5.2 Profit Distribution Between Microgrids-Cluster

In a coalitional game, every alliance S aims to ensure that each member of the game obtains an economic benefit; thus, the characteristic function of each MG union is represented by $v(\mathcal{S})$. Due to the coalition of MGs, it is essential to determine the characteristic function of each union, which indicates that each member makes a profit due to the coalitional mode. The characteristic function is defined as follows:

$$\boldsymbol{v}(\mathcal{U}) = \boldsymbol{\pi_U} - \sum_{\boldsymbol{\omega\epsilon S}}\boldsymbol{\pi_\omega} \quad (59)$$

where ω is a single MG in the coalition $\mathcal{S}$. When the MGs operate without the coalition mode, the entire profits acquired by the MGs are $\sum_{\omega\epsilon\mathcal{S}}\pi_\omega$. The proposed scheduling model for energy sharing and real-time reserve sharing for MGs-cluster in the coalitional game is super-additive (Kumar et al., 2017) as follows:

$$\boldsymbol{v}(\mathcal{S}) - \boldsymbol{v}(\mathcal{U}) = \boldsymbol{\pi_S} - \sum_{\boldsymbol{\omega\epsilon S}}\boldsymbol{\pi_\omega} + \boldsymbol{\pi_U} - \sum_{\boldsymbol{\omega\epsilon U}}\boldsymbol{\pi_\omega} = \boldsymbol{\pi_S} + \boldsymbol{\pi_U} - \sum_{\boldsymbol{\omega\epsilon S\cup U}}\boldsymbol{\pi_\omega} \le \boldsymbol{\pi_{S\cup U}} - \sum_{\boldsymbol{\omega\epsilon S\cup U}}\boldsymbol{\pi_\omega}$$
$$= \boldsymbol{v}(\mathcal{S}\cup\mathcal{U}) \quad (60)$$

This approach is described in **Equation 57** and the simulation results verify that the maximum profit is achieved by the alliance in which all MGs in the cluster participated. Hence for equal distribution of profits among all members of the MGs-figure, the Shapley value is the best approach (Anvari-Moghaddam et al., 2017). The Shapley value is formulated for the nth MG as follows:

$$\varnothing_{\boldsymbol{n}}(\boldsymbol{v}) = \sum_{\boldsymbol{S\subseteq\mathcal{N}\{n\}}}\frac{|\mathcal{S}|!\,(|\mathcal{N}| - |\mathcal{S}| - 1)!}{|\mathcal{N}|!}\left[\boldsymbol{v}(\mathcal{N}\cup\{\boldsymbol{n}\}) - \boldsymbol{v}(\mathcal{S})\right] \quad (61)$$

where $|\mathcal{N}|$ are the total number of MGs and the sum extends over all subsets S of S excluding the nth MG. $|\mathcal{S}|$ is the number of MGs in S . The formula can be interpreted as follows: considering that the coalition is formed 1 MG at a time, each MG demands its contribution $v(\mathcal{S}\cup\{n\}) - v(\mathcal{S})$ as fair compensation; it then uses the average of this contribution over different combinations in which the coalition can be formed. It should be mentioned that the MGCCC is the authorized entity for conducting the benefit distribution.

6 CASE STUDY

6.1 Case Description

A cluster of 4 MGs (see **Figure 1**) is used as a test system for the proposed model. Each MG comprises 1 DG, 1 ESS,1 WT, and 1 PV. The associated parameters of these components are listed in **Table 1**. **Figure 4** shows the forecast values of the output powers of the WT, PV, and load demands; their forecasting errors are 20%, 10%, and 10% (Li et al., 2018), respectively, Furthermore, the power mismatch among MGs due to unpredictable nature of PVs, WTs, and Load are shown in **Figure 5**. The service fee imposed by the MGCCC on both the buyer and seller MG is 0.005 $/kW (Sampath et al., 2018).

6.2 Simulation Results and Discussion

Since the MGs-cluster consists of a system of 4 MGs, 16 different alliances can be formed in the coalitional game. The turn-over of the coalition's MG (1,2,3), MG (1,2,4), MG (1,3,4), MG (2,3,4), and MG (1,2,3,4) are $61.10, $48.40, $48.53, $46.50, and $71.25 respectively, which is calculated by **Equation 61** and shown in **Table 2** and **Figure 6** The maximum obtained profit is $71.25, which is obtained by the coalition MG (1, 2, 3, 4). The results indicate that if all 4 MGs operate in a coordinated and coalitional

TABLE 1 | MGs-cluster parameter.

Parameters	MG1	MG2	MG3	MG4	Parameters	MG1	MG2	MG3	MG4
a_G^n ($/kW)	0.043	0.046	0.052	0.054	$p_{EESdc}^{n,max}$ (kW/h)	20	20	20	20
b_G^n ($)	0.09	0.08	0.07	0.07	$E_{EES}^{n,0}$ (kWh)	5	5	5	5
$c_{G,q\|q=pri}^{n,R}$ ($/kW)	0.039	0.060	0.040	0.040	$E_{EES}^{n,min}$ (kWh)	5	5	5	5
$c_{G,q\|q=sec}^{n,R}$ ($/kW)	0.011	0.020	0.010	0.010	$E_{EES}^{n,max}$ (kWh)	45	45	45	45
$R_{G,up}^n$ (kW/h)	80	60	40	40	η_c^n	0.95	0.95	0.95	0.95
$R_{G,down}^n$ (kW/h)	75	55	35	35	η_{dc}^n	0.95	0.95	0.95	0.95
$P_{G,min}^n$ (kW)	40	40	40	40	a_B^n	0.05	0.05	0.05	0.05
$P_{G,max}^n$ (kW)	200	150	100	100	$c_{B,q\|q=pri}^{n,R}$($/kW)	0.060	0.060	0.060	0.060
$m_{p,g}$ (mHz/kW)	7.50	10	15	15	$c_{B,q\|q=sec}^{n,R}$($/kW)	0.030	0.030	0.030	0.030
$p_{EESc}^{n,max}$ (kW/h)	25	25	25	25	$m_{p,k}$(mHz/kW)	30	30	30	30

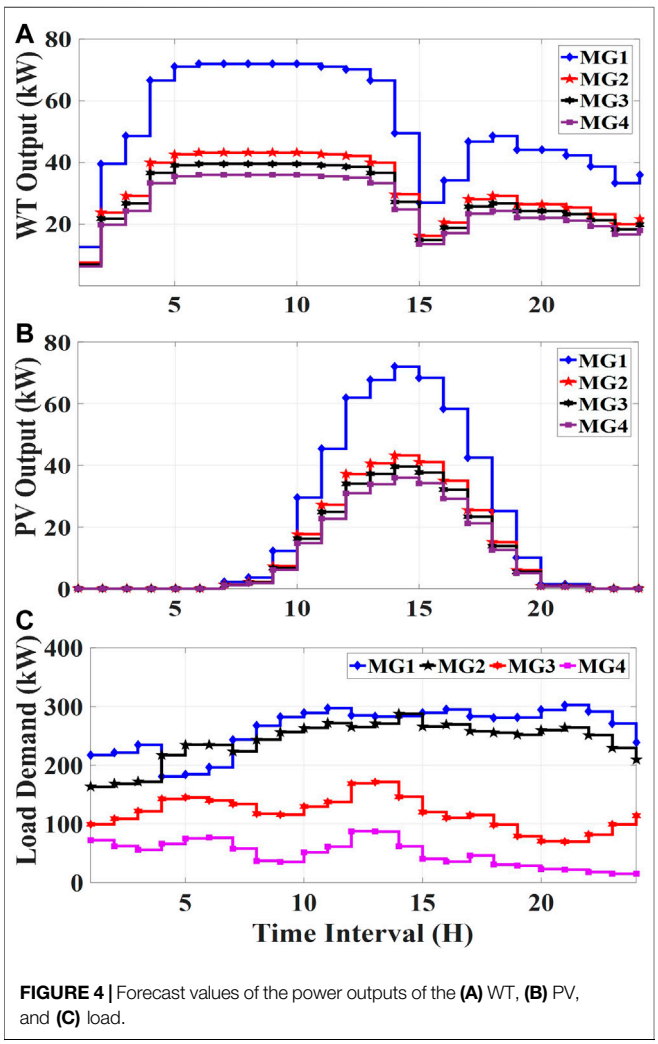

FIGURE 4 | Forecast values of the power outputs of the **(A)** WT, **(B)** PV, and **(C)** load.

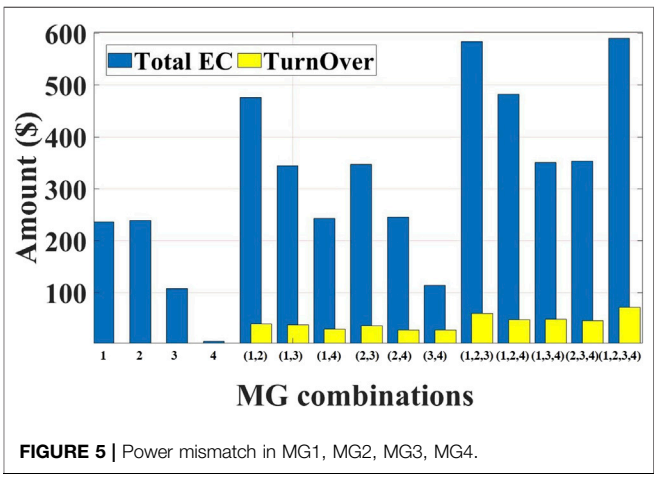

FIGURE 5 | Power mismatch in MG1, MG2, MG3, MG4.

manner, the combined profit is maximized. The total economic cost of MG4 is $6.64, demonstrating that MG4 compensates for all its expenses by selling its surplus electricity that is worth $64.42 and $33.02 in energy and reserve sharing respectively. To obtain an economic benefit and it also plays its part to keep the isolated MGs-cluster in equilibrium and stable.

The optimal results of jointed energy and reserve scheduling in term of MG (1,2,3,4) consist of day-ahead scheduling of DGs and ESSs, furthermore, the participation factor (PFs) of DGs and ESSs are shown in **Figures 7**, **8**, respectively The DGs participate in both energy and reserve scheduling but the DG in MG2 operates on a full load, as shown in **Figure 7A**. Therefore, the respective DG cannot participate in reserve energy as shown in **Figure 8A** However, as shown in **Figure 7B**, it is noted that ESSs do not participate in the energy scheduling, specifically MG1, MG2, and MG3, while they focus on participation in reserve energy sharing as presented in **Figure 8B**, therefore their PFs exceed 0.2 for all time interval. But MG4 will charge and discharge in the first to fourth and the 20th and 24th hour respectively. As a result, the participation of ESS in MG4 is reserve sharing is less than those of MG1, MG2, and MG3 during these time intervals.

The real-time outputs of all CDERs and the exchanged energy in period 5:00 to 5:15 based on the optimal plan are depicted in **Figure 9**. The output of the WTs in MG1 decreases from 52.2 kW to 41.76 kW, the DG output increases from 180 kW to 200 kW, the ESS discharges 3.26 kW, and 6.10 kW of reserve energy is purchased from MG3 through MGCCC to compensate for the mismatch. The load increases from 180.81 kW (planned value) to 198.89 kW (real-time value).

The real-time outputs of all CDERs and the exchanged energy in period 12:00 to 12:15 based on the optimal plan are shown in

TABLE 2 | Operational cost and RC for coalitions of MGs.

Alliance	MG1	MG2	MG3	MG4	MG(1,2)	MG(1,3)	MG(1,4)	MG(2,3)
DAOC of DGs($)	193.17	156.06	90.94	74.22	349.23	284.11	267.39	247.00
RC of DG($)	15.84	0.00	20.51	13.40	15.84	36.34	29.24	20.51
DAOC of EES($)	2.11	1.36	1.31	1.88	3.47	3.42	3.99	2.67
RC of EES($)	22.47	21.37	21.37	14.78	43.84	43.84	37.25	42.74
DAEX($)	3.10	60.43	−9.64	−64.62	63.53	−6.54	−61.52	50.79
RCEX($)	0.00	0.00	−16.59	−33.02	0.00	−16.59	−33.02	−16.59
Total EC($)	236.68	239.22	107.90	6.64	475.90	344.59	243.32	347.12
Turn Over($)	0.00	0.00	0.00	0.00	42.86	38.02	30.30	36.35

Alliance	MG (2,4)	MG (3,4)	MG (1,2,3)	MG (1,2,4)	MG (1,3,4)	MG (2,3,4)	MG (1,2,3,4)
DAOC of DGs($)	230.28	165.16	440.17	423.45	358.33	321.22	514.39
RC of DG($)	13.40	33.91	36.34	29.24	49.75	33.91	49.75
DAOC of EES($)	3.24	3.19	4.78	5.35	5.30	4.55	6.66
RC of EES($)	36.15	36.15	65.21	58.62	58.62	57.52	79.99
DAEX($)	−4.19	−74.26	53.89	−1.09	−71.16	−13.83	−10.73
RCEX($)	−33.02	−49.61	−16.59	−33.02	−49.61	−49.61	−49.61
Total EC($)	245.86	114.54	583.81	482.54	351.22	353.76	590.44
Turn Over ($)	28.44	28.39	61.10	48.40	48.53	46.50	71.25

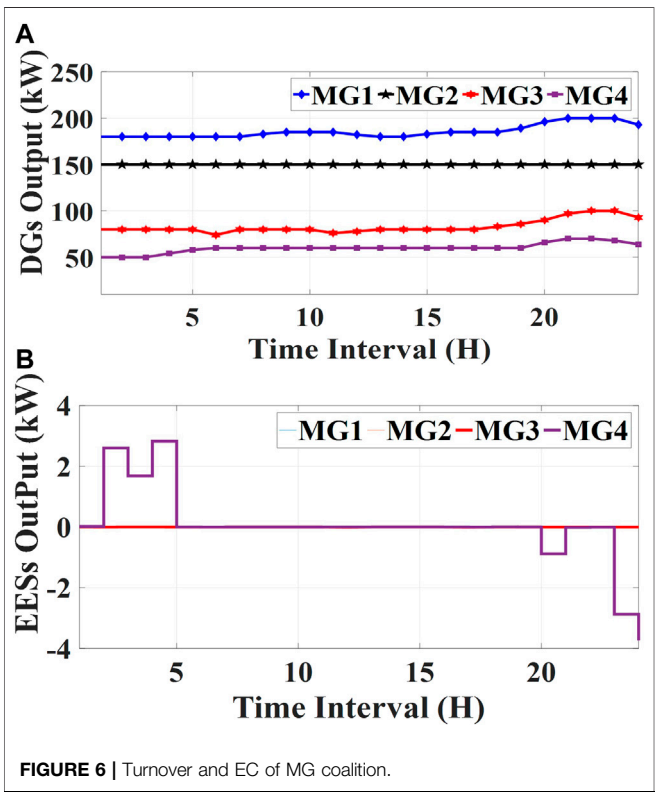

FIGURE 6 | Turnover and EC of MG coalition.

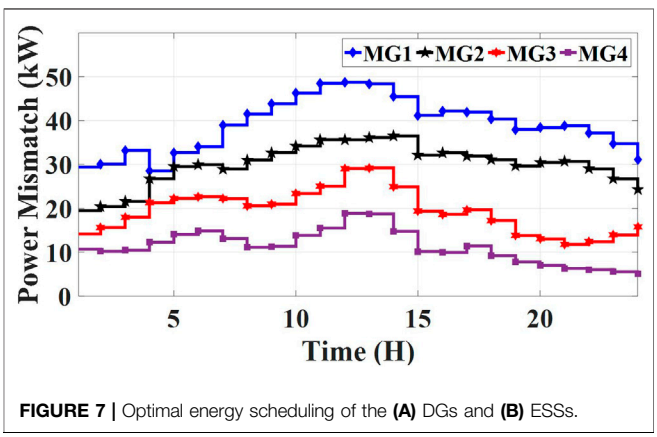

FIGURE 7 | Optimal energy scheduling of the **(A)** DGs and **(B)** ESSs.

subsection **Figure 9**. The forecast outputs and optimal schedule values are depicted in **Figures 4**, **7**. The WT output in MG1 increases from 70.2 kW (planned value) to 84.24 kW (real-time value), the load increases from 285.03 kW to 313.63 kW, and the PV output increases from 61.92 kW to 68.112 kW. The DG output increases from 182 kW to 200 kW, the ESS discharges 6.19 kW, 8.62 kW of reserve energy is purchased from MG3, and 14.03 kW is purchased from MG4 through MGCCC to compensate for the mismatch.

The real-time outputs of all CDERs and the exchanged energy in period 21:00 to 21:15 based on the optimal plan are shown in subsection **Figure 9**. The output of the WTs in MG1 increases from 42.1 kW (planned value) to 50.52 kW (real-time value), the load increases from 302.70 kW to 332.97 kW, and the PV output decreases from 1.44 kW to 1.296 kW. Since the DG was scheduled to operate on a full load, it cannot participate in reducing the mismatch. Therefore MG1 purchases 8.49 kW from MG3 and 25.14 kW from MG4 through MGCCC to compensate for the mismatch.

As shown in **Figure 10**, the frequency of the MGs for periods 5:00–5:15, 12:00–12:15, and 21:00–21:15 are stabilized from 49.89 *Hz*, 49.88 *Hz*, and 49.86 *Hz*–50 *Hz* respectively, after reserve sharing. **Figure 11A** depicts the energy sharing and **Figure 11B** depicts the reserve sharing among the MGs.

Using the obtained optimal coalitional energy and reserve scheduling solution for MG (1,2,3,4), we obtain the values of the

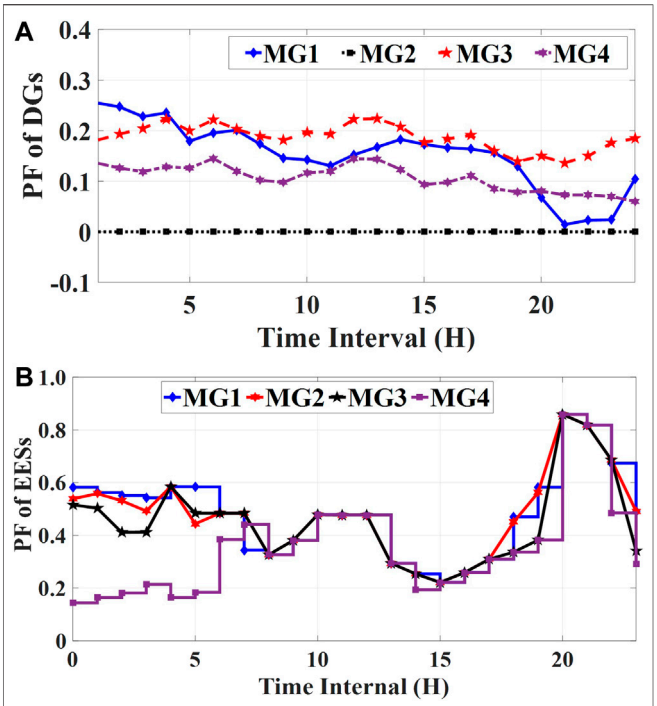

FIGURE 8 | Participation factor of **(A)** DGs and **(B)** ESSs.

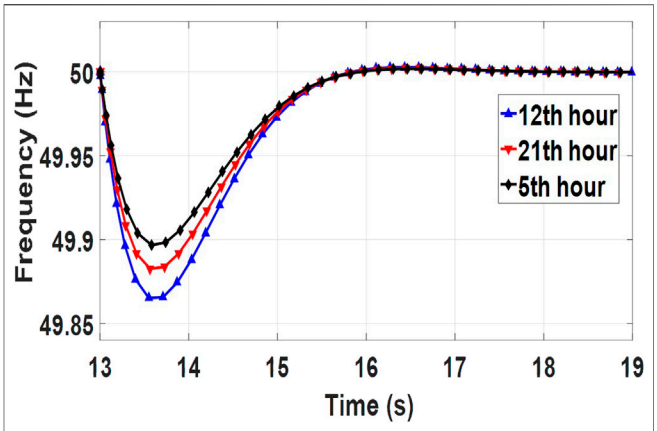

FIGURE 10 | Frequency Restoration in the fifth, 12th, and 21st hours.

day-ahead operational cost (DAOC) and Reserve Cost (RC) in term of DGs, ESSs and Power exchange cost (EX) for each MG which are shown in **Table 3**. Compared with the benefit values for MG1, MG2, MG3, and MG4 presented in **Table 2**. As presented in **Table 2** when MGs operate in isolated mode the turnover in of every MG is null as each MG tries to balance its generation and load as well as DGs also try to follow the load curve in both energy and reserve operation which is shown in **Figure 12**. In Cooperative mode, each MG tries to balance its generation and load as well to get some benefit by sell surplus energy to other MGs as compare the benefit of MG4 in (Isolated Mode) which is 0$ with the turn-over in (Cooperative Mode) which is 25.56$, the value of such benefit is 25.56-0 = 25.56$. The other benefit of the cooperative mode of operation is the smooth curve of DG which in other words reduces the operation cost of DG which is shown in **Figure 12**.

7 CONCLUSION

This study proposed a techno-economic framework for the optimal operation of isolated MGs-cluster by scheduling coalitional energy sharing and real-time reserve sharing for ancillary services such as frequency regulation caused by the uncertainty of PVs, WTs, and loads. The coalitional economic benefits of each member of a coalition are determined by shapely. A case study was conducted on the Isolated MGs-cluster and simulation results have been investigated in terms of energy and reserve sharing to stabilize the frequency of cluster power systems in real-time which is the technical aspect of our framework. Furthermore, we verify the effectiveness of the proposed coalitional sharing scheme for the economic operation of a cluster, compared with their isolated operation which explains

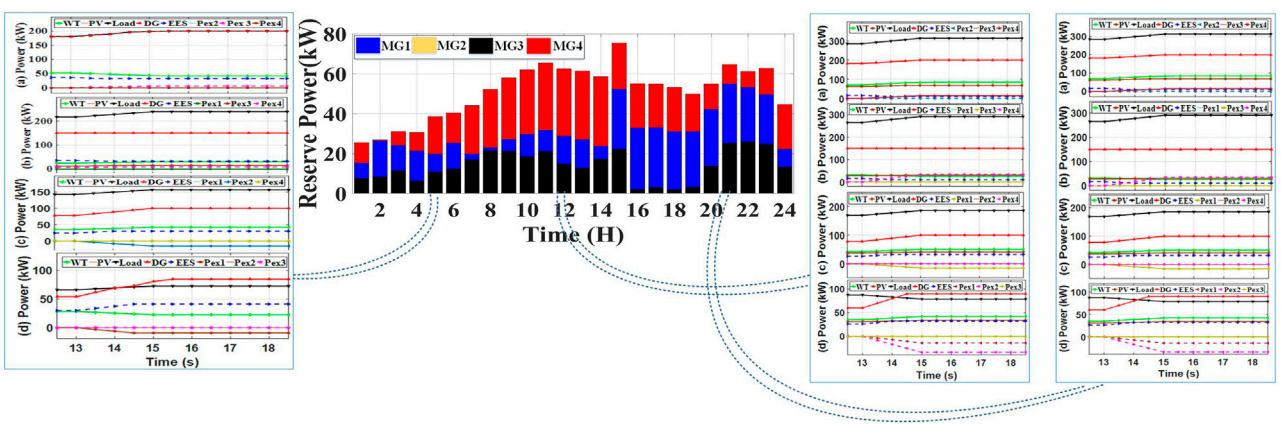

FIGURE 9 | Reserve sharing in the fifth, 12th, and 21st hours.

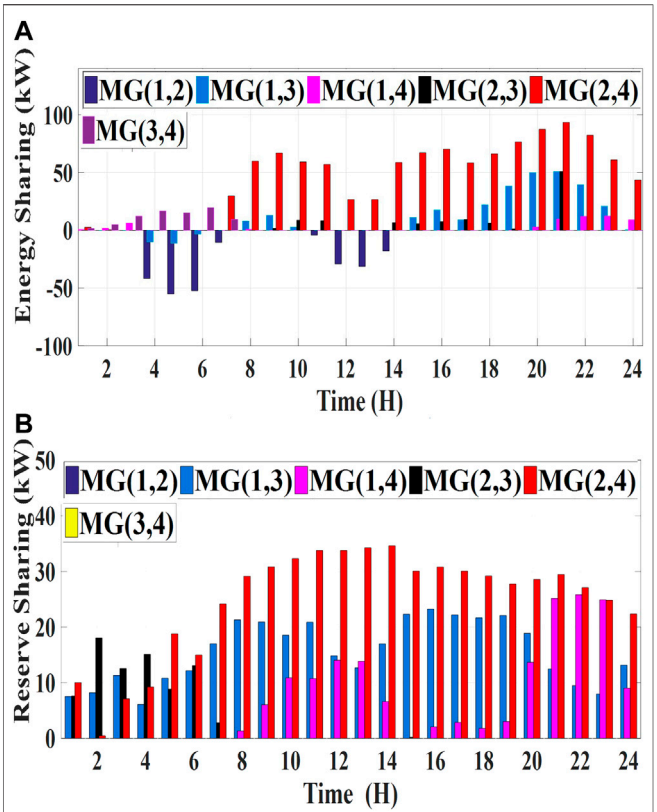

FIGURE 11 | Power exchange among MGs-Cluster MGs.

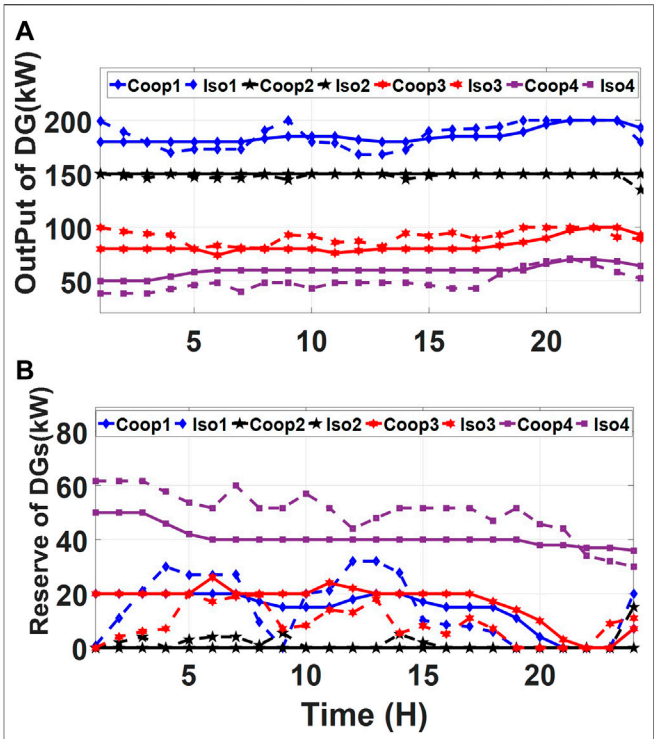

FIGURE 12 | Benefits of Coalitional operation of MGs-Cluster.

TABLE 3 | Operational cost and RC for the coalition MG (1, 2, 3, 4).

MG	DG		ESS		DAEX ($)	RCEX ($)	Turn over ($)
	DAOC ($)	RC ($)	DAOC ($)	RC ($)			
1	185.12	15.18	2.02	21.53	2.97	0.00	14.62
2	162.56	0.00	1.42	22.26	62.95	0.00	12.42
3	94.73	21.36	1.36	22.26	-10.04	-17.3	18.40
4	77.31	13.96	1.96	15.40	-67.32	-34.4	25.56

the economical aspect of our framework. As we are considering the frequency regulation therefore, we consider the active power for the whole system. Therefore, our future research direction is to include the control issues of voltage and reactive power in our system.

DATA AVAILABILITY STATEMENT

The original contributions presented in the study are included in the article/Supplementary Material, further inquiries can be directed to the corresponding author/s.

AUTHOR CONTRIBUTIONS

The author HQ is the Ph.D. scholar, who introduced the conceptualization of the idea, implemented the proposed scheme and contributed to concepts with the help of Professor NL and TZ supervised and finalized the proposed research. TW and ZU helped out in manuscript writing, original draft and verified the simulation results in accordance to the investigated case studies. All authors have read and agreed to the published current version of the manuscript.

REFERENCES

Aktas, A., Erhan, K., Ozdemir, S., and Ozdemir, E. (2017). Experimental investigation of a new smart energy management algorithm for a hybrid energy storage system in smart grid applications. *Elec. Power Syst. Res.* 144, 185–196. doi:10.1016/j.epsr.2016.11.022

Ali, M. S., Haque, M. M., and Wolfs, P. (2019). A review of topological ordering based voltage rise mitigation methods for LV distribution networks with high levels of photovoltaic penetration. *Renew. Sustain. Energy Rev.* 103, 463–476. doi:10.1016/j.rser.2018.12.049

Anvari-Moghaddam, A., Guerrero, J. M., Vasquez, J. C., Monsef, H., and Rahimi-Kian, A. (2017). Efficient energy management for a grid-tied residential microgrid. *IET Gener. Transm. Distrib.* 11 (11), 2752–2761. doi:10.1049/iet-gtd.2016.1129

Arani, M. F. M., and Mohamed, Y. A.-R. I. (2017). Dynamic droop control for wind turbines participating in primary frequency regulation in microgrids. *IEEE Trans. Smart Grid.* 9 (6), 5742–5751. doi:10.1109/tsg.2017.2696339

Basso, T., Hambrick, J., and DeBlasio, D. (2012). "Update and review of IEEE P2030 smart grid interoperability and IEEE 1547 interconnection standards", in *IEEE PES innovative smart grid technologies (ISGT).* (Washington, DC, United States: IEEE), 1–7.

Castilla, M., de Vicuña, L. G., and Miret, J. (2019). "Control of power converters in AC microgrids," in *Microgrids design and implementation.* (Switzerland: Springer), 139–170.

de Azevedo, R., Cintuglu, M. H., Ma, T., and Mohammed, O. A. (2017). Multiagent-based optimal microgrid control using fully distributed diffusion strategy. *IEEE Trans. Smart Grid.* 8 (4), 1997–2008. doi:10.1109/tsg.2016.2587741

Ding, T., Bie, Z., Bai, L., and Li, F. (2016). Adjustable robust optimal power flow with the price of robustness for large-scale power systems. *IET Gener. Transm. Distrib.* 10 (1), 164–174. doi:10.1049/iet-gtd.2015.0561

Faisal, M., Hannan, M. A., Ker, P. J., Hussain, A., Mansor, M. B., and Blaabjerg, F. (2018). Review of energy storage system technologies in microgrid applications: issues and challenges. *IEEE Access.* 6, 35143–35164. doi:10.1109/access.2018.2841407

Feng, X., Shekhar, A., Yang, F., Hebner, E. R., and Bauer, P. (2017). Comparison of hierarchical control and distributed control for microgrid. *Elec. Power Compon. Syst.* 45 (10), 1043–1056. doi:10.1080/15325008.2017.1318982

Gao, H., Liu, J., Wang, L., and Wei, Z. (2017). Decentralized energy management for networked microgrids in future distribution systems. *IEEE Trans. Power Syst.* 33(4), 3599–3610. doi:10.1109/tpwrs.2017.2773070

Ghadi, M. J., Ghavidel, S., Rajabi, A., Azizivahed, A., Li, L., and Zhang, J. (2019). A review on economic and technical operation of active distribution systems. *Renew. Sustain. Energy Rev.* 104, 38–53. doi:10.1016/j.rser.2019.01.010

Ghahramani, M., Nazari-Heris, M., Zare, K., and Mohammadi-Ivatloo, B. (2019). Energy and reserve management of a smart distribution system by incorporating responsive-loads/battery/wind turbines considering uncertain parameters. *Energy.* 183, 205–219. doi:10.1016/j.energy.2019.06.085

Guo, F., Wen, C., Mao, J., and Song, Y.-D. (2014). Distributed secondary voltage and frequency restoration control of droop-controlled inverter-based microgrids. *IEEE Trans. Ind. Electron.* 62 (7), 4355–4364. doi:10.1109/TIE.2014.2379211

Hamidi, A., Nazarpour, D., and Golshannavaz, S. (2017). Multiobjective scheduling of microgrids to harvest higher photovoltaic energy. *IEEE Trans. Ind. Inf.* 14 (1), 47–57. doi:10.1109/tii.2017.2717906

Hu, W., Wang, P., and Gooi, H. B. (2016). Toward optimal energy management of microgrids via robust two-stage optimization. *IEEE Trans. Smart Grid.* 9 (2), 1161–1174. doi:10.1109/tsg.2016.2580575

Ketabi, A., Rajamand, S., and Shahidehpour, M. (2017). Accurate power sharing for parallel DGs in microgrid with various-type loads. *Energy Equip. Syst.* 5 (1), 27–41. doi:10.22059/ees.2017.60847

Kumar, D., Zare, F., and Ghosh, A. (2017). DC microgrid technology: system architectures, AC grid interfaces, grounding schemes, power quality, communication networks, applications, and standardizations aspects. *IEEE Access.* 5, 12230–12256. doi:10.1109/access.2017.2705914

Lara, J. D., Olivares, D. E., and Canizares, C. A. (2018). Robust energy management of isolated microgrids. *IEEE Syst. J.* 13 (1), 680–691. doi:10.1109/JSYST.2018.2828838

Li, Y., Zhao, T., Wang, P., Gooi, H. B., Wu, L., Liu, Y., et al. (2018). Optimal operation of multimicrogrids via cooperative energy and reserve scheduling. *IEEE Trans. Ind. Inf.* 14 (8), 3459–3468. doi:10.1109/tii.2018.2792441

Li, Z., Cheng, Z., Liang, J., Si, J., Dong, L., and Li, S. (2019). Distributed event-triggered secondary control for economic dispatch and frequency restoration control of droop-controlled AC microgrids. *IEEE Trans. Sustainable Energy.* 11 (3), 1938–1950. doi:10.1109/tste.2019.2946740

Lin, P., Jin, C., Xiao, J., Li, X., Shi, D., Tang, Y., et al. (2018). A distributed control architecture for global system economic operation in autonomous hybrid AC/DC microgrids. *IEEE Trans. Smart Grid.* 10 (3), 2603–2617. doi:10.1109/tsg.2018.2805839

Liu, T., Tan, X., Sun, B., Wu, Y., and Tsang, D. H. (2018). Energy management of cooperative microgrids: a distributed optimization approach. *Int. J. Electr. Power Energy Syst.* 96, 335–346. doi:10.1016/j.ijepes.2017.10.021

Liu, Z., Yi, Y., Yang, J., Tang, W., Zhang, Y., Xie, X., et al. (2019). Optimal planning and operation of dispatchable active power resources for islanded multi-microgrids under decentralised collaborative dispatch framework. *IET Gener. Transm. Distrib.* 14 (3), 408–422. doi:10.1049/iet-gtd.2019.0796

Luo, L., Abdulkareem, S. S., Rezvani, A., Miveh, M. R., Samad, S., Aljojo, N., et al. (2020). Optimal scheduling of a renewable based microgrid considering photovoltaic system and battery energy storage under uncertainty. *J. Energy Storage.* 28, 101306. doi:10.1016/j.est.2020.101306

Lv, T., and Ai, Q. (2016). Interactive energy management of networked microgrids-based active distribution system considering large-scale integration of renewable energy resources. *Appl. Energy.* 163, 408–422. doi:10.1016/j.apenergy.2015.10.179

Lv, T., Ai, Q., and Zhao, Y. (2016). A bi-level multi-objective optimal operation of grid-connected microgrids. *Elec. Power Syst. Res.* 131, 60–70. doi:10.1016/j.epsr.2015.09.018

Ma, L., Liu, N., Zhang, J., Tushar, W., and Yuen, C. (2016). Energy management for joint operation of CHP and PV prosumers inside a grid-connected microgrid: a game theoretic approach. *IEEE Trans. Ind. Inf.* 12 (5), 1930–1942. doi:10.1109/tii.2016.2578184

Mohamed, A. A., Elsayed, A. T., Youssef, T. A., and Mohammed, O. A. (2017). Hierarchical control for DC microgrid clusters with high penetration of distributed energy resources. *Elec. Power Syst. Res.* 148, 210–219. doi:10.1016/j.epsr.2017.04.003

Mostafa, M. H., Aleem, S. H. A., Ali, S. G., Abdelaziz, A. Y., Ribeiro, P. F., and Ali, Z. M. (2020). Robust energy management and economic analysis of microgrids considering different battery characteristics. *IEEE Access.* 8, 54751–54775. doi:10.1109/access.2020.2981697

Pinzón, A. M. O., da Silveira, P. M., and Baghzouz, Y. (2018). "Simulation of microgrid hierarchical control", in *18th international conference on harmonics and quality of power (ICHQP).* (Ljubljana, Slovenia: IEEE), 1–6.

Pourghasem, P., Sohrabi, F., Abapour, M., and Mohammadi-Ivatloo, B. (2019). Stochastic multi-objective dynamic dispatch of renewable and CHP-based islanded microgrids. *Elec. Power Syst. Res.* 173, 193–201. doi:10.1016/j.epsr.2019.04.021

Purage, M. I. S. L., Krishnan, A., Foo, E. Y., and Gooi, H. B. (2019). Cooperative bidding-based robust optimal energy management of multimicrogrids. *IEEE Trans. Ind. Inf.* 16 (9), 5757–5768. doi:10.1109/tii.2019.2955991

Reddy, S. S., and Bijwe, P. (2016). Day-ahead and real time optimal power flow considering renewable energy resources. *Int. J. Electr. Power Energy Syst.* 82, 400–408. doi:10.1016/j.ijepes.2016.03.033

Rezaei, N., Ahmadi, A., Khazali, A. H., and Guerrero, J. M. (2018). Energy and frequency hierarchical management system using information gap decision theory for islanded microgrids. *IEEE Trans. Ind. Electron.* 65 (10), 7921–7932. doi:10.1109/tie.2018.2798616

Rezaei, N., and Kalantar, M. (2015). Stochastic frequency-security constrained energy and reserve management of an inverter interfaced islanded microgrid considering demand response programs. *Int. J. Electr. Power Energy Syst.* 69, 273–286. doi:10.1016/j.ijepes.2015.01.023

Rokrok, E., Shafie-Khah, M., and Catalão, J. P. (2018). Review of primary voltage and frequency control methods for inverter-based islanded microgrids with distributed generation. *Renew. Sustain. Energy Rev.* 82, 3225–3235. doi:10.1016/j.rser.2017.10.022

Sampath, L., Krishnan, A., Eddy, Y., and Gooi, H. B. (2018). Robust optimal energy and reserve management of multiple-microgrids via cooperative bidding. arXiv preprint arXiv:1812.00177.

Shi, Z., Liang, H., Huang, S., and Dinavahi, V. (2019). Multistage robust energy management for microgrids considering uncertainty. *IET Gener. Transm. Distrib.* 13 (10), 1906–1913. doi:10.1049/iet-gtd.2018.6594

Simões, M. G., Busarello, T. D. C., Bubshait, A. S., Harirchi, F., Pomilio, J. A., and Blaabjerg, F. (2016). Interactive smart battery storage for a PV and wind hybrid energy management control based on conservative power theory. *Int. J. Contr.* 89 (4), 850–870. doi:10.1080/00207179.2015.1102971

Toutounchi, A. N., Seyedshenava, S., Contreras, J., and Akbarimajd, A. (2019). A stochastic bilevel model to manage active distribution networks with multi-microgrids. *IEEE Systems J.* 13 (4), 4190–4199. doi:10.1109/jsyst.2018.2890062

Ullah, Z., Wang, S., Radosavljević, J., and Lai, J. (2019). A solution to the optimal power flow problem considering WT and PV generation. *IEEE Access.* 7, 46763–46772. doi:10.1109/access.2019.2909561

Vahedipour-Dahraie, M., Rashidizadeh-Kermani, H., Anvari-Moghaddam, A., and Siano, P. (2020). Flexible stochastic scheduling of microgrids with islanding operation complemented by optimal offering strategies. *CSEE J. Power Energy Sys.* [Epub ahead of print]. doi:10.17775/cseejpes.2019.02560

Wu, X., Xu, Y., He, J., Wang, X., Vasquez, J. C., and Guerrero, J. M. (2020). Pinning-based hierarchical and distributed cooperative control for AC

microgrid clusters. *IEEE Trans. Power Electron.* 35 (9), 9867–9887. doi:10.1109/tpel.2020.2972321

Xiao, H., Du, Y., Pei, W., and Kong, L. (2017). Coordinated economic dispatch and cost allocation of cooperative multi-microgrids. *J. Eng.* 2017 (13), 2363–2367. doi:10.1049/joe.2017.0753

Xie, J. Z., Chen, S., and Yang, Z. (2017). Multicast middleware for performance and topology analysis of multimedia grids. *J. Eng.* 2017 (6), 212–219. doi:10.1049/joe.2017.0090

Zhang, W., and Xu, Y. (2018). Distributed optimal control for multiple microgrids in a distribution network. *IEEE Trans. Smart Grid.* 10 (4), 3765–3779. doi:10.1109/tsg.2018.2834921

Conflict of Interest: The authors declare that the research was conducted in the absence of any commercial or financial relationships that could be construed as a potential conflict of interest.

frontiers in Energy Research

ORIGINAL RESEARCH
published: 09 March 2021
doi: 10.3389/fenrg.2021.630234

Research on the Application of SOP in Multi-Station Integrated System

Qunhai Huo[1,2]*, *Wenyong Wang*[1,2], *Yanhong Yang*[1], *Ming Ma*[3], *Jingyuan Yin*[1] and *Tongzhen Wei*[1,2]

[1]Institute of Electrical Engineering, Chinese Academy of Sciences, Beijing, China, [2]University of Chinese Academy of Sciences, Beijing, China, [3]Electric Power Research Institute of Guangdong Power Grid Corporation, Guangdong, China

The current large-scale access to distributed power and the rapid growth of electric vehicles are seriously affecting the reliability of distribution networks. The new multi-station fusion technology based on the flexible interconnection of the distribution network can effectively solve this problem. In this study, we design a multi-purpose station and a multi-function device using a soft normally open point (SOP). A new multi-station integration topology and a coordinated control strategy are developed using an active power signal (APS) and an energy management system (EMS). The coordinated control strategy involves sending out the corresponding operation mode command after the EMS receives the superior instruction or the APS of the local system and coordinating the operation mode of the SOP, energy storage DC/DC converter, and photovoltaic DC/DC converter, thereby ensuring stable and efficient operation of the multi-station fusion system. Finally, two typical cases are simulated to verify the feasibility and effectiveness of the proposed topology and control strategy.

Keywords: multi-station fusion, soft normally open point, active power signal, coordinated control strategy, multi-station integrated system, application of SOP

OPEN ACCESS

Edited by:
Hao Yu,
Tianjin University, China

Reviewed by:
Linquan Bai,
University of North Carolina at Charlotte, United States
Zhongguan Wang,
Tianjin University, China

***Correspondence:**
Qunhai Huo
huoqunhai@mail.iee.ac.cn

Specialty section:
This article was submitted to Smart Grids, a section of the journal Frontiers in Energy Research

Received: *17 November 2020*
Accepted: *25 January 2021*
Published: *09 March 2021*

Citation:
Huo Q, Wang W, Yang Y, Ma M, Yin J and Wei T (2021) Research on the Application of SOP in Multi-Station Integrated System. Front. Energy Res. 9:630234. doi: 10.3389/fenrg.2021.630234

INTRODUCTION

With the acceleration in the construction of the 5G infrastructure and the rapid development of the intelligent manufacturing industry (Giampieri et al., 2020), the quality requirements of the power of the distribution network are becoming increasingly stringent. Furthermore, the urban power grid is struggling to maintain pace with the rapid development of electric vehicles (Cha et al., 2020) and distributed generation (DG) (Ma et al., 2019), and problems such as unreasonable power grid structure are more becoming prominent (Abu-Elzait and Parkin, 2019). With the continuous economic growth, the demand for power continues to grow rapidly. The fluctuation of the power supplied by DG and the irregular large-scale access of electric vehicles to the distribution network causes the power flow to fluctuate (Tang et al., 2019). The high penetration access of DG (Chang and Chinh, 2020) may lead to providing excessive power to some equipment in the distribution network and even cause maloperation of such equipment. Therefore, it is difficult to satisfy the power quality and power supply reliability requirements of users.

Multi-station integration based on the flexible interconnection of the distribution network can solve the above problems. Several novel flexible power electronic devices can be applied to improve the controllability and flexibility of the power system (Cong et al., 2019; Long et al., 2016; Ouyang et al., 2020). Compared with the traditional distribution network, which relies on the sectionalized switch and tie switch (TS), the novel multi-station distribution network uses soft partition achieved by connecting soft normally open point. During the normal operation of the system, the power of an

SOP can be regulated between different interconnected distribution areas to realize mutual power flow and promote the global optimization of the energy under the steady-state condition (Li et al., 2018; Bai et al., 2018). Compared to traditional TS, SOP can enhance the controllability and improve the power quality of the distribution network, and improve the reliability of the power supply system.

On the research progress of multi-station fusion, reference (Xu et al., 2019) analyzed the optimal design and operation of an energy storage station under multi-station integration and reported the optimal design capacity and optimal operation strategy of the storage station based on multi-station integration. Reference (Zhang et al., 2019) discussed the connotation and characteristics of multi-station integration and a business model for multi-station integration based on the operation mode and business system. They verified the feasibility of the proposed business model with project examples. Reference (Wang et al., 2020) built a three in one DC power supply system based on an energy storage station, data center, and substation and compared it with the traditional high-voltage direct current system. However, the above literature is limited to the simple combination of multiple stations. The complementarity and integration of multiple function stations are not strong, the function of each function station is not fully played, the reliability of the system can be further strengthened, and the theoretical analysis of multi-station fusion and the innovation of topology structure is insufficient. At present, there are not enough research results in the realization of high-power supply reliability, power flow transfer and multi-purpose of one station.

In this paper, we propose a topology of the multi-station integration structure with a single DC bus based on SOP. The load is supplied hierarchically according to the demand. The issues of unidirectional flow and complex device coordinated control in traditional energy distribution networks are overcome through the coordinated control of SOP devices and other converter devices in the system. The coordinated control allows the power flow control among feeders and the highly reliable provision of sensitive loads in the system and promotes the overall optimization of the distribution network energy. The major contributions of this paper are as follows:

(1) From the topology and framework perspectives of power grids, a highly integrated multi-station system fusion topology based on the SOP is created. This results in an in-depth application of the SOP in the multi-station fusion system, and thus diverse load supplies with high-level power quality are achieved.
(2) The "APS plus EMS" coordinated control strategy is proposed, and the autonomous operation of the local system can be divided into three working modes, and each mode can be further divided into different sub-modes depending on the state of the system. These efforts can improve the flexibility of the system operation and the reliability of power supply for sensitive loads.
(3) The effectiveness of the proposed multi-station system topology and control strategies is verified through two case studies.

The remainder of this paper is organized as follows. The topology of multi-station integration is proposed in *Proposed Topology of Multi-Station Integration*. The coordinated control strategy of multi-station integration is established in *Coordinated control strategy of multi-station integration*. Case studies are presented in *Simulation Analysis of Different Cases*. Conclusion is drawn in *Conclusion*.

PROPOSED TOPOLOGY OF MULTI-STATION INTEGRATION

Different from the traditional AC/DC distribution network, in this study we use SOP as the key equipment of multi-station integration systems, which can solve the problems of the AC/DC distribution network by implementing the two-end power supply. SOP can respond to the running state of the system in real-time and optimize the power flow distribution of the system and are promising to meet the requirements of future flexible distribution networks for primary flexible equipment (Ji et al., 2017; Liang et al., 2018; Li et al., 2019). **Figure 1** shows the proposed multi-station integration topology with an SOP. The system is mainly composed of an AC power grid unit, energy management system (EMS), SOP, energy storage station, data center station, photovoltaic power station, 5G station, AC/DC load with different sensitivity levels, and electric vehicle charging station.

The proposed multi-station integration system is significantly more compact than the traditional hybrid AC/DC microgrid. Complementary function integration can achieve hierarchical power supply and overall performance improvement. The integration of the energy flow, information flow, and data flow in the system can improve the comprehensive utilization rate of resources. Furthermore, the multi-station integration system can achieve multi-purpose of one station and multi-function of one device and provides positive interaction and mutual benefits to power/energy suppliers, equipment providers, and users. The construction of multi-station integration systems requires full consideration of various factors, including investment optimization, land comprehensive utilization rate, energy price, power supply reliability, power quality, consumption of green energy, and comprehensive energy service.

The multi-station integration in one distribution system has changed the traditional mode of the AC/DC hybrid distribution network. In this system, the steps of generation, network load, and storage of power are highly integrated; the energy flow, information flow, and data flow are integrated, providing higher power supply reliability. Different sensitive loads make it easier to perform the hierarchical power supply function and significantly increase the comprehensive efficiency of the power grid. The power flow distribution can be flexibly and dynamically adjusted depending on the load conditions, equipment status, and other information, to adapt the access of plug-and-play loads, such as distributed power supplies and electric vehicles, to the distribution network. This can more efficiently promote the integration of the energy supply, distribution, and service, and balance the benefits to users and providers.

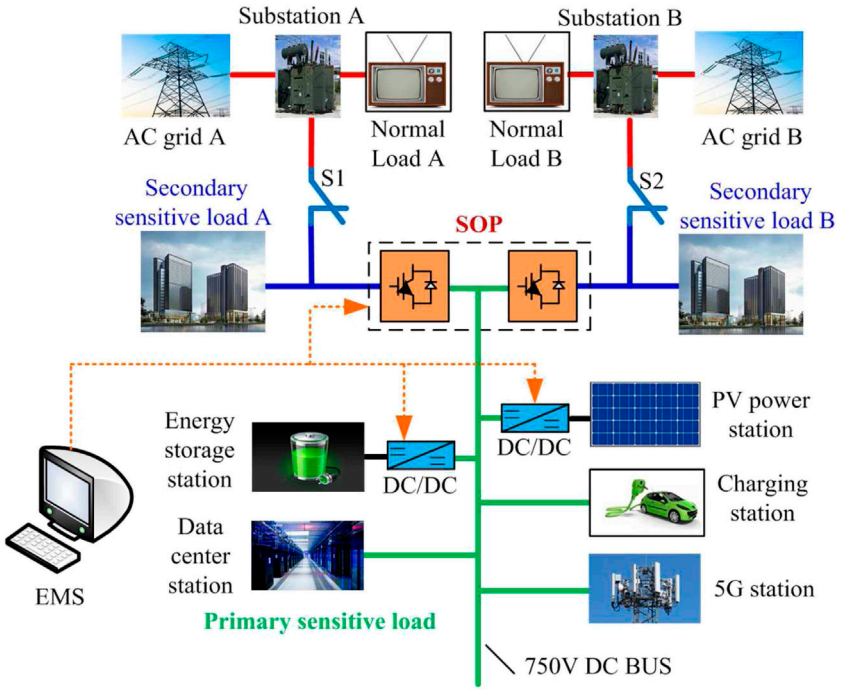

FIGURE 1 | Multi-station integration topology.

In the proposed topology, the SOP is used as an interconnection between two distribution feeders, and the distributed power supply, electric vehicle charging station, and 5G station are connected at the SOP DC terminal. To guarantee the uninterrupted power supply of important loads and realize the peak shaving and valley filling of the system in case of a fault, the DC terminal of the SOP is connected to the energy storage station. Moreover, different sensitive loads can be reasonably configured in the multi-station system, which enables the hierarchical power supply function and highly reliable power supply. The power supply quality of a single DC bus is the highest; here, the loads are defined as primary sensitive load, and the loads on the two sides of the SOP are defined as secondary sensitive load; the load at the substation is defined as the normal load. The optimal configuration of the hierarchical power supply can provide high quality power with low costs.

The proposed multi-station integration topology fully utilizes the DC bus of the SOP to facilitate access to distributed power, electric vehicles, and other equipment. However, the stability of this topology is affected when integrating multiple function stations. The control stability of the DC bus voltage is the basis for the stable operation of the multi-station integration system.

COORDINATED CONTROL STRATEGY OF MULTI-STATION INTEGRATION

The system control strategy is shown in **Figure 2**. The SOP described in this paper consists of back-to-back voltage source converters (VSCs). VSC1 and VSC2 of SOP can run in P_{-Q} mode, V_{-f} mode and V_{dc-Q} mode. The control objectives of the two VSCs of the SOP would be changed according to actual situations to realize the real-time control of voltage and power. One of the functions of the FMSS in the multi-station integration system is to transfer active power of the AC power grid and balance the load on both sides of the FMSS. When AC fault occurs, the energy is exchanged with the DC bus through the bidirectional DC/DC converter, and for the battery the three working modes switch according to the power balance in the system.

The photovoltaic DC/DC converter transfers the maximum power in the grid-connected mode. This can be achieved using the maximum power point tracking (MPPT) control technology or by switching to the idle mode to terminate the output power. For the MPPT control of the photovoltaic DC/DC converter, we use the conductance increment method to determine the change in the direction of voltage by comparing the instantaneous value of the current output conductance and the change in conductance. According to the power voltage curve of the photovoltaic cell, the extreme value is calculated.

Where P_{IN} and P_{IN_ref} are active power and its reference flowing into the SOP respectively, Q_2 and Q_{2_ref} are reactive power and the reference flowing from the SOP respectively, U_{dc} is the voltage value of DC bus, U_{dc_ref} is control command voltage of SOP DC bus or energy storage, I_{d1}, I_{q1}, I_{d2}, I_{q2},I_{d1_ref}, I_{q1_ref}, I_{d2_ref}, and I_{q2_ref} are axis components and reference values of AC currents of the VSC1 and VSC2, respectively, I_{dis_max} and I_{dis_min} are upper and lower limits of the battery discharge current respectively, I_{dis_ref} is reference value of the current loop, I_b is the charge and discharge current of the battery,

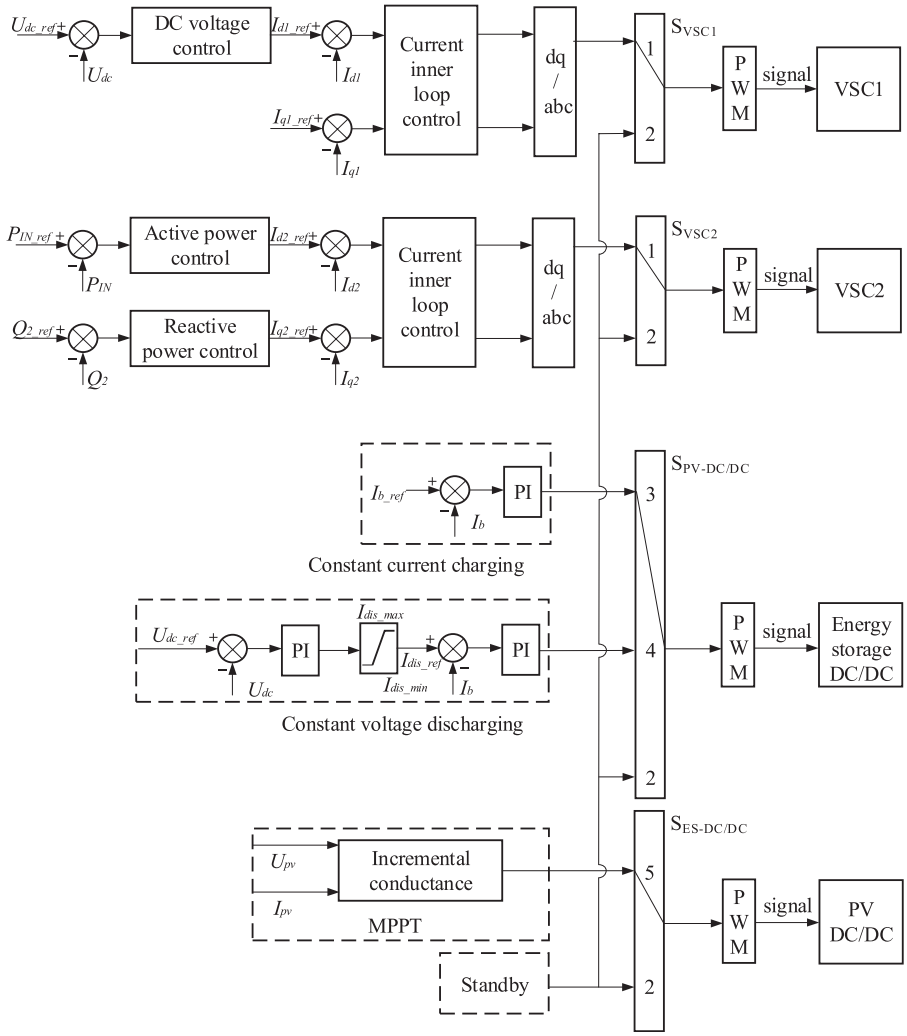

FIGURE 2 | The block diagram of system control strategy.

I_{b_ref} is reference value of charge and discharge current of the battery, I_{PV} is output current of the photovoltaic array, and U_{pv} is output voltage of the photovoltaic array.

The coordination between the stations essential for the stable operation and real-time power balance of the multi-station integration system. The stable operation of the SOP DC bus is affected by the various parts of the system, whose power status is closely related to the DC voltage. Accordingly, we adopt the "active power signal (APS) plus EMS" coordinated control strategy, as shown in **Figure 3**. This strategy allows the efficient power flow and stable control of the DC voltage and provides the maximum reliability of the power supply.

We denote the output power of the distributed power supply as P_{DG}; the power at the outlet side of the energy storage station as P_{ES}; the power consumed by the DC load as $P_{\mathrm{DC\_load}}$; the power exchanged between the SOP DC bus and the AC grids A and B as $P_{\mathrm{AB\_ex}}$, and the charging power of the DC bus of the energy storage station as $P_{\mathrm{DC\_bus}}$. The total power of the SOP DC can be expressed as

$$P_{\mathrm{DG}} = P_{\mathrm{DC\_bus}} + P_{\mathrm{DC\_load}} + P_{\mathrm{ES}} - P_{\mathrm{AB\_ex}}. \tag{1}$$

When the voltage of the SOP DC bus changes, the energy change of the DC bus capacitor ΔE_{dc} is

$$\begin{cases} \Delta E_{\mathrm{dc}} = \dfrac{C}{2}\left(U_{\mathrm{dc\_ref}}^2 - U_{\mathrm{dc}}^2\right), \\ \Delta E_{\mathrm{dc}} = T_0\left(P_{\mathrm{DG}} - P_{\mathrm{DC\_load}} - P_{\mathrm{AB\_ex}} - P_{\mathrm{ES}}\right), \end{cases} \tag{2}$$

where $U_{\mathrm{dc\_ref}}$ is the rated value of the DC bus, and T_0 is the system operation time.

From **Eq. 2**, U_{dc} can be obtained as follows:

$$U_{\mathrm{dc}}^2 = U_{\mathrm{dc\_ref}}^2 - \frac{2T_0}{C}\left(P_{\mathrm{DG}} - P_{\mathrm{DC\_load}} - P_{\mathrm{AB\_ex}} - P_{\mathrm{ES}}\right). \tag{3}$$

Equation 3 indicated that the DC bus voltage is affected by the power condition in the system. The stable DC bus voltage corresponds to the power balance of the system, so an unbalance in power flow leads to an abnormal bus voltage.

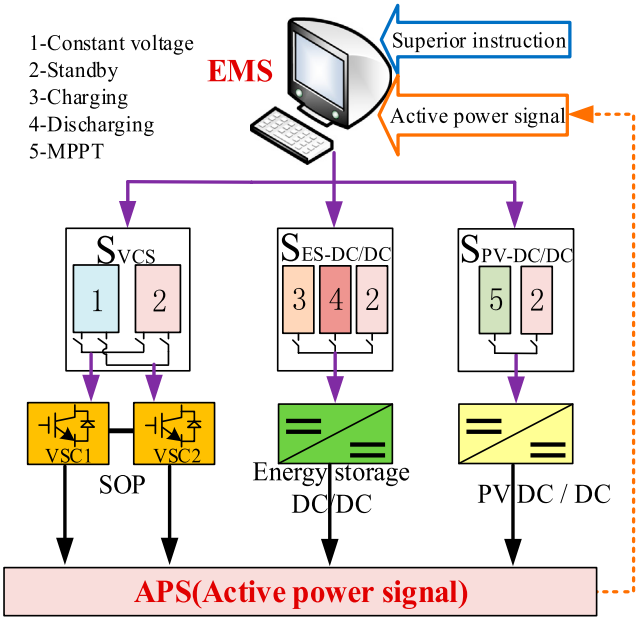

FIGURE 3 | Coordination control strategy of multi-station integration.

Therefore, the power balance of the system can be achieved by controlling the DC bus voltage balance, thereby ensuring reliable and stable operation of the multi-station integration system. Therefore, it is necessary to adopt an appropriate converter control strategy to manage the energy flow of the SOP. With a reasonable distribution of the SOP and distributed power output and the coordination of the energy storage device and the grid-connected converter control, the power balance in the system can be achieved.

The total power balance of the multi-station integration system can also be expressed as follows:

$$\begin{cases} \mathrm{SOC}_{\min} \le \mathrm{SOC} \le \mathrm{SOC}_{\max} \\ -P_{\max\_\mathrm{dischange}} \le P_{\mathrm{ES}} \le P_{\max\_\mathrm{change}}, \\ P_{\min\_pv} \le P_{pv} \le P_{\max\_pv}, \\ P_{\mathrm{IN}} \le P_{\max\_\mathrm{exchange}}, \\ P_{\mathrm{OUT}} \le P_{\max\_\mathrm{exchange}}. \end{cases} \tag{4}$$

where $\mathrm{SOC}_{\min}$ and $\mathrm{SOC}_{\max}$ are the lower and upper limits of the remaining capacity of the battery, respectively; $P_{\max\_\mathrm{dischange}}$ and $P_{\max\_\mathrm{change}}$ are the maximum discharging and charging power, respectively; $P_{\min\_pv}$ and $P_{\max\_pv}$ are the lower and upper limits of the output power of the photovoltaic power station, respectively; $P_{\min\_\mathrm{exchange}}$ is the maximum allowable switching power.

The following power relations exist in the AC and DC buses of the multi-station integration system:

$$\begin{cases} P_{\mathrm{AB\_ex}} = P_A + P_B - P_{\mathrm{AC\_load1}} - P_{\mathrm{AC\_load2}}, \\ P_{\mathrm{AC\_load1}} = P_A - P_{\mathrm{IN}}, \\ P_{\mathrm{AC\_load2}} = P_B + P_{\mathrm{OUT}}, \\ P_{\mathrm{AB\_ex}} = P_{\mathrm{IN}} - P_{\mathrm{OUT}}. \end{cases} \tag{5}$$

where P_{OUT} is the active powers flowing out of the SOP.

Equation 5 indicates that P_{IN} and P_{OUT} change when the system operation state changes. For example, if one side of the AC power grid is overloaded and the other side of the AC power grid is lightly loaded, power is transferred from the lightly side to the overloaded loaded side, increasing P_{IN}. When a fault occurs on one side of the AC power grid, the load in that side will be transferred through the SOP, increasing P_{IN} and P_{OUT}. In a multi-station integration system, any power change will change the active power through the SOP. Therefore, we combine the APS and EMS to judge the current working mode through the APS flowing in or out of the SOP. APSs are considered as dispatching signals of the EMS, and the operation mode of the power electronic devices in the control system are coordinated through the superior signals received by the EMS and the APS of the local system.

The coordination control strategy relies on the EMS as the general control layer, which is responsible for receiving the dispatching instructions of the upper-level grid and the APS of the local system. The EMS judges the system operation status according to the instructions of the upper-level or the APS and sends out the corresponding work mode instructions to coordinate the operation modes of the SOP, energy storage DC/DC converter, and photovoltaic DC/DC converter. The EMS operates according to the dispatching instruction received from the upper-level grid to realize the effective energy and active power flows and reactive compensation between the systems. When the EMS system does not receive the dispatching instruction from the upper-level grid, it operates the local system autonomously. In the autonomous operation mode, the EMS sends the corresponding control mode command through the APS received. In this study, the APS threshold interval is set according to the corresponding value of the active power in different operating conditions; then, the EMS judges the operation mode of the system according to the APS value.

With the above coordination control strategy, the autonomous operation of the local system can be divided into three working mode types, and each working mode type can be divided into different sub-modes depending on the state of the system. In this paper, $P_{\mathrm{IN\_ref}}$ denotes the reference value of the active power flowing into the SOP under the ideal operation of the system (i.e., the AC load on the two sides is equal; the DC load is constant, and the photovoltaic power station outputs the maximum power). The reference value P_{IN} is divided into different threshold intervals according to the three working modes. Among them, a_0 and b_0 are the reference coefficients ($a_0 \ge 1$ and $b_0 < 1$) determined according to the actual state of the system.

Operation mode 1: $b_0|P_{\mathrm{IN\_ref}}| < |P_{\mathrm{IN}}| < a_0|P_{\mathrm{IN\_ref}}|$. In this mode, the system is in the normal operation state. The SOP is in constant DC voltage mode, $S_{\mathrm{VSC1}} = 1$, and $S_{\mathrm{VSC2}} = 1$. The photovoltaic power station is in the MPPT mode, with $S_{\mathrm{PV\_DC/DC}} = 5$. Depending on the residual capacity of the SOC, the energy storage station can be in the constant voltage charging mode, with $S_{\mathrm{ES\_DC/DC}} = 3$, or the standby mode, with $S_{\mathrm{ES\_DC/DC}} = 2$.

Operating mode 2: $|P_{\mathrm{IN}}| > a_0|P_{\mathrm{IN\_ref}}|$. In this mode, when the AC loads on the two sides of the system are extremely unbalanced

TABLE 1 | System parameters.

Parameter	Unit	Value
AC voltage	V	380
Frequency	Hz	50
SOP DC voltage	V	750
Data center	kW	40
5G station	kW	10
PV station	kW	50
Secondary sensitive load A	kW	20
Secondary sensitive load B	kW	35

or one side of the AC grid is faulty, the system transfers a large amount of active power to the faulty side through the SOP to maintain the power supply of the load on the fault side. If necessary, the normal load is cut off, and the sensitive load is retained. The SOP is in constant DC voltage mode, with $S_{VSC1} = 1$ and $S_{VSC2} = 1$. The photovoltaic power station is in either MPPT mode, with $S_{PV\_DC/DC} = 5$, or standby mode, with $S_{PV\_DC/DC} = 2$. Depending on the residual capacity of the SOC, the energy storage power station works in constant voltage discharge mode, with $S_{ES\_DC/DC} = 4$, or standby mode, with $S_{ES\_DC/DC} = 2$.

Operating mode 3: $|P_{IN}| < b_0|P_{IN\_ref}|$. In this mode, both sides of the AC network are faulty, and the SOP works in the standby mode, with $S_{VSC1} = 2$ and $S_{VSC2} = 2$. If the power from the energy storage station and the photovoltaic station is enough to support the primary sensitive load power supply, the SOP can selectively transfer power depending on the load level, i.e., $S_{VSC1} = 1$ or $S_{VSC2} = 1$. The photovoltaic station works in either MPPT mode, with $S_{PV\_DC/DC} = 5$, or standby mode, with $S_{PV\_DC/DC} = 2$. According to the residual capacity of the SOC, the energy storage station works in either constant voltage discharge mode, with $S_{ES\_DC/DC} = 4$, or standby mode, with $S_{ES\_DC/DC} = 2$.

SIMULATION ANALYSIS OF DIFFERENT CASES

We designed a simulation model of the multi-station integration system in MATLAB/Simulink to analyze the operation in the different modes. We assumed that the data center contains ten cabinets, with a total power of 40 kW. The maximum output power of photovoltaic station was set to 50 kW; the power of the two 5G stations was set to 10 kW, and different AC and DC loads were considered. Two different operating modes were simulated. The rationality of the above-mentioned multi-station integration topology structure and the correctness of its control strategy were verified. The relevant parameters of the simulation model are shown in **Table 1**.

Case 1

The simulation of case 1 verifies operating mode 1. To simplify the analysis, the photovoltaic and data center stations balance the power generation and energy supply and demand. Initially, the energy storage station is fully charged and operates in the standby mode; the photovoltaic station operates in the MPPT mode, and all the output power is supplied to the data center and 5G station. In AC grid A, the secondary sensitive load A is set to 20 kW, and the normal load A is set to 30 kW. In AC grid B, the secondary sensitive load B is set to 35 kW, and the normal load B is set to 55 kW. At 0.5 s, the SOP starts the power flow control.

As shown in **Figure 4**, before the power flow control of the SOP starts, the power from the AC power grid on the two sides is unbalanced. AC power grids A and B send 50 and 90 kW of active power, respectively. Half a second after the power flow control is started, the active power from the AC power grid on the two sides reaches the balance state after the short-term power flow regulation, reducing the line loss of the distribution network system and the transformer pressure of the feeder upstream.

The results show that in operation mode 1, the system has good dynamic response capability when the DC load changes suddenly, which can ensure the stability of the DC voltage and the transfer capability of the system power flow. After 0.4 s, a 50 kW DC load is added, and after 0.7 s, a 30 kW DC load is cut off. The simulation results are shown in **Figure 5**.

As shown in **Figure 5A**, after a sudden increase of 50 kW in the DC load at 0.4 s, the active power flowing into VSC1 from AC grid A increases from 20 to 45 kW. After the 30 kW DC load is cut off at 0.7 s, the power flowing into VSC1 decreases by 15 kW. After a 0.02 s adjustment time, the system reaches a stable

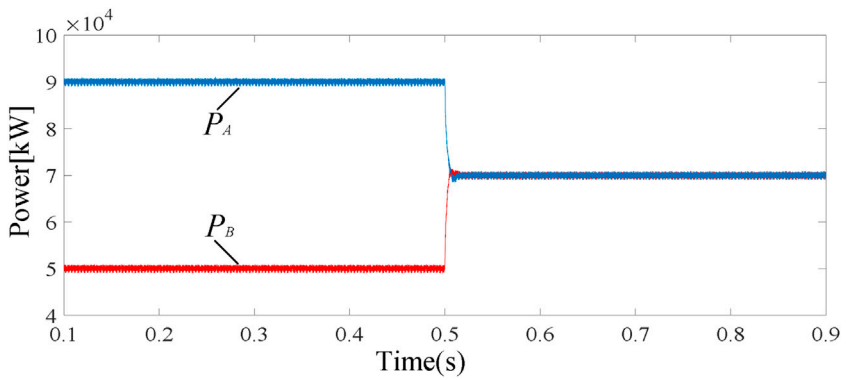

FIGURE 4 | Active power of AC grids A and B.

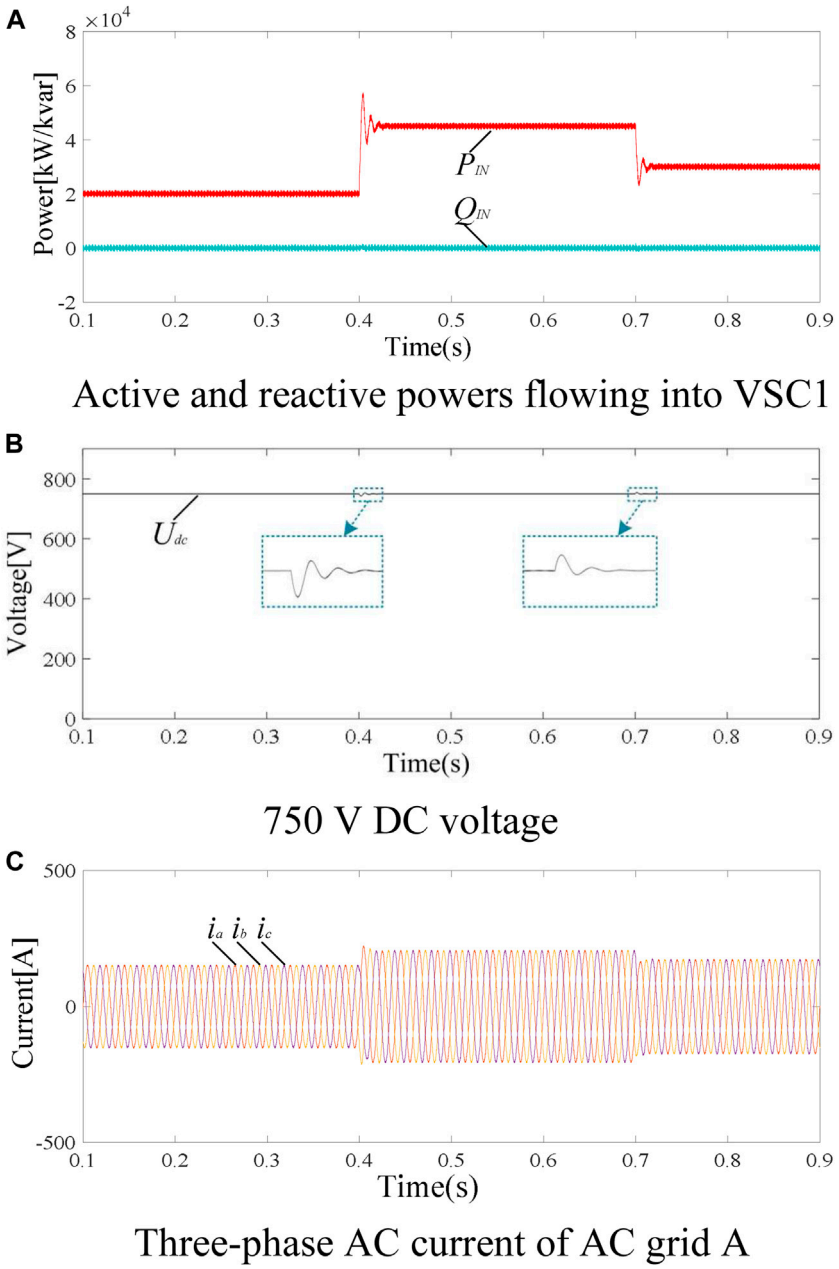

FIGURE 5 | DC load fluctuation simulation results **(A)** Active and reactive powers flowing into VSC1 **(B)** 750 V DC voltage **(C)** Three-phase AC current of AC grid A.

operation state. It can be seen from **Figure 5B** that the DC voltage of the SOP remains stable under the sudden changes in the load. In the dynamic response stage, the voltage fluctuation of the DC bus is within ±5 V, which ensures stable power transmission in the system. **Figure 5C** shows the current waveform of AC grid A.

It can be seen from the simulation results that the dynamic response of the system is perfect when the load changes suddenly, and it can track APS instructions accurately and quickly, so that the system operates in a stable state. Simulation results verify the effectiveness of the proposed topology and control strategy in mode 1.

Case 2

Case 2 verifies the sensitive load power supply capacity and the stability of the DC bus when one of the AC systems fails. In this case, the system switches from operation mode 1 to operation mode 2. To reflect the situation after the fault of AC grid B more intuitively, initially, the energy storage station is fully charged and operates in the standby mode. The photovoltaic station is in the MPPT mode, and all the output power is supplied to the data center and 5G station. The DC bus load is set as a 20 kW primary sensitive load. Loads of AC grid A are set as a 20 kW secondary sensitive load and a 30-kW normal load A. Loads of

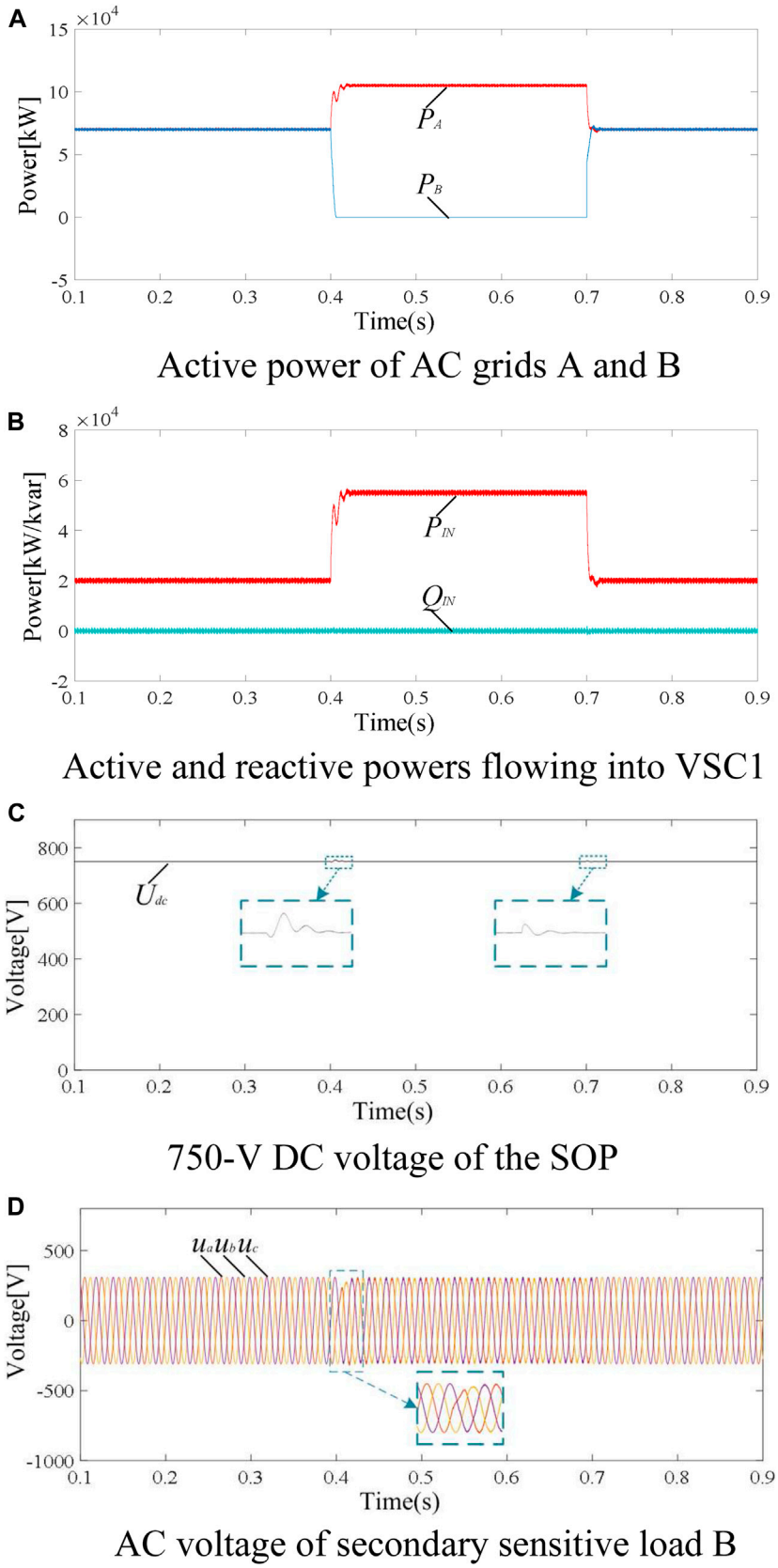

FIGURE 6 | AC grid fault simulation results **(A)** Active power of AC grids A and B **(B)** Active and reactive powers flowing into VSC1 **(C)** 750 V DC voltage of the SOP **(D)** AC voltage of secondary sensitive load B.

AC grid B are set as a 35 kW secondary sensitive load and 35 kW normal load. At 0.4 s, AC grid B fails, and the 35 kW normal load B is cut off. The secondary sensitive load B is maintained, and the fault is recovered at 0.7 s. The simulation results are shown in **Figure 6**.

As shown in **Figure 6A**, after the system fails at 0.4 s, the system supplies sensitive load power at the fault side through the SOP. As can be seen from **Figure 6B**, the power flowing into VSC1 increases from 20 to 55 kW in 0.4 s, which exceeds the preset upper limit. The EMS center judges the operation mode through the received APS and sends out the instruction of operation mode 2. The system cuts off the normal load B on the fault side, and the SOP carries out the power flow supply. When the system returns to the normal state in 0.7 s, it quickly stabilizes. **Figure 6C** shows that the DC voltage can remain stable when the AC system fails. In the dynamic response stage, the voltage fluctuation of the DC bus is within ±1%, ensuring the stable power transmission of the system. **Figure 6D** shows the voltage waveform of the secondary sensitive load B. When the fault occurs, the voltage fluctuates within a small range and quickly stabilizes after 0.02 ms.

It can be seen from the simulation results that when the system fails, because the SOP is used as the key equipment of the system, the system can still realize power flow transfer in case of failure, and maintains high reliability of power supply for sensitive loads. It can also perform good dynamic response characteristics of the system. The simulation results confirm that the multi-station integration topology and its control strategy described in this paper can effectively guarantee the stable operation of the system. The multi-station integration system has a highly reliable power supply capability for sensitive loads, such as those in data center stations.

Delaware Industrial Park in the United States has built as the first high-quality power park in the world, and has installed DVR, ASVC, transfer switch and other Distribution-Flexible AC Transmission Systems (D-FACTS) devices to realize the three-level power quality supply (Domijian et al., 2005). In this paper, only one SOP is used to realize the three-level power supply, and the comparison results show that the power quality level performed in this paper is better. In this paper, the response time is faster and the voltage fluctuation is smaller.

CONCLUSION

We proposed a topology structure of the multi-station integration system and simulated various scenarios that verified the feasibility of the coordinated control strategy. According to the multi-station integration topology, the "APS plus EMS" coordinated control strategy was proposed to achieve the stable operation of the system. We verified the rationality of the topological structure of the multi-station integration system. The topological structure fully guarantees the requirements of power supply reliability and system operation stability at different sensitive loads and can achieve effects of power flow in the system and power flow transfer under in the fault operation state.

In the future, we will investigate the capacity allocation of multi-station integration based on economic optimization. The construction of multi-station integration is of great importance to improve the operation and control ability of the distribution network. The results of this study are expected to promote the practical application of multi-station integration in the distribution network and accelerate the promotion and application of multi-station integration in the future intelligent distribution network.

DATA AVAILABILITY STATEMENT

The original contributions presented in the study are included in the article/Supplementary material, further inquiries can be directed to the corresponding author.

AUTHOR CONTRIBUTIONS

QH: Conceptualization, methodology, writing-original draft. WW: software, methodology; YY: methodology. MM: methodology. JY: validation. TW: Supervision.

FUNDING

This work is supported by the Strategic Priority Research Program of Chinese Academy of Sciences, Grant No. XDA 21050304 and Youth Innovation Promotion Association CAS (2017180).

REFERENCES

Abu-elzait, S., and Parkin, R. (2019). Economic and environmental advantages of renewable-based microgrids over conventional microgrids. 2019 IEEE green technologies conference (GreenTech), Lafayette, LA, United States, 3–6 April 2019. doi:10.1109/GreenTech.2019.8767146

Bai, L., Jiang, T., Li, F., Chen, H., and Li, X. (2018). Distributed energy storage planning in soft open point based active distribution networks incorporating network reconfiguration and DG reactive power capability. *Appl. Energ.* 210, 1082–1091. doi:10.1016/j.apenergy.2017.07.004

Cha, K.-S., Kim, D.-M., Jung, Y.-H., and Lim, M.-S. (2020). Wound field synchronous motor with hybrid circuit for neighborhood electric vehicle traction improving fuel economy. *Appl. Energ.* 263, 114618. doi:10.1016/j.apenergy.2020.114618

Chang, G. W., and Cong Chinh, N. (2020). Coyote optimization algorithm-based approach for strategic planning of photovoltaic distributed generation. *IEEE Access* 8, 36180–36190. doi:10.1109/access.2020.2975107

Cong, P., Tang, W., Lou, C., Zhang, B., and Zhang, X. (2019). Multi-stage coordination optimisation control in hybrid AC/DC distribution network with high-penetration renewables based on SOP and VSC. *J. Eng.* 2019, 2725–2731. doi:10.1049/joe.2018.8527

Domijian, A., Montenegro, A., Keri, A. J. F., and Mattern, K. E. (2005). Simulation study of the world's first distributed premium power quality park. *IEEE Trans. Power Deliv.* 20 (2), 1483–1492. doi:10.1109/TPWRD.2004.839182

Giampieri, A., Ling-Chin, J., Ma, Z., Smallbone, A., and Roskilly, A. P. (2020). A review of the current automotive manufacturing practice from an energy perspective. *Appl. Energ.* 261, 114074. doi:10.1016/j.apenergy.2019.114074

Ji, H., Wang, C., Li, P., Zhao, J., Song, G., Ding, F., et al. (2017). An enhanced SOCP-based method for feeder load balancing using the multi-terminal soft open point in active distribution networks. *Appl. Energ.* 208, 986–995. doi:10.1016/j.apenergy.2017.09.051

Li, Y., Pei, X., Kang, Y., Lu, Y., Xu, F., and Wang., C. (2019). Voltage support strategy of SOP under fault circumstance. 2019 IEEE applied power electronics conference and exposition (APEC), Anaheim, CA, United States, 17–21 March 2019. doi:10.1109/APEC.2019.8722092

Li, Y., Pei, X., Chen, Z., Yang, M., Lyu, Z., and Wang, C. (2018). The steady-state and fault ride-through control strategies of soft normally open point in distribution Network. IEEE energy conversion congress and exposition (ECCE), Portland, OR, United States, 23-27 September 2018. doi:10.1109/ECCE.2018.8557615

Liang, H., Zhang, K., Li, S., Ge, L., Wang, Q., and Han, T. (2018). Allowable DG penetration capacity calculation of SOP-based flexible distribution network. 2018 China international conference on electricity distribution (CICED), Tianjin, China, 17-19 September 2018. doi:10.1109/CICED.2018.8592392

Long, C., Wu, J., Thomas, L., and Jenkins, N. (2016). Optimal operation of soft open points in medium voltage electrical distribution networks with distributed generation. *Appl. Energ.* 184, 427–437. doi:10.1016/j.apenergy.2016.10.031

Ma, C., Dasenbrock, J., Többermann, J.-C., and Braun, M. (2019). A novel indicator for evaluation of the impact of distributed generations on the energy losses of low voltage distribution grids. *Appl. Energ.* 242, 674–683. doi:10.1016/j.apenergy.2019.03.090

Ouyang, S., Liu, J., Yang, Y., Chen, X., Song, S., and Wu, H. (2020). DC voltage control strategy of three-terminal medium-voltage power electronic transformer-based soft normally open points. *IEEE Trans. Ind. Electron.* 67 (5), 3684–3695. doi:10.1109/tie.2019.2922915

Tang, C., Liu, M., Dai, Y., Wang, Z., and Xie, M. (2019). Decentralized saddle-point dynamics solution for optimal power flow of distribution systems with multi-microgrids. *Appl. Energ.* 252, 113361. doi:10.1016/j.apenergy.2019.113361

Wang, B., Chen, Y., Liu, Y., Wang, H., Xu, L., Li, G., et al. (2020). Research on DC power supply system based on multi-station fusion. *Digital Commun. World* 2020 (2), 75–76. doi:10.3969/J.ISSN.1672-7274.2020.02.046

Xu, W., Cheng, H., Bai, Z., Miao, C., and Sun, F. (2019). Optimal design and operation of energy storage power station under multi-station fusion mode. *Distribution and utilization* 36 (11), 84–91. doi:10.19421/j.cnki.1006-6357.2019.11.12

Zhang, Y., Wang, B., Li, R., and Mi, X. (2019). Research on business mode and development path of multi-station integration. *Distribution and utilization* 36 (6), 62–66. doi:10.19421/j.cnki.1006-6357.2019.06.011

Conflict of Interest: MM was employed by the company Electric Power Research Institute of Guangdong Power Grid.

The remaining authors declare that the research was conducted in the absence of any commercial or financial relationships that could be construed as a potential conflict of interest.

frontiers in Energy Research

METHODS
published: 23 March 2021
doi: 10.3389/fenrg.2021.634551

Evaluation Method of Wind Power Consumption Capacity Based on Multi-Fractal Theory

Hongzhong Li[1], Yao Wang[1], Xinyu Zhang[2] and Guo Fu[1]*

[1]School of Electrical Engineering, Shanghai University of Electric Power, Shanghai, China, [2]East China Electric Power Design Institute Co., Ltd., China Power Engineering Consulting Corporation, Shanghai, China

An analysis model of wind power consumption capacity is established with the multi-fractal theory. Firstly, the fluctuation characteristics of wind power are described through multi-fractal parameters, and the correlation between wind power fluctuation characteristics and consumption capacity are analyzed. Afterwards, the swinging door algorithm (SDA) is applied to divide the wind power curve in the evaluation period, and the fluctuation process with similar characteristics is clustered. Further, a functional analysis model to evaluate wind power consumption capacity is mentioned based on the fluctuation clustering results. Finally, the effectiveness of the method is verified by an example of a regional power grid in China, and the influence of adjustable parameters in the model on the consumption capacity is quantitatively analyzed.

Keywords: multi-fractal theory, division of fluctuation process, fluctuation clustering, functional analysis model, wind power consumption

OPEN ACCESS

Edited by:
Peng Li,
Tianjin University, China

Reviewed by:
Yue Zhou,
Cardiff University, United Kingdom
Yanbo Chen,
North China Electric Power University, China

****Correspondence:***
Yao Wang
hushnowy@163.com

Specialty section:
This article was submitted to Smart Grids, a section of the journal Frontiers in Energy Research

Received: *28 November 2020*
Accepted: *01 February 2021*
Published: *23 March 2021*

Citation:
Li H, Wang Y, Zhang X and Fu G (2021) Evaluation Method of Wind Power Consumption Capacity Based on Multi-Fractal Theory. Front. Energy Res. 9:634551. doi: 10.3389/fenrg.2021.634551

INTRODUCTION

With the increase of power demands, the proportion of renewable energy in power grid is increasing, especially the wind power (Qazi et al., 2019). The installed capacity of wind power has reached 210 GW, accounting for 10.4% of the total in China by the end of 2019. The installed capacity is expected to reach 250 GW by the end of 2020, and the proportion of wind power in the energy supply system will increase year by year (Global Energy Interconnection Development and Cooperation Organization, 2020). However, the volatility and randomness of wind power bring severe challenges to the dispatching and operation of power system.

In recent years, the problem of "wind power curtailment" is becoming more and more serious, which has caused a waste of power generation resources and brought some economic losses. To ensure the safety and economy of power system, the reasonable wind power uncertainty model and unit commitment optimization method are established (Chen et al., 2019; Zhang et al., 2019a; Zhang et al., 2019b; Chen et al., 2020). In (Zhang et al., 2019a), the optimal unit commitment decision was obtained by considering the temporal and spatial correlation of wind load uncertainty prediction error. In (Zhang et al., 2019b), the time autocorrelation of wind power/load forecasting error and outage probability are considered in the unit commitment optimization method. These models not only reduce the operation cost of the optimization results, but also ensure the safe operation of the power system.

On the other hand, aiming at the problem of wind power curtailment, some literature focuses on how to improve the consumption capacity of wind power. In (Meena et al., 2017), a new bi-level optimization framework is proposed aim at the optimal configuration and operation management of wind power generation. To enhance the adaptability and load acceptance of wind power, Wu et al.

(Wu and Jiang., 2019) considered the joint planning, which includes installed capacity and location of wind power, expansion of transmission network, and location and scale of energy storage system. With the increase of coupling among multi-energy systems, some scholars also try to increase the wind power consumption capacity from the perspective of integrated energy (Wang and Li., 2017; Mu et al., 2019; Ma et al., 2020). There are different methods to improve the consumption capacity. However, how to evaluate the wind power quickly and accurately is the precondition for achieving reasonable dispatching decision and planning. Only on the basis of accurate assessment of the consumption capacity, can those methods be more meaningful.

So far, most of the studies use mathematical optimization models to evaluate the wind power consumption capacity (Chen et al., 2017; Koutroumpezis and Safigianni., 2010; Xie, et al., 2016; Wang, et al., 2018; Wang et al., 2020). Usually, many kinds of security operation constraints (Abad et al., 2018; Fu et al., 2018; Torquato et al., 2018; Zhan and Liu., 2019) are considered and different optimization algorithms are used to obtain the optimal solution of the objective function. In (Nguyen and Mitra, 2016), the influence of wind power generation on frequency regulation ability under different penetration levels is explored. In (Sun et al., 2018), a multi-objective optimization method for power system coordination is established, which can be applied to evaluate the wind power consumption capacity. In (Xie et al., 2016), a wind power consumption optimization model with security constraints and flexible demand response is established. Xu et al. (Xu et al., 2016) calculated the wind power consumption capacity based on the multi-scenario method in which a variety of constraints were considered. In (Fu et al., 2018), the system peak shaving capacity constraints were considered, and the optimization model is established based on the statistical characteristics of wind power output. The mathematical optimization method is complex in modeling, with a large amount of calculation and limited application. In addition, most of the evaluation models in the above studies are for a certain moment, only considering the power grid's consumption capacity at the extreme moment, but the wind power output also has strong volatility in other times. Therefore, the fluctuation characteristics of wind power in the whole period should be considered in the evaluation model.

On the basis of these studies, it is necessary to analyze the fluctuation characteristics of wind power from a long time scale, so as to improve the accuracy and adaptability of the assessment. Yang et al. (Yang et al., 2017) proposed an analysis method to divide and express the fluctuation process of wind power, but did not carry out quantitative analysis on the volatility of wind power. For the study of volatility, in (Shi et al., 2018), the fluctuation of wind power output data are analyzed by the probability density function (PDF) and discrete Fourier transform (DFT) in time and frequency domain. In (Zhang et al., 2017), fluctuating characters of the wind power are assumed to obey the versatile distribution. In (Lamsal et al., 2019; Li et al., 2019), the variation of the difference between the maximum and minimum power values within a certain time interval is used to describe the volatility of wind power.

Since the fluctuation of wind power varies with time, the fluctuation characteristics of wind power at different levels should be described by appropriate parameters. Multi-fractal theory (Harte and David, 2001) is an effective tool for studying the fluctuation characteristics of stochastic time series, and has been applied in many fields of power system. In (Teng et al., 2019), a multi-fractal spectrum is adopted to investigate wind speed characterizations. Liu et al. (Liu et al., 2014) examined the feasibility of applying the multi-fractal theory to analyse the electricity price fluctuation.

Thus, an evaluation method of wind power consumption capacity based on fluctuation characteristics analysis is carried out. Firstly, the singularity index of multi-fractal theory is adopted to describe the fluctuation characteristics of wind power. The matching degree between wind power and load curve is represented by the average Euclidean distance. The correlation between fluctuation parameters, average Euclidean distance and wind power consumption is verified based on historical data. On this basis, the fluctuation process is divided and clustered by the swinging door algorithm (SDA) and clustering algorithm, respectively. Finally, an evaluation model is established based on the fluctuation parameters. The method combines the fluctuation processes with the same fluctuation characteristics, greatly simplifies the calculation process. The consumption capacity of the power grid to a given wind power curve is analyzed, which is helpful for dispatchers to make reasonable decisions.

KEY INFLUENCING FACTORS

Fluctuation Degree of Wind Power Output

Multi-Fractal Theory

Multi-fractal is a kind of complex fractal structure which divides the non-uniform distribution area into multiple regions. It is composed of multiple non-uniform distribution sets with different singular indexes. The local characteristics of a system with complex fractals under different scales were described. Each scale can be represented by different parameters or dimensions. This series of parameters form a set, so that all different sets have different scales and fractal dimensions. Generally, the problems with fractal characteristics are described qualitatively and quantitatively by multi-fractal spectrum. The numerical value of each local detail and the probability distribution in the process of local detail change are calculated by Legendre transform.

The multi-fractal object is divided into N regions. x_i and P_i be the scale size of each region and the probability of physical quantity respectively. The relationship between x_i and P_i in different regions is expressed by scale index α_i:

$$\mathrm{P}_i = \mathrm{x}_i^{\alpha_i} \ (\mathrm{i} = 1, 2, 3, \ldots N), \tag{1}$$

When $x_i \to 0$, **Eq. 1** is changed into

$$\alpha = \lim_{x \to 0} \frac{\ln P}{\ln x}, \tag{2}$$

where α is the scaling index, which represents the fractal dimension of the local shape.

Fluctuation Degree

Based on multi-fractal theory, the local regularity of wind power output curve on different time scales is described by the singularity index. Wind power series $\{P_i\}$ with time length T, $i = 1, 2, 3, \ldots, T$, s is the time scale used to divide the series.

$$p_j(s) = \frac{I_j(s)}{\sum I_j(s)}. \tag{3}$$

Here, $p_j(s)$ is the probability of wind power output in the j^{th} interval. $I_j(s)$ is the wind power output of the j^{th} interval. $\sum I_j(s)$ is the sum of wind power output of all sections.

The singularity of wind power fluctuation in the j^{th} interval is characterized by local singularity index α_j, which reflects the irregularity of wind power in this interval. It satisfies the following conditions in the scale-free interval.

$$p_j(s) \propto s^{\alpha_j} \tag{4}$$

Since s is smaller than 1 in multi-fractal calculation, α_{min} and α_{max} correspond to the maximum and minimum probability subsets respectively. The difference between the two probability is used to describe the fluctuation and stability of the sequence distribution. Variation of wind power output in a certain section can be expressed by $\Delta\alpha$. The larger the $\Delta\alpha$, the more uneven the wind power output distribution and the greater the volatility.

$$\Delta\alpha = \alpha_{max} - \alpha_{min} \sim \frac{\ln p_{min}}{\ln s} - \frac{\ln p_{max}}{\ln s} = \frac{\ln(p_{max}/p_{min})}{\ln(1/s)}. \tag{5}$$

Matching Degree of Wind Power Output and Load Demand

The consumption capacity is closely related to the fluctuation of the wind power curve if the unit parameters have been determined. Wind power will be curtailed if the fluctuation range of wind power exceeds the regulation capacity of the unit. However, wind power may fluctuate greatly at both high and low output, a single fluctuation parameter can not accurately reflect the wind power consumption capacity. The matching degree of wind power output and load demand is also a key factor, which is measured by the similarity between load and wind power curve. The higher the similarity, the greater the wind power consumption. To compare the wave processes of different time scales, the average value of Euclidean distance of all data points is reflected to the matching degree. The calculation formula is as follows:

$$D_{av} = \frac{\sqrt{\sum_{i=1}^{N}(P_{W,i} - P_{L,i})^2}}{N}. \tag{6}$$

Here, N is the number of sampling points in the fluctuation duration. $P_{W,i}$, $P_{L,i}$ are the wind power and load power in the i^{th} point.

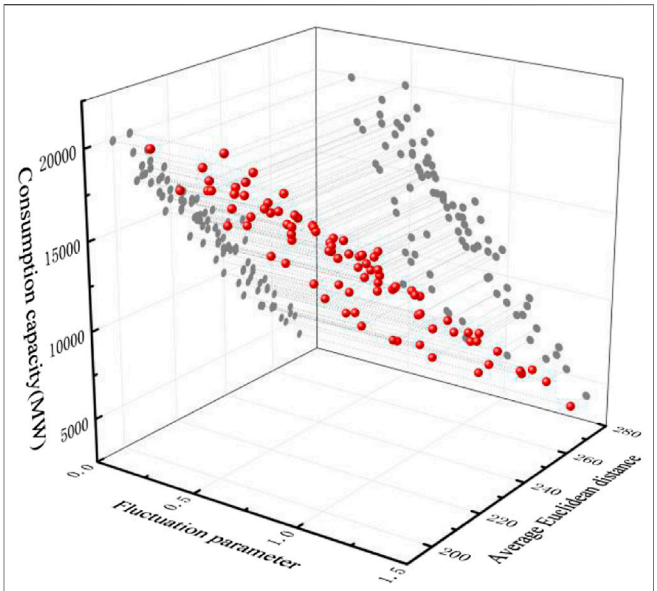

FIGURE 1 | Correlation between volatility parameters, average Euclidean distance and wind power consumption.

ANALYSIS ON FLUCTUATION CHARACTERISTICS OF WIND POWER CONSUMPTION

Correlation Analysis

Taking the data of a district in China in August 2019 as an example, the correlation between wind power consumption capacity and fluctuation characteristics is qualitatively analyzed by Pearson correlation coefficient (PCC). PCC is the most commonly used method to measure the correlation of series, and has many application examples in wind power output prediction (Vallée et al., 2011; Zhou et al., 2019; Wang and Zou, 2020). The correlation between any two variable sequences x and y can be calculated by **Eq. 7**.

$$r(x,y) = \frac{\mathrm{cov}(x,y)}{\sigma_x \sigma_y} = \frac{E(xy) - E(x)E(y)}{\sqrt{E(x^2) - E^2(x)}\sqrt{E(y^2) - E^2(y)}}, \tag{7}$$

where $r(x,y)$ is the correlation coefficient of x and y; $\mathrm{cov}(,)$ is the covariance operation; $E(\cdot)$ is the expected operation; σ_x and σ_y are the standard deviations of variables.

Figure 1 shows the calculation results of correlation analysis. With correlation coefficient $r_1 = -0.7977$, which shows that fluctuation parameters have strong negative correlation with wind power consumption, that is, the greater the parameter value, the smaller the wind power consumption. With correlation coefficient $r_2 = -0.8477$, similarly, there is a strong negative correlation between European distance and consumption.

Division of Fluctuation Process

The division of fluctuation process is the basis of studying the fluctuation characteristics of wind power output. The swinging

door algorithm (SDA) proposed in (Florita et al., 2013) is applied to divide the fluctuation process. The principle is as follows:

$$\begin{cases} D_u = \max\left(\dfrac{P(t) - P_0 - \varepsilon}{t}\right) \\ D_d = \min\left(\dfrac{P(t) - P_0 + \varepsilon}{t}\right) \end{cases} \quad t = 1, 2, 3, \ldots, T. \tag{8}$$

Here, D_u and D_d are the up and down swinging door respectively. ε is the window width. P_0 is the wind power at the initial time. $P(t)$ is the wind power at t time. The up and down swinging door are calculated from $t = 0$, and t_m satisfying **Eq. 9** is the end time of current fluctuation.

$$\begin{cases} t_m = \min t, \\ s.t.\ D_u \geq D_d. \end{cases} \tag{9}$$

According to the principle of swinging door algorithm, the next fluctuation process starts from t_m, the division is continued until the wind power data in the whole cycle is traversed. There may be an inflection point in a continuous and same trend fluctuation process, which will lead to the neglect of a data point and errors. Therefore, the traditional swinging door algorithm is improved.

The fluctuation trend before and after the termination point should be judged in the iterative process. That is, when each iteration process of fluctuation division is completed, it is necessary to judge the relationship between the change trend of the two fluctuation processes connected with the termination point. The termination condition of iteration division is changed from **Eqs. 9**, **10**:

$$\begin{cases} t_m = \min t, \\ s.t.\ D_u \geq D_d, \\ [P_W(t_m + 1) - P_W(t_m)] \cdot [P_W(t_m) - P_W(t_m - 1)] \geq 0, \end{cases} \tag{10}$$

where $P_W(t_m)$, $P_W(t_{m+1})$, $P_W(t_{m-1})$ are the wind power at time t_m, the next sampling time and the last sampling time respectively.

In **Eq. 8**, the window width ε affects the identification of continuous and identical trend fluctuations. Most of the division results will be small fluctuations if the selection is too small. Instead, the results will be large fluctuations and small ones ignored.

Clustering of Fluctuation Processes

The consumption capacity is significantly associated with volatility parameters and average Euclidean distance. The fluctuation process of wind power is clustered based on $\Delta\alpha$ and D_{av}. Essentially, the same fluctuation process should have similar consumption capacity in the clustering results.

A clustering algorithm with breadth first search neighbors (BF-SN) (Xue et al., 2015) is applied to cluster the fluctuation process. It is not needed to determine the number of clusters in advance in the algorithm, and the optimal parameters are easy to set. The steps are as follows:

(1) Input fluctuation process set, and $\Delta\alpha$ is the abscissa of each fluctuation process and D_{av} is the ordinate;
(2) Input the clustering parameters r and λ. Where r is the distance parameter to judge whether the two fluctuation processes are neighbors. Generally, the average distance between objects in the dissimilarity matrix can be taken as (Florita et al., 2013). λ is the parameter to judge whether the fluctuation process can be clustered into one class. $\lambda \in [0, 1]$, that is, if the fluctuation is joined to a certain class, X must be neighbors with the original fluctuation process of $\lambda\%$ in this class;
(3) Solve the similarity matrix. The similarity degree matrix is a quantitative representation of the similarity of any two fluctuation processes. Its diagonal elements are 1, and the non diagonal elements $d(X_i, X_j)$ represent the similarity between the fluctuation processes X_i and X_j;
(4) Search clustering. A new empty class is created and classified into this class from any fluctuation process X. All neighbors of X are searched according to the parameter r and whether they are classified into the class according to the parameter λ. When all the volatility processes except X are traversed, the clustering is completed once;
(5) Repeat step 4)to complete the clustering of all fluctuation processes.

EVALUTION MODEL

Wind Power Output Model

According to **Eqs. 3**, **4**, there is a one-to-one correspondence between wind power output $P_{W,i}$ and volatility parameters $\Delta\alpha_i$ in the i^{th} fluctuation process.

$$P_{Wi} = F(\Delta\alpha_i). \tag{11}$$

The functional relationship reflects the irregularity and distribution characteristics of wind power in the process of fluctuation.

Functional Analysis Model

State Space

The state of the system is judged according to the basic properties of the i^{th} fluctuation stage. Y represents the state set of the system in the whole evaluation period.

$$\{Y = y_1, y_2, \ldots, y_k | y_1, y_2, \ldots, y_k \in (0, 1)\}, \tag{12}$$

where y_k indicates whether the system satisfy the k^{th} constraint. If the system does not satisfy the constraint, $y_k = 0$, otherwise, $y_k = 1$.

The constraints are considered in the state space as follows:

Power Balance Constraints

$$P_{L,i} = P_{G,i} + P_{W,i} + P_{\text{line},i}. \tag{13}$$

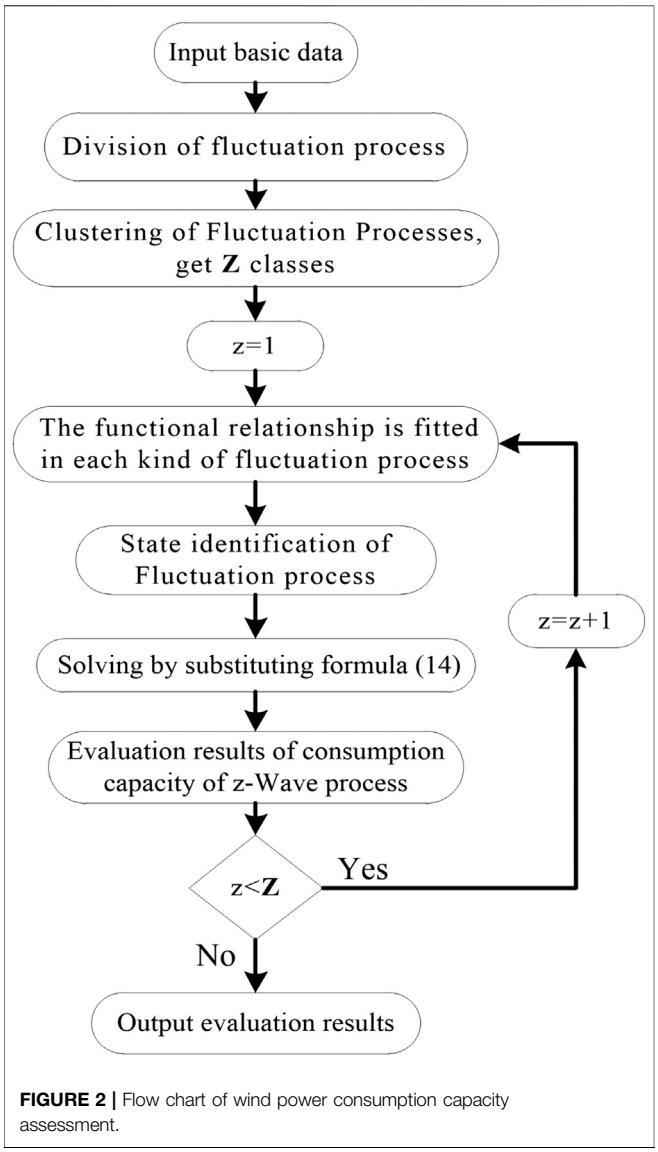

FIGURE 2 | Flow chart of wind power consumption capacity assessment.

Power Output Constraints

$$P_{G,\min} \le P_{G,i} \le P_{G,\max}. \tag{14}$$

Power Ramp Constraints

$$\begin{cases} P_{G,i-1} - P_{G,i} \le \Delta T \cdot R_{\text{down}}, \\ P_{G,i} - P_{G,i-1} \le \Delta T \cdot R_{\text{up}}. \end{cases} \tag{15}$$

Tie Line Power Constraints

$$0 \le P_{\text{line},i} \le P_{\text{line,max}}, \tag{16}$$

where $P_{L,i}$, $P_{G,i}$, $P_{W,i}$, $P_{\text{line},i}$ are load demand, the unit output, wind power output and tie line power of the i^{th} fluctuation process respectively; $P_{G,\min}$ and $P_{G,\max}$ are the minimum and maximum output of the unit; $P_{\text{line,max}}$ are the power limit of tie line; R_{down} and R_{up} are the climbing speed of the unit.

The proposed evaluation method is mainly used to calculate the wind power that the system can consume. If the system does not meet the power balance constraints, there may be two situations: excess power and power shortage. The former will lead to wind power being abandoned, and in the latter case, the system can consume all the wind power. However, the system will load shedding when the load demand can not be met. If the system satisfies the power balance constraints, y_1 will be 0; if the power is excessive, y_1 is one; if the power is insufficient, y_1 is −1.

Evaluation Model

For each kind of fluctuation process, a functional analysis model of consumption capacity evaluation is established according to the state set.

$$Q_i = \begin{cases} \int F(\Delta\alpha_i)\mathrm{d}t, \\ \int [F(\Delta\alpha_i) - C_{1,i}]\mathrm{d}t, \quad Y = \{0,1,0,1\}, \\ \int C_{2,i}\mathrm{d}t, \quad Y = \{1,0,0,0\}, \{1,0,1,0\}, \end{cases} \tag{17}$$

$$C_{1,i} = \Delta P_{W,i} - \Delta P_{L,i} - \Delta t \cdot R_{\text{down}}, \tag{18}$$

$$C_{2,i} = P_{L,i} - P_{G,\min} + P_{\text{line-max}}. \tag{19}$$

Here, $C_{1,i}$ is the wind power curtailment generated by the system due to insufficient climbing capacity of the unit. $C_{2,i}$ is the maximum consumption capacity of the wind power when the system has excess power. Δt is the duration. The solution flow is shown in **Figure 2**.

CASE STUDY

The effectiveness of the proposed method is verified by the actual power grid data. The grid structure is shown in **Figure 3**. There are three wind farms in the system with a total installed capacity of 350 MW, five thermal power units and the total installed capacity is 786 MW. The parameters of each generator set are shown in **Table 1**. Assuming that all units are in the starting state, the upper limit of tie line power is 50 MW. Load and wind power output curve are shown in **Figure 4**.

Division and Clustering of Fluctuation Processes

The fluctuation process of wind power is divided by SDA. Window width ε is taken as 5% of the installed capacity of wind power. A total of 41 fluctuation processes are obtained and numbered from left to right. The results of division are shown in **Figure 5**.

The volatility parameter $\Delta\alpha$ and average Euclidean distance D_{av} of each fluctuation process are calculated. The results are shown in **Table 2**. According to the calculation results, the process is clustered by breadth first search neighbor algorithm.

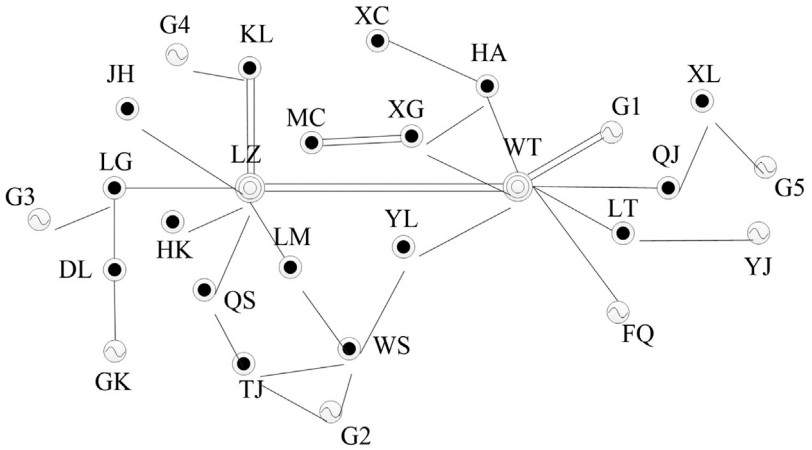

FIGURE 3 | Grid structure diagram.

TABLE 1 | General parameters of generator set.

Unit number	Maximum output/MW	Minimum output/MW	Climbing rate/(MW/15 min)
G_1	300	120	24
G_2	300	120	24
G_3	100	40	7.5
G_4	50	20	5
G_5	36	9	4
GK	150	0	\
FQ	100	0	\
YJ	100	0	\

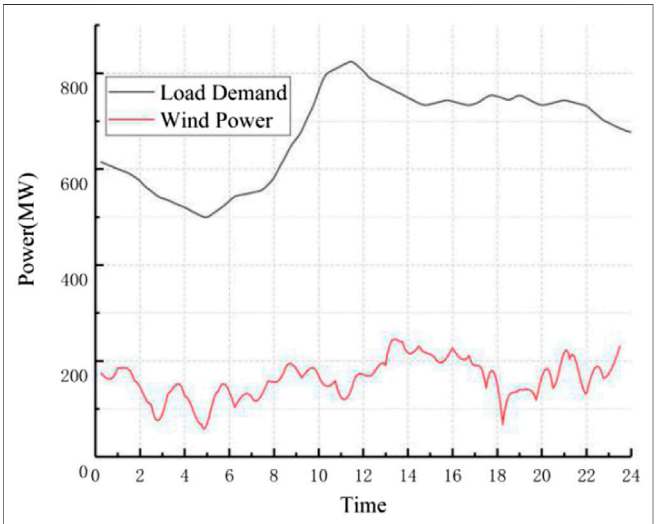

FIGURE 4 | Load curve and wind power output curve.

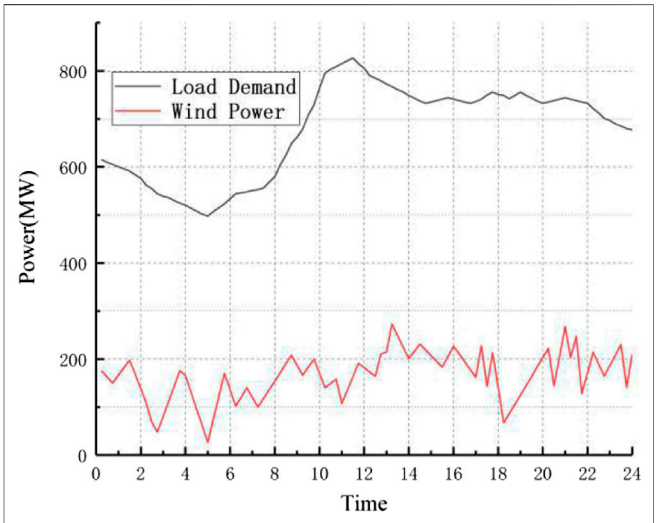

FIGURE 5 | Division results of fluctuation process.

Clustering parameters r and λ are 0.8 and 1, respectively, and seven categories are obtained. The clustering results of each process are shown in **Table 3**.

Calculation of Consumption Capacity

Function relationship between the wind power and singularity index in various wave stages is fitted. The wind power fitting function of 7 categories is replaced into the evaluation model, and

TABLE 2 | Clustering parameters.

Fluctuation process	Volatility parameter $\Delta\alpha$	Average euclidean distance D_{av}
1	0.12825	345.58
2	0.05803	224.08
3	0.0451	204.97
4	0.09167	233.89
5	0.09478	232.52
6	0.06923	182.69
7	0.16041	262.03
8	0.17606	305.66
9	0.18043	306.28
10	0.10285	304.41
11	0.06132	187.18
12	0.13755	302.49
13	0.08869	264.32
14	0.03097	260.42
15	0.12833	455.5
16	0.02609	289.17
17	0.02436	319.8
18	0.04972	288.12
19	0.11088	470.98
20	0.02389	187.97
21	0.12598	480.24
22	0.0945	338.6
23	0.18394	462.61
24	0.04178	318.74
25	0.08378	369.78
26	0.08797	332.22
27	0.25408	494.15
28	0.10617	380.34
29	0.02135	319.8
30	0.18068	446.74
31	0.16982	295.2
32	0.11103	298.69
33	0.17981	409.48
34	0.11198	391.09
35	0.1415	397.37
36	0.19435	301.14
37	0.08028	342.69
38	0.17825	325.26
39	0.08754	238.87
40	0.11569	290.05
41	0.17497	348.14

the consumption capacity in the evaluation period is obtained. Take category 5 as an example to illustrate the calculation process. The results are shown in **Figure 6**.

$$P_5(\Delta\alpha) = -1.281 \times 10^8 \cdot \Delta\alpha^4 + 7.064 \times 10^7 \cdot \Delta\alpha^3 - 1,428 \times 10^7 \cdot \Delta\alpha^2 + 1.251 \times 10^6 \cdot \Delta\alpha - 3.994 \times 10^4.$$

The state of this kind of fluctuation is $Y_5 = \{1, 0, 1, 0\}$ according to the basic data of each fluctuation process in Category 5. The power consumption is 253 MW·h, and the abandoned wind power is 64 MW·h. Similarly, the wind power consumption capacity of the whole grid is calculated.

To show the effectiveness of multi-fractal theory in describing the fluctuation degree of wind power, as a comparison, the volatility proposed in (Li et al., 2019) is used to describe the

TABLE 3 | Clustering results of fluctuation process.

Category	Number
1	31, 36
2	13, 25, 29, 37, 40
3	23, 33
4	16, 17, 18, 20, 39
5	4, 5, 7, 30, 41
6	2, 3, 6, 11, 14, 22, 24, 26, 32
7	1, 8, 9, 10, 12, 15, 19, 21, 27, 28, 34, 35, 38

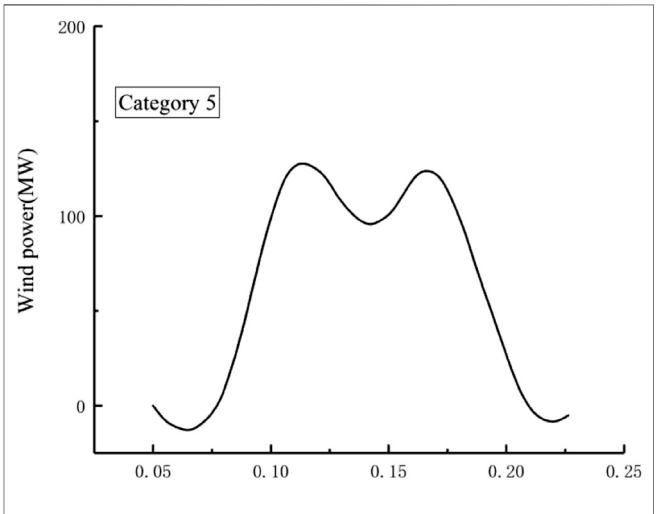

FIGURE 6 | Fitting results of wind power and singularity parameter.

fluctuation degree. The method is recorded as Method 1, and the calculation formula is as follows:

$$\alpha' = \frac{P_{t+1} - P_t}{P_C}, \tag{20}$$

where P_t denotes the output value at time t; P_C denotes the rated capacity of a wind farm.

The consumption capacity of Method 1 is evaluated by using the same evaluation procedure proposed in this paper.

In addition, the evaluation method used in (Sun et al., 2018) is recorded as Method 2. Without considering the load regulation characteristics in different time scales, the wind power consumption was evaluated with the maximum consumption capacity as the optimization objective. The results are shown in **Table 4**.

The fluctuation degree of wind power in Method 1 is expressed by the change degree of a certain period of time, which depends on the size of the time interval used. This may lead to the irregularity of wind power fluctuations that can not be well described. By comparing Method 1 with the method proposed, the relative deviations between the results and the actual data are 12.54% and 3.16% respectively. The results show that the multi-fractal theory can reflect the fluctuation process better and make the evaluation results closer to the actual data.

TABLE 4 | Calculation results of consumption capacity.

	Loadcapacity (MW · h)	Consumptioncapacity (MW · h)	Proportion of consumption (%)	Wind power curtailment ratio (%)
Actual data	16085	4014	24.96	3.57
Method 1	16085	3510	21.82	6.77
Method 2	16085	3969	24.67	3.92
Proposed method	16085	3887	24.17	4.48

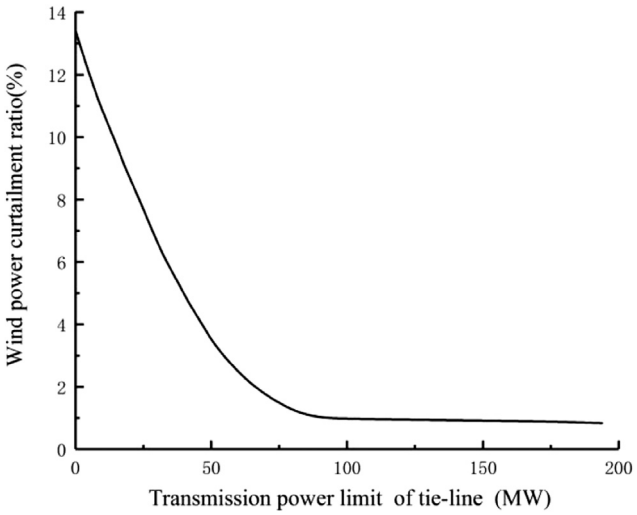

FIGURE 7 | Wind power curtailment ratio with different transmission power limit of tie-line.

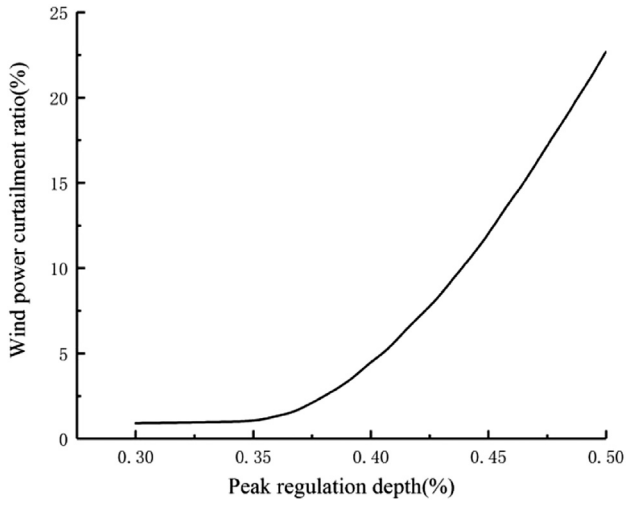

FIGURE 8 | Wind power curtailment ratio with different peak regulation depth.

The wind power consumption is calculated by the optimization problem in Method 2, the result is closest to the actual data, and the relative deviation is 1.12%. Compared with the optimization problem of long time scale, although there are errors between the proposed method and Method 2, the deviation between them is within the acceptable range of engineering application. The evaluation method proposed takes the fluctuation process as the unit for evaluation. Once the type of fluctuation process is determined, the current consumption can be evaluated according to the proposed functional model and the state space. It simplifies the calculation process of wind power energy consumption evaluation and reduces the amount of calculation, and has a wider applicability.

Analysis of Sensitive Factors of Consumption Capacity

Transmission Power Limit of Tie-Line

The results of wind power curtailment ratio of regional power grid are illustrated in **Figure 7** when the output power of tie line is (0, 200) MW. If the limit of transmission power is less than 100 MW, the wind power curtailment ratio is negatively correlated with P_{line}. The increase of P_{line} is equivalent to increasing the maximum consumption space of wind power, i.e. $P_L + P_{\text{line}} - P_{G\min}$, so that the system can consume the power curtailed at the low load. When P_{line} is greater than 100 MW, the ratio basically remains unchanged, which is caused by the insufficient climbing capacity of the unit.

Peak Regulation Depth of Unit

The calculation results of wind power curtailment ratio are shown in **Figure 8** when the unit peak load regulation depth is (30, 50%). The curtailment ratio is positively correlated with the peak shaving depth. If the peak shaving depth is less than 35%, the curtailment ratio does not change, the wind power transmission is blocked due to the transmission power of tie line reaching the upper limit. The influence principle of unit peak regulation depth on the consumption capacity is the same as that of tie line power upper limit, both of which can improve the maximum consumption space of wind power.

CONCLUSION

To guide the development of new energy such as wind and reduce the abandonment risk of wind, a functional analysis model of wind power consumption capacity assessment is established, which takes the singularity parameters of wind power as independent variables, and simplifies the calculation process of

wind power consumption assessment. Through the analysis of an example, the correctness and effectiveness of the refined consumption model proposed are proved. Moreover, the influence of the transmission power limit of tie-line and peak regulation depth of unit on wind power consumption capacity is analyzed quantitatively. The results show that the wind curtailment rate can be reduced to a certain extent by changing these two variables. Relevant research results can provide guidance for new energy development planning and construction.

DATA AVAILABILITY STATEMENT

The raw data supporting the conclusions of this article will be made available by the authors, without undue reservation.

AUTHOR CONTRIBUTIONS

The manuscript was written through the contributions of all authors. All authors have approved the final version of the manuscript.

REFERENCES

Abad, M. S. S., Ma, J., Zhang, D., Ahmadyar, A. S., and Marzooghi, H. (2018). Probabilistic assessment of hosting capacity in radial distribution systems. *IEEE Trans. Sust. Energ.* 9 (4), 1935–1947. doi:10.1109/TSTE.2018.2819201

Chen, X., Wu, W. C., Zhang, B. M., and Lin, C. H. (2107). Data-driven DG capacity assessment method for active distribution networks. *IEEE Trans. Power Syst.* 32 (5), 3946–3957. doi:10.1109/TPWRS.2016.2633299

Chen, Y. B., Zhang, Z., Chen, H., and Zheng, H. P. (2020). Robust UC model based on multi-band uncertainty set considering the temporal correlation of wind/load prediction errors. *IET Gener, Transm. Dis.* 14 (2), 180–190. doi:10.1049/iet-gtd.2019.1439

Chen, Y. B., Zhang, Z., Liu, Z. Y., Zhang, P., Ding, Q., Liu, X. Y., et al. (2019). Robust N-k CCUC model considering the fault outage probability of units and transmission lines. *IET Gener, Transm. Dis.* 13 (17), 3782–3791. doi:10.1049/iet-gtd.2019.0780

Florita, A., Hodge, B., and Orwig, K. (2013). "Identifying wind, solar ramping events," in 2013 IEEE green technologies conference. Denver, CO, April 4–5, 2013 (Piscataway, NJ: IEEE), 147–152. doi:10.1109/GreenTech.2013.30

Fu, K., Jia, Y., Han, X., Xiang, Y., and Wang, P. (2018). "Study on wind power consumption capacity of power grid considering risk and unit commitment," in IEEE Power & Energy Society General Meeting (PESGM). Portland, OR, August 5–10, 2018 (Piscataway, NJ: IEEE), 1–5. doi:10.1109/PESGM.2018.8586402

Global Energy Interconnection Development and Cooperation Organization (2020). Research on China's '14th five year plan' electric power development plan, Available at https://www.geidco.org/research/strategic/2020/2553.shtml (Accessed July 15, 2020).

Harteand David (2001). *Multifractals: theory and applications*. Boca Raton, FL: Chapman & Hall/CRC Imprint.

Koutroumpezis, G. N., and Safigianni, A. S. (2010). Optimum allocation of the maximum possible distributed generation penetration in a distribution network. *Electric Power Syst. Res.* 80 (12), 1421–1427. doi:10.1016/j.epsr.2010.06.005

Lamsal, D., Sreeram, V., Mishra, Y., and Kumar, D. (2019). Smoothing control strategy of wind and photovoltaic output power fluctuation by considering the state of health of battery energy storage system. *IET Renew. Power Genera.* 13 (4), 578–586. doi:10.1049/iet-rpg.2018.5111

Li, L., Wang, X., Zhang, L. N., Lei, X. H., Han, S., Liu, Y. Q., et al. (2019). Quantitative evaluation method for the complementarity of wind–solar–hydro power and optimization of wind-solar ratio. *Appl. Energ.* 189, 2019973–2019984. doi:10.1016/j.apenergy.2018.12.059

Liu, W. J., Chung, C. Y., and Wen, F. S. (2014). Multifractal based return interval approach for short-term electricity price volatility risk estimation. *Generation. Transm. Distribution, IET.* 8 (9), 1550–1560. doi:10.1049/iet-gtd.2013.0680

Ma, H., Xu, F., Chen, Q., Hu, K., Chen, L., Dai, Y. H., et al. (2020). Dispatch framework of power system with heat storage facilities in combined heat and power plants for wind power accommodation. *IET Renew. Power Genera.* 14 (3), 335–343. doi:10.1049/iet-rpg.2019.0595

Meena, N. K., Swarnkar, A., Gupta, N., and Niazi, K. R. (2017). Optimal accommodation and management of high renewable penetration in distribution systems. *J. Eng.* 2017 (13), 1–7. doi:10.1049/joe.2017.0659

Mu, Y. Q., Wang, C. S., Kang, G. Y., Wang, Z., Jiang, T., Li, J. F., et al. (2019). Research on sensitivity analysis of wind power consumption capability of integrated energy system based on unified optimal power flow model. *J. Eng.* 2019 (12), 8471–8476. doi:10.1049/joe.2019.0772

Nguyen, N., and Mitra, J. (2016). An analysis of the effects and dependency of wind power penetration on system frequency regulation. *IEEE Trans. Sust. Energ.* 7 (1), 354–363. doi:10.1109/TSTE.2015.2496970

Qazi, A., Hussain, F., Rahim, N. A. B. D., Hardaker, G., Alghazzawi, D., Shaban, K., et al. (2019). Towards sustainable energy: a systematic review of renewable energy sources, technologies, and public opinions. *IEEE Access* 9, 63837–63851. doi:10.1109/ACCESS.2019.2906402

Shi, J., Lee, W. J., and Liu, X. F. (2018). Generation scheduling optimization of wind-energy storage system based on wind power output fluctuation features. *IEEE Trans. Industry Appl.* 54 (1), 10–17. doi:10.1109/TIA.2017.2754978

Sun, F., Li, S. H., Ge, Y. Y., Fu, Y., Xie, C. J., Zhao, Q. S., et al. (2018). "Multi-objective optimization method for source-source coordination of power system considering wind power consumption" in 3rd international conference on smart city and systems engineering, Xiamen, China, December 29–30, 2018 (Piscataway, NJ: IEEE). doi:10.1109/ICSCSE.2018.00097

Teng, J., Zhao, X., Qian, M., Men, Y., Yu, Z., and Hou, Y. (2019). "Short-term wind power forecasting based on variable time window and feature extraction" in IEEE Sustainable Power and Energy Conference, Beijing, China, November 21–23, 2019. doi:10.1109/iSPEC48194.2019.8974948

Torquato, R., Salles, D., Oriente Pereira, C., Magalhaes Meira, P. C., and Freitas, W. (2018). A comprehensive assessment of PV hosting capacity on low-voltage distribution systems. *IEEE Trans. Power Deliv.* 33 (2), 1002–1012. doi:10.1109/TPWRD.2018.2798707

Vallée, F., Brunieau, G., Pirlot, M., Deblecker, O., and Lobry, J. (2011). Optimal wind clustering methodology for adequacy evaluation in system generation studies using nonsequential Monte Carlo simulation. *IEEE Trans. Power Syst.* 26 (4), 2173–2184. doi:10.1109/TPWRS.2011.2138726

Wang, C., Gong, Z., Liang, Y., Wei, W., and Bi, T. (2020). Data-driven wind generation admissibility assessment of integrated electric-heat systems: a dynamic convex hull-based approach. *IEEE Trans. Smart Grid* 11 (5), 4531–4543. doi:10.1109/TSG.2020.2993023

Wang, G., Liu, Y., Chen, D., Yang, Z., Geng, H., Li, H., et al. (2018). "Basics non-time series production scale semantic wind power consumption evaluation method," in 3rd international conference on Smart city and systems engineering. Xiamen, China, 6 May, 2019. doi:10.1109/ICSCSE.2018.00090

Wang, H. T., and Zou, B. (2020). Probabilistic computational model for correlated wind speed, solar irradiation, and load using bayesian network. *IEEE Access* 8, 51653–51663. doi:10.1109/ACCESS.2020.2977727

Wang, X. D., and Li, H. (2017). Multi-objectives combined electric heating dispatch model of wind power accommodation with heat storage device. *J. Eng.* 2017 (13), 1539–1545. doi:10.1049/joe.2017.0589

Wu, X. S., and Jiang, Y. W. (2019). Source-network-storage joint planning considering energy storage systems and wind power integration. *IEEE Access* 7, 137330–137343. doi:10.1109/ACCESS.2019.2942134

Xie, J., Wang, K., Feng, D. H., Zeng, D., Li, Y. P., and Yue, D. (2016). A security-constrained flexible demand scheduling strategy for wind power accommodation. *Int. Trans. Electr. Energ. Syst.* 26 (6), 1171–1183. doi:10.1002/etep.2123

Xu, Q. Y., Kang, C. Q., Zhang, N., Ding, Y., Xia, Q., Sun, R. F., et al. (2016). A probabilistic method for determining grid-accommodable wind power capacity based on multiscenario system operation simulation. *IEEE Trans. Smart Grid* 7 (1), 400–409. doi:10.1109/TSG.2014.2381271

Xue, Y., Sun, X. D., and Zhang, S. (2015). Modulation classification of communication signals based on broad first search neighbors clustering. *Telecommunication Eng.* 55 (1), 13–16. doi:10.3969/j.issn.1001-893x.2015.01.003

Yang, S., Li, C., Li, X. F., Huang, Y. H., Liu, C., and Wang, W. S. (2017). Wind power fluctuation characteristics of Three North regions based on clustering algorithm. *J. Eng.* 2017 (13), 2266–2270. doi:10.1049/joe.2017.0734

Zhan, X. Y., and Liu, C. (2019). Accommodation capability assessment of high-voltage direct current with a large-scale wind power integration system based on risk constraints of sub-synchronous oscillation. *J. Eng.* 2019 (16), 2131–2136. doi:10.1049/joe.2018.8710

Zhang, X. S., Yuan, Y., Hua, L., Cao, Y., and Qian, K. J. (2017). On generation schedule tracking of wind farms with battery energy storage systems. *IEEE Trans. Sust. Energ.* 8 (1), 341–353. doi:10.1109/TSTE.2016.2598823

Zhang, Z., Chen, Y. B., Liu, X. Y., and Wang, W. R. (2019a). Two-stage robust security-constrained unit commitment model considering time autocorrelation of wind/load prediction error and outage contingency probability of units. *IEEE Access* 7, 25398–25408. doi:10.1109/ACCESS.2019.2900254

Zhang, Z., Chen, Y. B., Ma, J., Liu, X. Y., and Wang, W. R. (2019b). Two-stage robust security constrained unit commitment considering the spatiotemporal correlation of uncertainty prediction error. *IEEE Access* 7, 22891–22901. doi:10.1109/ACCESS.2019.2895625

Zhou, S. Y., Zhao, Y., Gu, W., Wu, Z., Li, Y. P., Qian, Z. H., et al. (2019). Robust energy management in active distribution systems considering temporal and spatial correlation. *IEEE Access* 2019, 153635–153649. doi:10.1109/ACCESS.2019.2947415

Conflict of Interest: XZ was employed by the East China Electric Power Design Institute Co., Ltd, China Power Engineering Consulting Corporation.

The remaining authors declare that the research was conducted in the absence of any commercial or financial relationships that could be construed as a potential conflict of interest.

frontiers in Energy Research

ORIGINAL RESEARCH
published: 25 March 2021
doi: 10.3389/fenrg.2021.634912

Incentive Policy for Battery Energy Storage Systems Based on Economic Evaluation Considering Flexibility and Reliability Benefits

Shengxia Cai and Ying Li*

Zhou Enlai School of Government, Nankai University, Tianjin, China

The efficient application of battery energy storage system (BESS) technology can effectively alleviate the uncertainty and volatility caused by distributed generations (DGs) and loads, and reduce their adverse effects on the power grid. More efficient applications could delay equipment capacity upgrades, improve equipment utilization, save costs, and increase the system hosting capacity for renewable energy. However, the application of BESS is restricted by its high cost and limited policy support. It is, therefore, necessary to carry out an economic evaluation of BESS, considering its flexibility and improvement of reliability, alongside incentive policy research to promote its deployment. This study on BESS involves four key aspects: 1) It proposes a reliability-benefit model for BESS, considering the value of electricity in the national economy. 2) It describes a flexibility improvement benefit calculation model for BESS, built with the definition of flexibility indexes of distribution network related to BESS, and considering the capacity, charge, and discharge constraints. 3) A reliability improvement benefit calculation model of BESS was built, and the present study proposes a detailed calculation flow of economic evaluation model for BESS users considering net present value (NPV) index and dynamic payback period (DPP) index. 4) An impact analysis of different prices and incentive policies on BESS business models is also carried out, with the present study finally presenting an incentive policy based on flexibility and reliability improvement. The results of the IEEE 33-node test system show that flexibility and reliability improvement can effectively reflect the benefit and cost of BESS, and that incentive policies can help to promote the development of BESS technology.

Keywords: battery energy storage system, flexibility, reliabiity, economic evaluation, policy

OPEN ACCESS

Edited by:
Hao Yu,
Tianjin University, China

Reviewed by:
Changgang Li,
Shandong University, China
Wei Tian,
Illinois Institute of Technology, United States

****Correspondence:***
Shengxia Cai
Caishengxia77@nankai.edu.cn

Specialty section:
This article was submitted to Smart Grids, a section of the journal Frontiers in Energy Research

Received: *29 November 2020*
Accepted: *01 February 2021*
Published: *25 March 2021*

Citation:
Cai S and Li Y (2021) Incentive Policy for Battery Energy Storage Systems Based on Economic Evaluation Considering Flexibility and Reliability Benefits. Front. Energy Res. 9:634912. doi: 10.3389/fenrg.2021.634912

INTRODUCTION

Along with the expansion of industry on a global scale, comes excessive energy consumption, environmental degradation, and global warming, which seriously affect humans and the development of society. Traditional fossil energy generation has brought about an increasingly serious energy consumption crisis and problems of environmental pollution (Zhang et al., 2017; Xiao et al., 2018; Yang et al., 2018). In the face of global energy and environmental constraints, many countries have put energy conservation and energy efficiency in the foremost strategic position, making full use of as many renewable energies as possible to promote the efficient and clean use of

energy. Future power grids need to be flexible enough to adapt to the new situation of high penetration of renewable energy, multiple uncertain perturbations, even various natural and man-made disasters (Shao et al., 2017). Energy storage is one of the key technologies for a future power grid with high penetration of renewable energy due to its capability to separate the production and consumption of electrical energy from time and space (Li and Hedman, 2015). Rational use of energy storage to achieve multiple functional values can effectively mitigate the uncertainty and volatility caused by distributed generations (DGs) and loads, reducing the impact on the grid, and potentially delaying equipment capacity upgrades, improving equipment utilization, and saving costs (Kuleshov et al., 2019), which play a catalytic role in enhancing the flexibility of the distribution network.

Research and economic analysis of battery energy storage systems (BESS) have been carried out in terms of the method and intensity of subsidies (Fang et al., 2018), operating and maintenance costs (Bruninx et al., 2016), comprehensive environmental and other benefits (Lee et al., 2011), and the economy of participating in grid regulation (Yang et al., 2020). The literature (Li and Hedman, 2015) establishes an economic evaluation model for BESS with high penetration of renewable energy. The average cost of conventional generation is reduced when the system is connected to BESS, and BESS can increase the utilization of conventional power generation in the system. Other studies (Mahmoodi et al., 2015) have established the economics of microgrid systems where BESS participates in the regulation, and the proposed strategy could achieve the lowest cost operation of the system. Literature (Yan et al., 2016) establishes a costing model for grid power generation that includes BESS, which effectively reduces the operating cost of the system. Other literature on the subject (Xu and Tong, 2017) investigates the economic value of BESS, operated by a consumer who seeks to maximize the long-term expected payoff (utilities perceived from energy consumption minus energy cost) and define the value of storage as net benefits to the consumer obtained by optimally operating the storage.

Due to its flexible power input/output characteristics (Zhang et al., 2018), BESS is widely and flexibly applied on the grid side, user side, and power supply side, which can effectively achieve demand-side management (Shu and Jirutitijaroen, 2014), eliminate peak and valley differences between day and night (Lu et al., 2009), smooth load and power fluctuations (Bitaraf and Rahman, 2018), improve power equipment utilization, and reduce power supply costs (Cleary et al., 2015). The rapid development of BESS technology provides power systems with greater flexibility, safety, higher power quality, and self-healing capabilities. Literature (Kuleshov et al., 2019) evaluates the economic attractiveness of BESS and identifies the conditions under which solar BESS can operate profitably. Another study (Maghouli et al., 2016) considers the uncertainty of wind turbines in assessing the impact of BESS on the system, and the inclusion of BESS saves the operating costs of the system and increases the flexibility of the grid. In a study by Huang and Wang (2016), a value assessment methodology was proposed for BESS that aimed to facilitate large-scale PV energy access. The results show that energy storage can alleviate the grid modification workload and power constraints associated with large-scale distributed PV grid connections. Other literature by You et al. (2016) investigated the flexible economic dispatch of hydrogen BESS.

In order to promote the development of energy storage, many countries have introduced incentive policies. The United States has introduced the Better Energy Storage Technology Act, Best and the Promotional Grid Storage Act of 2019 to reduce costs and extend the life of energy storage systems. This policy focuses on the research and development of grid-scale energy storage systems and developed a battery recycling incentive to collect, store and transport waste lithium-ion batteries to promote sustainable energy development. The United Kingdom Department for Business, Energy and Industrial Strategy has invested heavily in the cost of energy storage, developing projects to improve the intelligence and flexibility of the grid, and has published the strategic report, Upgrading our Energy System: Smart Systems and Flexibility Plan (Ofgem, 2017). Currently, the energy storage market policy has entered the "post-guidance" stage, and the future commercialization and scale-up of energy storage in China will require strong support from policy and the market.

The main contributions of this paper are first, that it proposes a reliability-benefit model for BESS, considering the value of electricity in the national economy. A flexibility improvement benefit calculation model of BESS was then built with the definition of flexibility indexes of distribution networks related to BESS, considering capacity and charge and discharge constraints. A reliability improvement benefit calculation model of BESS was built with the detailed calculation flow presented, considering the net present value (NPV) index and dynamic payback period (DPP) index. Finally, the impact analysis of different prices and incentive policies on the BESS business models is carried out, and the incentive mechanism and policy based on flexibility and reliability improvement is presented.

The rest of the paper is organized as follows. *Benefit/Cost Evaluation of BESS in Distribution Network* introduces the benefit/cost evaluation of BESS in a distribution network. *Economic Evaluation and Optimization of BESS Allocation Considering its Value on Flexibility and Reliability Improvement* proposes the economic evaluation of BESS considering its flexibility and reliability values. *Economic Evaluation of BESS Considering its Flexibility and Reliability Improvement Benefits* discusses the case study, results, and incentive policy before *Incentive Mechanism and Policy for BESS Based on Economic Evaluation Considering its Flexibility and Reliability Improvement Benefits* outlines conclusions.

BENEFIT/COST EVALUATION OF BESS IN DISTRIBUTION NETWORK

Benefits of BESS

The roles that the BESS system plays in a distribution network can be summarized in terms of energy dimension, time dimension, and place dimension, respectively. From the perspective of the

energy dimension, it plays a role in power, electricity, and capacity support. From the perspective of time, it plays a role in static, dynamic, and instantaneous energy transfer support. From the perspective of place, it plays a role in the source, the user, and in grid support. Many benefits can be brought from BESS. In this paper, we focus on its benefits for flexibility and improving the reliability of the distribution network.

Flexibility Improvement Benefit for Peak Dispatching

The BESS deployment can improve the flexibility of the distribution network via the revenue from the auxiliary service of peak dispatching.

The flexibility improvement benefit for peak dispatching F_{fle} is:

$$F_{\text{fle}} = F_{\text{fle,dis}} - C_{\text{fle,ch}}, \tag{1}$$

where $F_{\text{fle,dis}}$, $C_{\text{fle,ch}}$ are the benefit of BESS discharging and the cost of BESS charging, respectively.

The mathematical model for the benefit of BESS discharging $F_{\text{fle,dis}}$ is:

$$F_{\text{fle,dis}} = \sum_{j=1}^{M} \sum_{k=0}^{K_j} \left(P_{\text{dis},jk} \cdot T_{\text{dis},jk} \cdot F_{\text{dis},jk} \right), \tag{2}$$

where $P_{\text{dis},jk,}$ is the power of the kth discharge of BESS j. $T_{\text{dis},jk}$ is the time of the kth discharge of BESS j, and $F_{\text{dis},jk}$ is the unit discharge benefit of the kth discharge of BESS j.

The mathematical model for the cost of BESS charging $C_{\text{fle,ch}}$ is as follows:

$$C_{\text{fle,ch}} = \sum_{j=1}^{M} \sum_{k=0}^{K_j} \left(P_{\text{ch},jk} \cdot T_{\text{ch},jk} \cdot C_{\text{ch},jk} \right), \tag{3}$$

where M is the number of BESS, K_j is the number of charging periods per day of BESS j. $P_{\text{ch},jk}$ is the time of the kth charge of BESS j. $T_{\text{ch},jk}$ is the time of the kth charge of BESS j and $C_{\text{ch},jk}$ is the unit charge cost of the kth charge of BESS j.

Reliability Improvement Benefit

The BESS deployment can also improve the reliability of the distribution network. The reliability benefits of BESS in the distribution network are mainly reflected in reduced outage losses when a system failure occurs. BESS can supply power to the load in a timely manner, which improves the reliability of load points. The reliability improvement benefit F_{rel} of BESS is as follows:

$$\begin{aligned} F_{\text{rel}} &= F_{\text{rel}}^{\text{before}} - F_{\text{rel}}^{\text{after}} \\ &= \sum_{j=1}^{n} \sum_{k=0}^{N_j} \left(P_{jk}^{\text{before}} \cdot T_{OFF,jk}^{\text{before}} \cdot C_{L,jk}^{\text{before}} \right) - \sum_{j=1}^{n} \sum_{k=0}^{N_j} \left(P_{jk}^{\text{after}} \cdot T_{OFF,jk}^{\text{after}} \right. \\ &\quad \left. \cdot C_{L,jk}^{\text{after}} \right), \end{aligned} \tag{4}$$

where n is the number of load points. N_j is the number of outages at load point j. P_{jk}^{before} and P_{jk}^{after} are the load power at the kth outage at load point j before and after the allocation of BESS, respectively. $T_{OFF,jk}^{\text{before}}$ and $T_{OFF,jk}^{\text{after}}$ are the kth outage time at load point j before and after the allocation of BESS, respectively. $C_{L,jk}^{\text{before}}$ and $C_{L,jk}^{\text{after}}$ are the average outage loss cost per kW at the kth outage at load point j before and after the allocation of BESS, which is determined jointly by the load type, outage time, and the value of electricity in the national economy. F_{rel} indicates the reliability improvement benefit after the BESS deployment.

Costs of BESS

Capital Costs

The capital costs of BESS for primary investment construction usually consist of two parts: the cost of a storage unit and the cost of the Power Conversion System (PCS).

$$C_{\text{IN}} = \sum_{i=1}^{N_{\text{ESS}}} \left(C_Q \cdot Q_i + C_P \cdot P_i \right), \tag{5}$$

where C_{IN} is the capital cost of BESS for investment. N_{ESS} is the number of BESS; C_Q and C_P are the cost of per capacity storage unit (Yuan/kWh) and the cost of unit power of PCS (Yuan/kW) respectively; Q_i and P_i are the capacity and the rated power of the ith BESS.

Operation and Maintenance Costs

Harmonize the time scales and discount the annual operation and maintenance (O&M) costs to present value considering the time value of money as follows.

$$C_{\text{O\&M}} = \sum_{n=1}^{Y} \eta \cdot C_{\text{IN}} \cdot (1+s)^n, \tag{6}$$

where $C_{\text{O\&M}}$ is the present value of the O&M cost of the BESS. η is the annual O&M cost as a percentage of the total investment cost. s is the discount rate, and Y indicates the useful life of the BESS equipment.

ECONOMIC EVALUATION AND OPTIMIZATION OF BESS ALLOCATION CONSIDERING ITS VALUE ON FLEXIBILITY AND RELIABILITY IMPROVEMENT

Impact of BESS Involvement on Flexibility Evaluation of Distribution Network

The impact of BESS on distribution network flexibility is studied from the perspective of two aspects of the flexible adequacy of the distribution network capacity and the voltage deviation at the nodes with the BESS involvement. Hence, the following two indicators, line capacity margin and node voltage deviation rate, are proposed to reflect the flexibility of regulating node voltage in distribution lines and distribution networks.

Flexibility Indexes of Distribution Network

Line Capacity Margin

The distribution line capacity margin reflects the upward flexibility of the distribution line to load fluctuations

$$M_{\mathrm{LCM},i}^{t}=\frac{P_{i,\max}^{\mathrm{line}}-P_{i,t}^{\mathrm{line}}}{P_{i,\max}^{\mathrm{line}}}\times 100\%, \tag{7}$$

where $M_{\mathrm{LCM},i}^{t}$ is the capacity margin of the ith distribution line at time t. $P_{i,\max}^{\mathrm{line}}$ is the maximum transmission power of line i. $P_{i,t}^{\mathrm{line}}$ is the power of the ith line at time t. $M_{LCM,i}^{t}$ generally refers to the line margin at the time corresponding to the peak load. $M_{\mathrm{LCM},i}^{t}\geq 0$ indicates that the line margin is sufficient and can adapt to load power fluctuations. $M_{\mathrm{LCM},i}^{t}<0$ indicates that the line margin is insufficient and line congestion will occur.

Node voltage deviation rate

The overall node deviation reflects the node voltage quality in one unit of time in the distribution network.

$$D_{\mathrm{dev}}=\frac{\left|U_{k,t}-U_{N}\right|}{U_{N}}\times 100\%, \tag{8}$$

where $U_{k,t}$ is the voltage at node k at time t. U_N represents the node voltage rated value during the period under investigation. The smaller D_{dev} is, the more favorable the effect of BESS on the flexibility of the distribution network.

Optimization Model for Improving Distribution Network Flexibility With BESS Participation in Dispatching

To study the impact of BESS on the flexibility of the distribution network, we consider the BESS $(\alpha P_{i,t}^{\mathrm{dis}}-\beta P_{i,t}^{\mathrm{ch}})$ in the distribution network to be an optimization variable and define the variable X as:

$$X=\left[\begin{array}{cccc}P_{i,t}^{\mathrm{dis}} & P_{i,t}^{\mathrm{ch}} & \alpha & \beta\end{array}\right], \tag{9}$$

where $P_{i,t}^{\mathrm{dis}}$ and $P_{i,t}^{\mathrm{ch}}$ are the discharging power and charging power of BESS respectively. α and β are charge/discharge state flag parameters, which are 0–1 variables and satisfy $\alpha+\beta\leq 1$.

Objective Functions

The first objective function is the total cost of the system operation, including the cost of purchasing power from the grid, the cost of grid losses, and the cost of BESS devices operating.

$$F_1(X)=\sum_{t=1}^{T}C_tP_t+\sum_{t=1}^{T}C_tP_t^{\mathrm{loss}}+\sum_{t=1}^{T}\sum_{i=1}^{N_{\mathrm{ESS}}}\left[\frac{C_i^{\mathrm{ESS}}}{M_i^{\mathrm{ESS}}}\left(\alpha P_{i,t}^{\mathrm{dis}}-\beta P_{i,t}^{\mathrm{ch}}\right)\Delta t\right], \tag{10}$$

where T is the total number of dispatching hours, T = 24 h. C_t is the hourly unit price. P_t is the power purchased from the power system. P_t^{loss} is the network loss. C_i^{ESS} is the ith BESS purchase cost, and M_i^{ESS} is the ith BESS charge/discharge cycle.

The second objective function is the node voltage deviation.

$$F_2(X)=\sum_{\mathrm{m}=1}^{N_{\mathrm{node}}}\sum_{\mathrm{t}=1}^{T}D_{\mathrm{dev}}, \tag{11}$$

where N_{node} represents the number of nodes in the system.

Constraints

(1) Charge state constraints of BESS

$$\begin{cases}S_{\mathrm{oc},t+1}=\dfrac{\left(\eta_{\mathrm{ESS}}^{\mathrm{ch}}\alpha P_t^{\mathrm{ch}}-\dfrac{\beta P_t^{\mathrm{dis}}}{\eta_{\mathrm{ESS}}^{\mathrm{dis}}}\right)\triangle t}{C_{\mathrm{ESS}}^{\mathrm{cap}}}+S_{\mathrm{oc},t}\left(1-\delta_{\mathrm{ESS}}\right), \\ S_{\mathrm{oc,min}}\leq S_{\mathrm{oc},t+1}\leq S_{\mathrm{oc,max}}\end{cases} \tag{12}$$

where P_t^{ch} and P_t^{dis} are the actual BESS charging and discharging power respectively. $S_{\mathrm{oc,t}}$ is the state of charge (SOC) of BESS at time t. δ_{ESS} is the self-discharge rate of BESS. $\eta_{\mathrm{ESS}}^{\mathrm{ch}}$ and $\eta_{\mathrm{ESS}}^{\mathrm{dis}}$ are the charging and discharging efficiency of BESS. $S_{\mathrm{oc,min}}$ and $S_{\mathrm{oc,max}}$ are the minimum and maximum charge states, respectively. α represents the 0–1 variable of BESS charging state, when α is 1, it means the BESS device is charging. β represents the 0–1 variable of BESS discharging state, when β is 1, it means the BESS device is discharging. The BESS device cannot be charged and discharged at the same time, therefore $\alpha+\beta\leq 1$. $C_{\mathrm{ESS}}^{\mathrm{cap}}$ is the size of BESS capacity.

(2) Flexibility constraints

$$M_{\mathrm{LCM},t}^{t}\geq 0, \tag{13}$$

(3) Power flow constraints

$$\begin{cases}P_{i,t}-V_{i,t}\sum_{i=1}^{N}V_{j,t}\left(G_{ij}\cos\theta_{ij}+B_{ij}\sin\theta_{ij}\right)=0 \\ Q_{i,t}-V_{i,t}\sum_{i=1}^{N}V_{j,t}\left(G_{ij}\sin\theta_{ij}-B_{ij}\cos\theta_{ij}\right)=0\end{cases}, \tag{14}$$

where $V_{i,t}$ and $V_{j,t}$ are the voltages of nodes i and j, respectively. G_{ij} and B_{ij} are the conductance and inductance between node i and node j, respectively. θ_{ij} is the phase-angle difference between node i and j.

(4) Node voltage constraints

$$V_{i,\min}\leq V_{i,t}\leq V_{i,\max}, \tag{15}$$

where $V_{i,\min}$ and $V_{i,\max}$ are the minimum and maximum value of node voltage, respectively.

Impact of BESS Involvement on a Reliability Evaluation of the Distribution Network

Islanding Division and Reliability Index

The BESS deployment can improve the reliability of the distribution network via the formation of a microgrid or isolated power system. When the outage occurs in the external power grid, it can keep the power supply service on some critical loads in islanding mode. Therefore, the islanding division is very important. A breadth-first search method (Li et al., 2018) is used to determine whether the current state can meet the power

demand of the islanded load during the outage period, taking into account the wind and photovoltaic (PV) power generation at the sequential Monte Carlo sampling moment and the SOC of the BESS. **Figure 1** shows the process of islanding division.

The system average interruption duration index (SAIDI) is the reliability index in this paper.

Determining the Reliability Benefit of BESS

Based on the sequential Monte Carlo method, the process for assessing the reliability of the distribution network is as follows:

(1) Import network topology parameters.
(2) Obtain time-series distribution of BESS SOCs based on flexibility scheduling results.
(3) Sample the normal operation time and repair time of each component of the simulation system, and find the minimum normal operation time of all components as the normal operation time of the system. Obtain the whole system operation fault sequence, and accumulate the total simulation time.
(4) Determine the loss of power due to a component failure according to the structure of the grid.
(5) Determine whether BESS is available based on SOC. If the BESS is available, the island is zoned as described above, to determine islanding division and load outages.
(6) Determine the simulation time, if it is less than the set time, go back to step 2, otherwise continue to step 7.
(7) Calculate reliability indexes and reliability benefits.

ECONOMIC EVALUATION OF BESS CONSIDERING ITS FLEXIBILITY AND RELIABILITY IMPROVEMENT BENEFITS

Economic Evaluation Index

The net present value (NPV) index and the dynamic payback period (DPP) are used to evaluate the economics of BESS owners. The specific evaluation metrics are as follows.

Net Present Value Index

The NPV takes into account the time value of money and discounts the net cash flows occurring each year over the life of the project to the sum of the present values at the same point in time, usually chosen as the total present value discounted to the beginning of the year of investment, based on a benchmark discount rate.

$$NPV(i_0) = \sum_{t=0}^{n} C_t^{\text{net}} (1 + i_0)^{-t}, \tag{16}$$

where C_t^{net} is the net cash flow in the tth year, and the investment year is 0. i_0 is the discount rate. When $NPV \geq 0$, the project is feasible, and when $NPV < 0$, the project is not feasible.

The annual net benefit of the BESS is set to R. C is the cost of BESS construction, and the NPV to the user over the whole life cycle is:

$$NPV(i_0) = \sum_{t=0}^{n} R(1 + i_0)^{-t} - C. \tag{17}$$

Dynamic Payback Period Index

The NPP, which takes into account the time value of money, is calculated by accumulating the present value of the project's net income from year to year at a benchmark rate of return until the time required to recover the entire initial investment.

In an investment project where the dynamic payback period is set to T_{p}, the computational model is as follows.

$$\sum_{t=0}^{Tp} C_t^{\text{net}} (1 + i_0)^{-t} = 0. \tag{18}$$

When annual net income is equal.

$$T_p = \frac{\lg R - \lg(R - C^* i)}{\lg(1 + i)}, \tag{19}$$

where R is the net income for each year, i is the benchmark rate of return, and C is the cost of BESS construction.

Economic Evaluation Process

In this paper, the maximum discharge depth of the battery is set to 80%. The annual net benefit R consists of three components, namely, F_{gov} for government subsidies of BESS projects, F_{rel} for the reliability improvement benefit, and F_{fle} for the peak power feed-in under the peak-transfer incentive policy. **Figure 2** shows the economic evaluation process of BESS considering its flexibility and reliability values.

INCENTIVE MECHANISM AND POLICY FOR BESS BASED ON ECONOMIC EVALUATION CONSIDERING ITS FLEXIBILITY AND RELIABILITY IMPROVEMENT BENEFITS

Case Analysis

Fundamental Data

A modified IEEE 33-node distribution system is used in this paper, as shown in **Figure 3**. This section converts the multi-objectives model into a single-objective optimization model using the linear weighted summation method, and adopts the particle swarm optimization algorithm to solve it. BESS economic evaluation is based on the benefits of flexibility through peak tariff and reliability assessment for reliability improvement benefit.

This paper analyzes the benefits of BESS in three scenarios.

Scenario 1: BESS only participates in cutting peaks and filling valleys.

Scenario 2: BESS participates in peak shifting based on time-of-use tariffs.

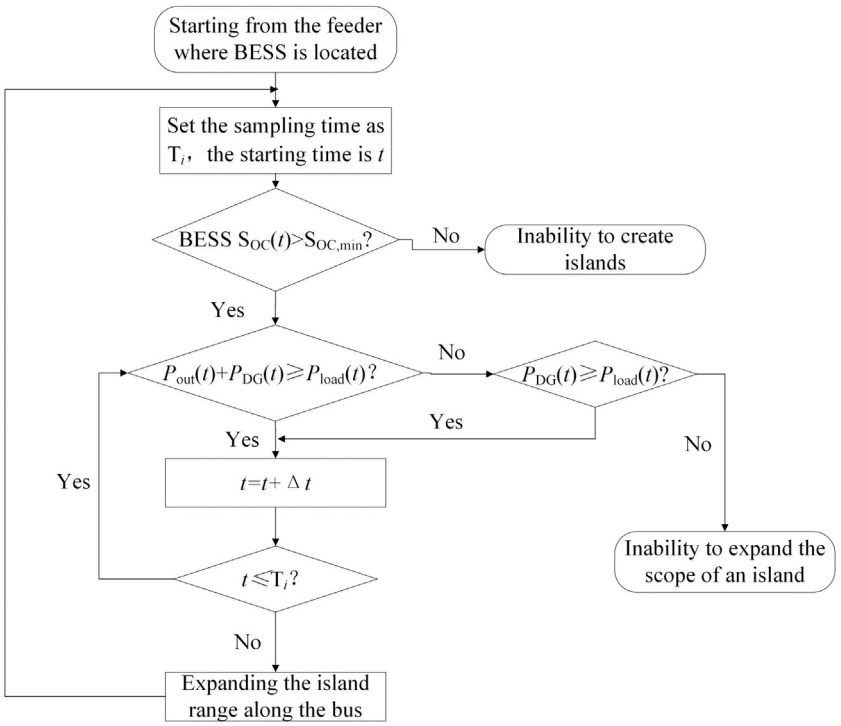

FIGURE 1 | Process of islanding division.

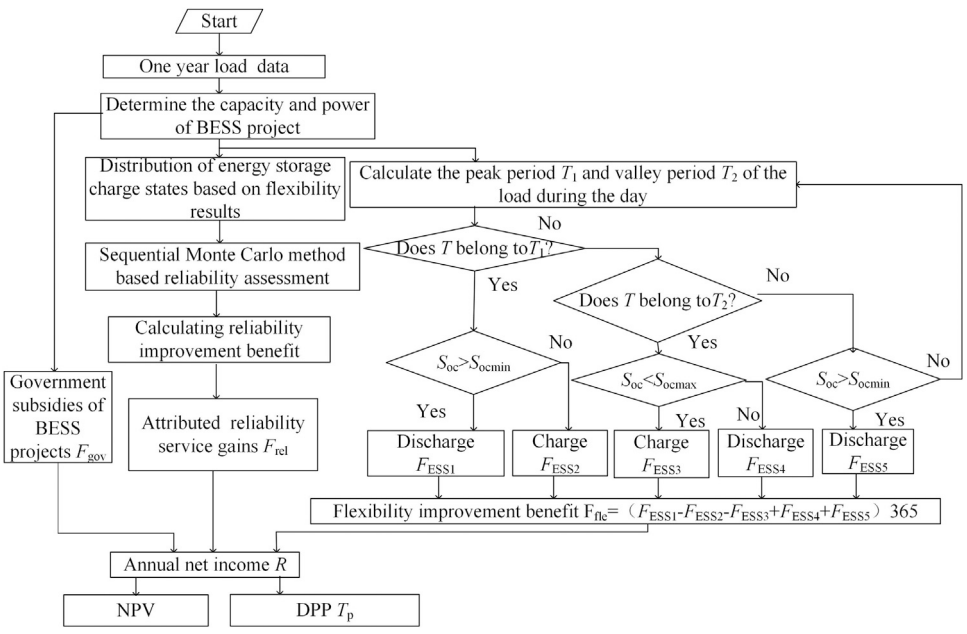

FIGURE 2 | Economic evaluation process of BESS considering its flexibility and reliability values.

Scenario 3: Reliability evaluation of BESS according to the distribution obtained in Scenario 2 to obtain reliability improvement benefit.

In the IEEE 33-node distribution system, 500 kW distributed PV is connected at nodes 2, 5, 10, 18, and 28, and 500 kW wind power is connected at nodes 17, 22, and 24, respectively. The rated power and

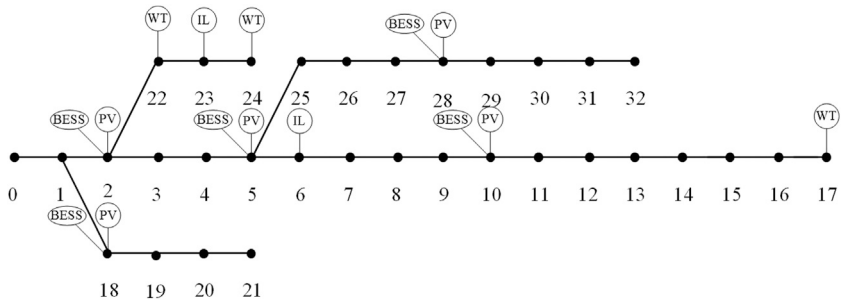

FIGURE 3 | An modified IEEE 33-node distribution system.

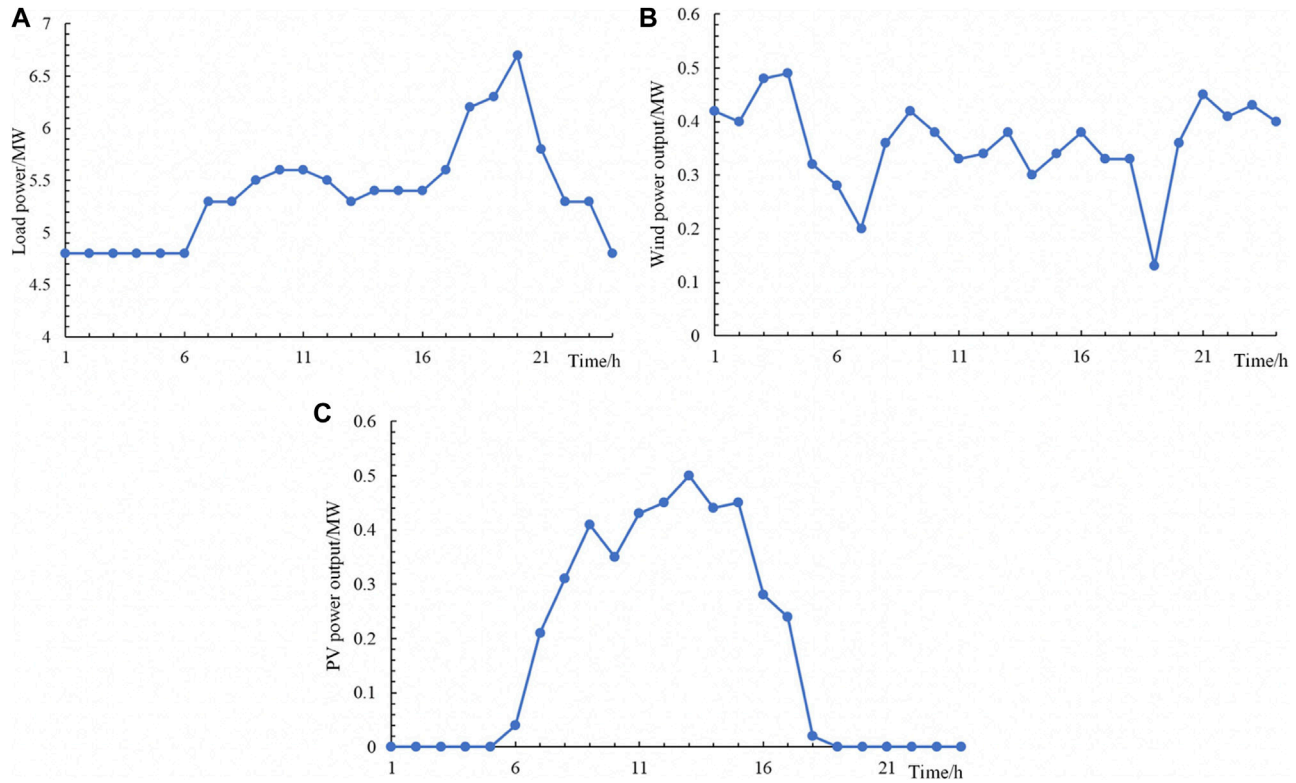

FIGURE 4 | The load, PV, and wind power curves on a typical day in a certain area. **(A)** The load curve on a typical day in a certain area. **(B)** Wind power output on a typical day in a certain area. **(C)** PV power output on a typical day in a certain area.

the rated capacity of the BESS is 150 kW and 800 kWh, which is connected to nodes 2, 5, 10, 18, and 28, respectively. The interruptible load is connected to nodes 6 and 23. The optimized scheduling cycle is 24 h. The power purchase tariff is a time-sharing tariff, based on the newly implemented time-sharing tariff for industrial loads in Tianjin power grid from October 5, 2020, in which 8:00–15:00 and 18:00–23:00 are peak periods with a tariff of 1.072 RMB yuan, 7:00–8:00 and 11:00–18:00 are flat periods with a tariff of 0.6836 RMB yuan, and 23:00–7:00 are valley periods with a tariff of 0.4042 RMB yuan.

The unit capacity cost of the BESS equipment is 2.5 million RMB yuan/MWh. The power cost is one million RMB yuan/MW. The operation and maintenance cost as a percentage of investment cost is 0.37%, and the availability of the BESS equipment is 95%.

The load, PV, and wind power curves for a typical day in a certain area are shown in **Figure 4**.

Flexibility Improvement Benefit for Peak Dispatching

Flexibility Improvement Results

The peak load moment is 19:00, and the line capacity flexibility index with or without BESS is analyzed comparatively, as shown in **Figure 5**. It can be seen that the line capacity flexibility is not enough without BESS, but after adding BESS, the line capacity and margin flexibility is greatly improved. The voltage change is

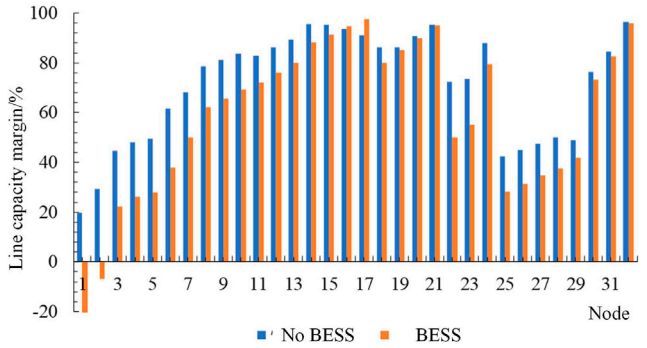

FIGURE 5 | Line capacity margin.

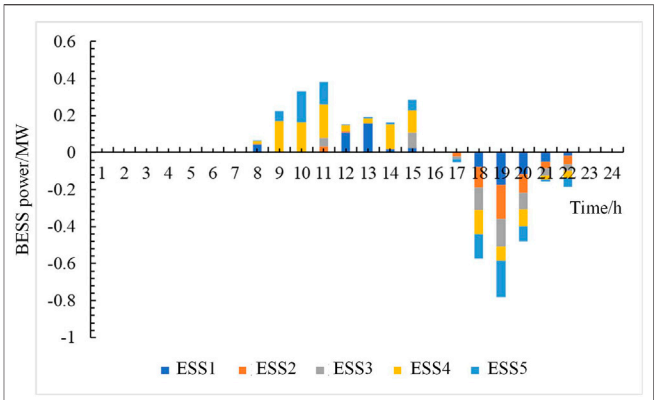

FIGURE 7 | Optimization scheduling results of Scenario 1.

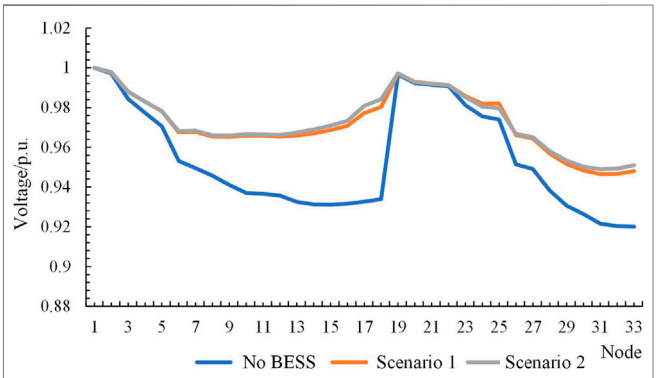

FIGURE 6 | Node voltage of the system.

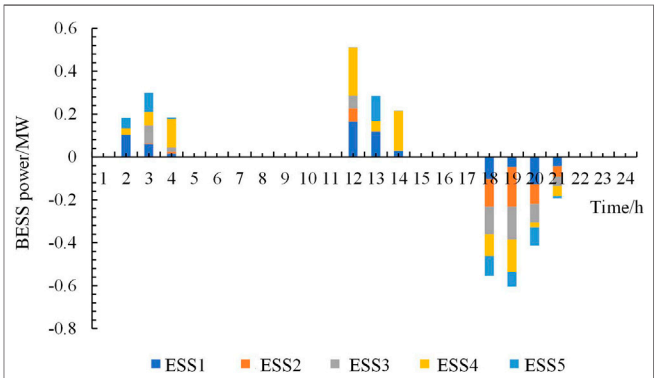

FIGURE 8 | Optimization scheduling results of Scenario 2.

TABLE 1 | Charging and discharging results of BESS in Scenario 2 and Scenario 3.

Hour	Scenario 2 (kWh)					Scenario 3 (kWh)				
	ESS1	ESS2	ESS3	ESS4	ESS5	ESS1	ESS2	ESS3	ESS4	ESS5
0	0	0	0	0	0	0	0	0	0	0
1	0	0	0	0	0	102.7	0.648	0.374	29.65	48.58
2	0	0	0	0	0	59.92	3.01	84.06	62.56	89.88
3	0	0	0	0	0	15.24	9.28	19.76	13.25	7.38
4	0	0	0	0	0	0	0	0	0	0
5	0	0	0	0	0	0	0	0	0	0
6	0	0	0	0	0	0	0	0	0	0
7	0	0	0	0	0	0	0	0	0	0
8	45.91	0.71	0	16.3	2.59	0	0	0	0	0
9	5.71	0.11	0.15	164.5	54.22	0	0	0	0	0
10	0.14	0.57	0	163.69	166.3	0	0	0	0	0
11	0.27	32.31	48.47	177.2	124.2	164.5	62.19	60.02	224.45	0
12	108.26	9.2	0.64	31.24	0	117.8	2.003	0	48.23	117.4
13	158.4	0	0	25.47	8.56	28.1	1.26	1.3	184.99	0.27
14	20.28	0.6	0	133.01	7.424	0	0	0	0	0
15	26.51	0.634	81.23	119.59	56.56	0	0	0	0	0
16	0	0	0	0	0	0	0	0	0	0
17	0	−19.04	−17.09	0	−16.13	−102.8	−129.0	−129.0	−100.6	−92.9
18	−76.05	−113.9	−122.7	−127.2	−133.4	−46.3	−184.9	−154.5	−150.2	−68.3
19	−174.4	−184.8	−151.0	−75.58	−195.1	−127.9	−91.1	−87.6	−21.2	−86.6
20	−118.1	−98.95	−91.19	−90.75	−80.8	−42.5	−49.98	−43.78	−46.22	−10.63
21	−49.07	−34.81	−39.34	−21.96	−10.84	0	0	0	0	0
22	−17.64	−46.71	−33.32	−42.27	−45.21	0	0	0	0	0
23	0	0	0	0	0	0	0	0	0	0

TABLE 2 | Benefit for peak dispatching.

Third party independent entities	Resource types at load side	Benefit for peak dispatching (RMB yuan/day)	Power for peak dispatching (kWh)
The whole system	Scenario 2	32.052 (without government subsidies)	4018.126
	Scenario 3	932.2676 (without government subsidies)	2779.06

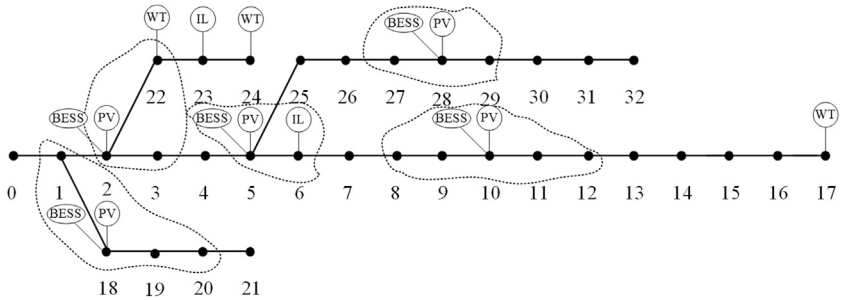

FIGURE 9 | Islanding division result.

TABLE 3 | Peak and valley tariffs for different load types in the Tianjin power grid.

Load classification	Voltage rating	Price to household			
		Spike	Peak	Flat	Valley
Large industry	Less than 1kV	1.072	0.977	0.6836	0.4042
	1–10 kV	1.0413	0.9491	0.6636	0.3961
General commercial and other	Less than 1 kV	—	1.0426	0.6768	0.3923
	1–10 kV	—	0.9441	0.6586	0.3891
Agricultural production	Less than 1 kV	—	0.8580	0.5860	0.3310
	1–10 kV	—	0.8355	0.5710	0.3235
Residential	Less than 1 kV	—	—	0.4900	0.5400
	1–10 kV	—	—	0.4800	0.5300

shown in **Figure 6**, and the voltage is also significantly improved after the BESS is added.

Flexible Resource Optimization Scheduling Results

Due to the integration of PV and wind power, the peak and valley moments of the net load have been changed. Scenario one only takes into account the actual net load changes without considering the time-sharing tariff of peak and valley. From **Figure 7**, it can be seen that the optimal scheduling results for scenario one are only for the net load cut. The optimized scheduling for Scenario 2 results in partial BESS being discharged and recharged at peak and valley times is shown in **Figure 8**, in addition to charging at the valley time when electricity prices are low. **Table 1** shows the specific charging and discharging results of BESS in Scenarios 2 and 3. From **Table 2**, it can be seen that the returns for Scenario 3 are much higher than those for Scenario 2.

Through the above analysis, the line capacity flexibility index and the flexible adaptability index of voltage deviation are improved to different degrees by the optimal scheduling of BESS using flexibility resources. The flexibility of line capacity margin without adding BESS is not as high as the system flexibility after adding BESS. After adding BESS, the line overload is eliminated, the flexibility of other line capacity margins is also improved to some extent, and the system voltage deviation is significantly improved. The different charging and discharging time of BESS makes the flexibility improvement benefit different, and the charging and discharging of BESS change according to the peak-valley tariff and the actual peak-valley difference of the power grid can improve the economy more.

Reliability Improvement Benefit

In this paper, we simulated the outage loss reduction for a certain BESS capacity and charge/discharge power based on the SOC distribution of BESS obtained from the flexible BESS optimization scheduling results, and analyze the reliability benefits of BESS. The results of islanding are shown in **Figure 9**, which shows that the BESS maximizes the power supply to the outage load nearby, improves the reliability of the system's power supply, and increases the power margin of the user side load. The average outage cost per unit of power lost during load point outages is determined by the load type, outage duration, and the value of electricity per kWh in the national economy.

Considering the different peak and valley time-sharing tariffs for load types, the load types include large industry, general commercial and other, agricultural production, and residential. The peak-valley time-sharing tariffs for the Tianjin power grid are shown in **Table 3**.

The system has a total of 32 lines and 31 load points with four load types: residential, commercial, agricultural, and industrial

TABLE 4 | Benefit for reliability improvement.

Third party independent entities	Resource types at load side	Benefit for reliability improvement (RMB yuan)	Power for reliability improvement (kWh)
The whole system	BESS	1,759,300	36,500

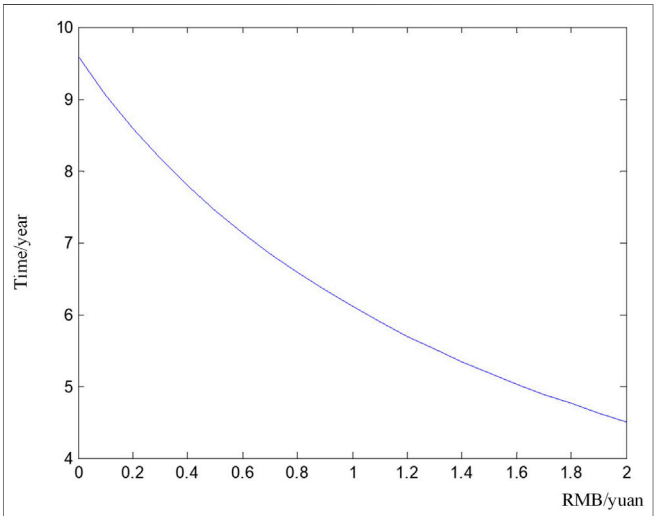

FIGURE 10 | DPP of BESS for government subsidy price changes.

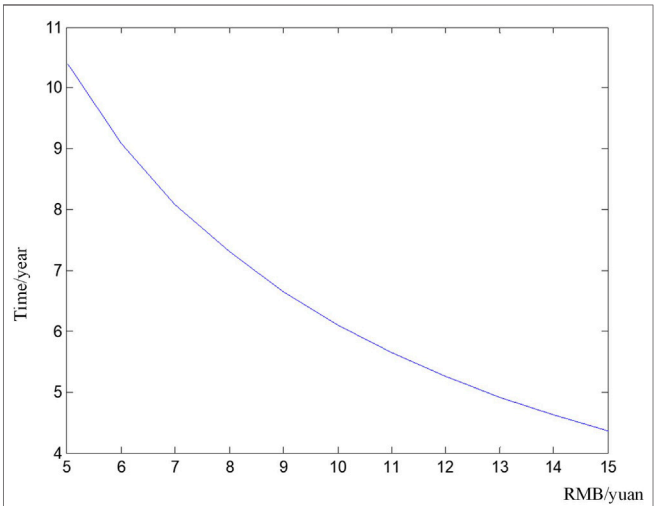

FIGURE 11 | Dynamic payback period for BESS in the face of changes in national electricity production.

loads. The BESS availability rate is taken as 95% and the Monte Carlo simulation sample size is taken as 20,000. The fault rate and average fault duration of each load point are calculated to obtain the annual average outage time. The fault rate of the line is 0.065, the fault rate of the transformer is 0.015, the fault rate of the breaker is 0.006, the repair time of the line is 5, the repair time of the transformer is 200, and the repair time of the breaker is 4. The average user outage time before adding BESS is calculated from the current grid data, and the average user outage time after adding BESS is calculated from the results of BESS islanding division and distribution network data. Further power for reliability improvement is calculated. The specific national economy generates industrial output per kWh of electricity reference. The reliability gains are 3–5 times the output value per kWh of electricity in the national economy. The reliability improvement gains are shown in **Table 4**.

Economic Evaluation Results

The NPV and DPP of a BESS project are analyzed based on the established economic model that considers flexibility gains and reliability improvement gains. Additionally, add a government subsidy factor to the flexibility gains and an electricity value factor to the reliability gains. The discount rate i is 10%. The formula for calculating the subsidy amount is as follows.

Subsidy amount (RMB yuan) = Average discharge power (kW) × Time (1–4 h) × Government subsidy factor (RMB yuan/kWh) + 0.5 × (Average discharge power (kW) ×Time (5–6 h) ×Government subsidy factor (RMB yuan/kWh))

Figure 10 analyzes the dynamic payback period in the subsidized price range of 0–2 RMB yuan/kWh for BESS discharges, with the DPP decreasing significantly as the subsidized price increases.

The range of national economic value of electricity is 5–15 RMB yuan/kWh with a DPP as shown in **Figure 11**. The larger the reliability gain, the shorter the DPP, considering the national economic electricity value of different industries. BESS can significantly improve system reliability gains.

From the above analysis, we can see that government price subsidies, feed-in tariffs, and the value of electricity production in the national economy are all important factors that influence the DPP of users.

Incentive Policy Suggestions for BESS Development

Improve the Electric Ancillary Services Market

An improved electric ancillary services market is advocated.

To reflect the benefits of BESS on the flexibility improvement of distribution network, it is recommended that the design takes into account not only the peak-valley price but also the flexibility price for peak dispatching.

Considering the value of BESS on reliability improvement, it is recommended that reliability price be designed so that BESS is encouraged to be deployed to support power grid operation and improve power supply performance. The reliability benefit evaluation of BESS to the grid should consider the influence of the value of electricity in the national economy.

Improve BESS Subsidy Programs

For low carbon goal achievement, more and more renewable energies are sometimes encouraged by financial subsidies. However, because of the intermittence and randomness characteristics of renewable energy resources, they bring more and more challenges to power grid operation. The frequency and voltage regulations need to be supported by traditional power plants, which contradict renewable energy requirements. In these situations, large-scale BES can be applied to regulate the frequency and voltage.

Subsidize large-scale BESS will help phase out less-efficient and high-pollution power plants. Power plant owners are encouraged to replace lost capacity with BESS or other clean energy sources. Reasonable government subsidies can accelerate the dynamic payback period of BESS and facilitate the rapid development of BESS projects.

Since the price of BESS is reducing, future policy should consider the impact of reducing the price of BESS. A decline in these costs will eventually make the BESS economically available without any subsidies. To promote the rapid development of BESS on a large scale, a detailed subsidy mechanism at multiple-stages that aims to reduce costs should be integral to its deployment. Establishing a BESS subsidy platform or launching an app to apply for subsidies could put this into practice, which could facilitate the simplification of subsidy procedures, visualization of subsidy programs, and diversification of compensation methods.

Improve BESS Investment Management Systems

It is suggested that investors and interested parties of BESS, and investment management structures be established. These would be responsible for managing investment in and the operation of BESS. This would also contribute to adjusting policy and the regulatory system for BESS as well as developing a licensing system.

BESS + diversified business models, including community energy trading based on BESS, virtual power plants, and power sale packages based on BESS services, are needed. We suggest that a BESS network like the grid is built. The integration of BESS networks and the power grid will help promote the development of BESS and the optimal dispatch of the power grid with more accuracy and reliability.

CONCLUSION

This paper presents an economic evaluation of BESS, considering improvements to its flexibility and reliability. Corresponding incentive mechanism research is proposed to promote its deployment. We analyzed the impact of BESS on active distribution networks along with the impact of BESS on the flexibility and reliability of the distribution network, providing a reference basis for the value of BESS in the distribution network. The following main conclusions were drawn from this study:

(1) Detailed calculation flow of economic evaluation model for users of BESS considering NPV evaluation index and dynamic payback period evaluation index, which provides a reference for the evaluation of distributed BESS value.
(2) Stimulate the BESS auxiliary regulation to participate in grid flexibility improvement. Participation in the peaking market will not only recover costs and profits by using time-of-use tariffs, but also increase the revenue of BESS by participating in peaking, which will shorten the payback time and promote the further development of BESS.
(3) To promote the participation of BESS reliability gains, the reliability gains of BESS are closely related to the value of electricity production in the national economy: the larger the value of electricity production in the national economy, the more obvious the reliability gains of BESS.
(4) The economics and flexibility of BESS provide incentives that reduce investment pressure on investors and shorten the payback costs, increase returns, and promote the healthy and flexible development of the BESS market.

DATA AVAILABILITY STATEMENT

The original contributions presented in the study are included in the article/Supplementary Material, further inquiries can be directed to the corresponding author.

AUTHOR CONTRIBUTIONS

SC: methodology, formal analysis, validation, writing original draft, editing, and visualization. YL: data curation, resources, writing, review, and editing. All authors contributed to the article and approved the submitted version.

FUNDING

This work was Supported by State Key Laboratory of Reliability and Intelligence of Electrical Equipment (No. EERI_KF2020006), Hebei University of Technology, and the National Natural Science Foundation of China (NSFC 51361135704).

REFERENCES

Bitaraf, H., and Rahman, S. (2018). Reducing curtailed wind energy through energy storage and demand response. *IEEE. Trans. Sustain. Energ.* 9 (1), 228–236. doi:10.1109/tste.2017.2724546

Bruninx, K., Dvorkin, Y., Delarue, E., Pandzic, H., Dhaeseleer, W., and Kirschen, D. S. (2016). Coupling pumped hydro energy storage with unit commitment. *IEEE Trans. Sustain. Energ.* 7 (2), 786–796. doi:10.1109/tste.2015.2498555

Cleary, B., Duffy, A., O'Connor, A., Conlon, M., and Fthenakis, V. (2015). Assessing the economic benefits of compressed air energy storage for mitigating wind curtailment. *IEEE. Trans. Sustain. Energ.* 6 (3), 1021–1028. doi:10.1109/tste.2014.2376698

Fang, X., Hodge, B.-M., Bai, L., Cui, H., and Li, F. (2018). Mean-variance optimization-based energy storage scheduling considering day-ahead and real-time LMP uncertainties. *IEEE Trans. Power Syst.* 33 (6): 7292–7295. doi:10.1109/tpwrs.2018.2852951

Huang, B., and Wang, C. (2016). "Value assessment of energy storage to support large scale PV integration," in IEEE PES asia-pacific power and energy engineering conference (APPEEC). Xi'an, China (IEEE), 2131–2136.

Kuleshov, D., Peltoniemi, P., Kosonen, A., Nuutinen, P., Huoman, K., Lana, A., et al. (2019). Assessment of economic benefits of battery energy storage application for the PV-equipped households in Finland. *J. Eng.* 2019 (18), 4927–4931. doi:10.1049/joe.2018.9268

Lee, J., Jeong, S., Han, Y. H., and Park, B. J. (2011). Concept of cold energy storage for superconducting flywheel energy storage system. *IEEE Trans. Appl. Supercond.* 21 (3), 2221–2224. doi:10.1109/tasc.2010.2094177

Li, Z., Li, Y., Zhang, D., and Yu, J. (2018). Influence analysis of energy storage device on reliability of distribution network and its optimal allocation. *Power Syst. Technology*, 42 (11), 3676–3683. doi:10.13335/j.1000-3673.pst.2018.0723

Li, N., and Hedman, K. W. (2015). Economic assessment of energy storage in systems with high levels of renewable resources. *IEEE. Trans. Sustain. Energ.* 6 (3), 1103–1111. doi:10.1109/tste.2014.2329881

Lu, M., Chang, C., Lee, W., and Wang, L. (2009). Combining the wind power generation system with energy storage equipment. *IEEE Trans. Industry Appl.* 45 (6), 2109–2115. doi:10.1109/TIA.2009.2031937

Maghouli, P., Soroudi, A., and Keane, A. (2016). Robust computational framework for mid-term techno-economical assessment of energy storage. *IET. Gener. Transm. Dis* 10 (3), 822–831. doi:10.1049/iet-gtd.2015.0453

Mahmoodi, M., Shamsi, P., and Fahimi, B. (2015). Economic dispatch of a hybrid microgrid with distributed energy storage. *IEEE. Trans. Smart Grid* 6 (6), 2607–2614. doi:10.1109/tsg.2014.2384031

Ofgem (2017). Upgrading our energy system-smart systems and flexibility plan. Available at: https://assets.publishing.service.gov.uk/government/uploads/system/uploads/attachment_data/file/633442/upgrading-our-energy-system-july-2017.pdf.

Shao, C., Shahidehpour, M., Wang, X., Wang, X., and Wang, B. (2017). Integrated planning of electricity and natural gas transportation systems for enhancing the power grid resilience. *IEEE. Trans. Power Syst.* 32 (6), 4418–4429. doi:10.1109/tpwrs.2017.2672728

Shu, Z., and Jirutitijaroen, P. (2014). Optimal operation strategy of energy storage system for grid-connected wind power plnts. *IEEE Trans. Sustain. Energ.* 5 (1), 190–199. doi:10.1109/tste.2013.2278406

Xiao, Y., Wang, X., and Bie, Z. (2018). Review on electricity market towards high proportion of renewable energy. *Proc. CSEE* 38 (3), 663–674. doi:10.13334/j.0258-8013.pcsee.172424

Xu, Y., and Tong, L. (2017). Optimal operation and economic value of energy storage at consumer locations. *IEEE. Trans. Automat. Contr.* 62 (2), 792–807. doi:10.1109/tac.2016.2572046

Yan, N., Xing, Z. X., Li, W., and Zhang, B. (2016). Economic dispatch application of power system with energy storage systems. *IEEE. Trans. Appl. Supercond.* 26 (7), 1–5. doi:10.1109/tasc.2016.2598963

Yang, J., Zhang, N., Wang, Y., and Kang, C. (2018). Multi-energy system towards renewable energy accommodation: review and prospect. *Automation. Electric. Power. Syst.* 42 (4), 11–24. doi:10.7500/AEPS20171002004

Yang, H., Shen, W., Yu, Q., Lu, J., Jiang, Y., Ackom, E., et al. (2020). Coordinated demand response of rail transit load and energy storage system considering driving comfort. *CSEE J. Power Energ. Syst.* 6 (4), 749–759. doi:10.17775/CSEEJPES.2020.02590

You, S., Hu, J., Zong, Y, and Lin, J. (2016). Value assessment of hydrogen-based electrical energy storage in view of electricity spot market. *J. Mod. Power Syst. Clean. Energ.* 4 (4), 626–635. doi:10.1007/s40565-016-0246-z

Zhang, C., Cheng, H., Liu, L., Wang, Z., Lu, J., and Zhang, X. (2017). Adaptability index and evaluation method for power transmission network structure with integration of high-penetration renewable energy. *Automation. Electric Power Syst.* 41 (21), 55–61. doi:10.7500/AEPS20170615005

Zhang, Z., Zhang, Y., Zhang, Y., Huang, Q., and Lee, W.-J. (2018). Market-oriented optimal dispatching strategy for a wind farm with a multiple stage hybrid energy storage system. *Csee Jpes* 4 (4), 417–424. doi:10.17775/cseejpes.2018.00130

Conflict of Interest: The authors declare that the research was conducted in the absence of any commercial or financial relationships that could be construed as a potential conflict of interest.

frontiers in Energy Research

ORIGINAL RESEARCH
published: 30 March 2021
doi: 10.3389/fenrg.2021.646975

A Two-Stage Dispatching Method for Wind-Hydropower-Pumped Storage Integrated Power Systems

Shuai Hu[1], *Yue Xiang*[1]*, *Junyong Liu*[1], *Jianhua Li*[2] *and Chang Liu*[3]

[1]College of Electrical Engineering, Sichuan University, Chengdu, China, [2]Southwest Electric Power Design Institute Co., Ltd. of China Power Engineering Consulting Group, Chengdu, China, [3]State Grid Sichuan Electric Power Research Institute, Chengdu, China

With the fossil energy crisis and environmental pollution, wind energy and other renewable energy have been booming. However, the strong intermittence and volatility of wind power make difficult of its integration into grid. To solve this problem, this study proposes a complementary power generation model of wind-hydropower-pumped storage systems, which uses hydropower and pumped storage to adjust the fluctuation of wind power. How to consider the uncertainty and unpredictability of wind power output and make more reliable hydropower generation plan and pumped storage generation plan is the key problem to be solved in the grid with the high proportion of renewable energy. The martingale model of forecast evolution is used to describe the uncertainty evolution of wind power in different regions. According to the flexible load in the region, the flexibility index is used to quantify flexibility, and the transaction price is set to be proportional to flexibility. The two-stage framework of day-ahead and real-time dispatching model is then developed. In the day-ahead stage, different regions trade with each other. If the power after trading is imbalanced, it will be supplemented by hydropower and the grid to meet the power demand. In the real-time stage, the pumped storage is added to quickly balance the deviation of wind power and load between the real-time and day-ahead stages. Finally, considering the positive effect of hydropower on wind power consumption in the grid, a benefit allocation method based on improved Shapley value method is proposed. Test cases are simulated to verify the rationality of the proposed dispatching model and the benefit allocation method. After the cooperation of hydropower and pumped storage, the average revenue growth is 3.02%. The improved benefit allocation scheme makes more benefit of hydropower and pumped storage and promotes the cooperation of multi-participants.

Keywords: integrated energy system, uncertainty, martingale model, benefit allocation, flexible load

OPEN ACCESS

Edited by:
Hao Yu,
Tianjin University, China

Reviewed by:
Lv Chaoxian,
China University of Mining and Technology, China
Shenxi Zhang,
Shanghai Jiao Tong University, China

***Correspondence:**
Yue Xiang
xiang@scu.edu.cn

Specialty section:
This article was submitted to Smart Grids, a section of the journal Frontiers in Energy Research

Received: *28 December 2020*
Accepted: *08 February 2021*
Published: *30 March 2021*

Citation:
Hu S, Xiang Y, Liu J, Li J and Liu C (2021) A Two-Stage Dispatching Method for Wind-Hydropower-Pumped Storage Integrated Power Systems. Front. Energy Res. 9:646975. doi: 10.3389/fenrg.2021.646975

INTRODUCTION

With the transformation of the global energy structure, the installed capacity of renewable energy has been increasing steadily (Bird et al., 2016). According to forecasts by the International Energy Agency, the proportion of renewable energy in global electricity consumption should be up to 30% by 2023 (International Energy Agency, 2018). Grid-connected power generation of large-scale renewable energy, which is represented by solar and wind energy, has become an unstoppable

development trend of new power systems. However, the uncertainty of renewable energy would cause the curtailment of power and the fluctuation of output. The utilization of renewable energy is impeded severely, and the dispatching of the power system is also influenced greatly. Hydropower, which has a strong regulation capability, is usually used as an adjustable power supply to ensure a stable and smooth output (Zhang et al., 2019). The pumped storage has the advantage of flexible schedulability and the ability of fast start-up and shut-down (Javed et al., 2020). Therefore, the complementary power generation system, which coordinates wind power with hydropower and pumped storage, can efficiently solve problems caused by the uncertainty of renewable energy and is important for the stability and economy of wind-hydropower-pumped storage (WHPS) systems.

In recent years, the modeling and optimization of complementary power generation system between renewable energy and other power have been conducted in many studies, mainly including hydro-wind (Denault et al., 2009; Lopes and Borges, 2014; Bayon et al., 2016; Shayesteh et al., 2016), hydro-solar-wind (Schmidt et al., 2016; Liu et al., 2019; Zhang et al., 2019), hydro-wind-thermal (Zhou et al., 2016; Zhang et al., 2017), solar-wind- pumped storage (Jakub et al., 2018; Xu et al., 2019), and wind-solar-storage (Lee and Wang, 2008; Lasemi and Arabkoohsar, 2020). The main idea is to combine renewable energy with hydropower and other flexible power and then improve the power grid's ability to consume renewable energy and schedulability. Gebretsadik et al. (Gebretsadik et al., 2016) proposed an operation model of wind power and hydropower to maximize the generation of integrated wind and hydropower. Li et al. (Li and Qiu, 2016) used hydropower to compensate for photovoltaic power as the great adjustable capability of hydropower. Panda et al. (Panda et al., 2017) developed a combined operation model of hydro-thermal-wind, and its optimal generation schedule is determined by a different algorithm. Biswas et al. (Biswas et al., 2018) proposed the optimization method of stochastic wind, solar, and small hydropower, considering intermittent and uncertain of renewable sources. Reddy et al. (Reddy, 2017) solved an optimal scheduling problem of the hybrid power system, concluding thermal generators, wind power, and solar power with batteries. Wang et al. (Wang et al., 2017) proposed the coordinated operation of the hydro-wind-photovoltaic system to overcome the bottleneck of new energy development.

Although these studies have researched the complementary operations of multi-power systems, the wind power uncertainties, which have made challenges of its large integration in the power system, still need to be considered thoroughly. Some researchers have investigated the uncertainty of wind power and emphasize the influence of wind power uncertainties on dispatching. Shahriari et al. (Shahriari et al., 2020) used the probabilistic method for wind power forecasting, which could quantify the uncertainty associated with wind forecast rather than deterministic forecast; probabilistic forecast is critical for users and dispatchers to make informed decisions. Zhang et al. (Zhang et al., 2014) verified that wind power forecast involves inherent uncertainty because of chaotic climatic and weather conditions, and probabilistic forecast is critical in the uncertainty atmospheric environment. Turk et al. (Turk et al., 2020) introduced that high level of uncertainty and fluctuation of renewable energy sources exist and proposed the scenario generation algorithm with corresponding probabilities to improve the utilization of wind energy. Li et al. (Li et al., 2020) discussed and classified the scenario generation method to address the uncertainties of energy systems with integrated wind power. In the above studies, the ways to describe the uncertainty of renewable energy can be classified as probabilistic forecasting, scenario generation, and uncertainty description by conditional value at risk. These methods usually assume that the error is fixed in a certain period. However, the weather system is dynamic and unstable, and wind power output is closely related to wind speed, temperature, wind direction, and other meteorological factors. The dynamic uncertainty of wind power should be updated as the forecast lead-time gradually increases. In current studies, only a few studies have considered the evolution of renewable energy uncertainty, which would have a certain impact on the dispatching results of multi-power systems.

In addition to the above problems, the complementary operation of wind power and hydropower can complement the output fluctuation caused by the uncertainty and improve the utilization of wind power. However, it may affect the hydropower adversely because of some reasons (e.g., the release of ecological water to the downstream river channel) and influence its ability of peaking capability. When wind power output is large, the hydropower generation would be reduced, and the possibility of hydroelectric spillage would be increased to ensure minimum ecological water delivery. The revenue of hydropower may be reduced through complementary operations. Therefore, how to make a reasonable allocation of benefit and stimulate the enthusiasm of hydropower to cooperation with wind power remains to be studied. Based on the basic principles of income distribution, the Shapley theory was developed by Shapley in 1953 (Liggett and Rumelt, 2009). In terms of benefit allocation between different units, some studies have been conducted. Shen et al. (Shen et al., 2018) allocated the appropriate benefit of multiple-reservoir cascaded hydropower plants by the game-theoretic Shapley method. Tan et al. (Tan et al., 2013) used the Shapley method to study the benefit allocation of wind power and thermal power; the result showed that the method realized the equitable allocation among the units fully. Wu et al. (Wu et al., 2019) proposed a benefit allocation mechanism based on Shapley value and nucleolus solution, and the corresponding effectiveness and applicability were proven. Kristiansen et al. (Kristiansen et al., 2018) used the Shapley value to access the benefits of fast-ramping gas turbine and hydropower, and the insights for energy policy designs could be gained through this way. However, the traditional Shapley method has some disadvantages. All stakeholders are assumed to have equal risks and status. Thus, the traditional Shapley value method should be improved according to the specific projects.

This study proposes a two-stage coordinated operation model of the WHPS system. Each of the three regions consists of wind power and flexible load. They trade with one another first. If there exist power shortage, the power can be provided from the hydropower or the grid; If there exist excess power, they can be sold to the grid in the day-ahead stage. In the real-time stage, considering the deviation of wind power and load between the real-time and day-ahead stages, the pumped storage, which can start and stop quickly, is used to balance the deviation. The main contributions of this study include the following:

Considering the constant updates and the evolution of wind power forecasting, the martingale model of forecast evolution (MMFE) is used to describe the evolution process of wind power forecasting uncertainty, and the synthetic ensemble forecasts are generated.
In the day-ahead stage, after regions trade with one another, if no balance is achieved, power is purchased or sold from hydropower or grid. In the real-time stage, the forecasting deviation of wind power and load between real-time and day-ahead is balanced by the pumped storage. The output fluctuation to the grid can be mitigated.
Considering the risk and cost factors of different members, the improved Shapley value method, which has a practical significance, is proposed to consider the characteristics of different participants fully and ensure their reasonable benefit allocation.

The rest of this paper is organized as follows. *Martingale Model of Wind Power Forecasting. Coordinated Operation Model of the WHPS System. Benefit Allocation Model by the Improved Shapley Value Method. Solution Method. Case Study* and compares the *Benefit Allocation of the Traditional Shapley Method and the Improved Shapley Method*. Finally, *Conclusion* concludes the paper.

MARTINGALE MODEL OF WIND POWER FORECASTING EVALUATION

The description of the forecast uncertainty of wind speed over time is vital for power grid dispatching. However, only a few methods can illustrate the evolution process of forecasting uncertainty. In this section, the MMFE is established for the evolution of the uncertainty of wind power forecasting over time. The MMFE was first proposed to simulate the uncertainty of supply chain demand forecasting (Heath and Jackson, 1994). This method is simple and effective; the mean value and covariance are used and are not invariant as traditional scene generation methods; the time-variation of wind power forecasting uncertainty is considered (Zhao et al., 2011).

Uncertainty of Wind Power Forecast

As time progresses, the forecasting information of wind power will be updated constantly. H is defined as the forecasting horizon, and $P_{w,t}^{\text{wind}}$ is defined as the forecasting value for wind power at time t, which is made at time w $(t = ws + 0, ws + 1, \cdots, ws + H)$. P_t^{wind} identifies the actual value of wind power, and $e_{w,t}$ denotes the forecasting error, which can be interpreted by **Eq. 1**.

$$e_{w,t} = P_{w,t}^{wind} - P_t^{wind} \tag{1}$$

The sequence of forecasting value with the forecasting horizon ranges from 0 to H, and the corresponding error made at time w can be expressed as follows:

$$P_{w,-}^{\text{wind}} = \left[P_{w,w}^{\text{wind}}, P_{w,w+1}^{\text{wind}}, \cdots, P_{w,w+H}^{\text{wind}}\right] \tag{2}$$

$$e_{w,-} = \left[e_{w,w}, e_{w,w+1}, \cdots, e_{w,w+H}\right] \tag{3}$$

Similarly, the wind power value of time t can be forecasted in the previous period. The sequence and the corresponding error are expressed as follows:

$$P_{-,t}^{\text{wind}} = \left[P_{t-H,t}^{\text{wind}}, P_{t-H+1,t}^{\text{wind}}, \cdots, P_{t,t}^{\text{wind}}\right] \tag{4}$$

$$e_{-,t} = \left[e_{t-H,t}, e_{t-H+1,t}, \cdots, e_{t,t}\right] \tag{5}$$

The improvement of forecasting value is defined as the difference of forecasting error between two adjacent time $w-1$ and w is expressed as follows:

$$u_{w,t} = e_{w,t} - e_{w-1,t} \tag{6}$$

Assuming that the current wind power forecasting value is accurate ($e_{t,t} = 0$), based on **Eqs. 4–6**, the following equation can be obtained.

$$\begin{cases} e_{t-1,t} = e_{t,t} - u_{t,t} = -u_{t,t} \\ e_{t-2,t} = e_{t-1,t} - u_{t-1,t} = -u_{t,t} - u_{t-1,t} \\ \cdots \\ e_{t-H,t} = -\sum_{i=1}^{H} u_{t-H+i,t} \end{cases} \tag{7}$$

Based on **Eqs. 1Eqs. 7** the forecasting value $P_{t,t}^{\text{wind}}$ can be expressed by the actual value and the improvement value, which is shown as follows:

$$\begin{cases} P_{t,t}^{\text{wind}} = P_t^{\text{wind}} \\ P_{t-1,t}^{\text{wind}} = P_t^{\text{wind}} - u_{t,t} \\ P_{t-2,t}^{\text{wind}} = P_t^{\text{wind}} - u_{t,t} - u_{t-1,t} \\ \cdots \\ P_{t-H+1,t}^{\text{wind}} = P_t^{\text{wind}} - \sum_{i=1}^{H-2} u_{t-i+1,t} \\ P_{t-HL,t}^{\text{wind}} = P_t^{\text{wind}} - \sum_{i=1}^{HL-1} u_{t-i,t} \end{cases} \tag{8}$$

The above formula can be transformed into the following equation:

$$\begin{cases} P_{t,t}^{\text{wind}} = P_{t-1,t}^{\text{wind}} + u_{t,t} \\ P_{t-1,t}^{\text{wind}} = P_{t-2,t}^{\text{wind}} + u_{t-1,t} \\ \cdots \\ P_{t-H+1,t}^{\text{wind}} = P_{t-H,t}^{\text{wind}} + u_{t-H+1,t} \end{cases} \tag{9}$$

Eq. 9 shows that, as time progresses from $t-H$ to t, the forecasting value $P_{w,t}^{\text{wind}}$ will update constantly as $u_{w,t}$ updates.

The MMFE

In the MMFE, the forecasting improvement value $u_{w,w+i-1}$ $(i = 1, 2, \cdots, H)$ can be expressed as follows:

$$U_{w,-} = \left[u_{w,w}, u_{w,w+1}, \cdots, u_{w,w+H-1}\right] \tag{10}$$

In the MMFE model, $U_{w,-}$ describes the uncertainty of wind power with four kinds of assumptions (Heath and Jackson, 1994): 1) The mean value of $u_{w,w+i-1}$ is zero (i.e., unbiased assumption), 2) $u_{w,w+i-1}$ obeys normal distribution (i.e., Gaussian distribution), 3) $u_{w1,w+i-1}$ is independent with $u_{w2,w+i-1}$ (i.e., temporal independence assumption), and 4) the distribution of $u_{w,w+i-1}$ does not change over time (i.e., stationarity assumption). On the basis of the above assumptions, the MMFE model can be expressed using the variance-covariance (VCV) matrix as follows:

$$VCV = \begin{bmatrix} \mathrm{var}_1 & \mathrm{cov}_{1,2} \cdots & \mathrm{cov}_{1,H} \\ \mathrm{cov}_{2,1} & \mathrm{var}_2 \cdots & \mathrm{cov}_{2,H} \\ \vdots & \vdots \ddots & \vdots \\ \mathrm{cov}_{H,1} & \mathrm{cov}_{H,2} \cdots & \mathrm{var}_H \end{bmatrix} \tag{11}$$

Given that VCV is a positive semi-definite matrix, it can be decomposed into the product of matrix V and its transpose by Cholesky decomposition (i.e., $VCV = V \times V^T$). The vector $U_{w,-}$ can be expressed through a mathematical transformation as follows:

$$[u_1\, u_2 \cdots u_H] = [x_1\, x_2 \cdots x_H] V^T \tag{12}$$

where $x_i\,(i = 1, 2, \cdots, H)$ is the independent random variable with the same standard normal distribution, VCV is the variance-covariance matrix of vector $U_{w,-}$, var_i is the variance of $u_{w,w+i-1}$, and $\mathrm{cov}_{i,j}$ is the covariance between $u_{w,w+i-1}$ and $u_{w,w+j-1}$. After obtaining $x_1\, x_2 \cdots x_H$ and $U_{w,-}$, combined with **Eq. 9**, the wind power forecasting value can be generated synthetically.

COORDINATED OPERATION MODEL OF THE WIND-HYDROPOWER-PUMPED STORAGE SYSTEM

The multi-power system investigated in this study is composed of hydropower, wind power, and pumped storage. The relationship among different members is shown in **Figure 1**. The hydropower output is a wide range. The pumped storage has flexible schedulability. The hydropower and pumped storage can ensure the smooth and stable output curve when wind power is strongly uncertain. Wind power and flexible loads form a region, when wind power output is greater than the load, the net power in the region is positive, this region can be considered as power supply. When wind power output is less than the load, the net power generation is negative, this region can be considered as the load. Three regions trade with one another firstly. If no balance is achieved after trading, power is purchased or sold from hydropower and grid in the day-ahead stage. In the real-time stage, the deviation of wind power and the load between the real-time and day-ahead stages are considered. The pumped storage, which can start and stop quickly, is used to balance the deviation. The power shortage in the region can be supplemented effectively by the above method, and the grid's ability to wind power consumption would be improved.

Modeling of the Wind-Hydropower-Pumped Storage Complementary Power Generation System

(1) Modeling of the Hydropower Station

The hydropower station has flexible regulation performance. The output can be expressed as the product of a constant, the generation efficiency of hydropower station, the net head, and the average power generation flow of the corresponding period. The output model can be expressed as follows:

$$P_{\mathrm{hyd},i,t} = 0.00981 \eta_i H_{i,t} Q_{i,t}^{\mathrm{H}} \tag{13}$$

where $P_{\mathrm{hyd},i,t}$ is the output of hydropower station i at time t, $Q_{i,t}^{H}$ is the average power generation flow, $H_{i,t}$ is the net head, and η_i is the power generation efficiency of the hydropower station i.

(2) Transformational relationship of hydropower station

The storage capacity of cascade hydropower stations should consider interval water. The interval water of the reservoir contains the natural water, generation flow, and the abandoned water of the upstream reservoir. The relationship equation is as follows:

$$V_{i,t} = V_{i,t-1} + 3600\left(Q_{i,t}^{S} - Q_{i,t}^{H} - Q_{i,t}^{d}\right) \tag{14}$$

$$V_{i,0} = V_{i,\mathrm{T}} + \Delta V_i \tag{15}$$

$$Q_{i,t}^{S} = I_{i,t} + Q_{i-1,t}^{H} + Q_{i-1,t}^{d} \tag{16}$$

where $V_{i,t}$ is the storage capacity of the reservoir i at time t, $V_{i,t-1}$ is the storage capacity of the reservoir i at time $t-1$, $Q_{i,t}^{S}$ is the interval water of the reservoir at time t, $I_{i,t}$ is the volume of natural water, $V_{i,0}$ is the initial water level, $V_{i,\mathrm{T}}$ is the final water level of the reservoir i, ΔV_i is the variance of storage capacity, $Q_{i,t}^{d}$ is the volume of abandoned water, $Q_{i,t}^{H}$ is the volume of generation flow, and $Q_{i-1,t}^{d}$ and $Q_{i-1,t}^{H}$ are the volume of abandoned water and the generation flow of the upstream reservoir, respectively.

(3) Inequality constraint of hydropower station

The output, storage capacity, and flow of the hydropower station have upper and lower limit constraints:

$$P_{\mathrm{hyd},i}^{\min} \le P_{\mathrm{hyd},i,t} \le P_{\mathrm{hyd},i}^{\max} \tag{17}$$

$$V_{i,\min} \le V_{i,t} \le V_{i,\max} \tag{18}$$

$$Q_{i,\min}^{H} \le Q_{i,\mathrm{t}}^{H} \le Q_{i,\max}^{H} \tag{19}$$

where $P_{\mathrm{hyd},i}^{\min}$ and $P_{\mathrm{hyd},i}^{\max}$ are the minimum and maximum output of hydropower station i, respectively; $V_{i,\min}$ and $V_{i,\max}$ are the minimum and maximum storage capacity, respectively, and

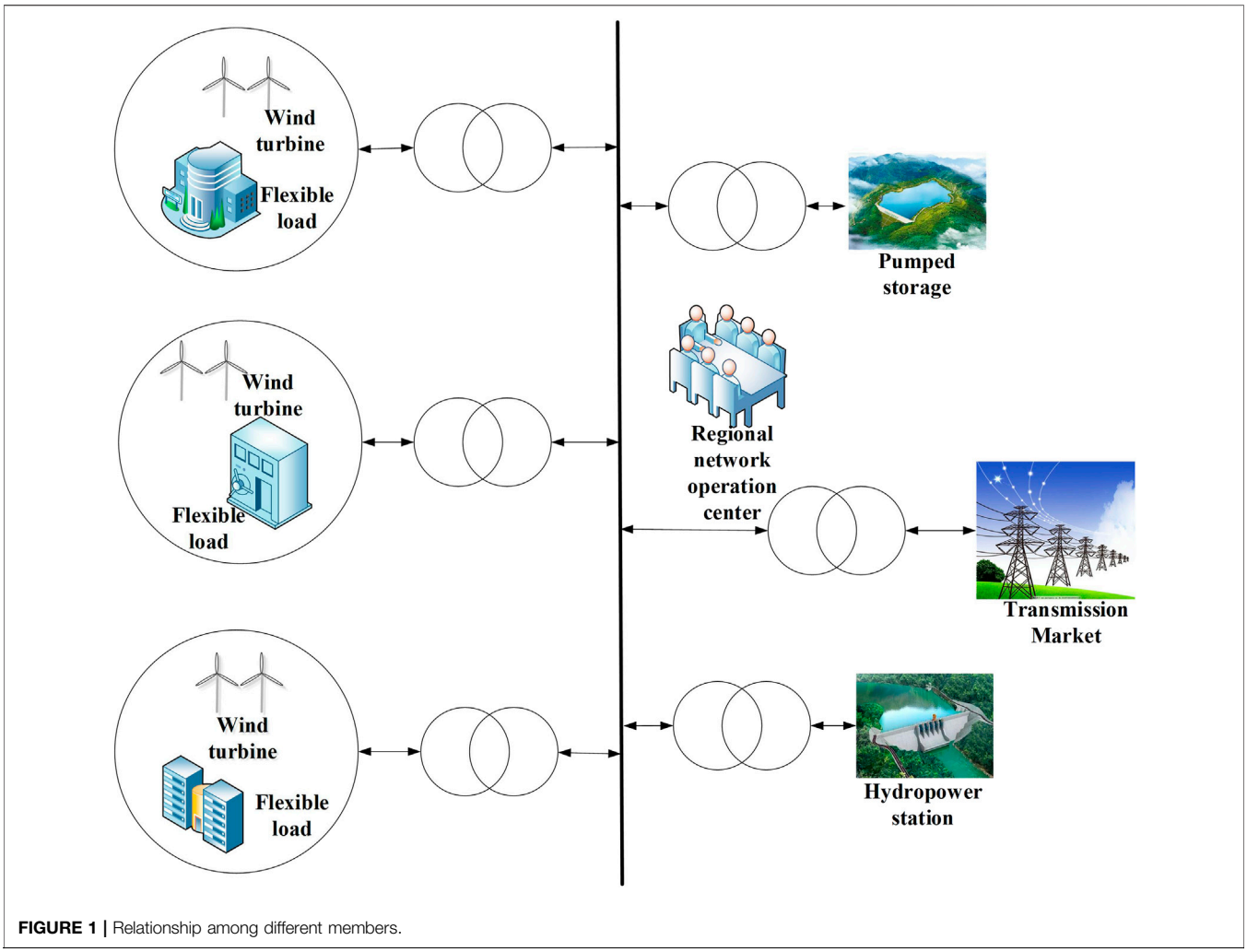

FIGURE 1 | Relationship among different members.

$Q^H_{i,\min}$ and $Q^H_{i,\max}$ are the minimum and maximum flow, respectively.

(4) Volume conversion constraints of pumped storage station

The pumped storage station can utilize the characteristics of power generation and pumping to realize the transfer of power generation and rapid regulation of the total output. The pumped storage station contains the upstream and downstream reservoirs, and their constraints are the same. Generally, only the upstream reservoir is constrained as follows:

$$V_{\mathrm{pm},k,t} = V_{\mathrm{pm},k,t-1} + \eta_{\mathrm{pm},k}\Delta t P_{\mathrm{pm},k,t} - \eta_{\mathrm{gn},k}\Delta t P_{\mathrm{gn},k,t} \tag{20}$$

where $V_{\mathrm{pm},k,t}$ is the volume of pumped storage i at time t; $V_{\mathrm{pm},k,t-1}$ is the volume of pumped storage i at time $t-1$; $\eta_{\mathrm{pm},k}$ and $\eta_{\mathrm{gn},k}$ are the power/water conversion coefficient at pumping and generation conditions, respectively; $P_{\mathrm{pm},k,t}$ and $P_{\mathrm{gn},k,t}$ are the pumping and generation power of the pumped storage station, respectively.

(5) Volume constraints of pumped storage station

The volume of the pumped storage station should be within a certain range, and it is the same at the beginning and end of the day. It can be expressed as follows:

$$V^{\min}_{\mathrm{pm},k} \le V_{\mathrm{pm},k,t} \le V^{\max}_{\mathrm{pm},k} \tag{21}$$

$$V_{\mathrm{pm},k,0} = V_{\mathrm{pm},k,\mathrm{T}} \tag{22}$$

where $V^{\max}_{\mathrm{pm},k}$ and $V^{\min}_{\mathrm{pm},k}$ are the maximum and minimum volume of the pumped storage, respectively, and $V_{\mathrm{pm},k,0}$ and $V_{\mathrm{pm},k,\mathrm{T}}$ are the initial and final volume of the pumped storage during the scheduling period, respectively.

(6) Working condition constraints of the pumped storage station

The working condition constraints of the pumped storage are generation and pumping, and the two kinds of condition never exist at the same time. The detailed constraint is as follows:

$$y_{\mathrm{pm},k,t} + y_{\mathrm{gn},k,t} \le 1 \;\; y_{\mathrm{pm},k,t}, y_{\mathrm{gn},k,t} \in \{0,1\} \tag{23}$$

When $y_{\mathrm{pm},k,t} = 1$, the pumped storage station is in the pumping condition. When $y_{\mathrm{gn},k,t} = 1$, the pumped storage station is in the generation condition. When $y_{\mathrm{pm},k,t} = y_{\mathrm{gn},k,t} = 0$, the pumped storage station is idle.

(7) Output constraints of pumped storage station

$$\begin{cases} y_{\mathrm{pm},k,t} P_{\mathrm{pm},k}^{\min} \le P_{\mathrm{pm},k,t} \le y_{\mathrm{pm},k,t} P_{\mathrm{pm},k}^{\max} \\ y_{\mathrm{gn},k,t} P_{\mathrm{gn},k}^{\min} \le P_{\mathrm{gn},k,t} \le y_{\mathrm{gn},k,t} P_{\mathrm{gn},k}^{\max} \end{cases} \tag{24}$$

where $P_{\mathrm{pm},k}^{\min}$ and $P_{\mathrm{pm},k}^{\max}$ are the minimum and maximum pumping power of pumped storage k, respectively, and $P_{\mathrm{gn},k}^{\min}$ and $P_{\mathrm{gn},k}^{\max}$ are the minimum and maximum generation power, respectively.

(8) Pumping/generation condition conversion downtime constraints

Generally, the continuous start and stop of pumped storage station is not carried out under pumping or generation conditions. For economic reasons, the pumped storage should be shut down for at least 1 h. The corresponding constraint is as follows:

$$\begin{cases} y_{\mathrm{pm},k,t} + y_{\mathrm{gn},k,t+1} \le 1 \quad t = 1, 2, \cdots, T-1 \\ y_{\mathrm{pm},k,t+1} + y_{\mathrm{gn},k,t} \le 1 \quad t = 1, 2, \cdots, T-1 \end{cases} \tag{25}$$

(9) Constraints of load in a region

$$P_{i,t}^{\mathrm{da,load,min}} \le P_{i,t}^{\mathrm{da,load}} \le P_{i,t}^{\mathrm{da,load,max}} \tag{26}$$

where $P_{i,t}^{da,load,\min}$ is the minimum value of load and $P_{i,t}^{da,load,\max}$ is the maximum value of the load.

(10) Constraints of tie line's volatility ratio

$$\frac{\left|P_{\mathrm{grid},t} - P_{\mathrm{grid},t-1}\right|}{P_{\mathrm{grid},t}^{\max}} \le K_{\mathrm{grid}}^{\max} \tag{27}$$

$$P_{\mathrm{grid},t} = P_{\mathrm{hyd},t} + P_t \tag{28}$$

$$P_t = \sum_{i=1}^{I} \left(P_{i,t}^{\mathrm{wind}} - P_{i,t}^{\mathrm{load}} \right) \tag{29}$$

where $P_t^{ch} = P_{grid,t}^{da} + P_{mar,t}^{re}$, $P_{grid,t}$ is the trading power with the grid at time t, $P_{\mathrm{grid},t-1}$ is the trading power with the grid at time $t-1$, $P_{\mathrm{grid},t}^{\max}$ is the maximum value of trading power with the grid, $K_{\mathrm{grid}}^{\max}$ is the tie line's volatility ratio, $P_{\mathrm{hyd},t}$ is the generation power of hydropower, and P_t is the net power of regions. The smaller the value of $K_{\mathrm{grid}}^{\max}$, the better the complementary effect of the complementary power generation system.

Objective Function

(1) Day-ahead stage

The coordinate operation of WHPS system uses multi-source complementary characteristics fully. Each kind of power supply is encouraged to play its role, and the goal of the economy and the stability of system operation are realized. In the day-ahead stage, considering the large peak regulation capacity and strong regulation capacity of the cascade hydropower stations, its joint operation with wind power is an effective way to solve large-scale wind power consumption. The power generation in the region meets the load in the region. If the power generation and load are unbalanced, different regions would trade with each other. After that, if power is redundant, the power is sold to the grid. If a power shortage is still experienced, the hydropower and grid can provide power. The specific objective of the economic operation is to minimize the generation cost in the dispatching period. The corresponding day-ahead objective function is as follows:

$$\begin{aligned} \max R_{V,t} = {} & \chi_{1,t} C_{1,t} P_{1,t} + \chi_{2,t} C_{2,t} P_{2,t} + \chi_{3,t} C_{3,t} P_{3,t} \\ & + \chi_{grid,t} C_{grid,t} P_{grid,t} + C_{hyd,t} P_{hyd,t} + C_{hyd,t}^{d} \end{aligned} \tag{30}$$

where $\chi_{i,t}$ is the state variable of region i. When redundant power exists in this region, the state variable is 1. When it is short of power, the state variable is 0. $C_{i,t}$ is the bidding price of region i, $P_{i,t}$ is the purchase or sale power of region i, $\chi_{grid,t}$ is the state variable of grid, $C_{grid,t}$ is the power price in the day-ahead stage, $P_{grid,t}$ is the purchase or sale of power of the grid, $C_{hyd,t}$ is the price of hydropower, $P_{hyd,t}$ is the output of hydropower, and $C_{hyd,t}^{d}$ is the cost of abandoned water. According to the understanding of its load regulation ability, each flexible load can predict the lower and upper limits of its total load in a certain period in the future, the minimum value of the load is express as $P_{i,t}^{da,load,\min}$, and the maximum value of the load is expressed as $P_{i,t}^{da,load,\max}$. The flexible load needs to report its load range $[P_{i,t}^{da,load,\min}, P_{i,t}^{da,load,\max}]$ to the stage organizer. $P_{i,t}^{da,load,\max} - P_{i,t}^{da,load,\min}$ represents the fluctuation of power that the load can bear. The flexibility indicator of the load is defined as follows:

$$\kappa_{i,t} = \frac{P_{i,t}^{\max} - P_{i,t}^{\min}}{P_{i,t}^{\max} + P_{i,t}^{\min}} \tag{31}$$

The net power generation or the load of region i as power supply or load is as follows:

$$P_{i,t}^{\mathrm{da}} = P_{i,t}^{\mathrm{da,wind}} - P_{i,t}^{\mathrm{da,load}} \tag{32}$$

where $P_{i,t}^{da,wind}$ is the wind power output of region i at time t and $P_{i,t}^{da,load}$ is the load of region i at time t. If $P_{i,t}^{da,wind} > P_{i,t}^{da,load}$, region i is the power supply. The bidding of each region is related to its flexibility. The higher the flexibility, the higher the bidding. The equation is $C_{i,t} = (1 + \kappa_{i,t})\lambda_{i,t}$, where $\lambda_{i,t}$ is the basic price. If $P_{i,t}^{da,wind} < P_{i,t}^{da,load}$, region i is the load. The higher the flexibility, the lower the bidding. The corresponding equation is $C_{i,t} = (1 - \kappa_{i,t})\lambda_{i,t}$. To reflect the relationship between regional flexibility and the final transaction price, the final transaction price is the data after the bidding and market clearing price are processed in proportion. The transaction price further reflects the flexibility of each region.

(2) Real-time stage

In the real-time stage, the pumped-storage, which is as a flexible power, can operate jointly with multiple regions containing wind farms to smooth the deviations of wind power and load between day-ahead and real-time stages. The optimization model is to optimize the trading power of pumped storage, grid, and three regions simultaneously. The optimization strategy considers the spot price, the start-up and shutdown cost of pumped storage, and other factors. The objective shown as follows minimizes the total operation cost of the system.

$$\max R^{re} = \sum_{t=1}^{T} R^{re}_{mar,t} - \sum_{t=1}^{T} C_{\mathrm{pm,t}} \tag{33}$$

where R_{re} is the net revenue in the real-time stage, $R^{re}_{mar,t}$ is the revenue from selling to the grid, $C_{\mathrm{pm,t}}$ is the cost of pumped storage.

Although the pumped storage unit starts and stops quickly, the working condition can be adjusted flexibly. However, physical loss will be caused in the process of frequent start-up and shutdown. The cost of pumped storage contains the start-up cost of generation and pumping and can be expressed as follows:

$$C_{\mathrm{pm}} = \sum_{t=1}^{T} \sum_{k=1}^{n_k} \left(C_{\mathrm{pm},k,t} + C_{\mathrm{gn},k,t} \right) \tag{34}$$

where $C_{\mathrm{pm},k,t}$ is the start-up/shut-down cost of pumping and $C_{\mathrm{gn},k,t}$ is the start-up/shut-down cost of generation. The revenue that sold to the grid can be expressed as follows:

$$R^{re}_{mar,t} = \sum_{t=1}^{T} P^{re}_{mar,t} \lambda^{re}_{t} \tag{35}$$

$$P^{\mathrm{re}}_{\mathrm{mar},t} = \sum_{i=1}^{I} \left(P^{\mathrm{re}}_{i,t} - P^{\mathrm{da}}_{i,t} \right) + \sum_{k}^{K} \left(P^{\mathrm{gn}}_{k,t} - P^{\mathrm{pum}}_{k,t} \right) \tag{36}$$

$$P^{\mathrm{re}}_{i,t} = P^{\mathrm{re,wind}}_{i,t} - P^{\mathrm{re,load}}_{i,t} \tag{37}$$

where $P^{re}_{mar,t}$ is the power sold to the grid in the real-time stage, λ^{re}_{t} is spot price at time t, $P^{da}_{i,t}$ is the net power in the day-ahead stage, $P^{re}_{i,t}$ is the net power in the real-time stage, $P^{gn}_{k,t}$ is the power generation of pumped storage, and $P^{pum}_{k,t}$ is the value of pumping.

BENEFIT ALLOCATION MODEL BY THE IMPROVED SHAPLEY VALUE METHOD

Cooperative Game Theory

Game theory is mainly used to study how to choose the best decision or group decision-making when interesting relations or conflicts between multiple decision-makers are observed (Yang et al., 2020). This method focuses on how many people cooperate to maximize the benefits of the alliance and how to distribute the benefits. A single agent participating in the market is faced with uncertain risks, such as its output and market price. However, given that the cooperative game alliance is composed of multi-agents, the multi-power complementary system can reduce its risk through internal regulation. Thus, additional benefits (i.e., cooperation surplus) are obtained. How to allocate the cooperative surplus reasonably is the key factor that affects whether different agents can reach a cooperative relationship.

Regarding the alliance $N = \{1, 2, 3, \cdots, n\}$ of n members, S is a subset of N, which represents a kind of combination. Assuming that the revenue of member i after the distribution is R_i, $R(S)$ is the revenue of S, and $R(\{\mathrm{i}\})$ is the revenue of member i without cooperation. Generally, an alliance can maintain cooperation needs to meet three conditions: 1) the individual revenue of each member is increased after cooperation, 2) the total revenue of alliance is increased after cooperation, and 3) the total benefit remains steady before and after benefit allocation.

$$R_i \geq R(\{i\}) \tag{38}$$

$$R(S) \geq \sum_{i \in S} R(\{i\}) \tag{39}$$

$$\sum\nolimits_{i=1}^{n} R_i = R(N) \tag{40}$$

The Traditional Shapley Value Method

The Shapley value method focuses on the marginal revenue of each member and determines the benefit that should be shared by all members by calculating the expected value of the marginal contribution of each member. Assuming n members in the alliance, they can be expressed as $N = \{1, 2, \ldots, n\}$, the formula for calculating the benefit allocated to member i is as follows:

$$v_i = \sum_{S \in N} \omega(|S|)\left[v(S) - v(S/i) \right], i = 1, 2, \ldots, n \tag{41}$$

$$\omega(|S|) = \frac{(n - |S|)!\,(|S| - 1)!}{n!} \tag{42}$$

where $\omega(|S|)$ is the weighting factor, $v(S)$ is the revenue of set S, $v(S/i)$ is the revenue when member i is deleted from set S, and $|S|$ is the number of members in set S.

Improved Benefit Allocation Model

The traditional Shapley value method has some shortcomings. The risks of different members in the alliance are regarded as equal, and other factors that need to be considered in the benefit distribution are simplified and ignored. In the actual cooperation alliance, the risk and cost factors of different members are different, and their willingness to participate in the alliance is also different. If all members are regarded as the same, the rationality of the final benefit allocation is affected. To make up for the shortcomings of the traditional Shapley method, in this study, the risk and cost factors are considered in the adjustment of the traditional Shapley value, and an improved benefit allocation model considering multi-factors is proposed.

Risk Factor

Risk sharing is a key problem in the process of the WHPS integrated power system. The greater the risk the participants take in the process of cooperation, the greater the expected benefits. The different risks of different members lead to the difficulty of benefit allocation in the system. Therefore, introducing the risk factor for reasonable benefit distribution is crucial.

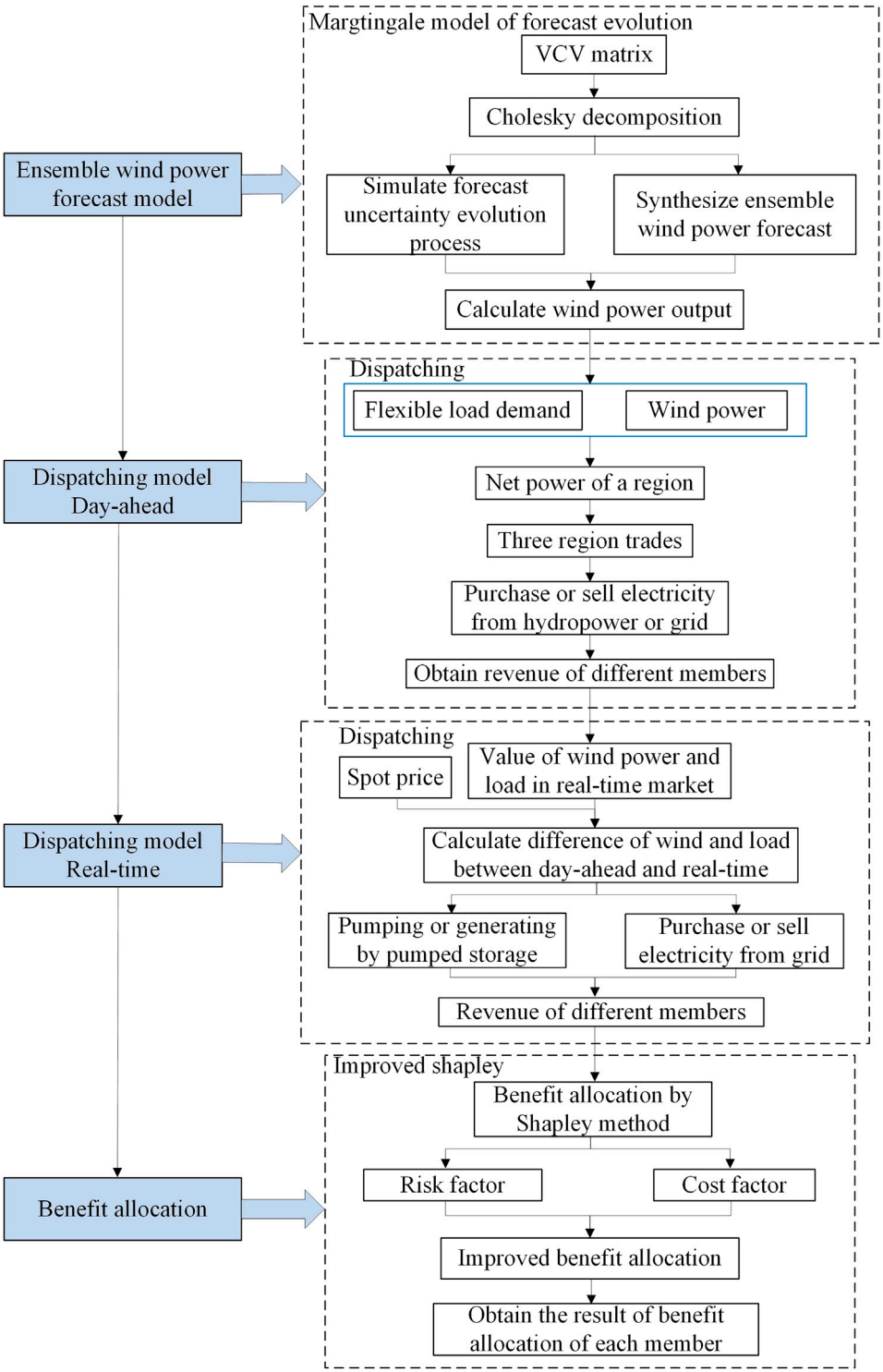

FIGURE 2 | Flowchart of dispatching and benefit allocation.

$$\varphi_i^R(V_i)' = R \times \Delta R_i + V_i \tag{43}$$

where R is the total revenue, ΔR_i is the difference between the risk taken by member i and the average risk (i.e., $\Delta R_i = R_i - \frac{R}{n}$), ΔR_i is also known as the risk correction factor, V_i is the allocated benefit of member i by traditional Shapley method, and $\varphi_i^R(V_i)'$ is the benefit allocation result by the improved Shapley method with considering risk factor.

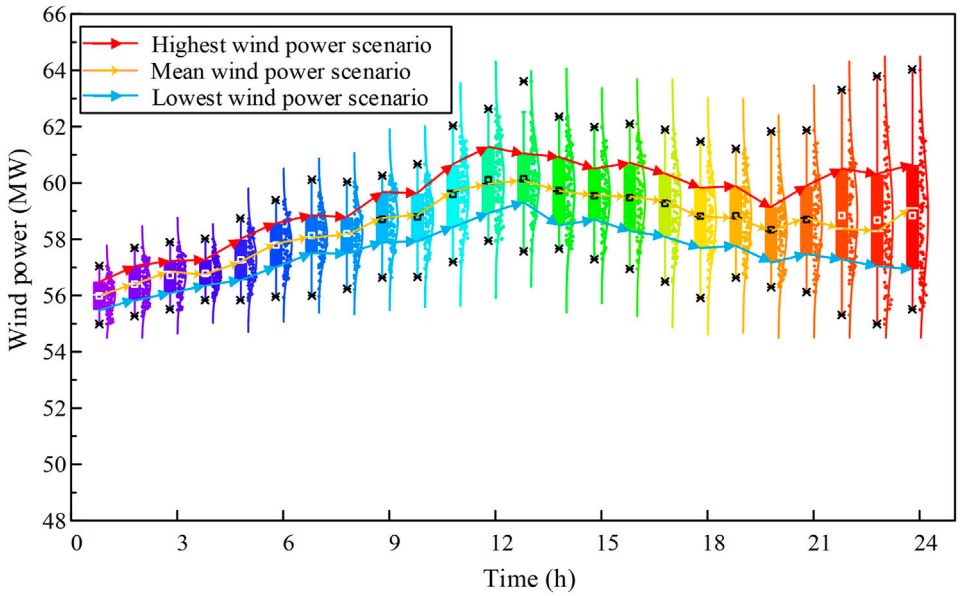

FIGURE 3 | Generated ensemble forecasts of wind power of region 1.

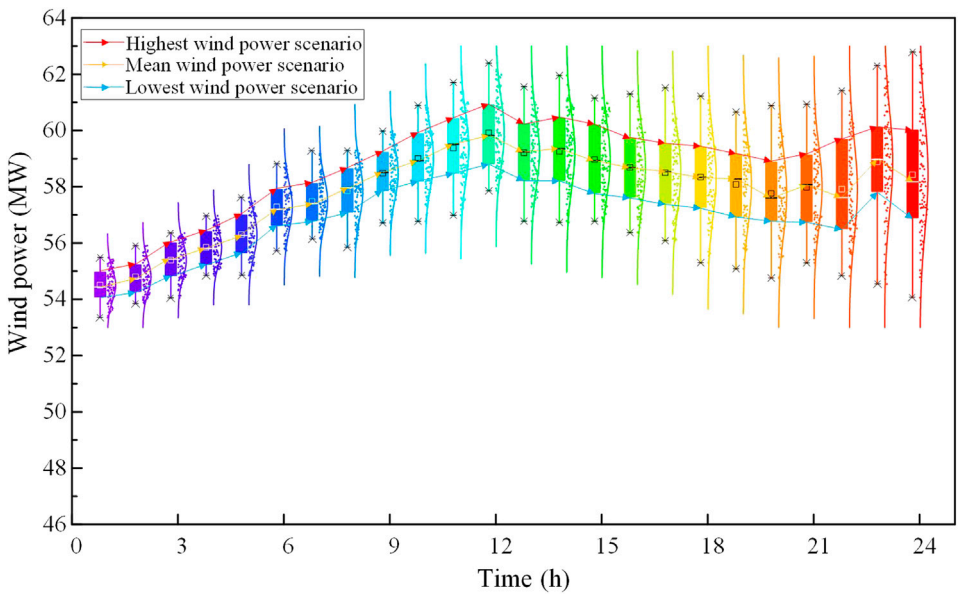

FIGURE 4 | Generated ensemble forecasts of wind power of region 2.

Cost Factor

The proposed cost factor focuses on the costs of all members in the actual operation process of the multi-power system. The benefit allocation of the participants is also affected by their cost. Generally, the higher the cost, the higher the expected benefits. The addition of the cost factor is beneficial to the rationality of benefit allocation. The equation is as follows:

$$\chi(V_i) = C \times \Delta C_i + V_i \tag{44}$$

where C is the total revenue, ΔC_i is the difference between the cost of member i and the average cost (i.e., $\Delta C_i = \frac{C_i}{C} - \frac{1}{n}$), ΔC_i is also known as the cost correction factor, and $\chi(V_i)$ is the benefit allocation result by the improved Shapley method with the cost factor.

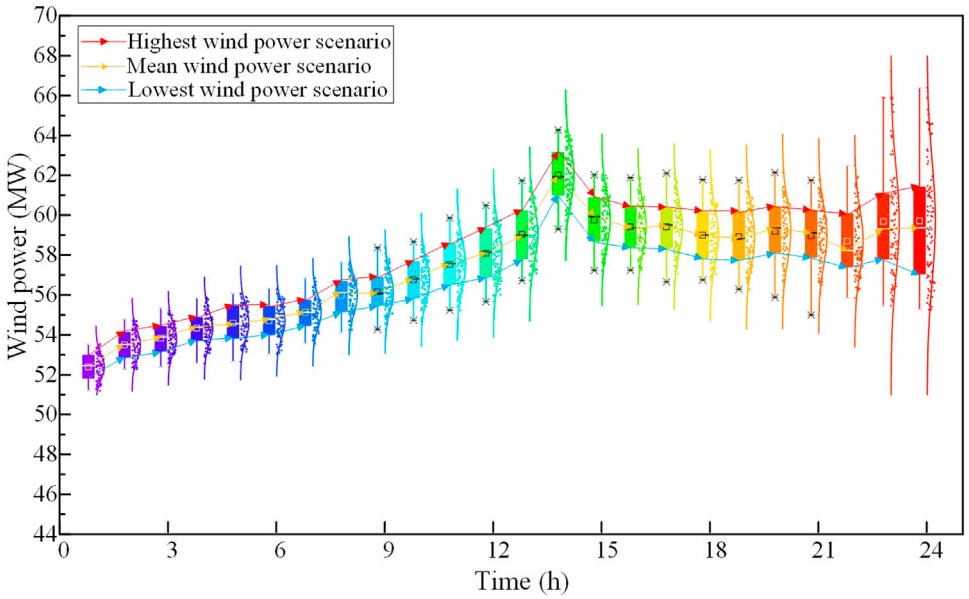

FIGURE 5 | Generated ensemble forecasts of wind power of region 3.

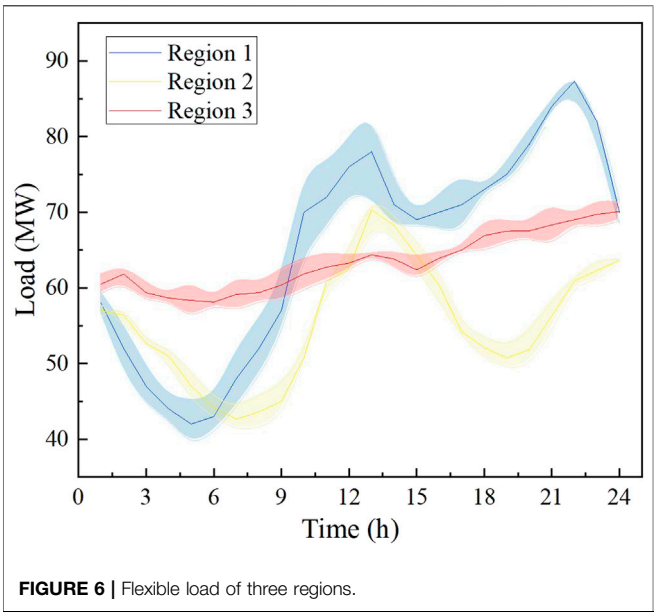

FIGURE 6 | Flexible load of three regions.

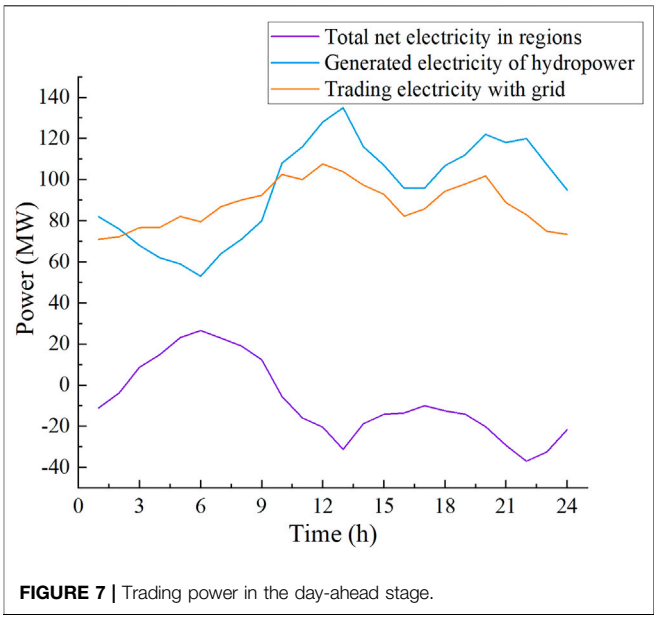

FIGURE 7 | Trading power in the day-ahead stage.

SOLUTION METHOD

Based on the martingale model, the scenario of the wind power output considering the evolution uncertainty of wind power forecasting is generated. In the day-ahead stage, the power supply and load demand of each region are analyzed, and the net power of this region can be calculated. Three regions trade with each other. If the power after trading remains unbalanced, it can be adjusted by purchasing power from hydropower or selling power to a large power grid. In the real-time stage, pumped storage is used to balance the deviation of wind power and load between the real-time and day-ahead stages quickly. An improved benefit allocation method that considers the risk and cost factors of each subject on the basic of Shapley value is put forward, which can reasonably allocate the benefits generated by the cooperation of multi-regions, the hydropower, and pumped storage. Using the uncertainty analysis formula of wind power in **Eqs. 9–12**, the revenue of the day-ahead stage shown in **Eqs. 30–32**, the revenue of the real-time stage shown in **Eqs. 33–37**, the improved benefit allocation of multi-members shown in **Eqs. 41–44**. Using the

TABLE 1 | Comparison of tie-line volatility.

Scenario	Maximum of tie-line volatility without hydropower	Maximum of tie-line volatility with hydropower	Mean value of tie-line volatility without hydropower	Mean value of tie-line volatility with hydropower
Scenario 1	0.9152	0.9063	0.6372	0.5828
Scenario 2	0.7482	0.5273	0.4822	0.3647
Scenario 3	0.1102	0.0937	0.0836	0.0724

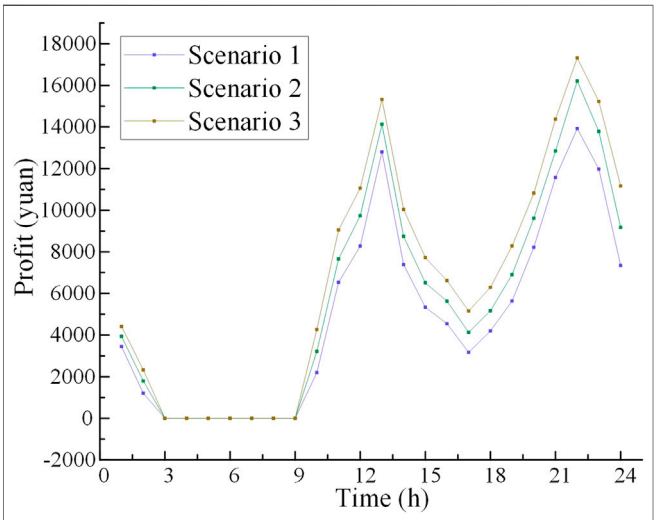

FIGURE 8 | Revenue of transaction between hydropower and multi-regions.

above model, Lingo is used to solve the problem. The revenue of each region after trading among the three regions in the day-ahead stage is obtained. The revenue, which is from three regions and the hydropower sale to the grid after hydropower is engaged in cooperation, can be obtained. In the real-time stage, the revenue of regions and pumped storage that sell to the grid can also be obtained. The result of the benefit allocation is obtained using the improved Shapley value method. The flowchart of dispatching and benefit allocation is shown in **Figure 2**.

The specific steps are as follows:

Using the MMFE to synthesize the ensemble wind power forecasting, this method keeps the statistical moments of the generated wind power sequence, such as mean and variance, and considers the evolution of wind power uncertainty over time.

The optimal dispatching of the day-ahead stage is carried out. First, according to its flexible load demand and wind power generation, the net power of each region is calculated. Next, if excess or shortage of power is experienced in the three regions, they will trade with each other. Then, if the three regions are balanced in power, the real-time stage is entered; if not, a shortage of power is experienced in the three regions, which can be supplemented by hydropower or by purchasing power from the grid. When the three regions have excess power, they can sell to the grid.

In the real-time stage, the deviation of wind power and load between the real-time and day-ahead stages is calculated. Considering the deviation and the spot price, the power generation and pumping of pumped storage are optimized, and the trading power between multi-regions and the grid is obtained. Through this method, the deviation is made up, the economy is improved, and the risk is reduced.

Considering that part of the interests of hydropower and pumped storage have been reduced to stabilize the fluctuation of wind power, the benefit generated after cooperation should be distributed among regions, hydropower, and pumped storage. Given that the traditional Shapley method does not consider the difference of different members, the risk and cost factors are introduced to obtain the improved benefit distribution scheme.

CASE STUDY

Basic Data

To show the change of wind forecast uncertainty over time, the proposed MMFE model is used to generate the ensemble forecasts of wind power synthetically. The time scale of wind power synthetic ensemble forecasts is 24 h, and the time interval is 1 h. **Figures 3–5** show the value of wind power in different regions over time in a day. As can be seen, with the increase of forecast lead time, the variance of wind power forecasting is also increased. Most of the time, the values of forecasted wind power are evenly distributed on both sides of the average value. As time progresses, the amount of data on two sides of the mean value gradually varies because of the increased uncertainty of the forecast over time. Three typical scenarios are then selected from the generated wind power for the later analysis. The first one is the value of the upper quartile, which is shown in red. The second one is the mean value, which is shown in yellow. The third one is the value of the lower quartile, which is shown in blue. **Figure 6** shows the mean value and the range of flexible load in the three regions.

Result Analysis

Trading Result in the Day-Ahead and Real-Time Stages

In the day-ahead stage, scenario 1 is taken as an example. The total net power of three regions, hydropower generation, trading power between multi-regions, and trading power of hydropower and multi-regions to the grid are shown in **Figure 7**.

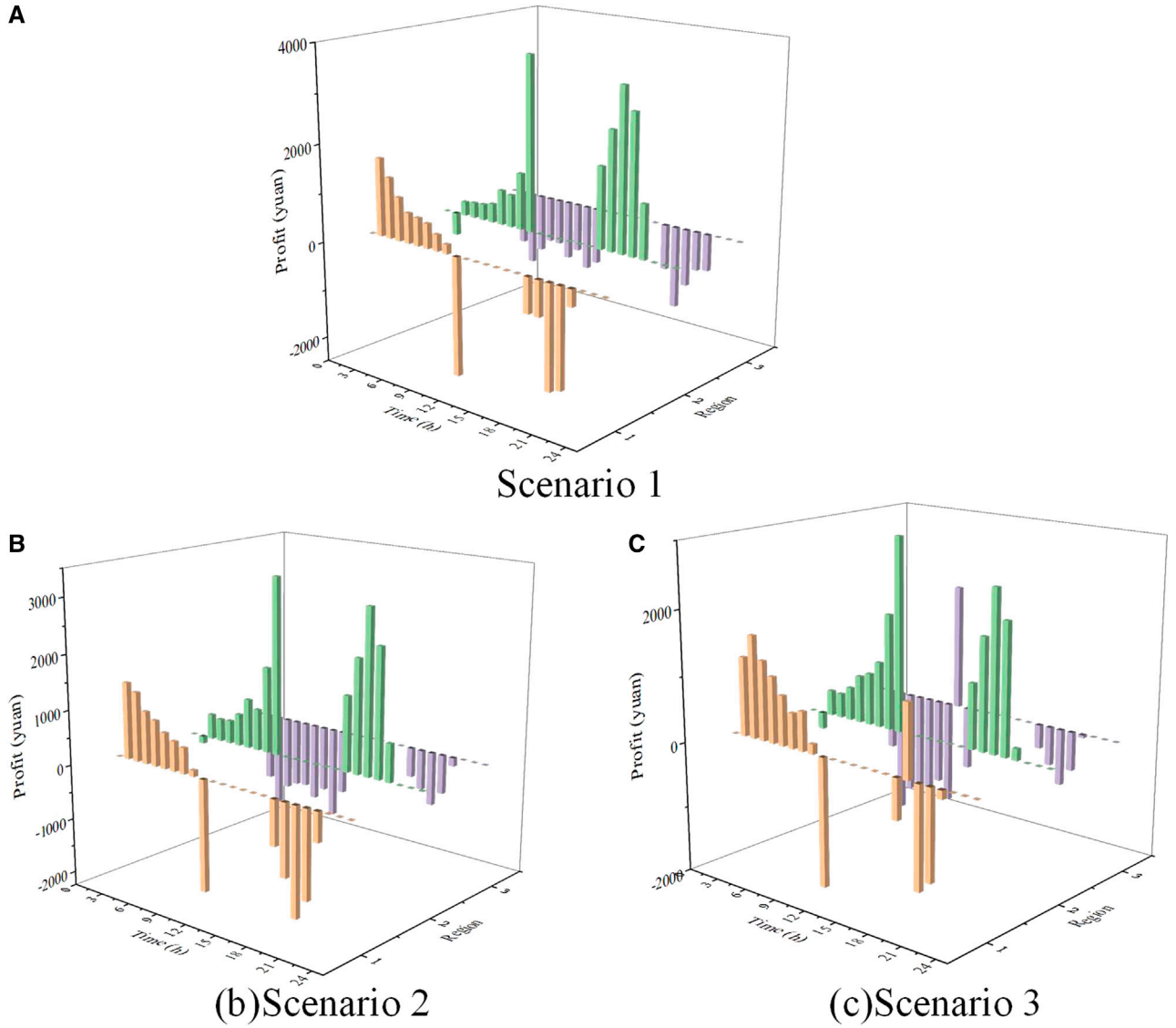

FIGURE 9 | Revenues of each region when the three regions trade with one another under scenario 1.

As shown in **Figure 7**, when the regional total net power is negative, the value of hydropower output is greater than the value of power trading with a large power grid. It illustrates that part of the hydropower output is to supplement the power shortage in the region and part of the power is sold to the grid, therefore, the role of hydropower is demonstrated. When the regional total net power is positive, the output of hydropower is less than that of power trading with the grid. The regional excess power will be sold to the grid, and the hydropower generation will also be sold to the grid. Furthermore, the fluctuation of tie lines trading with the grid will be reduced after hydropower is added, which indicates that hydropower can suppress the fluctuation of wind power effectively. The maximum and mean values of tie-line volatility under the three scenarios are shown in **Table 1**.

As shown in **Table 1**, after adding hydropower, the tie line volatility would be decreased in each scenario, which prove the function of multi power operation. The average of maximal tie line volatility with hydropower is reduced by 0.2463 after adding hydropower, and the average of mean tie line volatility with hydropower is reduced by 0.1831 after adding hydropower, which indicates the positive role of hydropower. The harmful impact on the grid is reduced. In the day-ahead stage, the revenue of transaction between hydropower and three regions is shown in **Figure 8**.

As shown in **Figure 8**, the revenue of transaction between hydropower and multi-regions is the highest under scenario 3. The revenue under scenario 1 is the lowest because of the minimum wind power output in scenario 3 and the additional hydropower output needed to supplement the regional power

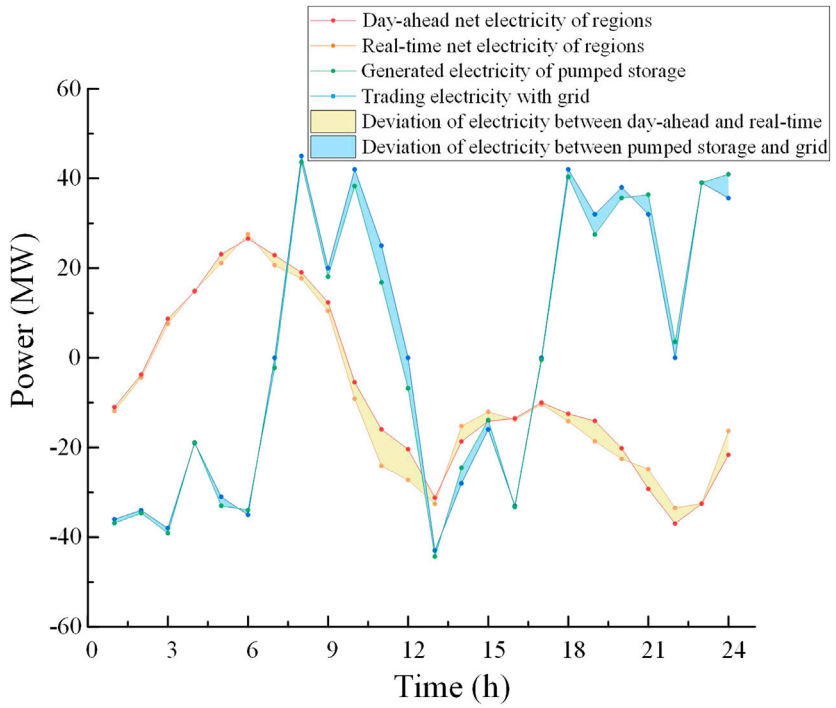

FIGURE 10 | Trading power in the real-time stage of scenario 1.

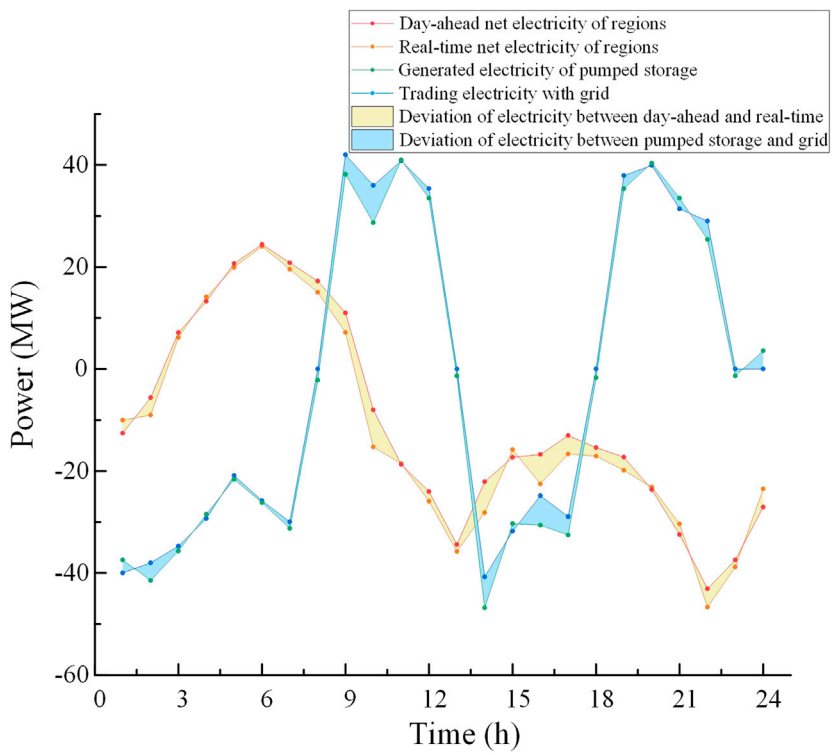

FIGURE 11 | Trading power in the real-time stage of scenario 1.

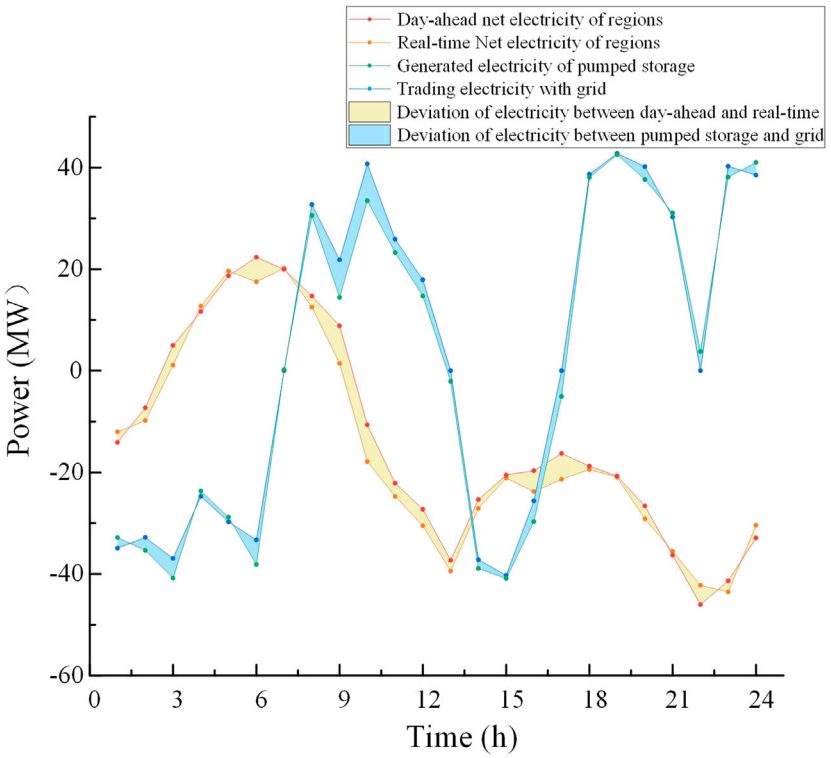

FIGURE 12 | Trading power in the real-time stage of scenario 1.

TABLE 2 | Result of benefit allocation.

Sequence	Set	Revenue in the day-ahead stage			Revenue in the real-time stage		
		Scenario 1	Scenario 2	Scenario 3	Scenario 1	Scenario 2	Scenario 3
1	{1}	−55789.0	−64073.2	−66032.4	−66842.7	−9268.6	−15058.3
2	{2}	11380.3	3621.7	1627.7	235.2	408.2	−12749.2
3	{3}	−28026.4	−37575.8	−65268.2	−5901.3	−4326.6	−3379.1
4	{4}	855714.2	883322.4	984828.9	\	\	\
5	{5}	\	\	\	24715.8	36882.6	42331.8
6	{1,2,3,4,5}	822782.6	817293.1	876779.5	12524.4	37,657.1	11345.7
Benefit growth rate		5%	4.1%	2.5%	2.6%	2.1%	1.8%

TABLE 3 | Comparison of revenue by different benefit allocation methods.

Category	Revenue in the day-ahead stage/yuan				Revenue in the real-time stage/yuan			
	{1}	{2}	{3}	{4}	{1}	{2}	{3}	{5}
Without cooperation	−55789.0	11380.3	−28026.4	855714.2	−6842.7	235.2	−5901.3	24715.8
Traditional Shapley	−50558.1	18415.6	−13388.6	868313.8	−6776.3	238.3	−5844.3	24906.7
Risk factor	−50677.5	18265.9	−13708.5	868902.8	−6778.9	237.9	−5845.8	24911.1
Cost factor	−50718.2	18177.5	−14035.7	869259.1	−6779.7	237.8	−5846.5	24912.8
Risk and cost factors	−50778.3	18105.3	−14068.8	869524.4	−6785.1	237.2	−5851.6	24923.9

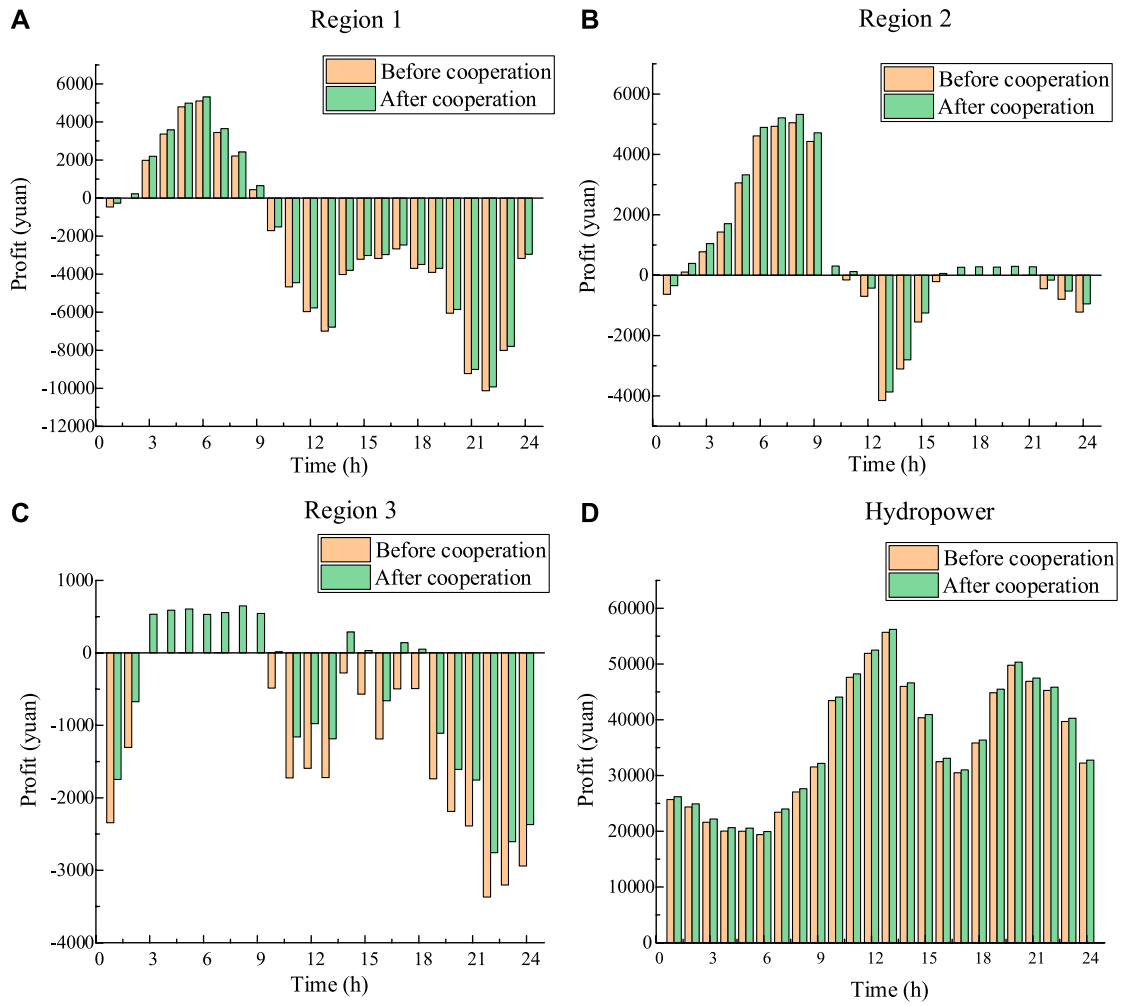

FIGURE 13 | Comparison of benefit before and after adding hydropower.

shortage. From 3:00 to 9:00, the revenue is zero, which indicates that the regions do not trade with hydropower. The regions and hydropower experience shortage of power or have excess power. Thus, they would purchase or sell power from the grid. From 11:00 to 15:00 and 21:00 to 23:00, the trading power suddenly increases because of the increase of load that residents use during this period. In the day-ahead stage, the revenues of each region when the three regions trade with one another are shown in **Figure 9**. The yellow column represents the revenue of region 1, the green column represents the revenue of region 2, and the purple column represents the revenue of region 3.

As shown in **Figure 9**, in the first several hours of the day, the revenue of regions 1 and 2 is positive, and the revenue of region 3 is negative. It illustrates that the wind power output in regions 1 and 2 is greater than the corresponding load and the wind power output in region 3 is less than the load. Thus, the excess power in region 1 is sold to region 3. From 11:00 to 16:00 and 22:00 to 24:00, the revenue of the three regions is zero, which illustrates that not trading occurs among regions at theses time, the regions all are in a state of excess or shortage of power, and they need to purchase or sell power from hydropower or grid to overcome the regional imbalance between the power supply and the load. From 17:00 to 21:00, the revenue of regions 1 and 3 is negative, and the revenue of region 2 is positive, illustrating that regions 1 and 3 are in the state of power shortage and region 2 has excess power. The sum of the income of the three regions is zero, meeting the balance of income and expenditure. In the real-time stage, the net power of regions in the day-ahead and real-time stages, the generated power of pumped storage, and the trading power with the grid are shown in **Figures 10–12**. The deviation of power between the day-ahead and real-time stages is shown by the yellow shadow, and the deviation of power between the output of pumped storage and the trading power of the grid is shown by the blue shadow.

As shown in **Figures 10–12**, the total net power of regions between the day-ahead and real-time stages has some deviation. When the total net power of regions in the real-time stages is

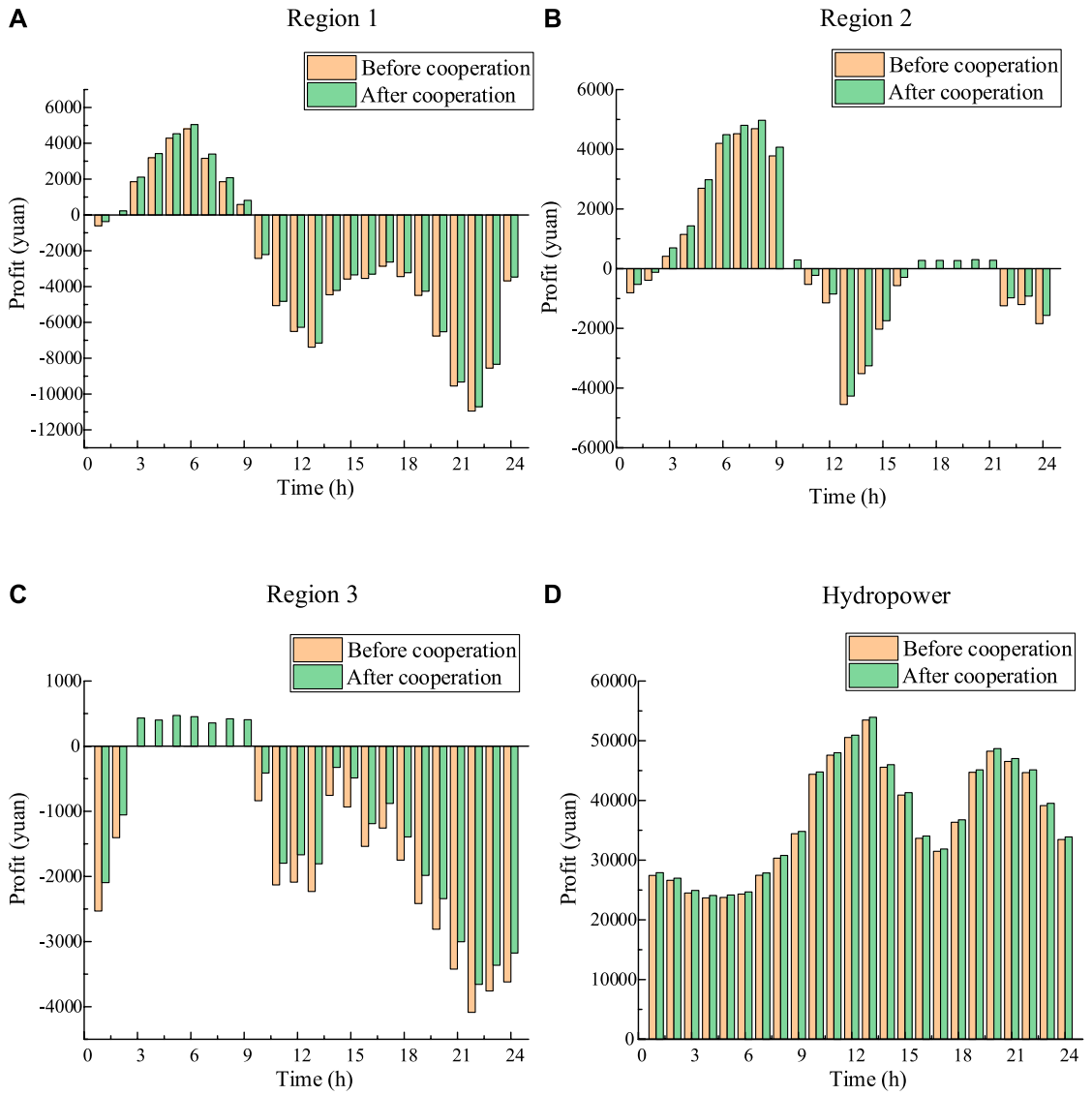

FIGURE 14 | Comparison of benefit before and after adding hydropower under scenario 2.

more than that in the day-ahead stage, the generation of pumped storage is less than the trading power with the grid, which illustrates that the excess power caused by forecasting error and the generation of pumped storage would be sold to the grid. When the total net power of regions in the real-time stage is less than that in the day-ahead stage, the generation of pumped storage is more than the trading power with the grid, one part of the pumped storage generation is sold to the grid, and another part of the pumped storage generation is used to make up the shortage of power in regions.

Benefit Allocation

The benefit allocation method based on the traditional Shapley value only considers the number of power traders. The positive effects of hydropower and pumped storage on wind power are not considered, for example, stabilizing wind generation fluctuation, reducing the fluctuation of tie line with grid, and supplementing the power shortage caused by the uncertainty of wind power. Thus, this section compares the basic Shapley value method and the improved Shapley value method.

Benefit Allocation Result by Traditional Shapley Value Method

The results of different members' benefits in the day-ahead and real-time stages, which are calculated by **Eqs. 7, 8,** are shown in **Table 2**. Symbols {1}, {2}, {3}, {4}, and {5} represent regions 1, 2, 3, hydropower, and pumped storage, respectively. The total benefit after cooperation is greater than the sum of individual benefits of each member before cooperation. The constraints of the cooperative game are satisfied.

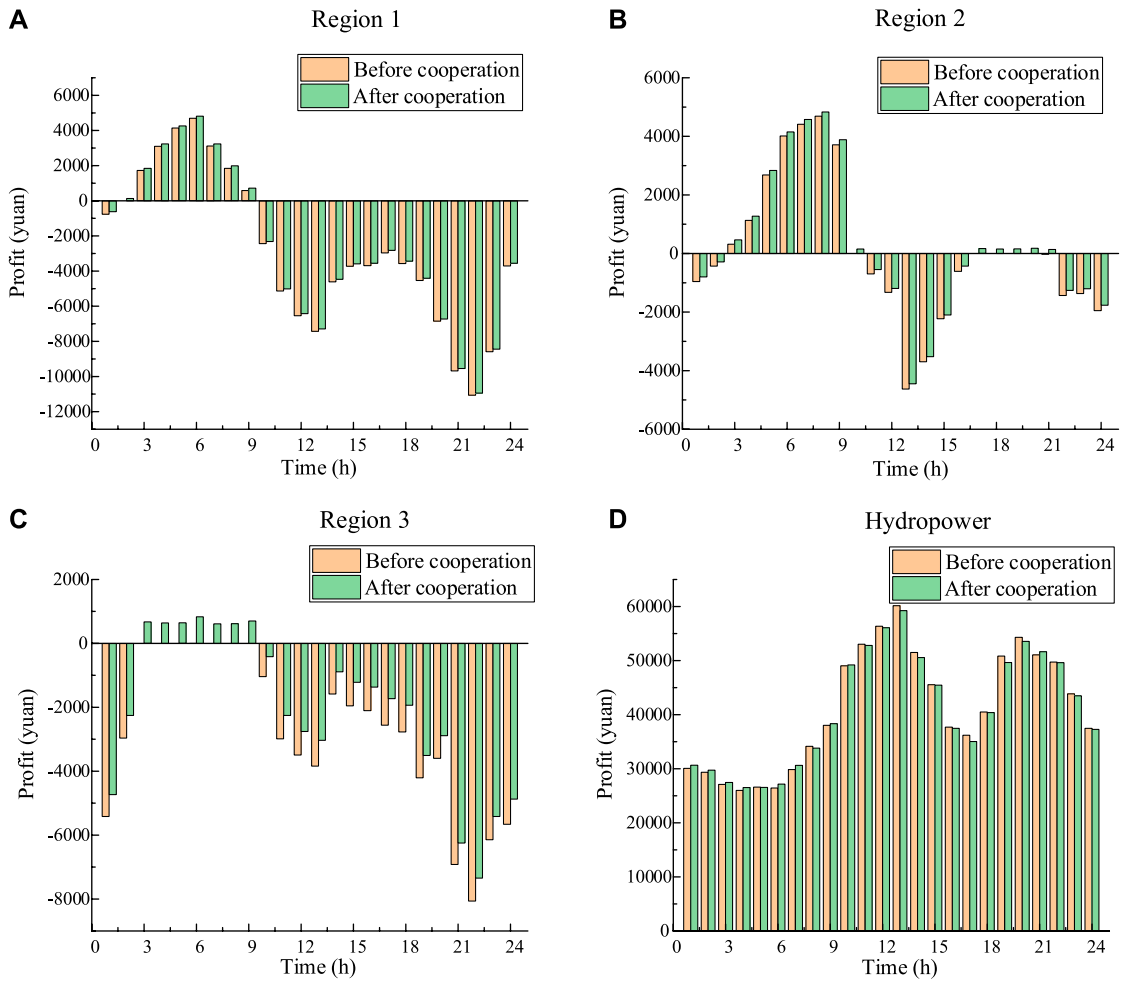

FIGURE 15 | Comparison of benefit before and after adding hydropower under scenario 1.

Improved Benefit Allocation Method

To show the performance of risk factor and cost factor in benefit allocation intuitively, the weighting coefficients of two factors are 1/2. Taking scenario 1 as an example, the benefit allocation results after adding the risk and cost factors are shown in **Table 3**.

As shown in **Table 3**, in the day-ahead stage, compared with the traditional Shapley method, the benefits of the three regions are reduced by 220.2, 310.2, and 680.2 yuan. The benefit of hydropower is increased by 1210.6 yuan. In the real-time stage, the benefit of pumped storage is also increased, which is in line with their role. The addition of hydropower and pumped storage has suppressed the fluctuation of renewable energy in regions but has lost part of its interests, which has a great risk. However, the benefit allocation scheme based on the traditional Shapley value method ignores the positive effects of hydropower and pumped storage. The improved Shapley method can promote the cooperation of all participants, and the allocation scheme is more reasonable.

Taking the day-ahead stage as an example, compared with the situation of noncooperation, the benefits of region 1, region 2, region 3, and hydropower are increased by 55230.9, 7035.28, 14637.8, and 12599.58 yuan, respectively. Considering the risk factor, the benefits of region 1, region 2, region 3, and hydropower are increased by 5010.7, 6725.06, 13957.6, and 13810.2 yuan, respectively. The benefit of each region and hydropower before and after adding hydropower in cooperation is shown in **Figures 13–15**.

As shown in **Figures 13–15**, the revenue of each participant after cooperation is greater than that before cooperation, which proves the rationality and effect of the cooperation. The revenue of the three regions is positive or negative in one day, which indicates that the difference between wind power output and load is fluctuating. When the revenue of a region is negative, it illustrates that power shortage is experienced after three regions trade with each other, and power should be purchased from the grid. When the revenue of a region is positive, which illustrates that the region has excess power, excess power would be sold to the grid. From 17:00 to 21:00 in region 2, the revenue of

the region before adding hydropower is zero, which illustrates that the power shortage or excess in this region is just balanced by the other two regions, and no excess power would be traded with the grid.

CONCLUSION

In this study, the framework of two-stage dispatching about wind power, which contains the day-ahead and real-time stages, is proposed. The MMFE is used to generate synthetic ensemble wind power forecasts. The forecasted values show that the uncertainty of wind power forecasting would be increased over time, which is coincident with the actual situation, and the rationality of the proposed MMFE model is proven. Three typical scenarios are selected for analysis. In the day-ahead stage, the regions trade with one another. If excess power is generated, it is sold to the grid, but if a power shortage is experienced, hydropower would provide power. Based on the first-stage optimization, in the real-time stage, deviations of wind power output and load between the day-ahead stage and the real-time stage are observed because of their uncertainty. The pumped storage, which has the advantages of flexible schedulability, is used to make up for the shortage of power or purchase the excess power caused by the deviation. In the day-ahead stage, after adding hydropower for cooperation, the revenue of regions and hydropower all increase, and the average growth of the revenue is 3.87%. In the real-time stage, after adding the pumped storage, the revenue of all participants increase, and the average growth of the revenue is 2.17%, which proves the positive effect of hydropower and pumped storage. Considering the positive effect, the region should give some economic compensation to hydropower and pumped storage. An improved Shapley value method is proposed for benefit allocation. The risk and cost factors are added to the traditional Shapley method. Compared with the traditional Shapley method, the allocated benefit of hydropower and pumped storage is higher, which is more in line with the actual situation.

DATA AVAILABILITY STATEMENT

The original contributions presented in the study are included in the article/Supplementary Material, further inquiries can be directed to the corresponding authors.

AUTHOR CONTRIBUTIONS

SH, YX: Conceptualization, Methodology; SH: Writing-Original draft preparation; JuL: Supervision; YX, JiL, CL: Writing-Reviewing and Editing.

ACKNOWLEDGMENTS

This work was supported by the National Key R&D Program of China (2018YFB0905200) and the National Natural Science Foundation of China (51807127).

REFERENCES

Bayon, L., Grau, J., Ruiz, M., and Suarez, P. (2016). A comparative economic study of two configurations of hydro-wind power plants. *Energy* 112 (1), 8–16. doi:10.1016/j.energy.2016.05.133

Bird, L., Lew, D., Milligan, M., Carlini, E., Estanqueiro, A., Flynn, D., et al. (2016). Wind and solar energy curtailment: a review of international experience. *Renew. Sust. Energy Rev.* 65, 577–586. doi:10.1016/j.rser.2016.06.082

Biswas, P., Suganthan, P., Qu, B., and Amaratunga, G. (2018). Multiobjective economic-environmental power dispatch with stochastic wind-solar-small hydro power. *Energy* 150, 1039–1057. doi:10.1016/j.energy.2018.03.002

Denault, M., Dupuis, D., and Couture-Cardinal, S. (2009). Complementarity of hydro and wind power: improving the risk profile of energy inflows. *Energy Policy* 37 (12), 5376–5384. doi:10.1016/j.enpol.2009.07.064

Gebretsadik, Y., Fant, C., Strzepek, K., and Arndt, C. (2016). Optimized reservoir operation model of regional wind and hydro power integration case study: Zambezi basin and South Africa. *Appl. Energy* 161, 574–582. doi:10.1016/j.apenergy.2015.09.077

Heath, D., and Jackson, P. (1994). Modeling the evolution of demand forecasts with application to safety stock analysis in production/distribution systems. *IIE Trans.* 26 (3), 17–30. doi:10.1080/07408179408966604

International Energy Agency (2018). Renewables 2018: analysis and forecasts to 2023, executive summary. Availble at: https://www.iea.org/reports/renewables-2018 (Accessed May 01, 2020).

Jakub, J., Mikulik, J., Krzywda, M., Ciapała, B., and Janowski, M. (2018). Integrating a wind- and solar-powered hybrid to the power system by coupling it with a hydroelectric power station with pumping installation. *Energy* 144, 549–563. doi:10.1016/j.energy.2017.12.011

Javed, M. S., Ma, T., Jurasz, J., and Amin, M. (2020). Solar and wind power generation systems with pumped hydro storage: review and future perspectives. *Renew. Energy* 148, 176–192. doi:10.1016/j.renene.2019.11.157

Kristiansen, M., Korpas, M., and Svendsen, H. (2018). A generic framework for power system flexibility analysis using cooperative game theory. *Appl. Energy* 212, 223–232. doi:10.1016/j.apenergy.2017.12.062

Lasemi, M., and Arabkoohsar, A. (2020). Optimal operating strategy of high-temperature heat and power storage system coupled with a wind farm in energy market. *Energy* 210, 118545. doi:10.1016/j.energy.2020.118545

Lee, D., and Wang, L. (2008). Small-signal stability analysis of an autonomous hybrid renewable Energy power generation/energy storage system part I: time-domain simulations. *IEEE Trans. Energy Convers.* 23 (1), 311–320. doi:10.1109/tec.2007.914309

Li, F., and Qiu, J. (2016). Multi-objective optimization for integrated hydro-photovoltaic power system. *Appl. Energy* 167 (1), 377–384. doi:10.1016/j.apenergy.2015.09.018

Li, J., Zhou, J., and Chen, B. (2020). Review of wind power scenario generation methods for optimal operation of renewable energy systems. *Appl. Energy* 280, 115992. doi:10.1016/j.apenergy.2020.115992

Liggett, T., and Rumelt, L. (2009). The asymptotic shapley value for a simple market game. *Econ. Theor.* 40 (2), 333–338. doi:10.1007/s00199-008-0374-4

Liu, Z., Zhang, Z., Zhuo, R., and Wang, X. (2019). Optimal operation of independent regional power grid with multiple wind-solar-hydro-battery power. *Appl. Energy* 235 (1), 1541–1550. doi:10.1016/j.apenergy.2018.11.072

Lopes, V., and Borges, C. (2014). Impact of the combined integration of wind generation and small hydropower plants on the system reliability. *IEEE Trans. Sust. Energy* 6 (3), 1–9. doi:10.1109/TSTE.2014.2335895

Panda, A., Tripathy, M., Barisal, A., and Prakash, T. (2017). A modified bacteria foraging based optimal power flow framework for hydro-thermal-wind

generation system in the presence of STATCOM. *Energy* 124 (1), 720–740. doi:10.1016/j.energy.2017.02.090

Reddy, S. (2017). Optimal scheduling of thermal-wind-solar power system with storage. *Renew. Energy* 101, 1357–1368. doi:10.1016/j.renene.2016.10.022

Schmidt, J., Cancella, R., and Pereira, A. (2016). An optimal mix of solar PV, wind and hydro power for a low-carbon electricity supply in Brazil. *Renew. Energy* 85, 137–147. doi:10.1016/j.renene.2015.06.010

Shahriari, M., Cervone, G., Clemente-Harding, L., and Delle Monache, L. (2020). Using the analog ensemble method as a proxy measurement for wind power predictability. *Renew. Energy* 146, 789–801. doi:10.1016/j.renene.2019.06.132

Shayesteh, E., Amelin, M., and Soder, L. (2016). Multi-station equivalents for short-term hydropower scheduling. *IEEE Trans. Power Syst.* 31 (6), 4616–4625. doi:10.1109/tpwrs.2016.2515162

Shen, J., Cheng, C., Zhang, X., and Zhou, B. (2018). Coordinated operations of multiple-reservoir cascaded hydropower plants with cooperation benefit allocation. *Energy* 153 (15), 509–518. doi:10.1016/j.energy.2018.04.056

Tan, Z., Song, Y., Zhang, H., and Shang, J. (2013). Joint delivery system of large-scale wind power and thermal power generation and its profit distribution model. *Autom. Electr. Power Syst.* 37 (23), 63–70. doi:10.7500/APES2013.01.123

Turk, A., Wu, Q., Zhang, M., and Stergaard, J. (2020). Day-ahead stochastic scheduling of integrated multi-energy system for flexibility synergy and uncertainty balancing. *Energy* 196, 117130. doi:10.1016/j.energy.2020.117130

Wang, X., Mei, Y., Kong, Y., Lin, Y., and Wang, H. (2017). Improved multi-objective model and analysis of the coordinated operation of a hydro-wind-photovoltaic system. *Energy* 134, 813–839. doi:10.1016/j.energy.2017.06.047

Wu, Z., Zhou, M., Yao, S., Li, G., Zhang, Y., and Liu, X. (2019). Optimization operation strategy of wind-storage coalition in spot market based on cooperative game theory. *Power Syst. Technol.* 43 (8), 2815–2824. doi:10.13335/j.1000-3673.pst.2019.0534

Xu, B., Chen, D., Venkateshkumar, M., Xiao, Y., Yue, Y., Xing, Y., et al. (2019). Modeling a pumped storage hydropower integrated to a hybrid power system with solar-wind power and its stability analysis. *Appl. Energy* 248 (15), 446–462. doi:10.1016/j.apenergy.2019.04.125

Yang, S., Tan, Z., Lin, H., Li, P., De, G., Zhou, F., et al. (2020). A two-stage optimization model for park integrated energy system operation and benefit allocation considering the effect of time-of-use energy price. *Energy* 195, 117013. doi:10.1016/j.energy.2020.117013

Zhang, C., Zhao, Z., Zhuang, J., and Wang, B. (2017). Risk-aware short term hydro-wind-thermal scheduling using a probability interval optimization model. *Appl. energy* 189, 534–554. doi:10.1016/j.apenergy.2016.12.031

Zhang, H., Lu, Z., Hu, W., Wang, Y., Dong, L., and Zhang, J. (2019). Coordinated optimal operation of hydro-wind-solar integrated systems. *Appl. Energy* 242, 883–896. doi:10.1016/j.apenergy.2019.03.064

Zhang, H., Lu, Z., Hu, W., Wang, Y., Dong, L., and Zhang, J. (2019). Coordinated optimal operation of hydro-wind-solar integrated systems. *Appl. Energy* 242, 883–896. doi:10.1016/j.apenergy.2019.03.064

Zhang, Y., Wang, J., and Wang, X. (2014). Review on probabilistic forecasting of wind power generation. *Renew. Sust. Energy Rev.* 32, 255–270. doi:10.1016/j.rser.2014.01.033

Zhao, T., Cai, X., and Yang, D. (2011). Effect of streamflow forecast uncertainty on real-time reservoir operation. *Adv. Water Resour.* 34 (4), 495–504. doi:10.1016/j.advwatres.2011.01.004

Zhou, J., Peng, Y., Wang, C., and Yuan, L. (2016). Short-term hydro-thermal-wind complementary scheduling considering uncertainty of wind power using an enhanced multi-objective bee colony optimization algorithm. *Energy Convers. Manag.* 123, 116–129. doi:10.1016/j.enconman.2016.05.073

Conflict of Interest: Author JiL was employed by the Southwest Electric Power Design Institute Co., Ltd. Of China Power Engineering Consulting Group. Author CL was employed by the State Grid Sichuan Electric Power Research Institute.

The remaining authors declare that the research was conducted in the absence of any commercial or financial relationships that could be construed as a potential conflict of interest.

frontiers in Energy Research

ORIGINAL RESEARCH
published: 20 April 2021
doi: 10.3389/fenrg.2021.634770

Analysis of Distributed Generation Accommodation in Flexible Distribution Networks

Jun Xiao[1], *Ying Wang*[1] *and Guoqiang Zu*[1,2]*

[1]Key Laboratory of Smart Grid of Ministry of Education, Tianjin University, Tianjin, China, [2]State Grid Tianjin Electric Power Research Institute, Tianjin, China

This work proposes a method to analyze distributed generation (DG) accommodation in a flexible distribution network (FDN). Firstly, the DG-load matching degree is proposed to quantitatively describe the power balance degree of DG and load in a distribution network. Secondly, the accommodation ratio of DG is proposed and divided into a DG-load accommodation ratio and DG-network-load accommodation ratio, to distinguish whether the index takes the network operational constraints into account. We derive the DG-load accommodation ratio directly from the matching degree and propose the simulation model of sequential production to solve the DG-network-load accommodation ratio. Finally, the cases of FDN under the scenarios of different matching degrees are studied and compared with those of the traditional rigid distribution network. The results show that the improvement of the accommodation ratio by upgrading the rigid distribution network to an FDN is conditional, which is related to not only the matching degree of the whole network but also that of each local network. The DG-network-load accommodation ratio will tend to the DG-load accommodation ratio if proper planning or optimization measures are taken. We find that the capacity of branches adjacent to the DG bus mainly limit the DG accommodation in the FDN, and it is recommended to relocate the DGs and enlarge the capacity of those branches.

Keywords: accommodation ratio, distributed generation, flexible distribution network, matching degree, DG-load accommodation ratio, DG-network-load accommodation ratio

OPEN ACCESS

Edited by:
Yang Mi,
Shanghai University of Electric Power, China

Reviewed by:
Yonghui Sun,
Hohai University, China
Tao Jiang,
Northeast Electric Power University, China
Zhenkun Li,
Shanghai University of Electric Power, China

***Correspondence:**
Guoqiang Zu
zuguoqiang_tju@163.com

Specialty section:
This article was submitted to Smart Grids, a section of the journal Frontiers in Energy Research

Received: *28 November 2020*
Accepted: *25 January 2021*
Published: *20 April 2021*

Citation:
Xiao J, Wang Y and Zu G (2021) Analysis of Distributed Generation Accommodation in Flexible Distribution Networks. Front. Energy Res. 9:634770. doi: 10.3389/fenrg.2021.634770

INTRODUCTION

The installed capacity of distributed generations (DGs) is rapidly increasing in distribution networks in recent years. Due to the intermittency and uncertainty of DGs, it is difficult to accommodate a large number of DGs in the traditional distribution networks (Stram, 2016).

The development of power electronics technology provides a new idea to solve this problem (Huang et al., 2011; Rueda-Medina and Padilha-Feltrin, 2013). The flexible power electronic equipment, such as the soft open point (SOP) (Zhu et al., 2018), is with great power flow control capability. SOPs refer to the flexible switches in distribution networks usually using back-to-back voltage source converters. SOPs are installed previously at normally open points (NOPs) of the distribution network (Cao et al., 2016). An SOP is able to provide the dynamic and continuous active/reactive power flow controllability and limit the short current (Escalera et al., 2020). The application of the SOP will promote the flexibility and controllability of the distribution system.

The SOP improves the capability of the distribution network to host high-penetration DGs (Shafik et al., 2019). The SOP relives the negative effect of intermittent DGs on the operation of distribution networks (Guo et al., 2020). In addition, through controlling the SOPs, the network losses can be reduced and the voltage levels can be well maintained (Flottemesch and Rother, 2004) without involving open/close switch operations. The SOPs can also avoid the power outage when the system is in fault and improve the system reliability (Barragan et al., 2012). Some pilot projects have demonstrated that the SOP is beneficial to a distribution network in many aspects, such as optimal power flow, load balancing, voltage regulation, power supply restoration, and accommodation of DG, which indicates its potential in the future distribution network (Western Power Distribution, 2016; SP Energy Networks, 2016).

The article (Xiao et al., 2018b) proposes the system-level concept of the flexible distribution network (FDN). An FDN is defined as the distribution network with flexible power flow controllability using multiterminal SOPs (including two-terminal SOPs). The article (Xiao et al., 2017a) proposes the total supply capability (TSC) of the FDN. The articles (Xiao et al., 2017b) and (Xiao et al., 2020) adopt the region method to observe the FDN and propose the model and observation approach of the dispatchable region of the FDN. However, the DG accommodation in the FDN has not been studied yet in the existing researches. This work analyzes the DG accommodation in the FDN, which will provide fundamental results for the planning scheme of the FDN to accommodate more DGs.

As for the assessment of the DG accommodation capability of distribution networks, the classical indices include the maximum admissible wind/solar power, wind/solar curtailment rate (Liu and Chu 2018; Ye et al., 2019), etc. However, these indices cannot reflect the essence of DG accommodation capability, which is determined by the location and power balance of DG and load, as well as network operational constraints. This paper proposes the concept of DG-load matching degree, to quantitatively describe the relative value of the power energy output from DG and load consumption in a distribution network. The DG accommodation ratio is proposed and divided into two subindices, including the DG-load accommodation ratio and DG-network-load accommodation ratio. DG-load accommodation ratio is derived directly from matching degree and DG-network-load accommodation ratio is solved by simulation model of sequential production. The proposed DG accommodation analysis method is simple and effective. It directly reflects the effect of DG accommodation capability caused by location and power balance between DG and load, as well as network operational constraints. The accommodation ratio of the traditional rigid distribution network and FDN are calculated and analyzed on case studies. The results discover the bottleneck of DG accommodation in the FDN, and the measures are proposed to remove these bottlenecks.

CONCEPTS OF MATCHING DEGREE AND ACCOMMODATION RATIO

The primary constraint of DG accommodation capability is to keep the real-time power balance of production and consumption. For an ideal distribution system without network operational constraints (i.e., thermal capacity constraints and voltage profile constraint), the DG accommodation capability is determined only by the load power. Therefore, the core idea of DG accommodation is to utilize load. The concept of DG-load matching degree is proposed in this section. Furthermore, the DG-load accommodation ratio and DG-network-load accommodation ratio are proposed to assess the influence of load on the DG accommodation.

Matching Degree

It is said the DG and load are "matched" in a distribution network during a period T only if the following condition is satisfied:

$$\left|P_{\mathrm{DG}}^{\mathrm{ge}}(t)\right| \le |P_{\mathrm{L}}(t)|, \ \forall t \in [0, T]. \tag{1}$$

Otherwise, it is said the DG and load are "unmatched" if

$$\left|P_{\mathrm{DG}}^{\mathrm{ge}}(t)\right| > |P_{\mathrm{L}}(t)|, \ \exists t \in [0, T]. \tag{2}$$

In **Eqs. 1**, **2**, T is the period of observation, and the unit is hour. $\left|P_{\mathrm{DG}}^{\mathrm{ge}}(t)\right|$ is the sum of maximum available output power of all the DGs at the moment t. $|P_{\mathrm{L}}(t)|$ is the sum of consumption power of all the load at the moment t. $\left|P_{\mathrm{DG}}^{\mathrm{ge}}(t)\right|$ is usually influenced by the weather conditions, such as light intensity and wind speed, as well as by the installed capacity. **Equations 1**, **2** show that if the DG and load are unmatched, definitely, there is a moment t, the output power of DGs has to be limited.

If the DG and load are matched in a distribution network, that is, **Eq. 1** is satisfied, the matching degree, represented by E_{Ω}, is defined as

$$E_{\Omega} = \frac{\int_0^T \left|P_{\mathrm{DG}}^{\mathrm{ge}}(t)\right| \mathrm{d}t}{\int_0^T |P_{\mathrm{L}}(t)| \mathrm{d}t} \times 100\% \ \text{("matched")}, \tag{3}$$

where, $\int_0^T \left|P_{\mathrm{DG}}^{\mathrm{ge}}(t)\right| \mathrm{d}t$ means the sum of maximum available output power energy of all the DGs during period T. $\int_0^T |P_{\mathrm{L}}(t)| \mathrm{d}t$ means the sum of consumption power energy of all the load during period T. The value range of E_{Ω} in **Eq. 3** is [0%, 100%]. Particularly, when $\left|P_{\mathrm{DG}}^{\mathrm{ge}}(t)\right| = |P_{\mathrm{L}}(t)|, \forall t \in [0, T]$, E_{Ω} = 100%. When $\left|P_{\mathrm{DG}}^{\mathrm{ge}}(t)\right| = 0, \forall t \in [0, T]$, $E_{\Omega} = 0\%$. The DG and load will be better matched if E_{Ω} is larger.

If the DG and load are unmatched in a distribution network, that is, **Eq. 1** is not satisfied, the matching degree is defined as

$$E_{\Omega} = -\frac{\int_0^T \left|P_{\mathrm{DG}}^{\mathrm{ge}}(t)\right| \mathrm{d}t - \int_0^T \min\left(\left|P_{\mathrm{DG}}^{\mathrm{ge}}(t)\right|, |P_{\mathrm{L}}(t)|\right) \mathrm{d}t}{\int_0^T \left|P_{\mathrm{DG}}^{\max}\right| \mathrm{d}t - \int_0^T \min\left(\left|P_{\mathrm{DG}}^{\mathrm{ge}}(t)\right|, |P_{\mathrm{L}}(t)|\right) \mathrm{d}t} \times 100\% \ \text{("unmatched")}, \tag{4}$$

where $\int_0^T \left|P_{\mathrm{DG}}^{\mathrm{ge}}(t)\right| \mathrm{d}t - \int_0^T \min\left(\left|P_{\mathrm{DG}}^{\mathrm{ge}}(t)\right|, |P_{\mathrm{L}}(t)|\right) \mathrm{d}t$ means the sum of the actual power energy curtailment of all the DGs during period T. $\int_0^T \left|P_{\mathrm{DG}}^{\max}\right| \mathrm{d}t - \int_0^T \min\left(\left|P_{\mathrm{DG}}^{\mathrm{ge}}(t)\right|, |P_{\mathrm{L}}(t)|\right) \mathrm{d}t$

means the sum of the power energy curtailment of all the DGs assuming that the power outputs of all the DGs keep their maximum value (installed capacity) during period T. The value range of E_Ω in **Eq. 4** is [−100%, 0%). Particularly, when $\left|P_{DG}^{ge}(t)\right| = \left|P_{DG}^{max}\right|, \forall t \in [0, T]$, $E_\Omega = -100\%$.

According to **Eqs. 1-4**, it can be seen that "$E_\Omega \geq 0$" is equivalent to "matched," while "$E_\Omega < 0$" is equivalent to "unmatched".

The DG output power is characterized by intermittency and uncertainty due to the uncertain weather conditions. Therefore, it is necessary to take uncertain weather conditions into account in the DG-load matching degree, which makes it to be calculated by an integral expression. Generally, the calculation speed can be improved by simplifying the integral. For example, the DG output curve can be simplified by assuming the DG output power is constant during a certain time. The result is relatively conservative, but the calculation speed is improved. In practical application, the speed and accuracy of calculation can be reasonably balanced according to the requirement of planning issues.

In distribution network planning, the DG-load matching degree can be applied to the primary capacity planning for the DG integrated in distribution networks. On the basis of the typical load curve of the distribution network, DG installed capacity can be obtained with the goal of maximum DG-load matching degree. The result is the maximum DG installed capacity such that the output power of the DG can be totally accommodated. When DGs are connected to the distribution network, the DG locations can be optimized by taking them as variables of the DG planning model.

Accommodation Ratio

The accommodation ratio is used in this work to assess the DG accommodation capability of a distribution network. The accommodation ratio, represented by λ_{DG}, is defined as the proportion of the actual output power energy to the maximum available output power energy of all the DGs in a distribution network during period T, as is shown in the following equation:

$$\lambda_{DG} = \frac{W_{DG}}{W_{DG}^{ge}} = \frac{\int_0^T |P_{DG}(t)| dt}{\int_0^T \left|P_{DG}^{ge}(t)\right| dt} \times 100\%, \quad (5)$$

where W_{DG}^{ge} is the sum of the maximum available output power energy of all the DGs during period T. W_{DG} is the sum of the actual output power energy of all the DGs during period T, which is also called accommodation power energy of the DG. $|P_{DG}(t)|$ is the actual output power of all the DGs at the moment t. $\lambda_{DG} \in [0,1]$. The DG accommodation capability of a distribution network will be better if λ_{DG} is larger.

Load power and network operational constraints are the key influences of DG accommodation capability. To analyze the influences separately, the accommodation ratio is divided into two subindices, including the DG-load accommodation ratio and DG-network-load accommodation ratio.

The DG-load accommodation ratio, represented by λ_{GL}, is equal to the accommodation ratio without any network operational constraints. The definition of the DG-load accommodation ratio is consistent with the matching degree, which reflects the overall DG-load power balance. The concept of DG-load accommodation ratio is similar to the "substation capacity-load ratio" (Xiao et al., 2018a), which is a classical index for distribution network planning, and also neglects the network operational constraints.

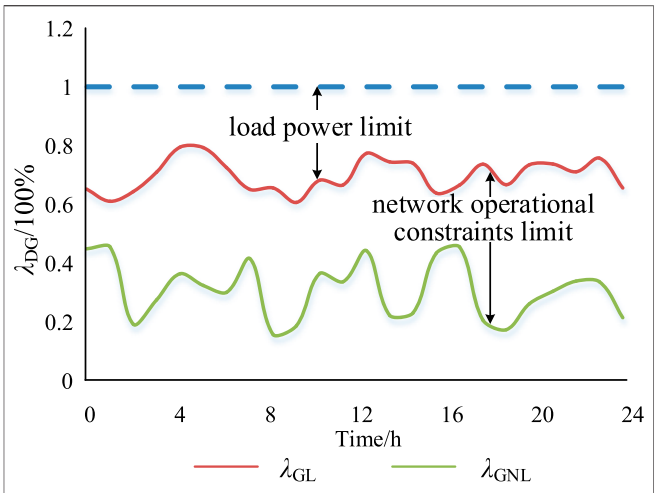

FIGURE 1 | Influences on DG accommodation of load power and network operational constraints.

The DG-network-load accommodation ratio, represented by λ_{GNL}, is equal to the accommodation ratio considering network operational constraints. The definition of the DG-network-load accommodation ratio reflects the effects of network operational constraints on the DG accommodation capability, which is effective supplementary to the DG-load accommodation ratio.

The DG-load accommodation ratio (λ_{GL}) and DG-network-load accommodation ratio (λ_{GNL}) are depicted in **Figure 1**. The area between the blue dot line (λ_{DG} = 100%) and red curve (λ_{GL}) is the power energy curtailment of the DG due to the load power limit. The area between the red curve (λ_{GL}) and green curve (λ_{GNL}) is the power energy curtailment of the DG due to the network operational constraints limit.

The DG-network-load accommodation ratio curve will tend to the DG-load accommodation ratio curve if proper planning or optimization measures are taken, such as regulating voltage and expanding feeder capacity. Particularly, $\lambda_{GNL} = \lambda_{GL}$ if the network operational constraints are completely eliminated.

The proposed accommodation ratio is similar to the existing DG penetration (Anderson et al., 2009). The DG penetration can be divided into power penetration, capacity penetration, and energy penetration. The power penetration and capacity penetration are the power ratios of DG to load (Anderson et al., 2009); the energy penetration (Moghaddam et al., 2018), which is most similar to the concept of accommodation ratio, is the energy ratio of DG to load. The accommodation ratio and energy penetration both utilize the power energy of the DG and load to analyze the DG accommodation capability. The difference

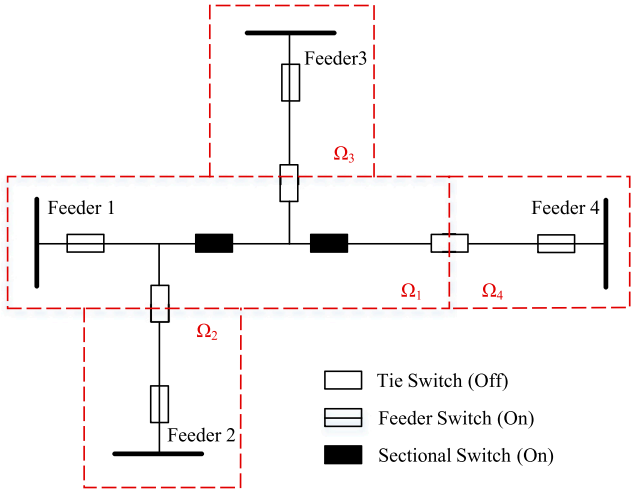

FIGURE 2 | Schematic diagram of the distribution network division.

is that the accommodation ratio, which reflects the utilization of DG, is the proportion of the actual output power energy to the maximum available output power energy of the DG, while the energy penetration, which reflects the supply capability of the DG in the distribution network, is the proportion of the maximum available output power energy of the DG to load consumption. Compared with energy penetration, the accommodation ratio can separately reflect the effects of load power and network operational constraints on the DG accommodation capability directly.

CALCULATION OF THE DG-LOAD ACCOMMODATION RATIO

Since the network operational constraints are not considered in the DG-load accommodation ratio, it can be directly deduced from the matching degree.

Firstly, a distribution network is usually not fully connective. However, it can be divided into several fully connective local networks. The division boundary is the normally open tie switches. As shown in **Figure 2**, the distribution network is divided into four local networks $\Omega_1, \ldots, \Omega_4$.

For a fully connective local network Ω, based on **Eqs. 3**-**5**, the DG-load accommodation ratio (λ_{GL}) can be formulated as

$$\lambda_{GL} = \begin{cases} 100\%, & E_\Omega \geq 0 \\ 100\% - \dfrac{C \cdot |E_\Omega|}{\int_0^T \left|P_{DG}^{ge}(t)\right| dt} \times 100\%, & E_\Omega < 0 \end{cases}, \quad C = \int_0^T \left(\left|P_{DG}^{max}\right| - |P_L(t)| + \left|\left|P_{DG}^{max}\right| - |P_L(t)|\right|\right)/2dt \tag{6}$$

where C is a constant. The detailed deduction is shown as follows:

(1) When $E_\Omega \geq 0$, that is, the DG and load are matched, $|P_{DG}(t)| = \left|P_{DG}^{ge}(t)\right|$, $\forall t \in [0, T]$.

$$\lambda_{GL} = \frac{\int_0^T |P_{DG}(t)| dt}{\int_0^T \left|P_{DG}^{ge}(t)\right| dt} \times 100\% = 100\%. \tag{7}$$

(2) When $E_\Omega < 0$, that is, the DG and load are unmatched, $|P_{DG}(t)| = \min\left(|P_L(t)|, \left|P_{DG}^{ge}(t)\right|\right)$, $\forall t \in [0, T]$.

$$\begin{aligned} \lambda_{GL} &= \frac{\int_0^T |P_{DG}(t)| dt}{\int_0^T \left|P_{DG}^{ge}(t)\right| dt} \times 100\% = \frac{\int_0^T \min\left(|P_L(t)|, \left|P_{DG}^{ge}(t)\right|\right) dt}{\int_0^T \left|P_{DG}^{ge}(t)\right| dt} \\ \times 100\%, &= \frac{\int_0^T \left|P_{DG}^{ge}(t)\right| dt + E_\Omega \left(\int_0^T \left|P_{DG}^{max}\right| dt - \int_0^T \min\left(|P_L(t)|, \left|P_{DG}^{max}\right|\right) dt \right)}{\int_0^T \left|P_{DG}^{ge}(t)\right| dt} \times 100\%, \\ &= 100\% + \frac{E_\Omega \cdot \int_0^T \left(\left|P_{DG}^{max}\right| - |P_L(t)| + \left|\left|P_{DG}^{max}\right| - |P_L(t)|\right|\right) \Big/ 2dt}{\int_0^T \left|P_{DG}^{ge}(t)\right| dt} \times 100\%, \\ &= 100\% - \frac{C \cdot |E_\Omega|}{\int_0^T \left|P_{DG}^{ge}(t)\right| dt} \times 100\%, \end{aligned} \tag{8}$$

where C is a constant, $C = \int_0^T \left(\left|P_{DG}^{max}\right| - |P_L(t)| + \left|\left|P_{DG}^{max}\right| - |P_L(t)|\right|\right)/2dt$.

It can be seen from **Eq. 6** that

(1) when $E_\Omega \geq 0$, that is, the DG and load are matched, the output power of the DG can be totally accommodated, and the DG-load accommodation ratio is 100%.
(2) when $E_\Omega < 0$, that is, the DG and load are unmatched, the DG-load accommodation ratio is determined by the matching degree and sum of the maximum available output power energy of DGs.

The FDN is fully connective because all the mechanical normally open tie switches are replaced with SOPs. Therefore, the DG-load accommodation ratio of the FDN can be directly calculated with **Eq. 6**.

However, for a rigid distribution network, which is not fully connective, the DG-load accommodation ratio should be calculated as follows. Assuming that a rigid distribution network is composed of N fully connective local networks $\Omega_1, \ldots, \Omega_i, \ldots, \Omega_N$,

(1) the DG-load accommodation ratio of each local network is calculated according to **Eq. 6**, and $\lambda_{GL,i}$, $i = 1, \ldots, N$ is obtained.
(2) $\lambda_{GL,i}$, $i = 1, \ldots, N$ is applied to **Eq. 5**, and $W_{DG,i}$, $i = 1, \ldots, N$ is obtained, where $W_{DG,i}$ is the sum of the actual output power energy of DGs in local network i during period T. Then, W_{DG} of the rigid distribution network can be calculated as

$$W_{DG} = \sum_{i=1}^{N} W_{DG,i}, i = 1, \ldots, N. \tag{9}$$

(3) W_{DG} is applied to **Eq. 5**, and the DG-load accommodation ratio of the rigid distribution network is obtained.

CALCULATION OF THE DG-NETWORK-LOAD ACCOMMODATION RATIO

Since the DG-network-load accommodation ratio takes the network operational constraints into account, it cannot be directly obtained based on the matching degree, which is different from the DG-load accommodation ratio. The simulation model of sequential production (Shu et al., 2017), which is usually used for the transmission network planning issue, is used here to solve the DG-network-load accommodation ratio. In this section, the calculation of the DG-network-load accommodation ratio of the FDN will be studied. The DG-network-load accommodation ratio of the rigid distribution network is just a bit different from that of the FDN in the network operational constraints (Wang et al., 2017) of the simulation model of sequential production.

Assumptions

This work is mainly focused on the urban distribution network, which is featured as high load density and short power supply range. Thus, the following assumptions are used:

(1) DC power flow (Purchala et al., 2005) is used. First, the network loss can be included in the power flow of the feeder outlets (Xiao et al., 2011) because the feeders are usually short in length and the network loss ratio is small in the urban power grid. Second, the voltage constraints can be neglected because the system and the DGs are all capable of regulating the bus voltage; thus, the voltage can be kept within the security limits (Shi et al., 2016).
(2) The power cannot flow reversely from 10 kV feeders to an upper-level substation because the upper-level power grid needs great changes for reverse power flow, such as relay protection settings, which is hardly realized in the short term (Fernandez et al., 2020).

Simulation Model of Sequential Production of the FDN

(1) Objective function

The objective is to maximize the sum of the actual output power energy of all the DGs during period T,

$$\max W_{\mathrm{DG}} = \int_0^T \sum_{k\in \boldsymbol{G}} \left|P_{\mathrm{DG},k}\right| \mathrm{d}t, \tag{10}$$

where $\left|P_{\mathrm{DG},k}\right|$ is the actual output power of the DG installed on node k at the moment t. $\boldsymbol{G}$ is the set of all the DG nodes.

(2) Network operational constraints

The network operational constraints include power flow constraints and security constraints. The power which flows out of bus, such as load consumption power, is noted as positive, while the power which injects into of bus, such as DG output power, is noted as negative. The power which flows from a substation to a feeder terminal is noted as positive. The power which flows from a feeder to the connected SOP is noted as positive. Due to the assumptions in *Assumptions*, the constraints are simplified as follows.

The branch flow $P_{\mathrm{B}i,j}$ can be expressed as the algebraic sum of the net power of downstream nodes and the power injected into the downstream SOPs. The power flow equations are formulated as follows:

$$\pm \left|P_{\mathrm{B}_{i,j}}\right| = \sum_{k,m\in \boldsymbol{\Omega}\left(\mathrm{B}_{i,j}\right)} \left(\pm|P_k| \pm \left|\Delta P_{i,m}\right|\right), \tag{11}$$

$$\pm|P_k| = \begin{cases} \left|P_{\mathrm{L},k}\right|, & k \in \boldsymbol{L} \\ -\left|P_{\mathrm{DG},k}\right|, & k \in \boldsymbol{G} \end{cases}, \tag{12}$$

$$\sum_{\mathrm{F}_i \in \boldsymbol{\Omega}(\mathrm{SOP}_m)} \pm \left|\Delta P_{i,m}\right| = 0, \tag{13}$$

where $\mathrm{B}_{i,j}$ is the branch j of feeder F_i. $\left|P_{\mathrm{B}_{i,j}}\right|$ is the power flow of $\mathrm{B}_{i,j}$. $\pm$ indicates the direction of power. $\boldsymbol{\Omega}(\mathrm{B}_{i,j})$ represents the set of downstream nodes and SOPs of $\mathrm{B}_{i,j}$. $\boldsymbol{L}$ and $\boldsymbol{G}$ represent the sets of all the load and DG nodes, respectively. $|P_k|$ is the net power of node k. $\left|P_{\mathrm{L},k}\right|$ is the load power of node k. $\left|\Delta P_{i,m}\right|$ is the power flow between F_i and SOP_m. $\boldsymbol{\Omega}(\mathrm{SOP}_m)$ represents the set of feeders connected to SOP_m. **Equation 11** is the power flow calculation of the branch. **Equation 12** is the node power equation. **Equation 13** is the equilibrium of active power from each terminal of the SOP.

Due to the assumptions in *Assumptions*, the voltage constraints are neglected. The security constraints of the FDN with DG installed are mainly thermal capacity constraints, including the feeder capacity constraints, node power constraints, DG output constraints, SOP capacity constraints, and the reverse power flow constraints.

$$\left|P_{\mathrm{B}_{i,j}}\right| \le C_{\mathrm{B}_{i,j}}, \quad \forall \mathrm{B}_{i,j} \in \boldsymbol{B} \tag{14}$$

$$\begin{cases} 0 \le \left|P_{\mathrm{L,k}}\right| \le \left|P_{\mathrm{k}}^{\max}\right|, & k \in \boldsymbol{L} \\ 0 \le \left|P_{\mathrm{DG,k}}\right| \le \left|P_{\mathrm{k}}^{\max}\right|, & k \in \boldsymbol{G} \end{cases} \tag{15}$$

$$0 \le \left|P_{\mathrm{DG},k}\right| \le \left|P_{\mathrm{DG},k}^{\mathrm{ge}}\right|, \quad k \in \boldsymbol{G} \tag{16}$$

$$\left|\Delta P_{i,m}\right| \le C_{\mathrm{SOP}_m}, \quad \forall \mathrm{SOP}_m \in \boldsymbol{S} \tag{17}$$

$$\pm \left|P_{\mathrm{B}_{i,1}}\right| \ge 0, \quad \forall \mathrm{B}_{i,1} \in \boldsymbol{B} \tag{18}$$

where $C_{\mathrm{B}_{i,j}}$ represents the capacity of $\mathrm{B}_{i,j}$. $\boldsymbol{B}$ is the set of all the branches. $\left|P_k^{\max}\right|$ is the maximum permitted power of node k. $\left|P_{\mathrm{DG},k}^{\mathrm{ge}}\right|$ is the maximum available output power of the DG installed on node k. C_{SOP_m} is the capacity of the SOP_m terminal. $\boldsymbol{S}$ is the set of all the SOPs. $\left|P_{\mathrm{B}_{i,1}}\right|$ is the power flow of the outlet of F_i. **Equation 14** is the constraint of branch capacity. **Equation 15** is the constraint of node power. **Equation 16** is the constraint of DG output. **Equation 17** is the constraint of SOP capacity. **Equation 18** is the constraint of reverse power flow.

Algorithm

The model in *Simulation Model of Sequential Production of the FDN* is linear, which can be solved by the linear programming software after identical deformation (Xiao et al., 2011). The

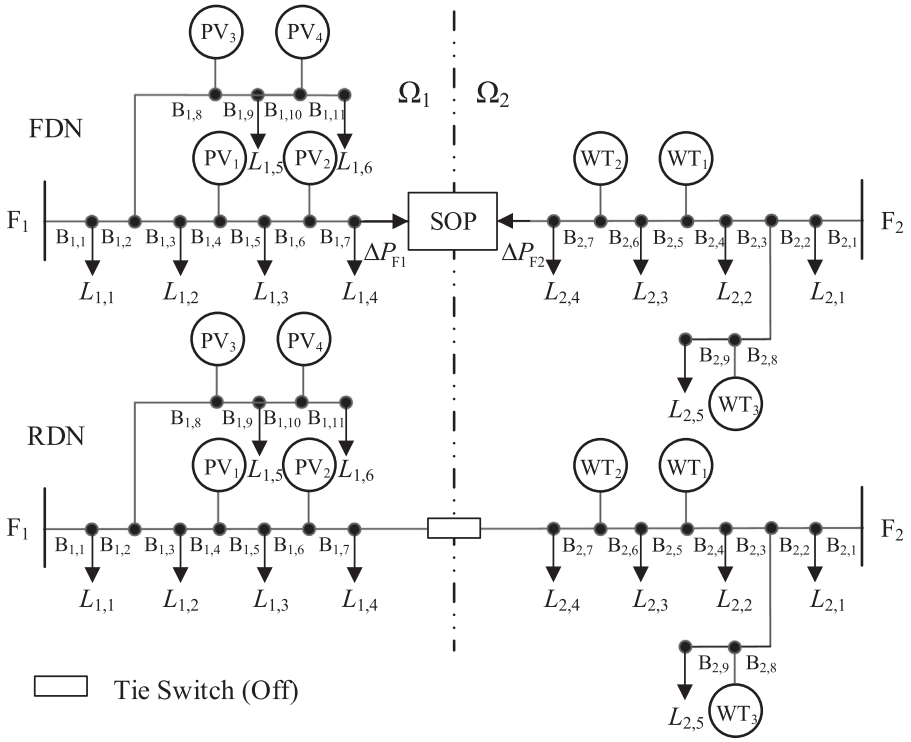

FIGURE 3 | Case grid of the FDN and RDN.

detailed deformation is shown in **Supplementary Material 1**. In this paper, LINGO is used to solve the model to obtain W_{DG}. W_{DG} is applied to **Eq. 5**, and the DG-network-load accommodation ratio is obtained.

CASE STUDY

In this section, cases of FDN with different matching degrees are studied. For three scenarios with different DG planning, the DG-load accommodation ratio and DG-network-load during 1 h are calculated, and their trends during one day are analyzed. Meanwhile, the DG-load accommodation ratio and DG-network-load accommodation ratio of a rigid distribution network are also analyzed as a comparison. The bottlenecks of the FDN to improve DG accommodation capability are analyzed, and the improvement measurements are proposed.

Case Grid

The case grid of the FDN is shown in **Figure 3**. For comparison, the case grid of a rigid distribution network (RDN) with the same topology is used, and the FDN is divided into two local networks corresponding to the RDN. The total daily power energy of the load is 597.8 MWh for both the FDN and rigid distribution network, and the details are shown in **Supplementary Tables S1** and **S2**. For both the FDN and rigid distribution network, each DG capacity is 8 MW and the distribution transformer capacity is 10 MVA. For the FDN, each terminal of the SOP is 10 MVA.

TABLE 1 | Three typical scenarios of case grids.

Scenario	The whole network, Ω_Σ	Local network 1, Ω_1	Local network 2, Ω_2
1	Matched	Unmatched	Unmatched
2	Unmatched	Unmatched	Unmatched
3	Matched	Matched	Matched

However, considering the uncertainty of DG output power caused by weather conditions, three typical scenarios are designed to represent the different matching degrees, as is shown in **Table 1**.

Scenario 1

Matching Degree Calculation

The daily curve of the maximum available output power of DGs and actual consumption power of the load is shown in **Figure 4**.

According to **Figure 4**, the matching degree (MD) is calculated using **Eqs. 3**, **4**. For the whole network, MD = 70.3%. For local network 1, MD = −5%. For local network 2, MD = −5.3%.

Daily Trend of the Accommodation Ratio

According to **Figure 4**, for the case grids of both the FDN and rigid distribution network (RDN), the DG-load accommodation ratio and DG-network-load accommodation ratio during each hour are calculated using **Eqs. 6**, **9**. Then, the DG-load

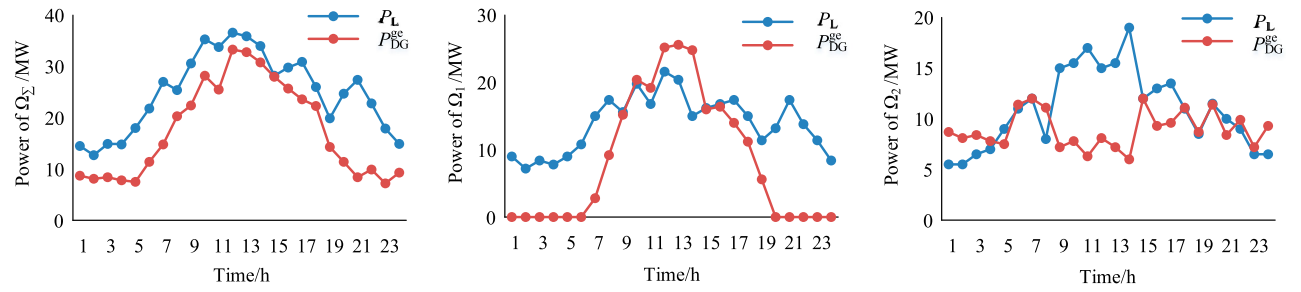

FIGURE 4 | Scenario 1: daily curve of the available output power of DGs and consumption power of the load.

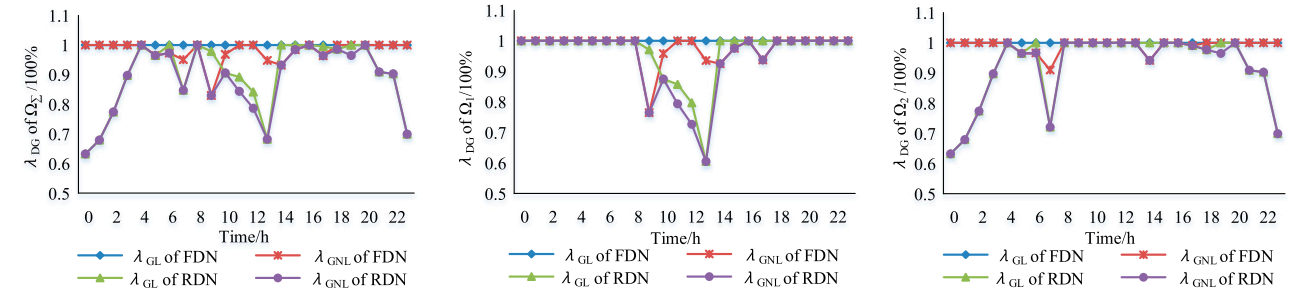

FIGURE 5 | Scenario 1: daily GLAR and GNLAR curve of both the FDN case and RDN case.

accommodation ratio (GLAR, represented by λ_{GL}) and DG-network-load accommodation ratio (GNLAR, represented by λ_{GNL}) of all 24 h are used to form the daily accommodation ratio curve, as is shown in **Figure 5**.

It can be seen from **Figure 5** that

(1) the DG-load accommodation ratio of the FDN is higher than that of the rigid distribution network during 66.7% of a day's period. The reason is that the FDN can adjust the power flow flexibly to increase DG accommodation.
(2) the DG-network-load accommodation ratio of the FDN is higher than that of the rigid distribution network during 58.3% of a day's period. The reason is that the FDN increases the DG accommodation by adjusting the power flow, while the increase extent of DG accommodation is limited by network operational constraints. For the PV accommodation of local network 1, it is focused in midday that the DG-network-load accommodation ratio of the FDN is higher than that of the rigid distribution network. For the WT accommodation of local network 2, it is focused from dusk to the next morning such that the DG-network-load accommodation ratio of the FDN is higher than that of the rigid distribution network.
(3) the DG-load accommodation ratio of the FDN can reach 100% anytime. The reason is that the FDN is capable to fully accommodate the DGs by adjusting the power flow flexibly, when the load and DG of the whole network are matched.
(4) the DG-network-load accommodation ratio of the FDN is lower than the DG-network-load accommodation ratio during 37.5% of a day's period. The reason is that network operational constraints limit the FDN adjusting power flow.

Analysis of the Daily Accommodation Ratio

According to **Figure 4**, for the case grids of both the FDN and rigid distribution network (RDN), the DG-load accommodation ratio (GLAR) and DG-network-load accommodation ratio (GNLAR) during a whole day are calculated using **Eqs. 6**, **9**, which is shown in **Table 2**.

It can be seen from **Table 2** that

(1) since matching degree of scenario 1 is positive, the daily DG-load accommodation ratio of the FDN is 100%.
(2) due to the network operational constraints, the daily DG-network-load accommodation ratio of local network 1 and local network 2 of the FDN case is reduced by 4.6% and 1.2%, respectively. The daily DG-network-load accommodation ratio of the whole network of the FDN is reduced by 2.9%.
(3) since matching degrees of local network 1 and local network 2 are all negative, the rigid distribution network case cannot fully accommodate all DGs, and the daily DG-load accommodation ratio of the rigid distribution network is lower than 100%.
(4) due to the network operational constraints, the daily DG-network-load accommodation ratio of local network 1 and local network 2 of the rigid distribution network case is reduced by 4.8% and 0.7%, respectively. The daily DG-network-load accommodation ratio of the whole network of the rigid distribution network is reduced by 2.7%.

TABLE 2 | Matching degree and daily accommodation ratio of scenario 1.

Scenario 1		The whole network, Ω_{Σ}	Local network 1, Ω_1	Local network 2, Ω_2
MD E_{Ω}		70.3% > 0	−5.0% < 0	−5.3% < 0
GLAR λ_{GL}	RDN	90.9%	89.5%	92.2%
	FDN	100%	100%	100%
GNLAR λ_{GNL}	RDN	88.2%	84.7%	91.5%
	FDN	97.1%	95.4%	98.8%

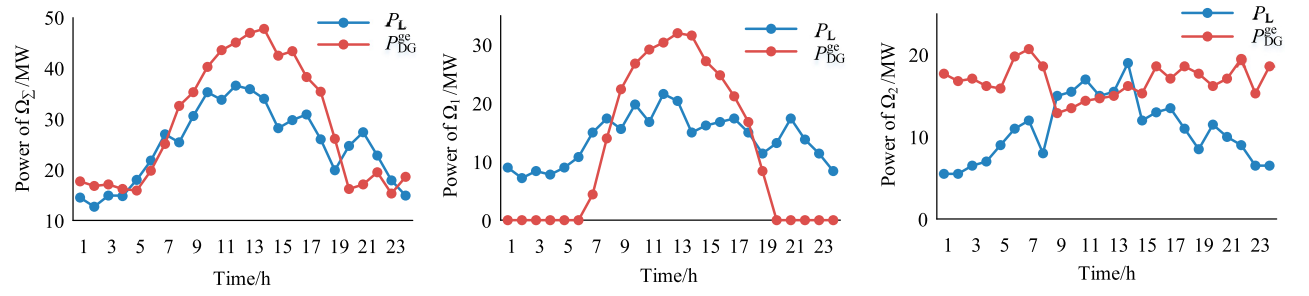

FIGURE 6 | Scenario 2: daily curve of the available output power of DGs and consumption power of the load.

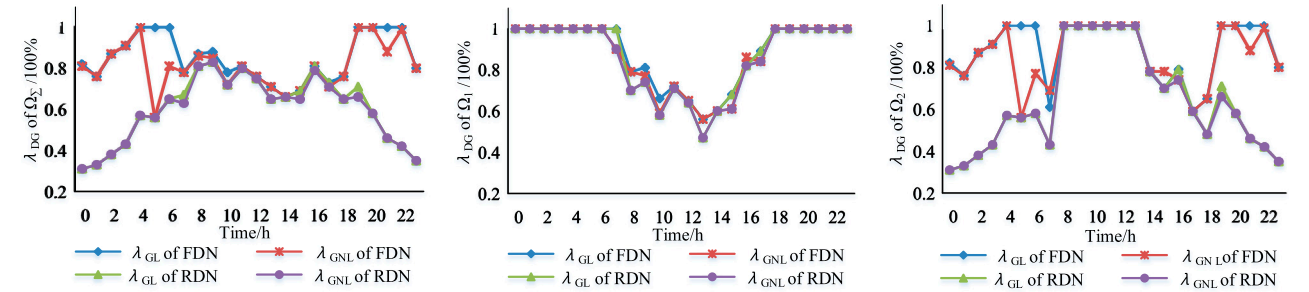

FIGURE 7 | Scenario 2: daily GLAR and GNLAR curve of both the FDN case and RDN case.

(5) compared with the rigid distribution network, the FDN can improve the daily DG-load accommodation ratio by 9.1% and daily DG-network-load accommodation ratio by 8.9%.

Scenario 2

Matching Degree Calculation

The daily curve of the maximum available output power of DGs and actual consumption power of the load is shown in **Figure 6**.

According to **Figure 6**, the matching degree (MD) is calculated using **Eqs. 3**, **4**. For the whole network, MD = −16.8%. For local network 1, MD = −20.3%. For local network 2, MD = −48.2%.

Daily Trend of the Accommodation Ratio

According to **Figure 6**, for the case grids of both the FDN and rigid distribution network (RDN), the DG-load accommodation ratio and DG-network-load accommodation ratio during each hour are calculated using **Eqs. 6**, **9**. Then, the DG-load accommodation ratio (GLAR, represented by λ_{GL}) and DG-network-load accommodation ratio (GNLAR, represented by λ_{GNL}) of all 24 h are used to form the daily accommodation ratio curve, as is shown in **Figure 7**.

It can be seen from **Figure 7** that

(1) the DG-load accommodation ratio of the FDN is higher than that of the rigid distribution network during 83.3% of a day's period. The reason is that the FDN can adjust the power flow flexibly to increase DG accommodation.

(2) the DG-network-load accommodation ratio of the FDN is higher than that of the rigid distribution network during 83.3% of a day's period. The reason is that the FDN increases the DG accommodation by adjusting the power flow, while the increase extent of DG accommodation is limited by network operational constraints. For the PV accommodation of local network 1, it is focused that the DG-network-load accommodation ratio of the FDN is just a little higher than that of the rigid distribution network in daytime. For the WT accommodation of local network 2, it is

TABLE 3 | Matching degree and daily accommodation ratio of scenario 2.

Scenario 2		The whole network, Ω_{Σ}	Local network 1, Ω_1	Local network 2, Ω_2
MD E_{Ω}		−16.8% < 0	−20.3% < 0	−48.2% < 0
	RDN	65.6%	69.6%	62.6%
GLAR λ_{GL}	FDN	81.9%	73.2%	88.1%
	RDN	64.8%	68.3%	62.2%
GNLAR λ_{GNL}	FDN	78.9%	71.0%	84.6%

focused from dusk to the next morning that the DG-network-load accommodation ratio of the FDN is much higher than that of the rigid distribution network.

(3) the DG-load accommodation ratio of the FDN cannot reach 100% during 70.8% of a day's period. The reason is that the FDN cannot fully accommodate the DGs by adjusting the power flow, when the load and DG of the whole network are unmatched.

(4) the DG-network-load accommodation ratio of the FDN is lower than the DG-load accommodation ratio during 37.5% of a day's period. The reason is that network operational constraints limit the FDN adjusting power flow.

Analysis of the Daily Accommodation Ratio

According to **Figure 6**, for the case grids of both the FDN and rigid distribution network (RDN), the DG-load accommodation ratio (GLAR) and DG-network-load accommodation ratio (GNLAR) during a whole day are calculated using **Eqs. 6**, **9**, which is shown in **Table 3**.

It can be seen from **Table 3** that

(1) since the matching degree of scenario 2 is negative, the daily DG-load accommodation ratio of the FDN is 81.9% (<100%).

(2) due to the network operational constraints, the daily DG-network-load accommodation ratio of local network 1 and local network 2 of the FDN case is reduced by 2.2% and 3.5%, respectively. The daily DG-network-load accommodation ratio of the whole network of the FDN is reduced by 3.0%.

(3) since matching degrees of local network 1 and local network 2 are all negative, the rigid distribution network case cannot fully accommodate all DGs, and the daily DG-load accommodation ratio of the rigid distribution network is lower than 100%.

(4) due to the network operational constraints, the daily DG-network-load accommodation ratio of local network 1 and local network 2 of the rigid distribution network case is reduced by 1.3% and 0.4%, respectively. The daily DG-network-load accommodation ratio of the whole network of the rigid distribution network is reduced by 0.8%.

(5) compared with the rigid distribution network, the FDN can improve the daily DG-load accommodation ratio by 16.3% and daily DG-network-load accommodation ratio by 14.1%.

Scenario 3

Matching Degree Calculation

The daily curve of the maximum available output power of DGs and actual consumption power of the load is shown in **Figure 8**.

According to **Figure 8**, the matching degree (MD) is calculated using **Eqs. 3**, **4**. For the whole network, MD = 46.4%. For local network 1, MD = 33.3%. For local network 2, MD = 63.1%.

Daily Trend of the Accommodation Ratio

According to **Figure 8**, for the case grids of both the FDN and rigid distribution network (RDN), the DG-load accommodation ratio and DG-network-load accommodation ratio during each hour are calculated using **Eqs. 6**, **9**. Then, the DG-load accommodation ratio (GLAR, represented by λ_{GL}) and DG-network-load accommodation ratio (GNLAR, represented by λ_{GNL}) of all 24 h are used to form the daily accommodation ratio curve, as is shown in **Figure 9**.

It can be seen from **Figure 9** that

(1) the DG-load accommodation ratio of the FDN is equal to that of the rigid distribution network anytime. The reason is that the rigid distribution network is capable of accommodating the DGs; thus, the FDN cannot increase DG accommodation by adjusting the power flow.

(2) the DG-network-load accommodation ratio of the FDN is higher than that of the rigid distribution network during 16.7% of a day's period. The reason is that DG accommodation in the rigid distribution network is limited by network operational constraints, and it is increased in the FDN by adjusting the power flow. For the PV accommodation of local network 1, it is focused in midday that the DG-network-load accommodation ratio of the FDN is higher than that of the rigid distribution network. For the WT accommodation of local network 2, it is focused from dusk to the next morning that the DG-network-load accommodation ratio of the FDN is higher than that of the rigid distribution network.

(3) the DG-load accommodation ratio of the FDN can reach 100% anytime. The reason is that the FDN is capable of fully accommodating the DGs, when the load and DG of the whole network are matched.

(4) the DG-network-load accommodation ratio of the FDN is lower than the DG-load accommodation ratio during 20.8% of a day's period. The reason is that network operational constraints limit the FDN adjusting power flow.

Analysis of the Daily Accommodation Ratio

According to **Figure 8**, for the case grids of both the FDN and rigid distribution network (RDN), the DG-load accommodation

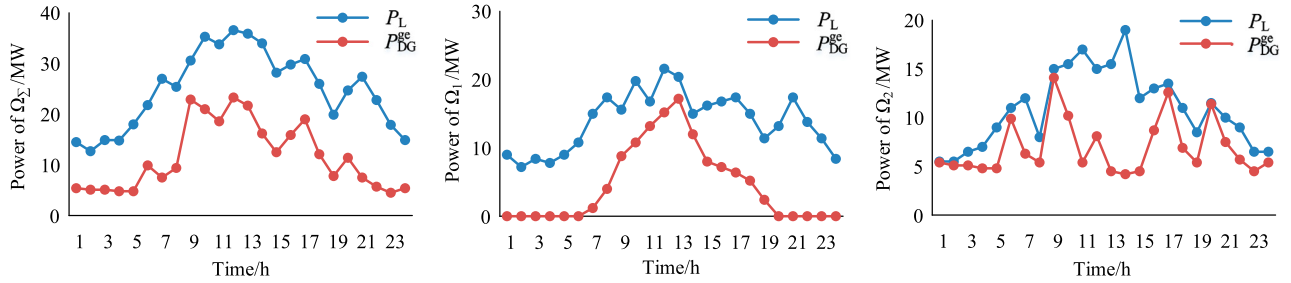

FIGURE 8 | Scenario 3: daily curve of the available output power of DGs and consumption power of the load.

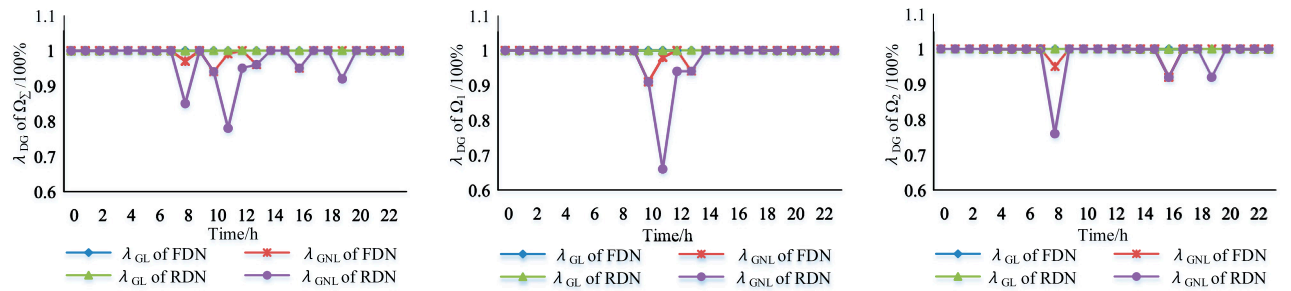

FIGURE 9 | Scenario 3: daily GLAR and GNLAR curve of both the FDN case and RDN case.

TABLE 4 | Matching degree and daily accommodation ratio of scenario 3.

Scenario 3		The whole network, Ω_Σ	Local network 1, Ω_1	Local network 2, Ω_2
MD E_Ω		46.4% > 0	33.3% > 0	63.1% > 0
GLAR λ_{GL}	RDN	100%	100%	100%
	FDN	100%	100%	100%
GNLAR λ_{GNL}	RDN	95.2%	92.8%	96.8%
	FDN	98.6%	98.0%	99.0%

ratio (GLAR) and DG-network-load accommodation ratio (GNLAR) during a whole day are calculated using **Eqs. 6**, **9**, which is shown in **Table 4**.

It can be seen from **Table 4** that

(1) since the matching degree of scenario 3 is positive, the daily DG-load accommodation ratio of the FDN is 100%.
(2) due to the network operational constraints, the daily DG-network-load accommodation ratio of local network 1 and local network 2 of the FDN case is reduced by 2.0% and 1.0%, respectively. The daily DG-network-load accommodation ratio of the whole network of the FDN is reduced by 1.4%.
(3) since matching degrees of local network 1 and local network 2 are all positive, the daily DG-load accommodation ratio of the rigid distribution network is 100%.
(4) due to the network operational constraints, the daily DG-network-load accommodation ratio of local network 1 and local network 2 of the rigid distribution network case is reduced by 7.2% and 3.2%, respectively. The daily DG-network-load accommodation ratio of the whole network of the rigid distribution network is reduced by 4.8%.
(5) compared with the rigid distribution network, the FDN cannot improve the daily DG-load accommodation ratio under scenario 3.

Overall Analysis for 3 Scenarios

In **Figure 10**, the results of the FDN and rigid distribution network (RDN) in three scenarios are summarized, including DG-load matching degrees (MDs, represented by E_Ω), DG-load accommodation ratios (GLARs, represented by λ_{GL}), and DG-network-load accommodation ratios (GNLARs, represented by λ_{GNL}).

According to the conclusion of *Scenarios 1–3* and **Figure 10**, it can be seen that

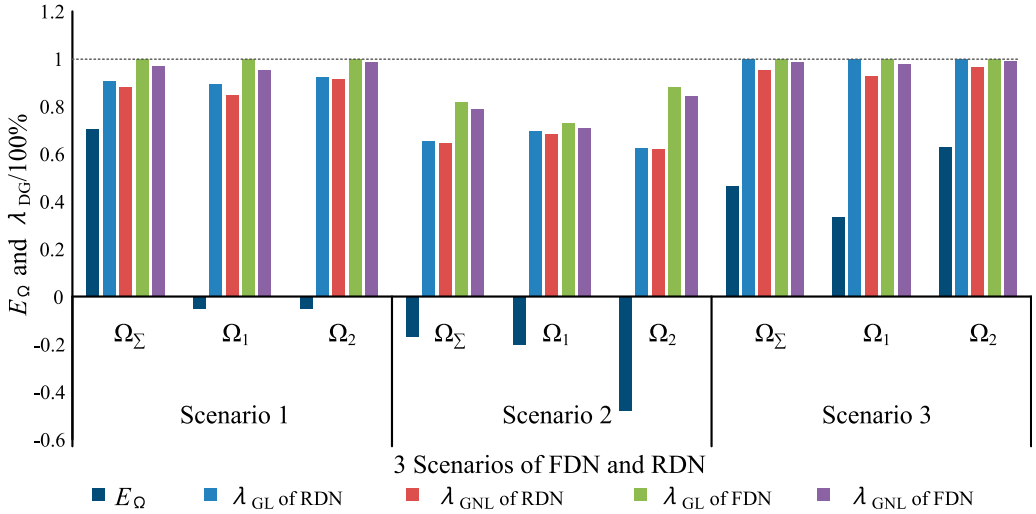

FIGURE 10 | MDs, GLARs, and GNLARs of all 3 scenarios for both the FDN and RDN.

(1) the DG-load accommodation ratio of a distribution network is determined by the matching degree of each local network. Particularly, since the FDN is overall connective, the DG-load accommodation ratio of the FDN is only determined by the overall matching degree.
(2) Only when at least one local network of a distribution network is DG-load unmatched can the DG-load accommodation ratio of the FDN be larger than that of the rigid distribution network. The increase extent of the DG-load accommodation ratio is determined by the matching degrees of the whole network and local networks together. Particularly, if the load and DG of every local network are matched, that is, the DG-load accommodation ratio of every local network reaches its maximum value 100%, it is evident that the DG-load accommodation ratio cannot be further improved by any measures, including the FDN upgrading. In this case, the rigid distribution network is capable of accommodating the DGs due to the perfect DG-load coordinated planning, although it is unusual in a real rigid distribution network.
(3) the increase extents of the hourly DG-load accommodation ratio and hourly DG-network-load accommodation ratio by the FDN fluctuate during one day. It can be seen that the improvements of the hourly DG-load accommodation ratio and hourly DG-network-load accommodation ratio are more obvious in midday and night because the output power of PVs and WTs is sequentially complementary and PVs and WTs are just located in different local networks in the cases.
(4) the DG-network-load accommodation ratio is always lower than the DG-load accommodation ratio in a real FDN. This is because the network operational constraints, such as thermal capacity constraints, limit the DG accommodation. According to the analysis of all three scenarios, we find that it is the branches adjacent to the DG bus that mainly limit the DG accommodation.

Measures to Improve the DG-Network-Load Accommodation Ratio of the FDN

To remove the bottlenecks of DG accommodation in the FDN, the following measures are proposed:

(1) If the locating of DGs is under discussion, it is recommended that the DGs should be integrated to the areas with enough load to ensure the output power of DGs can be accepted instead of exporting.
(2) If the locating of DGs is finished or measure 1 is not enough to remove the bottlenecks of DG accommodation, it is recommended that the capacity of branches adjacent to the DG bus should be properly enlarged according to the maximum output power of DGs. Besides, the capacity of SOP terminals should not be smaller than that of adjacent feeders.

For the cases in this work, the specific measures are as follows:

Measure 1: change the location of DGs, enlarge the capacity of feeders, and increase the capacity of the SOP terminal to 10.5 MVA, as is shown in **Table 5**.

Measure 2: based on measure 1, adjust the incremental capacity. The capacity of branch $B_{1,5}$ is increase by 0.9 MVA, $B_{1,7}$ 0.4 MVA, $B_{1,8}$ 4.8 MVA, $B_{2,4}$ 0.7 MVA, and $B_{2,7}$ 8.8 MVA. The capacity of the rest of the branches is increased as shown in **Table 5**. The details are shown in **Supplementary Table S3**.

The cases with overall higher capacity of DGs are also studied to verify the conclusion mentioned above, as is shown in **Supplementary Material 4**.

CONCLUSIONS

The FDN is a looped-operational distribution network using advanced power electronics technology, such as the SOP. This article studies the intermittent DGs accommodation in the FDN

TABLE 5 | DG location and feeder capacity improvement measures.

DG	PV_1	PV_2	PV_3	WT_1	WT_2	
Location	$L_{1,3}$	$L_{1,4}$	Between $B_{1,2}$ and $B_{1,3}$	$L_{2,2}$	$L_{2,4}$	
Branch	$B_{1,4}$	$B_{1,5}$	$B_{1,6}$	$B_{1,7}$	$B_{1,8}$	$B_{1,9}$
Capacity increase/MVA	0.9	0.9	1.0	0.4	1.2	1.2
Branch	$B_{2,4}$	$B_{2,5}$	$B_{2,6}$	$B_{2,7}$		
Capacity increase/MVA	0.4	0.4	0.1	0.1		

and makes comparison with the rigid distribution network. The main contributions are as follows:

(1) The matching degree is proposed to describe the relation of the load and location and size of the DG.
(2) The proposed index, accommodation ratio, is further divided into the DG-network-load accommodation ratio and DG-load accommodation ratio, to distinguish whether the index takes the network operational constraints into account.
(3) The calculation of the DG-load accommodation ratio is proposed based on the matching degree; the calculation of the DG-network-load accommodation ratio is proposed based on the simulation model of sequential production.
(4) The accommodation ratio of the FDN and rigid distribution network is studied on cases with different matching degrees, and it is concluded that:

   (a) the DG-load accommodation ratio is determined by the matching degree only. The DG-load accommodation ratio of the FDN is determined by the overall matching degree of the whole network. The DG-load accommodation ratio of the rigid distribution network is determined by the overall matching degree of the whole network, as well as the matching degrees of local networks.
   (b) when at least one local network of a distribution network is DG-load unmatched, the DG-load accommodation ratio of the FDN will be larger than that of the rigid distribution network because the SOP can redistribute the power flow among different local networks.
   (c) the DG-network-load accommodation ratio is determined by the matching degree and network operational constraints. The DG-network-load accommodation ratio will tend to the DG-load accommodation ratio if proper planning or optimization measures are taken, such as regulating voltage and expanding feeder capacity.
   (d) the branches adjacent to the DG bus mainly limit the DG accommodation in the FDN. It is recommended to relocate the DGs and enlarge the capacity of feeders.

Compared with traditional distribution network analysis, the proposed DG accommodation analysis method can reflect the essence of DG accommodation capability clearly, which is determined by the location and power balance of the DG and load, as well as network operational constraints. Under the guidance of DG-network-load coordination and planning, the advantages of the FDN can be maximized. Future research will consider the reverse power flow in the 35 kV and 110 kV network and the influences of voltage constraints and energy storage.

DATA AVAILABILITY STATEMENT

The original contributions presented in the study are included in the article/**Supplementary Material**; further inquiries can be directed to the corresponding author.

AUTHOR CONTRIBUTIONS

JX was responsible for conceptualization, methodology, investigation, formal analysis, validation, resources, reviewing and editing the manuscript, supervision, project administration, and funding acquisition. YW was responsible for conceptualization, methodology, investigation, software, validation, data curation, formal analysis, writing the original draft, visualization, and project administration. GZ was involved in investigation, validation, formal analysis, and writing the original draft, review, and editing.

FUNDING

This work was supported by the National Key Research and Development Program of China (2016YFB0900100), National Natural Science Foundation of China (51877144), and China Post-doctoral Science Foundation (2020M670668).

SUPPLEMENTARY MATERIAL

The Supplementary Material for this article can be found online at: https://www.frontiersin.org/articles/10.3389/fenrg.2021.634770/full#supplementary-material.

REFERENCES

Anderson, K., Coddington, M., Burman, K., Hayter, S., Kroposki, B., and Watson, A. (2009). *Interconnecting PV on New York City's Secondary Network Distribution System*. National Renewable Energy Laboratory, Golden, Colorado, USA.

Barragan, M., Mauricio, J. M., Marano, A., Nieves, M., Churio, J., Maza-Ortega, J. M., et al. (2012). "Operational benefits of multiterminal DC-links in active distribution networks," in Power and energy society general meeting, San Diego, CA, USA, July 22–26, 2012 (IEEE), 6.

Cao, W., Wu, J., Jenkins, N., Wang, C., and Green, T. (2016). Benefits analysis of Soft Open Points for electrical distribution network

operation. *Appl. Energy* 165, 36–47. doi:10.1016/j.apenergy.2015.12.022

Escalera, A., Prodanovic, M., Castronuovo, E. D., and Roldan-Perez, J. (2020). Contribution of active management technologies to the reliability of power distribution networks. *Appl. Energy* 267, 114919. doi:10.1016/j.apenergy.2020.114919

Fernandez, G., Galan, N., Marquina, D., Martinez, D., Sanchez, A., Lopez, P., et al. (2020). Photovoltaic generation impact analysis in low voltage distribution grids. *Energies* 13 (17), 4347. doi:10.3390/en13174347

Flottemesch, J., and Rother, M. (2004). "Optimized energy exchange in primary distribution networks with DC links," in Proceedings of the 2004 IEEE International conference on electric utility deregulation, restructuring and power technologies, Hong Kong, China, April 5–8, 2004 (IEEE), Vol. 1–2, 108–116.

Guo, X. M., Huo, Q. H., Wei, T. Z., and Yin, J. Y. (2020). A local control strategy for distributed energy fluctuation suppression based on soft open point. *Energies* 13 (6), 1520. doi:10.3390/en13061520

Huang, A. Q., Crow, M. L., Heydt, G. T., Zheng, J. P., and Dale, S. J. (2011). The future renewable electric energy delivery and management (FREEDM) system: the energy internet. *Proc. IEEE* 99 (1), 133–148. doi:10.1109/jproc.2010.2081330

Liu, P., and Chu, P. (2018). Wind power and photovoltaic power: how to improve the accommodation capability of renewable electricity generation in China?. *Int. J. Energy Res.* 42 (7), 2320–2343. doi:10.1002/er.4013

Moghaddam, I. N., Chowdhury, B. H., and Mohajeryami, S. (2018). Predictive operation and optimal sizing of battery energy storage with high wind energy penetration. *IEEE Trans. Ind. Electron.* 65 (8), 6686–6695. doi:10.1109/tie.2017.2774732

Purchala, K., Meeus, L., Van Dommelen, D., and Belmans, R. (2005). "Usefulness of DC power flow for active power flow analysis," in IEEE power engineering society general meeting, San Francisco, CA, USA, June 16, 2005, Vol. 1–3, 454–459.

Rueda-Medina, A. C., and Padilha-Feltrin, A. (2013). Distributed generators as providers of reactive power support-A market approach. *IEEE Trans. Power Syst.* 28 (1), 490–502. doi:10.1109/tpwrs.2012.2202926

Shafik, M. B., Chen, H., Rashed, G. I., El-Sehiemy, R. A., Elkadeem, M. R., and Wang, S. (2019). "Adequate topology for efficient energy resources utilization of active distribution networks equipped with soft open points," in IEEE Access, Vol. 7, 99003–99016.

Shi, Q., Hu, H., Xu, W., and Yong, J. (2016). Low-order harmonic characteristics of photovoltaic inverters. *Int. Trans. Electr. Energ. Syst.* 26 (2), 347–364. doi:10.1002/etep.2085

Shu, Y., Zhang, Z., Guo, J., and Zhang, Z. (2017). Study on key factors and solution of renewable energy accommodation. *Proc. Chin. Soc. Electr. Eng.* 37 (1), 1–8. doi:10.13334/j.0258-8013.pcsee.162555

SP Energy Networks (2016). Electricity NIC submission: SP energy networks – ANGLE-DC. Available at: https://www.ofgem.gov.uk/publications-and-updates/electricity-nic-submission-sp-energy-networks-angle-dc (Accessed November 30, 2015).

Stram, B. N. (2016). Key challenges to expanding renewable energy. *Energy Policy* 96, 728–734. doi:10.1016/j.enpol.2016.05.034

Wang, B., Xiao, J., Zhou, J., Zhou, H., Liu, Y., and Zu, G. (2017). Dispatchable region of distributed generators and microgrids in distribution systems. *Power Syst. Technol.* 41, 365–372. doi:10.13335/j.1000-3673.pst.2016.2430

Western Power Distribution (2016). Low carbon networks fund submission from Western Power Distribution–Network Equilibrium. Available at: https://www.ofgem.gov.uk/publications-and-updates/ (Accessed November 24, 2014).

Xiao, J., Gang, F., Deng, W., Huang, R., He, Y., and Yi, L. (2017a). Security region model for flexible distribution network. *Appl. Energy* 41 (12), 3764–3771. doi:10.1016/j.apenergy.2019.114425

Xiao, J., Gang, F., Huang, R., Shu, B., Yang, N., and Yu, X. (2017b). Total supply capability model for flexible distribution network. *Autom. Electr. Power Syst.* 41 (5), 30–38. doi:10.7500/AEPS20160713007

Xiao, J., Li, F., Gu, W. Z., Wang, C. S., and Zhang, P. (2011). Total supply capability and its extended indices for distribution systems: definition, model calculation and applications. *IET Gener. Transm. Distrib.* 5 (8), 869–876. doi:10.1049/iet-gtd.2010.0769

Xiao, J., Wang, Y., Luo, F., Bai, L., Gang, F., Huang, R., et al. (2018a). Flexible distribution network: definition, configuration, operation, and pilot project. *IET Gener. Transm. Distrib.* 12 (20), 4492–4498. doi:10.1049/iet-gtd.2018.5641

Xiao, J., Zhang, T., Zu, G. Q., Li, F. X., and Wang, C. S. (2018b). TSC-based method to enhance asset utilization of interconnected distribution systems. *IEEE Trans. Smart Grid* 9 (3), 1718–1727. doi:10.1109/TSG.2016.2598816

Xiao, J., Zu, G., Wang, Y., Zhang, X., and Jiang, X. (2020). Model and observation of dispatchable region for flexible distribution network. *Appl. Energy* 261, 114425. doi:10.1016/j.apenergy.2019.114425

Ye, L., Zhang, C., Xue, H., Li, J., Lu, P., and Zhao, Y. (2019). Study of assessment on capability of wind power accommodation in regional power grids. *Renew. Energy* 133, 647–662. doi:10.1016/j.renene.2018.10.042

Zhu, Z. S., Liu, D. C., Liao, Q. F., Tang, F., Zhang, J. J., and Jiang, H. G. (2018). Optimal power scheduling for a medium voltage AC/DC hybrid distribution network. *Sustainability* 10 (2), 318. doi:10.3390/su10020318

Conflict of Interest: The authors declare that the research was conducted in the absence of any commercial or financial relationships that could be construed as a potential conflict of interest.

NOMENCLATURE

Variables

$\lambda_{\mathbf{DG}}$ accommodation ratio of the DG

$\lambda_{\mathbf{GL}}$ DG-load accommodation ratio

$\lambda_{\mathbf{GL},i}$ DG-load accommodation ratio of local network i

$\lambda_{\mathbf{GNL}}$ DG-network-load accommodation ratio

$E_{\mathbf{\Omega}}$ DG-load matching degree of distribution network Ω

$\left|P_{\mathbf{DG}}^{\mathbf{ge}}(t)\right|$ sum of maximum available output power of all the DGs at the moment t

$\left|P_{\mathbf{DG},k}^{\mathbf{ge}}\right|$ maximum available output power of the DG installed on node k

$|P_{\mathbf{DG}}(t)|$ actual output power of all the DGs at the moment t

$\left|P_{\mathbf{DG},k}\right|$ actual output power of the DG installed on node k

$|P_{\mathbf{L}}(t)|$ sum of consumption power of all the load at the moment t

$\left|P_{\mathbf{B}_{i,j}}\right|$ power flow of $\mathrm{B}_{i,j}$

$\left|P_{\mathbf{B}_{i,1}}\right|$ power flow of the outlet of F_i

$|P_k|$ net power of node k

$\left|P_{\mathbf{L},k}\right|$ load power of node k

$\left|\mathbf{\Delta}P_{i,m}\right|$ power flows between F_i and SOP_m

$\boldsymbol{T}$ period of observation (unit is hour)

$W_{\mathbf{DG}}^{\mathbf{ge}}$ sum of the maximum available output power energy of all the DGs during period T

$W_{\mathbf{DG}}$ sum of the actual output power energy of all the DGs during period T (accommodation power energy of the DG)

$W_{\mathbf{DG},i}$ sum of the actual output power energy of DGs in local network i during period T

Indices and sets

$\pm$ direction of power

$\boldsymbol{\Omega_i}$ local network i

$\boldsymbol{\Omega_{\sum}}$ whole network

$\mathbf{B}_{\boldsymbol{i,j}}$ branch j of feeder F_i

$\mathbf{F}_{\boldsymbol{i}}$ feeder i

$\mathbf{SOP}_{\boldsymbol{m}}$ SOP m

$\boldsymbol{B}$ set of all the branches

$\boldsymbol{G}$ set of all the DG nodes

$\boldsymbol{L}$ set of all the load nodes

$\boldsymbol{S}$ set of all the SOPs

$\boldsymbol{\Omega}(B_{i,j})$ set of downstream nodes and SOPs of $\mathrm{B}_{i,j}$

$\boldsymbol{\Omega}(\mathrm{SOP}_m)$ set of feeders connected to SOP_m

Parameters

$C_{\mathbf{B}_{i,j}}$ capacity of $\mathrm{B}_{i,j}$

$C_{\mathbf{SOP}_m}$ capacity of the SOP_m terminal

$\left|P_k^{\mathbf{max}}\right|$ maximum permitted power of node k

$\left|P_{\mathbf{DG}}^{\mathbf{max}}\right|$ maximum output power (installed capacity) of all the DGs

frontiers in Energy Research

ORIGINAL RESEARCH
published: 22 April 2021
doi: 10.3389/fenrg.2021.647199

Multi-Objective Optimization and Dispatch of Distributed Energy Resources for Renewable Power Utilization Considering Time-of-Use Tariff

Qinhao Xing, Meng Cheng, Shuran Liu, Qianliang Xiang, Hailian Xie and Tailai Chen*

Department of Power Consulting in Smart Grids and Digitalization, ABB Investment (China) Ltd., Beijing, China

The intermittency of wind and solar power generation brings risks to the safety and stability of the power system. In order to maximize the utilization of renewables, optimal control and dispatch methods of the Distributed Energy Resources including the generators, energy storage and flexible demand are necessary to be researched. This paper proposes an optimization and dispatch model of an aggregation of Distributed Energy Resources in order to facilitate the integration of renewables while considering the benefits for dispatchable resources under time-of-use tariff. The model achieves multi-objective optimization based on the constraints of day-ahead demand forecast, wind and solar generation forecast, electric vehicles charging routines, energy storage and DC power flow. The operating cost, the renewable energy utilization and the revenues of storages and electric vehicles are considered and optimized simultaneously through the min–max unification method to achieve the multi-objective optimization. The proposed model was then applied to a modified IEEE-30 bus case, demonstrating that the model is able to reconcile all participants in the system. Sensitivity analysis was undertaken to study the impact of initial states of the storages on the revenues to the resource owners.

Keywords: flexible demand, multi-objectives optimal dispatch, renewable power utilization, distributed energy resouces, time-of-use tariff, min–max unification

OPEN ACCESS

Edited by:
Yue Zhou,
Cardiff University, United Kingdom

Reviewed by:
Rui Jing,
Institute of Urban Environment (CAS), China
Xiaolong Jin,
Technical University of Denmark, Denmark

****Correspondence:***
Qinhao Xing
qinhao.xing@hitachiabb-powergrids.com

Specialty section:
This article was submitted to Smart Grids, a section of the journal Frontiers in Energy Research

Received: *29 December 2020*
Accepted: *08 February 2021*
Published: *22 April 2021*

Citation:
Xing Q, Cheng M, Liu S, Xiang Q, Xie H and Chen T (2021) Multi-Objective Optimization and Dispatch of Distributed Energy Resources for Renewable Power Utilization Considering Time-of-Use Tariff. Front. Energy Res. 9:647199. doi: 10.3389/fenrg.2021.647199

INTRODUCTION

The continuous climate change is expediting the energy reform worldwide in order to develop a greener and sustainable future. In the power sector, the installation capacity of renewables, e.g. solar and wind, has been increased dramatically. According to the Renewables 2020 by IEA, 90% of the newly increased generation resources are renewable energy in 2020. The net increase of renewable generation capacity was predicted to be 7% in 2021 as historical high (IEA, 2020). China, as the second largest economy in the world, has announced the "China carbon-neutral Target" recently. By 2030, the non-fossil fuel resource will reach 25%. This indicates great market for renewables, i.e., the solar and wind generation reach 1200 GW by 2030 and hence approximately 75 GW new installation per year. By 2060, the carbon-neutral target will be reached.

However, the generation output from wind and solar relies on natural resources availability, which are usually intermittent and uncontrollable. Moreover, the substitution of fuel generation plants with renewable resources plants will threaten the power system transient stability by curtailing system inertia, since the renewable resources plants are electrically isolated from grid (Seneviratne and

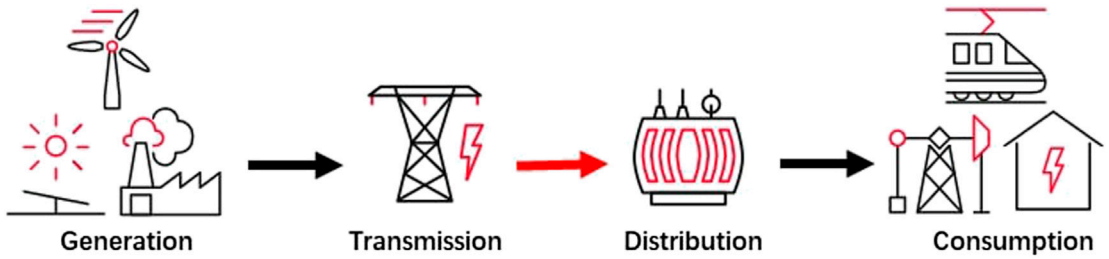

FIGURE 1 | Schematic diagram of the traditional power system.

Ozansoy, 2016). With the foreseeable high integration of renewables, two main challenges remain to be solved in order to operate the power system securely and efficiently. One is to enhance the utilization of renewable output, and the other is to maintain the system stability as a result of the uncontrollable generation output. It can be seen that the power system requires sufficient reserve with fast response to mitigate the impact of high renewable penetration.

Traditional power systems provide a unidirectional energy flow from generation to consumption as showed in **Figure 1**. Generation adjusts the power outputs in accordance to the variations of consumption, and in the meantime provides ancillary service to maintain the power system balance. Following the increasing integration of renewables, the replacement of conventional fossil-fuel generation reduces the available reserve capacity to flexibly adjust the generation output. The integration of renewables at the distribution level changes the power flow from unidirectional to bidirectional. The operation of power system is hence more complex to maintain the balance between generation and consumption.

In order to maintain the balance between generation and consumption, other mechanisms have been proposed in addition to the flexible regulation of conventional generators.

Energy storage is considered as a flexible and high-efficient dispatchable resource to maintain the power balance and hence improve the system security and reliability. The flexible charging and discharging of storage will counteract the instability of renewable generation, and in the meantime improve the renewable utilization. Castillo and Gayme (2014) listed the various ancillary services the energy storage is able to offer within economic-effective system penetrated by non-dispatchable renewable energy resources based on the definition of "grid-scale energy storage". Su and Abbas El Gamal (2013) modeled the exact power imbalance gap caused by wind power intermittent output, leading to a specific value of energy storage capacity needed to cover the imbalance through stochastic control. Wang et al., 2013 aggregated the battery energy storage and super-capacitor to stabilize the solar power output variations. Previous research study verified the necessity and feasibility to apply the energy storage with renewable integration.

In addition, flexible regulation of power consumption from the demand is also considered as an alternative option to maintain the power balance. One of the flexible demand regulation solutions is demand response (DR), which achieves customers shifting power usage following dispatch needs. Typical types of DR include industrial production lines (Alkadi et al., 2013) and temperature-controlled demand (Zhang et al., 2013).

Following the decarbonization in the transport sector, the Electric Vehicles (EVs) have been largely deployed and considered as a flexible demand as the power consumption of charging of an EV can be adjusted according to power system conditions.

Except for the technical feasibility evaluation, the business model of renewable generation, storage and flexible demand has also drawn attentions by researches. The economic dispatch at present always packaged or collaborated the storage and renewable generation when they used identical grid port and achieved the comprehensive revenue maximum. Chen and Zhao (2020) treated the storage-wind power integration as a single market participant, and the objective function included the profit of the integration to reach a maximum. Li et al., 2015 modeled different scenarios to compare the case of storage and wind power generation as one entity in the electricity market with the case of running storage and wind power generation independently. The results showed that the integrated case held a remarkable profit increase. Ge et al., 2020 established a solar power generation-storage cooperative game model. The offer-bid actions for the solar and storage to participate in electricity market were simulated. Yuan et al., 2016 proposed an economic dispatch model of virtual power plant consisting of wind and solar generation, gas and storage. The conclusion turned out that the storage is able to reduce the generation cost and improve the renewables utilization.

Likewise, DR encourages the end-users to curtail load during peak load period in response to financial incentives. PJM divided DR into Emergency Response and Economic Response based on dispatch needs and response capability, and accordingly provides different levels of compensation. DR resources are allowed to bid and compete with power market to achieve economic dispatch results (PJM INT, 2020). Similarly, the vehicle-to-grid technology (V2G) allows EV to adjust behaviors under electricity market circumstance for revenues. Ma et al., 2012 built the model of EV benefit, showing that the EV had minor impact to power system with significant profit gained. Ansari et al. (2015) introduced a bidding strategy of EV in ancillary service market based on the autoregressive integrated moving average model, which fully considered the uncertainties of market environment.

Considering the optimal dispatch of the energy storage and flexible demand, the future power system will be a system of friendly interaction among the generation source, load and energy storage, as present in **Figure 2** and named as an Integrated Energy System (IES). Through the continuous improvement in the electricity market mechanism and the digital technologies, most of the IESs are

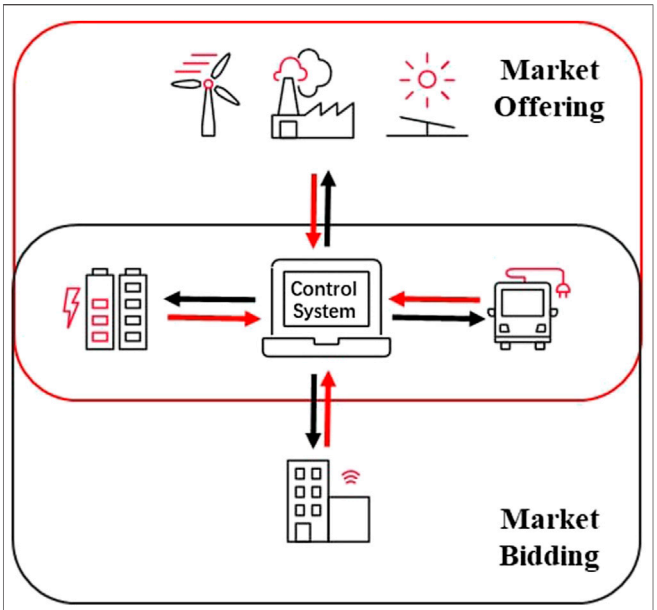

FIGURE 2 | Basic formation of integrated energy system.

operated by aggregators, who host multiple types of generations and flexible resources, supplying power for the load within regions, and seeking for the profit maximum. Under the energy dispatch of aggregators, the energy internet will be formulated which enables the generation, load and energy storage to participate in the energy trading and system operation to improve the utilization level of renewables efficiently and economically.

According to the literature review, a number of the studies have presented the technical feasibility of flexible resources coupling with PV or wind turbine for renewable energy utilization. There are also studies on the trading strategies based on system forecasting within electricity markets. However, most of the studies were focusing on the simple cooperation between one type of flexible resource with the conventional energy system. The interactions and dispatch of multiple energy resources under the regional energy aggregator have hardly been discussed in depth. Based on the discussion above, this paper established a coordinated optimal day-ahead dispatch model for regional IES based on the time-of-use (TOU) tariff considering the participation for the energy aggregator, energy resource owners, and the power flow distribution in grid. The model contains the distributed generators, storages and EVs. A multi-objective mixed-integer linear programming (MILP) problem was formulated considering the maximization of the whole system profit, maximization of renewable energy outputs and the maximization on revenues of storage/EVs' simultaneously based on the optimal method. Case studies on a modified IEEE 30-bus system were undertaken to verify the benefits of the proposed optimal dispatch method.

TYPICAL DISPATCH RESOURCES FOR OPTIMIZATION

The dispatchable resources of the IES in the model are depicted as follows.

(1) Thermal generation: As the main supplier of electricity, the thermal power output can be flexibly adjusted in order to achieve supply-demand balance of power in real time. Thermal generation plays an essential role for the stability and safety of power system.
(2) Wind generation: Wind power output is related to wind speed, thus presents significant volatility and uncertainty. In the meanwhile, the typical output curve usually shows an inverse-peak characteristic. As a result, storage devices are usually needed to mitigate the output variations of wind generation.
(3) Photovoltaic power stations: PVs typically operate and generate power output during daytime and reach the peak at midday. The operational cost of PVs is relatively low, compared with the fixed cost of PV equipment.
(4) Storage device: As the flexible dispatching device, energy storage plays an important role in the utilization of renewables, which supports to maintain the safety and efficient operation of power system. Energy storage devices can not only absorb the redundant power, but also play the role of reserve power during the peak period and achieve the load shifting of the power system.
(5) Load: Load is the consumer of electricity. Typical load curves reach a peak during midday and a valley in the evening. Various kinds of load show different external characteristic curves. Power system operations need to forecast the load variations, allowing the generation schedule to meet the load power requirements.
(6) Electric vehicles: Electric vehicles (EVs) can be treated as a special load, and the charging load behaviors are usually hard to predict in long time scale. Meanwhile, EVs can also be treated as energy storage device following the development of V2G technology. Incentive signals such as real-time price may encourage EV users to discharge during peak period in the daytime and charge during the valley load period at night. EVs will play an important role in terms of load shifting and improving system operating efficiency in the future.

FORMULATION OF THE OPTIMAL DISPATCH MODEL

Based on the operational constraints and distributed energy equipment mentioned above, this paper establishes an optimal day-ahead dispatch model and formed a MILP problem considering multiple objectives, including maximizing the total system profits, storage and EV profits, and renewable utilization level. The details of the optimization model are formulated as follows.

Objective Functions

Objective 1: Maximize the Profit of the Entire System

The total system profit is the interest of the aggregator, equal to the difference between revenue from load and energy cost. The revenue consists of the payment from load consumption and storage/EV electricity charge. The cost consists of the marginal costs, operating costs, start-up costs of thermal generators (Liu

and Du, 2018), the levelized cost of electricity (LCOE) for wind turbines and PVs, and the cost of electricity sold to the system from storage and EVs. The expression of objective 1 is as follows.

$$\max F_1 = \sum_{t=1}^{T} \left(\left(\sum_{d=1}^{D} Demand_{d,t} \cdot \mathrm{Price}_t + \sum_{es=1}^{ES} ESch_{es,t} \cdot \mathrm{Price}_t + \sum_{e=1}^{E} EVch_{e,t} \cdot \mathrm{Price}_t \right) - \left(\sum_{f=1}^{G_f} Genfuel_{f,t} \cdot fueloffer_t + \sum_{f=1}^{G_f} C_f + \sum_{f=1}^{G_f} STC_{f,t} \right) - \left(\sum_{w=1}^{G_w} Genwind_{w,t} \cdot windoffer_t \right) - \left(\sum_{s=1}^{G_s} Gensolar_{s,t} \cdot solaroffer_t \right) - \left(\sum_{es=1}^{ES} ESdis_{es,t} \cdot esprice_t \right) - \left(\sum_{e=1}^{E} ESdis_{es,t} \cdot ev\mathrm{Price}_t \right) \right) \tag{1}$$

where T is the total dispatch horizon, equal to 24. D represents the number of load buses. ES and E denote the number of storage devices and EVs respectively. G_f, G_w, G_s represent the number of thermal generator units, wind turbines and PVs. $Demand_{d,t}$ is the predicted power of the load d at period t. $Price_t$ is the electricity price at period t. $ESch_{es,t}$ is the charging power of the storage device es at period t. $EVch_{e,t}$ is the charging power of the EV cluster e at period t. $Genfuel_{f,t}$ represents the generation output of the thermal power unit f at period t. $Genwind_{w,t}$ indicates the output of the wind generation w at period t. $Gensolar_{s,t}$ represents the output of the PV panel s at period t. $ESdis_{es,t}$ is the discharge power of the storage device es at period t. $EVdis_{e,t}$ is the discharge power of the EV cluster e at period t. C_f indicates the operation cost of the thermal unit f. $STC_{f,t}$ indicates the start-up cost of the thermal unit f. $fueloffer_t$ denotes the marginal cost of thermal units at period t. $windoffer_t$ is the LCOE for wind turbines at period t. $solaroffer_t$ is the LCOE for PVs at period t. $esPrice_t$ is the discharge price of storage at period t. $evPrice_t$ is the discharge price of EV cluster at period t.

Objective 2: Maximize the Profit of Storage/EV Owners

In order to encourage the storage/EV owners to integrate the dispatch of energy, the profit of storage/EV owners is considered to be one of the objective functions during dispatch.

$$\max F_2 = \sum_{t=1}^{T} \left(\sum_{e=1}^{E} EVout_{e,t} \cdot ev\mathrm{Price}_t - \sum_{e=1}^{E} EVin_{e,t} \cdot \mathrm{Price}_t + \sum_{es=1}^{ES} SoCdis_{es,t} \cdot es\mathrm{Price}_t - \sum_{es=1}^{ES} SoCch_{e,t} \cdot \mathrm{Price}_t \right) \tag{2}$$

Objective 3: Maximize the Generation Output From Renewables

Considering the popularity of clean energy consumption, the generation output from renewable resources owners is considered to be one of the objective functions during dispatch.

$$\max F_3 = \sum_{t=1}^{T} \left(\sum_{w=1}^{Gw} Genwind_{w,t} + \sum_{w=1}^{Gw} Gensolar_{s,t} \right) \tag{3}$$

Constraints

System Constraints

Constraint 1: Power Balance

The real-time total power generation is required to meet the power consumption of demand.

$$\sum_{d=1}^{D} Demand_{d,t} + \sum_{es=1}^{ES} SoCch_{es,t} + \sum_{e=1}^{E} EVin_{e,t} = \sum_{f=1}^{G_f} Genfuel_{f,t} + \sum_{w=1}^{G_w} Genwind_{w,t} + + \sum_{s=1}^{G_s} Gensolar_{s,t} + \sum_{es=1}^{ES} SoCdis_{es,t} + \sum_{e=1}^{E} EVout_{e,t} \tag{4}$$

Constraint 2: Line Flow Capacity Limit

Line flow capacity refers to the allowable maximum power flow for a branch, which is decided by the power losses, wire temperature and system stability.

For clarification, the transmission line in this paper is modeled as a classical direct current (DC) power flow model (Stott et al., 2009). Thus the line voltage P.U. value is considered as 1, and the line flow capacity limit is considered a fixed constant value. The details of the approximations is briefly explained in the **Appendix**.

$$-Plimit_l \le SF \cdot Map\left(Genfuel_{f,t} + Gensolar_{s,t} + Genwind_{w,t} - Demand_{d,t} - EV_{e,t} - Storage_{es,t} \right) \le Plimit_l \tag{5}$$

$Plimit_l$ represents the line flow capacity of line l. SF is the shift distribution factor. Map is the position transformation matrix for the components (branches or nodes) of system.

Thermal Power Unit Constraints

Thermal power unit constraints include maximum/minimum output level constraints in **Eqs. 6** and **7**, ramping up/down constraints in **Eqs. 9**, minimum on/off time constraints in **Eqs. 10** and **11**, and start-up cost constraint in **Eq. 12**. Constraints **(13)**–**(17)** represent the thermal unit commitment status and the coupling relationships.

$$Genfuel_{f,t} \le I_{f,t} \cdot Genfuelub_f \tag{6}$$

$$Genfuel_{f,t} \ge I_{f,t} \cdot Genfuellb_f \tag{7}$$

$$Genfuel_{f,t} - Genfuel_{f,t-1} \le fuelru_f \tag{8}$$

$$-fuelrl_f \le Genfuel_{f,t} - Genfuel_{f,t-1} \tag{9}$$

$$I_{f,t} \ge \sum_{\tau=\max\left\{1,\ t-MT_f^{on}+1\right\}}^{t} P_{f,t} \tag{10}$$

$$1 - I_{f,t} \ge \sum_{\tau=\max\left\{1,\ t-MT_f^{off}+1\right\}}^{t} Q_{f,t} \tag{11}$$

$$STC_{f,t} \ge P_{f,t} \cdot Cstc_f \tag{12}$$

$$1 - I_{f,t-1} \ge P_{f,t} \tag{13}$$

$$I_{f,t-1} \ge Q_{f,t} \tag{14}$$

$$I_{f,t} - I_{f,t-1} \ge P_{f,t} - Q_{f,t} \tag{15}$$

$$0 \le P_{f,t}, Q_{f,t} \le 1 \tag{16}$$

$$I_{f,t} \in \{0, 1\} \tag{17}$$

$I_{f,t}$ is the binary on/off indicator for thermal power unit f. $P_{f,t}$ and $Q_{f,t}$ represent the start-up/shutdown indicators of thermal power

unit *f*. $Genfuelub_f$ and $Genfuellb_f$ represent the maximum/minimum output level constraints of thermal power unit *f*. $fuelru_f$ and $fuelrl_f$ represent the ramping up/down limit of thermal power unit *f*. MT_f^{on} and MT_f^{off} represent the minimum on/off time limit of thermal power unit *f*.

Wind Generation Constraints

Wind generation constraints include the maximum/minimum output constraints in **(18), (19)**.

$$Genwind_{w,t} \le Genwindub_w \tag{18}$$

$$Genwind_{w,t} \ge Genwindlb_w \tag{19}$$

$Genwindub_w$ and $Genwindlb_w$ represent the maximum/minimum output constraints of wind generation *w*.

PV Constraints

PV constraints include the maximum/minimum output constraints in **(20)(21)**.

$$Gensolar_{s,t} \le Gensolarub_s \tag{20}$$

$$Gensolar_{s,t} \ge Gensolarlb_s \tag{21}$$

$Gensolarub_s$ and $Gensolarlb_s$ represent the maximum and minimum output of PV *s*.

Storage Constraints

Storage constraints include the state of charge (SoC) constraints in **(22)**, charge/discharge power constraints in **(23)(24)**, charge/discharge efficiency in **(25)**, and the cyclic balance constraint in **(26)**, which requires the SoC of energy storage to return to the initial status in the final interval.

$$0 \le SoC_{es,t} \le 1 \tag{22}$$

$$\left(SoC_{es,t} - SoC_{es,t-1}\right) \cdot Capes_{es} = ESP_{es,t} \tag{23}$$

$$-ESdis_{es} \le ESP_{es,t} \le ESch_{es} \tag{24}$$

$$\min\{0, dces_{es} \cdot Storageout_{es,t}\} \le ESP_{es,t} \le \max\{0,\ ches_{es} \cdot Storagein_{es,t}\} \tag{25}$$

$$SoC_{es,0} = SoC_{es,24} \tag{26}$$

$Capes_{es}$ is the capacity of storage device *es*. $SoC_{es,t}$ is the state of charge of storage device *es* in *t*. $ESP_{es,t}$ is the charging/discharging energy of storage device *es* in *t*. $ESch_{es}$ and $ESdis_{es}$ denote the limits on charging/discharging power of storage device *es*. $ches_{es}$ and $dces_{es}$ are the charging and discharging efficiency of storage device *es*. $SoC_{es,0}$ is the initial state of charge of energy storage.

EV Constraints

For computational convenience, the optimization model assumes that EVs can participate in the dispatch throughout the whole 24 h horizon, and the battery material features of all EVs are same. The model considers the EVs as clusters based on geographical locations of EV charging stations. The constraints on EVs include the state of charge (SoC) constraints of EV clusters in **(27)**, charging/discharging power limits in **(28)(29)**, the efficiency constraints on charging and discharging in **(30)**, the constraints that simulate the driving habits of EV users in **(31)(32)**, and the cyclic balance constraint in **(33)**, which requires the SoC of EV cluster to return to the initial status in the final interval. In order to meet the travel demand of EV users, EVs is pre-set to guarantee more than 80 and 60% of battery charge at 7am and 16pm in this paper.

$$0 \le EV_{e,t} \le 1 \tag{27}$$

$$\left(EV_{e,t} - EV_{e,t-1}\right) \cdot Capev_e = EVP_{es,t} \tag{28}$$

$$-EVdis_e \le EVP_{es,t} \le EVch_e \tag{29}$$

$$\min\{0, dcev_e \cdot EVout_{e,t}\} \le EVP_{es,t} \le \max\{0, chev_e \cdot EVin_{e,t}\} \tag{30}$$

$$EV_{e,7} \ge 0.8 \tag{31}$$

$$EV_{e,16} \ge 0.6 \tag{32}$$

$$EV_{e,0} = EV_{e,24} \tag{33}$$

$Capev_e$ is the energy capacity of EV cluster *e*. $EV_{e,t}$ is the state of charge of EV cluster *e* in *t*. $EVP_{es,t}$ is the charging/discharging power of EV cluster *e* in *t*. $EVch_e$ and $EVdis_e$ represent the ramping up/down limits of EV cluster *e*. $chev_{es}$ and $dcev_{es}$ are the charging and discharging efficiency of EV cluster *e*. $EV_{e,0}$ is the initial state of charge of EV cluster.

Formulation of the Multi-Objective Problem

Many researches have been applying multi-objective optimization problem (MOP) as IES solution approaches. An elaborate literature review of MOP researches is present in Jing et al., 2019, which listed and summarized previous studies by objective considerations, modeling types, decision-making methods, and solving engines. The top 2 popular MOP solving methods are still genetic algorithm and weighted-sum algorithm. A figure of statistical results on occurrence frequency of MOP solving strategies and decision-making approaches, pointing out that most of the existing researches have been only focusing on problem modeling and algorithm formulation, while ignoring the decision-making discussion. Among the papers that have considered decision-making process, the most frequent method is still subjective decision-making.

This paper considers a weighed-sum algorithm in MOP with subjective decision-making on the weighing factors. The min–max unification on the objectives is applied to transfer the multi-objective problem to a single objective problem. It is

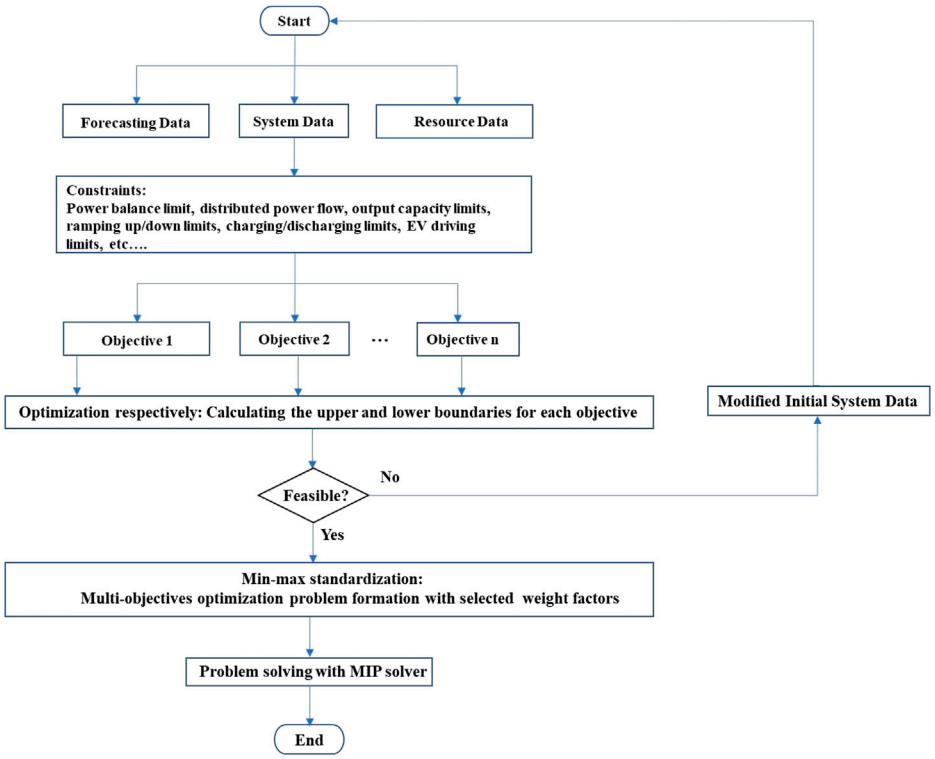

FIGURE 3 | Flowchart of the proposed multi-objective optimization model and the solution process.

necessary to standardize each objective function which neglect the magnitude differences of each objective function so that the weighting factors can be defined.

The min–max unification process is given below.

Minimum objective unification:

$$F_i^{'} = \left(F_i - F_{i,\min}\right) / \left(F_{i,\max} - F_{i,\min}\right) \tag{34}$$

Maximum objective unification:

$$F_i^{'} = \left(F_i - F_{i,\min}\right) / \left(F_{i,\max} - F_{i,\min}\right) \tag{35}$$

F_i and $F_i^{'}$ represent the actual value and the standardizing value of objective i. $F_{i,\max}$ and $F_{i,\min}$ are the maximum value and minimum value of objective i.

The reformulated problem with weight coefficient method is:

$$\max F = \sum_{i=1}^{n} \omega_i F_i^{'} \tag{36}$$

ω_i (i = 1,2,3, . . . n) are the weights of objectives set by the system operator, presenting the importance of each objective, where the sum of weights $\sum_{i=1}^{n} \omega_i = 1$.

Solution Approach

The flow chart in **Figure 3** depicts the proposed multi-objective optimization model and the solution process. Major steps of this method are summarized as follows.

Step 1: Input data of forecasting values, system data and resources parameters. The forecasting values include the forecasting wind power output, forecasting solar power output, and forecasting demand power output. The system data includes the network topology and line flow capacity limits. The resources parameters include the capacity limits, ramping limits, start-up costs, marginal costs, operational costs, and minimum on/off time requirements of thermal units. The capacity limits and LCOE for wind turbines and PVs, the state of charge capacity limits and charging/discharging power limits on energy storages and EVs are also the input data.

Step 2: Set system constraints including the power balance constraint, power flow limit constraints, maximum output capacity limits and ramping up/down limits for thermal units, wind generators and PVs, maximum capacity limits, charging/discharging limits and charging/discharging efficiency limits for energy storages and EVs, and EV driving habit limits.

Step 3: Solve each single-objective problem and calculate the upper and lower boundaries for all objective values. If the one or more optimization problems are infeasible, the input data needs to be modified and the whole process starts again.

Step 4: Combine the single objective problems using the min–max uniformization to formulate the one multi-objective problem with the pre-set weighting factors.

Step 5: The multi-objective problem is solved with the mix-integer programming solver.

TABLE 1 | Parameters of thermal generators and renewables.

Parameters	Thermal	PV	Wind
Maximum power output (MW)	150/200	70/50	80/80
Up ramping limit (MW)	45/40	14/11	12/7
Down ramping limit (MW)	40/30	15/9	13/8

TABLE 2 | Parameters of storage and EV.

Parameters	Storage	EV cluster
Capacity (MW·h)	80/90	10/10/10/10
Maximum charging power (MW)	30/35	1.2/1.5/1.8/1.3
Maximum discharging power (MW)	25/35	0.8/0.9/1.0/0.7
Charging and discharging efficiency	0.9	0.9

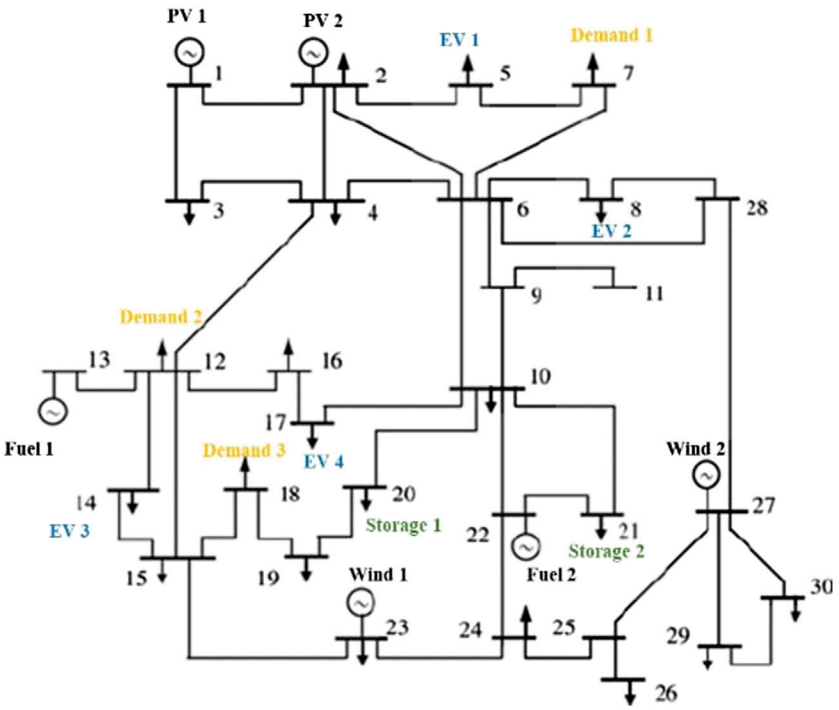

FIGURE 4 | Modified IEEE-30 bus system.

CASE STUDY

Case Overview

The case study was undertaken based on a modified standard IEEE-30 bus case, including 2 thermal generators, 2 PVs, 2 wind generators, 2 storage devices, and 4 EV clusters. The dispatch horizon span is 24 h, with each time interval of 1 h. The parameters of thermal generators and renewables are shown in **Table 1**. The parameters of storage devices and EVs are displayed in **Table 2**. **Figure 4** presents the system information of the modified IEEE-30 bus case. **Figure 5** shows the forecast of wind power, solar power and the load curve.

The MILP optimization problem contains 1,056 variables, including 144 binary variables. All algorithms are implemented in Yalmip based on MATLAB. The problem solved with CPLEX 20.1. The MILP gap is set as 0.1%.

The marginal generation costs on fuel generators, the levelized cost of electricity for wind turbines and PVs, utilization payment rates and storage/EV selling rate are present in **Table 3**. The levelized cost of electricity for wind power and solar power are based on the price from National Development and Reform Commission in China (National Development and Reform Commission., 2019; National Development and Reform Commission., 2020), and the marginal cost for fuel generation is the procurement price of fuel generation (National Energy Administration., 2018). While the production cost of wind and

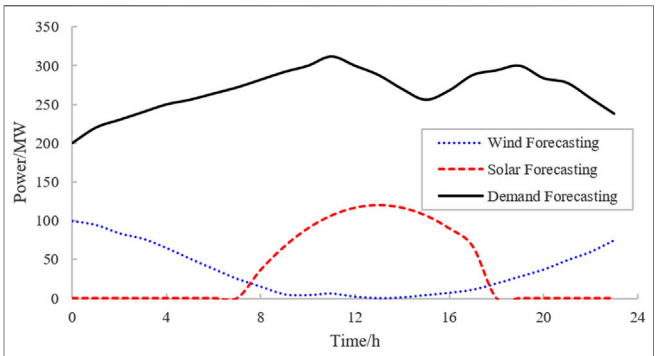

FIGURE 5 | Forecast Variation of Renewable Power and load level.

TABLE 3 | Generation marginal cost.

	Wind power (LCOE)	Solar power (LCOE)	Fuel generation (marginal)
Cost (RMB/MW·h)	290	350	441

TABLE 4 | Electricity price and storage/EV Selling Rate with TOU Tariff.

Time-of-use tariff	Peak (9:00–14:00, 18:00–21:00)	Flat (6:00–9:00, 14:00–18:00, 21:00–23:00)	Valley (0:00–6:00, 23:00–24:00)
Demand payment rate (RMB/kW·h)	1.0994	0.7510	0.4126
Storage/EV selling rate (RMB/kW·h)	0.8795	0.6008	0.3300

solar power is close to zero, the levelized cost of electricity for wind and solar power represents the average net present cost over equipment life time circle and tends to be raised to cover the fixed investments (e.g. equipment investment, installation fees, labor cost).

The utilization payment rate follows the industrial TOU tariff, showing in **Table 4**. It is assumed that the storage/EV can sell power to the system with 0.8 times of the tariff.

Results and Analysis of Multi-Objective Optimization

As aforementioned, the optimization model is first standardized by solving three single-objective optimization problems to maximize system profit, maximize the profits of storage and EV owners, and maximize the output of renewables. The function values under different objectives optimized with mentioned constraints and data are shown in **Table 5**. The upper and lower bounds for the three single-objective optimization problems are $F_{1,max} = 2176.5$, $F_{1,min} = 1610.7$, $F_{2,max} = 50.5$, $F_{2,min} = -254.1$, $F_{3,max} = 2639.9$, $F_{3,min} = 1811.0$.

Table 5 shows that F_1 and F_3 are positively correlated, showing that maximizing system profit will increase the output of renewables as a result of the lower costs of renewables. F_1 and F_2 are negatively correlated, namely the strategy of maximizing grid profits will reduce the profits of storage devices and EVs, and vice versa. If the profit of storage devices and EVs owners takes the priority, the grid will first purchase power from storage devices and EVs instead of the cheaper thermal power units during peak hours. The profit of generators is hence decreased. Therefore, the single-objective optimization of F_1 and F_2 is incompatible.

The results shown in **Table 4** are used as input parameters to solve the multi-objective optimization model which is a mixed-integer programming problem solved by CPLEX. The weighting factors are set as $[\omega_1, \omega_2, \omega_3] = [0.3,0.3,0.4]$ for F_1, F_2, and F_3, representing their importance in the objective function (35). The optimization result is shown in **Table 6**, demonstrating this multi-objective optimization method can fully take the factors of different subjects into account.

TABLE 5 | Function values with different optimization objectives.

Objectives	F_1/kRMB	F_2/kRMB	F_3/MW·h
$F = \max F_1$	2,176.5	−254.1	2,124.2
$F = \max F_2$	1,610.7	50.5	1,811.0
$F = \max F_3$	1,902.4	−111.5	2,639.9

TABLE 6 | Objective values under multi-objective optimization.

Objective number	Optimal result value
F_1/kRMB	1,945.0
F_2/kRMB	46.1
F_3/MW·h	2,639.9

$$\max F = \omega_1 \frac{F_1 - F_{1,\min}}{F_{1,\max} - F_{1,\min}} + \omega_2 \frac{F_2 - F_{2,\min}}{F_{2,\max} - F_{2,\min}} + \omega_3 \frac{F_3 - F_{3,\min}}{F_{3,\max} - F_{3,\min}} \tag{37}$$

Figures 6 and **7** show the charging/discharging schedule obtained from the multi-objective optimization, which demonstrates the energy storage and EVs are quite active under the incentive of TOU tariff to gain much profits from charging/discharging behaviors. The TOU tariff is present as broken line, and the changing/discharging power is showed as bar.

Another two case studies were carried out to verify the benefits of the optimal dispatch with various dispatchable resources. The case settings are given below, where Scenario 3 is the identical case mentioned above.

Scenario 1: Thermal power units are included in the system, without renewables, storage devices, or EVs.
Scenario 2: The system includes thermal power units and renewables, without storage devices or EVs.
Scenario 3: Thermal power, renewables, storage and EVs are all included in the system.

The profits of power system and the owner of storage devices/EVs in each scenario are compared in **Table 7**. Considering scenarios 1 and 2, the cost of power supply dramatically decreases

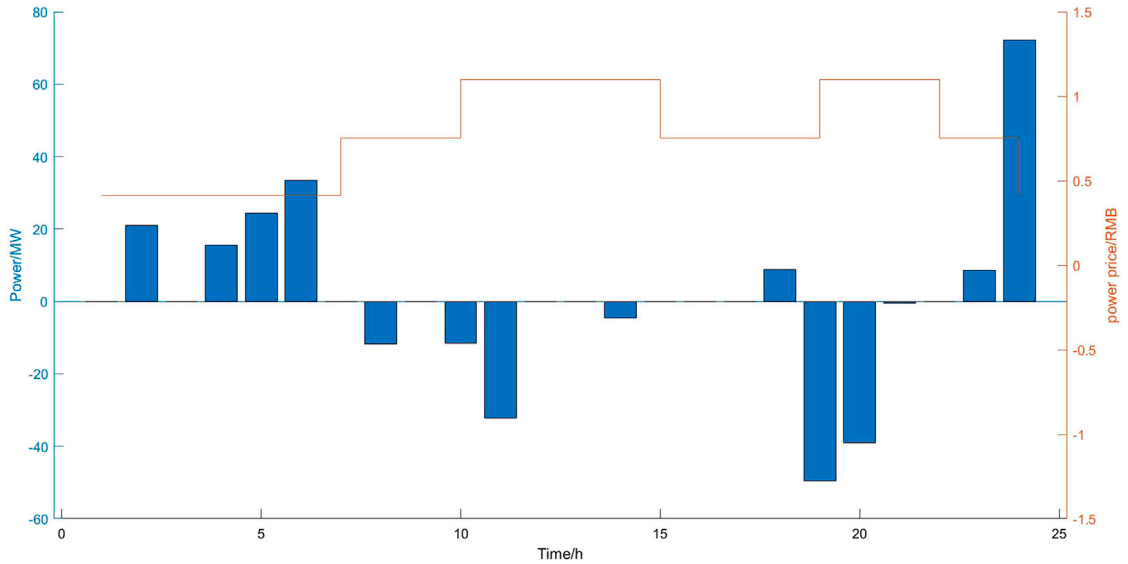

FIGURE 6 | Charging and discharging of storage.

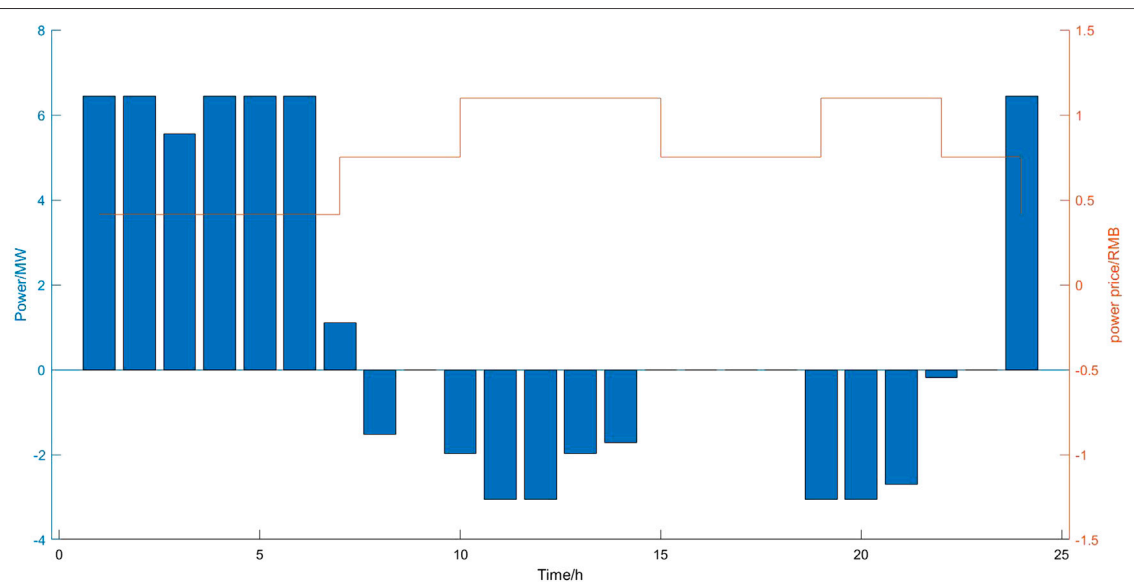

FIGURE 7 | Charging and discharging of EV clusters.

with the participation of renewables, which holds a comparative lower cost and leads to higher revenue. Scenarios 2 and 3 show that with the participation of storage devices and EVs, the profit of the power system slightly decreases. It is because a part of the profit of the power system is transferred to the owner of storage devices and EVs. Moreover, the total profit of the power system and storage/EV increases slightly.

With the renewable generation penetrated in scenario 2 and 3, the storage/EV may stabilize the variation of renewable generation output, as well as a flatter output of fuel generation output. **Figure 8** shows the overall output curves of thermal power units with and without storage device/EV. Due to the lower LCOE for renewable generation, the thermal units tend to be utilized after renewable generation reaches the maximum output capability, leading to the severe fluctuation of thermal output in scenario 2 synchronized with the

TABLE 7 | Profits of grid and storage/EV under each scenario.

Profit/kRMB	Power system	Storage/EV
Scenario 1	1,375.7	–
Scenario 2	1,799.3	–
Scenario 3	1,763.2	46.1

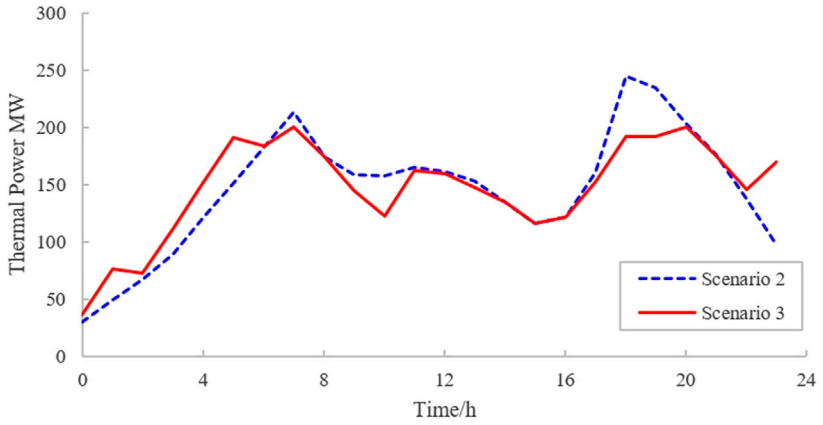

FIGURE 8 | Comparison of thermal power output curves.

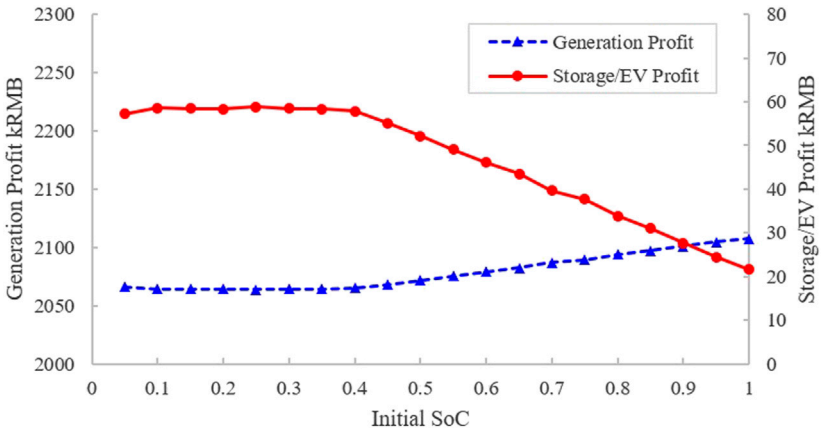

FIGURE 9 | Influence of initial charging status of storage/EV on profits.

fluctuation of wind/solar forecasting. With the participation of storage and EVs in scenario 3, it can be seen that the output of the thermal power units is smoother due to storage and EVs buffering the variations of renewable output. The system peak-valley gap is also reduced significantly, and thus improves the operating efficiency of the power system.

Impacts of the Initial Charging Status of Storage Device

The initial charging status of the energy storage device will impact the charging behaviors of the storage device over the whole dispatch horizon, which in turn affects the overall profitability of the grid and storage/EV. **Figure 9** shows the evaluation of various initial charge of storage on the profits of different entities based on Scenario 3. The storage/EV profit is almost constant when the initial SoC is less than 0.4, while shows a linear decrease with the increase of initial charging status. The generation profit shows a completely opposite trend with storage/EV profit. Thus, from the perspective of storage/EV owners, an initial SoC lower than 0.4 would promise a better revenue from the dispatch of energy aggregator.

Figure 10 presents a further proof of the conclusion made above, which compared the charging/discharging activities of two cases: initial SoC = 0.3 and initial SoC = 0.7. The magnitudes of charging/discharging activities in the former case present a more active storage in the dispatch, leading to better revenue and profit for the owner.

CONCLUSION

This paper proposes an optimization and dispatch model of the energy aggregator of DERs including generators, flexible electric charging loads and energy storages in order to facilitate the integration of renewables while considering the benefits for all energy resources under the time-of-use tariff. A multi-objective optimal dispatch model was developed considering the constraints of the DER operational requirements, power network flows and the end user comforts. Based on the IEEE 30-bus system, by integrating significant renewable

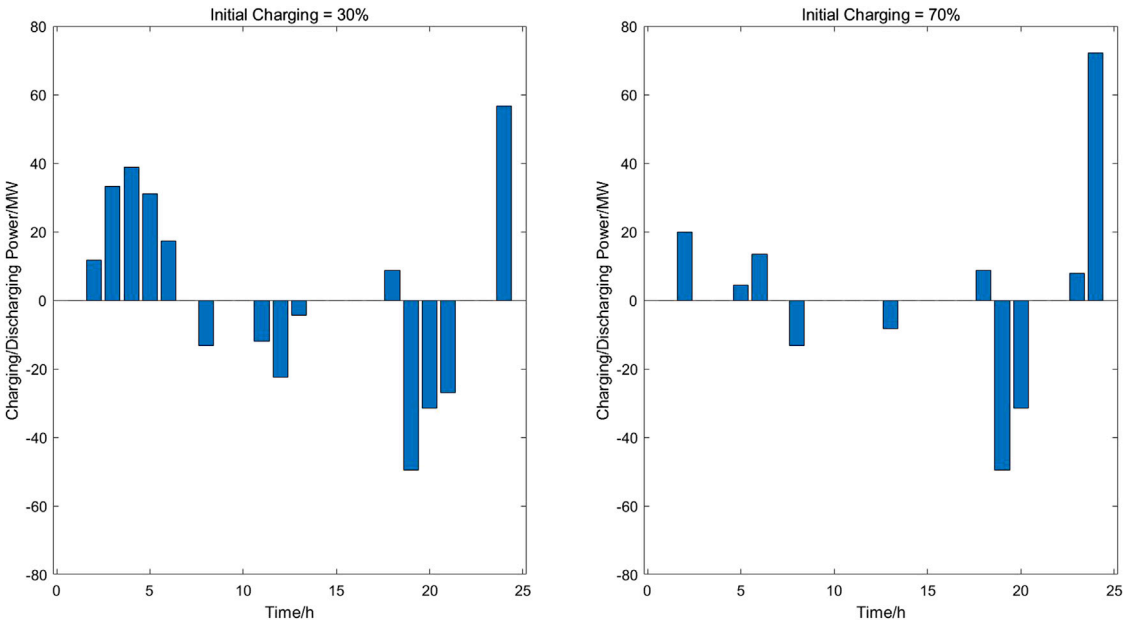

FIGURE 10 | Charging and discharging behaviors under different initial charging status.

resources, case studies were carried out to verify the benefits of the proposed model and dispatch methods.

The multi-objective optimization results were obtained in the case studies, which verifies that both the benefits of the aggregation and the storage device/EV were optimized. Results also showed that through the dispatch of the energy storage devices and EVs, the fluctuations of renewables were smoothed, the peak-valley difference of the system was reduced. In the meantime, the frequent regulations of conventional generators were reduced. A sensitivity analysis was undertaken which indicates that the initial state of charge for the storage has an impact on the charging/discharging schedules, thus may impact the profit of the storage/EV owners for participating in the dispatch.

DATA AVAILABILITY STATEMENT

The raw data supporting the conclusions of this article will be made available by the authors, without undue reservation.

AUTHOR CONTRIBUTIONS

QX contributed toward supervision, conceptualization, methodology and writing—review and editing. MC and SL contributed toward supervision, review and editing. QX contributed toward model building. HX and TC contributed toward data collection and initial analysis.

FUNDING

This research was fully funded by the National Natural Science Foundation of China under Grant 51961135101.

ACKNOWLEDGMENTS

The authors would like to sincerely acknowledge the kind supports and research exchanges from Tianjin University and other project cooperative members.

REFERENCES

Ansari, M., Al-Awami, A. T., Sortomme, E., and Abido, M. A. (2015). Coordinated bidding of ancillary services for vehicle-to-grid using fuzzy optimization. *IEEE Trans. Smart Grid* 6 (1), 261–270. doi:10.1109/tsg.2014.2341625

Castillo, A., and Gayme, D. F. (2014). Grid-scale energy storage applications in renewable energy integration: a survey. *Energy Convers. Manag.* 87, 885–894. doi:10.1016/j.enconman.2014.07.063

Chen, Y., and Zhao, D. (2020). Multi-objective optimization model for multi-form energy storage coordinated scheduling with wind power. *Electr. Meas. Instrumentation* 11, 1–9. doi:10.2172/1762045

Alkadi, N. E., Starke, M. R., and Ma, O. (2013). *Assessment of industrial load for demand response across western interconnect*. New York, NY, United States. Oxford University Press. https://www.osti.gov/servlets/purl/1111445.

Ge, R., Zhang, L., and Chai, J. (2020). Cooperative game model of energy storage power station and photovoltaic power station in power market environment. *Renew. Energy Resour.* 38 (04), 545–553. doi:10.1016/s0038-092x(98)90019-6

IEA. (2020). Renewables 2020. Available at: https://www.iea.org/reports/renewables-2020 (Accessed December 5, 2020).

Knight, D. G., Crisan, O., and Higgins, T. J. (1972). Power systems engineering and mathematics. *IEEE Trans. Syst. Man, Cybern. SMC* 3 (6), 650.

Li, D., Liu, J., and Liu, Y. (2015). Power market linkage game analysis considering wind and storage. *Power Syst. Technol.* 39 (004), 1001–1007. doi:10.17950/ijer/v3s10/1003

Liu, C., and Du, P. (2018). Participation of load resources in day-ahead market to provide primary-frequency response reserve. *IEEE Trans. Power Syst.* 33 (5), 5041–5051. doi:10.1109/tpwrs.2018.2818948

Ma, Y., Houghton, T., Cruden, A., and Infield, D. (2012). Modeling the benefits of vehicle-to-grid technology to a power system. *IEEE Trans. Power Syst.* 27 (2), 1012–1020. doi:10.1109/tpwrs.2011.2178043

National Development and Reform Commission. (2019). Notice of the National development and reform Commission on improving the on-grid tariff policy for wind power. Available at: https://www.ndrc.gov.cn/xxgk/zcfb/tz/201905/t20190524_962453.html (Accessed January 11, 2021).

National Development and Reform Commission. (2020). Notice of the National Development and Reform Commission on matters related to the 2020 photovoltaic power grid tariff policy. Available at: https://www.ndrc.gov.cn/xxgk/zcfb/tz/202004/t20200402_1225031.html (Accessed January 11, 2021).

National Energy Administration. (2018). 2018 National electricity price regulatory. Available at: http://www.nea.gov.cn/138530255_15729388881531n.pdf (Accessed January 11, 2021).

PJM INT. (2020). Manual 11: energy and ancillary services market operations. Available at: https://www.pjm.com/markets-and-operations/demand-response/~/media/documents/manuals/m11.ashx (Accessed December 10, 2020).

Seneviratne, C., and Ozansoy, C. (2016). Frequency response due to a large generator loss with the increasing penetration of wind/PV generation – a literature review. *Renew. Sustain. Energy Rev.* 57, 659–668. doi:10.1016/j.rser.2015.12.051

Stott, B., Jorge, J., and Alsaç, O. (2009). DC power flow Revisited. *IEEE Trans. Power Syst.* 24 (3), 1290–1300. doi:10.1016/j.rser.2015.12.051

Su, H.-I., and Abbas, E. G. (2013). Modeling and analysis of the role of energy storage for renewable integration: power balancing. *IEEE Trans. Power Syst.* 28 (4), 4109–4117. doi:10.1109/tpwrs.2013.2266667

Wang, H., Yang, X., and Zhang, M. (2013). A hybrid energy storage control strategy to smooth the fluctuations of photovoltaic systems. *Power Syst. Technol.* 37 (009), 2452–2458. doi:10.3390/su11051324

Yuan, G., Chen, S., and Liu, Y., (2016). *Virtual power plant economic dispatch based on time-of-use power price*. London: Power System Technology.

Zhang, W., Lian, J., Chang, C.-Y., and Kalsi, K. (2013). Aggregated modeling and control of Air conditioning loads for demand response. *IEEE Trans. Power Syst.* 28 (4), 4655–4664. doi:10.1109/pesgm.2014.6939498

Conflict of Interest: Author QX, MC, SL, QX, HX, and TC were employed by the company ABB Power Grids Investment (China) Ltd.

The handling editor declared a past co-authorship with one of the authors MC.

APPENDIX

The typical alternating current (AC) transmission model is showed in **Appendix Figure A1**. The expressions of AC transmission line power flow are in Eq. 38.

$$p_2 - p_1 = gv_1v_2\cos(\theta_2 - \theta_1) + bv_1v_2\sin(\theta_2 - \theta_1) \quad (38)$$

p_1 and p_2 represent the real power injections in nodes. v_1 and v_2 represent the voltages. θ_1 and θ_2 represent the phase angles. z, y, r, x, g and b represent the impedance, admittance, resistance, reactance, conductance, and susceptance respectively.

The DC power flow derivation is showed in Knight et al., 1972, which is based on multiple approximation: line conductance ignored, phase angle close to zero, line voltage P.U. set as constant, and line susceptance equal to the reciprocal of reactance. The formations are present in **(39)**-**(42)**. The DC transmission line power flow is **Eq. 43**. **Appendix Figure A2** shows the DC transmission line model.

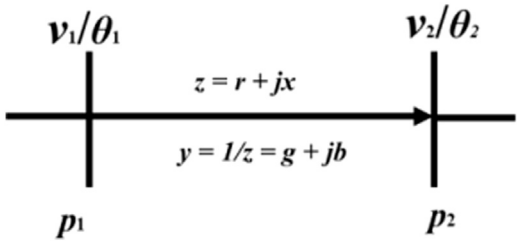

FIGURE A1 | AC transmission line model.

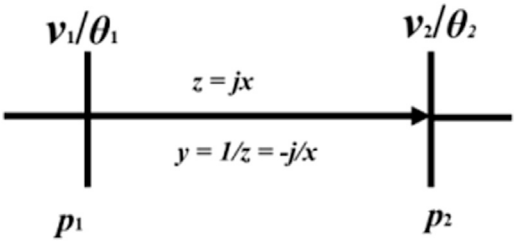

FIGURE A2 | DC transmission line model.

$$g = 0 \quad (39)$$

$$\sin(\theta_2 - \theta_1) \approx \theta_2 - \theta_1 \quad (40)$$

$$v_1, v_2 \approx 1 \quad (41)$$

$$b \approx -1/x \quad (42)$$

$$p_2 - p_1 = -(\theta_2 - \theta_1)/x \quad (43)$$

NOMENCLATURE

$\boldsymbol{T}$ total dispatch horizon, equal to 24

$Plimit_l$ the line flow capacity of line l in MW

$\boldsymbol{SF}$ the shift distribution factor matrix

$\boldsymbol{Map}$ the position transformation matrix for branches of system

$\boldsymbol{D}$ the number of load buses

$\boldsymbol{ES}$ the number of energy storage devices

$\boldsymbol{E}$ the number of EV clusters

G_f the number of thermal units

G_w the number of wind turbines

G_s the number of PVs

$Demand_{d,t}$ the predicted power of the load d at period t in MW

$Genfuel_{f,t}$ the output of the thermal unit f at period t in MW

$Genwind_{w,t}$ the output of the wind turbine w at period t in MW

$\boldsymbol{\alpha}$ efficiency factor of wind generator

$Wind_t$ wind power at period t in MW

$Gensolar_{s,t}$ the output of the PV panel s at period t in MW

$\boldsymbol{\beta}$ the efficiency factor of PV

$Solar_t$ solar power at period t in MW

$ESP_{es,t}$ the charging/discharging energy of storage device es at period t in MWh

$ESch_{es,t}$ the charging power limit of the storage device es at period t in MW

$ESdis_{es,t}$ the discharge power limit of the storage device es at period t in MW

$EVP_{e,t}$ the charging/discharging energy of the EV cluster e at period t in MWh

$EVch_{e,t}$ the charging power limit of the EV cluster e at period t

$EVdis_{e,t}$ the discharge power limit of the EV cluster e at period t

$Price_t$ the electricity price at period t in RMB/kWh

C_f the operation cost of the thermal unit f in RMB

$STC_{f,t}$ the start-up cost of the thermal unit f in RMB

$fueloffer_t$ the marginal cost of thermal units at period t in RMB/MWh

$windoffer_t$ the levelized cost of electricity for wind turbines at period t in RMB/MWh

$solaroffer_t$ the levelized cost of electricity for PVs at period t in RMB/MWh

$esPrice_t$ the discharge price of storage at period t in RMB/MWh

$evPrice_t$ the discharge price of EV cluster at period t in RMB/MWh

$I_{f,t}$ the binary on/off indicator for thermal unit f

$P_{f,t}$,$Q_{f,t}$ the start-up/shutdown indicators of thermal unit f

$Genfuelub_f$, $Genfuellb_f$ the output upper/lower bound of thermal unit f in MW

$fuelru_f$, $fuelrl_f$ the ramping up/down limit of thermal unit f in MW

MT_f^{on}, MT_f^{off} the minimum on/off time limit of thermal unit f

$Genwindub_w$, $Genwindlb_w$ the output upper/lower bound of wind turbine w in MW

$Gensolarub_s$, $Gensolarlb_s$ the output upper/lower bound of PV s in MW

$Capes_{es}$ the capacity of storage device es in MWh

$SoC_{es,t}$ the state of charge of storage device es at period t

$ches_{es}$, $dces_{es}$ the charging/ discharging efficiency of storage device es

$Capev_e$ the energy capacity of EV cluster e in MWh

$EV_{e,t}$ the state of charge of EV cluster e at period t

$chev_{es}$, $dcev_{es}$ the charging/discharging efficiency of EV cluster e

frontiers in Energy Research

ORIGINAL RESEARCH
published: 26 April 2021
doi: 10.3389/fenrg.2021.646869

A Distributed and Robust Optimal Scheduling Model for an Active Distribution Network With Load Aggregators

Jidong Wang[1], Qiuming Xu[1], Huiling Su[2] and Kaijie Fang[2]*

[1]Key Laboratory of Smart Grid of Ministry of Education, Tianjin University, Tianjin, China, [2]State Grid Jiangsu Electric Power Co., Ltd. Marketing Service Center, Nanjing, China

Increasing penetration of distributed generation (DG) has brought more uncertainty to the operation of active distribution networks (ADNs). With the reformation of the power system, increasingly more flexible loads access to distribution network through load aggregators (LAs), which becomes an effective way to solve these issues. Since LAs and ADNs are separate entities with different interests, the traditional centralized and deterministic optimization methods fail to meet the actual operational requirements of ADNs. Based on the linear power flow model, a robust optimal dispatching model of ADNs considering the influence of renewable DG's uncertain output on voltage security constraints is established. Then, an independent optimal scheduling model for LAs is modeled based on the analysis of the composition and characteristics of flexible load in LAs. LAs and ADNs, as two different stakeholders, use a distributed modeling method to establish different economic optimization goals. The optimization problem is solved by decoupling the coupling exchanging power between LAs and ADNs into virtual controllable loads and virtual DGs. Finally, with the case study of a modified IEEE 33-bus system, the correctness and effectiveness of the proposed method are verified. The effects of the robust level and demand response incentive on the results are also analyzed.

Keywords: distributed generation, active distribution network, load aggregator, robust optimization, distributed optimization, demand response

OPEN ACCESS

Edited by:
Yue Zhou,
Cardiff University, United Kingdom

Reviewed by:
Yan Li,
Pennsylvania State University (PSU), United States
Wei Zhou,
Dalian, University of Technology, China

****Correspondence:***
Jidong Wang
jidongwang@tju.edu.cn

Specialty section:
This article was submitted to Smart Grids, a section of the journal Frontiers in Energy Research

Received: *28 December 2020*
Accepted: *16 February 2021*
Published: *26 April 2021*

Citation:
Wang J, Xu Q, Su H and Fang K (2021) A Distributed and Robust Optimal Scheduling Model for an Active Distribution Network With Load Aggregators. Front. Energy Res. 9:646869. doi: 10.3389/fenrg.2021.646869

INTRODUCTION

With continuously increasing penetration of renewable energy, the uncertainty and intermittency of clean energy challenge the operation of distribution network (Ehsan and Yang, 2019). With the marketization of electric power industry on the demand side and the development of new information and communication technology in recent years, flexible resources in demand side have attracted extensive attention due to its economy and flexibility (Asensio et al., 2018a; Asensio et al., 2018b), which provides a solution for the economic and stable operation of ADNs in the accommodation of renewable energy. Different from the traditional inelastic load, the flexible load, such as smart home appliances, electric vehicles, and energy storage, can respond to the dispatching requirements of the power grid by adjusting its power or transferring its power consumption time (Zhang G. et al., 2019). With Demand Response (DR) technology, the flexible load can improve the

economy and stability performance of the distribution system (Parizy et al., 2019; Delavari and Kamwa, 2018) and provide auxiliary services like frequency regulation (Wang et al., 2017), voltage regulation (Zhong et al., 2019), and reserve capacity (Tomasson and Soder, 2020).

Since the low electricity consumption level and DR efficiency of an individual user (Adrian et al., 2018), the flexible load can participate in the DR program through the load aggregators (LAs) (Herre et al., 2020), which promotes the massive participation of flexible loads in the demand side and in guiding the users to consume electricity properly and economically (Wang et al., 2020).

There are many studies on the role of flexible load in the operation of ADNs. In Jiang et al. (2018), the working mode of integrated smart buildings with heating, ventilation, and air-conditioning (HVAC) systems is proposed according to the heat storage characteristics of thermostatically controlled loads. The power loss and voltage fluctuation of the ADN can be decreased by utilizing the flexibility of the smart buildings. A multi-objective scheduling model for ADN based on source-network-load coordination scheduling is proposed in the article(Yong et al., 2018). The operating cost, renewable energy utilization rate and users' satisfaction are considered as the optimization objectives. In the study by Kong et al. (2020), interruptible loads (ILs) are applied to increase the power supply capability and renewable energy utilization rate of the ADN, considering the uncertainty of distributed generation (DG). The above studies greatly exploit and utilize the capacity of demand side resources and improve the operational status of the ADN. However, most of the present works adopt centralized optimization methods, which are hard to adapt to the widely spread and scattered regional distribution system due to their heavy computational burden and poor expansibility with the increasing access of the flexible load. And in the centralized optimization, the benefits of different subjects are hard to be reconciled. To reflect the different interests of diverse subjects and the decentralized and autonomous characteristics of ADNs, the distributed optimization methods are applied into the optimal scheduling of ADNs.

In the studies of distributed optimization, the article by Meyer-Huebner et al. (2019) proposes a distributed optimal power flow algorithm of the ADN with multiple distributed resources but ignores the different interests of diverse stakeholders. In the study by Du et al. (2018), as a new distributed demand side resource, the source-load dual characteristic of Microgrid (MG) is discussed, and cooperative game theory is applied to realize the benefit assignment between the MG and the ADN. The article by Yu and Hong (2017) proposes a novel incentive-based demand response model from the view of a grid operator to enable system-level dispatch of demand response resources by adjusting the electricity price. Those literatures take the dynamic game process between two stakeholders into consideration. However, some private information, such as cost functions and network topologies, needs to be exchanged in the bargain process, which makes it hard to guarantee the privacy of data. In the study by Wang Z. et al. (2016), the distributed optimal scheduling of the ADN is realized with merely the knowledge of each MG's expected exchange power in case of securing privacy of each MG. However, the effect of economic incentives to DR participants has not been taken into fully consideration. In the study by Wang D. et al. (2016), the marginal cost of proper constraints is utilized to form an updated price, with which the electricity cost can be reduced and the frequent transitions between battery charging/discharging states can be avoided. However, the method is essentially "source changing with load" mode and lack of interaction, which results in a low DR efficiency.

At the same time, the risk brought by renewable energy's uncertain output cannot be ignored. At present, stochastic programming and robust optimization are two main methods to deal with the uncertainty of DGs' output. In the study by Zhang Y. et al. (2019), the ellipsoid set is applied to describe the uncertainty of photovoltaic (PV) and wind turbine (WT), and the terminals of the ellipsoid are introduced into the stochastic optimization as extreme scenarios. The uncertainty of WT is considered by Cobos et al. (2018), and a robust scheduling model is established, which introduces variable cost depending on the uncertain WT output into the objective function. In the study by Liu et al. (2018), a two-stage robust optimization model of the min-max-min structure is established to obtain the scheduling scheme with the lowest operating cost under the worst scenario. However, stochastic programming and robust optimization methods still have their limitations. A large amount of calculation is inevitable in stochastic optimization, and the optimization effect heavily depends on scenarios selection. The traditional robust optimization mostly adopts the Soyster framework, which is also known as the completely robust optimization, whose feasible solutions are too conservative (Wang et al., 2018). Besides, the mentioned studies mainly focus on the power unbalance problem caused by the uncertain output of renewable DG, without considering whether the power flow security constraints of the system can be satisfied under the uncertainty.

To this end, two main questions arise:

(1) The traditional centralized optimization model failed to give full consideration of the benefits and autonomous characteristics of the LA inside the ADN. Therefore, a research question is raised on how to make use of the LA's DR ability while giving consideration to the different benefits and autonomous characteristics of both the ADN and the LA.
(2) How to reduce the conservativeness of traditional robust optimization and make the effective optimal scheduling plan for the ADN while considering the influence of uncertain parameters on the power flow constraints?

This article tries to answer these questions and presents an effective, robust, and distributed optimal scheduling for ADNs connected with multiple LAs by coordinating the controllable devices in power supply and demand sides, while addressing the uncertain DG output. The contributions of this article are summarized as follows:

(1) This study proposes a distributed optimal scheduling model with DR incentive. In this model, the ADN and LAs are modeled as several stakeholders with different

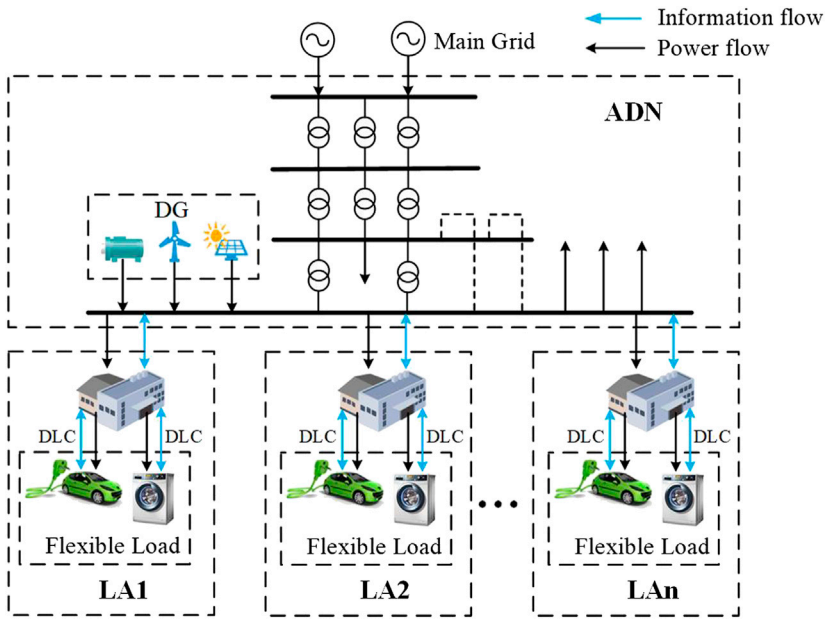

FIGURE 1 | Architecture for the ADN with LAs.

benefits and solve their own optimal scheduling problem autonomously and independently.

(2) A robust optimization method is applied to deal with the uncertainty brought by renewable DG in the power flow constraints of the ADN. Via the robust optimization, the schedules with different robust levels can be obtained to make a trade-off between the voltage violation rate and power supplying cost by adjusting the robust coefficient, which can make the result less conservative.

(3) Analytical target cascading (ATC) theory is applied to solve the distributed optimization problem without the knowledge of private data inside the LA and the ADN. The impact of DR incentive on LAs and ADNs is also analyzed. The ADN can further improve DR efficiency by adjusting DR incentive to an appropriate value.

The remainder of this article is organized as follows. In *Optimal Scheduling Models of Active Distribution Network and Load Aggregator*, the dispatching model of the ADN and the LA and the interaction model between them are established. The Bertsimas robust optimization and ATC theory are applied to solve the proposed problem in *Solution Process*. In *Case Study*, case studies are conducted to demonstrate the correctness and effectiveness of the model. Concluding remarks are presented in *Conclusion*.

OPTIMAL SCHEDULING MODELS OF ACTIVE DISTRIBUTION NETWORK AND LOAD AGGREGATOR

The structure of ADNs connected with LAs is shown in **Figure 1**. To improve the DR capacity, the LA directly combines the flexible loads (shiftable load and interruptible load) of different users in the region, the power consumption of which is adjusted based on the DR incentive to meet the scheduling requirements of the ADN. Through direct load control (DLC) technology, the LA properly arranges the power consumption plan of each flexible load and coordinates the power exchanged with the distribution network, so as to minimize the total operation cost of itself. With the goal to minimize the total cost while meeting the total power demand, the ADN controls the operational state and output power of controllable units based on the power demand of LAs and other power demand and the renewable DGs' output in the distribution network.

Normally, LAs and ADNs are with their own scheduling functions and taken as different stakeholders. There is a strong coupling relationship between the LA and the ADN, because the power interaction between them makes their economic dispatching affect each other. The detailed dynamic economic dispatching models of the ADN and the LA are given below.

Optimal Scheduling Model for Active Distribution Network

Objective Function of the Active Distribution Network Optimal Dispatching

The requirement of ADNs' optimal dispatching is to reduce its power supply cost while meeting its load. The ADN needs to decide its electricity procurement schedule and the operation state of its controllable unit. The ADN's comprehensive cost F_{ADN} can be calculated as **Eq. 1**, and the subentry cost of **Eq. 1** can be calculated as **Eqs. 2–5**

$$\min F_{ADN} = C_{DG} + C_{grid} + C_{loss} + C_{ex} \tag{1}$$

$$C_{DG} = \sum_{t=1}^{T} \sum_{i=1}^{|N_{DG}|} \left[a_i^{DG} \left(P_{i,t}^{DG} \right)^2 + b_i^{DG} P_{i,t}^{DG} + c_i^{DG} \right] \Delta t \quad i \in N_{DG} \tag{2}$$

$$C_{grid} = \sum_{t=1}^{T} c_t^{grid} P_t^{grid} \Delta t \tag{3}$$

$$C_{loss} = \sum_{t=1}^{T} \sum_{j=1}^{|N_b|} c_{loss} P_{j,t}^{loss} \Delta t \tag{4}$$

$$C_{ex} = \sum_{t=1}^{T} \sum_{i=1}^{|N_{LA}|} \left(c_{DR} P_{i,t}^{DR} - c_t^{DN} P_{i,t}^{b} \right) \Delta t \quad i \in N_{LA} \tag{5}$$

C_{DG} is the cost function of controllable DG in the ADN and expressed as the quadratic function of their active output $P_{i,t}^{DG}$. N_{DG} is the set of nodes with controllable DG. The function $|S|$ represents the number of elements in the set S. C_{grid} is the electricity purchase cost. c_t^{grid} is the time-of-use (TOU) price of the main grid. P_t^{grid} is the injected power from the main grid. C_{loss} is the network loss cost andc_{loss} is the unit network loss cost. P_t^{loss} is the network losses. N_b is the set of branch lines. C_{ex} is the interaction cost with LAs, and contains two parts: DR compensation for LAs participating in the DR program and the profit from selling electricity to LAs. The term $c_{DR} P_{i,t}^{DR}$ represents the DR compensation for LAs participating in the DR program. $P_{i,t}^{DR}$ is the shedding power of the LA at node i. The calculation of $P_{i,t}^{DR}$ and the mechanism of DR are illustrated in *Constraints of the Active Distribution Network Optimal Dispatching*. c_{DR} is the DR incentive for unit shedding power and is set by the ADN. The term $c_t^{DN} P_{i,t}^{b}$ represents the profit from selling electricity to LAs. $P_{i,t}^{b}$ is the purchasing power of node i and c_t^{DN} is the electricity price inside the ADN. N_{LA} is the set of LA nodes.

Constraints of the Active Distribution Network Optimal Dispatching

(1) Constraints of controllable DG

The constraints of power output **Eq. 6**, ramp rate **Eq. 7**, and running time **Eq. 8** are considered:

$$\begin{cases} P_{i,\min}^{DG} \cdot u_{i,t}^{DG} \le P_{i,t}^{DG} \le P_{i,\max}^{DG} \cdot u_{i,t}^{DG} \\ Q_{i,\min}^{DG} \cdot u_{i,t}^{DG} \le Q_{i,t}^{DG} \le Q_{i,\max}^{DG} \cdot u_{i,t}^{DG} \end{cases} \quad i \in N_{DG} \tag{6}$$

$$-r_{i,\max} \le P_{i,t}^{DG} - P_{i,t-1}^{DG} \le r_{i,\max} \quad i \in N_{DG} \tag{7}$$

$$\begin{cases} \sum_{k=1}^{T_{i,on}^{DG}-1} u_{i,t+k}^{DG} \ge \left(u_{i,t+1}^{DG} - u_{i,t}^{DG} \right) \cdot T_{i,on}^{DG} \\ \sum_{k=1}^{T_{i,off}^{DG}-1} \left(1 - u_{i,t+k}^{DG} \right) \ge \left(u_{i,t}^{DG} - u_{i,t+1}^{DG} \right) \cdot T_{i,off}^{DG} \end{cases} \quad i \in N_{DG} \tag{8}$$

$u_{i,t}^{DG}$ is the binary variable representing the running state of controllable DG at node i equal to 1 when controllable DG is on, while 0 means the DG is off. $P_{i,\max}^{DG}$ and $P_{i,\min}^{DG}$ ($Q_{i,\min}^{DG}$, $Q_{i,\max}^{DG}$) are its maximum and minimum active (reactive) output. $r_{i,\max}$ is the maximum ramp rate. $T_{i,on}^{DG}$ and $T_{i,off}^{DG}$ are the minimum continuous working time and the minimum off time.

(2) Constraints of renewable DG

The cubic set is adopted to define the uncertain output of PV and WT (Ding et al., 2017).

$$\begin{cases} P_{i,t}^{PV} = \widehat{P}_{i,t}^{PV} + \mu_t^{PV} \xi_{t,\max}^{PV} & i \in N_{PV} \\ P_{i,t}^{WT} = \widehat{P}_{i,t}^{WT} + \mu_t^{WT} \xi_{t,\max}^{WT} & i \in N_{WT} \\ \left| \mu_t^{PV} \right| \le 1, \quad \left| \mu_t^{WT} \right| \le 1 \end{cases} \tag{9}$$

$P_{i,t}^{PV}$ and $P_{i,t}^{WT}$ are the actual outputs of PV and WT at node i. $\widehat{P}_{i,t}^{PV}$ and $\widehat{P}_{i,t}^{WT}$ are the predicted outputs. $\xi_{t,\max}^{PV}$ and $\xi_{t,\max}^{WT}$ are the maximum prediction errors of PV and WT. μ_t^{PV} and μ_t^{WT} are the uncertain variables used to adjust the range of uncertain prediction error. N_{PV} and N_{WT} are the sets of nodes installed with PV and WT.

(3) Power flow constraints

A distribution network is normally configured to be a radial/tree-like topology, which means that each network node has only one parent node. **Figure 2** shows a line diagram of a radial power network. The power flows corresponding to **Figure 2** can be described by DistFlow branch equations. However, the traditional DistFlow model is nonlinear, which makes the problem difficult to solve. To make relevant problems computationally tractable and meanwhile guarantee an acceptable calculation result, the linearized DistFlow model is adopted here (Song et al., 2019).

$$\begin{cases} P_{n,t}^{br} = P_{n+1,t}^{br} + P_{n,t}^{nd} \\ Q_{n,t}^{br} = Q_{n+1,t}^{br} + Q_{n,t}^{nd} \\ V_{n+1,t} = V_{n,t} - \dfrac{\left(r_{n+1} P_{n+1,t}^{br} + x_{n+1} Q_{n+1,t}^{br} \right)}{V_0} \end{cases} \tag{10}$$

$P_{j,t}^{br}$ and $Q_{j,t}^{br}$ are the active and reactive power at the sending end of branch j, while r_j and x_j are the resistance and reactance of the same branch line. $P_{i,t}^{nd}$ and $Q_{i,t}^{nd}$ are the total active and reactive load at node i, while $V_{i,t}$ is the voltage magnitude. V_0 is the rated voltage magnitude of the distribution system.

According to the definition of robust optimal scheduling, the voltage security must be ensured as the prediction errors of renewable DG change, which is expressed as follows:

$$\begin{cases} \max\limits_{\mu} V_{n,t}(P, Q, \mu) \le V_{\max} \\ \min\limits_{\mu} V_{n,t}(P, Q, \mu) \ge V_{\min} \end{cases} \tag{11}$$

Except for the voltage safety constraint, the branch current constraint is also considered in some studies. However, the current carrying capacity of the branch line is usually two to three times larger than its rated current. Besides, the voltage drop will increase as the branch current increase. Therefore, the branch current constraint will also be satisfied if the voltage security constraint is satisfied.

For node i, its total active and reactive load can be calculated as follows:

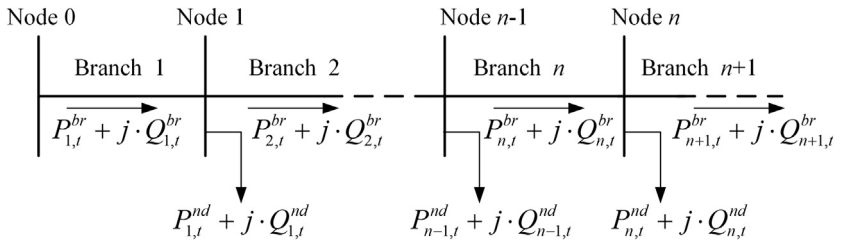

FIGURE 2 | Diagram of a radial power network.

$$\begin{cases} P^{nd}_{i,t} = P^{b}_{i,t} - P^{r}_{i,t} - P^{PV}_{i,t} - P^{WT}_{i,t} - P^{DG}_{i.t} \\ Q^{nd}_{i,t} = Q^{b}_{i.t} - Q^{DG}_{i.t} \end{cases} \tag{12}$$

Since the network losses are much smaller than line flow terms $P^{br}_{n,t}$ and $Q^{br}_{n,t}$, the node voltage is insensitive to the network loss terms which can be neglected in the voltage constraints **Eq. 10** of the linear DistFlow model (Zhong et al., 2019). However, to accurately calculate the cost of the ADN, this article considers the network losses in the objective function of the ADN. By using the approximation $V_{n,t} \simeq V_0$, the network loss power of the ADN can be expressed as **Eq. 13**, which is a commonly used expression with the employment of the adopted linear DistFlow constraint (Fu and Chiang, 2018).

$$P^{loss}_{j.t} \approx \frac{r_j\left(P^{br}_{j,t}\right)^2 + x_j\left(Q^{br}_{j,t}\right)^2}{V_0^2} \quad j \in N_b \tag{13}$$

(4) DR constraint

When the TOU price of the main grid is higher than the selling price inside the ADN, the higher cost will be caused by the higher power purchasing price from the main grid. Therefore, the ADN hopes to reduce its cost by compensating and encouraging LAs to reduce their power consumption in the above period or to transfer their power consumption time to other periods. In this article, the ADN releases DR incentive in the corresponding period to encourage LAs to participate in the DR program. After LAs reduce their power consumption in the DR period set by the ADN, they will get DR compensation according to their reduction. The DR mechanism is shown in **Eq. 14**

$$P^{DR}_{i,t} = u^{DR}_{t} \cdot \left(P^{0}_{i,t} - P^{b}_{i,t}\right) \ i \in N_{LA} \tag{14}$$

u^{DR}_t is the binary variable which represents the DR period set by the ADN, while 1 means the DR program is implemented in the period t. $P^0_{i,t}$ is the load of LA node i before DR. **Eq. 14** describes the DR mechanism: LAs will only gain DR compensation by reducing their power consumption in the DR period set by the ADN, but will not gain any DR compensation if they reduce their power consumption in other periods. This DR mechanism encourages LAs to reduce their power in the DR period or transfer their load to other periods, which will reduce the cost of the ADN by the means of peak shifting and valley filling.

There is a product form of the binary variable and continuous variable in **Eq. 14**. We apply the Big-M method to transfer **Eq. 14** into a linear constraint **Eq. 15** where M is a large enough constant.

$$\begin{cases} 0 \le P^{DR}_{i,t} \le M \cdot u^{DR}_{t} \\ P^{0}_{i,t} - P^{b}_{i,t} - M \cdot \left(1 - u^{DR}_{t}\right) \le P^{DR}_{i,t} \le P^{0}_{i,t} - P^{b}_{i,t} + M \cdot \left(1 - u^{DR}_{t}\right) \end{cases} \tag{15}$$

Thus, in the optimal scheduling model for ADNs, the decision variables are $x_{ADN} = [P^{DG}_{i,t}, Q^{DG}_{i,t}, u^{DG}_{i,t}, P^{grid}_{t}, u^{DR}_{t}, P^{DR}_{i,t}, P^{b}_{i,t}]$. The objective is to minimize **Eq. 1** while satisfying the constraints **Eqs. 6–13**, **15**.

Optimal Scheduling Model for Load Aggregator

Objective Function of Load Aggregator's Optimal Dispatching

Based on the electricity selling price and the DR incentive of the ADN, the LA adjusts its power consumption plan of the flexible load to minimize its comprehensive cost **Eq. 16**, which includes electricity purchasing cost, DLC cost and the profit from participating in the DR program. The subentry cost can be calculated as **Eqs. 17–19**

$$\min F_{LA,i} = C_{b,i} + C_{DLC,i} - C_{DR,i} \tag{16}$$

$$C_{b,i} = \sum_t c^{DN}_t P^{b}_{i,t} \Delta t \tag{17}$$

$$C_{DLC,i} = \sum_t \left[a_{il,i}\left(P^{il}_{i,t}\right)^2 + b_{il,i}P^{il}_{i,t}\right]\Delta t + \sum_t \left[a_{sh,i}\left|P^{sh}_{i,t} - P^{sh0}_{i,t}\right|^2 + b_{sh,i}\left|P^{sh}_{i,t} - P^{sh0}_{i,t}\right|\right]\Delta t \tag{18}$$

$$C_{DR,i} = \sum_t c_{DR} P^{DR}_{i,t} \Delta t \tag{19}$$

$P^{il}_{i,t}$ is the shedding power of the interruptible load. $P^{sh0}_{i,t}$ and $P^{sh}_{i,t}$ the power of the shiftable load before and after DR. $a_{il,i}$ and $b_{il,i}$ ($a_{sh,i}$, $b_{sh,i}$) are the quadratic and linear cost coefficient of the interruptible load (shiftable load). It is assumed that all LAs have reached their optimal scheduling plan without DR incentive, which means that LAs cannot further reduce their cost by changing its power consumption plan without DR incentive (Guo et al., 2020). As a result, the linear cost coefficients of the interruptible load and shiftable load in **Eq. 18** must obey the following constraint:

$$\begin{cases} b_{il,i} \geq c_t^{DN} \\ b_{sh,i} \geq \max\left\{\left|c_{t_1}^{DN} - c_{t_2}^{DN}\right|\right\} \ t_1, t_2 \in [1, T] \end{cases} \tag{20}$$

Constraints of Load Aggregator's Optimal Dispatching

(1) Constraints of interruptible load

In order to meet the basic demand of users, the shedding power of the interruptible load cannot be larger than the maximum shedding power.

$$0 \leq P_{i,t}^{il} \leq \alpha_{il} \cdot P_{i,t}^{il,0} \tag{21}$$

$P_{i,t}^{il,0}$ is the consumption power of the interruptible load before DR. α_{il} is the maximum shedding ratio.

(2) Constraints of shiftable load

$$0 \leq P_{i,t}^{sh} \leq P_{i,t}^{sh,\max} \tag{22}$$

$$\sum_t P_{i,t}^{sh} \Delta t = \sum_t P_{i,t}^{sh0} \Delta t \tag{23}$$

Constraint **Eq. 22** represents the power range of the shiftable load. Constraint **Eq. 23** indicates that the total energy consumption of the shiftable load remains unchanged after load shifting. In order to remove the absolute value function in **Eq. 18**, an auxiliary variable $\Delta P_{i,t}^{sh}$ and a relevant constraint are introduced into the model.

$$\Delta P_{i,t}^{sh} \geq \max\left\{P_{i,t}^{sh} - P_{i,t}^{sh0}, -P_{i,t}^{sh} + P_{i,t}^{sh0}\right\} \tag{24}$$

Equation 18 can be transferred into **Eq. 25**

$$C_{DLC,i} = \sum_t \left[a_i^{il}\left(P_{i,t}^{il}\right)^2 + b_i^{il} P_{i,t}^{il}\right]\Delta t + \sum_t \left[a_i^{sh}\left(\Delta P_{i,t}^{sh}\right)^2 + b_i^{sh} \Delta P_{i,t}^{sh}\right]\Delta t \tag{25}$$

When $F_{LA,i}$ reaches its optimal value, the equality $\Delta P_{i,t}^{sh} = \left|P_{i,t}^{sh} - P_{i,t}^{sh0}\right|$ is satisfied.

(3) DR constraint

$$P_{i,t}^{DR} = u_t^{DR} \cdot \left(P_{i,t}^0 - P_{i,t}^b\right) \tag{26}$$

The Big-M method is applied to linearize constraint **Eq. 26**, which is the same as the linearization of **Eq. 14**.

(4) Power balance constraint in LA

$$P_{i,t}^b = P_{i,t}^{fix} + P_{i,t}^{sh} + P_{i,t}^{il0} - P_{i,t}^{il} \tag{27}$$

$P_{i,t}^{fix}$ is the inelastic load of LA.

Thus, in the optimal scheduling model for LAs, the decision variables are $x_{LA,i} = [P_{i,t}^{il}, P_{i,t}^{sh}, \Delta P_{i,t}^{sh}, P_{i,t}^{DR}, P_{i,t}^{b}]$. The objective is to minimize **Eq. 16** while satisfying the constraints **Eqs. 21–27**.

SOLUTION PROCESS

Robust Counterpart for Power Flow Constraints

If node n is the leaf node of ADN, $P_{n+1,t}^{br} = 0$ and $Q_{n+1,t}^{br} = 0$ can be derived according to **Figure 2**. As a result, the first two equations in **Eq. 10** can be further expanded as follows:

$$\begin{cases} P_{n,t}^{br} = P_{n+1,t}^{br} + P_{n,t}^{nd} = P_{n,t}^{nd} \\ P_{n-1,t}^{br} = P_{n,t}^{br} + P_{n-1,t}^{nd} = P_{n,t}^{nd} + P_{n-1,t}^{nd} \\ \vdots \\ P_{1,t}^{br} = P_{2,t}^{br} + P_{1,t}^{nd} = P_{n,t}^{nd} + P_{n-1,t}^{nd} + \ldots + P_{1,t}^{nd} \end{cases} \tag{28}$$

We denote N_n as the set of nodes in the distribution network topology. According to **Eq. 28**, the linear relationship between line transmitting power and node load can be obtained:

$$\begin{cases} P_{k.t}^{br} = \sum_{i=k}^{N_n} P_{i,t}^{nd} \\ Q_{k.t}^{br} = \sum_{i=k}^{N_n} Q_{i,t}^{nd} \end{cases} \tag{29}$$

The last equation in **Eq. 10**, which represents the relationship between the line transmission power and the node voltage magnitude, can be further expanded into:

$$\begin{aligned} V_{n+1,t} &= V_{n,t} - \frac{\left(r_{n+1} P_{n+1,t}^{br} + x_{n+1} Q_{n+1,t}^{br}\right)}{V_0} \\ &= V_{n-1,t} - \frac{\left(r_n P_{n,t}^{br} + x_n Q_{n,t}^{br}\right)}{V_0} - \frac{\left(r_{n+1} P_{n+1,t}^{br} + x_{n+1} Q_{n+1,t}^{br}\right)}{V_0} \\ &\vdots \\ &= V_0 - \frac{\left(r_1 P_{1,t}^{br} + x_1 Q_{1,t}^{br} + \ldots + r_{n+1} P_{n+1,t}^{br} + x_{n+1} Q_{n+1,t}^{br}\right)}{V_0} \end{aligned} \tag{30}$$

According to the graph theory, we can obtain $|N_b| = |N_n| - 1$ from the radial topology of distribution network. By plugging **Eqs. 12** and **29** into **Eq. 30**, the relationship between node voltage magnitude and each controllable resource's power can be gained, which can be described in a matrix expression:

$$\begin{aligned} \boldsymbol{V}_t &= \boldsymbol{V}_0 - \boldsymbol{B}_1^R \boldsymbol{P}_t^{br} - \boldsymbol{B}_1^X \boldsymbol{Q}_t^{br} = \boldsymbol{V}_0 - \boldsymbol{B}_1^R \boldsymbol{B}_2 \boldsymbol{P}_t - \boldsymbol{B}_1^X \boldsymbol{B}_2 \boldsymbol{Q}_t \\ &= \boldsymbol{V}_0 - \boldsymbol{B}_X\left(\boldsymbol{Q}_t^b - \boldsymbol{Q}_t^{DG}\right) - \boldsymbol{B}_R\left(\boldsymbol{P}_t^b - \tilde{\boldsymbol{P}}_t^{PV} - \tilde{\boldsymbol{P}}_t^{WT} - \xi_{t,\max}^{PV} \boldsymbol{\mu}_t^{PV} - \xi_{t,\max}^{WT} \boldsymbol{\mu}_t^{WT} - \boldsymbol{P}_t^{DG}\right) \\ &= \boldsymbol{V}_0 + \xi_{t,\max}^{PV} \boldsymbol{B}_R \boldsymbol{\mu}_t^{PV} + \xi_{t,\max}^{WT} \boldsymbol{B}_R \boldsymbol{\mu}_t^{WT} + \begin{bmatrix} \boldsymbol{B}_R & \boldsymbol{B}_X \end{bmatrix} \begin{bmatrix} \boldsymbol{P}_t^{DG} - \boldsymbol{P}_t^b \\ \boldsymbol{Q}_t^{DG} - \boldsymbol{Q}_t^b \end{bmatrix} + \begin{bmatrix} \boldsymbol{B}_R & \boldsymbol{B}_X \end{bmatrix} \begin{bmatrix} \tilde{\boldsymbol{P}}_t^{PV} + \tilde{\boldsymbol{P}}_t^{WT} \\ 0 \end{bmatrix} \\ &= \boldsymbol{V}_0 + \boldsymbol{A}\boldsymbol{x}_t + \tilde{\boldsymbol{A}}_t^{PV} \boldsymbol{\mu}_t^{PV} + \tilde{\boldsymbol{A}}_t^{WT} \boldsymbol{\mu}_t^{WT} + \boldsymbol{A} \begin{bmatrix} \tilde{\boldsymbol{P}}_t^{PV} + \tilde{\boldsymbol{P}}_t^{WT} \\ 0 \end{bmatrix} \end{aligned} \tag{31}$$

$$\begin{cases} \boldsymbol{A} = \begin{bmatrix} \boldsymbol{B}_R & \boldsymbol{B}_X \end{bmatrix} \\ \tilde{\boldsymbol{A}}_t^{PV} = \xi_{t,\max}^{PV} \boldsymbol{B}_R, \ \tilde{\boldsymbol{A}}_t^{WT} = \xi_{t,\max}^{WT} \boldsymbol{B}_R \\ \boldsymbol{x}_t = \left[-\boldsymbol{P}_t^b + \boldsymbol{P}_t^{DG}, \ \boldsymbol{Q}_t^{DG} - \boldsymbol{Q}_t^b\right]^{\boldsymbol{T}} \end{cases} \tag{32}$$

The uncertain variables and controllable variables are separated in **Eq. 31**. $\boldsymbol{V}_t = [V_{2,t} \ldots V_{n,t}]$ is a vector consisting of nodes' voltage magnitude of the nodes except the root node (assuming that the voltage magnitude of substation node is always equal to V_0). $\boldsymbol{V}_0$ is a vector whose elements are all equal to V_0. $\boldsymbol{P}_t^{br}$ and $\boldsymbol{Q}_t^{br}$ are the active and reactive line flow vectors. $\boldsymbol{P}_t$ and $\boldsymbol{Q}_t$ are the

active and reactive node load vectors. $\boldsymbol{B}_1^R$ and $\boldsymbol{B}_1^X$ are the coefficient matrixes of **Eq. 30**. $\boldsymbol{B}_2$ is the coefficient matrix of **Eq. 29**. We denote $\boldsymbol{B}_R = \boldsymbol{B}_1^R \boldsymbol{B}_2$ and $\boldsymbol{B}_X = \boldsymbol{B}_1^X \boldsymbol{B}_2$.

Soyster intially gained the solutions under the worst situation of uncertain parameters through linear robust optimization (Wang et al., 2018). The traditional robust optimization methods adopt the Soyster robust framework (Peng et al., 2014; Liang et al., 2019), which is too conservative in most situations. To reduce the conservativeness, this article adopts the Bertsimas robust optimization framework in which the result with different robust levels can be obtained by adjusting the robust coefficient. According to the principle of the Bertsimas robust optimization and **Eq. 31**, the voltage security constraints **Eq. 11** have to be satisfied despite of the uncertainty of renewable DG's output. As a result, the robust counterpart of voltage security constraints of node i is expressed as follows:

$$\begin{cases} \boldsymbol{A}(i,:)\boldsymbol{x}_t + \max\limits_{\mu_t^{PV},\mu_t^{WT}} \boldsymbol{\theta}_t(i) \le \overline{\boldsymbol{b}}_t(i) \\ \boldsymbol{A}(i,:)\boldsymbol{x}_t + \min\limits_{\mu_t^{PV},\mu_t^{WT}} \boldsymbol{\theta}_t(i) \ge \underline{\boldsymbol{b}}_t(i) \\ \underline{\boldsymbol{b}}_t(i) = V_{\min} - V_0 - \sum\limits_{j \in N_{PV} \cup N_{WT}} \boldsymbol{B}_R(i,j) \cdot \left(\widehat{P}_{j,t}^{PV} + \widehat{P}_{j,t}^{WT} \right) \\ \overline{\boldsymbol{b}}_t(i) = V_{\max} - V_0 - \sum\limits_{j \in N_{PV} \cup N_{WT}} \boldsymbol{B}_R(i,j) \cdot \left(\widehat{P}_{j,t}^{PV} + \widehat{P}_{j,t}^{WT} \right) \\ \boldsymbol{\theta}_t(i) = \sum\limits_{\boldsymbol{j} \in \boldsymbol{N}_{PV}} \tilde{\boldsymbol{A}}_t^{PV}(i,j)\mu_t^{PV} + \sum\limits_{\boldsymbol{j} \in \boldsymbol{N}_{WT}} \tilde{\boldsymbol{A}}_t^{WT}(i,j)\mu_t^{WT} \\ -1 \le \mu_t^{PV}, \mu_t^{WT} \le 1 \\ z_t^{PV} \ge \max\{-\mu_t^{PV}, \mu_t^{PV}\}, \quad z_t^{WT} \ge \max\{-\mu_t^{WT}, \mu_t^{WT}\} \\ z_t^{PV} + z_t^{WT} \le \Gamma \end{cases} \tag{33}$$

z_t^{PV} and z_t^{WT} are the auxiliary variables, which are introduced to remove the absolute value function in **Eq. 9**. Γ is the robust coefficient. Γ belongs to $[0, |N_{un}|]$, where N_{un} is the set of uncertain sources. Assuming that the prediction error percentage of same kind renewable DGs at different nodes is same at the same time, we can derive $|N_{un}| = 2$. The optimal result under different robust levels can be obtained by adjusting Γ. By introducing auxiliary variables, the uncertain variables in the robust counterpart **Eq. 33** can be eliminated according to strong dual theory. Constraint **Eq. 33** is converted into the constrain types with only deterministic variables and controllable variables, which is shown in **Eq. 34**. Besides, the constraints of auxiliary variable, which is shown in **Eq. 35**, should also be considered in the optimization model.

$$\begin{cases} \boldsymbol{A}(i,:)\boldsymbol{x}_t + \overline{\boldsymbol{\alpha}}_t^{PV}(i) + \underline{\boldsymbol{\alpha}}_t^{PV}(i) + \overline{\boldsymbol{\alpha}}_t^{WT}(i) + \underline{\boldsymbol{\alpha}}_t^{WT}(i) + \Gamma\boldsymbol{\gamma}_t(i) \ge \underline{\boldsymbol{b}}_t(i) \\ \boldsymbol{A}(i,:)\boldsymbol{x}_t + \overline{\boldsymbol{\alpha}}_t^{PV}(i) + \underline{\boldsymbol{\alpha}}_t^{PV}(i) + \overline{\boldsymbol{\alpha}}_t^{WT}(i) + \underline{\boldsymbol{\alpha}}_t^{WT}(i) + \Gamma\boldsymbol{\gamma}_t(i) \le \overline{\boldsymbol{b}}_t(i) \end{cases} \tag{34}$$

$$\begin{cases} \overline{\boldsymbol{\alpha}}_t^{PV}(i) - \underline{\boldsymbol{\alpha}}_t^{PV}(i) + \overline{\boldsymbol{\beta}}_t^{PV}(i) - \underline{\boldsymbol{\beta}}_t^{PV}(i) \ge \sum\limits_{j \in \boldsymbol{N}_{PV}} \tilde{\boldsymbol{A}}_t^{PV}(i,j) \\ \overline{\boldsymbol{\alpha}}_t^{WT}(i) - \underline{\boldsymbol{\alpha}}_t^{WT}(i) + \overline{\boldsymbol{\beta}}_t^{WT}(i) - \underline{\boldsymbol{\beta}}_t^{WT}(i) \ge \sum\limits_{j \in \boldsymbol{N}_{WT}} \tilde{\boldsymbol{A}}_t^{WT}(i,j) \\ -\overline{\boldsymbol{\beta}}_t^{PV}(i) - \underline{\boldsymbol{\beta}}_t^{PV}(i) + \boldsymbol{\gamma}_t(i) \ge 0, \quad -\overline{\boldsymbol{\beta}}_t^{WT}(i) - \underline{\boldsymbol{\beta}}_t^{WT}(i) + \boldsymbol{\gamma}_t(i) \ge 0 \end{cases} \tag{35}$$

$\overline{\boldsymbol{\alpha}}_t^{PV}(i)$, $\underline{\boldsymbol{\alpha}}_t^{PV}(i)$, $\overline{\boldsymbol{\beta}}_t^{PV}(i)$, $\underline{\boldsymbol{\beta}}_t^{PV}(i)$, $\overline{\boldsymbol{\alpha}}_t^{WT}(i)$, $\underline{\boldsymbol{\alpha}}_t^{WT}(i)$, $\overline{\boldsymbol{\beta}}_t^{WT}(i)$, $\underline{\boldsymbol{\beta}}_t^{WT}(i)$, and $\boldsymbol{\gamma}_t(i)$ are the nonnegative dual variables corresponding to inequality constraint in **Eq. 33**.

Distributed Optimization Based on Analytical Target Cascading Method

Since the ADNs and LAs are physically connected to each other, the power interaction $P_{i,t}^b + jQ_{i,t}^b$ between the ADN and the LA makes the optimal scheduling of the ADN and the LA affects each other and difficult to be solved independently. To decouple the problem, the exchanging power is equivalent to the virtual controllable load and virtual controllable DG. The decoupling scheme is shown in **Figure 3**. From the perspective of the ADN, the purchasing power of each LA $P_{i,t}^b + jQ_{i,t}^b$ can be regarded as a virtual controllable load $P_{i,t}^D + jQ_{i,t}^D$ which is controlled by the ADN. From the perspective of the LA, the purchasing power at the bus can be regarded as a virtual controllable generator $P_{i,t}^G + jQ_{i,t}^G$ supplying electricity to its users and controlled by the LA at the same bus. As a result, the coupling purchasing power $P_{i,t}^b + jQ_{i,t}^b$ can be decoupled into virtual controllable load $P_{i,t}^D + jQ_{i,t}^D$ and virtual generator $P_{i,t}^G + jQ_{i,t}^G$, and solved in the optimal scheduling model of the ADN and the LA, respectively.

ATC is a parallel processing algorithm to solve the coordination problem with distributed hierarchy and performs well in convergence and stability despite the system scale. ATC can realize the parallel coordinated solution of different stakeholders and can ensure the security of private data inside each stakeholder. In the iterative process of ATC, the upper system (which is the ADN in this article) solves its scheduling problem and sends target information to the lower system (which is the LA in this article). The lower system calculates the response information according to the target information and feeds it back to the upper system. The upper system updates its scheduling problem based on the feedback results. The optimization is processed alternately in these two hierarchies, until the setting convergent condition is met. Since the ADNs and LAs only need to interact with expected exchange power with each other in the framework of ATC, the private data, like the topology parameter of the ADN and the cost functions of LAs, will not be exposed.

When the ADN solves its own optimal scheduling problem, the virtual controllable load term $\underline{P_{i,t}^D} + j\underline{Q_{i,t}^D}$ is optimized by the ADN, and the optimized value $\overline{P_{i,t}^D} + j\overline{Q_{i,t}^D}$ of the virtual load variable is sent to LA i in the form of parameters. While minimizing its own cost, the LA needs to consider the coordination between the virtual controllable DG and virtual controllable load. The Lagrange penalty function is introduced to the objective function of the LA to express the deviation between the virtual DG $P_{i,t}^G + jQ_{i,t}^G$ and the virtual load $\overline{P_{i,t}^D} + j\overline{Q_{i,t}^D}$ optimized by the ADN. As a result, the objective function of the LA is relaxed into **Eq. 36**

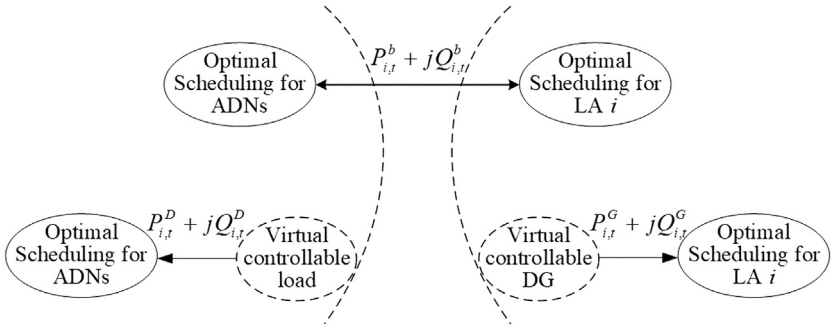

FIGURE 3 | Decomposition scheme of the ADN and the LA.

$$\min F_{LA,i} + \gamma \sum_{t=1}^{T}\left[\left(P_{i,t}^G - \overline{P_{i,t}^D}\right)^2 + \left(Q_{i,t}^G - \overline{Q_{i,t}^D}\right)^2\right] + \sum_{t=1}^{T}\left[\omega_{i,t}\left(P_{i,t}^G - \overline{P_{i,t}^D}\right) + \tau_{i,t}\left(Q_{i,t}^G - \overline{Q_{i,t}^D}\right)\right] \tag{36}$$

γ, $\omega_{i,t}$, $\tau_{i,t}$ are the Lagrangian multipliers. If the deviation between the virtual generator $P_{i,t}^G + jQ_{i,t}^G$ of LA i and the virtual load $\overline{P_{i,t}^D} + j\overline{Q_{i,t}^D}$ optimized by the ADN is not small enough, the Lagrange penalty function will increase the cost of LA i, which makes the result not optimal.

Similarly, if the ADN is connected with $|N_{LA}|$ LAs, $|N_{LA}|$ Lagrangian penalty functions are introduced into the objective function of the ADN, representing the deviation between the virtual load $P_{i,t}^D + jQ_{i,t}^D$ controlled by the ADN and the optimized virtual generator $\overline{P_{i,t}^G} + j\overline{Q_{i,t}^G}$ of each LA. The objective function of the ADN is relaxed into **Eq. 37**

$$\min F_{ADN} + \gamma \sum_{t=1}^{T}\sum_{i=1}^{|N_{LA}|}\left[\left(P_{i,t}^G - \overline{P_{i,t}^D}\right)^2 + \left(Q_{i,t}^G - \overline{Q_{i,t}^D}\right)^2\right] + \sum_{t=1}^{T} \times \sum_{i=1}^{|N_{LA}|}\left[\omega_{i,t}\left(P_{i,t}^G - \overline{P_{i,t}^D}\right) + \tau_{i,t}\left(Q_{i,t}^G - \overline{Q_{i,t}^D}\right)\right] \tag{37}$$

Therefore, in the scheduling model based on ATC, the optimal scheduling of the LA consists of **Eqs. 36**, **21–27**, and the optimal scheduling of the ADN consists of **Eqs. 37**, **6–13**, **15**. Each system solves its own optimal scheduling problem independently and exchanges boundary variables $\overline{P_{i,t}^D} + j\overline{Q_{i,t}^D}$ and $\overline{P_{i,t}^G} + j\overline{Q_{i,t}^G}$ until the convergence condition is satisfied.

Based on the principle of ATC, we can obtain the parallel solving process which is shown in **Figure 4**. The setting convergence condition of the coupling constraint is expressed as:

$$\sum_{t=1}^{T}\sum_{i=1}^{|N_{LA}|}\left[\left|\overline{P_{i,t}^G}(k) - \overline{P_{i,t}^D}(k)\right|^2 + \left|\overline{Q_{i,t}^G} - \overline{Q_{i,t}^D}(k)\right|^2\right] \le \varepsilon \tag{38}$$

ε is the convergence accuracy. k is the iteration times. When the convergence condition is not satisfied, the Lagrangian multipliers will be updated as follows:

$$\begin{cases} \omega_{i,t}(k+1) = \omega_{i,t}(k) + \gamma\left[\overline{P_{i,t}^G}(k) - \overline{P_{i,t}^D}(k)\right] \\ \tau_{i,t}(k+1) = \tau_{i,t}(k) + \gamma\left[\overline{Q_{i,t}^G}(k) - \overline{Q_{i,t}^D}(k)\right] \end{cases} \tag{39}$$

Considering that LA will not participate in the DR program when there is no DR incentive ($c_{DR} = 0$),the coefficients of augmented

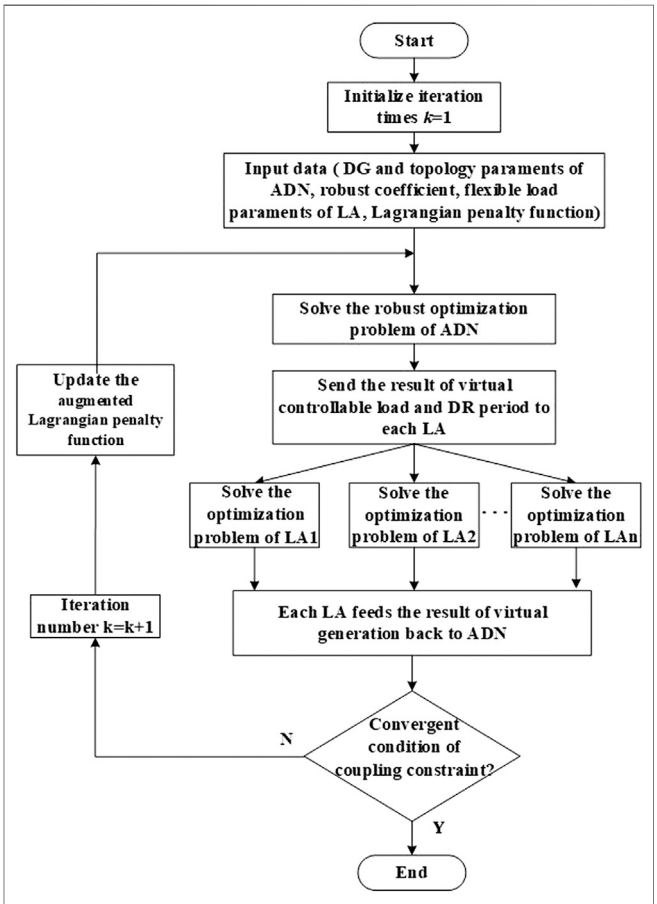

FIGURE 4 | Flow chart of distributed economic dispatch based on ATC.

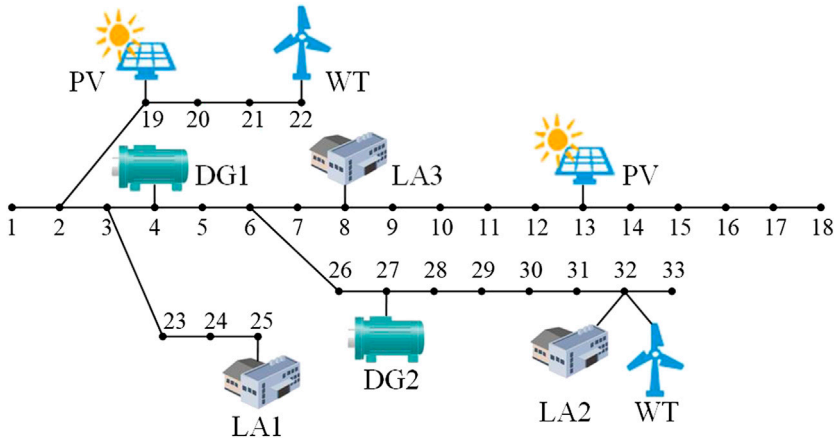

FIGURE 5 | Topology of a modified 33-bus system connected with three LAs.

Lagrangian penalty in LA's optimal dispatching problem are modified as follows:

$$\begin{cases} \gamma_{LA} = c_{DR}\eta\gamma \\ \omega_{i,t}^{LA} = c_{DR}w_{i,t}, \quad \tau_{i,t}^{LA} = c_{DR}\tau_{i,t} \end{cases} \tag{40}$$

η is the constant whose value is larger than 1. By applying **Eqs 20**, **40**, LA will participate in the DR program only when $c_{DR} > 0$.

CASE STUDY

Case Introduction

This section focuses on simulation in the case of grid-tied LA. The IEEE 33-bus distribution system connected with three LAs is used as the simulation system, shown in **Figure 5**. The normalized daily load and forecast output of PV and WT can be found in the article by Yong et al. (2018). The ADN is a 12.66 kV system. The upper and lower limit of voltage magnitude are set to 1.05 and 0.95 pu, respectively. The total load of the ADN is 3.715 MW + j·2300 MVar. The installed capacity of PV and WT are both 300 kW. The maximum prediction error is 30% of its predicted value. The robust coefficient Γ is set to 1.2. The DR incentive is 0.4 ¥/kWh. The interruptible load and shiftable load are both 20% of the total load in LA. The trading price between the ADN and the LA is 0.55 ¥/kWh. The parameters of controllable DG and flexible load are shown in **Tables 1** and **2**. The TOU price of the main grid is given in the article (Liang et al., 2019). The problem is solved by adopting commercial software CPLEX 12.9.0 through YALMIP in MATLAB on a 1.8 GHz, 16 GB machine, whose convergent gap value is set to 10^{-4}. The convergence accuracy of ATC is set to 10^{-4}.

Result Analysis

Optimal Scheduling Result

Figure 6 shows the output of controllable DG. DG1 is off during 1–7 h and t = 24 h, as the TOU price in the main grid during these periods are lower than the unit cost of DG1. Due to the ramping rate constraints, DG1 gradually increases its output since t = 6 h until it reaches its maximum value before the peak period. Compared to DG1, DG2 starts increasing its output at t = 2 h due to its higher capacity. DG1 and DG2 both maintain high output during 10–21 h and gradually decrease their output since t = 21 h, with the end of the peak period. Seen from the DGs' marginal price in **Figure 7**, the marginal cost of controllable DGs is higher than the TOU price in some period. This is because the controllable DGs have to generate more power to protect the ADN from voltage violation caused by the fluctuating output of renewable DG. With the increasing output of DG, the voltage drop on the distribution line will be decreased due to the less power transmitted through the distribution line.

According to the result, u_t^{DR} is equal to 1 during 7–23 h, as the trading prices between the ADN and the LA during these periods are lower than the TOU price in the main grid. Denote $\Delta P_{i,t}^{LA}$ as the variation of the LA's purchasing power after the DR program. The calculation of $\Delta P_{i,t}^{LA}$ is given as follows:

$$\Delta P_{i,t}^{LA} = P_{i,t}^{b} - P_{i,t}^{0} \quad (i \in N_{LA}) \tag{41}$$

Figure 8 shows $\Delta P_{i,t}^{LA}$ of each LA. Under the DR incentive, the LA reduces its power consumption in the flat and peak periods and transfers part of the load from the DR period to the valley period, which demonstrates LA's role in peak shifting and valley filling under DR incentive. The LA can obtain additional income by participating in DR, which will also help the ADN reduce its higher power supplying cost in peak and flat periods and make extra electricity selling profit in the valley period.

Performance of ATC

Figure 9 illustrates the convergence performance of the ATC algorithm for the ADN-LA power exchange. The applied distributed optimization scheduling method is stably convergent after 112 times iteration, which means it does not require many computing resources. By applying the ATC algorithm, the optimization times of the LA and the ADN and

TABLE 1 | Parameters of controllable DG.

No.	Technical parameters			Cost coefficients		
	$P^{DG}_{i,max}$/kW	$P^{DG}_{i,min}$/kW	$r_{i,max}$/(kW/h)	a_i^{DG}/(¥/kW^2)	b_i^{DG}/(¥/kW)	c_i^{DG}/¥
1	500	0	100	0.0005	0.46	0
2	800	100	100	0.0007	0.50	0

TABLE 2 | Parameters of flexible load in LA.

LA	Interruptible load		Shiftable load	
	a_i^{il}/(¥/kW^2)	b_i^{il}/(¥/kW)	a_i^{sh}/(¥/kW^2)	b_i^{sh}/(¥/kW)
1	0.008	0.55	0.010	0.15
2	0.010	0.55	0.012	0.18
3	0.013	0.55	0.015	0.20

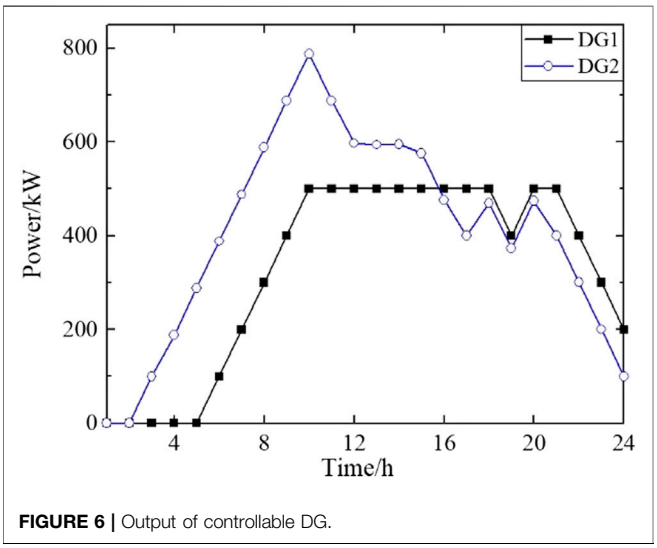

FIGURE 6 | Output of controllable DG.

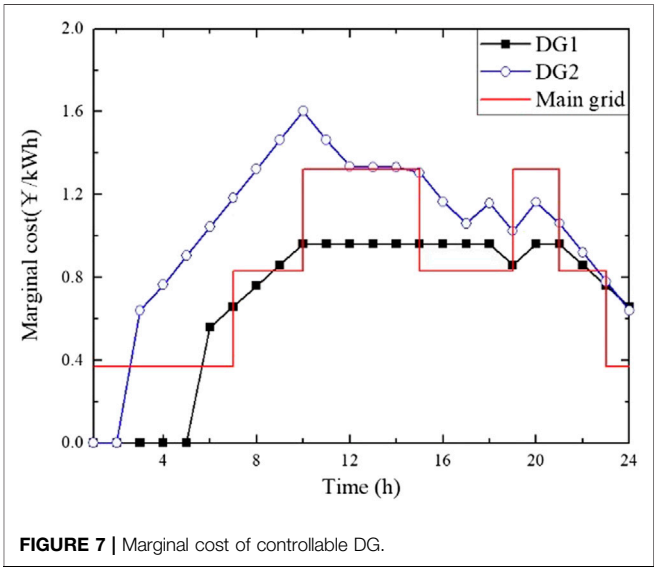

FIGURE 7 | Marginal cost of controllable DG.

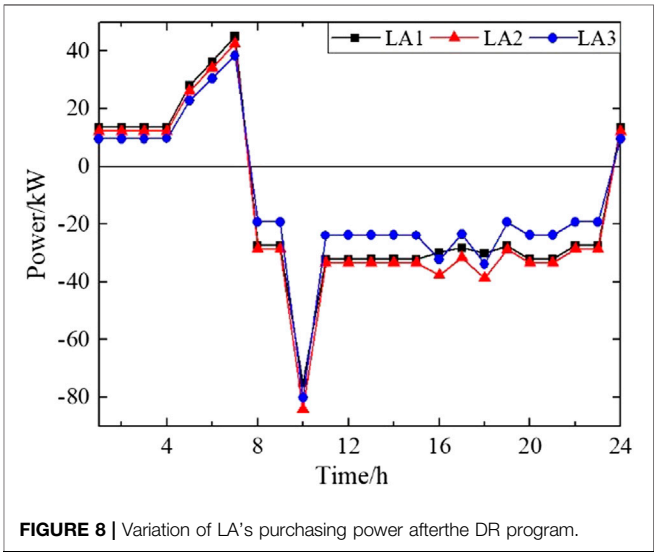

FIGURE 8 | Variation of LA's purchasing power afterthe DR program.

the communication burden between them can be reduced. Besides, the LA and the ADN only need to send their expected purchasing power to each other in the iteration process. The privacy data inside the LA, such as the cost function of the LA, is unknown to the ADN. As a result, the privacy and security of users' data can be guaranteed.

To further demonstrate the effectiveness of the proposed method, three scheduling models are used to calculate the operating costs of the ADN and each LA. The three scheduling models are as follows:

(1) Centralized DLC model: assuming that the ADN can directly control the flexible load of users and that the ADN and LAs are regarded as the same stakeholder, the total cost of the ADN and LAs is taken as the objective function, and the centralized optimization method is applied to solve the problem.
(2) The "Source changing with load" model (Wang D. et al., 2016): LAs solve their optimal scheduling problem based on the electricity price and DR incentive of the ADN. Then the ADN makes its scheduling plan according to the result of LAs' optimal scheduling problem.
(3) The distributed optimization method based on ATC in this article.

The results of different scheduling models are compared in **Table 3**. The total cost of the centralized DLC method is the lowest

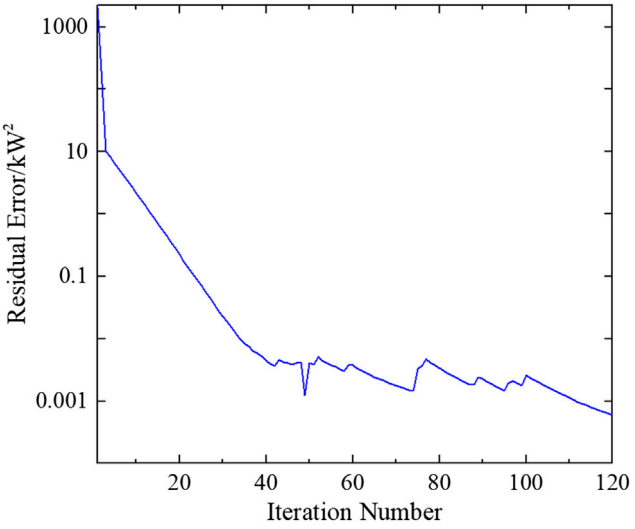

FIGURE 9 | Convergence curve of ATC.

among **Table 3**, but the cost of each LA is higher than that of other methods, which means the total cost is decreased at the expense of each LA. Besides, the ADN needs to collect the relevant parameters of the flexible load under the centralized DLC model, which makes it difficult to guarantee the privacy of users. The benefits of each LA can be ensured under the "source changing with load" model. However, the cost of the ADN and total cost of this model are the highest due to the lack of enough interaction between the ADNs and LAs. Under the distributed optimization model based on ATC where the optimal scheduling problems of the ADNs and LAs are decoupled and solved independently, the economic benefits of LAs and the ADNs can be reconciled, and the privacy and security of users' electric power data can be guaranteed. Although it takes more time to gain the results through distributed optimization due to its iterative process, the distributed method based on ATC is still fast enough to be applied in the day-ahead optimal scheduling and is more applicable than the centralized optimization for its advantage in guarantying the security of the private data inside each subject.

Robustness and Economy Analysis

To further study the influence of robust level on the optimization results, uncertainty analysis is presented in this article. We denote the violation rate to quantitatively measure the influence of uncertain parameters on voltage security. The violation rate is calculated as **Eq. 42** through the Monte Carlo simulation where all uncertain parameters are assumed to follow uniform distribution.

$$\alpha_{vio} = \frac{|N_{vio}|}{|N_{total}|} \times 100\% \tag{42}$$

N_{total} is the set of 1,000 renewable DGs' output scenarios generated by the Monte Carlo simulation. The randomly generated output of renewable DG and the optimal scheduling results are substituted into the topology of the ADN for power flow calculation to obtain the power flow distribution of the ADN. N_{vio} is the set of scenarios where the voltage safety constraint is not satisfied.

When Γ takes different values, different solutions with different levels of robustness can be obtained (compared in **Table 4**). For the ADN, different levels of robustness make it possible to make trade-offs between the economy and voltage level.

It can be seen from **Table 4** that the cost of the ADN increases with the increasing Γ. The rise in cost was mainly due to the increasing cost of controllable DG. Controllable DG needs to increase its output and reduce the transmission power through distribution network lines, which indicates the role of controllable DG in voltage supporting under uncertain environment. When Γ is less than 1.2, the violation rate goes on declining rapidly, while the cost of the ADN rises with the increasing Γ. This result demonstrates that the ADN has to cost more to improve its power quality under an uncertain environment. However, declining speed of the violation rate is close to 0 when Γ is larger than 1.2, which means the ADN has to cost much more to reach a higher robust level when the current robust level is relatively high.

The robust optimization model proposed in this article is equivalent to the deterministic optimization model when Γ is equal to 0. The cost of the ADN is the least in **Table 4** when no uncertainties are considered. However, it does not mean that the solution obtained by deterministic optimization is better than that by robust optimization. The voltage violation rate of deterministic optimization exceeds 90%, which results in the poor power quality caused by insufficient voltage support. The robust optimization model is equivalent to the completely robust optimization model when Γ is equal to 2 in which all uncertainty is considered. While short time voltage violation is allowed in the practical operation of distribution network, the result of completely robust optimization model is too conservative for considering every possible situation, resulting in its highest cost. However, the completely robust optimization model is applicable in the system with high reliability and quality requirements. Therefore, the ADN can select the appropriate robust level according to the practical operation requirements for power supplying.

Effect of DR Incentive

Table 5 shows the effect of DR under different DR incentive. With the increase of DR incentive, the total DR power is also increasing, which means that LAs are more willing to participate in the DR program with higher incentive. LAs can help the ADN reduce power supply cost by peak shifting and valley filling. When the c_{DR} is less than 0.4, the operating cost of the ADN will decrease with the increasing DR incentive. Although the ADN has to pay more compensation to LAs with the higher c_{DR}, more benefit will be brought to the ADN by the higher participation of LAs in the DR program. However, when c_{DR} is larger than 0.4, the benefit brought by the higher DR participation is less than the compensation. As a result, the cost of the ADN starts to increase as c_{DR} increases from 0.4. Therefore, the ADN can further reduce its operation cost by making the appropriate DR incentive according to the response of LAs.

TABLE 3 | Comparison of cost and solving time with different methods.

Methods	Cost of each stakeholders/¥					Solving time/s
	ADN	LA1	LA2	LA3	Total cost	
1	26,385.0	3,552.4	1,840.7	1,740.3	33,518.4	1.43
2	27,536.0	3,454.5	1,721.8	1671.2	34,383.5	3.21
3	26,878.9	3,458.1	1,743.4	1691.0	33,771.4	461.97

TABLE 4 | The economy and violation rate of schedules under different robust levels.

Γ	C_{DG}/¥	C_{grid}/¥	C_{loss}/¥	C_{ex}/¥	F_{ADN}/¥	α_{vio}/%
0	12,274.8	18,986.7	506.0	−5,506.3	26,261.2	90.6
0.4	12,763.6	18,648.6	499.1	−5,499.6	26,411.7	45.1
0.8	13,468.0	18,161.9	490.2	−5,494.9	26,625.1	17.9
1.2	14,241.9	17,644.2	481.0	−5,488.2	26,878.9	2.6
1.6	15,043.4	17,146.5	472.4	−5,487.1	27,175.2	0.4
2	15,826.0	16,692.6	464.9	−5,491.8	27,491.6	0

TABLE 5 | Effect of DR under different DR incentive.

c_{DR}/(¥/kWh)	Total DR power/kW	F_{ADN}/¥
0	0	27,488.2
0.2	974.3	27,036.2
0.4	1,467.2	26,878.9
0.6	1,922.3	27,145.0
0.8	2,257.6	27,655.2
1	2,486.8	28,285.8

CONCLUSION

In this article, a distributed and robust optimal scheduling model of the ADN with LAs is proposed. The global optimal scheduling of the whole distribution system is realized by the autonomous energy management of the ADN and the LA. In the meanwhile, the influence of renewable DG's uncertain output on the voltage security constraints is also considered in the optimal scheduling model of the ADN.

Numerical simulations on a modified IEEE 33-bus system have verified the effectiveness of the proposed method. The simulation results show that the proposed distributed optimization framework of ADN with LA performs well in convergence and reconciling the interest of the LA and the ADN compared to the traditional centralized DLC model and "source changing with load" model. Besides, the economy and the voltage violation rate of scheduling plans with different robust levels are compared quantitatively. The proposed robust optimization method allows the ADN to make a trade-off between the economy and voltage level, by choosing the schedules with different robust levels. Finally, the costs of the ADN under different DR incentive are also compared. The ADN can further reduce its operation cost by making appropriate DR incentive according to the response of LAs.

DATA AVAILABILITY STATEMENT

The original contributions presented in the study are included in the article/Supplementary Material, further inquiries can be directed to the corresponding author.

AUTHOR CONTRIBUTIONS

JW contributed toward supervision, conceptualization, and writing—review and editing. QX contributed toward methodology, software, data curation, and writing—original draft. HS and KF contributed toward writing—review and editing.

FUNDING

This work was supported by the Science and Technology Project from State Grid Jiangsu Electric Power Co., Ltd. (J2020115).

ACKNOWLEDGMENTS

The authors would like to thank the Science and Technology Project from State Grid Jiangsu Electric Power Co., Ltd. (J2020115).

REFERENCES

Adrian, C. F. C., Alexis, G., Andrea, M., and Georges, K. (2018). Stochastic operation of home energy management systems including battery cycling. *Appl. Energy* 225, 1205–1218. doi:10.1016/j.apenergy.2018.04.130

Asensio, M., Pilar, M. D. Q., Munoz-Delgado, G., and Contreras, J. (2018a). Joint distribution network and renewable energy expansion planning considering demand response and energy storage part I: stochastic programming model. *IEEE Trans. Smart Grid* 9, 655–666. doi:10.1109/TSG.2016.2560339

Asensio, M., Pilar, M. D. Q., Munoz-Delgado, G., and Contreras, J. (2018b). Joint distribution network and renewable energy expansion planning considering demand response and energy storage part II: numerical Results. *IEEE Trans. Smart Grid* 9, 667–675. doi:10.1109/TSG.2016.2560341

Cobos, N. G., Arroyo, J. M., Alguacil, N., and Wang, J. (2018). Robust energy and reserve scheduling considering bulk energy storage units and wind uncertainty. *IEEE Trans. Power Syst.* 33, 5206–5216. doi:10.1109/TPWRS.2018.2792140

Delavari, A., and Kamwa, I. (2018). Sparse and resilient hierarchical direct load control for primary frequency response improvement and inter-area oscillations damping. *IEEE Trans. Power Syst.* 33, 5309–5318. doi:10.1109/TPWRS.2018.2795462

Ding, T., Li, C., Yang, Y., Jiang, J., Bie, Z., and Blaabjerg, F. (2017). A two-stage robust optimization for centralized-optimal dispatch of photovoltaic inverters in active distribution networks. *IEEE Trans. Sustain. Energy* 8, 744–754. doi:10.1109/TSTE.2016.2605926

Du, Y., Wang, Z., Liu, G., Chen, X., Yuan, H., Wei, Y., et al. (2018). A cooperative game approach for coordinating multi-microgrid operation within distribution systems. *Appl. Energy* 222, 383–395. doi:10.1016/j.apenergy.2018.03.086

Ehsan, A., and Yang, Q. (2019). State-of-the-art techniques for modelling of uncertainties in active distribution network planning: a review. *Appl. Energy* 239, 1509–1523. doi:10.1016/j.apenergy.2019.01.211

Fu, Y. Y., and Chiang, H. D. (2018). Toward optimal multi-period network reconfiguration for increasing the hosting capacity of distribution networks. *IEEE Trans. Power Deliv.* 33, 2294–2304. doi:10.1109/TPWRD.2018.2801332

Guo, K., Gao, C., Lin, G., Lu, S., and Feng, X. (2020). Optimization strategy of incentive based demand response for electricity retailer in spot market environment. *Autom. Electr. Power Syst.* 44, 28–35. [in Chinese, with English summary]. doi:10.7500/AEPS20190726002

Herre, L., Mathieu, J. L., and Soder, L. (2020). Impact of market timing on the profit of a risk-averse load aggregator. *IEEE Trans. Power Syst.* 35, 3970–3980. doi:10.1109/TPWRS.2020.2971866

Jiang, T., Li, Z., Jin, X., Chen, H., Li, X., and Mu, Y. (2018). Flexible operation of active distribution network using integrated smart buildings with heating, ventilation and air-conditioning systems. *Appl. Energy* 226, 181–196. doi:10.1016/j.apenergy.2018.05.091

Kong, X., Yong, C., Wang, C., Li, P., Yu, L., and Chen, Y. (2020). Multi-objective power supply capacity evaluation method for active distribution network in power market environment. *Int. J. Electr. Power Energy Syst.* 115, 1–11. doi:10.1016/j.ijepes.2019.105467

Liang, J., Lin, S., Liu, M., Song, Y., Fan, G., He, S., et al. (2019). Distributed robust optimal dispatch in active distribution networks. *Power Syst. Technol.* 43, 1336–1344. [in Chinese, with English summary]. doi:10.13335/j.1000-3673.pst.2018.1375

Liu, Y., Guo, L., and Wang, C. (2018). A robust operation-based scheduling optimization for smart distribution networks with multi-microgrids. *Appl. Energy* 228, 130–140. doi:10.1016/j.apenergy.2018.04.087

Meyer-Huebner, N., Suriyah, M., and Leibfried, T. (2019). Distributed optimal power flow in hybrid ac-dc grids. *IEEE Trans. Power Syst.* 34, 2937–2946. doi:10.1109/TPWRS.2019.2892240

Parizy, E. S., Bahrami, H. R., and Choi, S. (2019). A low complexity and secure demand response technique for peak load reduction. *IEEE Trans. Smart Grid* 10, 3259–3268. doi:10.1109/TSG.2018.2822729

Peng, C., Xie, P., Zhan, J., and Sun, H. (2014). Robust economic dispatch of microgrid using improved bacterial foraging algorithm. *Power Syst. Technol.* 38, 2392–2398. [in Chinese, with English summary]. doi:10.13335/j.1000-3673.pst.2014.09.012

Song, Y., Zheng, Y., Liu, T., Lei, S., and Hill, D. J. (2019). A new formulation of distribution network reconfiguration for reducing the voltage volatility induced by distributed generation. *IEEE Trans. Power Syst.* 35, 496–507. doi:10.1109/TPWRS.2020.3012367

Tomasson, E., and Soder, L. (2020). Coordinated optimal strategic demand reserve procurement in multi-area power systems. *Appl. Energy* 270, 1–12. doi:10.1016/j.apenergy.2020.114984

Wang, D., Guan, X., Wu, J., Li, P., Zan, P., and Xu, H. (2016). Integrated energy exchange scheduling for multimicrogrid system with electric vehicles. *IEEE Trans. Smart Grid* 7, 1762–1774. doi:10.1109/TSG.2015.2438852

Wang, F., Xiang, B., Li, K., Ge, X., and Dehghanian, P. (2020). Smart households' aggregated capacity forecasting for load aggregators under incentive-based demand response programs. *IEEE Trans. Ind. Appl.* 56, 1086–1097. doi:10.1109/TIA.2020.2966426

Wang, J., Li, P., Fang, K., and Zhou, Y. (2018). Robust optimization for household load scheduling with uncertain parameters. *Appl. Sci. Basel* 8, 1–16. doi:10.3390/app8040575

Wang, J., Zhang, H., and Zhou, Y. (2017). Intelligent under frequency and under voltage load shedding method based on the active participation of smart appliances. *IEEE Trans. Smart Grid* 8, 353–361. doi:10.1109/TSG.2016.2582902

Wang, Z., Chen, B., Wang, J., and Kim, J. (2016). Decentralized energy management system for networked microgrids in grid-connected and islanded modes. *IEEE Trans. Smart Grid* 7, 1097–1105. doi:10.1109/TSG.2015.2427371

Yong, C., Kong, X., Chen, Y., Cui, K., Cui, K., and Wang, X. (2018). Multiobjective scheduling of an active distribution network based on coordinated optimization of source network load. *Appl. Sci. Basel* 8, 1–23. doi:10.3390/app8101888

Yu, M., and Hong, S. H. (2017). Incentive-based demand response considering hierarchical electricity market: a Stackelberg game approach. *Appl. Energy* 203, 267–279. doi:10.1016/j.apenergy.2017.06.010

Zhang, G., Jiang, C., and Wang, X. (2019). Comprehensive review on structure and operation of virtual power plant in electrical system. *IET Gener. Transm. Distrib.* 13, 145–156. doi:10.1049/iet-gtd.2018.5880

Zhang, Y., Ai, X., Fang, J., Wen, J., and He, H. (2019). Data-adaptive robust optimization method for the economic dispatch of active distribution networks. *IEEE Trans. Smart Grid* 10, 3791–3800. doi:10.1109/TSG.2018.2834952

Zhong, W., Xie, K., Liu, Y., Yang, C., and Xie, S. (2019). Topology-aware vehicle-to-grid energy trading for active distribution systems. *IEEE Trans. Smart Grid* 10, 2137–2147. doi:10.1109/TSG.2018.2789940

Conflict of Interest: Author HS and KF were employed by State Grid Jiangsu Electric Power Co., Ltd. Marketing Service Center. The authors declare that this study received funding from Science and Technology Project of State Grid Jiangsu Electric Power Co., Ltd. (J2020115). The funder had the following involvement: reviewing and editing. All authors declare no other competing interests.

The remaining authors declare that the research was conducted in the absence of any commercial or financial relationships that could be construed as a potential conflict of interest.

The handling editor declared a past co-authorship with the authors JW and KF.

Advantages of publishing in Frontiers

OPEN ACCESS
Articles are free to read for greatest visibility and readership

FAST PUBLICATION
Around 90 days from submission to decision

HIGH QUALITY PEER-REVIEW
Rigorous, collaborative, and constructive peer-review

TRANSPARENT PEER-REVIEW
Editors and reviewers acknowledged by name on published articles

Frontiers
Avenue du Tribunal-Fédéral 34
1005 Lausanne | Switzerland

Visit us: www.frontiersin.org
Contact us: frontiersin.org/about/contact

REPRODUCIBILITY OF RESEARCH
Support open data and methods to enhance research reproducibility

DIGITAL PUBLISHING
Articles designed for optimal readership across devices

FOLLOW US
@frontiersin

IMPACT METRICS
Advanced article metrics track visibility across digital media

EXTENSIVE PROMOTION
Marketing and promotion of impactful research

LOOP RESEARCH NETWORK
Our network increases your article's readership